Position Measurement in the ALEPH Inner Tracking Chamber

by

Ann Patricia Heinson

A thesis submitted for the degree of
Doctor of Philosophy of the University of London
and
Membership of the Diploma of Imperial College

August 1988

Imperial College
London

ABSTRACT

This thesis describes work done on the position measurement systems used in the ALEPH Inner Tracking Chamber (ITC). ALEPH is one of four experiments on the LEP collider at CERN. The ITC is a cylindrical small cell multiwire drift chamber, which will be used for tracking charged particles and triggering the ALEPH detector. The thesis is divided into five chapters. Chapter 1 forms a short introduction to the following chapters. In chapter 2, a detailed description of the design and construction of the ITC is given.

Chapter 3 presents work done on the position measurement in the r-ø plane of the ITC. A small prototype chamber was built, and then tested at CERN in a high magnetic field with a beam. Results from the analysis of the data are presented, and the resolution obtained is studied as a function of high voltage, magnetic field, gas type, track angle, choice of discriminator and the drift relation used.

Chapter 4 presents the results from investigations made into the z position measurement along the wires, using a method of timing. The z position of a track is found by taking the difference between the times of arrival of the signals at each end of the sense wire. Experimental results from a long test rig are set out, using a wide range of test pulse sizes. Emphasis is laid on the nonlinearities produced by various discriminator types and the resolution obtainable. Results from a computer simulation of the z measurement system are compared with the data, and predictions made from the simulation about the optimum type of discriminator for the best z measurement obtainable.

Finally in chapter 5, the behaviour of the ITC triggers is investigated, when subjected to background noise from the beam. This is done using random data from PETRA, recorded in the vertex detector in TASSO.

CONTENTS

Chapter 3   The Small Test Chamber

LIST OF FIGURES

Appendix B   Electron Drift Paths in the ITC Hexagonal Cells

Chapter 4   z Position Measurement

Appendix C   Transmission Line Theory

Appendix D   The Skin Effect

Fig 4.D.1 Cross Section Through Sense Wire
Fig 4.D.2 Change in Series Resistance of a Conductor with Signal
           Frequency

Appendix E   The Reflection and Transmission Coefficients

Fig 4.E.1 Mismatched Termination of a Transmission Line

Chapter 5   Simulation of the ITC Trigger –
               Using Data from the TASSO Vertex Detector

LIST OF TABLES

Chapter 1

INTRODUCTION

The work presented in this thesis involves detailed measurements and models of the position measurement systems to be used in the Inner Tracking/Trigger Chamber of ALEPH. In this introduction, I would like to place this work in context by explaining a little of the new accelerator LEP at CERN, and the ALEPH detector.

1 The LEP Collider

The Large Electron-Positron Collider, or LEP, is the latest of a series of e^+e^- accelerators, and is being built at CERN, Geneva [1.1]. The reason for building e^+e^- accelerators is that lepton annihilation is very clean. According to the Standard Model, leptons are point-like structureless particles. These accelerators are therefore very suitable for testing new theoretical predictions. LEP will be the largest particle accelerator to be built to date, with a circumference of ~ 26.7 km. It is planned to start running by mid 1989. Phase 1 of LEP will have an energy per beam of ~ 46 GeV. This gives a centre of mass energy of ~ 92 GeV, and LEP will thus be tuned to the Z^0 resonance and produce a Z^0 in each collision. Z^0s are the neutral intermediate vector bosons from the Glashow–Salam–Weinberg Electroweak Theory [1.2], and they have never been produced in large enough quantities before to enable them to be studied in detail. LEP is also expected to be suitable to search for and hopefully study the top quark and the Higgs boson [1.3]. The Higgs is responsible, via the Higgs–Kibble mechanism within Electroweak theory for the non-zero masses of the W^+, W^- and Z^0.

On the LEP collider, there are eight intersection regions, four of which will initially have an experiment, known as ALEPH, DELPHI, L3 and OPAL. Imperial College is a member of the ALEPH collaboration. Figure 1.1 shows a plan of the area around CERN with the LEP accelerator marked onto it.
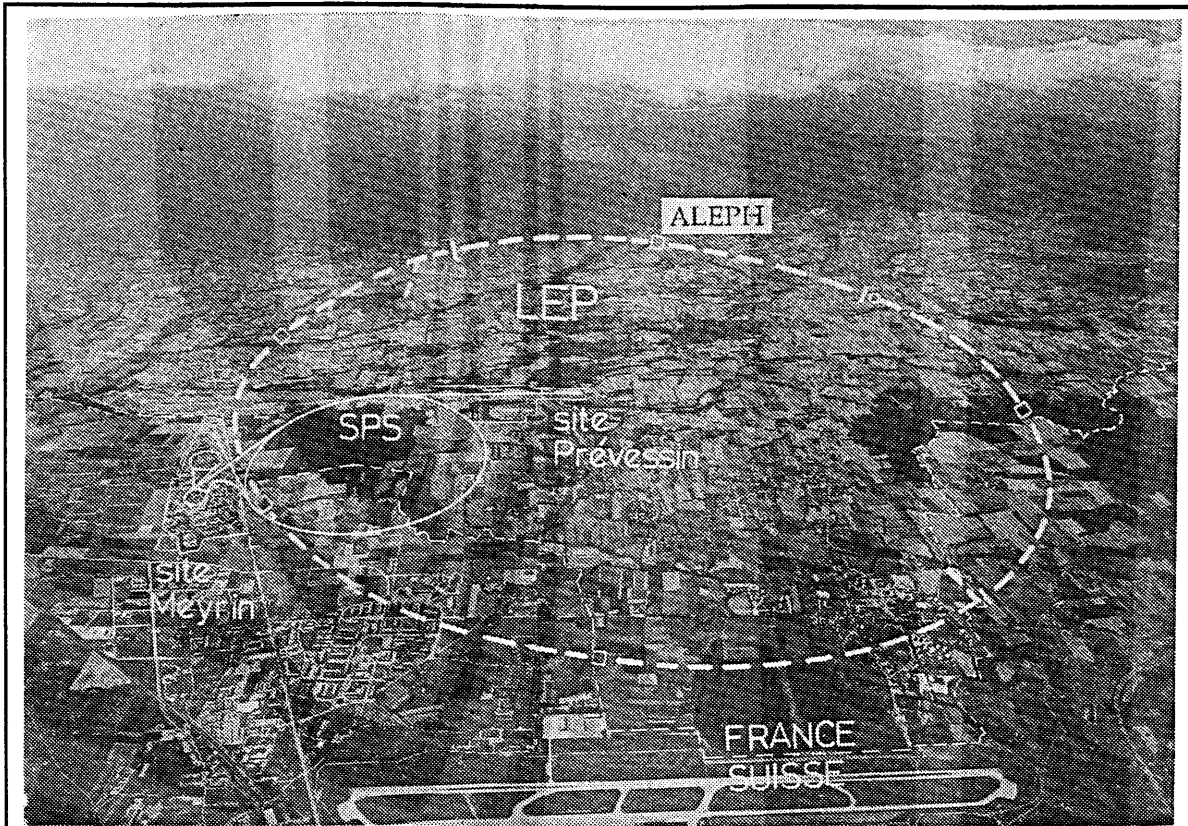
Fig 1.1   Aerial View of CERN Showing the Position of the LEP Accelerator

2   The Experiment ALEPH

The ALEPH collaboration is made up of research teams from twenty nine institutions based in eleven countries world-wide. The ALEPH detector will be situated in the northern-most intersection area, known as Pit 4. This is the deepest of the experimental pits, under the Jura mountains. The detector will be ~ 140 m underground. Figure 1.2 shows a view of the ALEPH detector with its subdetectors.
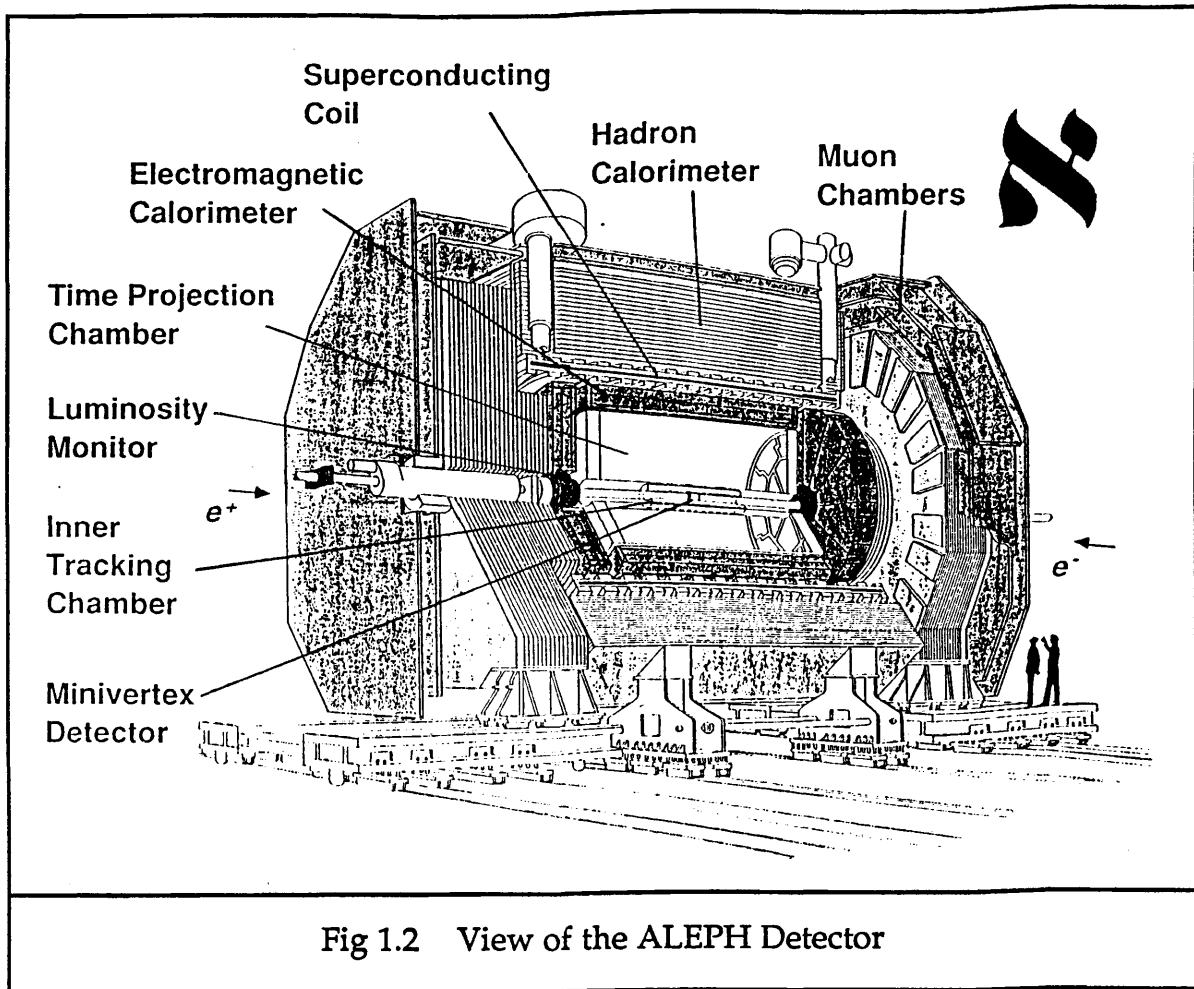
Fig 1.2   View of the ALEPH Detector

The main design criterion for ALEPH is for it to cover as much of the solid angle around the interaction point as is practical. This is important because at the very high centre of mass energies expected, particles will be produced in jets distributed over the whole sphere. The event rate will be very low, at ~ 1 Hz, and so ALEPH is designed to accumulate for each event as much information as possible. The strong points of the ALEPH detector are the precision of the charged momentum measurement, good electron, photon and muon identification and high spatial resolution. These will be achieved using a superconducting coil magnet and several types of detector arranged in layers like a tubular onion.

The following brief description of these subdetectors starts with the smallest innermost one and works outwards [1.4].

a) Mini Vertex Detector

This solid state detector is mounted on the beam pipe very close to the interaction point. It is constructed from two layers of double-sided silicon microstrip detectors. It will be used to localise the vertices of short-lived particles.

b) Inner Tracking/Trigger Chamber (ITC)

This subdetector is a large cylindrical multiwire drift chamber. It lies just outside the mini vertex detector, surrounding the beam pipe. It forms an essential part of the Level 1 trigger for ALEPH, and also provides good spatial resolution and track separation of charged particles.

c) Time Projection Chamber (TPC)

This very large subdetector forms the heart of the ALEPH tracking system. It is 6 m long, with an active volume 4.4 m long and 3.6 m in diameter. It is a gas drift chamber. Electrons liberated in the gas from ionisation, drift parallel to the beam axis and are measured at the end planes. The reconstructed tracks provide high resolution measurement of charged particle momenta, directions and ionisation. This detector forms part of the Level 2 trigger.

d) Electromagnetic Calorimeter

This detector surrounds the TPC with a segmented barrel and two end caps. The calorimeter consists of lead sheets interspersed with proportional wires. It measures the energy of electromagnetic showers, with some degree of position localisation, and provides electron identification. It also forms part of the Level 1 trigger.

e) The Magnet

The next layer in the ALEPH detector is the superconducting solenoid magnet. This is 6 m long and 5 m in diameter and provides a uniform axial magnetic field of strength 1.5 Tesla.

f) Hadron Calorimeter

This outer calorimeter surrounds the magnet. It consists of streamer tubes sandwiched between iron sheets. It is designed to measure the energy and locality of hadrons entering it, and is also useful for muon identification, as these energetic particles are not absorbed by the iron. The hadron calorimeter forms part of the Level 1 trigger.

g) Muon Detectors

The muon detectors cover almost the whole of the ALEPH detector, and consist of a double layer of streamer tubes. 160,000 tubes are needed to do this, and they are used for muon identification.

h) Luminosity Monitors

A small luminosity monitor is mounted at each end of the ALEPH detector around the beam pipe, inside the e–γ calorimeter endcaps. Each monitor consists of a tracking detector based on multilayers of square drift tubes, and a luminosity calorimeter based on lead sheets like the electromagnetic calorimeter. These monitors will determine the luminosity of the beams by measuring the rate of Bhabha events at small scattering angles. The luminosity monitors form part of the Level 1 trigger for ALEPH.

The aim of the ALEPH collaboration is to have all these detectors (with the possible exception of the mini vertex detector) completed and installed ready for the startup of LEP. All the readout and trigger electronics should be complete and all the data acquisition software should be tested and ready to enable physics results to be obtained as early as possible. The offline data reduction and analysis programs should be ready, together with the associated Monte Carlo model of the detector and the particle generators. These will enable comparison between the real events found in the detector and the predictions of the Standard Model.

As can be seen from this brief overview, the ALEPH project is extremely complex and ambitious. It can only be achieved by putting together thousands of small contributions such as the one presented here in this thesis.

Chapter 2

THE INNER TRACKING / TRIGGER CHAMBER – DESIGN AND CONSTRUCTION

1 General Description

The inner tracking/trigger chamber of ALEPH is a large cylindrical multiwire drift chamber, known as the ITC. The ITC has 5136 wires, which are 2 metres long, and all are parallel to the beam. It will be operated in a magnetic field of 1.5 Tesla also parallel to the beam. Its overall length is 4.638 m and its outer diameter is 0.570 m. The ITC has three dimensional position measurement, using the drift times recorded on the wires to produce r-ø tracks and a method of time differences to find the z coordinates along the sense wires. Figure 2.1 shows a cross section through the ITC.

1.1 Aims of the ITC

One purpose of the ITC is to act as part of the first trigger in ALEPH. It produces an online signal to trigger the outer position measurement detector, the TPC, within ~ 3 µs of a beam crossing, using three dimensional space points to indicate whether there were any tracks produced in it.

Another aim of the ITC is to produce high resolution tracking during the offline reconstruction, using all the drift time and time difference information. The ITC produces accurate r-ø points on up to 8 layers for tracking in the radial region between 160 and 260 mm. These tracks are used to improve the angular resolution of the Time Projection Chamber (TPC) tracks to the interaction point, and they also give some improvement to the overall momentum resolution.
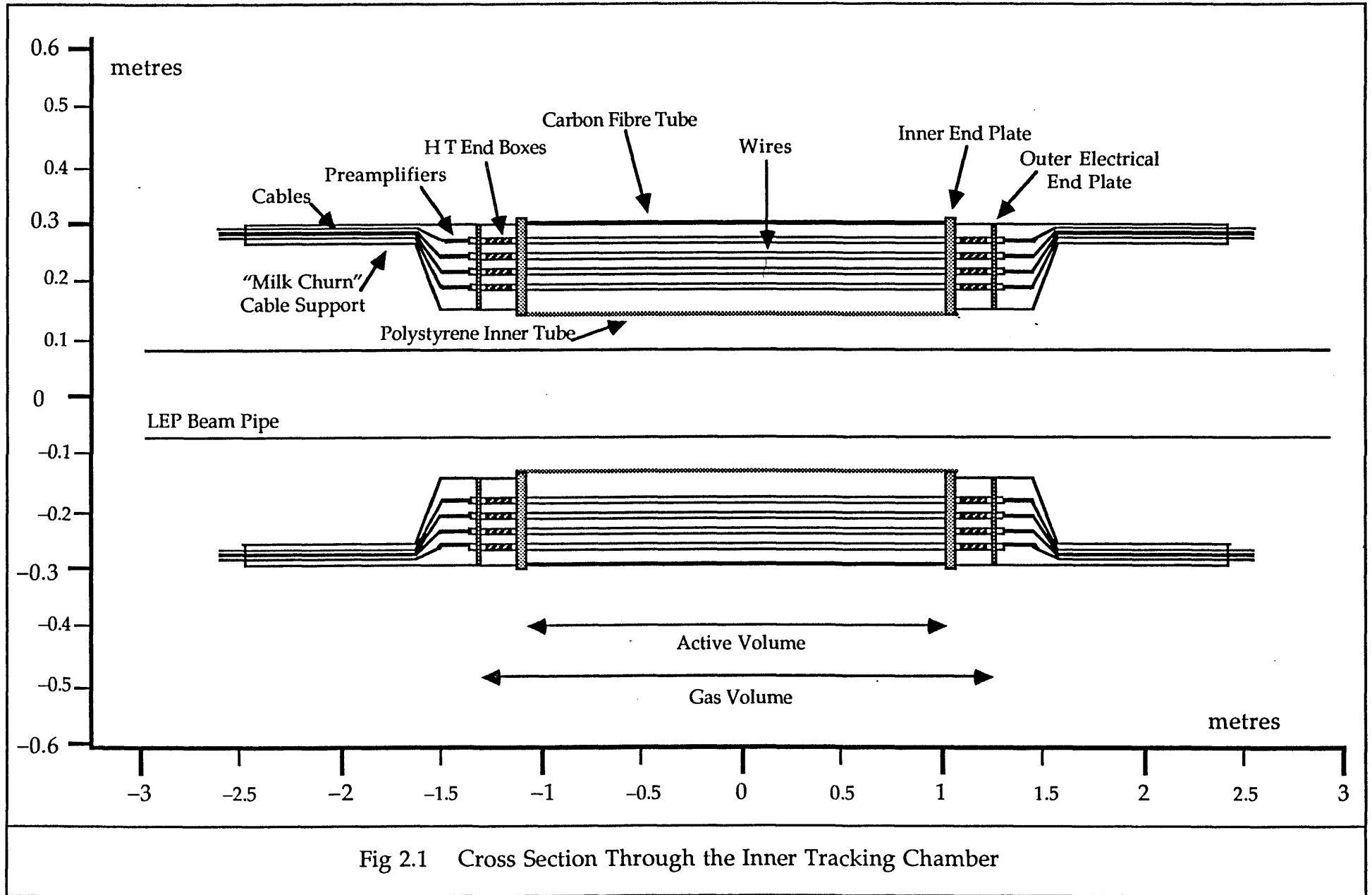
Fig 2.1   Cross Section Through the Inner Tracking Chamber

The detector is designed to cover as much of the solid angle as possible. For a track crossing all 8 layers of cells, the acceptance angle θ is 14.7° around the z axis.

1.2 Coordinate System used in the ITC

The coordinate system adopted when describing the ITC is that which is conventionally used in e^+e^- experiments. The z direction is defined as being along the axis of the beam pipe in the e^+ direction, with the origin at the interaction point in the centre of the detector. The plane orthogonal to the z direction is usually known as the r-ø plane, where r is the radius from the z axis and ø is the angle around the z axis, but it is occasionally also described in terms of x and y, where the x direction is horizontal and the y direction is vertical. The angle ø is 0° in the x direction. The angle θ is used to describe the angle of a track to the z direction, with θ = 0° being along the positron beam. These directions and angles can be seen in figure 2.2.

Fig 2.2   The Coordinate System Used in the ITC
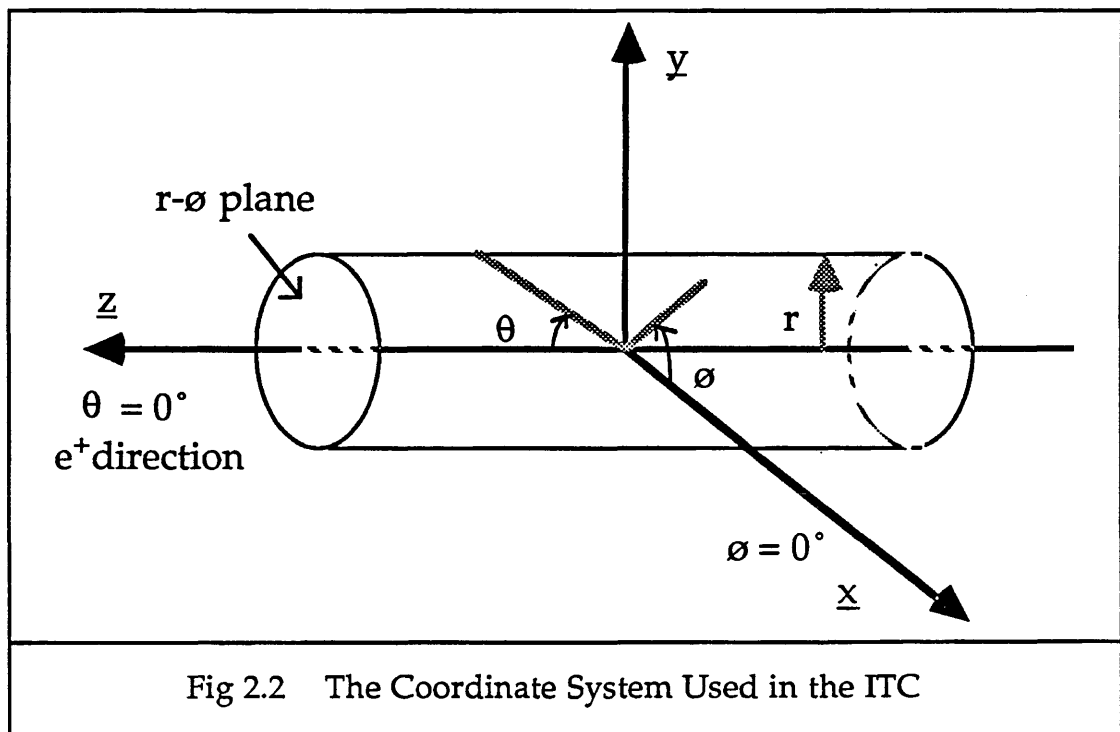
1.3 Constraints on the Design of the ITC

In the design of any large engineering project, there are certain factors which constrain the final outcome. Some of these are detailed here for the ITC.

1.3.1 Radiation Length

It is desirable to minimise the Coulomb scattering in the ITC, which is when charged particles are scattered from the nuclei of the detector material, in order not to degrade the momentum resolution. Also, it is desirable to minimise the Bremsstrahlung radiation from electrons interacting with the nuclei, since the photons produced will have high energy, and consequently pair production will dominate their absorption. These extra e^+e^- pairs will make track finding more complicated and could produce false triggers. In order to minimise both of these effects, the detector must be built of materials which have long radiation lengths. A radiation length X_0 is defined as the thickness of a medium which reduces the mean energy of a beam of electrons by a factor e. The amount of material in the detector must be kept to a minimum in order to minimise the fraction of a radiation length through which particles from the interaction must travel.

1.3.2 Volume Available

The ITC must fit inside the TPC, which has an inner diameter of 60 cm, and a length of ~ 4.7 m. The inner diameter of the ITC must leave a large enough gap around the beam pipe for the Mini Vertex Detector to be fitted in. The innermost layer of cells must be sufficiently far from the beam pipe to avoid noise hits from debris produced by spurious electromagnetic interactions in the beam pipe.

1.3.3 Materials to be Used

There are other restrictions on the materials which can be used to build the chamber, apart from having to minimise the percentage radiation length. Firstly, the whole chamber has to operate in a high magnetic field of 1.5 Tesla. Therefore, no magnetic materials such as iron can be used in the chamber. This includes any alloy which contains iron.

Secondly, there are certain types of molecule which, when present in the gas of a drift chamber, seriously degrade the operation of the chamber. Of special note is silicon. If this gets into a chamber, from a sealant or other source, it diffuses into the gas and is deposited onto the wires. These deposits cause first of all a loss of gain, possibly followed by an increase in noise, discharge around the wires or breakage of the wires [2.1].

There is one other restriction on the material which can be used in the ITC. The ITC can only be supported from the outer flanges of the TPC. These are nearly 5 m apart. There can be no supports nearer the centre of

the detector to support its weight, since these would just increase the percentage of radiation length and decrease the momentum resolution of the TPC, without contributing any information on the interactions. Therefore, the whole chamber must be light enough to be supported in this way from far out at each end, and rigid enough not to sag significantly in the middle. The ITC, including all the electronics on its ends, weighs ~ 271 kg, and the sag at the centre of the chamber is 0.4 mm, when supported only at the outer ends.

1.3.4 Trigger Speed

When LEP runs with 4 bunches, there will be 22.5 μs between bunch crossings in each experiment. The level 1 physics trigger in ALEPH consists of the ITC, the e - γ calorimeter, the hadron calorimeter and the luminosity monitors, and is designed to reduce a beam crossing rate of 44 kHz to a level 1 trigger rate of 500 Hz. When a level 1 YES is produced, the system is forced into a 50 μs dead time while the next trigger levels are operated and checked, thus losing the next two beam crossings. The level 1 trigger processor must produce its signal very quickly because the TPC needs such a fast signal to prepare its gates for the drifting electrons in it. The ITC has two levels of trigger. The r-ø trigger processor operates in ~ 1 μs. The more complex r-ø-z space point trigger processor will operate in ~ 3 μs.

1.3.5 Resolution

Within the constraints of a fast trigger, the resolution needs to be as good as possible in order to avoid ambiguities in tracking, both within the ITC and for connecting tracks found in other detectors. The resolutions aimed for are 100 μm in the r-ø plane and < 5 cm in the z direction along the sense wires.

1.3.6 Two Track Resolution

The ITC is operated with single hit electronics and readout. This means that the first signal to arrive on any wire is timed, and any subsequent signals are not read out until the readout equipment is reset for the next beam interaction. Two track resolution is limited to the cell size at a few millimetres. The cells have been designed to be small, so that the chamber is fast, but this also helps improve the two track resolution.

1.3.7 Reliability

The ITC must be designed to operate in inaccessible conditions for many years. If a wire were to break, it must not incapacitate the whole

chamber, since the ITC forms a vital part of the level 1 trigger. Many months of valuable beam time would be lost if the ITC had to be removed from the TPC, to replace or even just remove a broken wire. The design of the ITC must also allow for segmented control of the high voltage supply, so that if a sector of the chamber were to become too noisy or was shorted by a broken wire, it could be turned off without affecting the rest of the detector.

1.3.8 Remote Operation

Every aspect of the ITC, from gas flow, pressure and temperature, to high voltage supply must be monitorable and controllable from the surface of the experimental area, 140 m above the detector itself. Also, it must be possible to calibrate the detector by remote control, automatically and reliably.

1.3.9 Cost

About 70 % of the cost of the ITC is taken up by the electronics, including the cables, amplifiers, readout and processors. This imposes a tight constraint on the number of channels, and thus on the number of sense wires in the ITC. The small cells chosen mean that large numbers of them could fit into the available volume. The total number of sense wires chosen is 960, to be read out on both ends. This number of cells does not fill the volume of the chamber, but will be enough for the tracking to work, and will keep the cost of the ITC within an affordable budget.

1.3.10 Time Constraints

The ALEPH detector must be operationally ready by the time that the LEP accelerator is turned on in 1989. For the ITC, this means that it had to be mechanically complete by May 1987, ready to be transported to CERN for beam tests in August 1987. Enough of the electronics had to be built and tested by then for these tests to be carried out. The remaining electronics and readout must be ready by Spring 1989, when the tracking detectors will be aligned using cosmic rays.

2   Mechanics

The following section provides a detailed description of the design and construction of the mechanical structure of the ITC. Figure 2.3 shows the

ITC after it was wired, and before the outer shell was slid over the chamber.
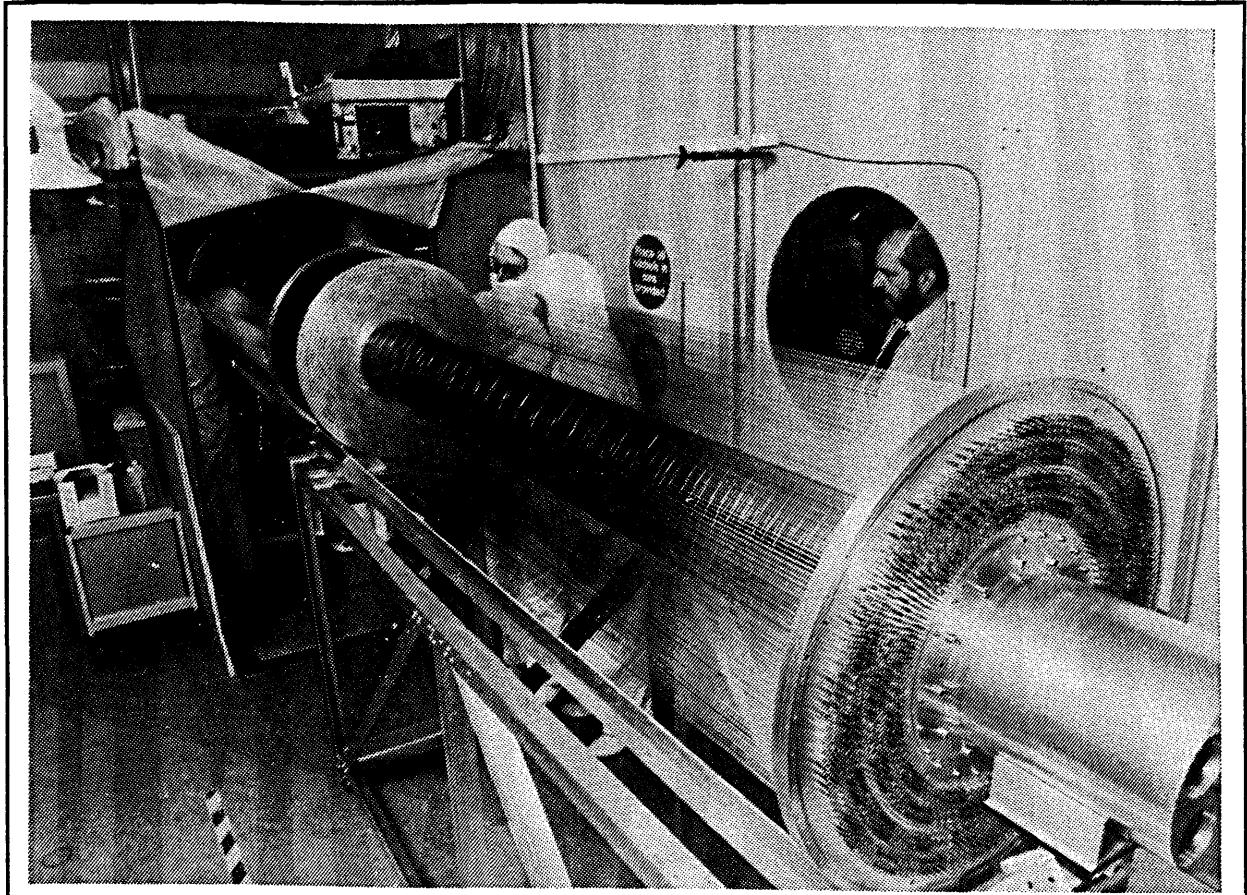
Fig 2.3   The ITC After Wiring was Complete

2.1   End Plates

The two inner end plates of the ITC hold the ends of the chamber wires in the cell pattern, as shown in figure 2.4.

The end plates are 570 mm and 600 mm in diameter and 2.5 cm thick. The smaller end plate goes inside the outer carbon fibre tube and the larger one holds the carbon fibre tube in place.

2.1.1   Material

The end plates are made of an aluminium alloy called Alcoa Alca Plus, a cast alloy of aluminium with zinc, which is heat treated. The aluminium alloy was chosen because it is easy to machine and is lightweight. It also has a long radiation length and a low density, so a 2.5 cm thick end plate does not form a very large fraction of a radiation length. For this aluminium alloy, the density is 2.8 g/cm^3, (cf. pure aluminium at 2.7 g/cm^3), and

the radiation length of aluminium $X_0 = 24.01$ g/cm^2. The radiation length of a material is often quoted as a distance, X_0/ρ, which is ~ 8.575 cm for the end plate material.
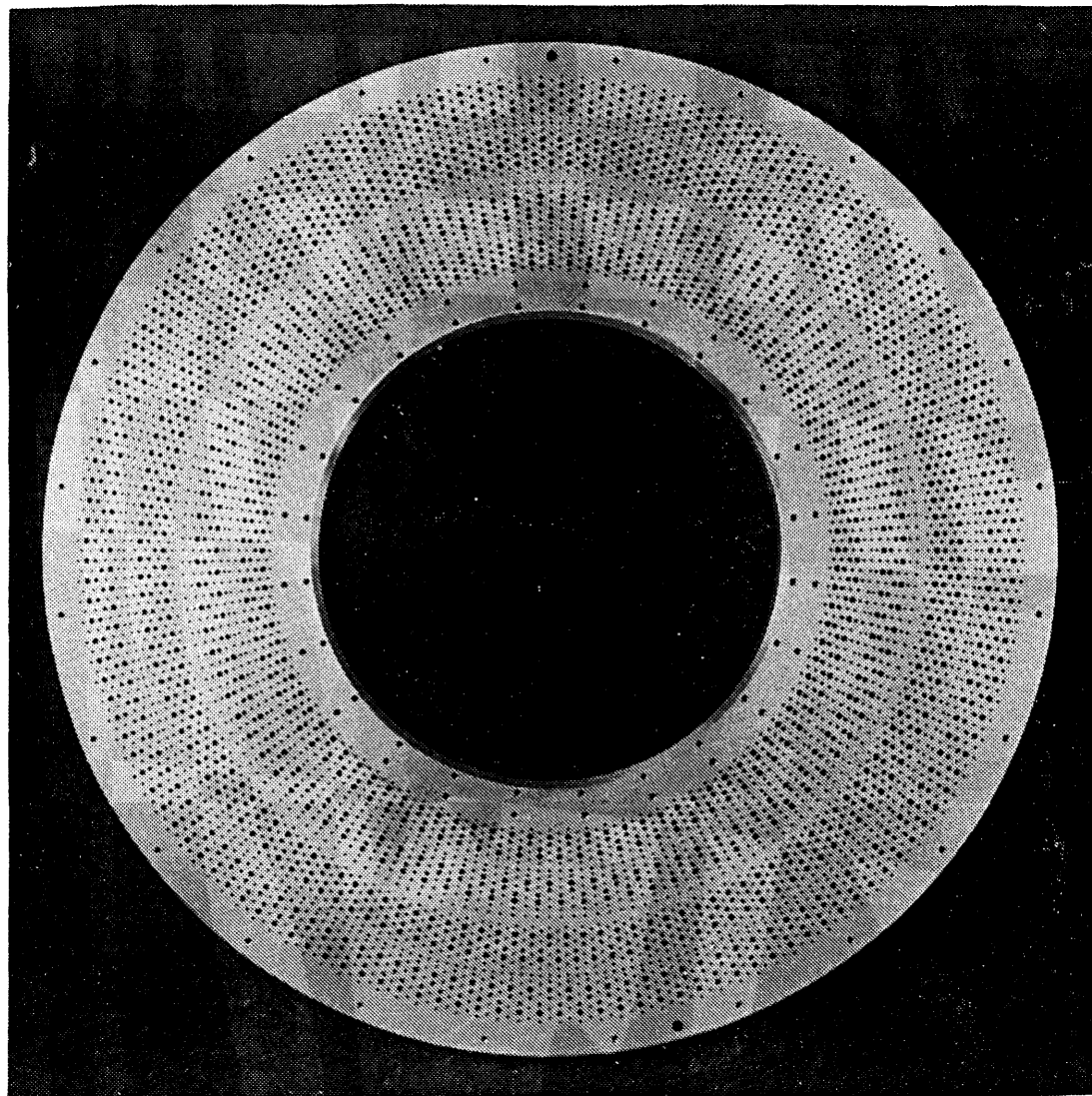
Fig 2.4   ITC End Plate from the Inside, Showing Cell Layout

2.1.2   Deflections of the End Plate

The end plate thickness is chosen to be as thin as possible, to minimise the fraction of radiation length presented, whilst being strong enough to bear the tension from the wires, during and after the wiring, without bending. The end plates are made from two 1" thick sheets of metal, machined down to $25 \pm .13$ mm thickness. The deflection of the outer rim of the end plates during wiring is calculated to be ~ 300 μm, when the load is born by an inner wiring mandrel. When all the wires are strung in place, and the tension load has been transferred to the outer tube, the deflection of the inner rim of the end plates is calculated to be ~ 180 μm [2.2].

These initial and final deflections have to be taken into account when calculating the weights needed to produce the tensions in the wires, to ensure that the final tensions and sagitta are approximately even across the chamber.

Once the chamber is fully wired, the force on each end plate is 9418 N.

Before any wires were strung into the chamber, a trial assembly was held. The load from the wires was simulated by 50 long springs which were fixed in between the end plates to produce the same deflection as expected from the wires. The springs were designed to produce a load of 10^4 N on each end plate. The load of these springs was then transferred from the inner wiring mandrel to the outer carbon fibre tube. After transfer of the load, the wiring mandrel was removed and a thin, low mass inner tube was inserted in its place. This trial assembly was successfully achieved.

2.1.3 Accuracy of the Hole Positions

The two end plates are each drilled with 960 sense wire holes, 3840 field wire holes, 336 guard wire holes and 336 holes for the gas flow. The most important holes for accuracy are the sense wire holes. The azimuthal position of the sense wires is critical, since the tracking takes place in that direction, whereas the radial error is not so critical. Some of the sense wire holes were surveyed at CERN, and after fitting the hole positions with concentric circles whose centres were made to coincide, 23 sense wire holes were found to be outside the tolerance of ± 25 µm azimuthally, and 18 holes were outside the tolerance radially. These holes were evenly distributed across both end plates. The maximum deviation of a hole from its ideal position after fitting is 38 µm [2.3].

2.1.4 Cell Layout

The chamber is divided into 8 concentric layers of cells, with these layers being paired, to give 4 double layers of cells. The four inner layers have 96 cells per layer, and the four outer layers have 144 cells per layer. Consequently, the cell radius in each layer is slightly different from layer to layer. Layer 1 is the innermost layer at the smallest radius, and layer 8 is the outermost layer. The cells with the longest drift distance are in layer 4 and those with the shortest drift distance are in layer 5.

The numbers of cells per layer have been chosen to be divisible by 16, to make the electronics easy to produce in modular units.

The cells within each bilayer are staggered to allow resolution of the ambiguity of the drift times, to decide which side of a cell a particle passed through.

The radii of the sense wire layers, after fitting concentric circles through them to allow for expansion and contraction of the end plates during the drilling, are shown in table 2.1, together with the ideal radii at which the holes were drilled.

Table 2.1 Radii of the Sense Wire Layers in the ITC			
Layer	Nominal Radii / mm	Plate A Radii / mm	Plate B Radii / mm
1	161.100	161.082	161.085
2	172.000	171.991	171.982
3	187.000	186.988	186.981
4	197.900	197.882	197.875
5	216.800	216.775	216.772
6	230.100	230.085	230.074
7	246.900	246.874	246.869
8	260.200	260.177	260.173

Figure 2.5 shows a section of the ITC end plate, with sense, field and calibration wire positions, plus the three layers of alternate guard wires and gas holes.

2.1.5 Cell Design

The cell design chosen for the ITC is made up of small, flattened hexagonal close-packed cells. Hexagonal cells were chosen because they have the best uniformity of electric field, relative to other designs such as rectangles.

Figure 2.6 shows a close up of part of a bilayer of these hexagonal cells. It shows the double layer of field wires between the cell layers. The extra layer of field wires was inserted to reduce the electric field on the surface of the field wires and also to reduce the electrostatic forces on the sense wires. It is important to keep the electric field on the field wires below ~ 20 kV/cm, above which carbon fibre whiskers can grow [2.4]. With a sense wire voltage of 2.2 kV, the electric field on the field wires is between 10 and 13 kV/cm, depending on the cell size and the position of the field wire within the cell, which is well below the critical level.

Fig 2.5   Layout of ITC End Plate Holes

Fig 2.6   ITC Hexagonal Cell Design, Showing Bilayer Layout
and Cell Staggering Between Sublayers
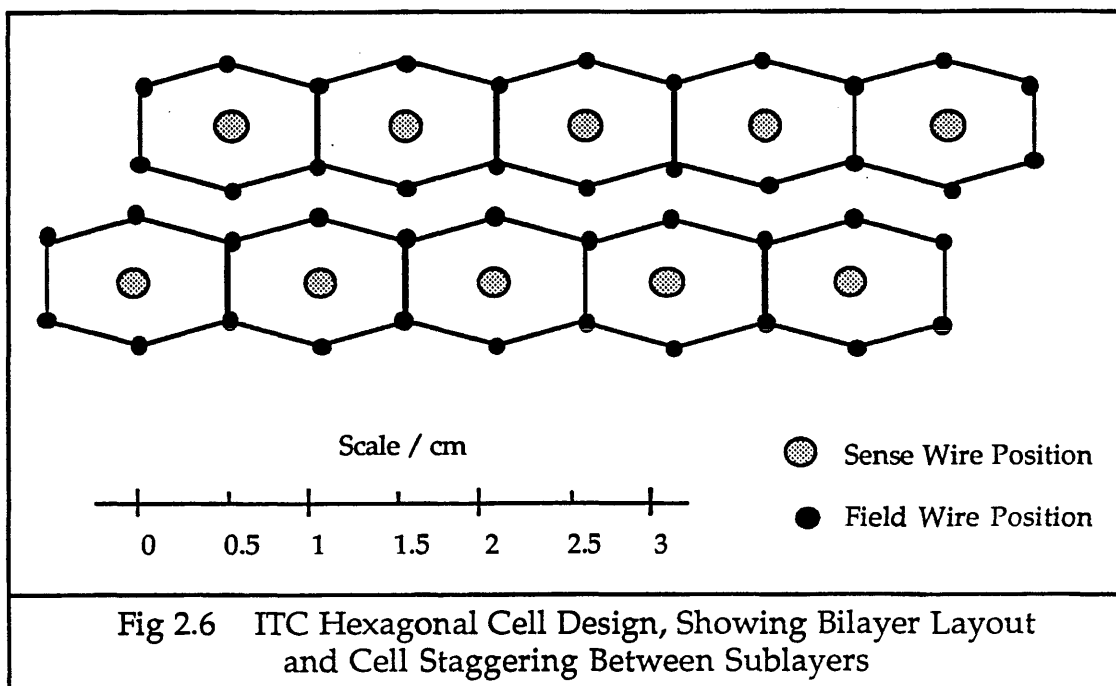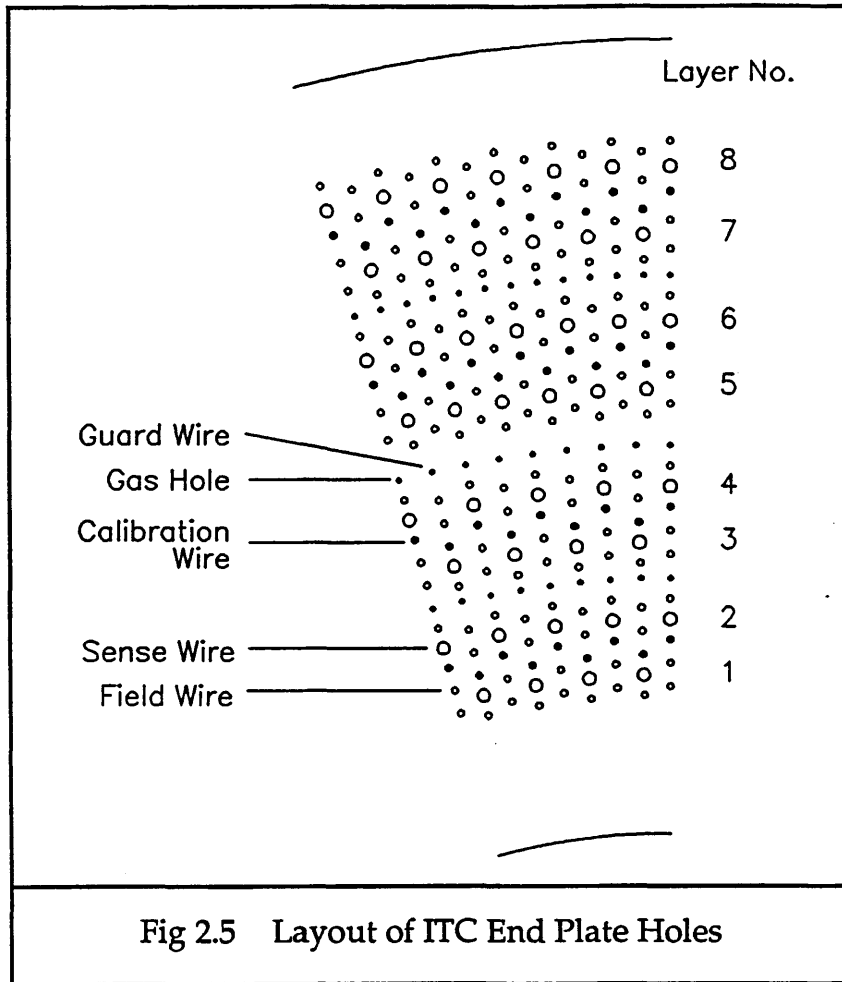
The field on the sense wires is between 225 and 227 kV/cm, depending on the cell size. The electric field on the sense wires has to be high to generate the electron avalanche. The electrostatic force per unit length on

the sense wires is 17 μN/m, and from 148 to 257 μN/m on the field wires. This can be compared to the gravitational forces on the sense wires of 134 μN/m and 479 μN/m on the field wires.

This hexagonal design produces a reasonably uniform distribution of charges on the field wires that define the electric field in the cell. The design also has acceptable drift time characteristics. Appendix B after Chapter 3 contains an investigation into the electric fields and electron drift paths found in the cells.

2.2 Inner Tube

The inner tube forms the inner wall of the ITC, and is the gas seal. It does not bear any of the load from the wires, and consequently it has been designed to be of as low mass and percentage radiation length as possible. It is made from two layers of 1 mm thick polystyrene, with a 25 μm coating of aluminium foil over both the inner and outer surfaces, and layers of epoxy resin between each of the layers of material to hold it all together. On the inner surface there is a 100 μm thick layer of mylar. The foil lining provides electrical screening of the chamber from radio frequency noise. It also provides an equipotential surface to ensure that the electric field in the innermost layer of cells is uniform at all places around the layer. The low mass inner tube is 2.08 m long, has a mean diameter of 256 mm and is just over 2 mm thick.

Because the inner tube is so thin and fragile, there is a danger that it may be broken by the Mini Vertex Detector, when that detector and the beam pipe are positioned into the ITC. Therefore, two inner tubes have been produced, so that there is a spare one in case of accidents. The mylar layer inside the low mass tube is to help strengthen it for the installation process.

2.3 Outer Tube

The main design criterion of the outer tube is to bear the load of 33309 N/m^2 in the longitudinal direction from the tension in the ~ 5000 wires. It also has to form the gas seal at the outer surface of the chamber. It has to be light weight, with a small percentage radiation length. To fulfil all these requirements, the outer tube is made of 2 mm thick filament wound carbon. It is 2.019 m long and 570 mm in diameter. There was some concern

that the carbon fibre tube might twist when under the load, but calculations and tests of the tube itself have shown that any torsion produced is negligible.

The carbon fibre tube is coated inside and out with aluminium foil, which screens the chamber from any radio frequency signals and also provides an even grounded potential surface for the electric field in the outermost layer of cells.

2.4   Wiring Mandrel

The wiring mandrel is a long aluminium tube which had the end plates mounted onto it during the wiring process, but does not form part of the final chamber. It was mounted on a wall, supported at its ends, on a pivot. The pivot allowed the chamber to be positioned horizontally for wiring and vertically for gluing the wires into the end plates.

The alignment of the end plates on the wiring mandrel was very critical, to ensure that the wires were strung parallel to the z axis, with uniform tension. They were made parallel by precision machining of the mandrel and the plates themselves. The rotation of the end plates relative to each other was minimised by using an optical measuring method, and reduced to < 30 μm at the maximum diameter.

Once all the wires were strung into place between the end plates, the carbon fibre tube was slid over the chamber and attached to the end plates. The wiring mandrel was then detached from the end plates and the load was transferred from the mandrel to the outer tube. Next, the mandrel was slid out from the centre of the chamber, and replaced with the polystyrene inner tube.

2.5   Electrical End Plates

This outer pair of end plates and short section of aluminium cylinder form the gas seal at the ends of the chamber. The end plates support the high tension end boxes inside the gas volume, and connect them through to the preamplifiers outside the gas volume. They are made of 1 cm thick aluminium alloy.

2.6 Chamber Supports

There are several parts of the ITC which are present purely for support. At each end, attached to the electrical end plates and reaching out to the end of the detector are two cable supports made of aluminium, shaped like milk churns. These route the cables from the preamplifiers to the outside of the TPC and support them out of the line of the luminosity monitors, which are situated up and down stream of the interaction point along the beam pipe, inside the ALEPH detector, to detect very low angle particles.

At the end of the "milk churns" are flanges which have lines inscribed on them to allow the alignment and survey of the ITC position within the TPC. The chamber supports are also essential to support the ITC from the outer edges of the TPC.

2.7 Wires

In the ITC there are four types of wire used to construct the drift cells and the guard wire layers. In the separated hexagonal cell design, each sense wire is surrounded by six field wires, four of which are shared with neighbouring cells in the same layer. One of the six field wires in each cell is also used as a calibration wire. In each of the three gaps between the four bilayers of cells, there is a layer of guard wires.

2.7.1 Sense Wires

There are 960 drift cells in the ITC, and there is a sense wire in the centre of each cell. They are operated at a potential of 2 - 2.5 kV. They are designed to provide a high electric field close around them in the cell, in order to give a large gain to the charge in the signal. The electric field around the sense wire is increased by decreasing the diameter of the wire, but the diameter reduction is limited by the fact that the wire must be strong enough to bear its own weight under tension. To satisfy these conditions, 30 μm diameter tungsten wire has been chosen. The tungsten has been gold plated to improve the surface quality of the wire.

2.7.2 Field Wires

There are 3840 field wires in the ITC, of which 960 are also used as calibration wires. The purpose of the field wires is to shape the electric field in the cell around each sense wire. The normal field wires are connected at both ends to the earthed end plates. Unlike for the sense wires, it is

desirable for the electric field at the surface of the field wires to be as low as possible. This reduces the possibility of the growth of carbon fibres on the surface of the wires. A low field is achieved by making the field wire diameter as large as possible, without making the wires too heavy to be supported, or introducing too much material into the chamber which would increase the fraction of radiation length too much. Consequently, the field wires chosen for the ITC are made from 147 μm diameter aluminium alloy wire. The alloy contains manganese and magnesium and has a density of 3.19 g/cm^3. The field wires are gold plated to improve the surface quality by preventing aluminium oxide forming on the wire surface. Aluminium oxide is a white powdery substance and an insulator, so if it were present, then the electric field around the field wires would be irregular. The gold plating also ensures that there is good electrical contact, to earth the field wires at the crimp in the crimp pin which holds them in place. The diameter of the wire varies by a few microns along the wire, due to the variability in the thickness of the gold plating.

To check the quality of the gold plating of the field wires, photographs were taken of the surface of the wires in several areas using an electron microscope. These showed both smoothly gold plated areas and also some areas where the gold plating was so thin and patchy that bare aluminium could be seen. Spectral analysis was performed on some of these areas, and elemental aluminium was found, together with copper, which must have either been added to the aluminium alloy during manufacture, or introduced onto the wire during the wire drawing out process.

Aluminium wire is very soft, and if any small kink is seen in it, that section of the wire must be discarded and not used in the chamber. Kinks can be caused by just touching the wire. If a section with a kink is used as a field wire, then there is a high probability of the wire breaking at the kink.

Another difficulty experienced when using aluminium wire is its tendency to creep. That is, when the wire is held under tension, its length increases by ~ 15 % over several days. This must be taken into account when the weights needed to produce the final tensions are calculated.

Tests were performed on the aluminium field wires to find the maximum weight they could support before exceeding their elastic region of extension, entering the plastic region and breaking. The maximum weight which could be supported was 713 ± 10 g for the field wires, just before breakage, and the limit of proportionality was reached at 310 g.

2.7.3 Calibration Wires

The calibration wires form a subset of the field wires. One quarter of the field wires are also calibration wires, which means one field wire per hexagonal cell is a calibration wire. The calibration wires are identical to the field wires, except that they are insulated from the end plates with a small sleeve of acetal resin, and are connected together with a soldered zig-zag of wire wrapped around the pins on the outside of the end plate. They are grouped together in blocks of 8 wires on the inner 4 cell layers, and in blocks of 12 on the outer 4 layers, giving 96 blocks in all. The use of the calibration wires is described in Chapter 4.

2.7.4 Guard Wires

There are three layers of guard wires in the ITC. Each one consists of a layer of longitudinally strung 100 μm diameter copper/beryllium wires, with 147 μm aluminium wire wrapped around them in hoops to form a cage. The aluminium hoops were glued onto the long straight support wires at 6 points around each hoop. There are 51 hoops along the length of the chamber in each layer. Fourteen of these at each end of the chamber are 2 cm apart and the remaining 23 hoops in the middle of the chamber are 6 cm apart. Care was taken when winding the hoops not to pull too tightly and make the guard wire cage smaller in the centre than at the ends.

The three guard wire cages are intended to catch any wire that might break, so that damage is limited to only a small region of the chamber.

2.8   Wire Fixing

2.8.1 Aims

a) Position Accuracy

The sense wires must be wired in place so that their positions are not significant in the overall resolution of the chamber. For an overall r-ø resolution of 100 μm, the sense wire positions must be less than ~ 50 μm azimuthally from their ideal positions.

b) Reliability

The wires must be fixed in the end plate so that they do not slip out of whatever is used to hold them there, and the fixing must not weaken the wire so that it will be likely to break. The wires were put into the chamber in London. They had to withstand the journey in a van from there to

Geneva. They must then not slip or break for the lifetime of the chamber in ALEPH.

c) Electrical Connections

There are two points to be considered under this heading. The first is the grounding of the field wires to the end plate, and electrical insulation of the high voltage sense wires and the calibration wires from the end plate. These objectives must be reliably achieved as an intrinsic part of the wire fixings, and not need lots of extra materials and labour to effect.

. Secondly, it must be simple to connect the end electronic units onto the sense and calibration wires, in order to distribute the high voltage and read out the timing signals.

d) Cost, Availability and Ease of Use

Of course, along with the above constraints, the usual ones of cheapness, availability and ease of use apply. Components can only be designed if a manufacturer can be found to make ~ 13500 of them including spares. In order to string the 5000 wires, the fixing method must be fast and foolproof. All these considerations have led to the following methods being adopted for fixing the wires in the end plates.

2.8.2 Crimping and Gluing

It was decided to have two ways of fixing the wires in the end plates. This "belt and braces" approach ensures that if one method fails, there is a second to back it up and prevent any wires coming loose in the chamber. The principal method is to crimp the wires inside a specially designed pin which fits into the end plate directly for the field wires, or within a plastic feedthrough, for the sense wires. The second method is to glue the wire inside the end plate before it reaches the crimp. Therefore, if a crimp joint should create a weak point in a wire and it should snap, or if the crimp should be too loose and the wire slip through it, then nothing will happen to the wire in the chamber, as the glue will hold it securely in place.

The system of pins and feedthroughs to hold the wires is a modified version of a design used by the Cornell CLEO II drift chamber group [2.5].

Figure 2.7 shows a crimp pin in a feedthough in the end plate.
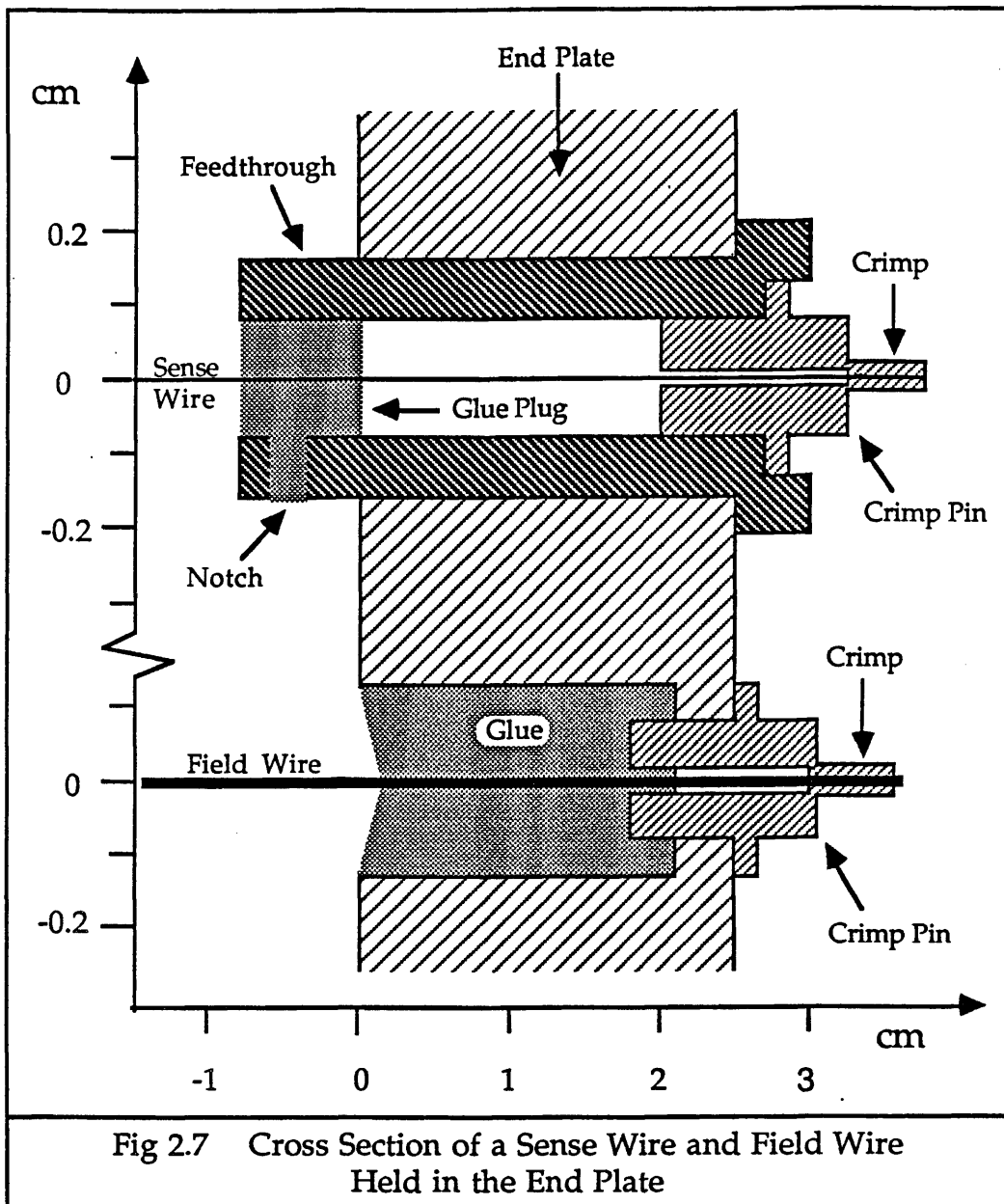
Fig 2.7 Cross Section of a Sense Wire and Field Wire
Held in the End Plate

a) Crimp Pin

A crimp pin was derived for the ITC from the CLEO II design. It is
made of a copper tube, with most of its length covered in a thicker outer
brass tube, and the whole pin is gold plated for good electrical contact. There
are two types of crimp pin. One has a 100 μm diameter centre hole for the
30 μm sense wire and the other has a 200 μm hole for the 147 μm field wire
and 100 μm guard wire.

The crimp itself was made in the thinnest section of the pin with a
specially designed and built crimp tool.

The inner and outer diameters of the pins were measured, and the
ones outside the tolerances specified were separated out. Some of those
discarded were later used in the Small Test Chamber. The pins were
manufactured in several batches, and in some batches, all the pins had

inner diameters of about 250 μm instead of 200 μm, with a very wide spread of values. The outer diameters also had a very large spread, and many were too fat to fit in the holes drilled in the end plates. The large inner diameter pins necessitated the production of a new crimp tool to enable them to be used without the wire slipping out.

One quarter of the field wire pins, for use with the calibration wires, were inserted into short cut-down feedthroughs which had been thinned down, so that the calibration wires would be insulated from the end plates.

b) Feedthrough

The sense wire pins were mounted in long acetal resin tubes known as feedthroughs or bushings. The plastic used to make them, called ULTEM 1000, was chosen because it has very low mould shrinkage (0.5 % − 0.7 %), enabling the feedthroughs to be manufactured within very small tolerances. The feedthroughs are mounted in the end plates and protrude into the chamber volume by 8 mm. They ensure that the sense wires, which are at a potential of 2 - 2.5 kV do not come close to the end plates, so there is no possibility of a breakdown in the chamber, with sparking.

The feedthroughs were made in a mould used by the CLEO II drift chamber group, and then cut down in length to be more suitable for the thinner end plate of the ITC. The short wide end of the feedthrough in which the pin is inserted was machined thinner, so that the feedthroughs would fit between the field wire pins in the close-packed small cell arrangement on the outside of the end plates. A notch was cut near the tip of each feedthrough to help the gluing process. The tip of the glue syringe nozzle was inserted in the notch to glue the sense wire into the feedthrough.

c) Crimp Tool

Two specially designed crimp tools were initially built to crimp the wires into the pins. One was for the sense wire pins with 100 μm holes, and the other for the field wire pins with 200 μm holes. A third tool later had to be made for the large batch of 250 μm hole pins. Each tool was designed to be simple to use. The crimp tool essentially looked like a pair of pliers, but there was a mechanism built in to limit the gap between the crimping heads. Therefore, when the handles were squeezed gently together, the crimping heads moved together and then out again. The tool was then slid off the newly crimped pin with the handles still held together, so that a second crimping operation did not occur when the handles were allowed to

move apart. There was also a disk attached near the jaws of the crimp tool which was adjusted and fixed in position to ensure that when the disk was held against the end plate, the crimp heads were the correct distance along the pin and were held parallel to the end plate. The crimp tools were very elegant and simple to use, and made the process of crimping over 10000 wire ends in pins into an operation which could be repeated with consistent quality control.

d) Glue

An acetal resin was used to glue the wires into the end plates and feedthroughs. The glue type used was R.S. High Strength Epoxy. On the inside of the end plates, around each field wire position a hole 2.1 cm deep had been counterbored for the glue. This hole was almost completely filled with glue. The sense wires had glue injected into the tip of the feedthrough which formed a small plug inside. The glue was put into these holes with a syringe and long plastic nozzle, and was forced out of the syringe and through the nozzle under pressure from a gas cylinder. This was operated with a foot pedal, leaving both hands free to support the syringe and keep the nozzle steady. One layer of sense wires or one or two layers of field wires were glued in one session, with the chamber held in a vertical position on the wiring mandrel and pivot. The glue was then left to harden for ~ 6 hours, before the chamber was inverted and the other ends of those wires were glued.

2.9   The Wiring Process

The wiring process was carefully planned and adhered to, in order to avoid wastage of the wire from mistakes, or damaged wire ending up in the chamber. The wiring was done in shifts of two hours, with two people forming a shift. People worked in the same pairs, each person at the same end of the chamber, over the 6 months that it took to wire the ITC, so that they got used to each other's method of working. This enabled them to become very fast and efficient.

The whole chamber was wired and assembled in a clean room, complete with air lock outer door and air conditioning, and everyone wore complete clean suits from head to toe, and clear plastic gloves at all times. This was to keep dirt and grease out of the chamber, since they can degrade its performance.

The ITC was held in a horizontal position for wiring. This was the only

direction it could be done in, because there was no suitable room with a tall enough ceiling to do the wiring vertically in the Blackett Laboratory at Imperial College.

For each wire, a length about 3 m long was unrolled from the reel of wire and cut off. It was threaded through the end plates and pins from the inside of the chamber outwards, in order to avoid scraping the length of wire which ended up in the chamber through the holes and damaging its surface plating. The sense wires had to be threaded using a needle, since they were so thin. The central 2 m section of the wire was not touched by gloved hands or tools and neither was it allowed to touch the end plates at all. If the wire was an aluminium field wire, it was checked especially carefully for kinks before the tension was applied. Once the wire was threaded through the pins, and feedthroughs if it was a sense wire, it was clamped at one end, outside the chamber, and run over a small pulley wheel at the other end. To this end was attached a weight to give the wire the correct tension. The weights were made from lead shot in small plastic bottles, with a wire hook attached around the neck of the bottle, and a tiny flat-plated clamp was used to carefully fix the weight to the wire. Under-tightening of the clamp let the weight slip off the wire, and over-tightening caused the wire to break. The far end of the wire was then crimped into position, and the spare bit of wire between the pin and the clamp was clipped off at the tip of the pin. The crimping process was then repeated at the weight end.

All wires at the same radius were wired sequentially, to ensure that there was never an imbalance of forces between one side of the chamber and the other, which might pull the end plates over in the direction of the extra cluster of wires. The origin of the numbering scheme was marked onto a flange on the end of the wiring mandrel, which was about 15 cm further out from the end plate, and also engraved onto the end plate itself. This extra, temporary flange was made of perspex, with two concentric rings of holes drilled through it, corresponding to the cell positions in the inner and outer layers. When a dowel fixed to the support tripod of the mandrel was pushed into one of these holes, it held the chamber at the correct angle for wiring or frequency testing the corresponding wire.

After stringing a wire, the chamber was rotated one notch on the perspex end flange, to raise the wire just strung, so as to be ready for the next wire. After a couple of months' experience of wiring the chamber by a wiring team, a field wire could be put into the chamber in 2 minutes, and a sense wire took 3.5 minutes.

The numbering system used for the wires identified sense wires, field

wires and calibration wires separately, so that the numbering system for the sense wires can be used for the readout and the subsequent track reconstruction. The sense wires are numbered sequentially from 1 to 960, starting at the innermost layer, layer 1, and spiralling outwards. Within bilayers, the wires are grouped into blocks for the HT distribution system and the preamplifier cards. Thus, wires 1–8 and 97–104 form block 1, and so on.

2.10 Wire Tension and Sag

The three types of wire in the chamber all have different weights, but have to have the same amount of sag due to gravity, in order to keep the cell dimensions constant from end to end of the chamber. Therefore, each type of wire is wired with a different tension. The wire tensions after relaxation of the wires and transfer of the load are approximately 60 g for the sense wires, giving a sagitta of 114 μm at the centre of the wire, and 200 g for the field wires, giving a sagitta of 126 μm. The wires are not stiff, and so hang in parabolas in the chamber. The sagitta were calculated using :

$$\text{Sagitta} = \frac{M g L^2}{8 T}$$

M = mass per unit length of wire
g = acceleration due to gravity
L = length of wire
T = tension of wire

The tension on the sense wires gives a high voltage stability limit of 4.6 kV, which is a much higher voltage than will ever be used. The guard wires had a tension of 400 g, giving a sagitta of 88 μm, but they are also pulled ~ 1 mm by the hoops.

The weights used to produce these uniform final tensions had to be varied from layer to layer of the wires. They are shown in Table 2.2. The detailed engineering calculations from which these weights were obtained included allowances for the inward movement of the outer edges of the end plates as more and more wires were strung into place, and also for the inward movement of the inner edges of the end plates when the load transfer took place.

Table 2.2 Masses Used to Achieve Uniform Final Wire Tensions										
Wire Type	Sense	Sense	Sense	Sense	Field	Field	Field	Field	Guard	Guard	Guard
Wire Layers	1 & 2	3 & 4	5 & 6	7 & 8	1 & 2	3 & 4	5 & 6	7 & 8	1	2	3
Mass used / grammes	68	66	63	58	267	256	239	214	460	440	400
Initial Frequency f / Hz	55.3	54.5	53.2	51.1	56.9	55.7	53.9	51.0	63.3	61.9	59.0

Frequency Tests

Once a wire was strung, its tension could be measured by forcing it to vibrate at its resonant frequency and using the relationship between tension and frequency.

$$f = \frac{1}{2L}\sqrt{\frac{T}{M}}$$

This gives frequencies of ~ 52 Hz for the sense wires, ~ 51 Hz for the field wires and ~ 60 Hz for the guard wires, at the given final tensions. For the aluminium field wires, these frequencies have gradually decreased over a period of a few hours from the initial values straight after wiring, because of the creep of the wires. The creeping slowed down after a few days. Tests were made of this effect, and the results can be seen in figure 2.8.

After 19 days, there is a discontinuity in the tension measured. This is due to the removal of the test rig from one room to another.

The creep of the wire was taken into account when calculating the weights needed to produce the final tensions. The wires were forced to oscillate in the chamber by clamping a mechanical vibrator to one of the end plates. A set of frequency tests was performed after wiring each layer of wires, on the wires just strung. Each wire in the layer just wired was observed in turn through a telescope, and the frequency of the vibrator was adjusted until the resonance of the wire was found. If this was not within one or two Hertz of the theoretical frequency, then the wire was cut out and replaced.
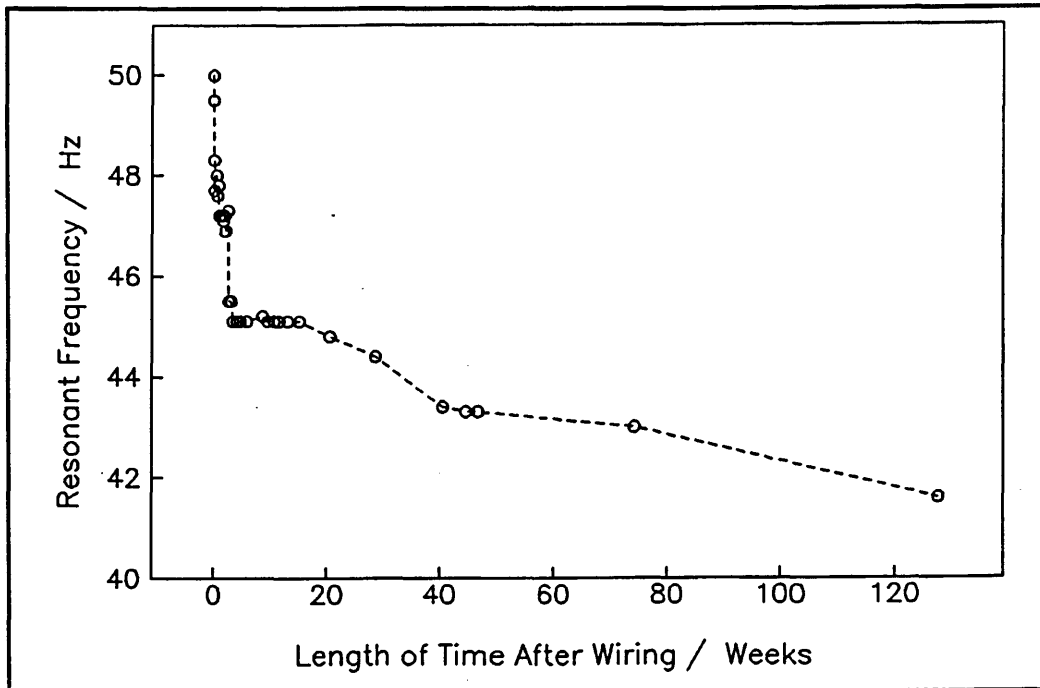
Fig 2.8   Graph of the Creep of the Aluminium Wires

Every wire was frequency tested twice before it was glued into place. The first frequency test was performed straight after a layer of wires was strung into the chamber. The second test took place the next morning, before the gluing was started.

The frequencies of some of the wires in each layer were also measured after the transfer of the load, to check that the final tensions, and therefore the sagitta, did not vary significantly from layer to layer. These measurements could not use the method of mechanical vibration and optical finding of the resonant frequency, since the wires were inside the carbon fibre tube and so no longer visible. Instead, a DC magnetic field was applied across the chamber, and an alternating current was passed through the wires. The wires vibrate when the current frequency is equal to the resonant frequency, and the resistance of the wire drops. The resonant frequencies found were approximately equal across all the layers for each wire type, confirming the tension calculations as correct.

2.11   Position Accuracy

The position accuracy of the sense wires with respect to the chamber, and especially with respect to each other is of great importance to the overall position resolution in the r-ø plane of the ITC. Therefore, the contribution from each component to that accuracy had to be measured and

controlled. The errors from each component add in quadrature to give a measure of the overall spread in the position of the sense wires.

a) Sense Wire Position in Pin

· Assuming a flat distribution of the position of the 30 μm diameter sense wires across the 100 μm diameter pin holes, then the position of the sense wire in the pin hole contributes an error to the sense wire position of $\sigma = 20$ μm.

b) Concentricity of Hole in Pin

Attempts were made to measure the concentricity of the holes in the sense wire pins, but it was very difficult, so not many were measured. The difference between the axes of the hole and the pin was found to be always less than 20 μm. Assuming a flat distribution across this range, pessimistically to be ± 20 μm wide, then the contribution to the sense wire position error is $\sigma \sim 10$ μm.

c) Concentricity of Hole in Feedthrough

The concentricity of every feedthrough was checked, and if it was worse than 30 μm, then the feedthrough was discarded. Assuming a flat distribution across this range, then the contribution to the sense wire position error is $\sigma \sim 17$ μm.

d) Spread of Hole Positions in End Plates

The surveyed hole positions were fitted using concentric circles, and the resulting spread of azimuthal displacement of the sense wire holes from their nominal positions is $\sigma = 10.4$ μm for one end plate and $\sigma = 12.0$ μm for the other.

These four contributions to the azimuthal spread of the sense wire positions in an end plate give a total spread of $\sigma = 30$ μm.

There are two other contributions which also affect how well known the sense wire positions are.

e) Angular Displacement of End Plates with Respect to Each Other

This was measured after assembly of the end plates onto the wiring mandrel to be ~ 0.0066°, which gives an azimuthal difference of sense wire positions between the ends of between 19 μm for layer 1 to 30 μm for layer 8.

f) Spread of Sense Wire Sagitta

After transfer of the load, the resonant frequency of some of the sense wires in each layer was measured, to check that the tension calculations had been correct. From these measurements, the spread of the sense wire sagitta is $\sigma \sim 7\,\mu m$.

2.12 Gas

Three commonly used gas mixtures in drift chambers are argon-ethane 50%-50%, argon-carbon dioxide 80%-20%, and argon-carbon dioxide 90%-10%. It is expected that the ITC will be operated with the argon-ethane mixture.

The gas chosen for the operation of a drift chamber has a critical influence on its operational characteristics. The criteria used to choose a gas are as follows.

a) Diffusion

In a drift chamber it is desirable to have low diffusion of the drifting electrons through the gas, in order not to degrade the resolution. Any gas in which the electrons remain thermal at high values of the electric field satisfy this, including hydrocarbons, CO_2, and mixtures of noble gases with large fractions of these quenchers [2.6].

b) Operating Plateau

The operating plateau of a chamber is the range of conditions in the chamber which give a saturated drift velocity of electrons in the gas, and consequently have a steady drift relation. The electron drift velocities as a function of electric field for argon-ethane and argon-carbon dioxide, are shown in figures 2.9 [2.7] and 2.10 [2.8].
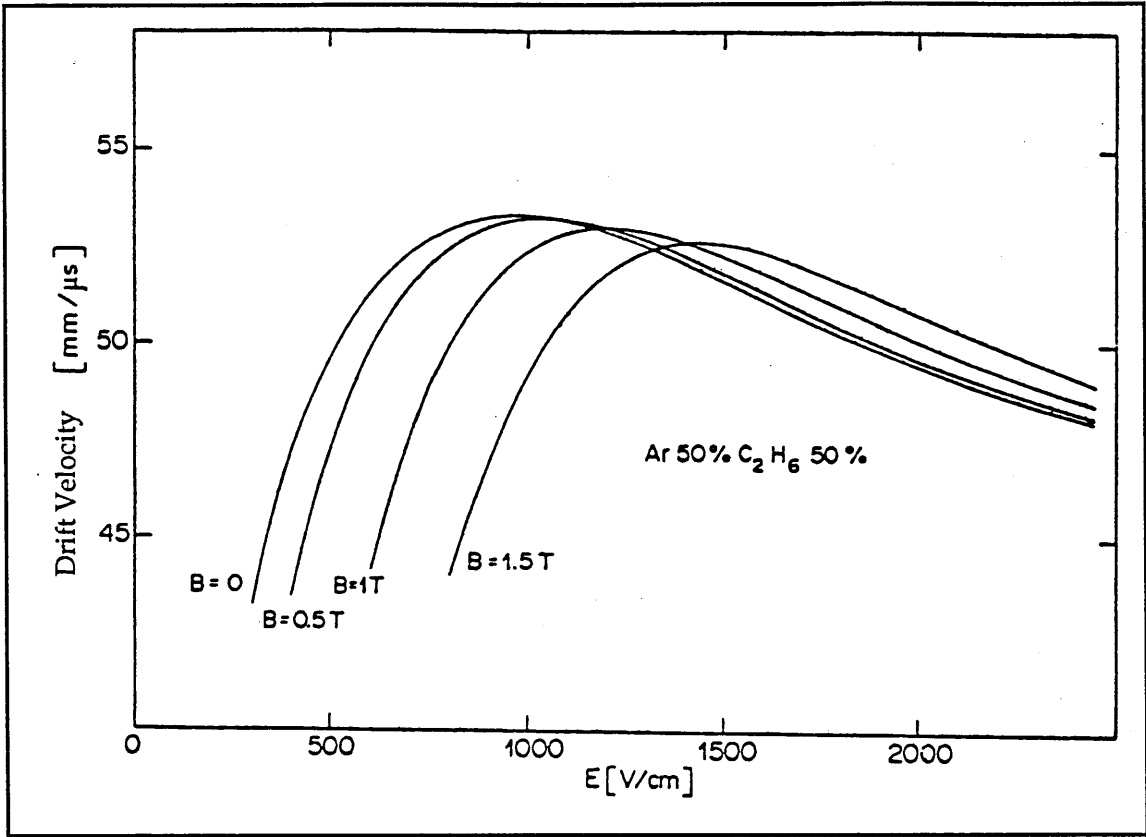
Fig 2.9   Drift Velocity at Various Electric and Magnetic Fields
in Argon-Ethane 50%-50%
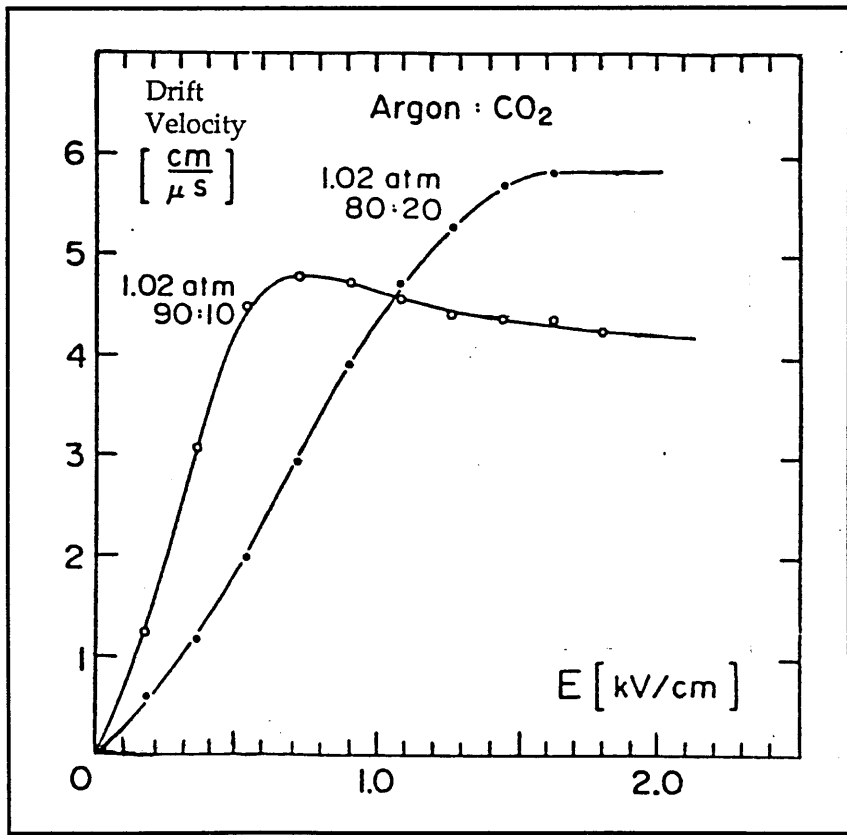
Fig 2.10   Drift Velocity at Various Electric Fields
in Argon-Carbon Dioxide

For the argon-ethane gas mixture, it can be seen that in order to operate with a saturated electron drift velocity in the ALEPH magnetic field of 1.5 T, it will be necessary to have the sense wire voltage much higher than when running with no magnetic field, in order to sufficiently raise the electric field across the cell.

For the argon-carbon dioxide 90%-10% gas mixture, the region of saturated drift velocity is reached at a lower electric field than for argon-ethane 50%-50%, with no applied magnetic field. The argon-carbon dioxide 80%-20% mixture needs a higher electric field to saturate the electron drift velocity, and saturates at a faster velocity than the mixture with less CO_2 in it.

If a gas has a long operating plateau, then small fluctuations in the electric field across the cell or from cell to cell, or small changes in the sense wire voltage from wire to wire or in time, will not affect the drift relation of the electrons in the gas.

The electric field and the gas type are also chosen in conjugation to give the drift cell a high gain < 10^6 on the number of drifting electrons.

Another factor which will affect the drift velocity is the percentage of each gas type in the gas mixture. A 1 % variation in the percentage of argon is the maximum tolerable change which would not significantly affect the drift velocity.

The temperature of the gas will also affect the drift velocity. For most gases, variations of 0.1 % - 0.2 % in the drift velocity per °C are typical. Therefore, a significant 1 % - 2 % shift in drift velocity requires a 10°C gas temperature change. A change this large should never happen. The temperature of the gas will be monitored for offline corrections to the drift velocity, but not controlled. Six platinum resistance (100 Ω at 0°C) temperature sensors have been installed inside the chamber in order to do this monitoring.

c) Impurities in the Gas

Some gases containing organic molecules have caused serious problems for drift chambers in the past. Large polymers can form in the gas which do not break up between ionisations, and so accumulate and degrade the electron drift behaviour and gain of the chamber [2.9]. Sometimes carbon fibres form on field wires if the electric field is too high on the surface of the wire, which cause a complete breakdown of the chamber [2.4]. In other detectors, silicon deposits have built up on the wires causing a loss of gain in the chamber [2.1].

One known method of eliminating some of these problems is the

addition of a small amount of alcohol to the gas. This can be done by bubbling the gas through liquid alcohol before it enters the chamber. This seems to cure the previously mentioned problems of large polymers and carbon fibres, although it is not well understood how this happens. The gases can also be bubbled through water, which reduces leakage currents in the gas and extends the lifetime of the chamber.

The carbon fibre growths are never observed when using argon-carbon dioxide, which is the most common reason for using it, despite its shorter, steeper plateau than that of argon-ethane.

The ITC will probably have argon-ethane 50%-50%, because of its longer plateau for operation, giving better drift relation characteristics.

3 Electronics

The various units which make up the electronics in the ITC will be briefly described here. They will be described in greater detail in later chapters of this thesis. A schematic diagram of the end electronics and readout of the ITC can be seen in figure 2.11.

3.1 High Tension End Box

This is a passive unit which capacitively couples the sense wires in the ITC to the preamplifiers on the ends of the chamber, outside the gas volume. There are 60 end boxes at each end of the ITC. They connect the high voltage supply with the sense wires and keep the field wires and end plates earthed. They have been designed to cover blocks of 16 sense wires only, so that if a wire should start to draw current in operation, for instance one near the beam pipe which has been damaged by radiation from the high intensity of particles, then the high voltage on that block of wires can be independently switched off, leaving the rest of the chamber working normally.

Each end box is connected to 34 wires. There are 16 sense wire connections, covering a block of cells 8 x 2 in one bilayer. Then there is one field wire per cell, on the outer side of each cell, that is earthed through an end box connection. The remaining 2 connections are also to field wires on the end of each block of cells, to make sure that every signal track on the end box is surrounded on both sides with a pair of earthed copper strips.

The end boxes are made from a 50 μm thick sheet of Kapton, coated on both sides with a 25 μm thick layer of adhesive, and a 35 μm thick layer of copper. Areas of copper are etched away, leaving strips of copper on both sides of the sheet, which form the coupling capacitances. The sheet is then folded into a box to cover the block of 2 layers of 8 cells, and the whole box
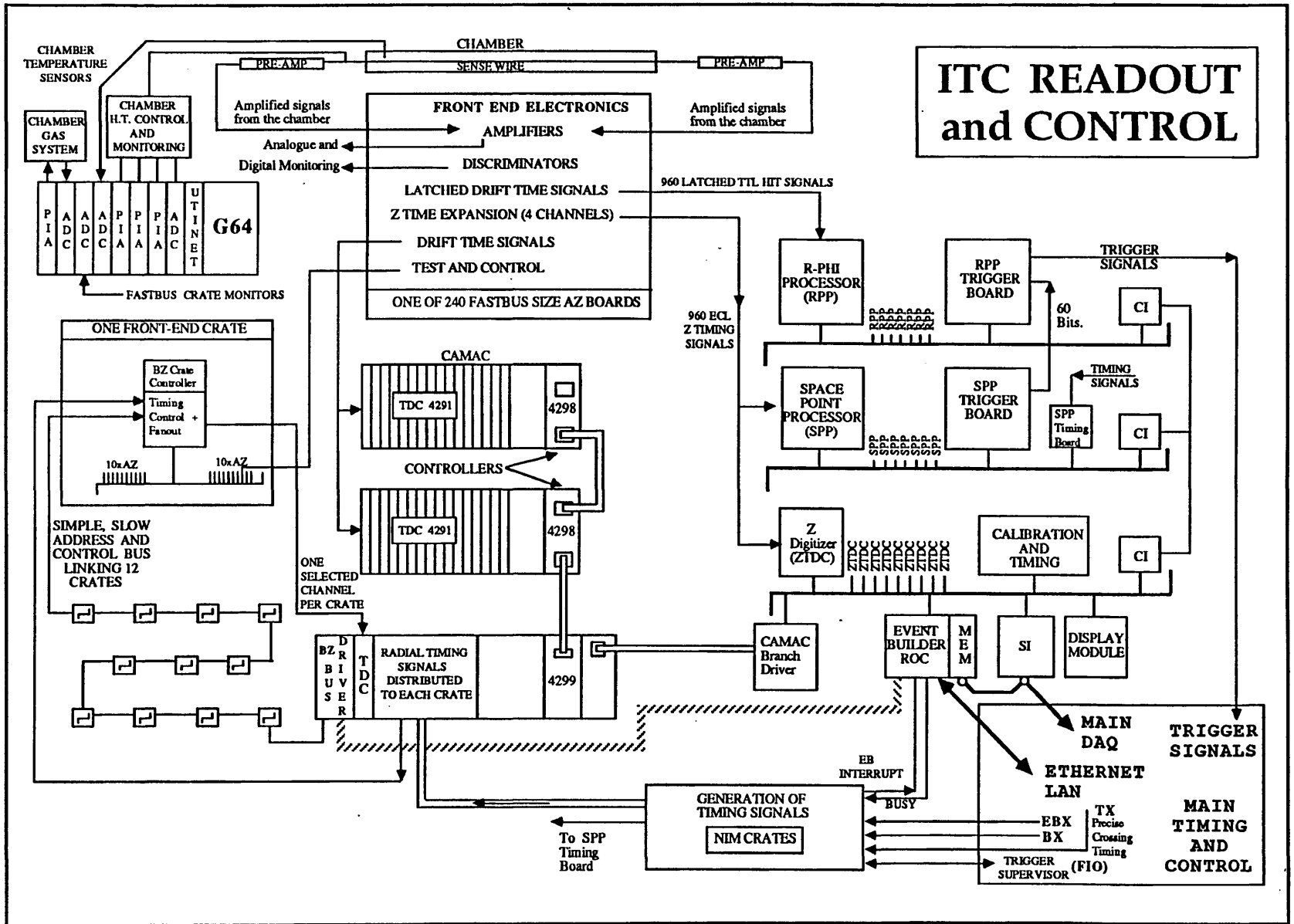
Fig 2.11   The Data Acquisition System of the ITC

is covered in a thin layer of conformal coating. This coating prevents corona discharge from the strips. The copper strips behave like transmission lines.

3.2 Preamplifier

Outside the gas chamber of the ITC, there are 60 charge sensitive preamplifiers at each end. These drive the chamber signals down the cables to the main amplifiers. The preamplifiers are outside the gas volume to avoid cooling problems. The voltage gain of the preamplifier is ~ 2 for high signal frequencies, and the current gain is ~ 100. The rise time is ~ 10 ns.

3.3 Main Amplifier/Discriminator

The signals from the long cables are fed into the main amplifiers, which are on the so called Az boards (shown in figure 2.11) in crates in the electronics barrack in the ALEPH pit. The signals are amplified, then passed into discriminators, which produce a signal when a threshold is passed. Different types of discriminator under consideration are discussed and investigated in detail in Chapter 4.

4 Readout

There are two sets of readout electronics for position measurement. One set is for the r-ø plane coordinates and the second set is for the z direction along the sense wires. There are also two trigger processors. They both form part of the level 1 trigger for ALEPH. The simplest and fastest trigger uses masks on the r-ø plane hits. The space point trigger processor uses all three coordinates to reconstruct tracks.

4.1 r-ø Measurement System

The r-ø measurement system has to perform two jobs in the ITC. It has to produce a hit pattern for the r-ø trigger processor within ~ 150 ns of a beam crossing, to enable the full r-ø trigger to be produced in ~ 1 μs, and it

also has to measure the drift time for each hit in the chamber, for reconstruction of the tracks. To do this, a LeCroy TDC (time-to-digital converter) CAMAC system is used. The r-ø measurement system and the resolution obtainable will be covered in Chapter 3.

4.2   z Measurement System

The z position measurement system uses a novel time difference method in order to produce online positions for each hit along the wires, within an error of < 5 cm, for use in the space point trigger processor. The signals from each end of a hit wire are read out and the difference between their times of arrival is found. This process and the nonlinearities involved are investigated in Chapter 4. The time differences, one for each hit, then undergo a "time expansion" process. The times measured from each cell layer are multiplied by a factor inversely proportional to the radius of that layer. This ensures that all z times from any one track emanating from the interaction point, arrive simultaneously at the space point trigger processor. The time expansion process is explained in more detail in Chapter 5.

4.3   r-ø Trigger Processor

The r-ø trigger is the fast trigger from the ITC which forms part of the level 1 trigger for ALEPH. The processor works by mapping a grid of masks of hits onto the cell layers, and if there is a set of from four to eight radial hits in a line, then a positive signal is produced. The r-ø trigger will be examined in more detail in Chapter 5.

4.4   Space Point Trigger Processor

The z times are fed into the space point processor with the hit wire information. This produces a trigger signal if a reconstructed track is found in three dimensions. This trigger also forms part of the level 1 trigger of ALEPH. This trigger is more complex than the r-ø trigger, but produces far less false triggers from noise in the chamber.

5 General Notes

5.1 Position Alignment of the ITC

The ITC has to be positioned inside the TPC as close as possible to its centre. Ideally, the two axes will be aligned, the centres will coincide, and there will be no twist in θ or ϕ. This physical positioning will be achieved after the ITC has been inserted inside the TPC, by a survey of alignment marks made on the outer flanges of the ITC supports. These marks correspond to the wire positions inside the chamber. The position of the ITC will be carefully adjusted until the ITC alignment marks match up with the TPC alignment marks. This can be done to ~ 250 μm.

Once the chamber is physically aligned, and cabled up, cosmic rays will be used to perform a software alignment. This will produce a set of calibration coefficients which can be used in the offline track reconstruction to help identify tracks found in the ITC with those found in the TPC.

This software alignment can be achieved to a few μrad in all rotations, and to a few μm in the x and y directions, but cannot be done for the z direction as no trigger can be provided, and the z resolution is too poor [2.10].

5.2 Total Percentage Radiation Length

Calculations have been made of the total percentage radiation length contributed by the ITC to the ALEPH detector. The percentage radiation lengths presented to particles travelling from the interaction point are shown in figure 2.12, for the whole of the length of the chamber and for the central section with $\theta > 20°$ [2.11].

For tracks crossing all 8 cell layers and not entering the end plates, with $\theta > 17°$, the fraction of radiation length varies from 0.013 X_0 to 0.045 X_0. Over three quarters of this is from the carbon fibre outer tube.
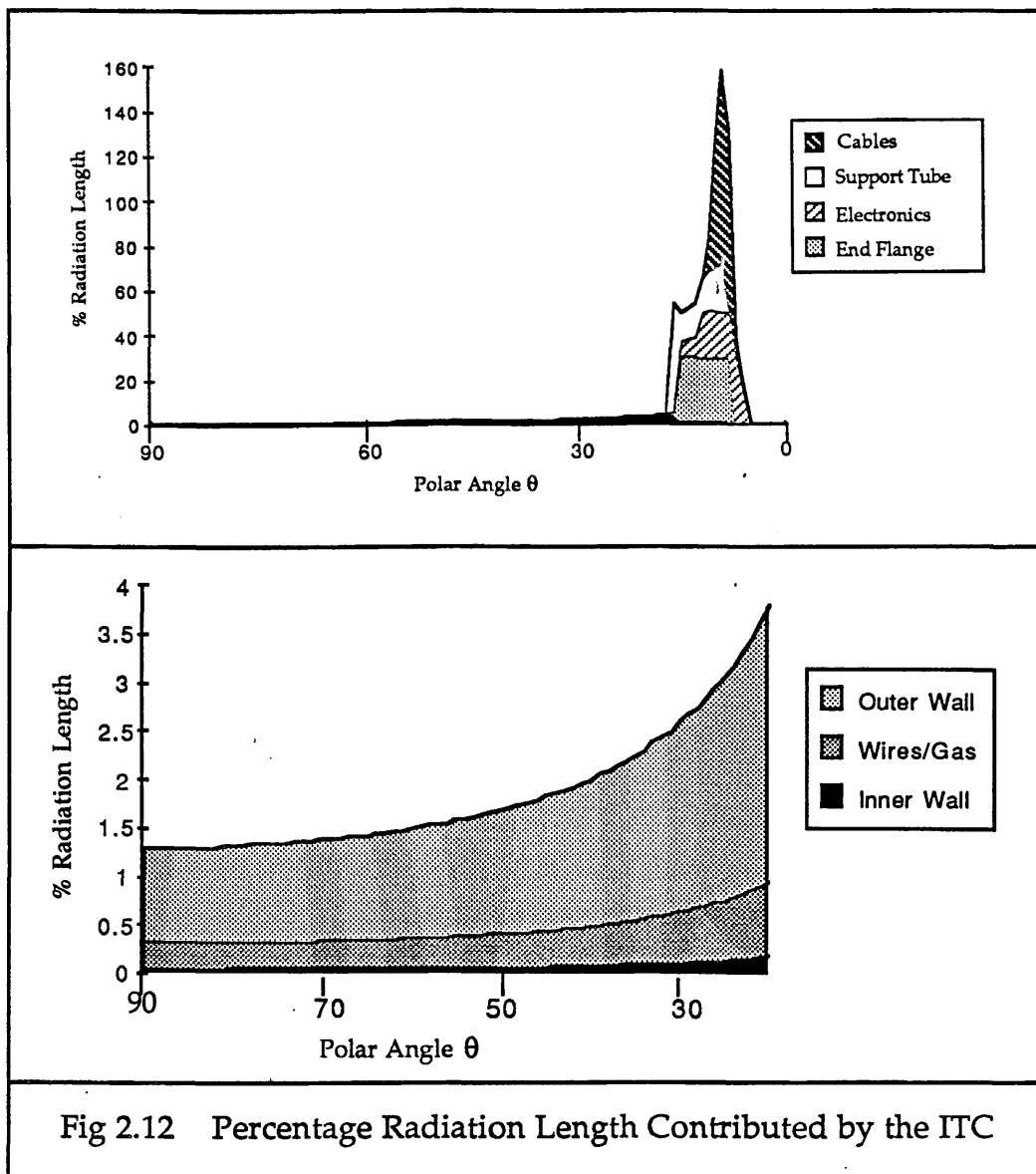
Fig 2.12 Percentage Radiation Length Contributed by the ITC

5.3 Overall Resolution

5.3.1 r-ø Resolution

The overall r-ø resolution aimed for in the ITC is 100 μm. This is defined as the root mean square of the residuals from a large number of fitted tracks and their drift time coordinates. There are several different effects which contribute to this value. These are as follows :

a) Position of the sense wires

b) Resolution of the TDCs

c) Diffusion of electrons in the gas

d) Knowledge of the space-time drift relationship

The position of the sense wires will contribute about ~ 40 μm to the error. The knowledge of the position coordinates of individual wires can be improved by offline iteration. This is explained in Chapter 3.

The contribution to the position error from the 0.5 ns TDCs is, for a uniform distribution across the bins, ~ 7 μm, provided there is no drift of the TDC timing after autotrimming.

Diffusion of the electrons in the gas occurs both along the direction of the electric field and transverse to it. The transverse diffusion is greater than the longitudinal diffusion, the exact ratio being dependent on the gas mixture in use. Over the very short drift distances in the ITC cells, the diffusion of the electrons will be < ~ 30 μm, and so will not form a significant contribution to the overall resolution [2.12].

The contribution to the uncertainty in r-ø position which can be reduced, is knowledge of the form that the drift relation should take to best represent the drift paths of the electrons in the electric and magnetic fields. Chapter 3 contains work done to find a good drift relation.

5.3.2 z Resolution

The z resolution aimed for is < 5 cm. The principal use for this third coordinate is in the space point trigger, so it does not need to be measured with such high accuracy as the r-ø coordinates. There are several contributions to this value of 5 cm resolution. These include :

a) Noise on the signal
b) Variations in capacitance on the ends of each wire
c) Accurate adjustment of discriminator slewing with pulse size
d) Threshold level of the discriminators
e) Resolution of the TDCs
f) Accuracy and stability of calibration

The noise on the signal is introduced by high frequency interference and the intrinsic noise from the electronics components. This must be held to a minimum. It will have a dominating effect if dual threshold discriminators are used.

The variation in the behaviour of individual components in the end electronics will have a small effect on the z resolution.

If constant fraction discriminators are used, then they must be carefully set up in order to be used sensibly.

If dual threshold discriminators are used, then the threshold level set will affect the z resolution. A high threshold will improve the resolution

but lose the timing from small signals.

The resolution of the FASTBUS LeCroy 1870 TDCs used for the ITC with 5 nsec bins, (and time expansion), will give ~ 0.2 cm limit on the z resolution.

Chapter 4 contains work done on understanding and improving the z resolution obtainable.

6 Summary

The ITC, a 2 m multiwire drift detector, has been successfully wired and assembled at Imperial College. It has been transported to CERN and tested for reliability at high voltage without any wires breaking or other problems occurring.

There are a few wires from which the signals cannot be read out at both ends, and the only known causes for this are bad connections between the sense wires and the preamplifiers, due to poor contacts or broken tracks on the HT boxes. This leaves 8 wires which are dead for z measurement, but all 960 wires can produce r-ø drift times.

The ITC has been operated in a test beam at CERN in the Summer of 1987. Preliminary analysis of data has produced resolutions at the levels aimed for.

Chapter 3

THE SMALL TEST CHAMBER

1   Introduction

This chapter describes the work done with a small test chamber, which was built to assess the construction processes for the ITC and to test the behaviour of the design in a high magnetic field.

1.1   The Need for a Test Chamber

There had already been one test chamber built for the ITC, early in 1984. This full-length detector had been designed to compare two different z measurement systems which were then under consideration. To do this, the long test chamber was taken to CERN in the summer of 1984 and operated in a particle beam. However, this chamber did nothing to test the r-ø measurement system, since it had an old cell design and was not operated in a magnetic field. It was also built from components similar to those used in the TASSO vertex detector, including the wire type, wire fixing method with solder spills in the feedthroughs and different designs of high voltage end box and preamplifier. Consequently, another test chamber was needed with which the construction methods could be tried out and the new components tested. Using the data acquired with the new design electronics and hexagonal cells, the r-ø measurements obtained in a magnetic field could then be assessed.

1.2   What Was Done to Meet this Need

It was decided that the best way to achieve all these aims was to construct a test chamber using all the latest designs and components. Since the z measurement system had already been proved to work with the

previous long test chamber, it was unnecessary to build a full-length chamber with 2 m wires. Therefore, it was decided to construct the new test chamber with wires only 40 cm long. This also meant that the whole small test chamber was compact enough for a suitable magnet to be found into whose aperture it would fit. Because no z position measurements were to be made, it was necessary to have readout electronics on one end of the sense wires only. This reduced the number of prototype end boxes and preamplifiers needed, and also reduced the amount of data to be read in and recorded.

The small test chamber was built at Imperial College in the late Spring of 1986 and tested in the ALEPH test beam, inside a large magnet, in July 1986. Approximately 4 million triggers of data were recorded during 10 days of beam time. This was despite several problems which occurred with the operation of the chamber during this period. These problems will be fully explained later in the chapter.

In this chapter, there is first a brief description of the small test chamber, followed by a detailed discussion of how the chamber was wired and assembled. This trial run formed the basis of the technique for wiring the ITC itself. Next, the tests carried out on the chamber, both at Imperial College and at CERN are described and the results presented. After this, the analysis of the data is explained, together with what information can be extracted from the data, and the methods used to obtain it. Finally, the results from the analysis are presented and the behaviour of the chamber under various running conditions is shown. Conclusions are then drawn as to the implications from this work for the construction and operation of the ITC.

Throughout this chapter the small test chamber will sometimes be referred to as the STC.

2 Construction of the Small Test Chamber

2.1 A Brief Description of the Detector

Many aspects of the design of the STC are the same as for the ITC. These have already been described in Chapter 2 and need not be repeated here.

The basic structure of the STC can be seen in figure 3.1.

Fig 3.1   The Small Test Chamber
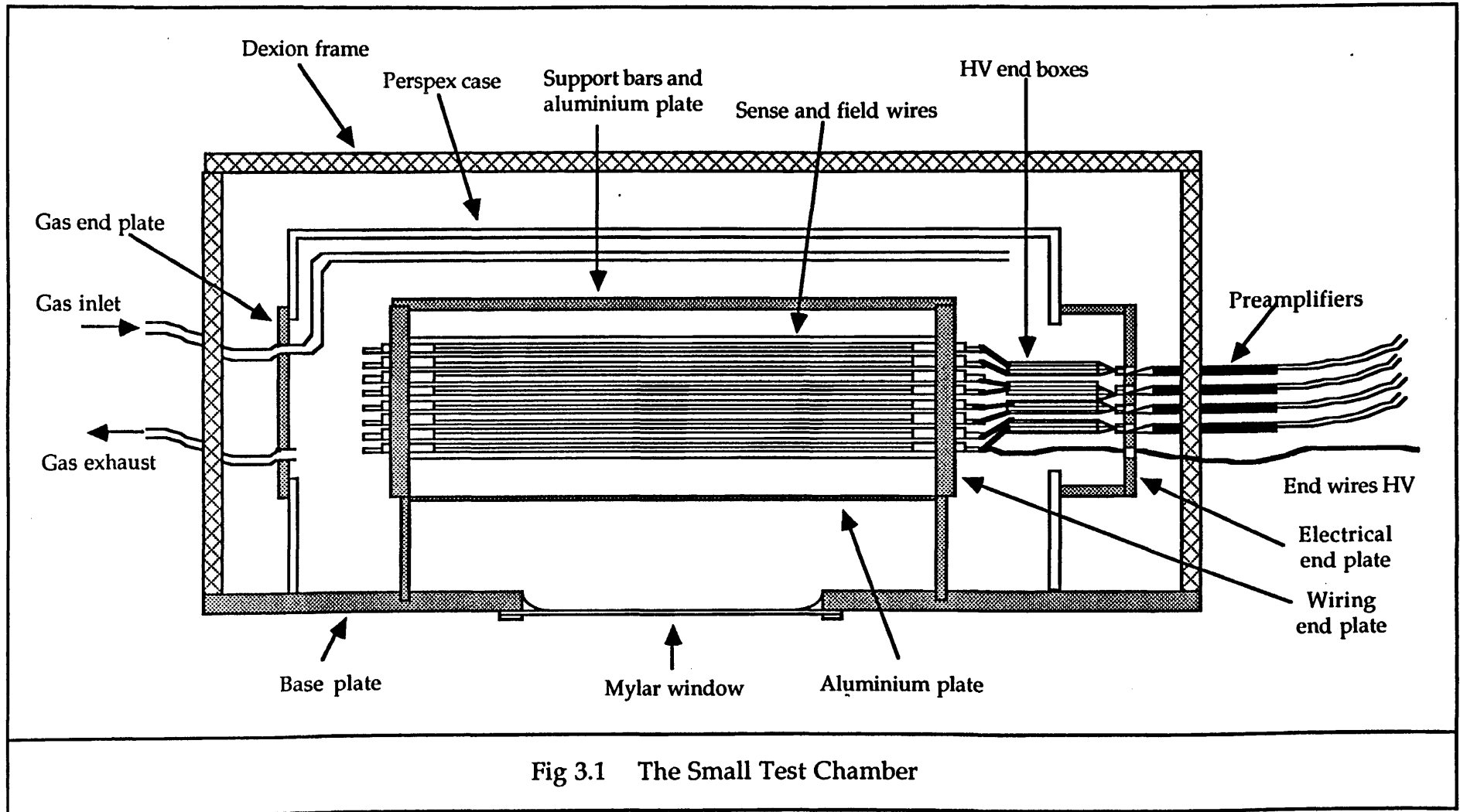
The wires are strung between two aluminium end plates, which are mounted in a thick aluminium base plate. The end plates are held apart by two aluminium load-bearing rods. The wires are fixed in the end plates using the crimp and glue method. The sense wires are 30 μm diameter gold plated tungsten and the field wires are 147 μm diameter gold plated aluminium. Four high voltage end boxes are attached to one end of the sense wires and field wires. These have the preamplifiers attached outside, via connectors embedded in an aluminium outer end plate. The whole of the base is covered by a large clear perspex box, which is gas tight. The box has 4 windows in it, one at each end of each of the long sides, which allow access to the chamber once assembled. Around the aluminium base there is a framework of Dexion which completely surrounds the perspex box, and allows the chamber to stand alone on any of its faces. In the centre of the aluminium base plate there is a rectangular window covered in mylar. This is to reduce the amount of material in the path of the beam or cosmic rays to reduce Coulomb scattering and Bremsstrahlung.

Figure 3.2 shows a photograph of the small test chamber after wiring but before the perspex case was attached. The sense wires attached to the read out system have black feedthroughs. The edge sense wires have yellow feedthroughs. On the right hand side of the picture, the end boxes can be seen, and the daisy chain of wires supplying high voltage to the edge sense wires. The vertical wires which can just be seen are strips of aluminium wire glued across the guard wires to represent the guard wire cage in the ITC.

Figure 3.3 shows the end plate arrangement of hexagonal cells. This is the r-ø plane, and tracks crossing the wire planes perpendicularly, in this plane, have ø = 0°. The angle between the track and the wires is θ.
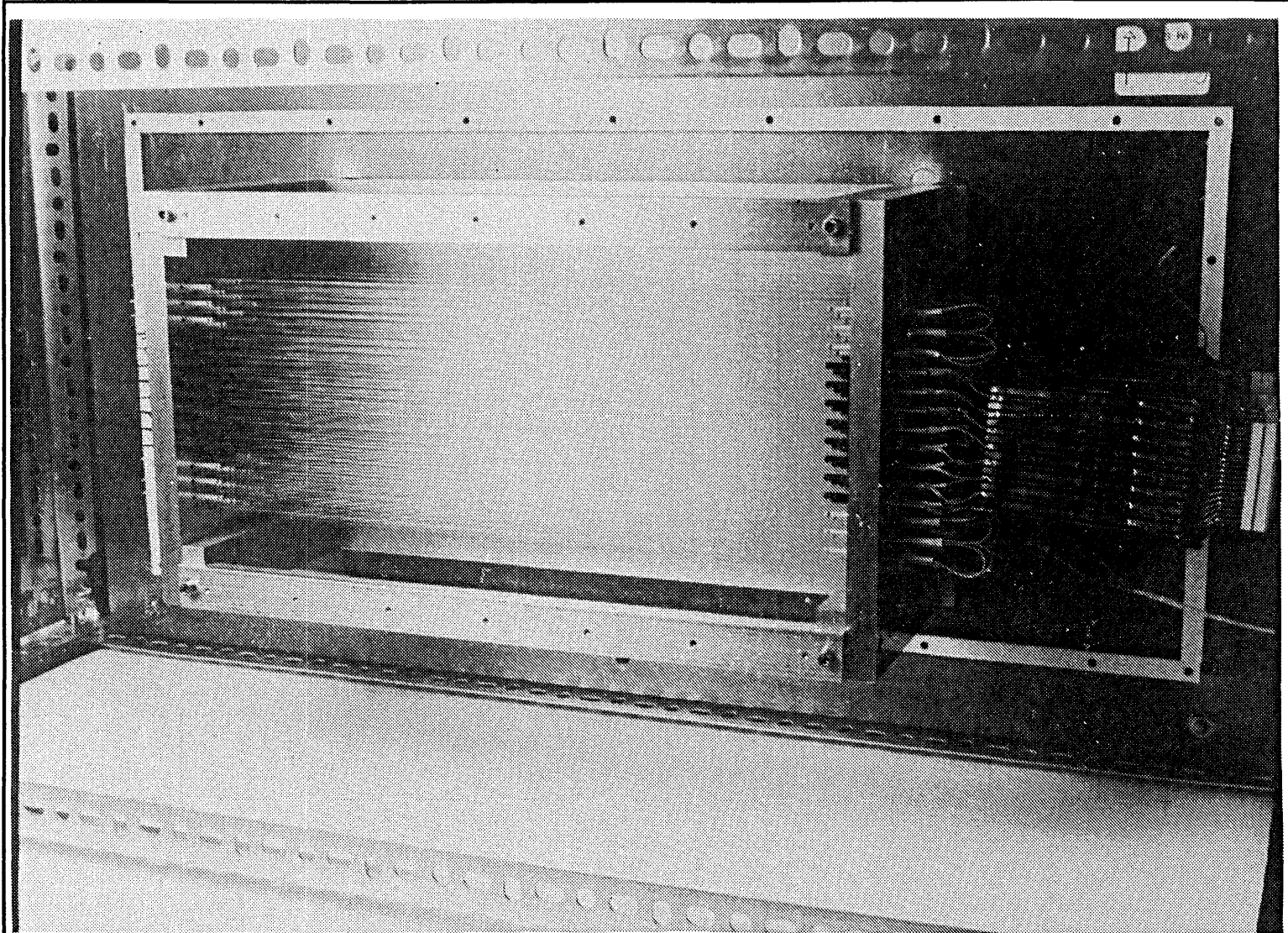
Fig 3.2   The Small Test Chamber

67
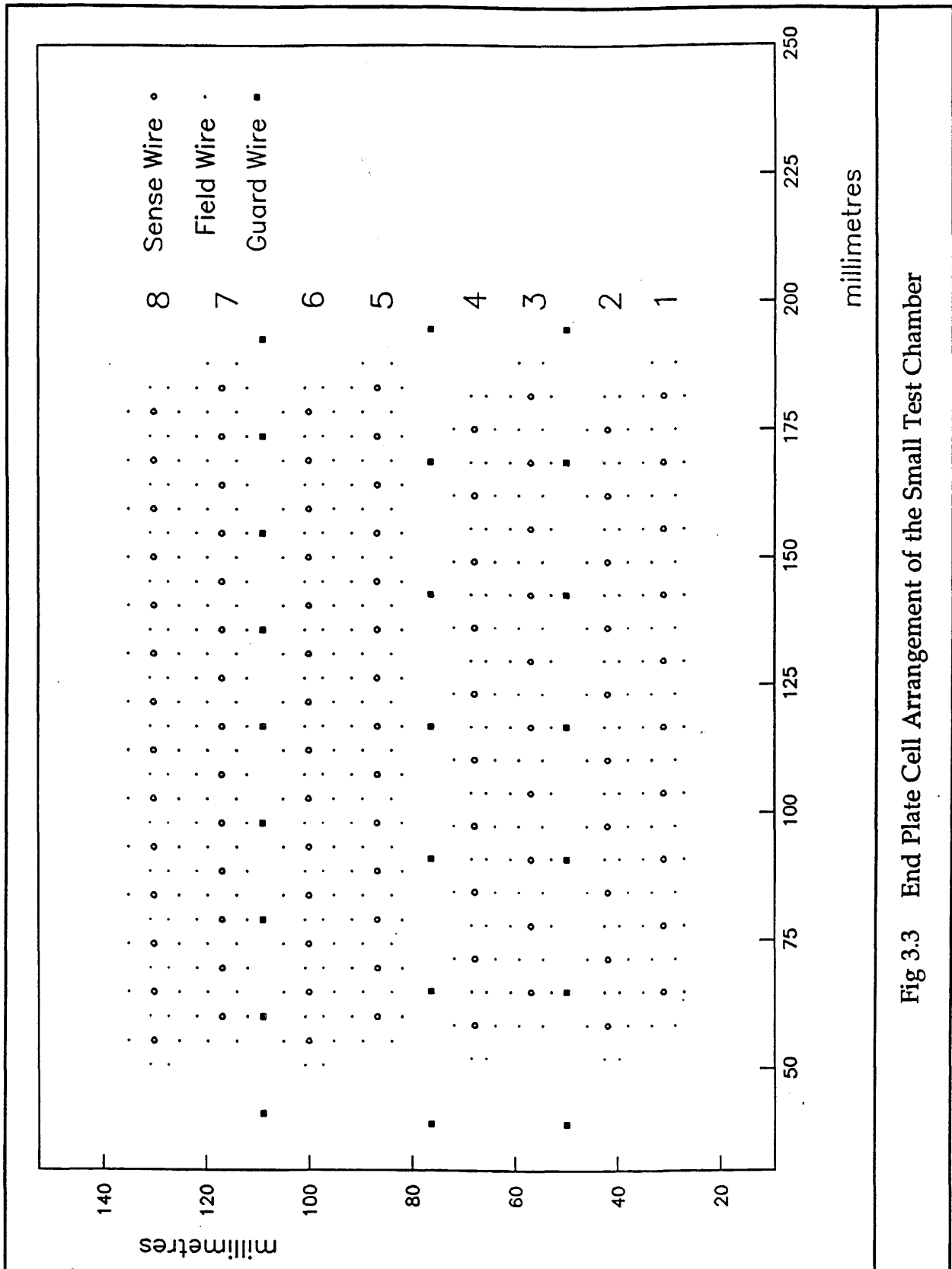
Fig 3.3   End Plate Cell Arrangement of the Small Test Chamber

There are 96 hexagonal cells in the STC. These are arranged in 8 layers, split into 4 bilayers, and between each bilayer is a guard wire layer. The 4 layers nearest the base of the chamber consist of large cells, whose dimensions are those of layer 4 in the ITC (numbering from the centre outwards 1–8). These cells have the longest drift distances in the ITC, of

68

~ 6.5 mm ($\underline{B}$ = 0 T, ⌀ = 0°, θ = 90°). The upper 4 layers of the STC consist of small cells. These have the same dimensions as those of layer 5 in the ITC. These cells have the shortest maximum drift distances in the ITC, of ~ 4.7 mm ($\underline{B}$ = 0 T, ⌀ = 0°, θ = 90°). The dimensions and squashed hexagonal shape of these cells can be seen in figure 3.4.

All Dimensions
in Millimetres

Fig 3.4   Dimensions of the Cells in the STC
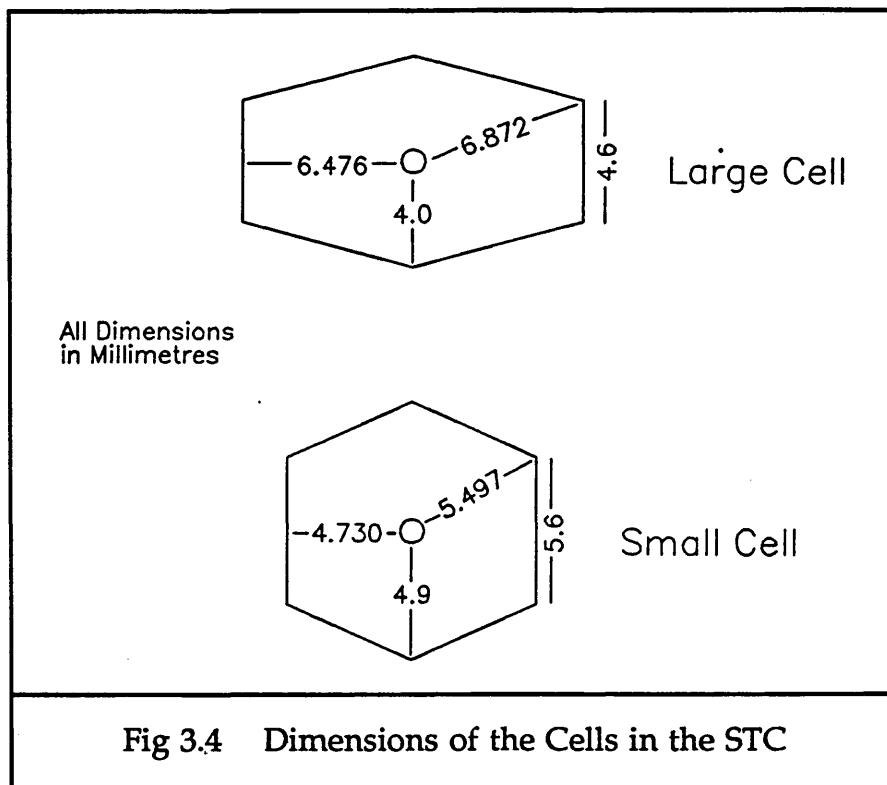
Not all of these 96 cells were attached to the readout system. Only the central 8 from each layer were read out. Thus only one end box and one preamplifier (which both have 8 channels per side) were needed to read out each bilayer of cells. The remaining cells on each end of the layers had high voltage on them, to avoid edge effects in the electric field affecting the end active cells. Another precaution was taken to ensure there were no differences between the ITC and this small chamber regarding the electric field in the cells. Two thin sheets of aluminium were fixed above and below the block of wires, at the same distances as those between the aluminium coating on the polystyrene inner tube of the ITC and the inner layer of cells, and between the carbon fibre outer tube and the outer layer of cells. These sheets created equipotential surfaces to keep the electric fields smooth.

2.2 Wiring the Chamber

The 96 sense wires, 400 field wires and 43 guard wires were strung in place within 35 days in April and May 1986. All the wiring took place in a small clean room, with a team of 4 wirers, who wore complete clean room overclothes, shoes, hoods and plastic gloves. Wiring was done in approximately 3 hour shifts, with each shift being just one person at a time. It was found that the chamber was too small for two people to work on it at the same time. Wires were strung horizontally, with the chamber base clamped vertically to a large table. The stringing method, using a small weight, a clamp and the crimp tools was the same as described in the ITC chapter. The time taken to insert a field wire started at ~ 15 minutes per wire, and ended at ~ 5 minutes. Sense wires, with their extra assembly of feedthroughs and greater difficulty of threading, started out needing ~ 20 minutes to be threaded in place, but required only ~ 8 minutes by the last layer. All these times were improved upon in the ITC, where the wiring was done by 2 people, one at each end of the chamber, and where there were ~ 10 times as many wires to be strung.

The major problem encountered when wiring the STC proved to be the pins and feedthroughs used for the wires. These were chosen from the rejects of those for the ITC. Every pin and feedthrough had its inner and outer diameters measured by hand, and they were then sorted into various categories. Those used in the ITC had acceptable tolerances of these diameters. However, there were not sufficient of these good components for the STC as well, and consequently, most of the pins available for the STC were too large for the holes. The field wire pins were mostly very tight in their holes in the end plates and had to be rammed in hard with a specially designed tool. If the wiring went wrong and a field wire had to be cut out, it was very difficult to remove the pins and some had to be drilled out. The small shards of metal from the drilling were cleaned out using a spray called Inhibisol, a cleaning fluid based on 1.1.1. Trichlorethane. The use of Inhibisol nearly destroyed the operation of the whole chamber, but we were unaware, during the wiring, of the problems to come. This was a big mistake, as will be made plain in Section 3.4.2.2 later. The sense wire pins also caused problems, since they were often too large for the feedthrough inner holes, and also had to be forced in with the pusher. The problem caused by these large pins during the wiring was to slow up the whole process, since many pins had to be tried and rejected before usable ones could be found.

After each 2 layers of wires were in place, they were glued at each end

of the chamber. The quantities of glue needed and the time taken for it to set (~ 6 hours until firm) were measured and applied to the gluing in the ITC.

The tension of each wire in a layer was measured at the end of wiring that layer, in order to check that there had been no slippage through the crimp. To do this, a variable frequency oscillator was clamped to one of the tension-bearing rods between the end plates and each wire in turn was observed through a telescope. The frequency was varied until the wire was observed to vibrate at resonance. Because the small chamber wires were only 40 cm long, the resonant frequencies were about 5 x times those found in the ITC. Initially they were ideally 252 Hz for the sense wires and 265 Hz for the field wires. By the time the frequencies were measured the wires had crept somewhat, especially the aluminium field wires, and the frequencies measured were mainly lower. The frequencies measured for the field wires and one layer of sense wires can be seen in figure 3.5. The spread of measured values for the field wires is larger than the variation in tension from the wiring process, because the measurements were taken at different numbers of hours after the wiring of each layer.

After the frequency tests were performed, any unsatisfactory wires found were replaced and retested. A wire was considered to be unsatisfactorily wired if its resonant frequency was more than ~ 20 Hz too high or too low. If the frequency was too high, then usually the feedthrough had been tweaked, which pulled it out of the end plate slightly, after the wire had been inserted. If the frequency was too low, then either the wire was slipping in one of the crimps, or the wire had been inserted with a feedthrough pulled slightly out of the end plate, and this had later gone into its hole further. There was one more operation carried out on the sense wires after the frequency tests. It was felt that a knowledge of the actual positions of the sense wires relative to each other within each layer would give a useful indication of how accurately the positioning of the sense wires had been achieved.

This was done using the same telescope as for the frequency tests, but using the vertical measurement scale and vernier on its support stand. These measurements were difficult to make and at the very limits of accuracy of the telescope scale. Measurements were made at the centre of the wires and at each end near the feedthroughs. They indicate an RMS shift from ideal of ~ 70 μm. However, it is hoped that the sense wire positions in the ITC are better than this because only good concentrically bored pins and feedthroughs were used, and the end plate holes were drilled on a more accurate drilling machine at CERN.
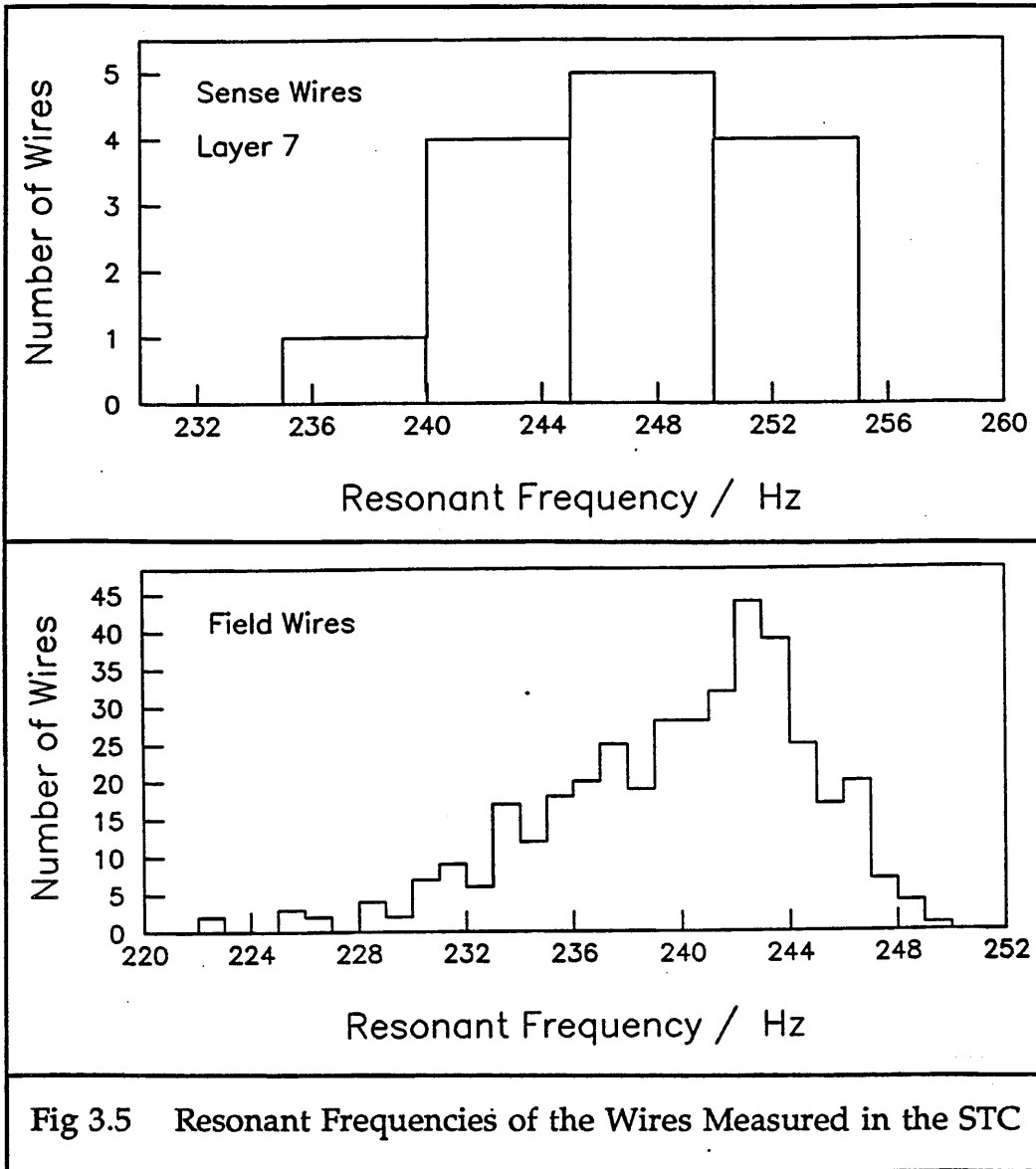
Fig 3.5   Resonant Frequencies of the Wires Measured in the STC

Optical measuring was not used to check the sense wire positions in the ITC. This decision was partly based on the results from the STC, and was also made because of the increased difficulties of measuring the positions of wires not in a plane. For the outer sense wire layers, with many wires behind them, it would have been almost impossible to be sure of focussing on the right wire.

Once the small test chamber had been completely wired and glued, the next stage of assembly was to attach the high tension end boxes.

Throughout the wiring of the chamber and also during the subsequent electrical assembly, a detailed log book was kept of everything that happened to the chamber and each wire in it by whoever was on shift at the time. This was in case there were any problems with any of the wires, such as breakage. If a complete history of each wire were to be available, then diagnostics would be easier and prevention of the problem recurring might be possible.

2.3 Electrical Assembly

On one end of the chamber, four high voltage end boxes were attached to the sense wire pins and some of the field wire pins. Because of the difficulty experienced in getting the correct lead onto the correct pin without crossing them or getting one out of step, a colour coding scheme was implemented for the leads of boxes produced subsequently. The end boxes only provided high voltage connections to the central 64 sense wires. The edge cells were connected to the high tension via a daisy chain of connectors and insulated wire. Once the internal electronics were attached, the whole chamber was sprayed with alcohol to ensure there was no dust or fibres on the wires, and then the perspex case was put on over the top and screwed onto the base plate with strips of glued rubber around the join as a gas seal.

Then it was attempted to connect the outer connectors of the end boxes to the electrical end plate. Unfortunately, although the end box leads had been cut in a former of the right length for the gap in the small test chamber between the two end plates, the leads were cut for small cells. Once they were spread out to reach across the large cells, the whole box was too short and would not reach the outer end plate. The two boxes on the large cells had to be removed, by cutting them open and cutting all the connecting leads off the box. The connectors were then delicately removed from the pins. New boxes with longer leads were hurriedly made and reattached.

Unfortun_ately, these new boxes proved to be too rigid and long for straight lines of cells and once the end boxes were attached at both of their ends they buckled up. However, they operated successfully in this distorted state, so no fresh attempts were made to replace them.

Several pins were bent during the first removal process and one came right out of the plate, leaving a sense wire protruding from the glue in its feedthrough. This pin was successfully replaced with a bored out one, and soldered, but it was felt that any more damage would be for no gain.

Finally, once the chamber was fully assembled, the four preamplifiers were attached to the connectors outside the electrical end plate and fixed between brass rod supports. When the chamber was tested using cosmic rays as a charged particle source, one side of one preamplifier was found to have very low amplification due to a fault in its construction, and so the whole unit had to be replaced.

The final stages of assembly included attaching insulated connectors over each of the sense wire pins at the far end of the chamber from the

electronics, to prevent any worry of sparks from the high voltage points to the nearby field wire pins. The gas end plate was attached to the perspex case at the opposite end from the electrical end plate, and gas pipes and high voltage cables for the edge cells were attached to their appropriate connectors. The chamber was then ready for testing.

2.4   Conclusions from the Construction

Despite the teething problems which occurred while the new wiring techniques were being used and during the electrical assembly, the methods chosen for securing the wires in the end plates were found to be simple, quick and clean. It was found as expected that great care had to be taken when using the aluminium wire to prevent anything touching it in the portion destined to end up inside the chamber, as any kink thus produced was a great weakness, and made the wire liable to break.

Mechanical oscillation of the chamber which forced the wires to resonate was found to be a satisfactory method of checking their tensions. When a tension was found to deviate by more than ~ 20 Hz from the mean value, the wire was removed and replaced. This minimised the likelihood of breaking or slipping of the wires.

The problems experienced with using pins which had too large an outer diameter led to the time saving precaution being taken for the ITC of every pin being tried in an end plate hole before a batch was given to the wiring teams.

Due to the problems experienced with the end boxes, great care was taken to cut the leads for each one to fit exactly one bilayer of cells, with the correct left/right orientation for each end of the ITC, so that they fitted the gap between the end plates. The wires to the connectors were alternated in colour to avoid getting them on the wrong pins, and had a coloured band attached to every other lead to avoid getting them out of step on the pins. This made them easier to attach. Also, techniques were devised for removing the end boxes, but these techniques were not needed on the ITC.

The successful mechanical construction of the small test chamber gave good reason to believe that the assembly of the ITC would be equally successful.

3 Testing of the Small Test Chamber

3.1 Introduction

The small test chamber was built with the intention of operating it in a charged particle beam in a magnetic field at CERN. Before these tests could be carried out, several checks had to be made on the chamber to ensure that it would work reliably during the short period of beam time. These initial tests and the responses of the chamber are described in the next section. Following that, the setup at CERN for the tests is described. Finally, the beam runs themselves are detailed, and problems found during the tests are explained in detail. Conclusions are then drawn for the building and running of the ITC.

3.2 Initial Tests at Imperial College

3.2.1 Checking for Gas Leaks

The whole chamber had first of all to be made gas tight before any tests could be performed. The gas used was argon-ethane 50%-50%, which was passed through a gas mixer rack, although it was premixed, in order to allow the pressure and flow rate to be regulated. From there it went into the chamber at the far end from the electronics, and there was an exhaust pipe at this end too, to take the gas back to the gas rack. It went through a flowmeter, so that it was known that gas was actually going through the chamber. When the gas was turned on, however, no matter how much gas went into the chamber, none came back out. It leaked very badly.

To try to halt the leak of gas, every window was removed and its rubber O-ring carefully cleaned with alcohol and replaced with even pressure of the screws. If a screw was too tight, then gaps appeared a few centimetres around it. The perspex lid was significantly tightened onto the base plate by using steel screws which could be turned hard without shearing. These were replaced one by one with the softer, but non-magnetic brass ones. Finally, every joint in the chamber walls around the end plates and windows was smeared with a silicone sealant. The chamber was now sufficiently gas tight to be operated. The gas was left to flow through it for many hours to flush out all the air.

3.2.2 Raising the Sense Wire Voltage

A check had to be made on the insulation of the sense wires from the rest of the chamber. This was done by filling the chamber with carbon dioxide, applying voltage to the sense wires and gradually increasing it, while measuring the total current drawn by the chamber. The leakage current can be seen in figure 3.6 as a function of sense wire potential.

Fig 3.6   Leakage Current versus Sense Wire Potential with Carbon Dioxide in the STC
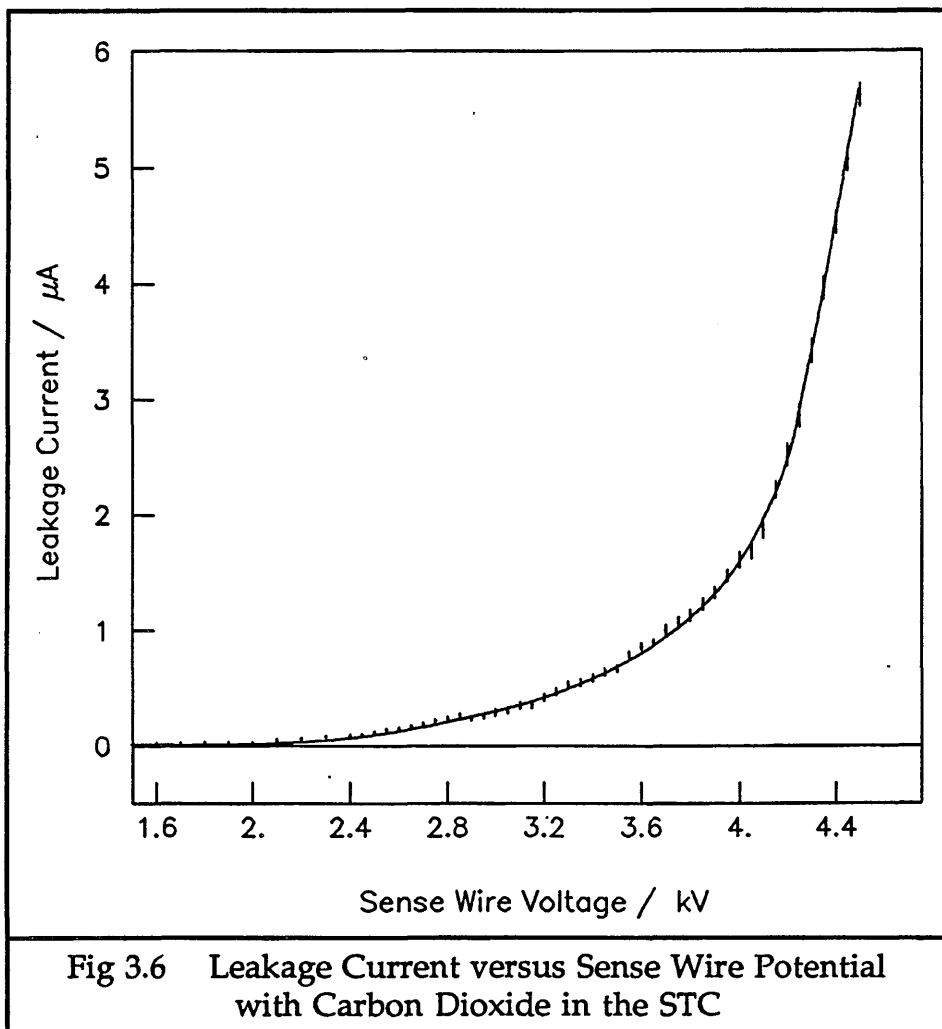
The rapid increase in current after the sense wire voltage reaches about 4 kV is caused by a change in the properties of carbon dioxide. When the electric field gets above about 1.7 kV/cm the drift velocity of electrons in CO_2 starts to increase rapidly. Therefore, the gas starts to break down and the currents are flowing through the gas, and not through the plastic insulators.

3.2.3 Inspecting the Signals at the Discriminators

This piece of work was done using an earlier form of the small test chamber. However, the results have important implications for the running of the ITC, so are presented here. The analogue signals at the

discriminators were observed and recorded. From this an idea can be gained of the range of pulse heights expected in the ITC. How the signals are produced on the sense wires from the electrons in the gas is summarised in Appendix A at the end of this chapter. How the signals travel from where they were generated to the discriminator is described in detail in Chapter 4.

The signals at the discriminator inputs were inspected by sending the analogue signal from the output of the main amplifier card into an oscilloscope. The oscilloscope was equipped with a freeze frame facility, so that drawings could be made of one signal before resetting for the next one. Cosmic rays passing through the chamber were used as a source of charged particles. The gas used was a mixture of argon and ethane from separate cylinders, whose exact ratios were unknown but were approximately 50%-50%. The sense wire voltage was 2.28 kV. A trigger was provided from three scintillators. These were positioned one above and two below the chamber. All had to register a signal within a short time window for a cosmic ray to trigger the data acquisition system. The scintillators were so positioned that the cosmic rays that were registered on all three of them passed very nearly ($\pm \sim 5°$) perpendicularly through the chamber.

Some of the signals seen are reproduced in figure 3.7.

The range of pulse heights seen was from ~ 20 mV to ~ 240 mV, giving a factor of 12 across the range for straight through tracks. For the range of pulse heights expected in the ITC, this range must be multiplied by a factor of ~ 1.7 to allow for the extra length of tracks which cross the cells at a steep $\emptyset$ angle (those with low momenta spiralling in the magnetic field) and by a factor of ~ 5 to allow for tracks which run along the sense wires with a small θ angle. This gives a total pulse height range expected in the ITC of ~ 100.
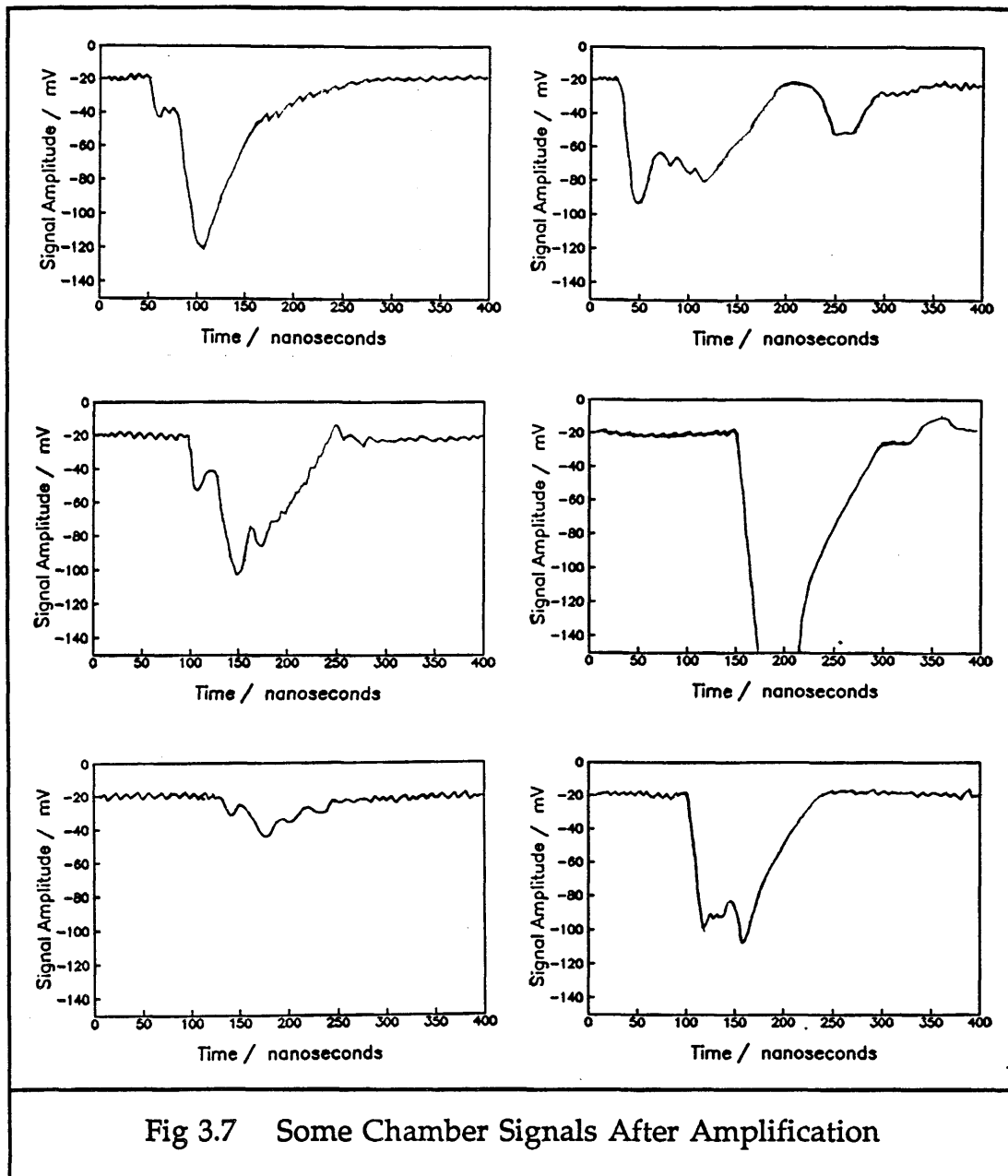
Fig 3.7   Some Chamber Signals After Amplification

3.3   The Setup at CERN for the Tests

The chamber, a small computer and all the equipment needed to produce a trigger and read in and record the data were driven out to CERN in the middle of June 1986. The chamber survived the journey intact and no wires broke or came loose. It was then prepared for the beam time at the start of July.

3.3.1   The Test Beam

The test beam used was in the West Area at CERN, beam number X7. The test area belonged to DELPHI (another LEP experiment) and was just upstream from the ALEPH area. This is because DELPHI had a large test

magnet which was not in use by them at that time.

The beam was produced by syphoning off protons from the SPS collider and colliding them with a target. This produced, for 10^{12} incident protons, a beam of 10^2 - 10^4 tertiary electrons and hadrons, with a maximum momentum of 100 GeV/c. The momentum of the beam could be controlled by computer from the DELPHI control room. Also, the ratio of hadrons (mainly pions) to electrons could be controlled. We chose to have a momentum of 50 GeV/c, with mainly hadrons from a lead absorber. The beam profile could also be controlled by altering the position of the collimators. The beam profile was approximately 2 cm x 5 cm, elliptical, with the larger dimension horizontal. The test beam came in spills, with ~ 300 particles per spill spread over ~ 2 seconds, and one spill every 14 seconds.

3.3.2   The Magnetic Field

The DELPHI test magnet is a very large magnet which can be operated to produce a uniform horizontal field transverse to the beam direction, of up to 1 Tesla. The inner aperture is 128 cm wide, 79 cm high and 204 cm long. This was just wide enough for the small test chamber with the preamplifiers attached to fit in horizontally so that the $\underline{B}$ field ran parallel to the chamber wires. The magnet was controlled from inside the DELPHI control room.

3.3.3   Data Acquisition Methods

The chamber was set up inside the magnet. The gas was piped into it and returned via long plastic pipes to the gas mixer rack about 20 m away, near the control room. The high voltage was distributed to the 4 bilayers and the edge cells via a box next to the magnet, and then all the cables ran from the box across the test beam area, over the wire cage surrounding the area, and into the racks of electronics which were situated just outside the cage. From here, the drift time signals and scintillator time signals passed down a 20 m flat twisted pair cable to an LSI-11 computer at the far end of the control room. The data acquisition system can be seen in figure 3.8.
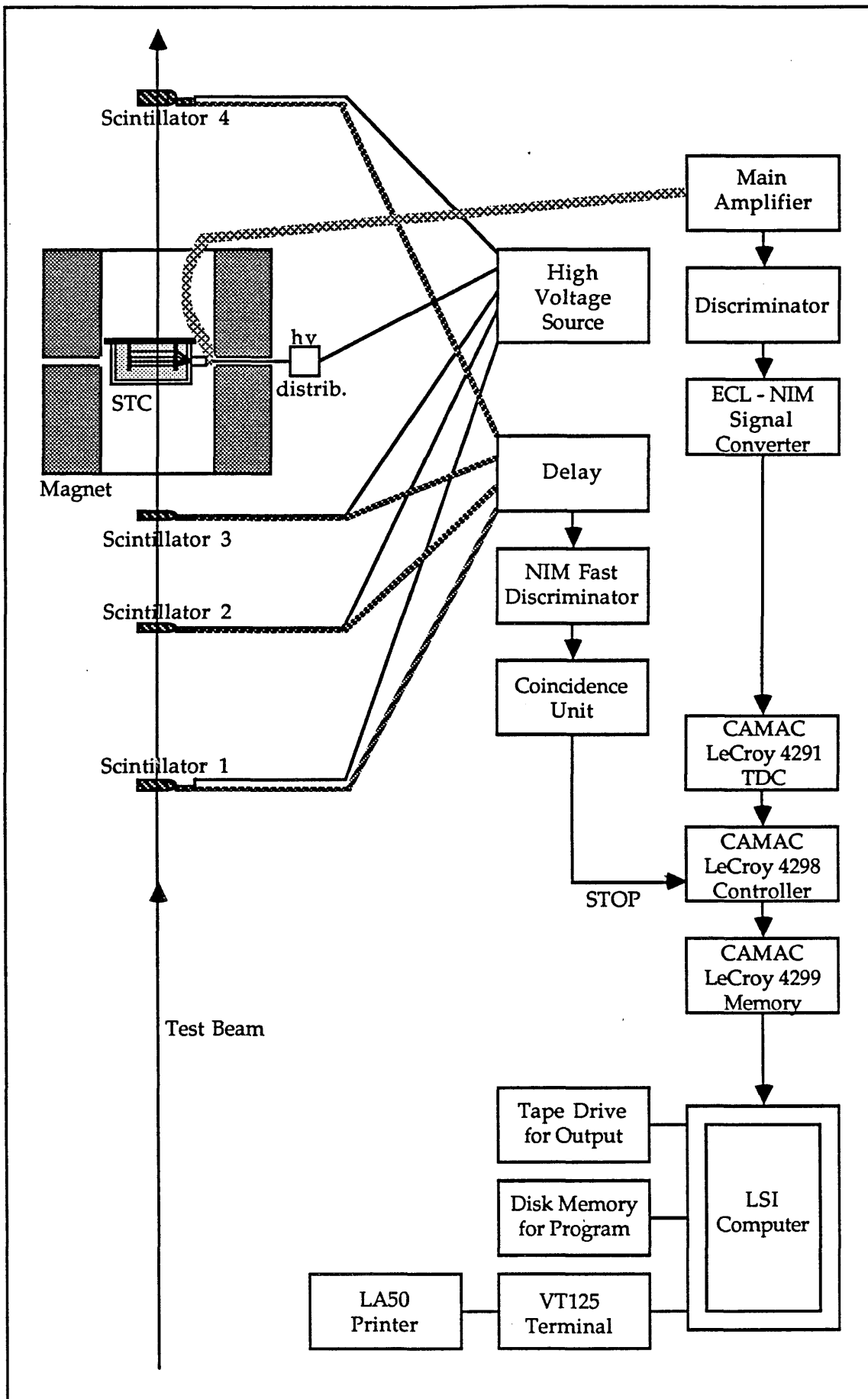
Fig 3.8   The Data Acquisition System of the STC

The triggers from each beam spill were digitised by the LeCroy CAMAC 4291 half nanosecond Time to Digital Converters, or TDCs, read in by the LeCroy 4298 Controller and buffered by the LeCroy 4299 Memory unit. After each beam spill, the LSI read in the data from the 4299 buffer and recorded it on magnetic tape. The computer also filled histograms with some of this data, so that it was possible to see online the number of sense wire hits per trigger, the number of hits per wire overall, the TDC time distributions, and where the tracks actually were in the chamber on a wire map. The reading in and recording of data from a beam spill always took priority over filling and plotting histograms.

3.3.4 The Trigger

The trigger for the data acquisition electronics was provided by four scintillators. These were set up to be in the line of the beam, with three paddle scintillators upstream from the chamber and one slightly smaller paddle scintillator downstream. These all produced a signal ~ 50 ns long, each time a particle passed through them. The four signals had to have a window of overlap several nanoseconds wide to produce a trigger. The first and last scintillators were ~ 14 m apart. Hadrons in the beam travel in air at approximately the speed of light. Therefore, the delay between the signals from the first and last scintillators was ~ 46 ns. The   ⌐ signal from the scintillator furthest downstream always arrived last, and therefore set the trigger time. The arrival of these signals can be seen in figure 3.9.

Fig 3.9   Production of the Signal to Stop the TDCs
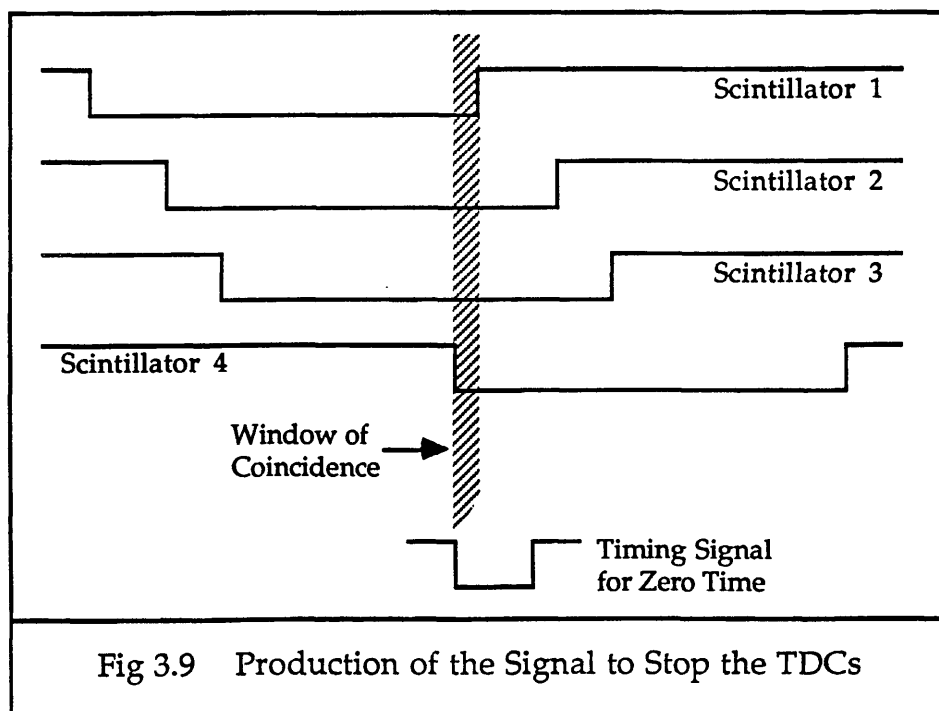
The photomultipliers attached to each scintillator were operated at voltages from 1.35 kV to 1.70 kV.

The TDCs were operated in COMMON STOP mode, so the signal from the scintillator coincidence was delayed by a suitable time to arrive just after all the electron drift times had been recorded.

The timing from the scintillators had a jitter which can be seen for one of the scintillators in figure 3.10.

Fig 3.10   Signal Times from One of the Scintillators
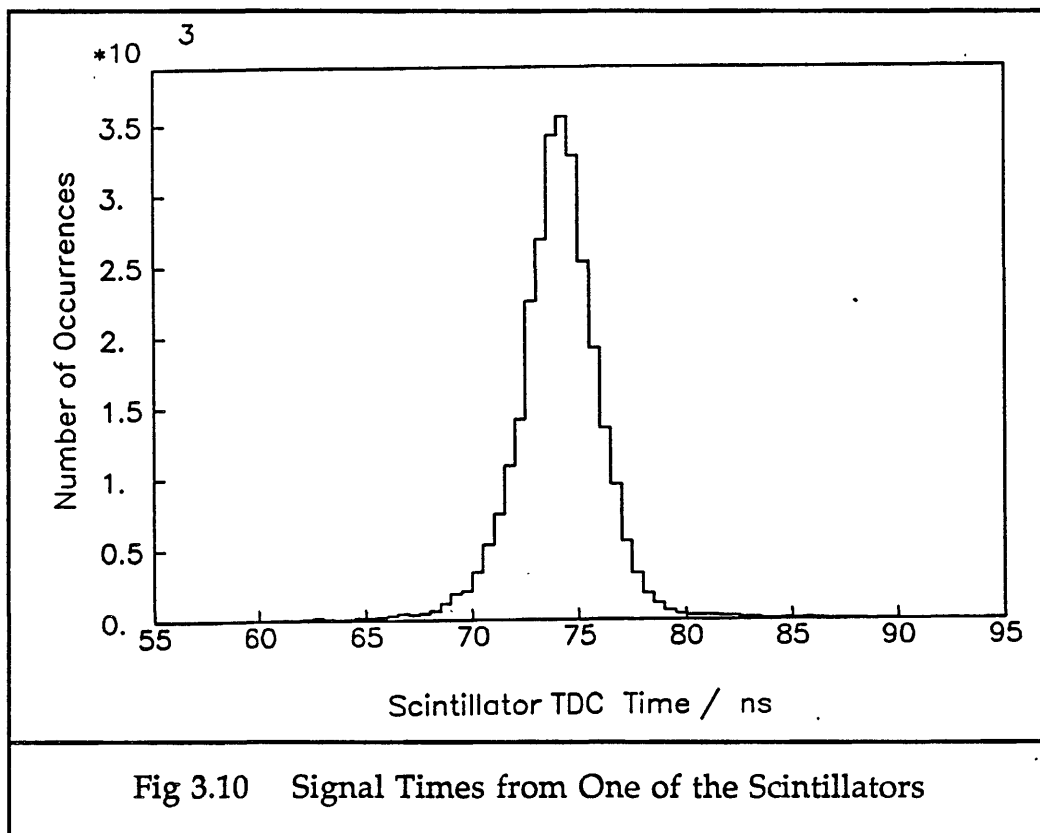
This jitter, with a spread of ~ 3.5 ns, has a detrimental effect on the timing and consequently on the resolution of the chamber.

3.3.5 Plateauing the Chamber

Plateauing the chamber had to be done after each time the chamber was opened up, because the gas became contaminated, and also after each subsequent run until the plateau voltage was stable. It involved measuring the efficiency of several sense wires as a function of the high voltage applied to them. If the voltage was too low, the wires would become inefficient and not record a drift time for every charged particle passing through that cell. If the voltage was too high, then the sense wires would produce hits when there was no track to generate them. The range of voltages in between these extremes forms the operating plateau on which it is desirable to run the chamber.

There are several factors which affect how long the plateau is and at what voltage it starts. The shape of the plateau is determined by which type of gas is used. However, details such as at which voltage the plateau starts are strongly affected by any contaminant impurities in the gas, such as air, from when the chamber had most recently been opened up. It took many hours for the gas to flush through and the plateau to become fairly stable. When there was even a small amount of air in the chamber, the sense wires needed ~ 100 V higher voltage for the chamber to be operated efficiently. This is because the molecules in air absorb a lot of the electron energy and so quench the electron avalanche.

A typical plateau for argon-ethane 50%-50% can be seen in figure 3.11.

Fig 3.11   Efficiency Plateau for Argon-Ethane 50%-50%
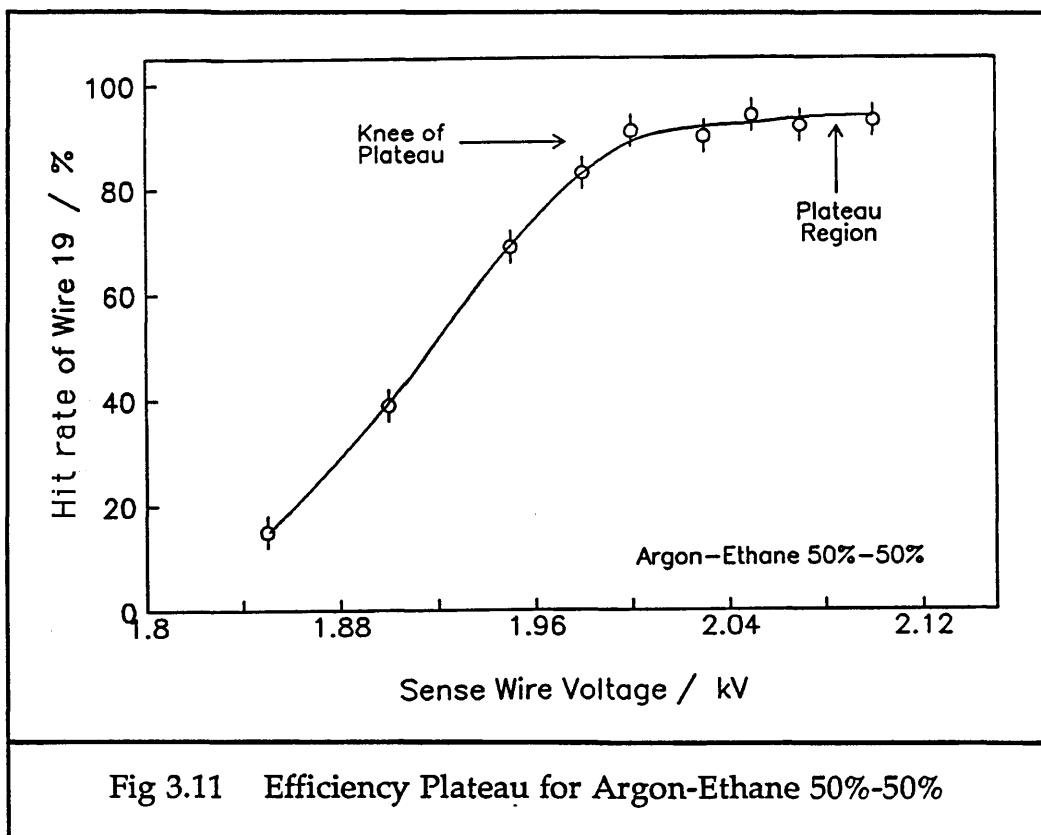
This has a fairly long flat plateau. It can be compared with an example plateau from argon-carbon dioxide 90%-10% shown in figure 3.12. For this run, the track angle ∅ was ~ 28°.

Fig 3.12 Efficiency Plateau for Argon-Carbon Dioxide 90%-10% Track Angle ø = 28°
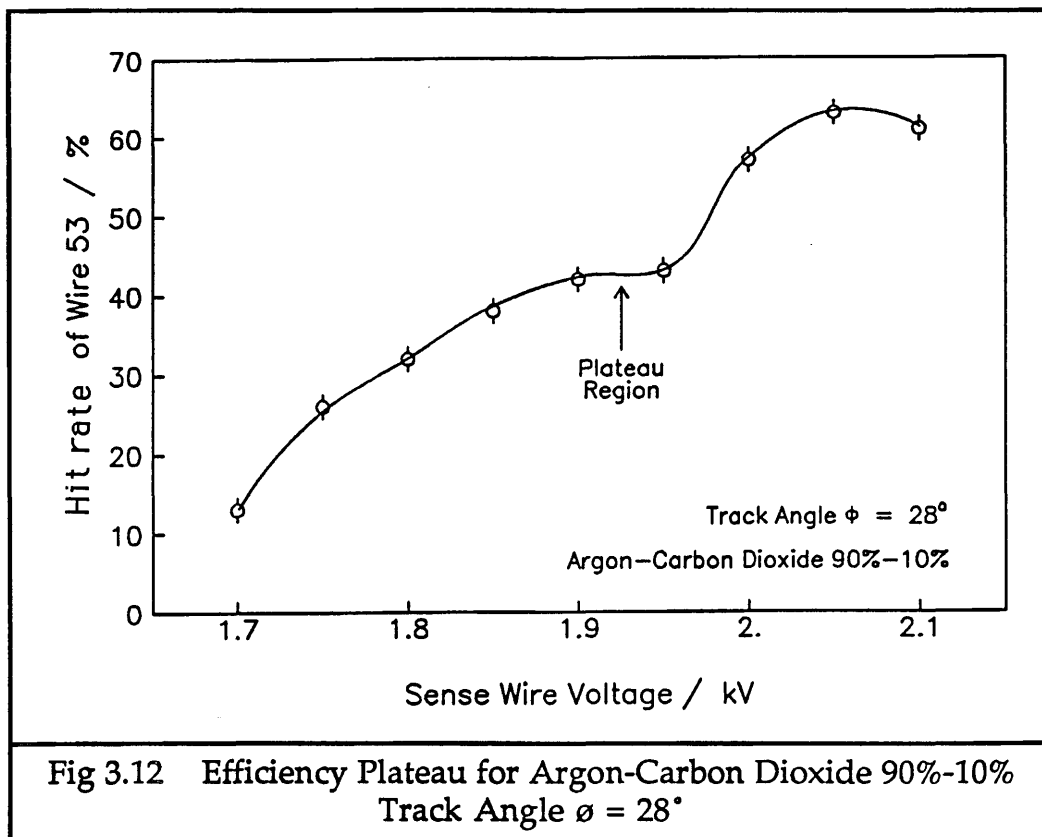
·The efficiencies were found by using two scalers to count hits and triggers for a fixed amount of time. One scaler counted the total number of triggers from the NIM scintillator coincidence unit. The other scaler was attached to the output from one channel on a discriminator board for a wire near the centre of the chamber. This scaler counted how many times that particular wire registered a signal. The ratio of these two counts provides a measure of the efficiency of the chamber. Of course, since not all the beam particles pass through the cell being monitored, the ratio need not be approaching the real chamber efficiency of at least 95 %. However, since the beam profile does not change between the scaler counts at each sense wire voltage, the plateau can still be found by just seeing where the ratio saturates. For example, from figure 3.11, it was chosen to operate the chamber at 2.10 kV, so that the chamber was well above the knee at the edge of the plateau.

3.4   Data Taking and the Problems Encountered

3.4.1   The Series of Tests Made

From 5 pm on Friday 4th July 1986 until 6 am Monday 14th July, there were ~ 153 hours of data taking in the beam. 198 runs were recorded, each with a different set of conditions. There were several variables that could be

84

controlled which affected the behaviour and operation of the chamber. 70 % of the runs were done using argon-ethane 50%-50% as the chamber gas, 18 % used argon-carbon dioxide 80%-20% and the remaining 12 % of the runs were done with argon-carbon dioxide 90%-10%.

Another parameter affecting the resolution of the chamber is the type of discriminator used after the amplification of the signals. Two types of discriminator are under consideration for use with the ITC. These are the dual threshold type and the constant fraction type. The difference in behaviour of these two discriminators has a very marked effect on the z position measurement. This is investigated later, in Chapter 4. However, it was felt that any effect the discriminator type had on the drift time measurements and the r-ø resolution should also be tested. Therefore, the first 35 % of the runs were taken using constant fraction discriminators, and the remaining 65 % used dual threshold ones.

The magnetic field was varied from 0 Tesla up to 1 Tesla, the full strength available. From measurements across this range it was hoped to predict the ITC behaviour in the 1.5 Tesla magnetic field in which it is to be operated. The sense wire voltage was also varied to alter the electric field in the drift cells, with runs on the voltage efficiency plateau, with the voltage below the knee of the plateau, and with it so high that the chamber was rather noisy. The purpose was to see how the sense wire voltage affected the drift relation and the resolution obtainable.

Finally, the last variable which was changed during this set of tests was the angle of the beam to the chamber. The chamber was rotated around a horizontal axis perpendicular to the beam to vary the angle ø of the tracks through the cells. This simulated the tracks of low momentum charged particles in the ITC, coiling around in the strong magnetic field.

It was not possible to simulate tracks with a small angle θ to the beam with the magnetic field applied, since then the magnetic field would not run parallel to the chamber wires as in the ITC.

The results from these tests will be presented after the problems which occurred during the running have been described and the solutions explained.

3.4.2 Problems Found During the Tests

The tests did not go smoothly. There were many problems, some of which were fairly easily solved but had important implications for the ITC. Others were very difficult to solve, lost much beam time and greatly reduced the quality of the data taken.

3.4.2.1 Preamplifier Problems

During the initial setting up and testing of the ITC at CERN, before the magnet and beam were available, problems were encountered when attempting to "autotrim" the TDCs and associated cables. An autotrim test is done by the Controller unit in order to calibrate out any differences in the readout cable lengths. The Controller sends out a signal which is fanned out to each of the preamplifier channels. From there, the signals travel back to the TDCs along the usual readout routes. The time of arrival of each signal is measured by a TDC channel, and any offset between these times due to uneven cable lengths is corrected by the Controller which produces calibration times. These times are internally incorporated into every time read out subsequently, until another autotrim test is performed or until the power for the unit is switched off, when the calibration times are lost. When the first autotrim test was performed on the STC readout system at CERN, four of the channels, all in one layer of the chamber, on one side of a preamplifier, twisted pair cable and one discriminator card, would not autotrim to produce a constant start time and end of range time. These channels consistently overflowed, underflowed, or produced bad time values. The problem had to be caused by either bad connections somewhere in the circuit, causing the signals not to arrive at all, or by something oscillating, causing the timing signals to arrive at the wrong times. All connections were checked between every part of the circuit, and the problem was isolated to the preamplifiers. When a square pulse was injected into the preamplifiers from a pulse generator and the analogue output checked from the TDCs, all channels worked except eight, which formed one layer in the chamber, and these showed nothing at all. However, most of these produced a digital output, some of which were delayed. After inspection of each signal at every stage through the system, it transpired that a small differentiated signal was actually being produced on the bad channels, which was sufficiently large to produce a digital signal. Also, reflections were seen on some of the channels' digital outputs. Many of the channels had 3 - 4 ns noise and jitter on the digital output. This can be seen in figure 3.13.
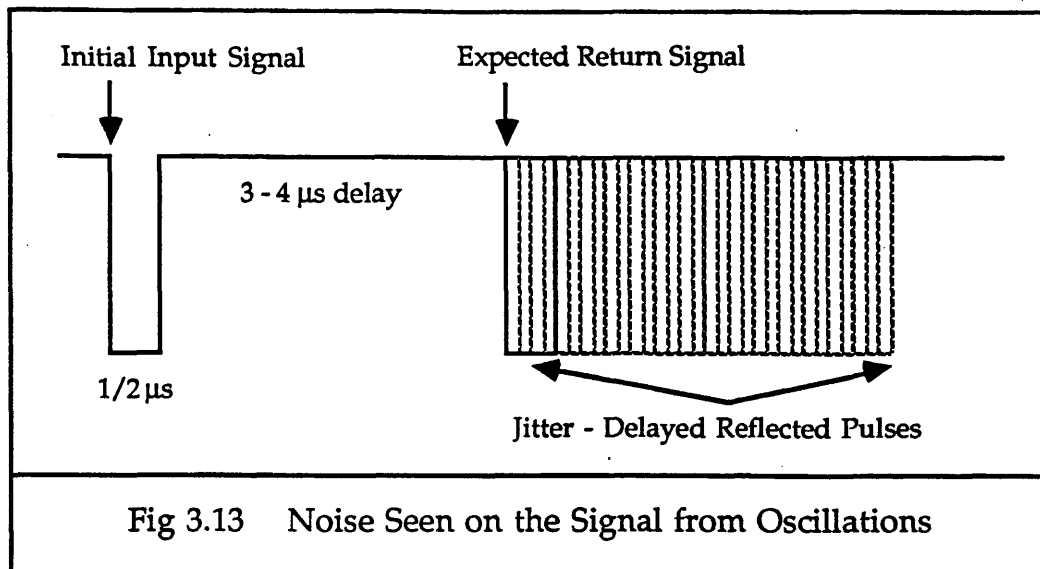
Fig 3.13   Noise Seen on the Signal from Oscillations

The symptoms experienced turned out to have two causes. The first was that one of the connectors in the cable to one of the preamplifiers for the calibration signal was broken. This meant that there was a short circuit, and the channels on that side of the board were only being calibrated by a reflection of the calibration signal on the other side of the preamplifier. This damaged connector was replaced. This cured the reflections seen on some of the signals, the poor autotrimming and the lack of analogue signals on one set of eight channels. However, it did not remove the delayed jitter and noise seen on nearly every channel. This was caused by oscillations in the preamplifier circuits. Some of the amplified signal was feeding back at low frequency and causing the oscillations. This was greatly reduced by a modification being made to every channel of the preamplifiers. A capacitor was soldered on between the signal line and earth, which helped to stabilise the circuit. Adding the capacitor reduced the gain by ~ 15 %, and the oscillation was reduced by a factor of between 2 and 3. During the soldering of the extra capacitors onto the preamplifier boards, one of the channels was damaged. Consequently, no times could be read out from wire 21, which was in the centre of a large cell layer.

It was important that the problem of preamplifier oscillation was identified and the design of the preamplifier changed to correct it before the ITC was assembled. There is no access to the preamplifiers on the ends of the ITC for removing them to make modifications, once the cable supports are in place.

3.4.2.2 Leakage Currents

At the same time as the problems with the signals from the preamplifiers were being diagnosed and treated, there occurred a very major breakdown of the STC itself. The chamber had argon-ethane 50%-50% flowing through it, and the sense wire voltage was being raised slowly over many hours. It had reached 2.25 kV when suddenly and unexpectedly the chamber tripped due to a current greater than the threshold of 10 μA being drawn. The behaviour was checked and the current drawn was found to be Ohmic in nature, with ~ 0.8 μA being drawn for every 100 V applied. The chamber was left with 500 V on the sense wires and drawing ~ 4 μA, but after a few hours it tripped again. The chamber continued to behave like this sporadically over the next two days, with the leakage currents coming and going. The currents were isolated down to layers 3 and 4, the bilayer of large cells in the middle of the chamber. This layer contained a pin which had been pulled out of the end plate when removing the end boxes, and which had been replaced with a bored out pin soldered in. It was thought that maybe the heat from the soldering iron had damaged the feedthrough. This had happened before with an old batch of feedthroughs in an earlier test chamber. This pin was the penultimate one in its sense wire layer, and so fairly accessible through one of the windows in the perspex case. Therefore, it was decided to remove the high voltage connector from it and see if the current drawing problem was solved.

Before the tools arrived from London to do this, the chamber tripped again, and this time the current was found to be coming from layers 1 and 2, the other bilayer of large cells. This current also had markedly Ohmic characteristics, with ~ 1.5 μA being drawn for every 100 V applied to the sense wires.

Since current was now being drawn by two bilayers, the theory about the soldered pin was abandoned. Instead, it was decided that there may have been some dirt in the chamber which was connecting the sense wires to earth or creating very high electric fields in the gas near a sense wire, and causing the breakdown. It was decided to apply a negative high voltage to the sense wires and attempt to burn off anything inside the chamber which should not have been there. The gas was also changed to just argon, which as an inert gas, would remove the possibility of the previously present ethane from breaking down or polymerising and allowing a current to flow through the gas. Unfortun_ately, applying a high negative voltage of up to 1 kV had no effect on the leakage currents, which were still ~ 25 μA in total.

Various strategies were now proposed and tried out to clean the

chamber of any hairs or dirt that may have got in. The chamber was removed from the experimental area during a period of access, and inspected. A large number of small white fibres were seen on the wires. It was not known what these were or where they had come from, but maybe they were from the gas pipes, or from the cotton wool buds which were used to clean glue off the end plate during the gluing. It was decided to attempt to blow these off the wires with a jet of gas, while the high voltage was still on the sense wires, so it could be seen if the leakage current dropped when they went. The preamplifiers were removed, and a window in the perspex case opened. However, when the high voltage was applied to the sense wires, sparks were seen between the end plate and the chamber frame. The electrical end plate had only been earthed via the preamplifiers, and was now 250 V higher than the earthed base plate and frame. This sparking was prevented by connecting the electrical end plate to the frame with a roll of aluminium foil. Making this connection also reduced the noise in the preamplifiers later, with an improvement of x 5 for the worst channels.

A pipe was then taken from the argon source, with a hole cut in the side of it near the end, and the end was sealed off. It was slid carefully down the inside of the chamber through the open window. This produced a jet of argon which could be sprayed across each layer of cells from end to end of the wires, in an attempt to dislodge the white fibres. While this was being sprayed, the current fell gradually and then dropp_ed suddenly so that it was negligible on the meter. It was hoped that the fast fall to nearly nothing was caused by the white fibres falling off the wires. The chamber was closed up and left with 500 V on all the sense wires and argon flowing through it to flush out all the air. There were negligible leakage currents. After a few hours, slowly ramping up the sense wire voltage, the chamber started to draw large leakage currents again. The processes of using just argon, applying a negative voltage and spraying the wires with the gas pipe were repeated without success. The cylinder of premixed argon-ethane was replaced with gas from two separate cylinders for a while, in case the premixed cylinder was contaminated in some way. It was also attempted to clean the wires with alcohol and a fine nozzle spray bottle was used to fill the chamber with alcohol vapour. The drops of alcohol condensed on the wires and ran down to one end, because the chamber was supported at a steep angle. However, even this did not stop the chamber from drawing current.

Individual white crinkly fibres could be seen inside the chamber connecting the sense wires to the field wires. It was believed that these were

causing the leakage currents. All previous attempts to remove them had failed. A final attempt was made to move one particularly large one, using a long piece of solder, but the fibre seemed to be stuck in a blob of glue on the guard wires. It was eventually moved so it only touched a field wire, but still the chamber would not function properly.

Finally, it was decided to find out if individual sense wires were drawing current, and if so, to disconnect them from the high voltage. This was done by cutting off the plastic covers on the sense wire pins at the far end of the chamber from the electronics, and applying a probe to the bare pins. The probe had ~ 300 V on it from the high voltage power supply, and the current trip was set high, at 125 μA. One wire was found to cause a current to be drawn, but only sporadically, when wobbled with the probe. The feedthroughs of this wire and others were then inspected using a magnifying glass and a probe light. A wide crack was seen on the feedthrough of the wire drawing current, which ran from the open end of the feedthrough all the way down to the plate. Two other feedthroughs were also then found to have hairlines down them. The cracked feedthrough can be seen in figure 3.14.

Fig 3.14   Cracks Running Along a Feedthrough from the STC
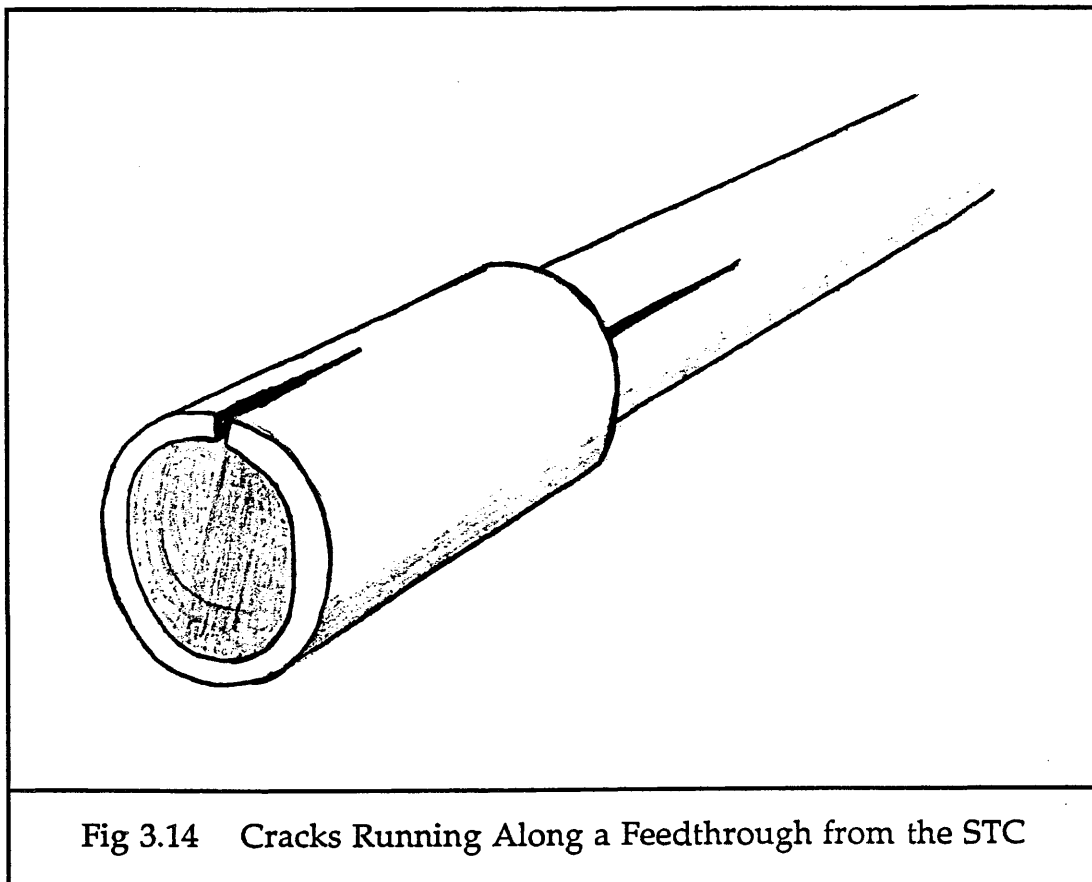
To deal with this wire, the chamber was opened up near the end boxes, and the high voltage lead was pulled off the wire with the cracked

feedthrough. The high voltage connector was covered in insulating tape and the chamber resealed. Gas was passed through it and the sense wire voltage was slowly ramped up. However, within a few hours the chamber tripped again with more leakage currents. The leaking bilayer was disconnected and the chamber was used for the first time in the magnet and beam, because the beam time allocated for use had started. Two days later, the chamber tripped again. The current drawn was not Ohmic, but flickered, and can be seen in figure 3.15. This looked like the sort of current drawn when carbon fibres are growing on the wires, conducting and then breaking off and falling away. No carbon fibres were seen, however.

Fig 3.15   Leakage Current Drawn by the Small Test Chamber
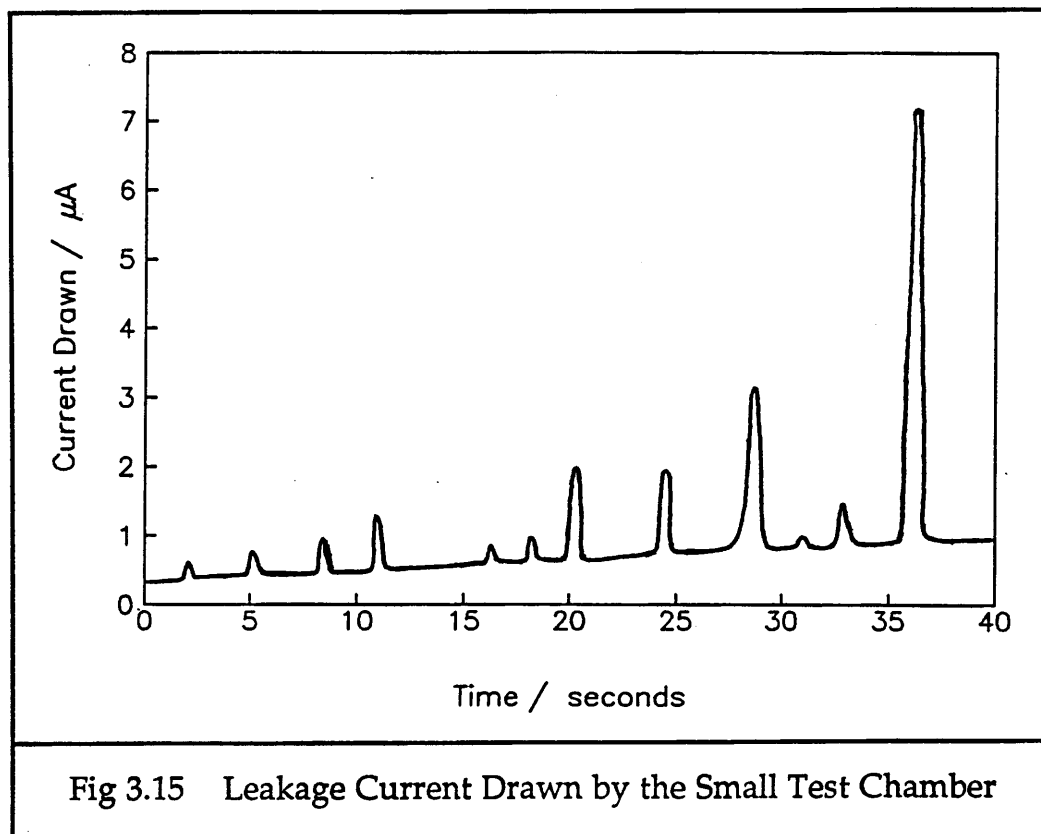
The layers containing the disconnected wire were now also drawing current. After a few hours, the current drawn became Ohmic again. The chamber was opened up and two offending wires were identified and disconnected. In doing this, the high voltage connector on a neighbouring wire was accidentally pulled and this later caused the wire to break. The broken wire was removed completely from the chamber.

This process of the chamber drawing current, and wires being identified and removed from the high voltage supply was repeated until it became evident that a lot of beam time was being lost not only from fixing the chamber, but also from having to allow many hours for the air to be flushed out of the chamber afterwards. For all the work done, more and

more feedthroughs were breaking down in the four large cell layers. The rate of breakdown can be seen in figure 3.16.
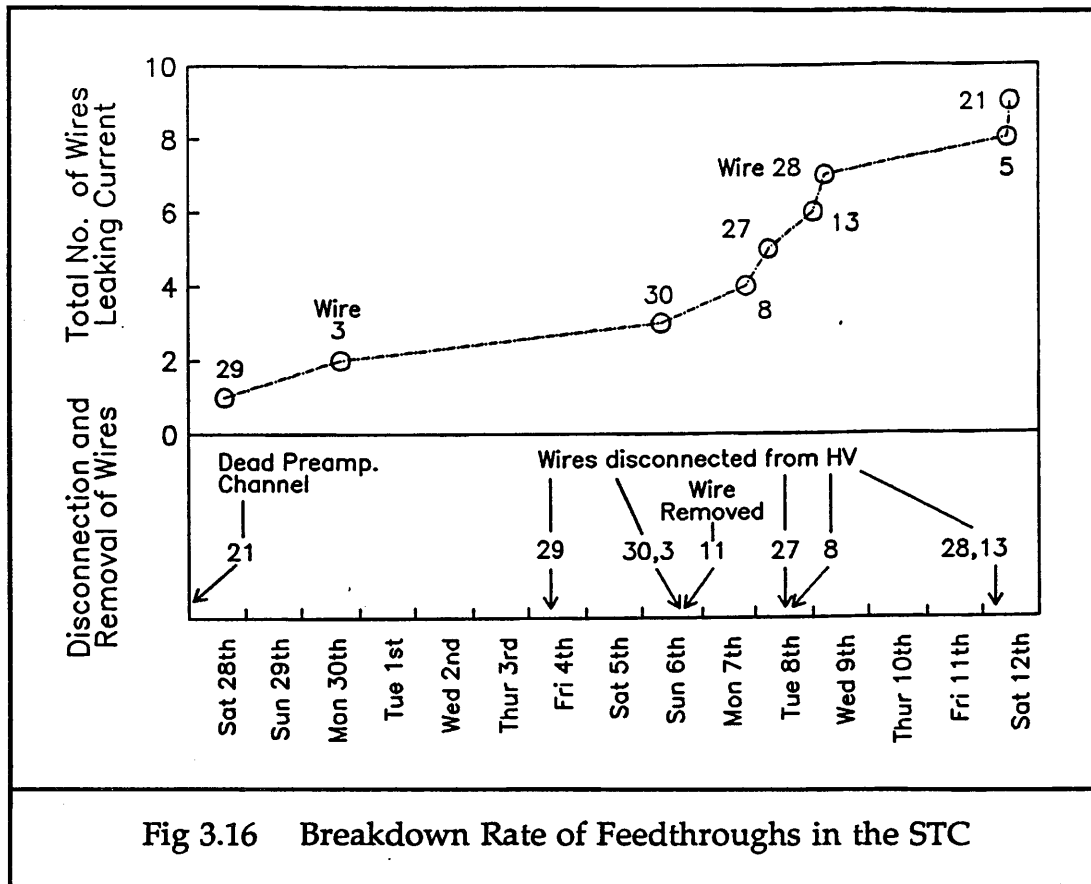
Fig 3.16   Breakdown Rate of Feedthroughs in the STC

Eventually it was decided not to fix any more wires, but to run the chamber with just the 4 layers of small cells operating.

The position in the chamber of the wires which were disconnected from the high voltage is shown in figure 3.17. It can be seen that they were unfortun.ately rather central to the chamber, and so considerably degraded the quality of measurements made on the remaining large cells.

This problem with cracked feedthroughs and leakage currents caused much concern. It could not be allowed to happen in the ITC itself. Many theories were put forward as to why feedthroughs in only the large cells were breaking down and not those in the small cells. The end boxes which had been removed and replaced were on the large cell layers. More problems had occurred on these layers with too large pins, since it was not known then that not all the pins were too large.

Fig 3.17   Position of Dead Wires in the
           Small Test Chamber

Eventually the cause of the cracks in the feedthroughs was identified. When a field wire pin had got stuck in the end plate, after a mistake in the wiring, and had been forced out, the metal shards remaining had been cleaned out by spraying the proprietary cleaner Inhibisol through the hole. This fine spray covered the plastic feedthroughs each time, as well as the hole it was aimed through. Tests at Imperial College of spraying the feedthroughs with Inhibisol, after the leakage problems occurred, subsequently showed that the plastic reacted with the Inhibisol and cracked very rapidly.

Fortunately for the small chamber tests, better batches of pins were probably used for the small cells. Because the wirers were more experienced, and had less problems with the pins, there had been little or no need to use the Inhibisol on the second half of the chamber to be wired.

The main conclusion drawn for the construction of the ITC was to avoid the use of Inhibisol completely. Also, the pins used were chosen with smaller outer diameters, which meant that not only was it quicker to do the wiring, but also that when mistakes were made, it was easier to remove the pins from the plate.

As a corollary to this section of problems, diagnostics and solutions, when the STC was returned to Imperial College, the 4 layers of sense wires in the large cells were cut out and the feedthroughs at each end of the

chamber were removed and inspected. A large number of cracked feedthroughs were found. It was suggested that the fat pins in the feedthroughs added stress to the plastic and contributed to the cracking. This was tested by measuring the outer diameter of the pins in the 42 feedthroughs which had cracked in the large cells of the STC, and comparing these with the outer diameters of the pins from the feedthroughs at the other end of those wires. The two distributions can be seen in figure 3.18.
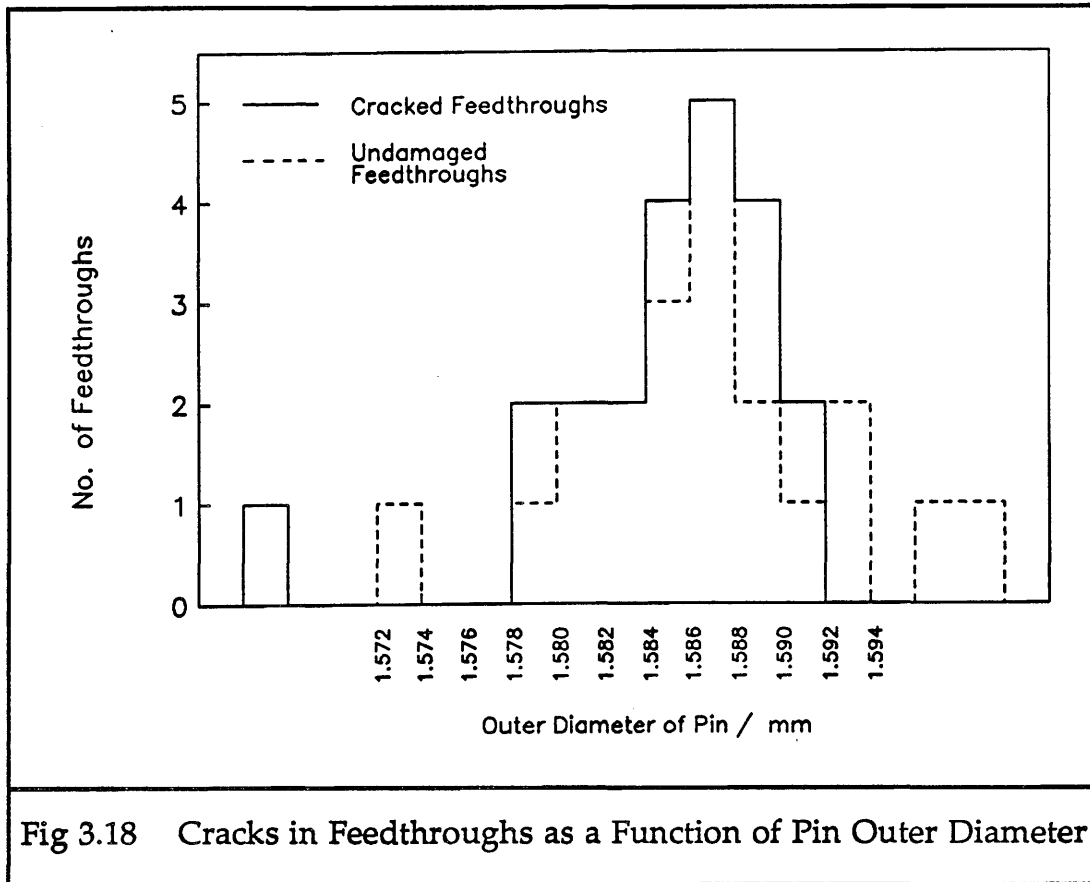
Fig 3.18   Cracks in Feedthroughs as a Function of Pin Outer Diameter

As can be seen in figure 3.18, there is no significant difference between the two distributions of pin outer diameters for the cracked and the undamaged feedthroughs. Therefore, the fat pins did not directly contribute to the cracking of the feedthroughs, only indirectly, since the Inhibisol needed to be used more often for these pins. Some of the feedthroughs which had leaked current were found to have a small round hole through the crack, from the inside of the feedthrough right through to the outside, like a lightning burn. This was ~ 1 mm in diameter, and had been gold plated on its inner surface from the gold plating on the pin. There were 6 feedthroughs with these burn holes.

3.4.2.3 Gas Leaks

When compared with the problems of leakage currents as described in the previous section, the gas leaks of the chamber were relatively unimportant. Every time the chamber was opened to clean the wires, or remove a sense wire from the high voltage supply, air got into the chamber, and the gas seals around the windows were weakened. This has no consequences for the ITC, which has no windows, and cannot be opened up. However, for the STC, it meant that because of the gas leaks there were many hours spent with the chamber gas contaminated, when no useful data could be taken. Each window and its O-ring had to be cleaned with alcohol and resealed with silicone sealant. This took a long time and was not always very successful. Consequently, during some data runs, the chamber voltage operating plateau was shifting, and the chamber was very inefficient if the voltage was not raised many tens of Volts above its nominal position for uncontaminated gas.

3.4.2.4 Moving the Timing Scintillator

There was one more problem experienced which affected the quality of the data taken. This was due to the magnetic field and the position of the timing scintillator. The timing scintillator was the one furthest downstream in the beam. This was because its signals arrived last, due to the time of flight of the particles in the beam between scintillators. However, when the magnet was switched on, it bent the path of the beam downwards. This meant that a scale of positions for this scintillator had to be found and marked onto its support. Its height then had to be changed according to the scale, every time the magnetic field was altered. If this was not done, then the trigger did not operate on individual particles which had just left one track through the chamber, but on the beam halo. This resulted in these mistriggered runs having very erratic STOP signals for the TDCs and lots of hits.

3.5 Conclusions from the Tests

The most immediate conclusion to be drawn from the tests was from the cracked feedthroughs and leakage currents. It would be a complete disaster if this were to happen in the ITC. The chemical spray cleaner Inhibisol was banned from use anywhere near the feedthroughs. It is now a year after the wiring of the ITC and so far similar problems have not occurred.

The problem of oscillation experienced with the preamplifiers led to modifications being made in the circuit which reduced this. This was easy to implement because the main production of the preamplifiers had not started. Only a few prototypes had been specially built for the STC.

General conclusions may also be drawn from the tests. Apart from the problems with the leakage currents, the chamber operated very well in the test beam and magnetic field. Histograms of data were produced online whilst runs were in progress, and from these it could be seen that the chamber ran cleanly without excess noise or other problems. The readout electronics operated well as a system. In total, about 4 million triggers were recorded during this short period, despite the problems encountered.

The following section will describe the aims of the data analysis and how it was carried out.

4   Analysis of the Test Data

4.1   What can be Obtained from the Test Data ?

The single most important result that can be obtained from the test data is how best to parameterise the drift relation of the electrons in the electric and magnetic fields. If a form of this relation can be found which gives satisfactory resolution across the whole of the cell, then this can be directly applied to the ITC without having to repeat the work with the data from the ITC once ALEPH is running.

Other results that can be obtained from the test data are things like finding corrections to the wire coordinates for comparison with the measured offset of the wires, and investigating the differences in the chamber resolution produced by using different types of discriminator. The behaviour of the chamber as a function of track angle through it can be evaluated. The methods used to obtain these results will be presented in this section, together with the investigations into the drift relation.

4.2   Variables Used in the Analysis

The variables which distinguish one data run from another are :
    a)   gas mixture in the chamber
    b)   electric field in the cells

c) magnetic field in the cells

d) discriminator type used

e) threshold level on discriminator

f) track angle through chamber

However, none of these is used directly in the analysis. For every run, certain pieces of information were recorded and are used in the analysis. For each trigger, these are :

a) scintillator times which produced the trigger

b) which wires were hit

c) time recorded on the TDC for each hit

d) total number of hits

This information allows detailed reconstruction of the tracks, and from this, the way the chamber performed can be evaluated.

4.3 How the Fitting Program Works

The fitting program has an iterative structure and works in two distinct stages. The first stage involves reading through the data, and for every trigger, sorting the data and separating the scintillator timing hits from the drift times in the cells. With the drift times, a track is found and fitted, using a weighted fitting method to determine the ambiguity of each hit in the cells. An individual zero time is then found for the track, to counteract the intrinsic jitter of the scintillators. This process is repeated for all triggers, with cuts being applied to the data to remove hits from noise, leaving a final set of triggers for which well-fitting tracks have been found. The second stage of the process takes all the drift distances and drift times from these good tracks and finds the best fit drift relation of the form under investigation. The process is then repeated, using the latest drift relation to generate the drift distances from the drift times. The resolution of the chamber slowly improves with increased number of iterations, although the rate of improvement gradually slows down. All subsequent results show values calculated after 10 iterations.

Figure 3.19 shows the overall structure of the fitting program.

Initialise - open files, read in run parameters, chamber parameters, drift relations, cuts, output wanted.

Set up histograms (if requested)

Zero everything to do with overall iteration

Read in next event

Zero everything to do with track fitting

Sort out scintillator times.

Unpack data

Make first cuts - TDC times greater than lower limits
Number of hits in range wanted

Fit track

Make second cuts - Tzero within limits
Track angle ø within limits

Store drift distances for later fitting

Print out event values (if requested)

Calculate resolutions and efficiencies

Find the best fit drift relation

Print out iteration results

Output histograms (if requested)

Fig 3.19   How the Fitting Program Works

4.3.1   Track Fitting

Track fitting forms the first phase of the analysis program. It can be considered to be divided into several distinct stages. In the program, these are each written as separate subroutines. The stages of finding and fitting a track can be seen in figure 3.20. The tracks to be fitted are all straight lines over the short length of the chamber, even when the magnetic field is at 1 Tesla, due to the high particle momentum.

```
┌──────────────────────────────────────────────────────────────────┐
│   Make first fit through all hit wire coordinates                  │
├──────────────────────────────────────────────────────────────────┤
│   Discard hit wires which are too far from track                   │
├──────────────────────────────────────────────────────────────────┤
│   First cuts - Discard event if there are too few hits left        │
├──────────────────────────────────────────────────────────────────┤
│   Make weighted fits to wire coordinates and hit positions         │
│   using linear drift velocities to get the ambiguities             │
├──────────────────────────────────────────────────────────────────┤
│   Find the best Tzero                                              │
├──────────────────────────────────────────────────────────────────┤
│   Make best fit using full drift relation, best Tzero and track angle │
├──────────────────────────────────────────────────────────────────┤
│   Calculate residuals                                              │
├──────────────────────────────────────────────────────────────────┤
│   Second cuts - Discard hit with largest residual, if larger than limit given │
└──────────────────────────────────────────────────────────────────┘
```

Fig 3.20   Track Fitting Method for Tracks in the Small Test Chamber

This process has been chosen as the most straight forward one of several tried. A linear drift relation is used for the whole process except the last fit, when the full drift relation under consideration is used.

4.3.1.1 Identifying the Hits Associated with a Track

Throughout the runs, there are between 4 and 8 layers of the chamber working, and almost every trigger has only one track in the chamber. Therefore, initial cuts are made on the number of hits in a trigger, before the track fitting starts. Due to the very poor quality of the data recorded from the large cells, which will be demonstrated later, it has been decided not to use any of the drift times from the large cells in the track fitting. They bias the results from the small cells, and no very useful knowledge is obtained about the behaviour of the large cells. Consequently, analysis is only carried out using the four layers of small cells in the chamber. One cut used in the program is that every trigger must have at least 4 hits before attempting to fit a track. An upper cut at 10 hits is also made to prevent time wasting on very noisy triggers. For steep angled tracks where there are 2 or 3 hits per layer, this upper limit is increased to 16.

The TDC times are also checked, and if they are smaller than some set minimum, indicating a very long drift time which appears from the TDC time distribution to be part of a noisy tail, then these times are not included in the count of whether there are sufficient hits. The value of this minimum varies with cell size, magnetic field applied and discriminator type.

Once a trigger has passed these cuts, the track finding is very simple. Since there is almost only one track per trigger, and this passes straight through the chamber across the sense wire layers, it is unnecessary to use a very sophisticated algorithm to associate hits with the track. It is also very cumbersome and unnecessary to use even the wire layer information. The fastest, most straightforward and thorough way of finding an initial approximation to where the track is, is to assume that every hit belongs to the track and fit a straight line through the sense wire coordinates of every hit wire. A cut is then made on any hit wire which is further than 10 mm (for the small cells) from the track. A cut of 13 mm would be suitable for the large cells, if used. These distances are a little larger than the maximum drift distances in each cell size. This cut removes less than 1 % of the hits in a standard run with the magnetic field on. An example of this can be seen in figure 3.21.

After this process, the event with its remaining hits is passed on for track fitting.

Fig 3.21   Removal of a Noise Hit from the Set of Hits to be Used for the Track Fitting
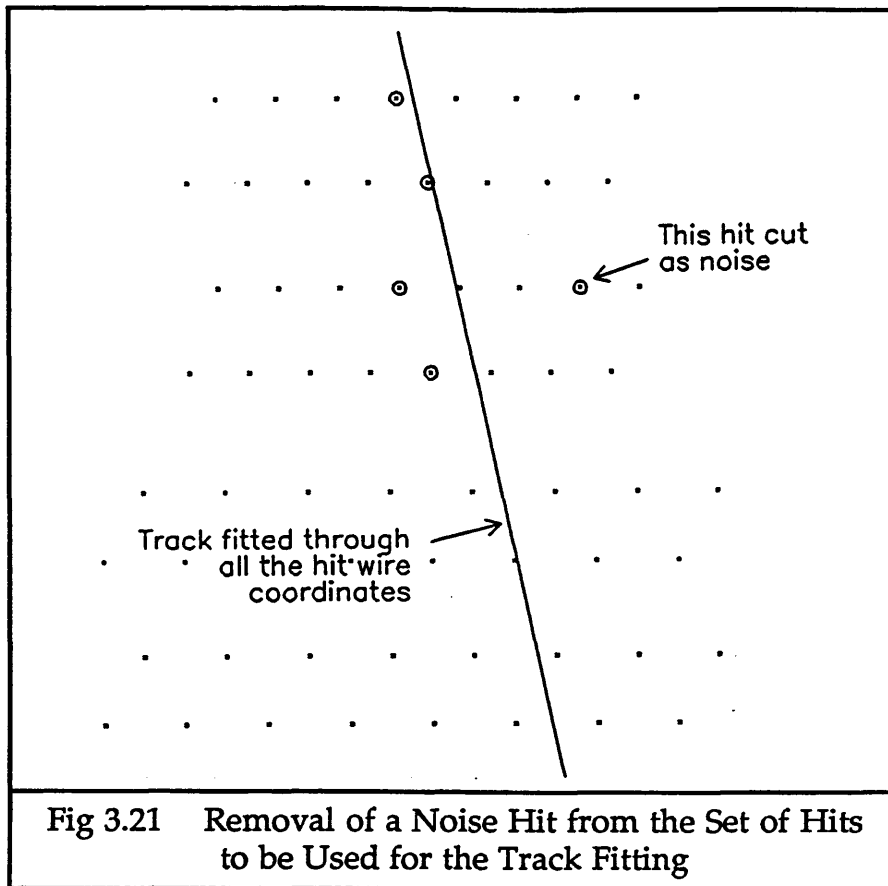
4.3.1.2   Choosing the Hit Ambiguities

Due to the design of the drift cells, every hit has an associated ambiguity, since it is not known through which side of the cell the charged particle passed. It is especially difficult to determine the ambiguity when the track lies very close to the sense wire, when a small shift in the zero time for instance, might shift a track enough for it to appear to swap sides for these hits. Also, the drift times in cells where the track was very close to the sense wire have an intrinsically larger error than those times in the middle of the cell, due to primary ionisation statistics. Consequently, special care must be taken with hits with very short drift times. Misassigning the ambiguity very easily causes the residual distance between the hit position and the fitted track to be too large, and the hit is rejected later.

A sample track with reconstructed drift distances can be seen in figure 3.22. The circles drawn around each hit wire, with radii equal to the calculated drift distances, indicate that the signal in the cell could have started from any position at that distance from the wire. Since the track direction is known to within a few degrees, this reduces the possible track coordinates to two positions on opposite sides of the cell. All the possible hit positions are indicated with small crosses. The best fit track is shown. Two hits from large cells are shown included in this track. The other two large cell layers have no high voltage applied, and so produce no drift times.

101

Fig 3.22   Track Fitted Through Hits, showing All
Possible Positions due to the Ambiguities
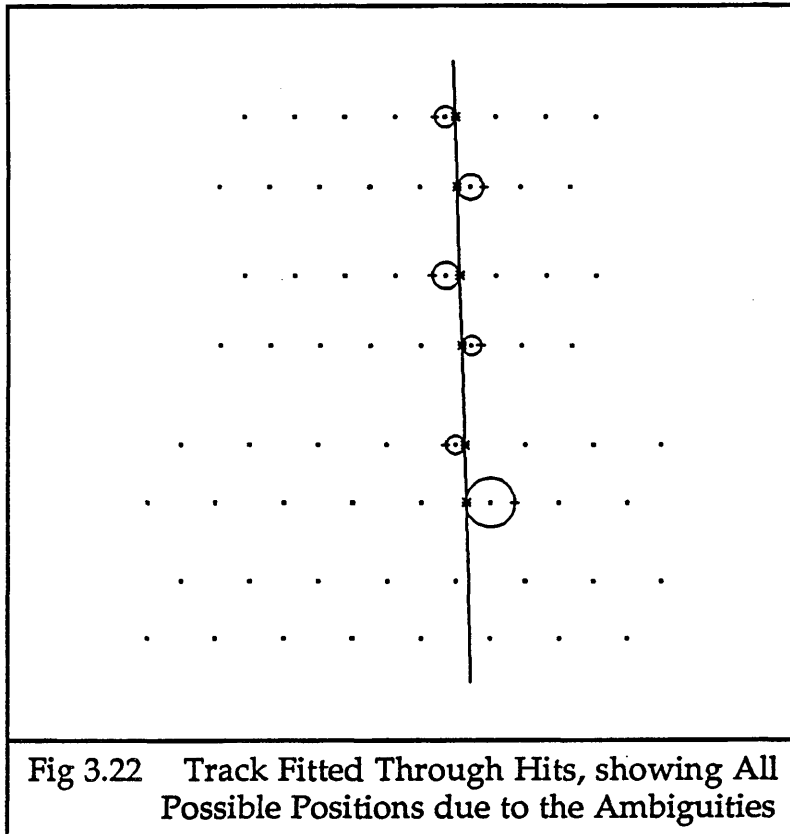
The method used to determine these ambiguities uses a series of weighted fits. A track is fitted three times during this process.

Stage 1

A straight line fit is made through the wire coordinates, weighting most heavily those wires with a very short drift time. The track must lie fairly close to these wires, and consequently the ambiguities for those wires with long drift times are found. The weighting function used is :

$$Weight = \frac{1000}{(Resolution^2 + Drift\ Time^2)}$$

The resolution factor, set arbitrarily at 20 ns, is to ensure that the weight for a zero drift time does not blow up.

An initial set of ambiguities is produced from this fit.

Stage 2

The drift distances are now calculated from the drift times, using a linear drift relation. A track is fitted through these hit points using the ambiguities from stage 1. The hits with large drift times are now most heavily weighted, because their ambiguities are most likely to be correct.

The weighting function used for this stage is :

$$Weight = \frac{Drift\ Time^2}{1000}$$

The factor of 1000 in each weighting function is necessary to prevent the fitting routine from overflowing.

The final hit ambiguities are then found from which side of the sense wires this second fitted track lies.

Stage 3

The angle of the track is found from the previous fit, and new hit positions are then found using linear drift relations, the track angle and the final ambiguities. A final unweighted fit is performed through these points, and the final track angle found afterwards.

4.3.1.3 Finding the Best Zero Time, t_0

The TDCs were operated in COMMON STOP mode, with a signal from the last scintillator forming the stopping signal. It is important to determine when the zero time is, to within a TDC bin of 1/2 ns, in order not to produce all the drift distances in a trigger too long or too short. However, since the stop signal was produced from a scintillator which had an intrinsic jitter of ~ 3.5 ns, (shown in figure 3.10), this degrades the overall resolution obtainable. An individual zero time is found for each track, giving an improvement in the resolution of $\sim 16\ \mu m$. This was done after the weighted fits, whilst still using only the linear drift relations, by minimising the sum of the squares of the residuals as they are calculated at this point in the track fitting. A residual is defined as the perpendicular distance from the hit position to the fitted track. The hit position is calculated as the drift distance produced from the drift time, with the linear drift relation, extended at the appropriate angle from the sense wire to the fitted track.

The following calculation shows how the best t_0 was found for each track. Index "i" is the count over the hits used for the track fit.

residual from hit to track	$= r_i$
$\perp$ distance from track to sense wire	$= d_i$
zero time	$= t_0$
TDC time	$= t_{TDCi}$
linear drift velocity	$= v_d$

103

$$\text{calculated drift distance} = v_d \, (t_0 - t_{TDCi})$$

$$r_i = d_i - v_d \left(t_0 - t_{TDCi} \right)$$

$$S = \sum_{i=1}^{nhits} r_i^2 = \sum_i \left(d_i - \frac{v_d}{r}(t_0 - t_{TDCi}) \right)^2$$

$$\frac{dS}{dt_0} = 2 \sum_i \left(v_d^2 \, t_0 - v_d \left(d_i + v_d \, t_{TDCi} \right) \right) = 0$$

$$t_0 = \frac{\sum_i v_d \left(d_i + v_d t_{TDCi} \right)}{nhits \times v_d^2}$$

From this, a new value of the zero time is found, and if different from the starting value by more than a TDC bin of 1/2 ns, the weighted fitting is redone and an iterative procedure continued up to a given maximum number of times, such as 5, until the value of the zero time has converged. Approximately 94.6 % of triggers have reached their final value of t_0 after only one iteration (although a second one has to be done so that the t_0 values are known to have converged). A further 5.2 % of triggers need one more iteration to find the final value.

A typical distribution of zero times after fitting can be seen in figure 3.23. This has a width of ~ 4 ns, which is comparable to the scintillator jitter.
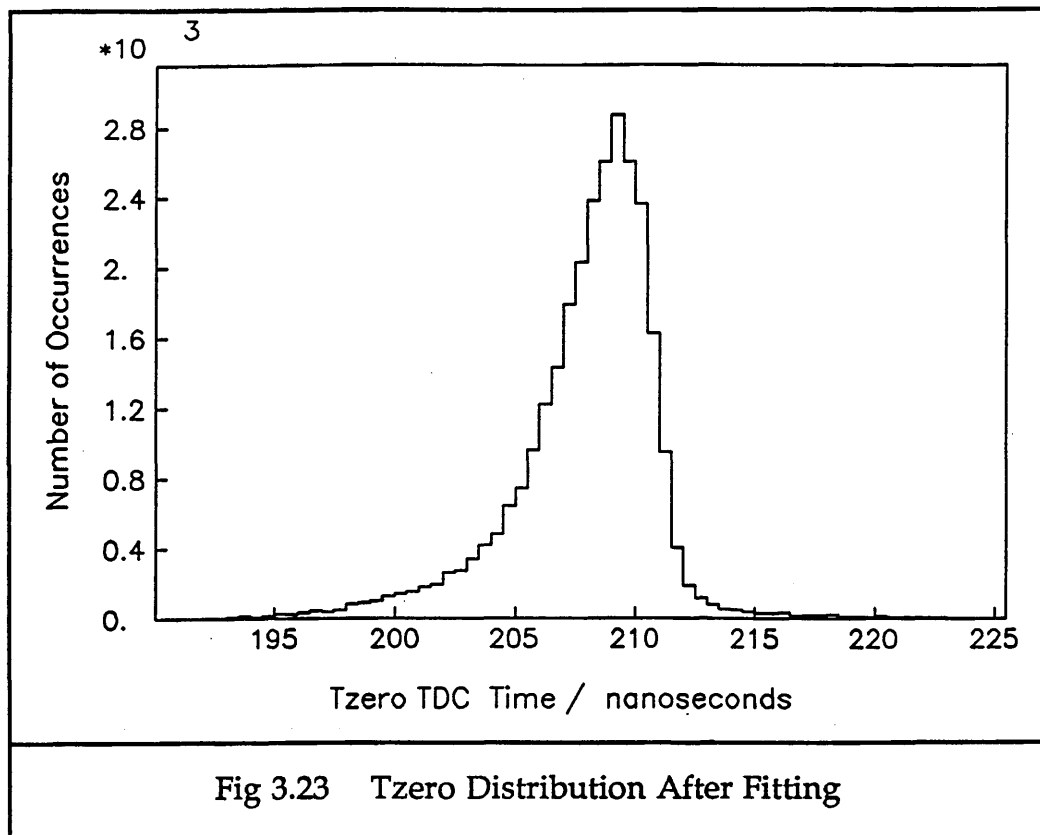
Fig 3.23   Tzero Distribution After Fitting

4.3.1.4   Fitting the Best Track

It is only once the stage has been reached when the ambiguities are known, the zero time has been found and the track angle calculated, that the full drift relation is used to construct the drift distances from the drift times.

Finding the best fit track is just the straightforward process of doing a straight line least squares fit through the hits. The hit positions are calculated using the zero time to produce the drift times, the ambiguities and track angle for the direction from the sense wire, and the full drift relation to reconstruct the drift distances from the drift times.

Once the best fit track is found, the residuals are calculated simply as the perpendicular distance between each hit and the track, using the final full drift relation to calculate the drift distance. They are compared with a given cut on the maximum residual length, (300 μm was used for this analysis), and a hit is rejected if its residual is greater than this value. After this process, provided that the track still has enough hits to satisfy the minimum required, then its zero time and angle through the chamber are compared to the mean values for each. If they are too far off, (± 20 ns for t_0, $\pm 3°$ for $\emptyset$), then the track is rejected. Values associated with tracks passing all these cuts are stored for later overall calculations. The residuals are used to calculate the resolution across each size cell. The perpendicular distances between sense wires and the tracks are stored as a function of their drift

times, in order to find the new drift relation.

At this point, various diagnostic aids are available, such as printing out on the screen all the parameters associated with the track, or displaying a graphic cross-sectional view of the track, its hit points and all the hit wires in the chamber.

The whole track finding and fitting process is repeated for every trigger in the run. Counts are made of whereabouts in the process hits are rejected from the track, and where whole tracks are cut, in order to monitor both the behaviour of the program and the behaviour of the chamber.

4.3.2 Finding the Best Drift Relation

The second phase of the analysis program is to find the best fit drift relation to the drift distances and times generated from the individual track fitting. It is very important for good resolution in the ITC to know how to parameterise the electron drift relation. If a form can be found for the drift relation which models well the electron drift behaviour across all parts of the cell, then very few genuine hits will be cut from the fitting, and high resolution tracks will improve vertex finding from long lived decays of heavy quarks and resonances.

4.3.2.1 The Method Used to Find the Best Drift Relation

a) Linear Drift Velocities

First of all, before any more elaborate drift relations are tried, a simple linear one is used on the data. This is used to generate drift distances for the first part of the track fitting, whilst the hit ambiguities and track zero time are found. Even for later iterations when a drift relation with more coefficients is used to find the best fit track, the same linear velocities are still used. Consequently, it is very important to find the best linear velocities for each run. The linear velocities are not the same as the mean drift velocity of electrons in the gas. (Eg. argon-ethane 50%-50% has a mean electron drift velocity of ~ 53 μm/ns at atmospheric pressure, with E ~ 1 kV/cm and $\underline{B}$ = 0 T. When $\underline{B}$ = 1.0 T, the mean electron drift velocity reduces slightly to ~ 52 μm/ns, and when $\underline{B}$ = 1.5 T, then the mean electron drift velocity is ~ 49 μm/ns and is no longer saturated.) The coefficient of a linear drift relation is smaller than these linear drift velocities, because the mean paths of the electrons are not straight lines in the cells from where they were ionised to the nearest sense wire. The electrons' mean paths are in large arcs across the cell, due to the magnetic field acting on them. This means that the perpendicular drift distance from track to sense wire is

much shorter than the distance travelled by the electrons for which the drift time was measured. The electron drift paths in the ITC hexagonal cells are shown in Appendix B, at the end of this chapter. The best mean linear velocities found for argon-ethane 50%-50% are ~ 45 μm/ns when $\underline{B}$ = 0 Tesla, and ~ 42 μm/ns when $\underline{B}$ = 1 Tesla, for the smallest cells. Large cells had ~ 47 μm/ns for $\underline{B}$ = 0 Tesla and ~ 40 μm/ns for $\underline{B}$ = 1 Tesla, for the same running conditions as the small cells.

The method used to find the best linear drift velocities is unfortun_ately fairly slow, but it improves the overall resolution by ~ 27 μm. First of all, several runs of the program are made through one set of data, each run having a different fixed zero time and linear drift velocity. The value of the zero time is not allowed to vary from track to track at this stage. For example, if from inspection of the TDC time distribution histograms, the zero time, t_0, is found to be ~ 210 ns, then runs will be made for 208.5 ns $\leq t_0 \leq$ 211.5 ns in half integer steps, and at each t_0 the velocity will be set at 40, 42 and 44 μm/ns (if $\underline{B}$ = 1 Tesla) for the small cells. The residuals from each run are divided up into sets, one for each drift relation region, (ie. one region for each side of each size cell), and in each set, the residuals are signed according to whether the drift distance prediction undershot or overshot the track. A very loose cut is made on hits whose residuals are larger than 1 mm. The means of these residual distributions are found, and the best drift velocity for that t_0 occurs where the mean = 0 μm.

The residual signs are calculated by multiplying the residual as calculated from the sense wire to the track, which is signed by which side of the track it is on, by the hit ambiguity for that cell.

Figure 3.24 shows the mean of the residuals plotted against the drift velocity, for several trial values of t_0. This is an example plot from one drift relation region in one run. These are different for every t_0, every drift relation region and every run.

In figure 3.24, where each line crosses the axis, that is, where each distribution of residuals is centred, is the best linear drift velocity for that t_0.

A further set of runs on the data is then made. Each set of best drift velocities corresponding to one t_0 is used, and the t_0 jitter is reintroduced. This produces a resolution for each drift relation region, plus measures of how efficient the drift relation is at keeping hits and tracks. The set of linear drift velocities to be used for all subsequent analysis of data from that run, is chosen to be where the smallest RMS of residuals occurs. This is despite whether the efficiencies are good or bad, since they will be improved when a better drift relation is used later.

Fig 3.24   Mean Residuals versus Mean Linear Drift Velocity
to give the Best Drift Velocity at Each Tzero
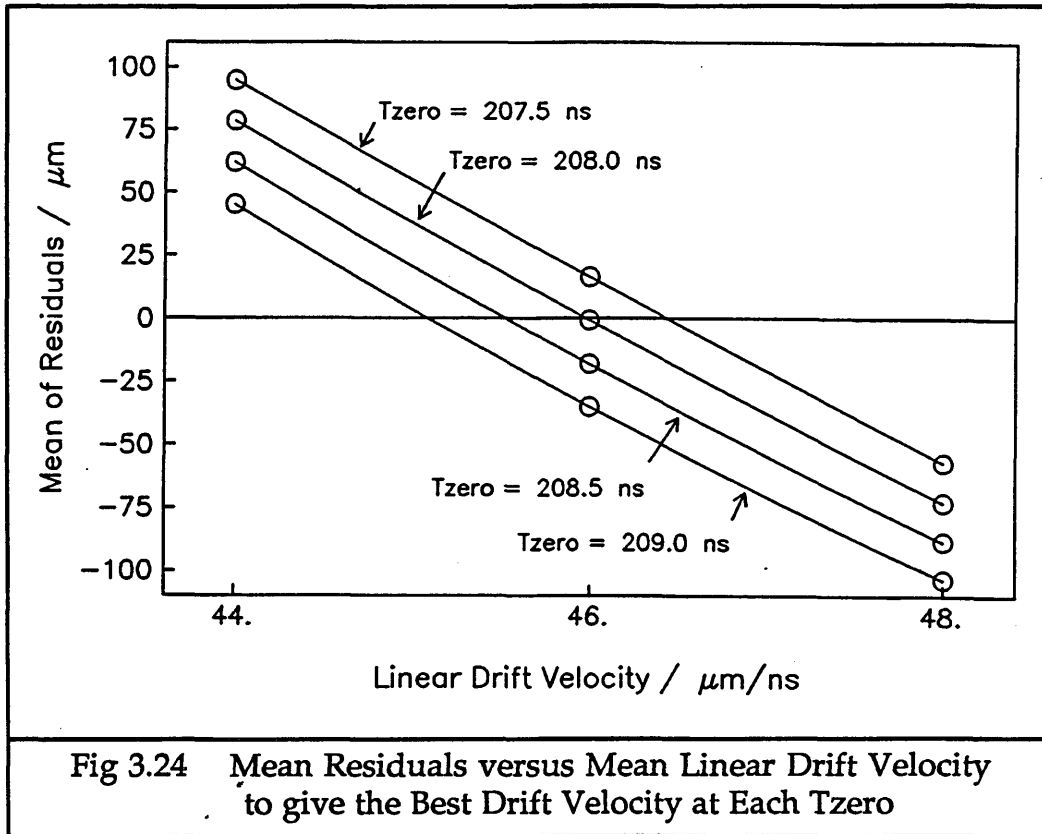
b) Higher Order Drift Relations

Once a set of linear drift velocities has been chosen, the next stage in the process is to try fitting drift relations with more than one coefficient. This is because a linear drift relation does not model the electron drift very well at the edges of the cell near the field wires.

The best fit higher order drift relation is found by fitting the relation under consideration to the weighted means of the drift distances at each drift time using the method of least squares. The weights used are :

$$\text{Weight} = \frac{n \cdot f}{\sigma_{n-1}^2} \qquad f \sim 10^{-20}$$

The integer n is the number of hits at that drift time used to calculate the mean drift distance. The scaling factor f is necessary to avoid overflows in the standard least squares fitting routine. σ_{n-1}^2 is the variance of the drift distances being calculated at the drift time under consideration.

Once the best fit drift relation is found for this iteration, the track fitting process is repeated, using this relation to generate the final drift distances. A new drift relation is fitted, and the whole iterative process is repeated many times. This iterative procedure can be seen in figure 3.19, which shows the overall structure of the analysis program. The number of

iterations needed to gain the smallest RMS of the residuals for these runs is ~ 10. However, the efficiency of the program keeping a track continues to increase by one or two per cent up to at least 100 iterations. The RMS of the residuals increases by a couple of microns after this large number of iterations. Since it is impractical to analyse every data set with this number of iterations, it has been decided to stop each track fitting run after 10 iterations.

4.3.2.2 Results for the Best Drift Relation

a) The Number of Drift Relations Needed

There were two sizes of drift cells used in the small test chamber. These corresponded to the smallest and largest cells in the ITC. It is necessary to have separate drift relations, both linear and higher order, for each size of cell. It was also decided to split the cells into two halves, and have separate drift relations for each half. This is because, when the magnetic field is on, the electron paths in the cells are no longer symmetric in each half. Therefore, if all layers had been working properly with no dead wires, there would have been four separate drift velocities and drift relations for each run. However, the dead wires with no high voltage on them changed the electric field in the cells around them. Therefore, most of the large cells no longer had electric fields similar to those in the ITC or to each other. Consequently, the quality of the data taken with the large cells was so poor that it was decided not to use the drift times from the large cells in the track fitting.

b) Parameterising the Drift Relation

All attempts to parameterise the drift relations were done on runs whose conditions most resembled those expected for the ITC in ALEPH. That is, the runs used had :

    a) argon-ethane 50%-50% gas
    b) sense wire voltage plateaued at 2.07 kV
    c) constant fraction discriminators
    d) magnetic field at 0 or 1 Tesla
    e) for simplicity, tracks perpendicular to the cells and wires.

This enabled comparisons to be made between different forms of drift relations.

i) Polynomial Drift Relation

The first form tried for parameterising the drift relations was a polynomial. Figure 3.25 shows the relationship between the RMS of residuals and mean of residuals as a function of the maximum power of the polynomial used, with no magnetic field. The cut used on the maximum residuals allowed was 300 µm. It also shows for the same data the two measures used to assess how well the drift relation is coping with the data : the mean number of hits per track, and the percentage efficiency of keeping a track after all the cuts, which started off with between 4 and 10 hits. Figure 3.26 shows these same relations for a run where $\underline{B} = 1$ Tesla.

From these figures, it can be seen that there are only small improvements in how well the electron drift relation is modelled, as extra coefficients for higher powers of t are introduced, so it is not very critical which is the highest power of t used.

The polynomial drift relation used for all of the following analysis is of the form :

$$\text{Drift Distance} = a + b\,t + c\,t^2 + d\,t^3 + e\,t^4 + f\,t^5 + g\,t^6 + h\,t^7$$

where $\quad t = \text{Drift Time} = t_0 - t_{TDC}$
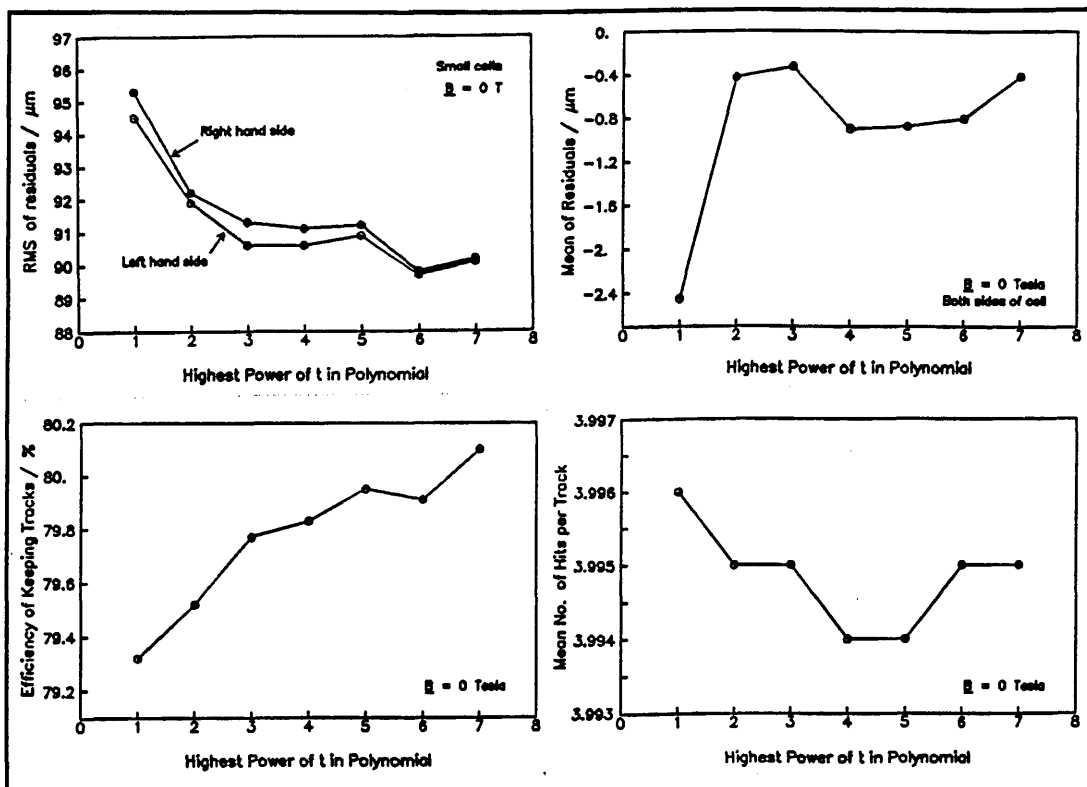
Fig 3.25   The Effects of Increasing the Power of the Drift Time in the
            Polynomial Drift Relations with B = 0 Tesla
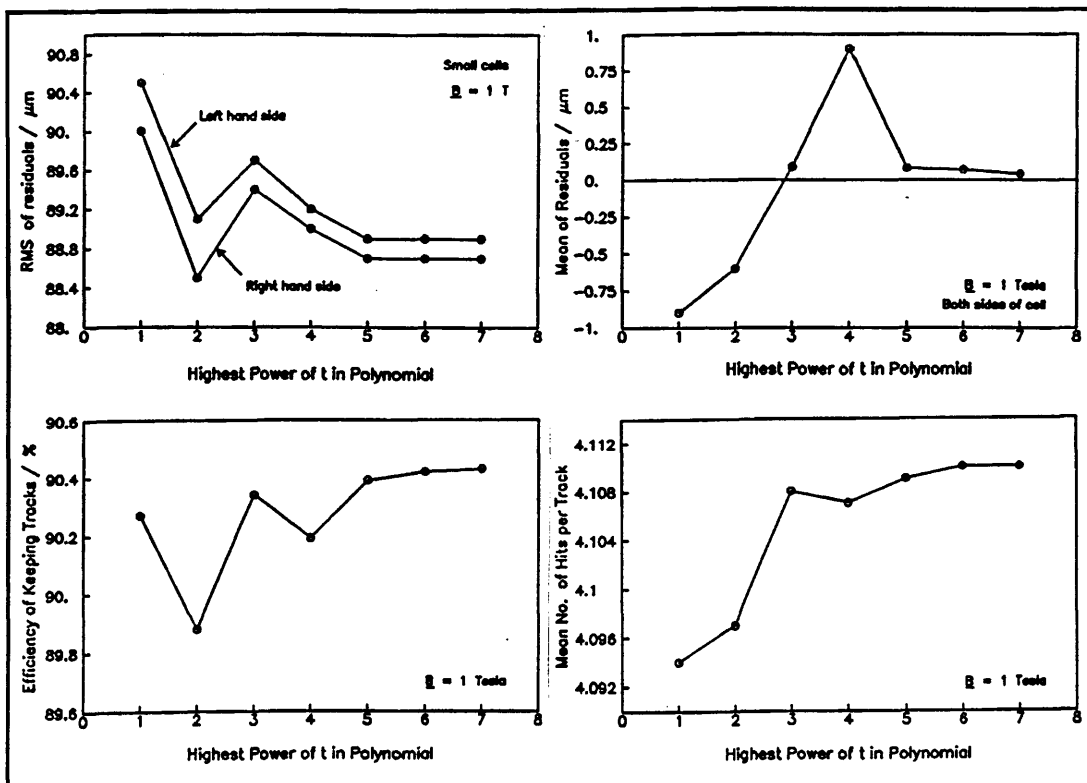
Fig 3.26   The Effects of Increasing the Power of the Drift Time in the
            Polynomial Drift Relations with B = 1 Tesla

For these two runs, the best linear and polynomial drift relations can be seen in the following plots. Figure 3.27 shows the best linear relations for the standard run with $\underline{B}$ = 0 T. There are two sets of data on the plot, one for each side of the small cells. There are 50766 hits in the distribution for the left hand side of the cells and 50902 hits for the right hand side. Figure 3.28 shows the data and best linear relations for the standard run with $\underline{B}$ = 1 T. There are 45303 hits in the distribution for the left hand side of the cells and 45876 hits for the right hand side. The lines shown are not the best fit to the data, but the drift velocities used to generate the drift distances from the drift times initially. The drift distances on the plot are the perpendicular distances from the sense wire to the best fit track.

There are several features of these drift distance - drift time plots which are worth commenting on.

Firstly, each of the points on the plots corresponds to one drift time measured, in 1/2 ns increments from the 1/2 ns TDC bins. Each point has the value of the mean drift distance measured at that time. The error bars are the statistical errors on the means.

Secondly, when the magnetic field is on, the electron paths in the cells become longer and consequently larger drift times are measured.

Thirdly, near the sense wire there are two opposing processes going on. The primary ionisation statistics for tracks very close to the sense wire mean that tracks which should produce a very small or zero drift time sometimes produce a much larger drift time. This effect tends to pull the points downwards on the plot over the last few hundred microns. However, opposing this effect is one due to the division of the cells into two halves. Every time a track is very close to the sense wire, it will sometimes be assigned the wrong ambiguity. This means that part of the spread of drift distances for the short times is removed from one plot and entered on the one for the opposite side of the cell. This causes the mean drift distances for times up to ~ 10 ns to be calculated larger than they really are and pulls up the drift relation tail near the sense wire. This second effect can be seen to dominate the effect from ionisation statistics over the last ~ 100 μm of the cell near the sense wire.

Fig 3.27   Drift Distance-Time Plot from a Linear Drift Relation
for Small Cells with B = 0 Tesla

Fig 3.28   Drift Distance-Time Plot from a Linear Drift Relation
for Small Cells with B = 1 Tesla
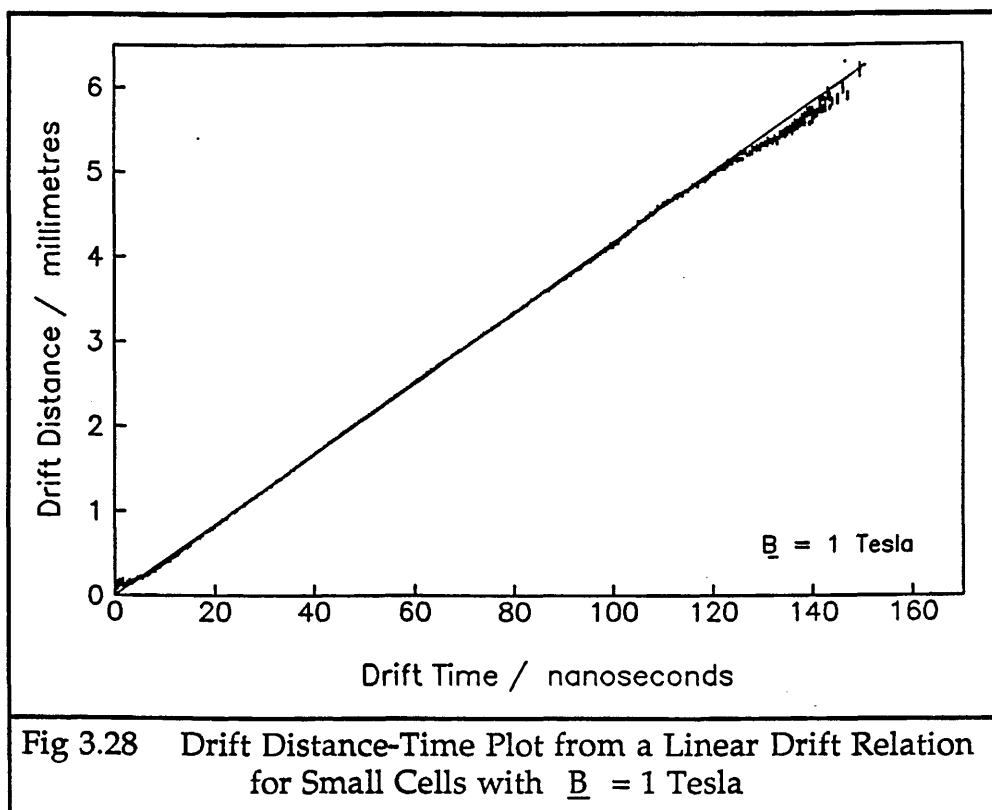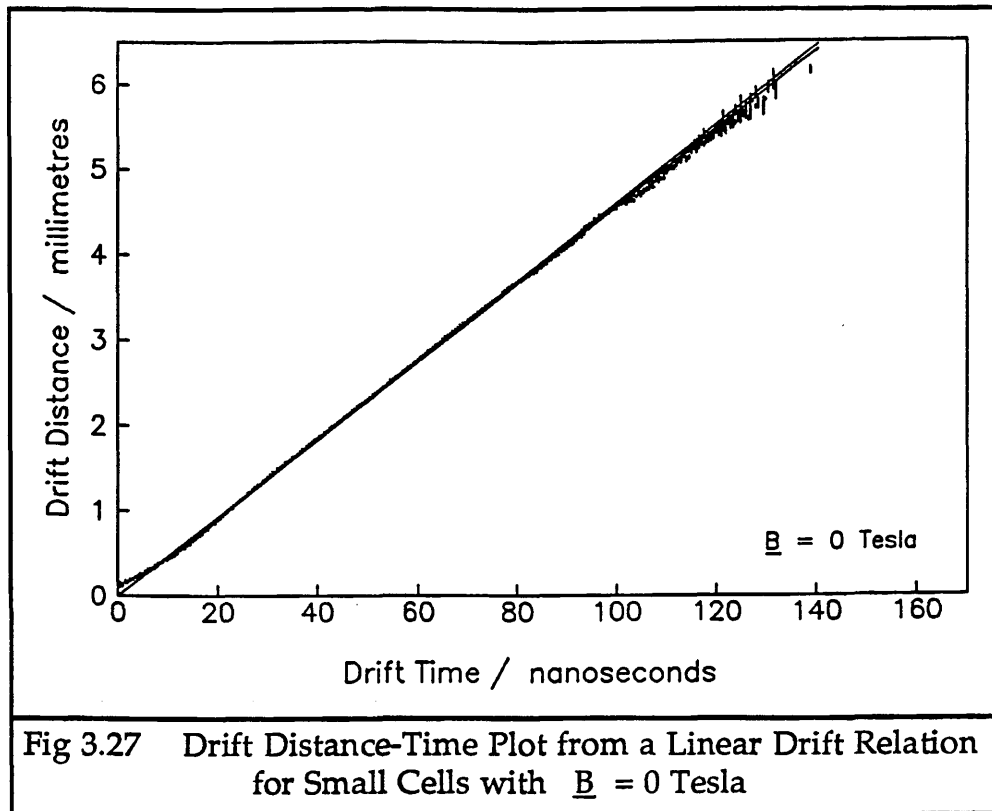
A final fit drift relation can be seen superimposed on its data in figure 3.29 for the standard run with $\underline{B}$ = 0 T. This has 51546 hits for the left hand side of the cells and 51571 hits for the right hand side. These values have increased by 1.5 % and 1.3 % repectively over those obtained with a

linear drift relation, as shown in figure 3.27 for the same data set. Figure 3.30 shows the final fit drift relation for the standard run with $\underline{B} = 1$ T. This has 45589 hits in the distribution for the left hand side of the cells and 46318 hits for the right hand side. These values have increased by 0.6 % and 1.0 % respectively over the number of hits kept with the linear drift relations. The drift relation used here was a polynomial to the power 7 in drift time.

The line shown is not a best fit to the data, which would be the drift relation after 11 iterations, instead of only 10. It is the drift relation used to generate the drift distances during the track fitting.

There are two things worth noting about these distributions. Firstly, across almost all the cell the two drift relations for the left hand side and right hand side of the cells are almost identical. There is no strong assymetry in the electric fields on either side of the cell, and the electron drift paths must be fairly similar even when the magnetic field is applied. At the outer extremities of the cells, near the field wires, only a small number of hits are kept, due to the large intrinsic errors on the drift times caused by the low electric field there (see Appendix B at the end of this chapter). Therefore, the divergence between the two drift relations is probably not indicative of a fundamental difference in the electron drift paths from one side of the cell to the other. Rather, it just reflects which hits from a large distribution have been kept by the fitting program.

Secondly, the drift relation over most of the length of the cell is almost linear. Using a polynomial with eight coefficients instead of a linear drift relation improves the RMS of the residuals by only one or two microns, so the best linear drift relation is almost as good as the polynomial for the vast majority of the hits across most of the cell. This improvement in the resolution is very small for such a lot of extra work involved in a more complex fitting program needing several hours to run on the computer in order to iterate on the values of the drift relation coefficients. Near the sense wire, the higher order drift relation fits better the longer drift distances produced by very small drift times. However, this is a disadvantage, since this upturned tail is only produced as a consequence of splitting the cells into left and right halves. Zero length drift times should not really produce drift distances of ~ 100 μm. Near the field wires, the drift distances get shorter for long drift times. However, no extra hits are kept in this region. Since the hits from this region probably have a large intrinsic error on them, it may be possible to keep more by having two separate limits on the maximum acceptable residual allowed. The purpose of cutting hits with too large residuals is to remove hits from the track fitting which

are not really associated with the track in question. Although a cut on residual size of 300 μm is valid across most of the cell, for hits with very long drift times it might have been more appropriate to use a cut of perhaps 500 μm or more in order not to lose so many hits from this region of the cell.
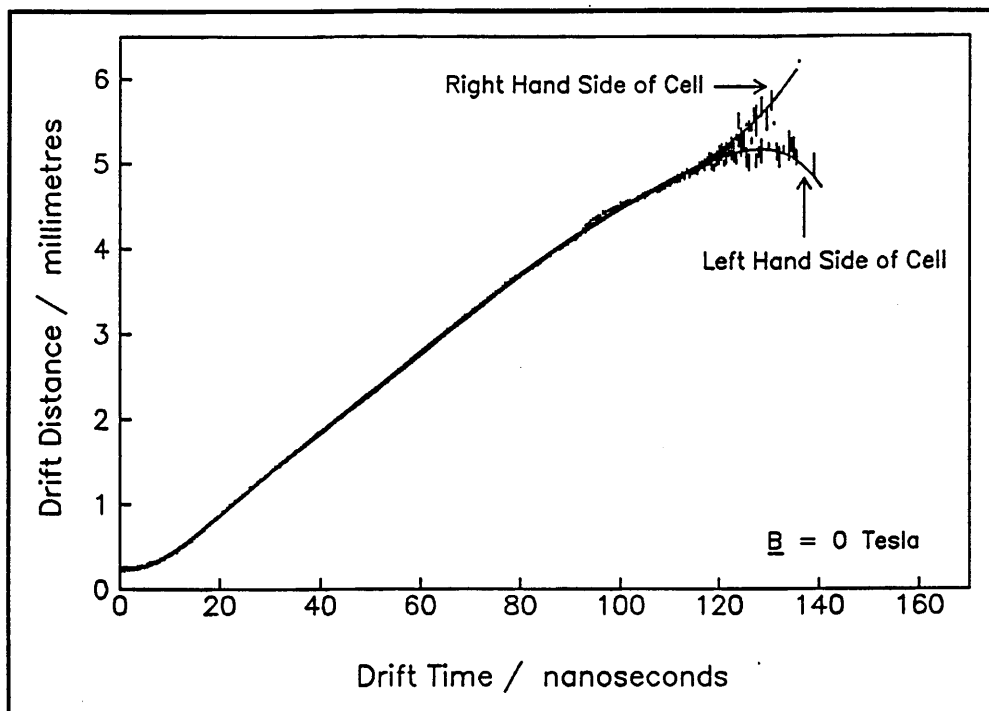
Fig 3.29   Drift Distance-Time Plot from a Polynomial Drift
Relation for Small Cells with B = 0 Tesla
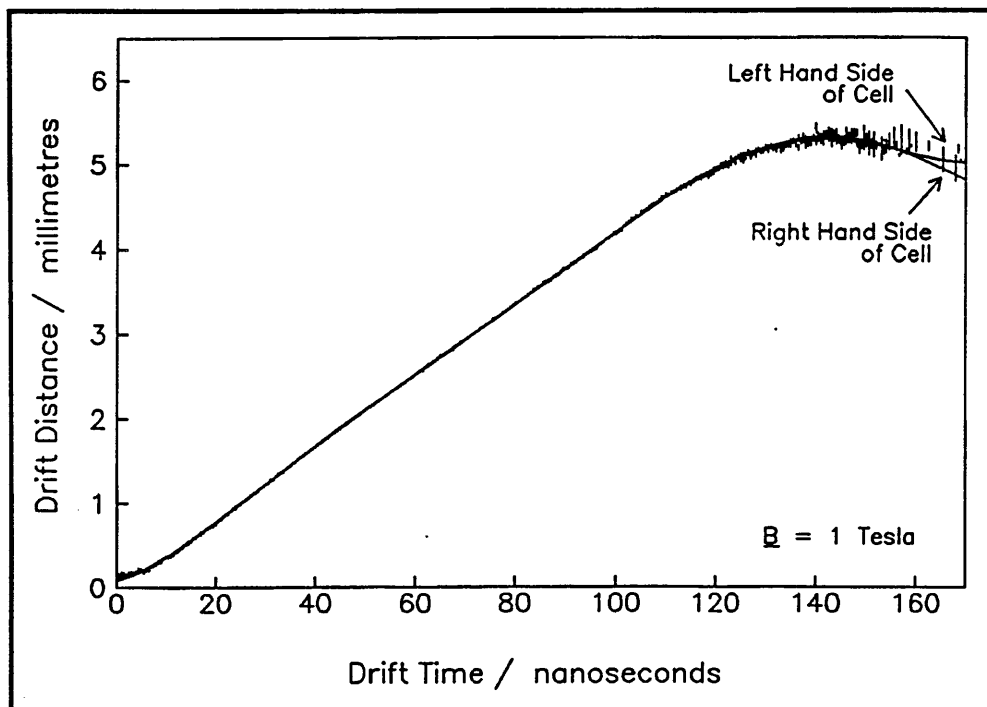
Fig 3.30   Drift Distance-Time Plot from a Polynomial Drift
Relation for Small Cells with B = 1 Tesla

ii) Cubic Spline Drift Relation

A cubic spline is a function composed of several cubic polynomials which join together smoothly up to the second derivative at places called "knots" which are chosen by the user. The coefficients by which a spline is identified are not those of its constituent cubics, but are the coefficients of the spline's associated B-spline. These B-spline coefficients are produced from the NAG (Numerical Algorithms Group) fitting routine E02BAF. They are then used to reconstruct drift distances from drift times using NAG routine E02BBF. If three knots are used, giving four cubics, then there are seven B-spline coefficients which define the spline. These are in the range 0.04 < B-spline coeff < 8.0, for this work.

There was an addition made to the spline to try and compensate for the tail of the drift time distribution caused by the arbitrary dividing of the cells into left and right hand sides. For these short drift times, a short straight stub was introduced into the drift relations to cover the drift times from 0 ns to 5 ns.

Two sets of knots were tried. These were chosen by inspection of the linear drift relation plots. The first set was chosen so the knots were fairly near some perceived feature, bend or kink. The second set of knots was chosen so the knots were in the middle of long straight smooth stretches of the relation. Two sets were chosen for these two runs to check whether it was critical where the knots were. Table 3.1 shows the two sets of knots for each magnetic field strength.

Table 3.1 Knots Used for the Cubic Splines				
Selection Number	Magnetic Field / Tesla	Drift Relation Area	Knots /ns	Stub / ns
1	0	Left Right	20, 70, 110 20, 70, 110	5
1	1	Left Right	30, 90, 120 35, 80, 110	5
2	0	Left Right	30, 70, 100 30, 70, 100	5
2	1	Left Right	30, 90, 120 30, 90, 120	5

Table 3.2 compares the results from the two best fit splines and stubs with the results from the best fit polynomial $\leq t^7$. All the values of the RMS of residuals are calculated from the residuals left after a cut on those greater than 300 µm has been made.

Table 3.2 Comparison Between Polynomial and Two Cubic Spline Drift Relations for $\underline{B} = 0$ T and $\underline{B} = 1$ T					
Magnetic Field	Drift Relation used	Mean no. of hits per track	Efficiency of keeping a track which started with sufficient hits	RMS of Residuals /µm Small Cells	
				Left	Right
$\underline{B} = 0$ T	Poly - nomial	3.995	80.10 %	90.1	90.2
	First spline	3.995	79.20 %	88.8	89.1
	Second spline	3.994	79.31 %	89.3	89.8
$\underline{B} = 1$ T	Poly - nomial	4.110	90.43 %	88.9	88.7
	First spline	4.106	90.27 %	88.9	88.6
	Second spline	4.106	90.27 %	88.8	88.5

The cubic splines produce a very small improvement in the RMS of the residuals, and also cut out a very few tracks more than when a polynomial drift relation is used. However, using a cubic spline makes the fitting program much slower, since library routines have to be called every time a drift distance is needed.

The drift relation plots for the splines are very similar to those for the polynomials shown in figures 3.29 and 3.30.

Since the improvements gained by using cubic splines over polynomials are so small, and they increase the complexity of the program and the time needed to analyse the data, it was decided to do all subsequent analysis using a polynomial drift relation, although using the best linear drift velocity would also have been acceptable.

iii) Polynomial Drift Relation with a Short Stub

The short stub was tried with the polynomial drift relation, to see if there was any improvement in the drift relation for the part of the cell near the sense wire, and a subsequent improvement in resolution obtainable. The stub was inserted from 0 ns to 10 ns.

In table 3.3, the results with the polynomial plus stub are compared

117

with those from just a polynomial drift relation.

Table 3.3	Comparison Between Polynomial and Polynomial with Stub for $\underline{B}$ = 0 Tesla and $\underline{B}$ = 1 Tesla				
Magnetic Field	Drift Relation Used	Mean no. of hits per track	Efficiency of keeping a track which started with sufficient hits	RMS of Residuals / μm Small Cells	
				Left	Right
$\underline{B}$ = 0 T	Poly - nomial	3.995	80.10 %	90.1	90.2
	Poly. + stub	3.994	79.90 %	90.3	90.4
$\underline{B}$ = 1 T	Poly - nomial	4.110	90.43 %	88.9	88.7
	Poly. + stub	4.107	89.84 %	88.8	88.9

As can be seen, adding a short stub to the drift relation to cover the region near the sense wire degrades the overall resolution very slightly, and also slightly worsens the track-keeping efficiency and reduces the mean number of hits per track. Therefore, the short stub will not be used in any of the following analysis and results.

4.4   Correcting the Sense Wire Coordinates

The position of the sense wires within the planes of the layers is a factor which can affect the resolution obtainable, if the coordinates used do not correspond well with the actual positions. When the chamber was built, optical measurements were made of where the sense wires were relative to each other. These were not good enough to use to correct the wire coordinates due to the limits of resolution of the scale on the travelling telescope used. However, it is also possible to make corrections to the sense wire coordinates using the track fitting program. This was done using the 24 data runs taken with no magnetic field.

For each run, the drift relation used was a quadratic. An individual t_0 was found for each track. Once the best drift relation was found by iteration, the mean of the residuals for each wire was calculated. The residuals were signed not as before, by whether the hit over or undershot the track, but

simply by which side of the track they were on. This meant that the mean of the distribution corresponded to the position of the sense wire. If the mean was not at zero, then it was used as a correction to the wire coordinate. This correction was only made to a wire coordinate if there were at least 500 residuals in the distribution, to avoid spurious corrections from low statistics.

The wire coordinate shifts were found for all 24 runs, and the averages of these shifts for each wire were used as the corrections. This produced a new set of sense wire coordinates and the iterative process was repeated 3 times. After the last set of corrections, the mean shift of each layer was found and used to correct all the sense wire coordinates in that layer.

The distribution of the shifts, from ideal sense wire position to final corrected position can be seen in figure 3.31.

Fig 3.31   Offsets of Sense Wire Positions from Iterations of the Fitting
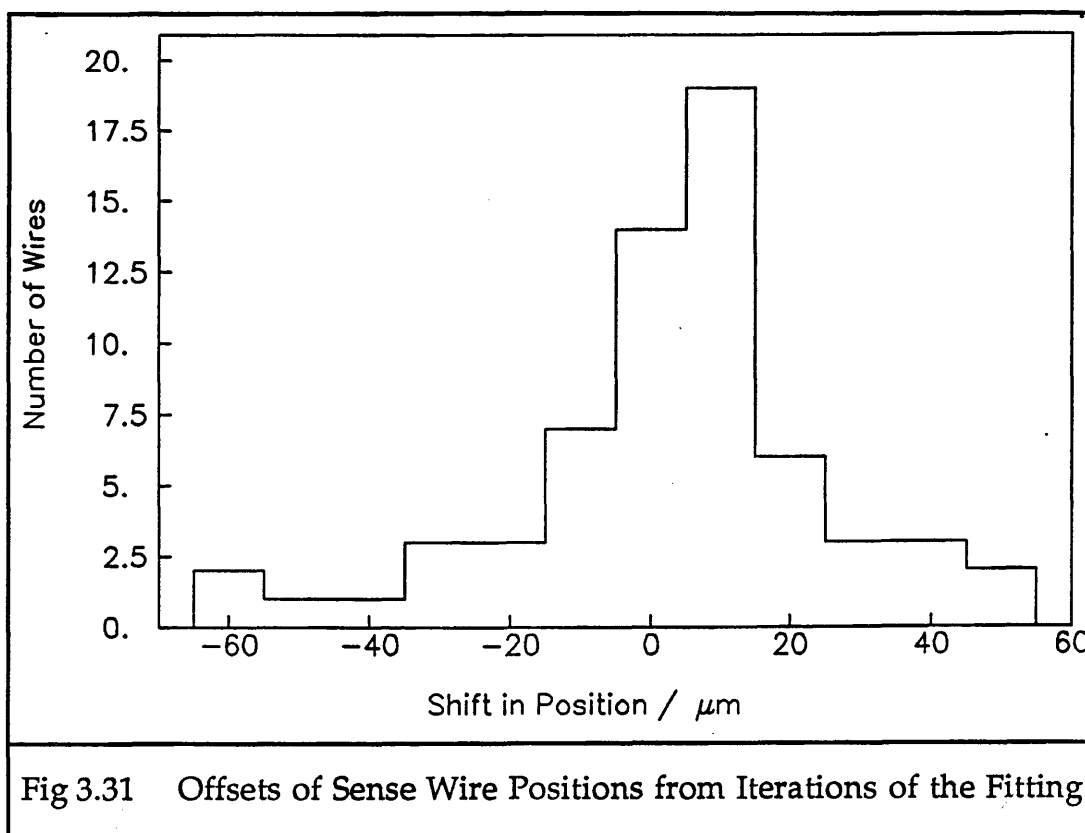
This was a very early piece of work, done before it was realised how bad the large cell drift times were, and so all hits were used in the track.fitting.

It should be noted that the wire coordinate corrections from the track fitting were not very consistent from run to run. This was partly because when different numbers of layers were in operation, an offset wire in one layer would change the offsets for the others along the tracks, relative to the offsets when that layer was not in operation. Also, between some runs, the chamber was opened up and the sense wire pins were wobbled in their

feedthroughs while looking for the source of leakage currents. This means that the actual position of the sense wires may have changed from one set of runs to the next.

5 Results from the Test Data

The following section will present the results from the test beam runs at CERN with the small test chamber.

5.1 Information from the Raw Data

There are several things worth commenting on from the raw data, before any track fitting or analysis is presented.

5.1.1 Steady Zero Time

By looking at the plots of scintillator time distribution, it is possible to check that the mean zero time for the whole of a run was constant. If the TDCs had jumped or drifted, then the times measured from the scintillators would be in distributions with more than one peak. Also, it is possible to check that the same scintillator produced the stop signal each time throughout the run, since the distribution of its times should be less than 1 ns wide, because it starts and stops itself.

No runs were found which suffered from these problems.

5.1.2 Raw TDC Times

The TDC time distribution is dependent on cell size, magnetic field strength, track angle, gas type and discriminators used. The differences for each controllable variable will be presented in later sections with the analysis results. However, some of the details will be investigated here.

A fairly standard TDC time distribution can be seen in figure 3.32. This is for the small cells in argon-ethane 50%-50%, with the chamber sense wire voltage plateaued at 2.07 kV, constant fraction discriminators and $\underline{B} = 1$ Tesla. Ideally, this distribution would be "box" shaped. There would be no inefficient areas of the cell near the sense wire or field wires, and no loss of short drift times due to ionisation statistics. However, several effects can be seen. There is a small tail of very long drift times, which is due to either electrons leaking from a track in one cell into a neighbouring cell, or

just from noise picked up in the cables and circuits, and electronic crosstalk.

Fig 3.32   TDC Time Distribution for Small Cells in Argon-Ethane
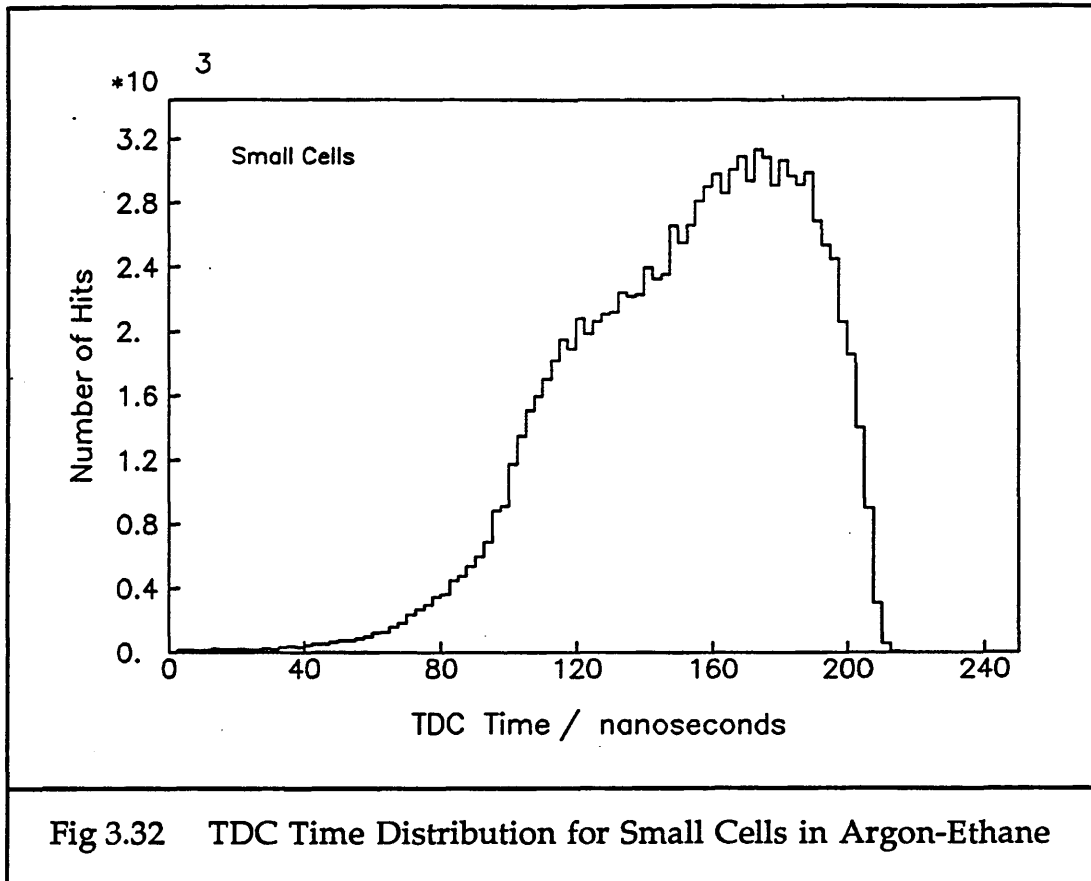
Since the t_0 is not constant, the right hand side of the distribution does not rise abruptly. Also contributing to the slope on this edge of the distribution are tracks which pass very close to a sense wire. These hits sometimes produce longer drift times than they could do, due to the lack of a liberated electron very close to the sense wire from the primary ionisation statistics. These extra times form a surfeit of medium drift times further back from the t_0 edge. A third contributing factor to the slope at the right hand side of the distribution is the lack of efficiency of the cell very close to the sense wire. At this sense wire voltage, the electric field is not high enough to produce enough electrons quickly enough in the avalanche to generate a signal large enough to be measured at the discriminators.

The following two figures illustrate the source of some of the problems experienced with analysing the large cell data. They show the TDC time distributions for the large cells next to "dead" cells with no high voltage on the sense wire, (figure 3.33), and for the large cells not next to dead cells (figure 3.34), for the same run as the previous small cell TDC times plot.
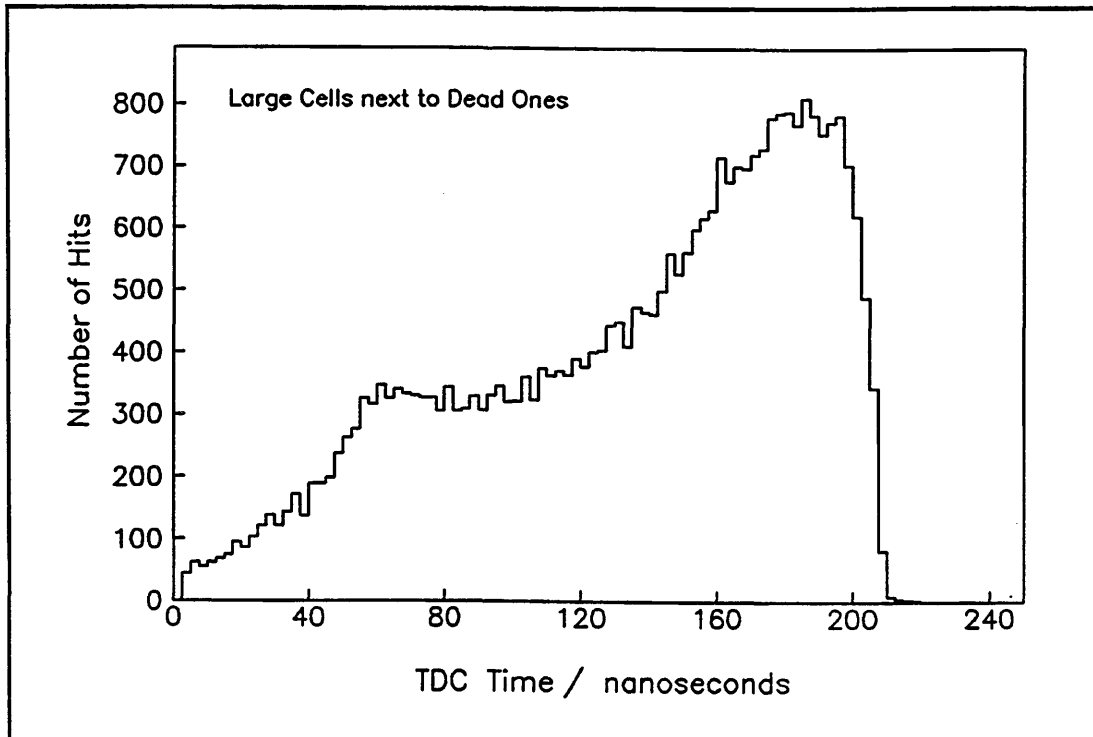
Fig 3.33   TDC Time Distribution for Large Cells Next to Dead Cells
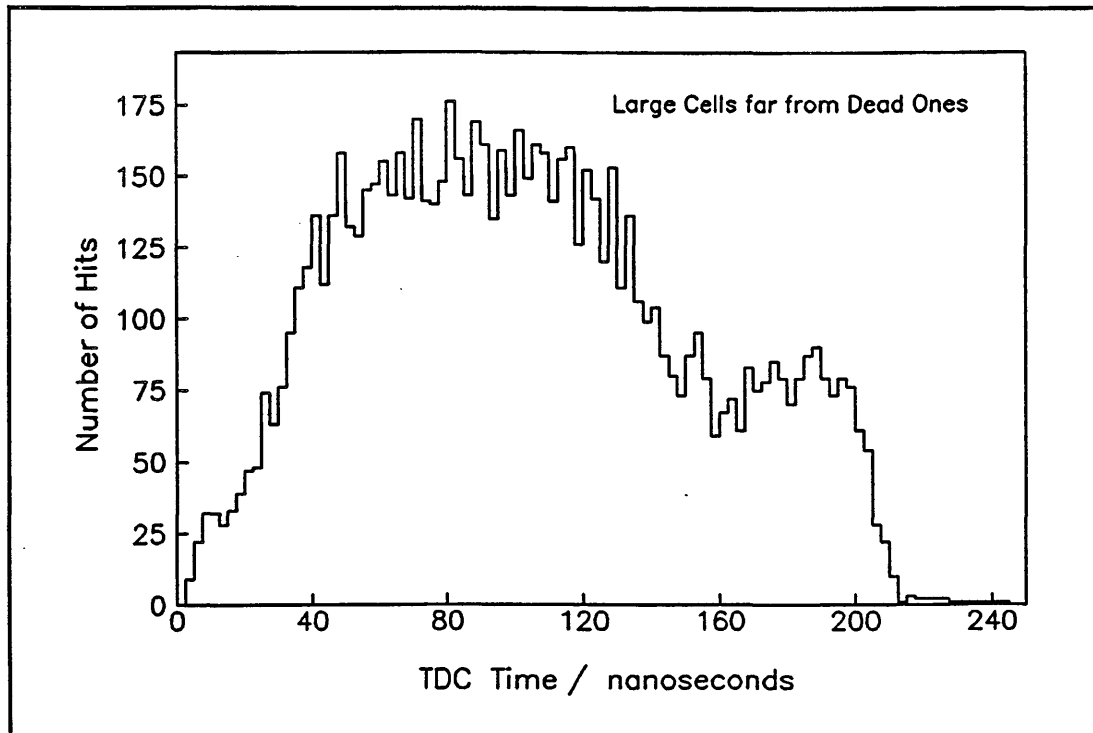
Fig 3.34   TDC Time Distribution for Large Cells Far From Dead Cells

In figure 3.34 for the large cells not near the dead cells, where the electric field is hopefully not too affected, the beam edge effects with few hits near the sense wires, can clearly be seen. This is caused by nearly all the

large cells not near dead cells being near the edges of the block of cells, and so only having particles in the edges of the beam pass through them.

The beam profile across the cell layers can be seen in figure 3.35, which shows the number of hits per layer for this same run. The staggering of the cells can be seen by the apparent shift of the centre of the beam across the chamber layer by layer. Also, the different cell sizes can be seen, from the apparently wider beam in layers 5–8 of small cells than in layers 3 and 4 of large cells. The beam does not get wider as it enters the small cells, it just passes through more cells in each layer.

The large cells in layers 1 and 2 had no high voltage on their sense wires, so no hits were recorded there.
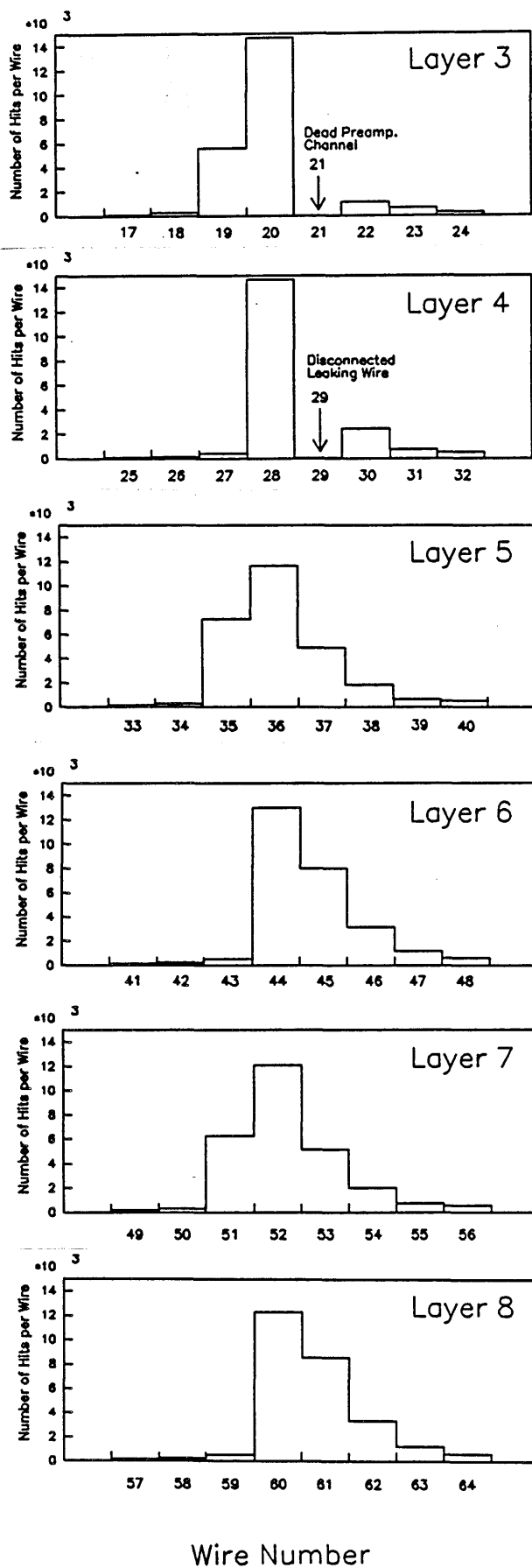
Fig 3.35   Number of Hits per Wire, Showing
Beam Profile

5.2   Some Notes on Noise in the Detector

When the STC, or ITC is running with charged particles passing through producing tracks, there are sometimes extra hits read out which are not associated with these tracks. These extra hits can have a variety of causes. It is not necessary or even always possible to identify the cause of each individual hit, but there are probably five sources of these hits in the ITC. These can be divided into two categories : those which occur inside the chamber, and those which occur somewhere in the cables or electronics.

a)   Extra Hits Caused by Steep Angle Tracks

Figure 3.36 shows how there can easily be more than one hit in a layer, when a particle travels through that layer at a steep $\emptyset$ angle. The curved lines are electron paths in a 1.5 T magnetic field.

Fig 3.36   Steep Angle Track Producing Two Hits on One Layer
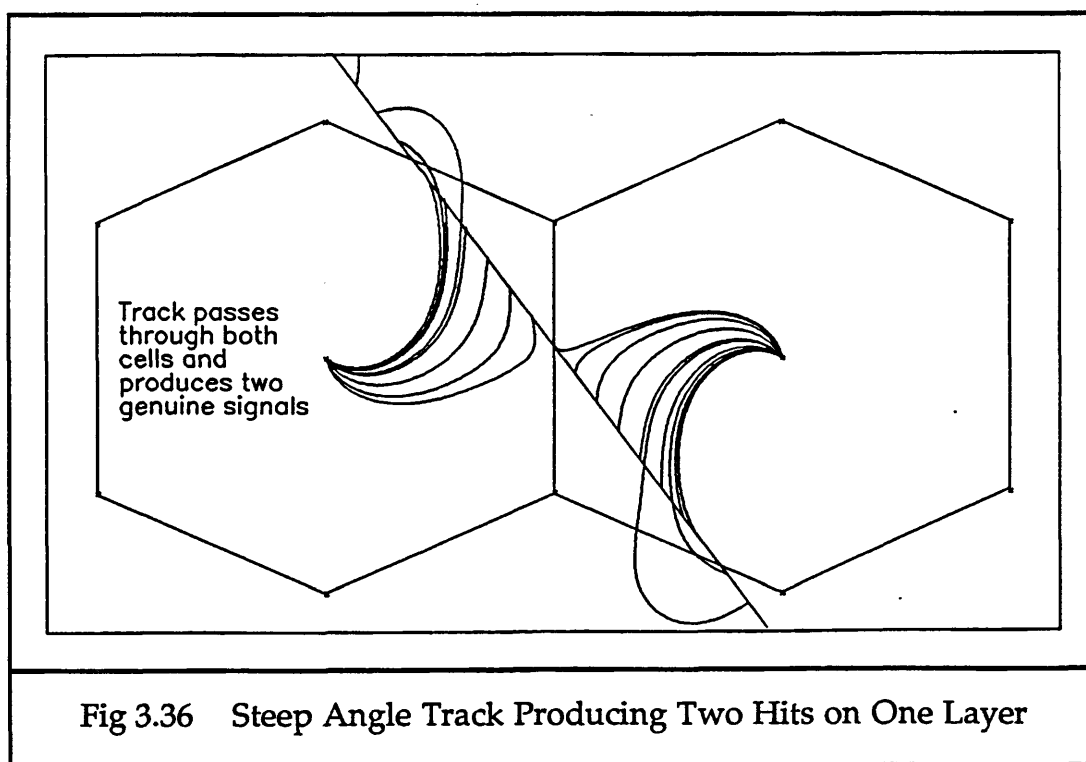
This is not really an extra hit not associated with the track, since provided an appropriate track-finding algorithm is used, then the drift times from both sense wires can be used to reconstruct the track. The TDC times measured here can take any value, and will not necessarily be the same.

b) Extra Hits Caused by Electron Leakage into Neighbouring Cells

Figure 3.37 shows another source of extra hits in the chamber, which are usually associated with a track, and which are sometimes known as crosstalk. The electron paths shown are with $\underline{B} = 1.5$ T.

Fig 3.37   Leakage of Electrons from One Cell to the Next
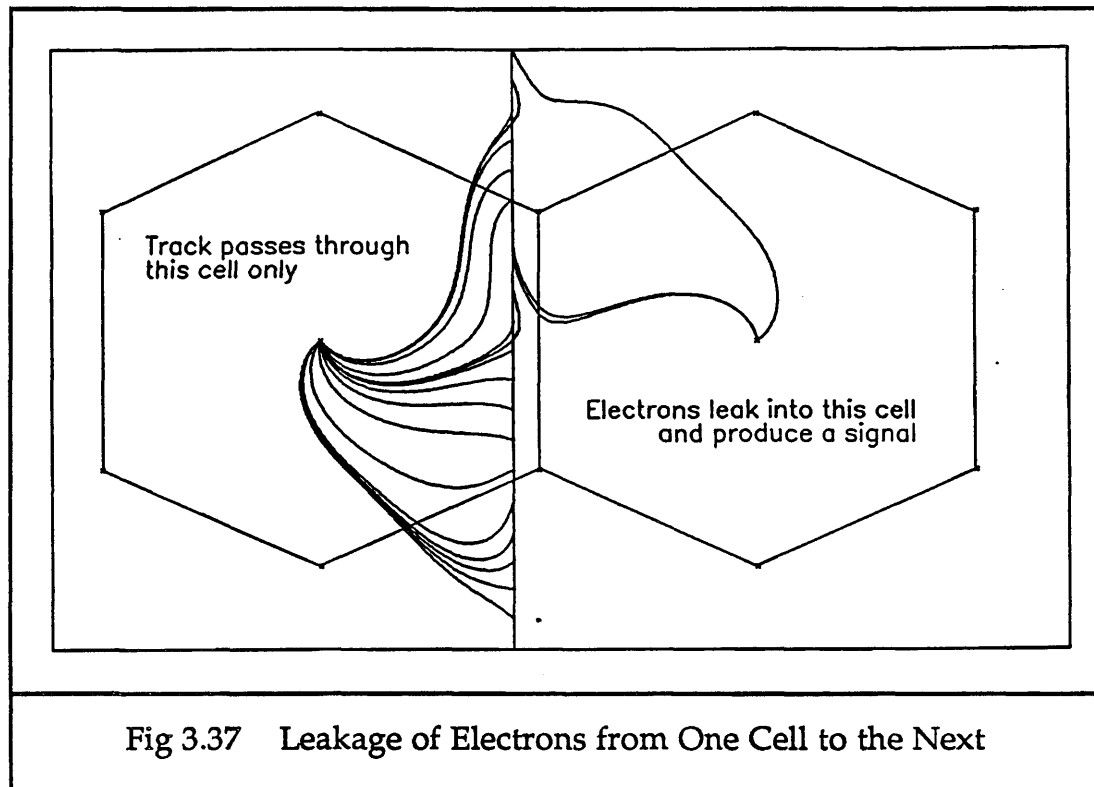
Here, the charged particle has passed through only one cell in the layer, but has still produced two hits. This is a different case to the previous one, since the extra hit will now have an extremely long drift time which may well cause the TDC channel to overflow. If it is recorded as a drift time, then it will not lie on the drift relation curve from tracks with drift distances originating inside the cell. Therefore, the drift distance reconstruction from the drift time may well be very inaccurate and have a large residual if the hit is used in the track fitting. The TDC time signature for this type of crosstalk is one fairly large drift time and one extremely large drift time, on neighbouring cells.

c) Extra Hits Caused by Free Electrons in the Gas

When a charged particle passes through the gas, it ionises some of the atoms and molecules, and the signals from the free electrons produced are read out from the sense wires to give a drift time. If the particle was not produced at the same time as the trigger was generated, but earlier, say, then it could still produce signals which are read out, but all drift times will seem much longer than they really were, due to the late arrival of the STOP

126

signal. This will produce spurious hits which may or may not appear to form a track. There may only be one hit produced if all the others are too long for the maximum TDC scale. Consequently, odd hits may be seen in the chamber which are not apparently associated with any track.

If the charged particle not associated with the triggered event travels through after the particles from the interaction point, then very short drift times will be measured. Consequently, TDC times of any value may be produced by this source of extra hits in the chamber.

d) Extra Hits Caused by Random Noise

This source of noise hits can occur on any wire, regardless of where in the chamber the real track is. An example can be seen in figure 3.38.

Fig 3.38   A Random Noise Hit in the Chamber
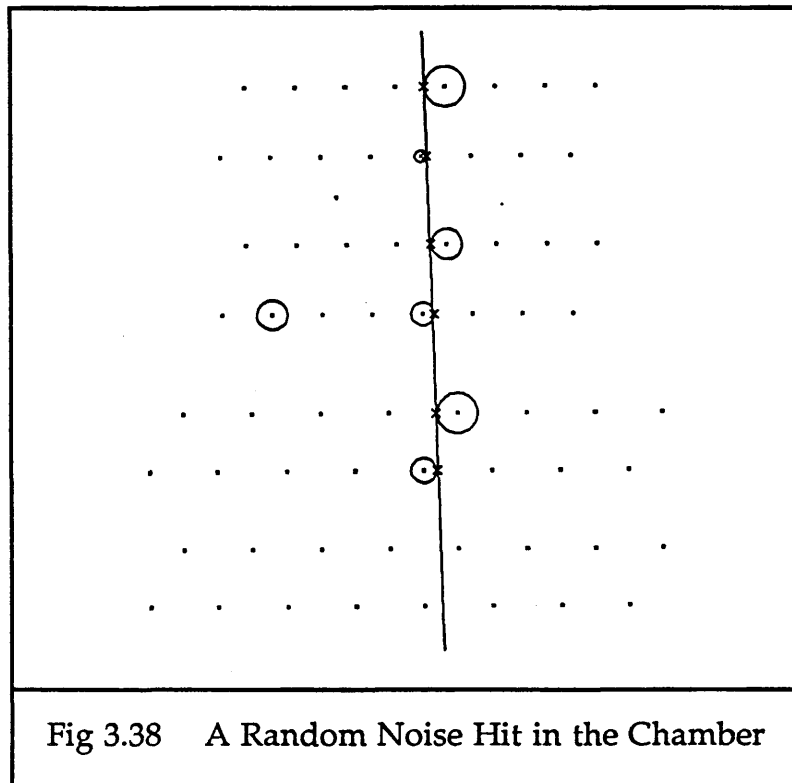
These noise hits can be read out by a discriminator operating with a low threshold, generating a few of its signals from interference on its input channel instead of from real chamber pulses. The TDC time measured can be of any value. This source of noise may appear as a hit on a wire with no high voltage on it, since it is generated outside the chamber.

e) Extra Hits Caused by Electrical Crosstalk

The fifth source of noise identified is illustrated in figure 3.39. It is seen as two or more neighbouring cells in a layer having drift times which do not belong on a track.
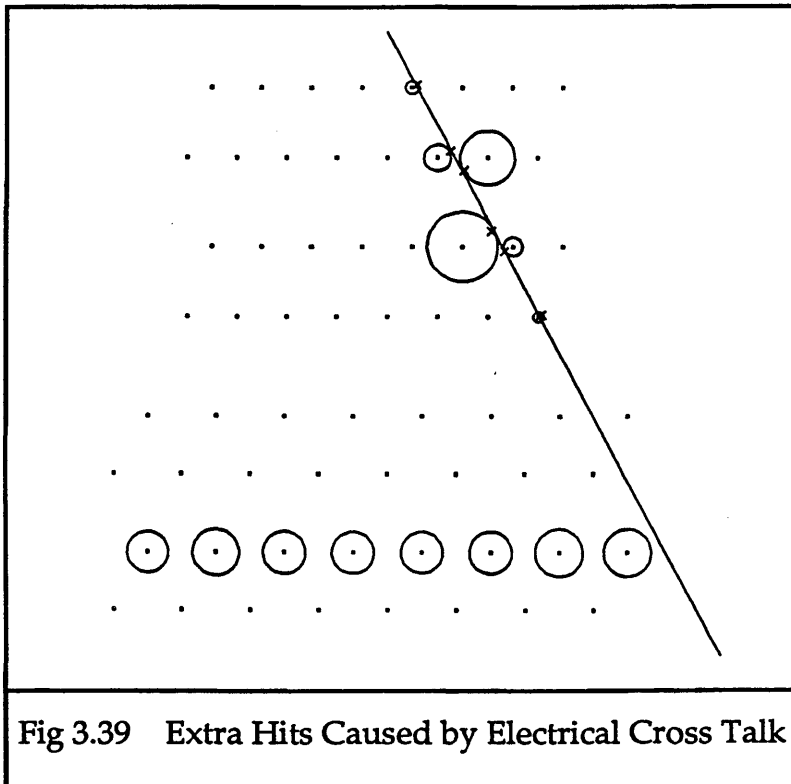
Fig 3.39   Extra Hits Caused by Electrical Cross Talk

This sort of crosstalk occurs somewhere in the amplifiers, cables or on the discriminator boards, between neighbouring channels, which is why it appears as an extra hit or hits anywhere in the chamber. The TDC times can take any value.

Measuring How Much Noise is Present

Without much work, it is difficult to identify how much of each source of extra hits is present in a data run. However, it is useful to know how much noise is present overall. One way of measuring this is to calculate the number of hits which are present in the chamber and rejected by the track finding as being too far from the initial track fitted through all the hits, as a fraction of the total number of hits present in all the triggers before fitting. This can be quoted as a percentage noise figure, calculated separately for each cell size.

For some of the data runs in the small chamber, it is possible to distinguish different types of noise. Several of the runs used later in the discriminator threshold analysis have one or two triggers in which a whole layer of large cell sense wires record a time on the TDC. None of these wires had high voltage attached to them at the time. One wire had started to leak current through its feedthrough, but had not been disconnected from the end box, and one channel was for the wire which had been broken and completely removed from the chamber. The TDC times measured are very similar to each other for each run. The times from each set of noise hits lie

within a range of 20-30 ns of each other, forming a small cluster.

Another set of runs showed a different pattern of noise hits. These 5 runs, with the sense wire voltage at 2.40 kV on the small cells only, showed hits in different triggers on a different large cell layer to those previously. Figure 3.40 shows the pattern of noise hits across this layer for these 5 runs.

Fig 3.40   Number of Noise Hits per Channel
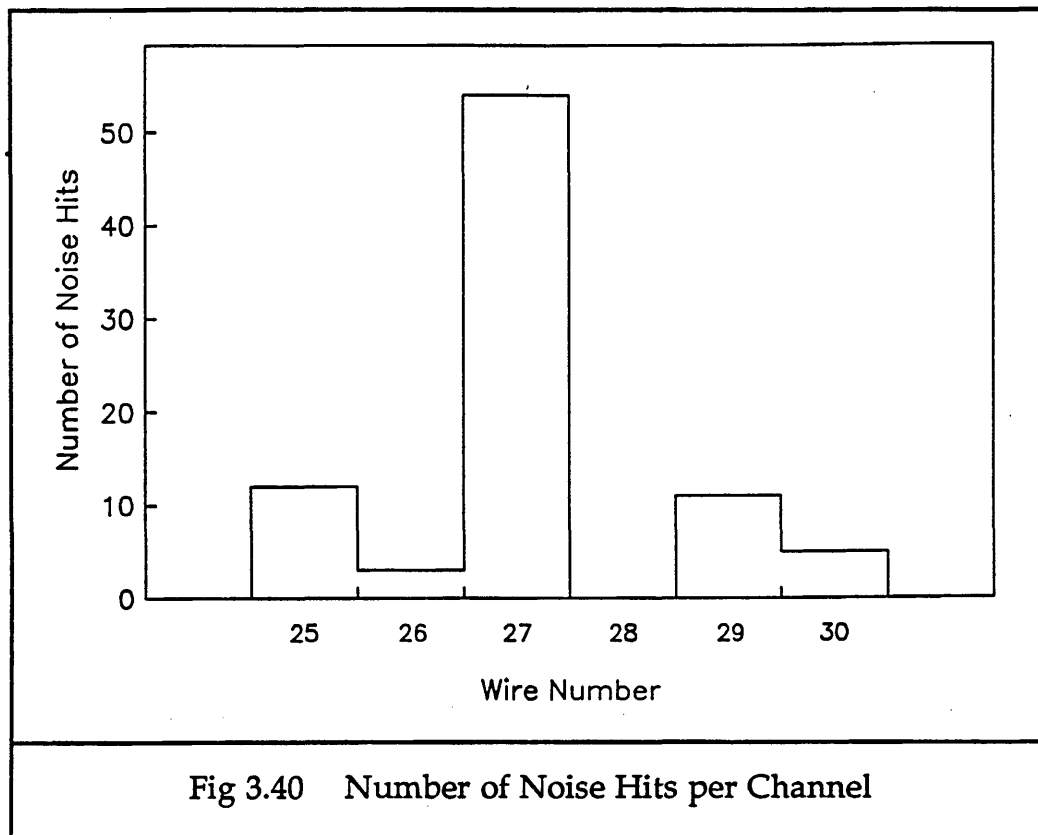
In figure 3.40, none of the wires have high voltage on them. Wires 27, 29 and 30 have been disconnected from the end box because their feedthroughs had broken down. One of wire 28's feedthroughs had also broken down, but it had not then been disconnected.

The TDC times recorded for these runs do not show the same clustering effect as before. They are spread out for each run in ranges between 80 ns and 110 ns. For this second set of runs, the percentage of noise hits on these dead wires, as a fraction of the total number of small cell hits, is dependent on the magnetic field applied. This can be seen in figure 3.41.

Fig 3.41   Noise Hits in Large Cells versus Magnetic Field
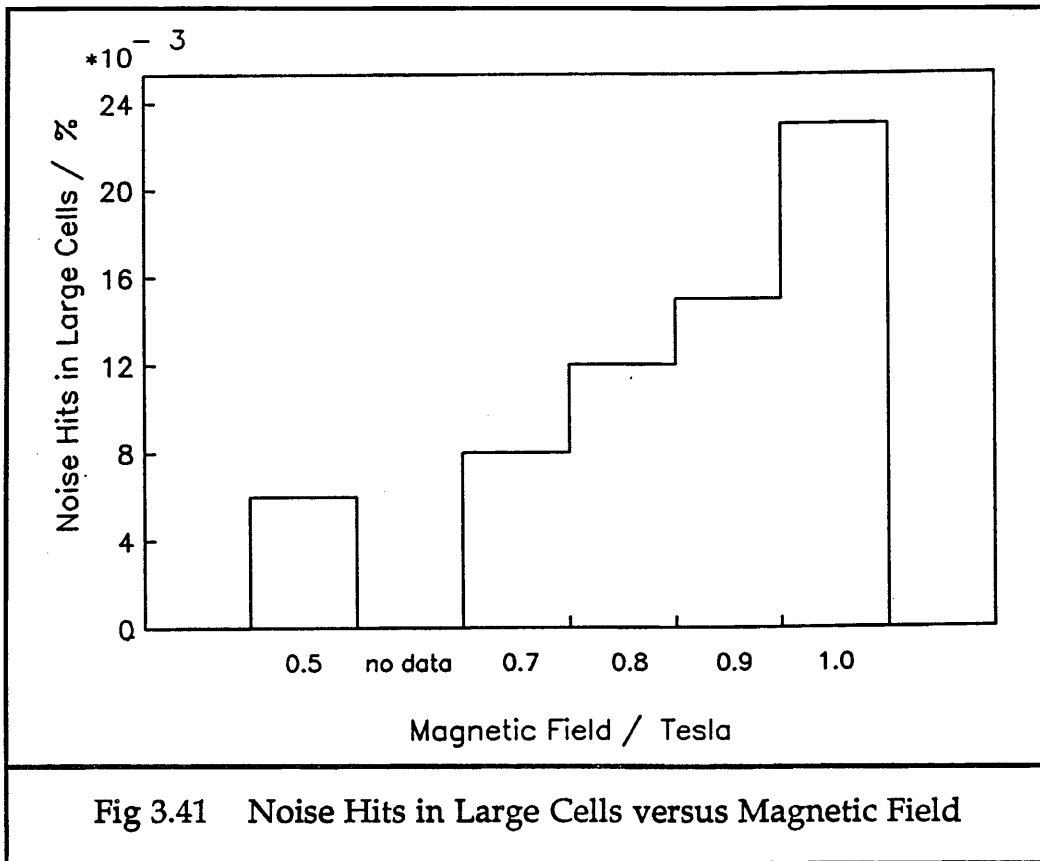
For both of these sets of runs, the noise cannot be coming from inside the chamber. There is no high voltage on the wires, so no electron amplification can occur to produce a signal. Some wires were disconnected from the readout and one was not there at all. Consequently, these noise hits must come from electrical crosstalk or interference. Since the number of noise hits from the first set of data is independent of the discriminator threshold, this implies that all these extra hits are from quite large signals, and are probably not just from noise on the discriminator input. Random noise would also not produce the clustering effect in the TDC times, or probably the restriction of the noise hits to just one layer of cells. The noise in the second set of runs increases as the magnetic field rises. This implies that crosstalk is occuring inside the magnet, probably on the preamplifier or across one of the connectors. The level of crosstalk, at 0.023 % with $\underline{B}$ = 1 Tesla, is very low.

5.3   The Performance of the Small Test Chamber with Argon-Ethane

5.3.1   How Well the Drift Relation Works Across the Cells

For all the figures in this section, the chamber is operated under standard conditions, which are the same as those for which the higher order drift relations were tested. These conditions are :

a)   argon-ethane 50%-50% gas
b)   sense wire voltage plateaued at 2.07 kV
c)   constant fraction discriminators
d)   magnetic field at 1 Tesla
e)   for simplicity, tracks perpendicular to the cells and wires.

For this standard run, the results for the best linear drift velocity and best polynomial drift relation are summarised in table 3.4.

Table 3.4 Comparison of Linear and Polynomial Drift Relations, with $\underline{B} = 1$ Tesla					
Drift Relation	RMS of Residuals /μm Small Cells		Efficiency of keeping a track which started with sufficient hits	Mean no. of hits per track	Noise hits
	Left	Right			
Linear	90.5	90.0	90.27 %	4.094	0.80 %
$\leq t^7$	88.9	88.7	90.43 %	4.110	0.80 %

The following figures show how the drift relations fit as a function of drift distance for this run. Figure 3.42 shows the mean of the residuals across the left hand side of the cell when a linear relation is used and figure 3.43 shows the mean of the residuals across the right hand side. Figures 3.44 and 3.45 show the mean of the residuals for the two sides of the cell when a polynomial drift relation is used. Figures 3.46 and 3.47 show the RMS of the residuals across each side of the cell when a linear relation is used. Figures 3.48 and 3.49 show the RMS of the residuals for each side of the cell when a polynomial drift relation is used.

Fig 3.42   Mean of Residuals across Left of Cell, Linear Relation

Left Hand Side of Cell

Linear Drift Relation

$\underline{B}$ = 1 Tesla
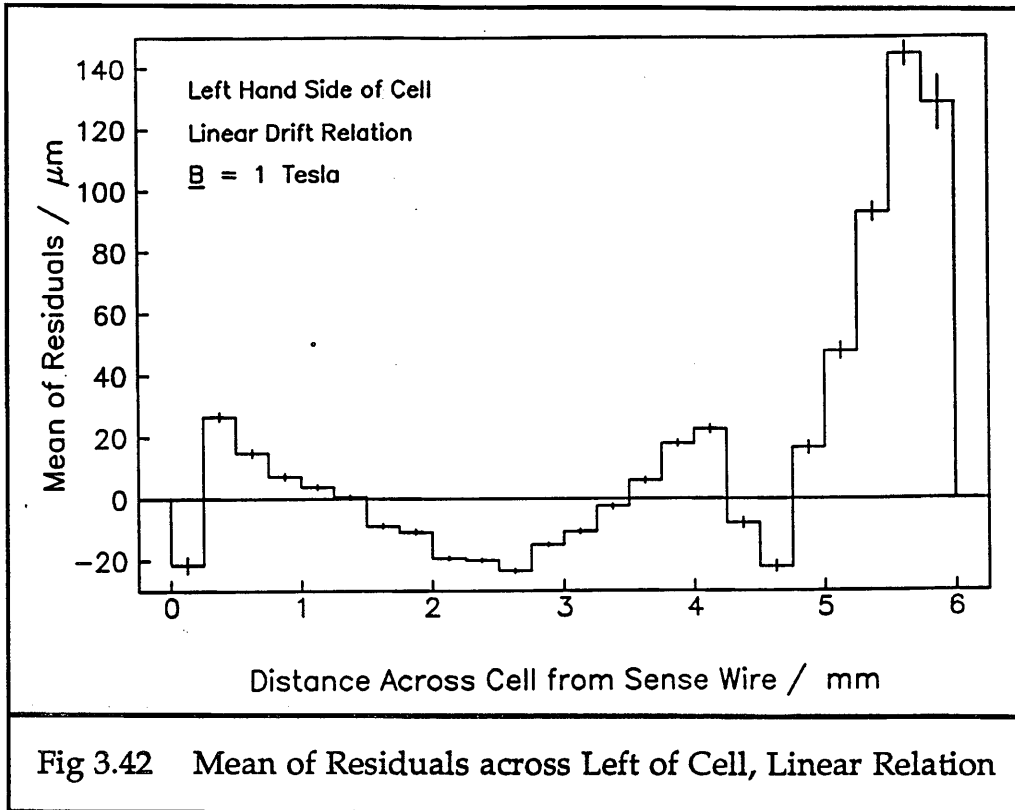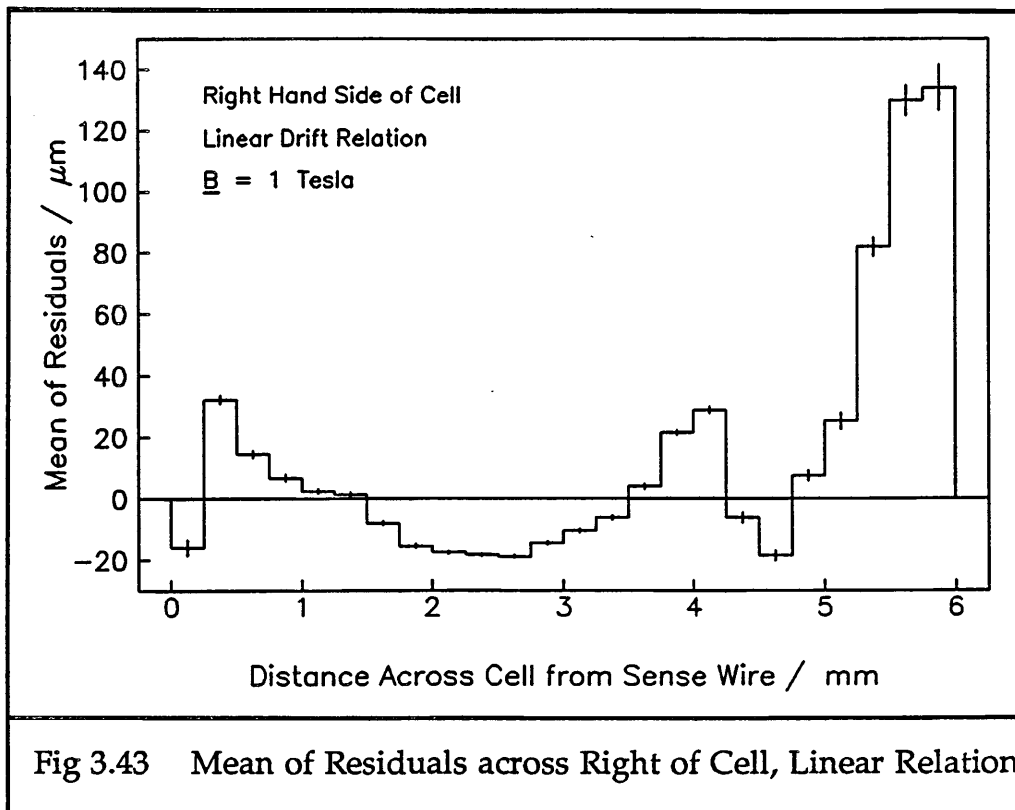
Fig 3.43   Mean of Residuals across Right of Cell, Linear Relation

Right Hand Side of Cell

Linear Drift Relation

$\underline{B}$ = 1 Tesla

Fig 3.44   Mean of Residuals across Left of Cell,
Polynomial Drift Relation

Fig 3.45   Mean of Residuals across Right of Cell,
Polynomial Drift Relation

Fig 3.46   RMS of Residuals across Left of Cell, Linear Relation

Fig 3.47   RMS of Residuals across Right of Cell, Linear Relation
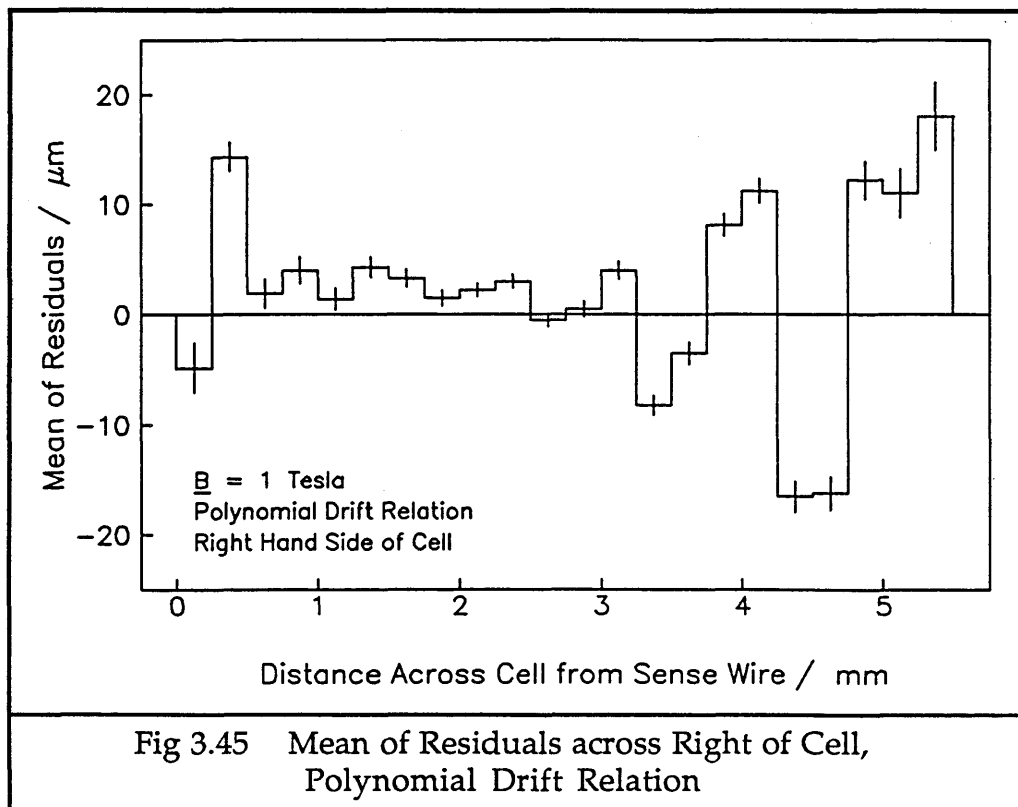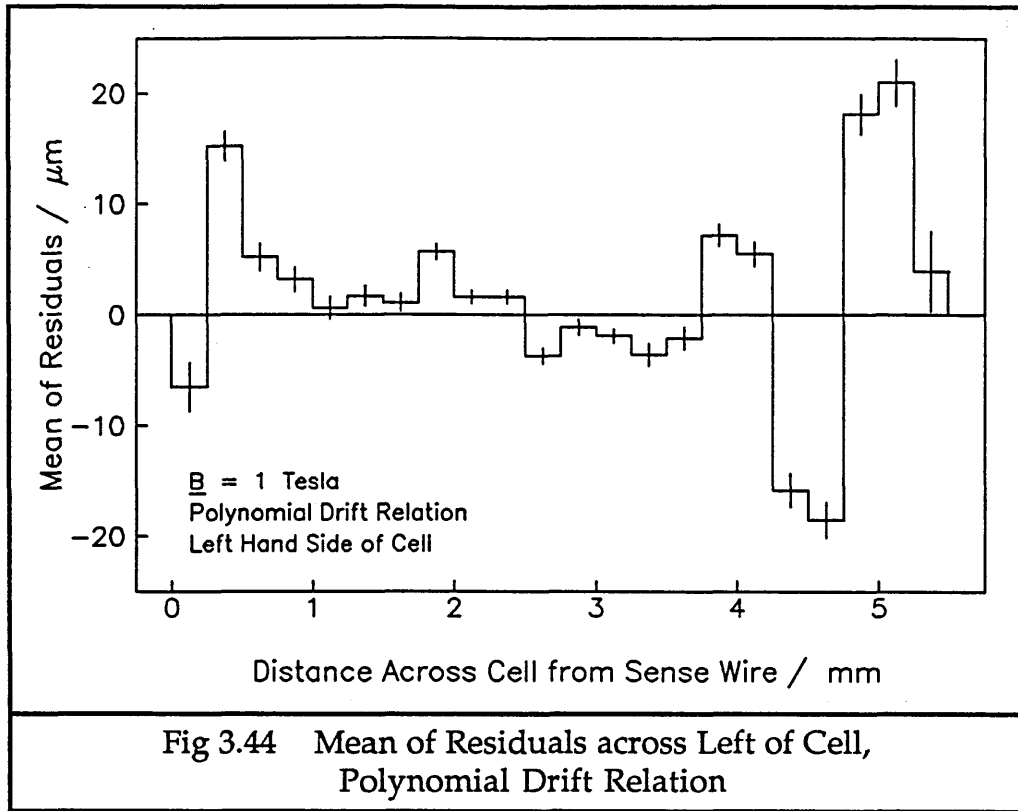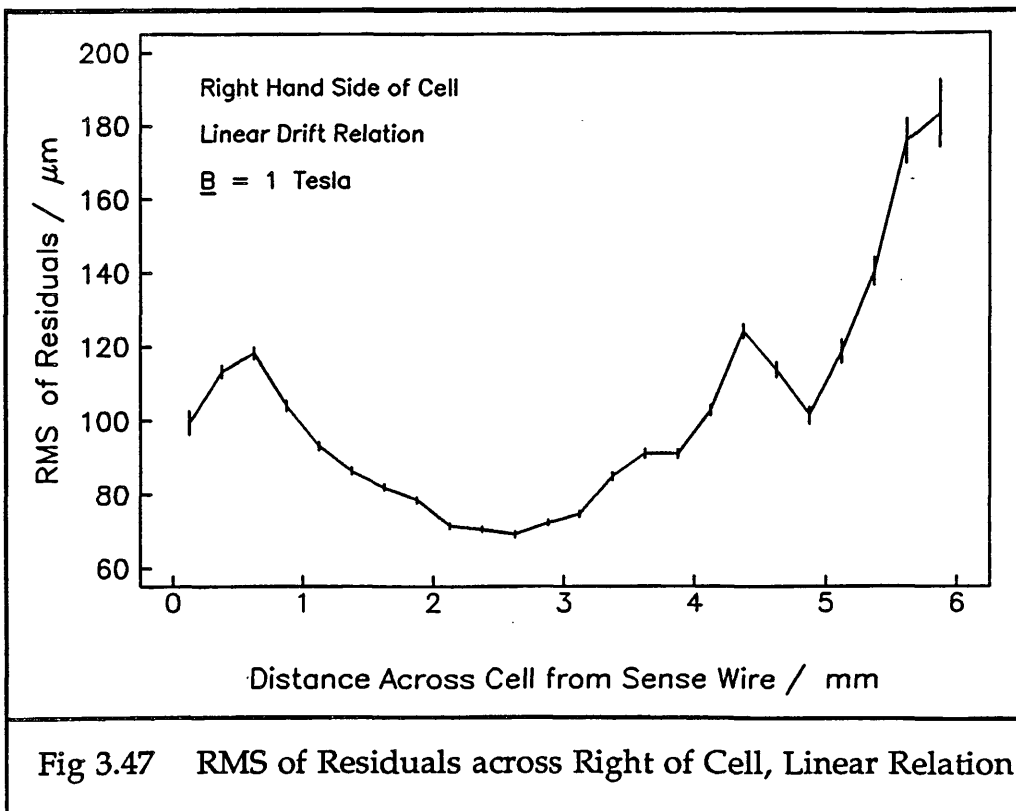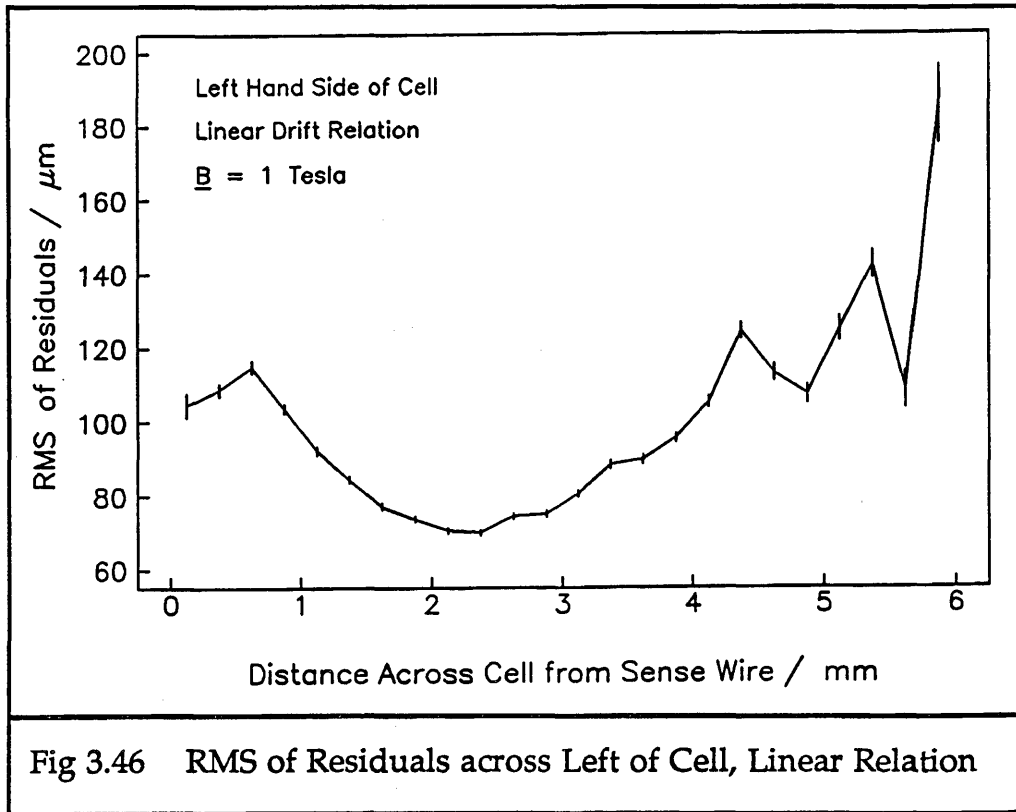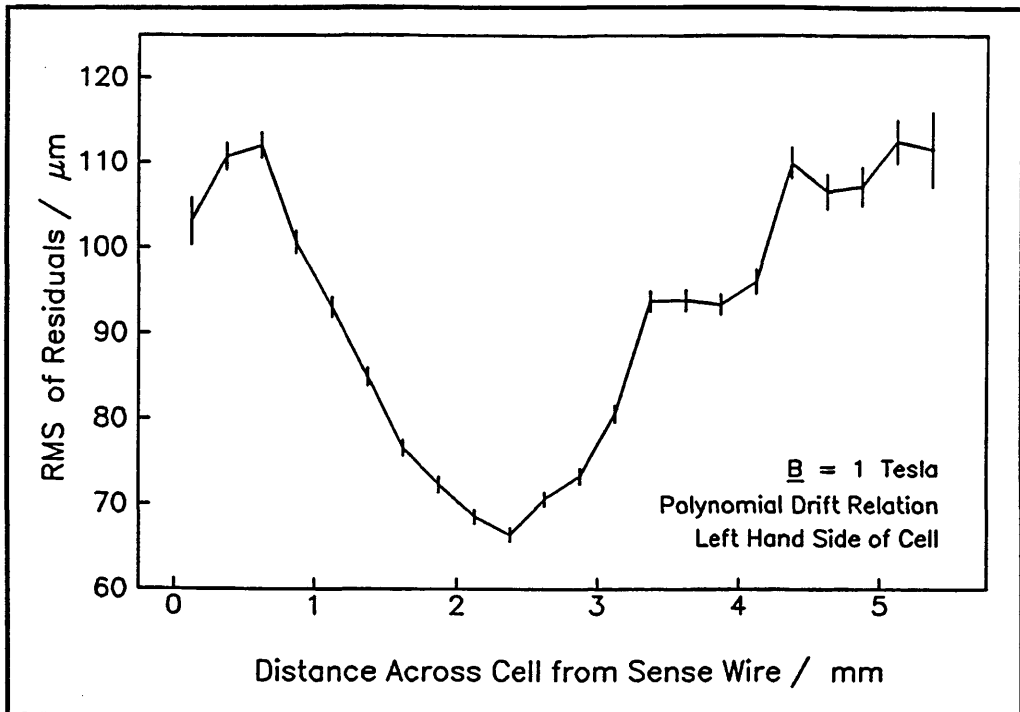
Fig 3.48 RMS of Residuals across Left of Cell,
Polynomial Drift Relation
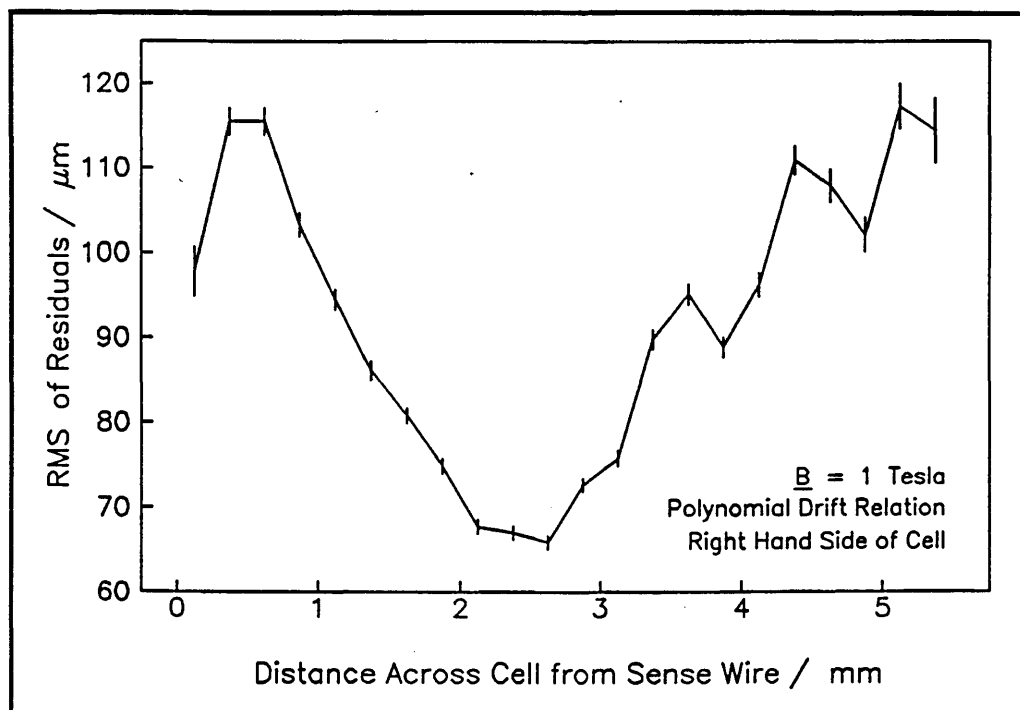
Fig 3.49 RMS of Residuals across Right of Cell,
Polynomial Drift Relation

The main difference between the results from these two drift relations is that with the linear relation there are a few hits at very long drift times which are very badly fitted by the drift relation. When the higher order relation is used, these hits are either cut or the zero time jitter assigns them

shorter drift times, and they are no longer seen. Over most of the cell, apart from at this very great distance out from the sense wire, both the linear and the polynomial drift relations seem to work equally well in modelling the data.

When considering the change of RMS of residuals across the cell, it can be seen that this is best about 2.5 mm away from the sense wire. Beyond this distance, the effects of uneven electric field around the field wires are seen and the resolution gets worse. It can therefore be predicted that for the large cells, this region of low RMS of the residuals in the centre of the drift distance range would be longer, and possibly lower than that seen in these small cells.

Figure 3.50 shows the distribution of hits across the cell for the previous eight plots. Each distribution contains approximately 50000 hits. The loss of hits close to the sense wire and near the field wires can be seen, although the cell was not 100 % efficient across its whole length when the data was taken originally. The distribution of hits with drift distance after the track fitting cuts can be compared with the TDC time distribution before the cuts, in figure 3.32. It is reversed with respect to the TDC times, because the TDCs were operated in COMMON STOP mode, making the smallest TDC times correspond to the longest drift distances.
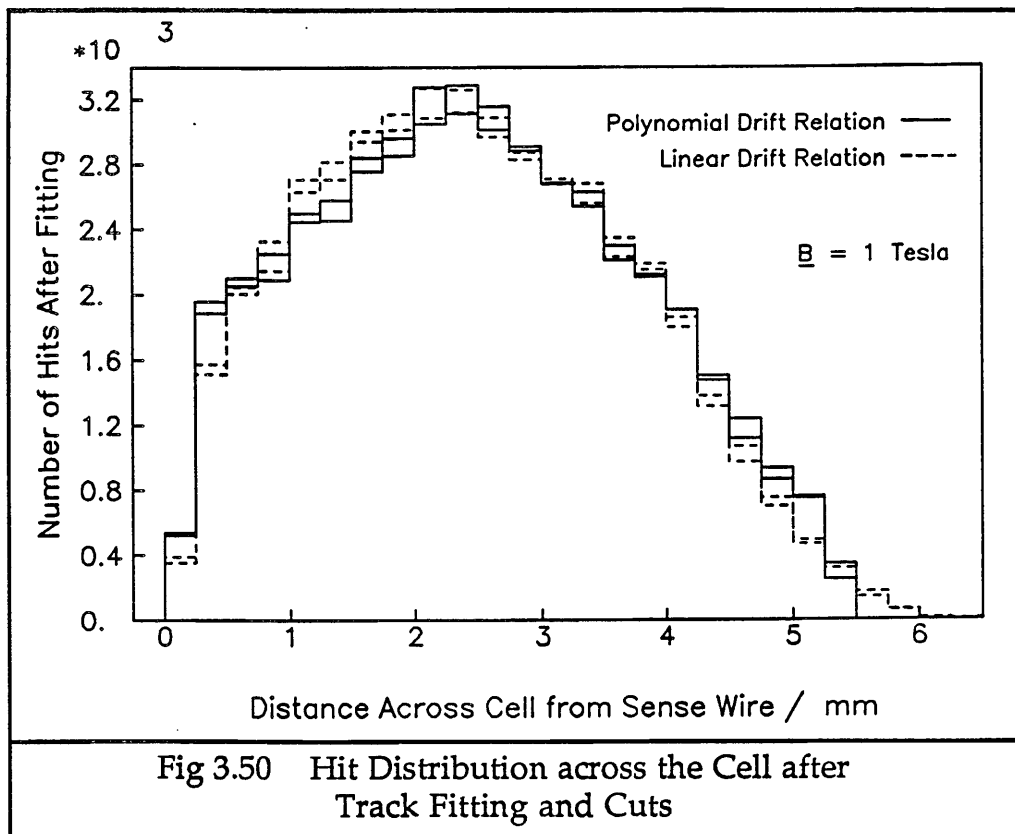
Fig 3.50   Hit Distribution across the Cell after
Track Fitting and Cuts

136

5.3.2 Changes with the Sense Wire Voltage

The effect of raising the sense wire voltage on the TDC time distribution recorded can be seen in figure 3.51. These two sets of data were taken with dual threshold discriminators, threshold level 1 V, and the magnetic field at 1 Tesla. The track angle ø was ~ 0°, and the gas was argon-ethane 50%-50%. The main effect is to improve the efficiency of the chamber near the sense wire, which can be seen from the much steeper edge at the zero time point, just past 200 ns. Across the body of the cell, the TDC time distribution becomes much flatter at the higher sense wire voltage, indicating a more uniform efficiency over a greater area of the cell. There are slightly more long drift times read out, probably indicating that hits are being produced in cells next to those through which the charged particle passed.

Fig 3.51   TDC Time Distributions with Different
Sense Wire Voltages
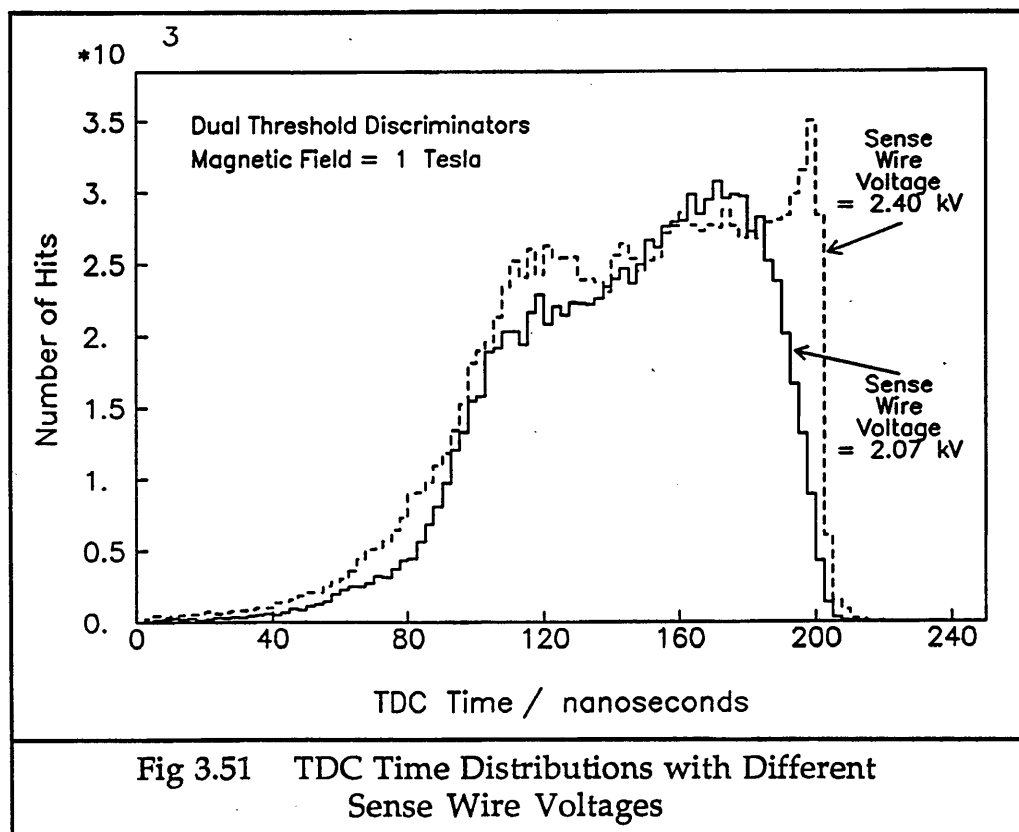
When the drift relations for these two runs are examined, they are found to be very similar over much of the length of the cell, only differing slightly near the sense wire and field wires, the regions of low efficiency where there are less hits, with a larger range of values. These two drift relations for the left hand side of the cell can be seen in figure 3.52.

Fig 3.52   Electron Drift Relations with Different
Sense Wire Voltages, Magnetic Field = 1 Tesla
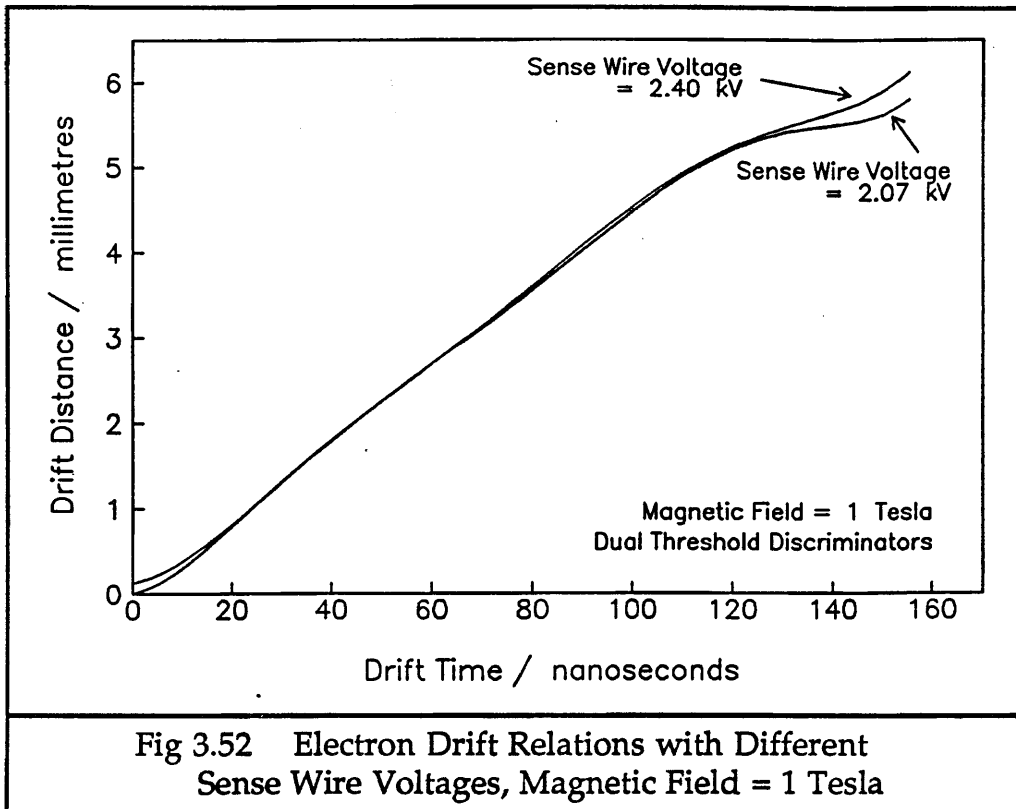
Figure 3.53 shows another example of how little the drift relation changes over most of the cell. These three runs had the same conditions as the previous two, except that constant fraction discriminators were used and the magnetic field was 0 Tesla. The range of voltages is less than before, because the chamber was breaking down and leaking current, so much caution was being taken with the voltage level on the wires.

The usual reason for raising the sense wire voltage is to improve the resolution of the chamber, and the resulting decrease in the RMS of the residuals is shown in figure 3.54 for the two sets of data. One of the reasons for the improvement in resolution as the sense wire voltage is raised is the increased gain near the sense wires. This produces larger, steeper rising pulses, which are better for timing at the discriminators. Also, the electric field around the field wires has a steeper gradient, leading to less variation of drift times from this area of the cells.
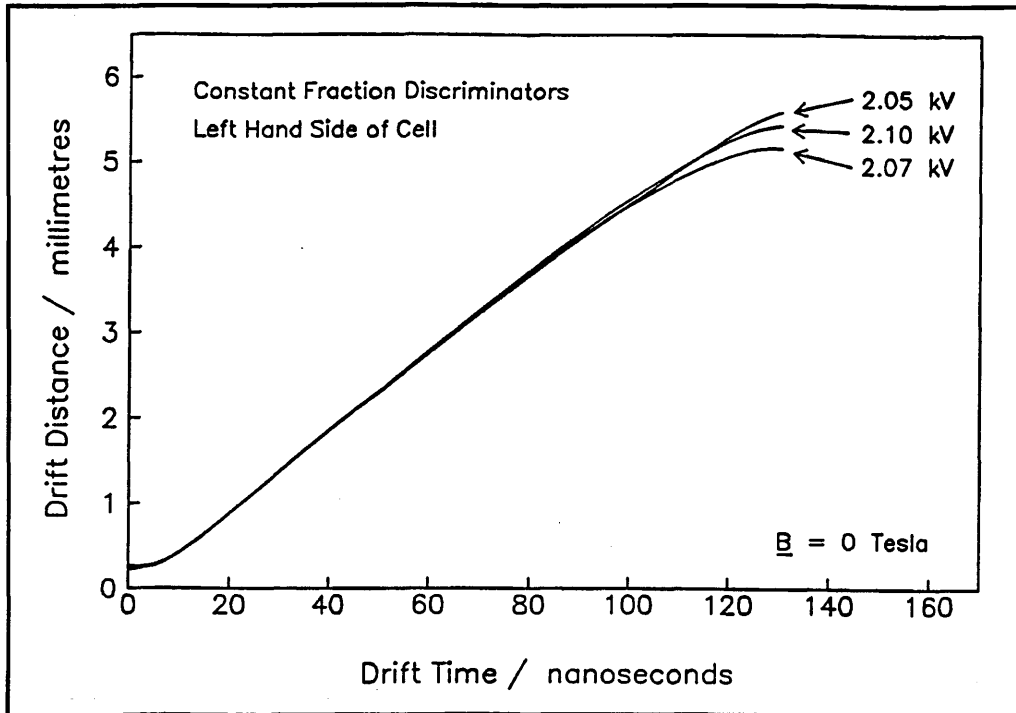
Fig 3.53   Electron Drift Relations with Different Sense Wire Voltages, Magnetic Field = 0 Tesla
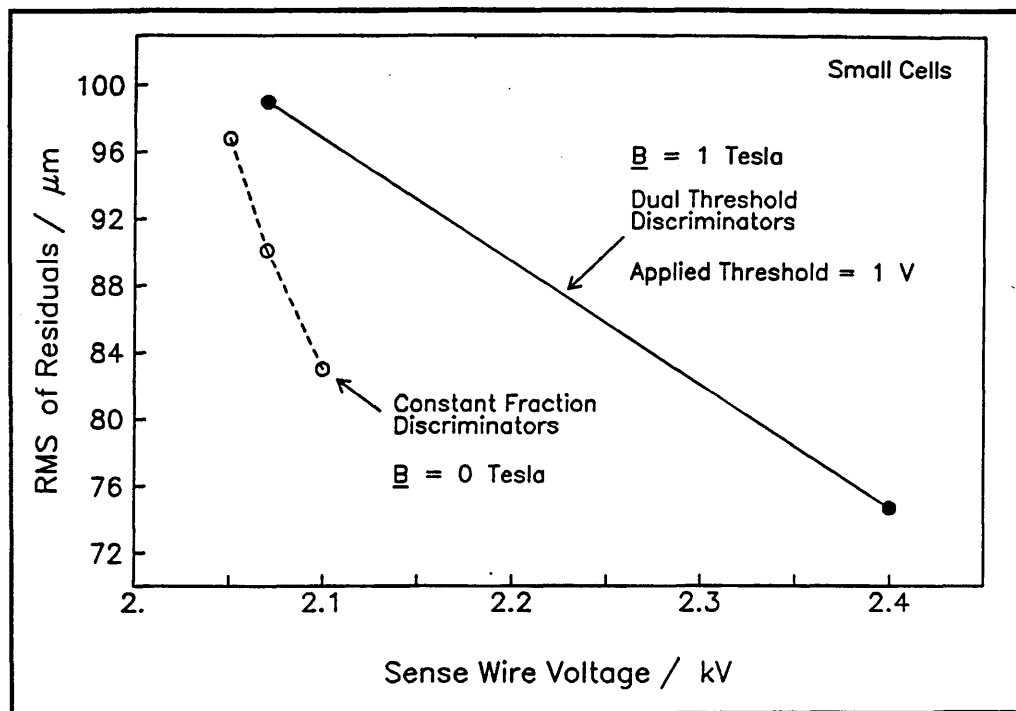
Fig 3.54   RMS of the Residuals versus Sense Wire Voltage

Changing the sense wire voltage does not affect the mean number of hits per track or the amount of noise found in the chamber, when constant fraction discriminators are used across the low range of voltages tested. With the dual threshold discriminators and the much larger increase in

sense wire voltage from 2.07 kV to 2.40 kV, the mean number of hits per track increases from 4.162 to 4.629. The percentage of noise hits increases from 0.69 % to 2.20 %. More hits are included in the track fitting because the signals at the discriminators are larger, with smaller variation in their arrival times from the same parts of the cell. The amount of noise increases because if electrons stray from one cell into a neighbouring one, they are more likely to be amplified in the gas into a signal large enough to be read out.

5.3.3 Changes with the Magnetic Field

Running the chamber with the magnetic field at 1 Tesla produces several changes in its behaviour from when there was no magnetic field applied. The most basic change happens to the paths of the drifting electrons, as shown in Appendix B at the end of this chapter. The TDC time distributions with field at 0 T and 1 T can be seen in figure 3.55, for small cells, straight through tracks, plateaued voltage at 2.07 kV, argon-ethane 50%-50% gas and constant fraction discriminators. The distributions have been scaled to have the same number of entries as each other, for comparison. The shift in TDC times measured between 0 and 1 Tesla here is actually rather small.

Figure 3.56 shows the change in the TDC time distribution when the magnetic field is increased from 0 to 1 Tesla, for the data sets taken with dual threshold discriminators and sense wire voltage of 2.40 kV. The difference is larger in this situation, with both distributions having fairly flat tops, but when the field is applied, many more longer drift times are recorded. Also, the tail of noise hits is smaller when the magnetic field is applied than when there is no field.
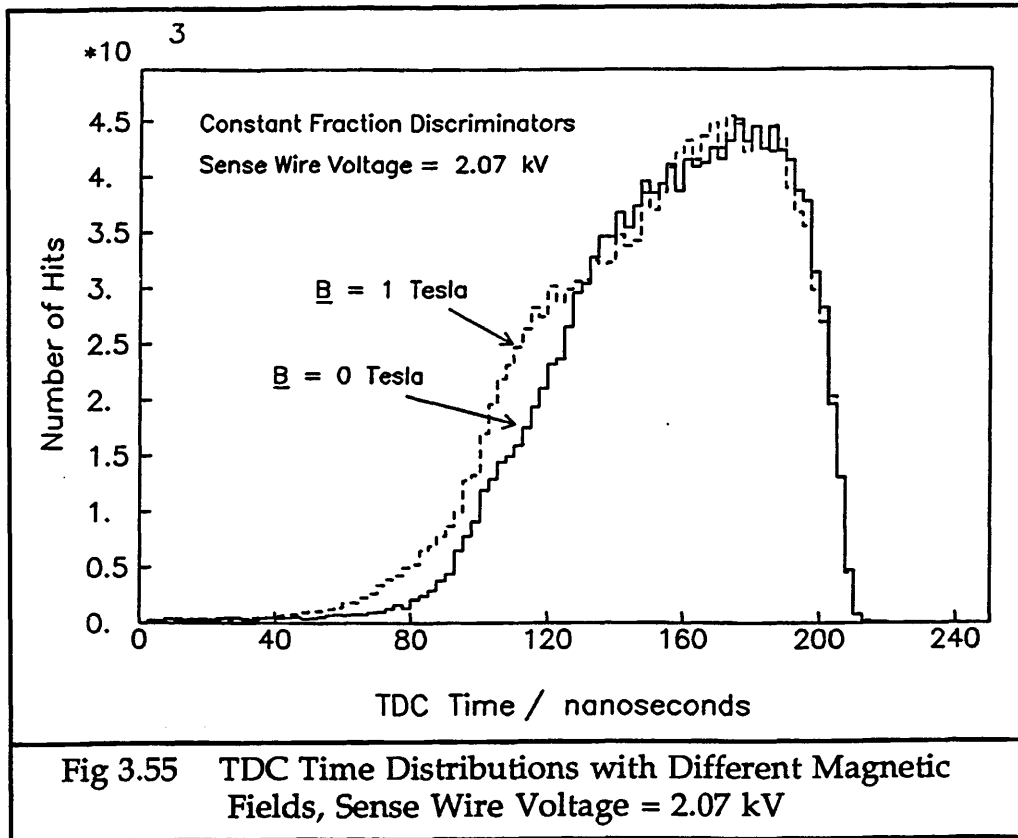
Fig 3.55   TDC Time Distributions with Different Magnetic
Fields, Sense Wire Voltage = 2.07 kV
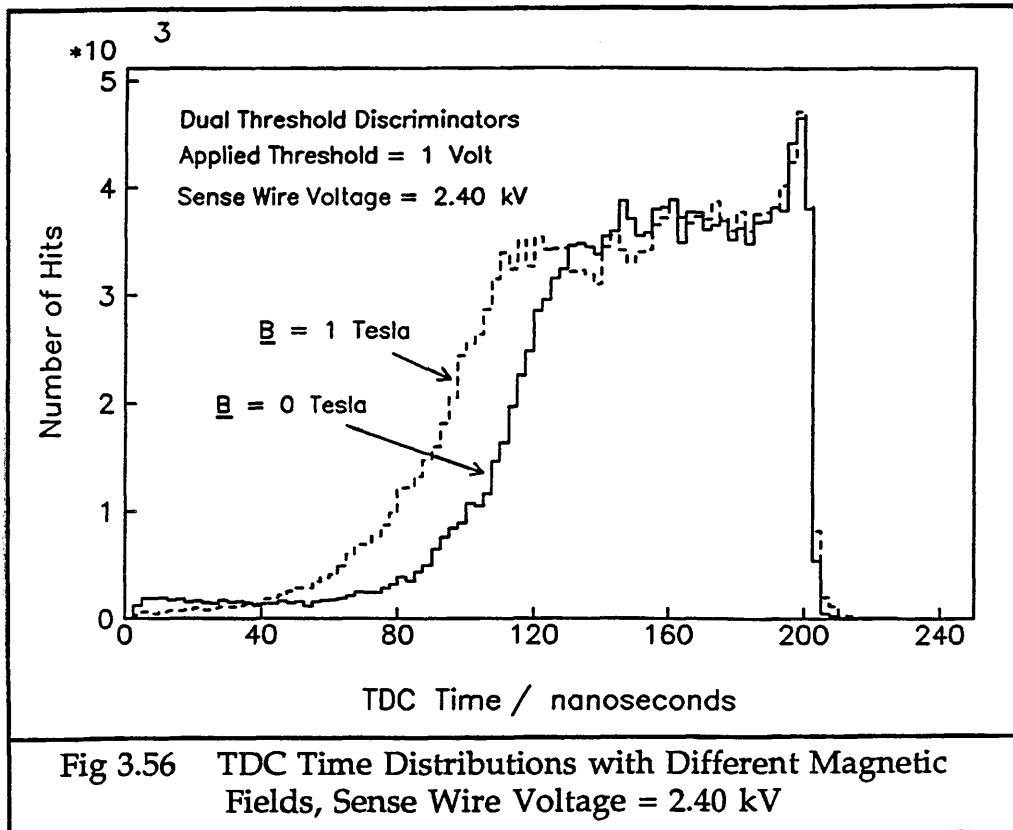
Fig 3.56   TDC Time Distributions with Different Magnetic
Fields, Sense Wire Voltage = 2.40 kV

The presence of the magnetic field means that the electrons experience
the Lorentz force perpendicular to their direction of travel when there is no
magnetic field, and their paths towards the nearest sense wire become very

much longer. This leads to longer drift times being measured and the mean linear velocity of the electrons with the magnetic field at 1 Tesla goes down. This can be seen in figure 3.57. The runs have straight through tracks, and argon-ethane 50%-50% gas. At the low sense wire voltage of 2.07 kV, the reduction of the best mean linear drift velocity is larger than when the sense wire voltage is at 2.40 kV.
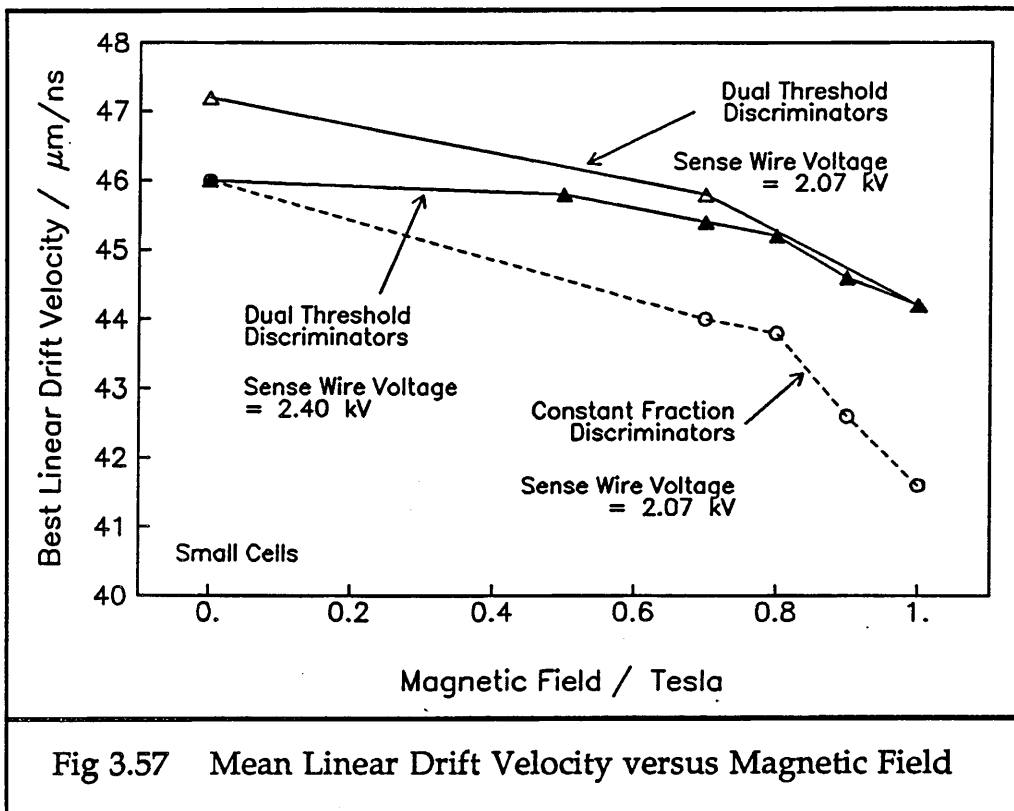
Fig 3.57   Mean Linear Drift Velocity versus Magnetic Field

Figure 3.58 shows the polynomial drift relations for the left hand sides of the small cells for three of the runs taken with constant fraction discriminators at various values of the magnetic field. Over most of the cell, the drift relation can be seen to need slower velocities to represent it as the magnetic field increases, and longer drift times are found. The longest drift times found in each run have very large errors on them from the region of low electric field in the cell around the field wires. Consequently the precise form of the drift relation here is not very significant.

As the magnetic field increases, the mean number of hits per track increases. This is shown in figure 3.59. When the sense wire voltage is fairly low, then this effect is noticable but not very large. At the higher sense wire voltage, the increase in the mean number of hits per track is such that more than half the tracks have five hits included in the track fitting after the cuts, with only four layers of cells working.

142
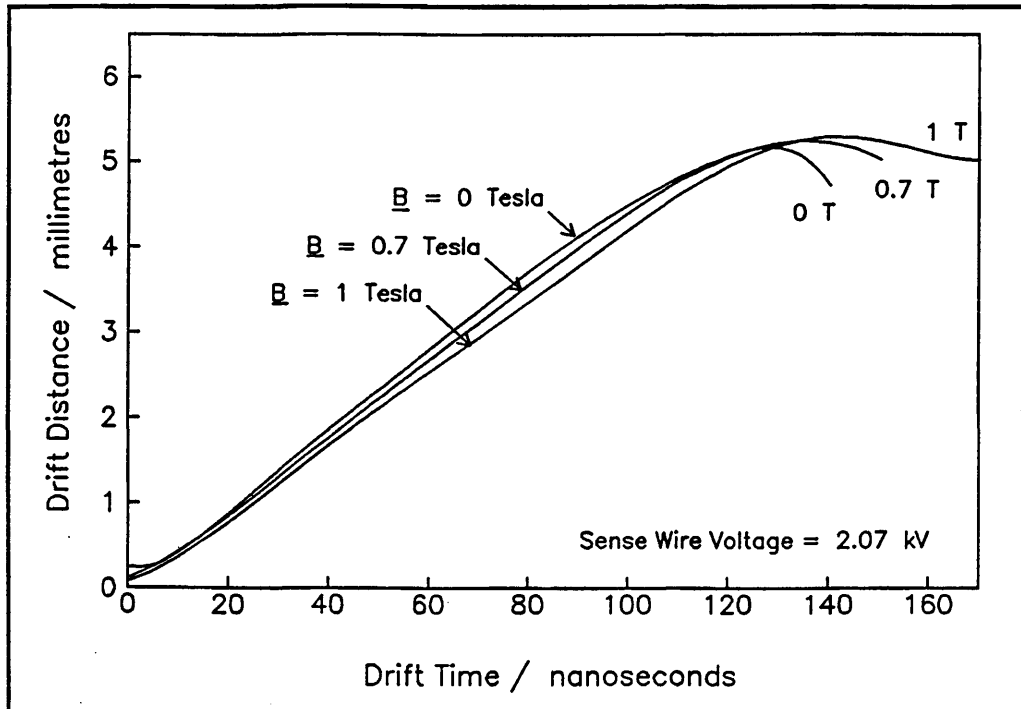
Fig 3.58   Electron Drift Relations at Different Magnetic Fields
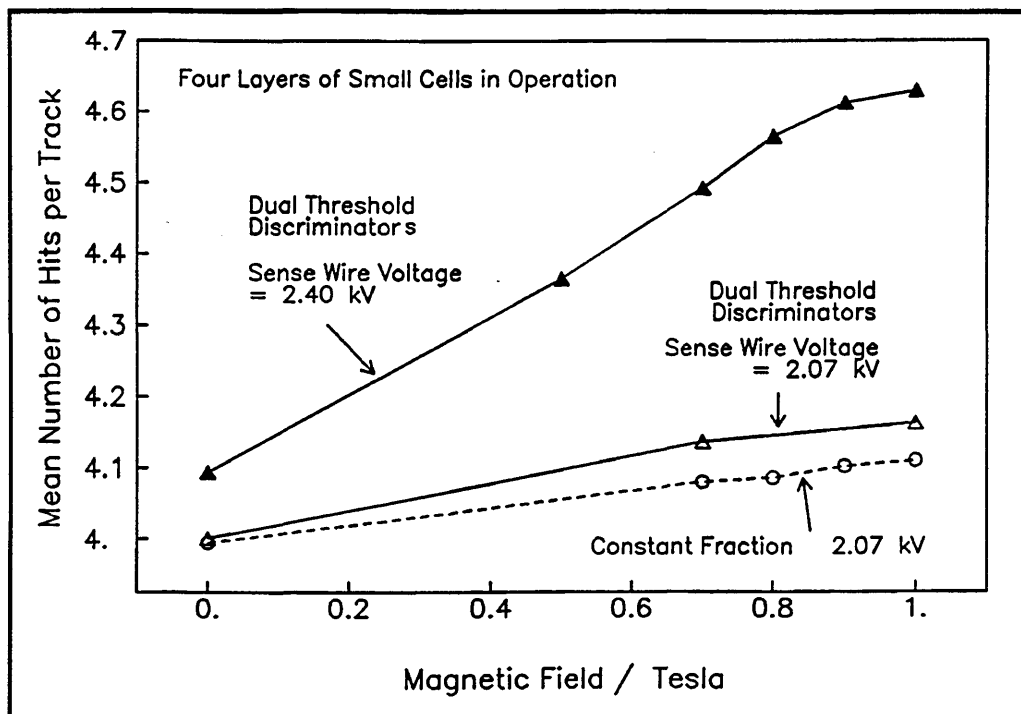
Fig 3.59   Mean Number of Hits per Track versus Magnetic Field

The amount of noise hits found in the chamber as a function of magnetic field is shown in figure 3.60. For each of the three sets of runs examined, the amount of noise reduces as the magnetic field increases. When the sense wire voltage is low and the magnetic field is 1 Tesla, then

the level of excess hits in the chamber is less than 1 % of the total number of hits recorded over the whole run. This figure rises to ~ 2 % when the sense wire voltage is at the higher level. The noise hits at 0 Tesla are not just the extra hits not used in the track fitting, since the way of defining a noise hit does not change when the magnetic field is 0 or 1 Tesla, and the cut used to see whether a hit wire is too far from a first fitted track is 10 mm for all the analysis. The explanation for the decrease in noise when the magnetic field is applied is not obvious, but the field may affect the preamplifiers in some way, reducing any crosstalk. This is at variance with the effect seen on the large cells, where the amount of noise hits increases as the magnetic field increases. However, with the effect on the large cells, the overall level of noise is nearly 2 orders of magnitude lower than that seen on the active small cells.

Fig 3.60   Percentage Noise Hits versus Magnetic Field
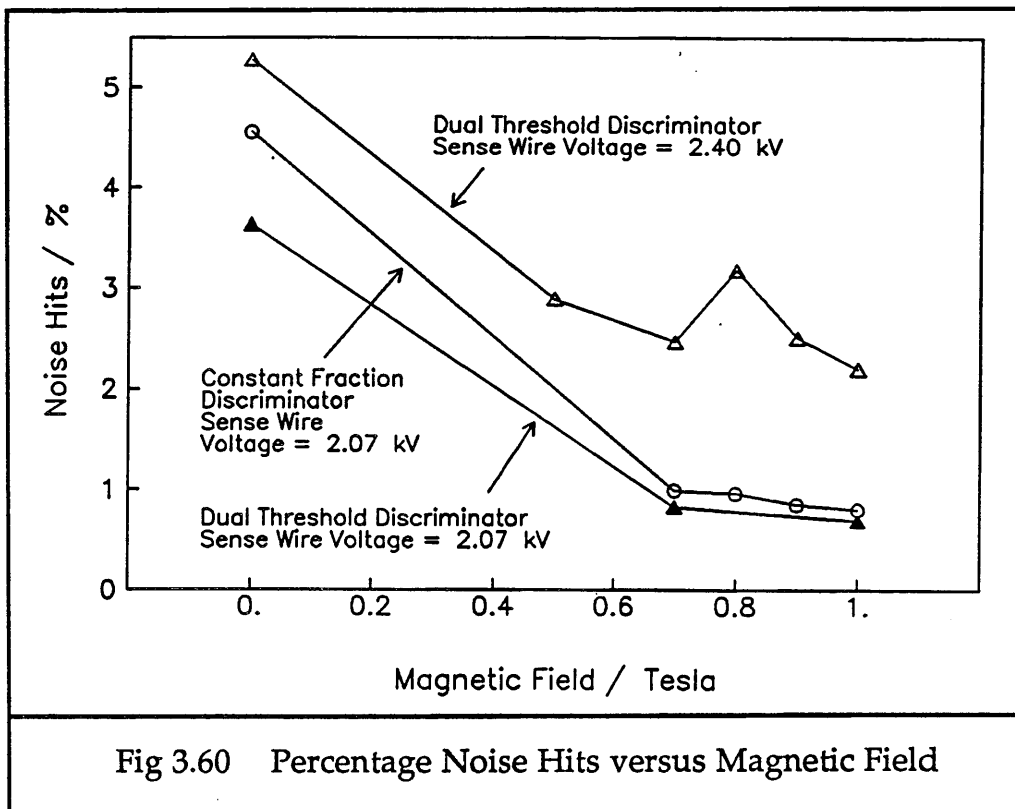
When the magnetic field is applied to the chamber, there is no significant change in the RMS of the residuals for all three sets of data which can be considered to be an effect of the magnetic field. The actual levels found will be presented in the next section as a demonstration of discriminator dependent results.

5.3.4 Changes with Discriminator Type

The two types of discriminator used were :

i) constant fraction   fraction = 1/2   delay = 5 ns

ii) dual threshold   applied threshold = 1 V

                                       (internal thresholds = 19 mV and 41 mV)

Figure 3.61 shows two TDC time distributions for small cells. One was taken with constant fraction discriminators and the other with dual threshold, with both runs having the same sense wire voltage of 2.07 kV and magnetic field of 1 Tesla. As can be seen, there is almost no difference at all between these two distributions. The dual threshold discriminators produce very slightly more of a hump of drift times at the edge of the cell, where the TDC time is around 110 ns.
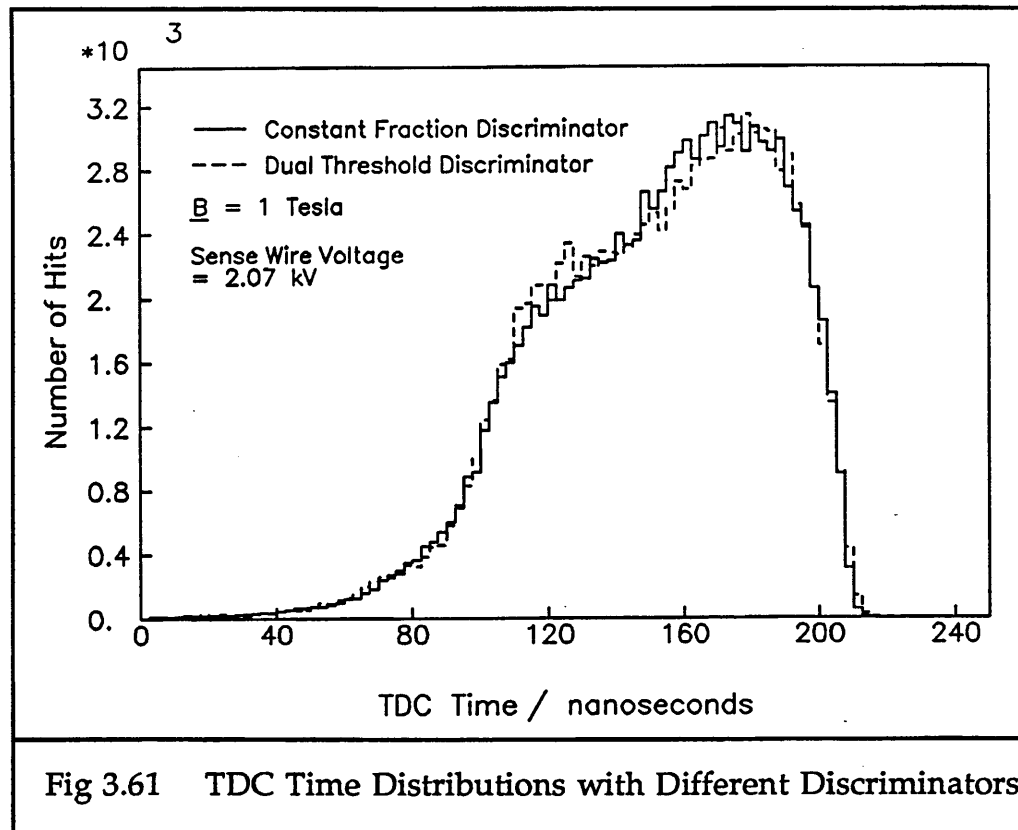
Fig 3.61   TDC Time Distributions with Different Discriminators

Figure 3.62 shows the RMS of the residuals for the small cells, measured with each type of discriminator. The constant fraction discriminators produce values which are several microns smaller than those from the dual threshold discriminators when the sense wire voltage is at 2.07 kV. When the sense wire voltage is increased to 2.40 kV, then the dual threshold discriminators perform much better than the constant fraction ones. Unfortuneately, data is not available for the constant fraction

discriminators with sense wire voltage this high for comparison.

Fig 3.62   RMS of Residuals with Different Discriminators
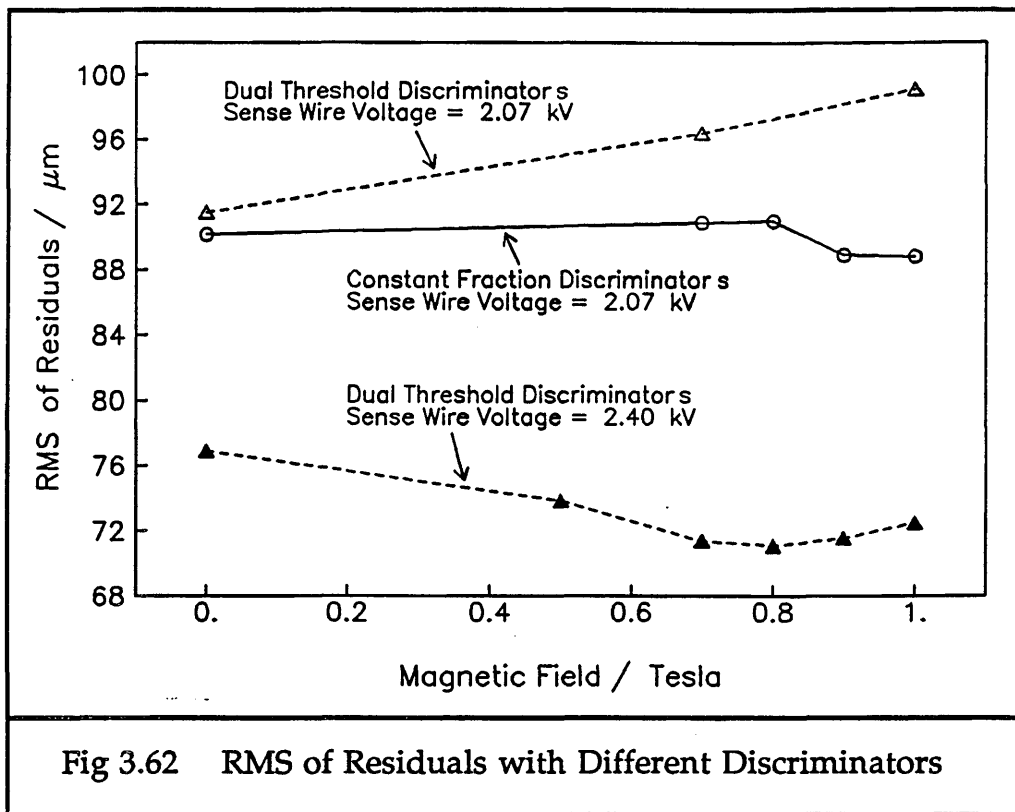
5.3.5 Changes with the Discriminator Threshold Level

There are several effects which result from raising the threshold on the dual threshold discriminator. Firstly, the distribution of TDC times changes. Two TDC time distributions for applied thresholds of 1 Volt and 4.5 Volts can be seen in figure 3.63.

The zero times for these two TDC time distributions are the same, because the scintillator signals go through a separate discriminator system to produce the STOP signal than that used by the chamber signals. When the external threshold is raised from 1 V to 4.5 V, the rise of the TDC distribution at the very short drift times near the zero time becomes less steep, and is shifted along by ~ 5 ns. This effect can be explained by the slewing of the timing from the discriminator.

As the threshold is raised, the timing is taken from higher up the signal where there is more variability in shape. The signal reflections on the 40 cm sense wires in the small test chamber arrive very rapidly, compared with those on the 2 m wires in the ITC. Therefore, they affect the signal leading edge lower down than in the longer chamber, and these effects can be seen by the discriminators. The resolution obtained would be expected to get worse as the threshold is increased because of the reflections, and this is indeed seen, in figure 3.64.

Fig 3.63 TDC Time Distributions with Different
Discriminator Threshold Levels

Fig 3.64 RMS of Residuals versus Discriminator
Threshold Level
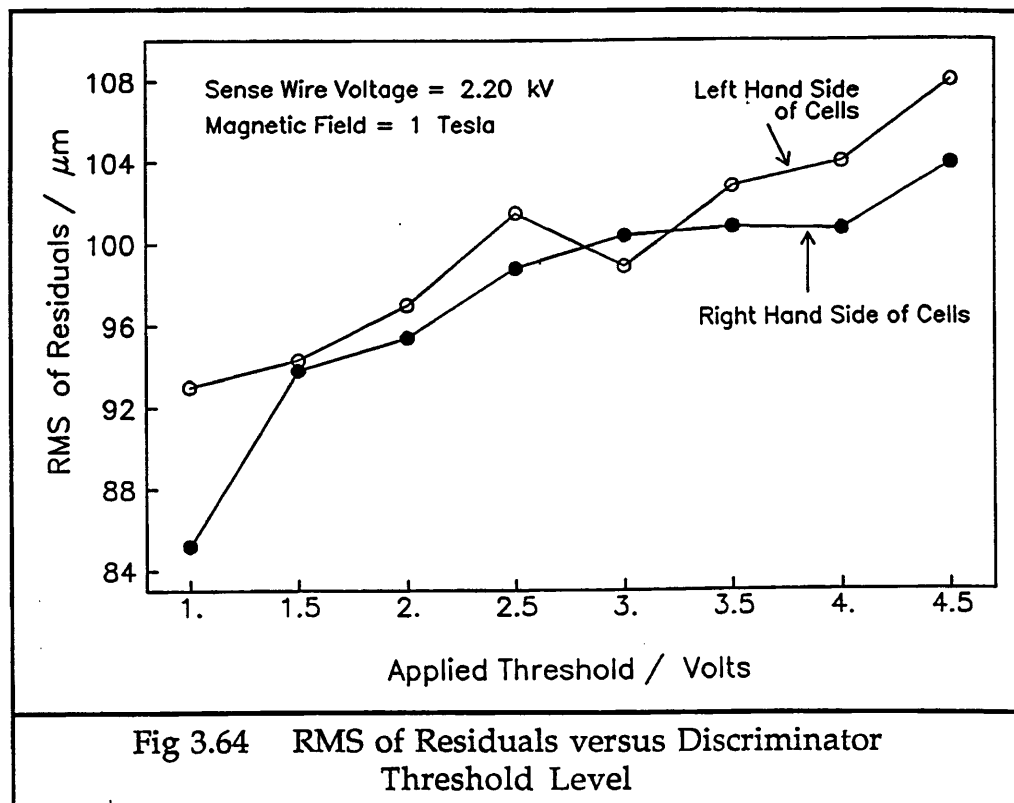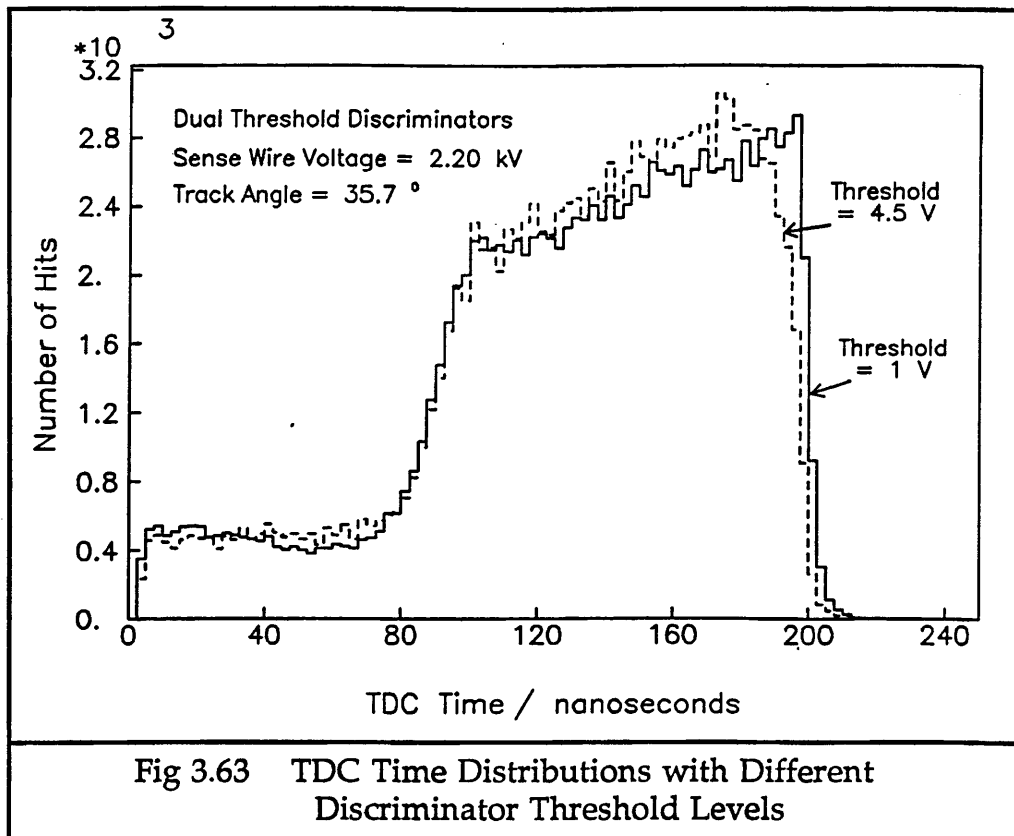
The runs used to produce figure 3.64 all have argon-ethane 50%-50% gas, a 1 Tesla magnetic field, and track angles of $\theta = 90°$ and $\phi = 35.7°$.

Another possible result of changing the threshold is a change in the

number of noise hits found. Raising the threshold would be expected to decrease the number of noise hits, if the source of noise was from interference on the signal. However, the amount of noise seen is found to be independent of the threshold applied, and so the noise hits must be caused by some sort of crosstalk. The noise level is at about 1.5 % of the total number of hits measured. The mean number of hits per track is also found to be independent of the discriminator threshold level.

5.3.6 Changes with Track Angle

During the tests at CERN, the angle of incidence between the beam and the chamber was varied to simulate various types of tracks expected in the ITC. This was done by tilting the chamber at an angle to the beam on concrete blocks and aluminium frameworks inside the magnet. The angle $\emptyset$ of the track in the r-$\emptyset$ plane was varied from 0°, which is perpendicular to the wires, to ~ 49°.

Results are presented here for the varying $\emptyset$ angle runs. Four runs were analysed at different track angles. All the runs had argon-ethane 50%-50% gas, dual threshold discriminators with a threshold of 1 V, a magnetic field applied of 1 Tesla and sense wire voltage of 2.07 kV.

The change in the TDC time distributions with track angle $\emptyset$ can be seen in figure 3.65. As the track angle increases, the tail of long drift times gets larger and larger, since the maximum perpendicular distance between the tracks and the sense wires increases with $\emptyset$. Apart from this, there is very little change between the distributions.

Figure 3.66 shows the polynomial drift relations for the left hand sides of the small cells at these $\emptyset$ angles. Across most of the cell length, the gradients of the drift relations are very similar to each other. However, the way each relation handles the very long drift times is not very consistent as a function of the track angle.

With such varying drift relations, especially at the edges of the cells, it would seem that the quality of the data for these very long drift times was not very uniform. Consequently, the overall resolution as indicated by the RMS of the residuals would be expected to get worse with increasing track angle. This happens and is shown in figure 3.67.

Fig 3.65   TDC Time Distributions with Different Track Angles

Fig 3.66   Electron Drift Relations with Different Track Angles

149

Fig 3.67   RMS of Residuals versus Track Angle
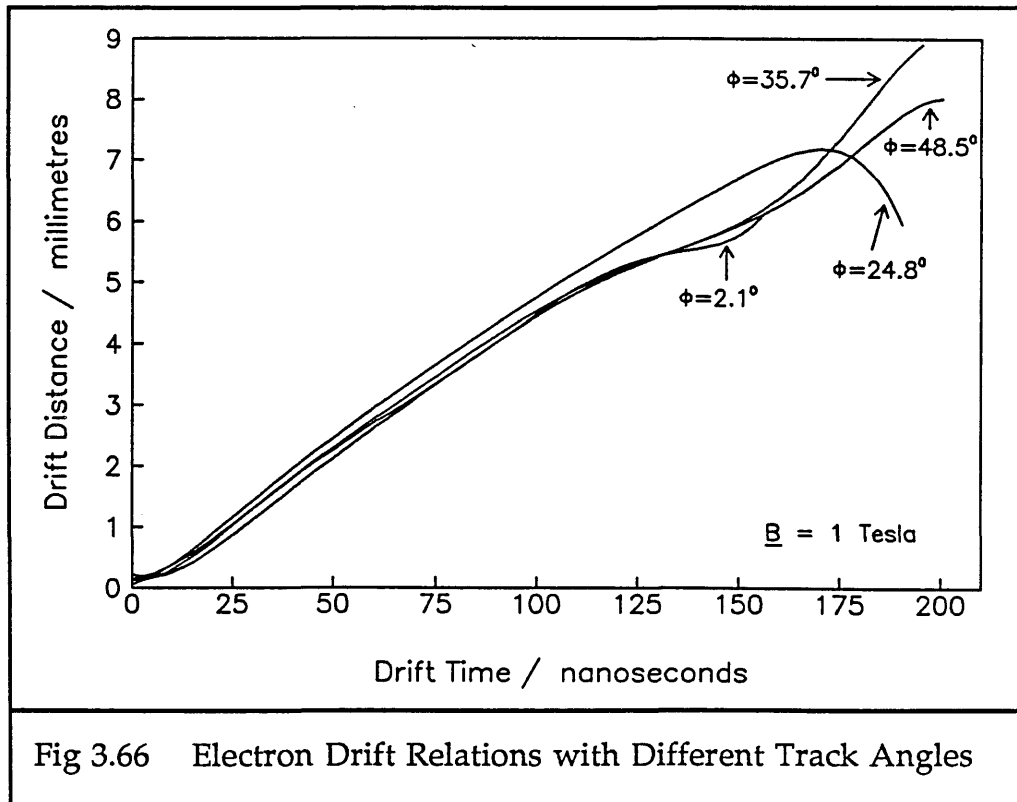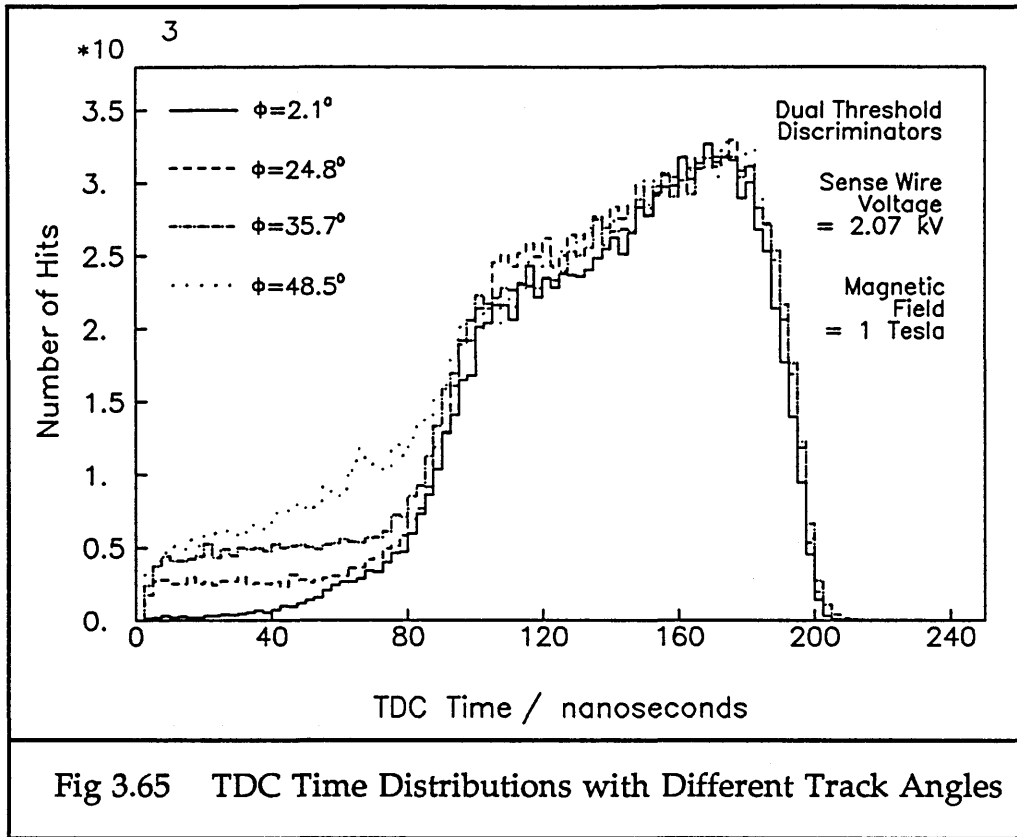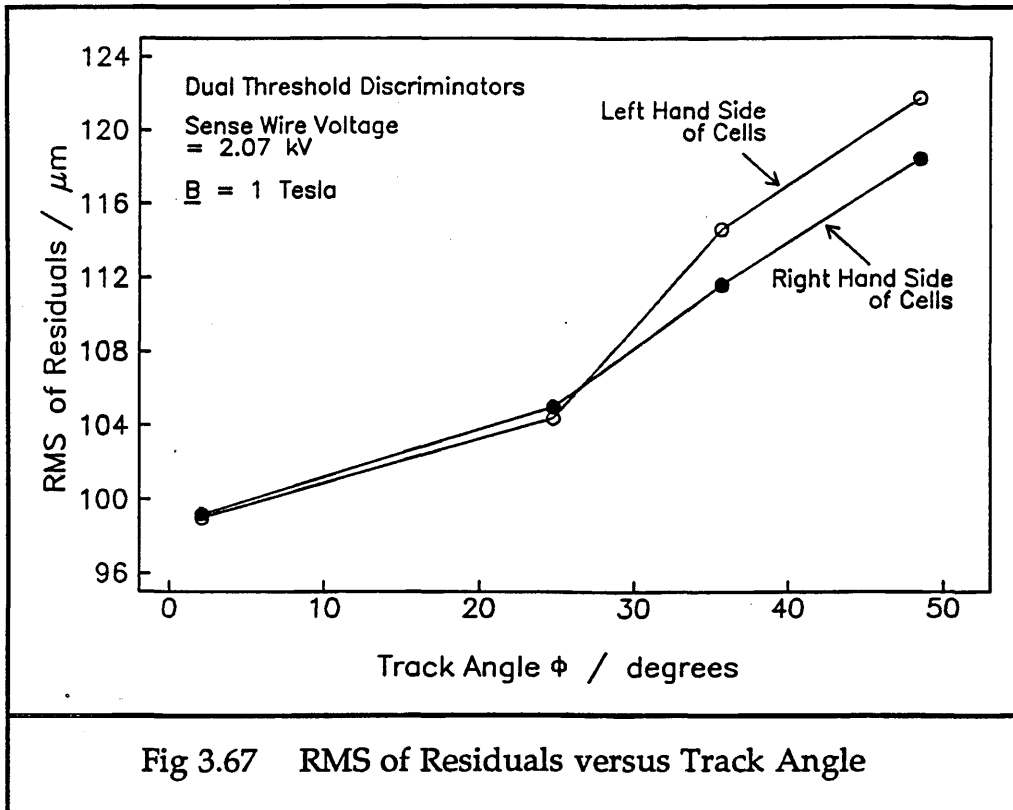
Figure 3.68 shows the mean number of hits per track as a function of track angle ø. When the track angle is very steep, then it passes through more cells in each layer, and the number of hits would be expected to rise. This is found.

Fig 3.68   Mean Number of Hits per Track versus Track Angle
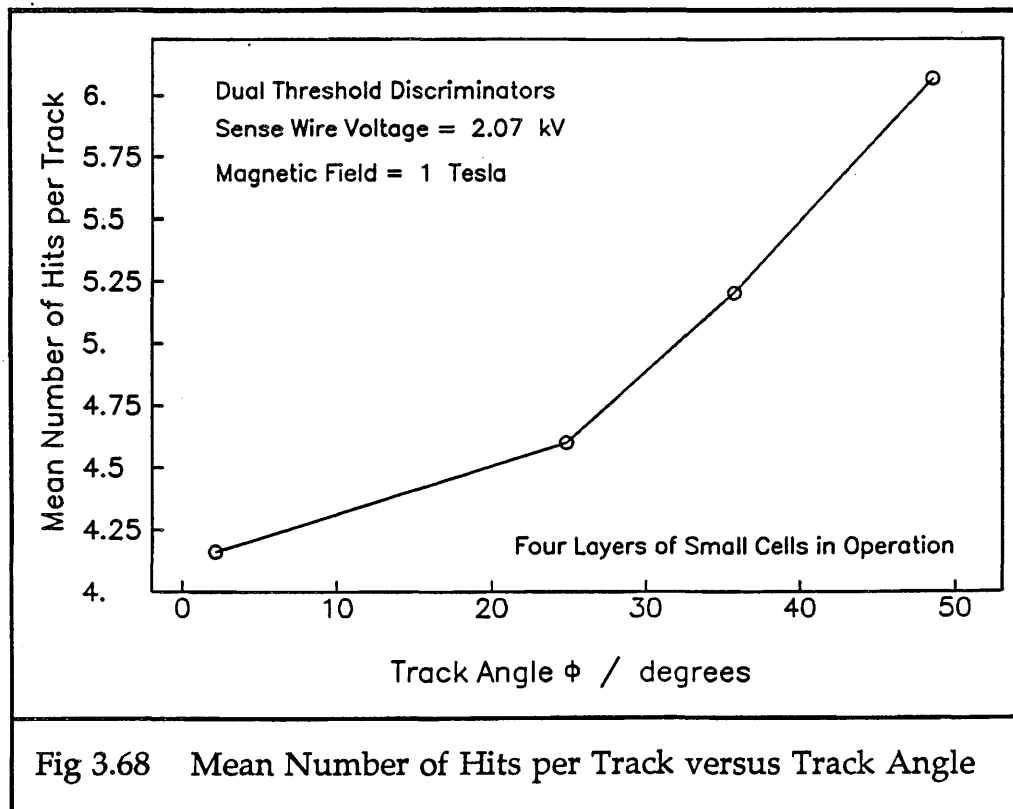
Changing the track angle does not change anything which affects the sources of noise in the chamber, such as stray electrons, crosstalk or interference on the signals. Consequently, the noise level would not be expected to change with ∅. The percentage of noise hits between these runs does vary, but this is due to different beam conditions during the data taking, (these runs were not taken consecutively, but on different days), and the changes found are not dependent on the track angle.

Some of these steep angle tracks can be seen in figure 3.69.

Fig 3.69   Some Examples of Steep ∅ Angle Tracks
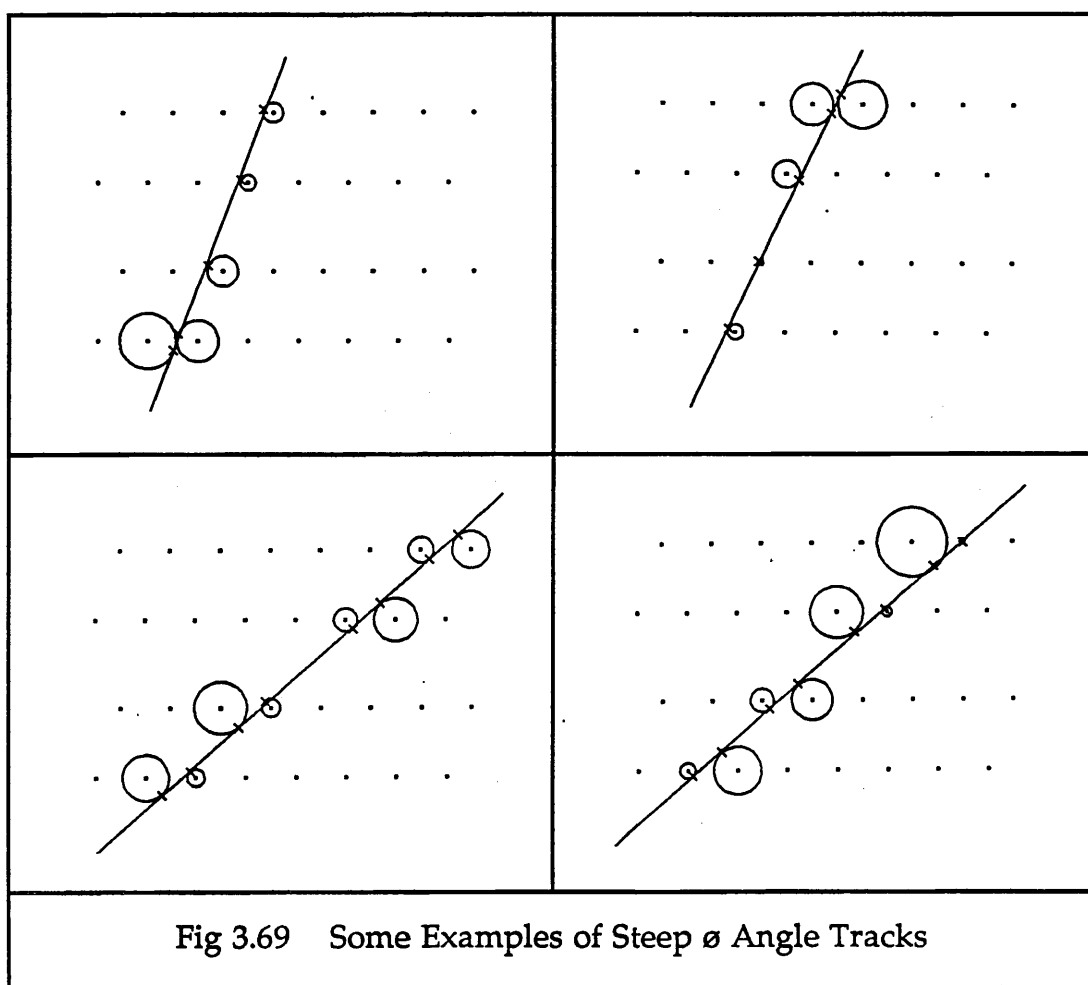
5.4   The Performance of the Small Test Chamber with Argon-Carbon Dioxide

5.4.1   Comparison of the TDC Time Distributions

Two different mixtures of argon-carbon dioxide were used in the CERN tests with the STC. These were 80%-20% and 90%-10%. Both these mixtures (and the argon-ethane mixture) contained a very small amount of alcohol, because the gas was bubbled through a flask of it before entering the

chamber. The alcohol acted as a quencher, absorbing secondary electrons in the gas volume.

The argon-carbon dioxide gas mixtures produced very different shaped TDC time distributions to those obtained with argon-ethane. Figure 3.70 shows the small cell TDC time distributions for argon-ethane 50%-50% and argon-carbon dioxide 90%-10%, with track angle $\emptyset = 0°$. Both runs were taken with dual threshold discriminators, threshold level 1 V. The argon-ethane run has sense wire voltage of 2.40 kV. The argon-carbon dioxide run has sense wire voltage of 1.90 kV. This gas mixture cannot take such high voltages as the argon-ethane mixture, without the chamber getting very noisy.
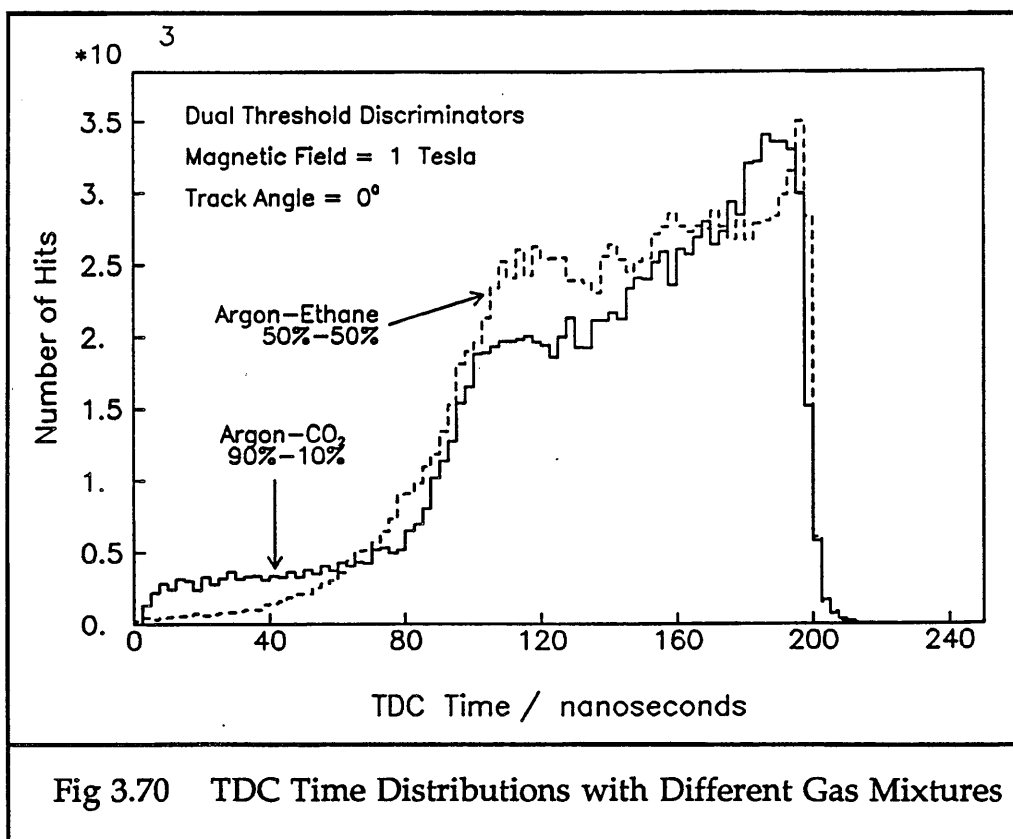
Fig 3.70   TDC Time Distributions with Different Gas Mixtures

Comparing the TDC time distributions in figure 3.70, the main difference is that across the body of the cell, the distribution is much less flat with the argon-carbon dioxide gas mixture, showing that the chamber is less efficient than with the argon-ethane mixture. Another difference is that there is a much larger tail of long drift times in the argon-carbon dioxide distribution. This is due to the much larger region of the cells around the field wires where the electric field is too weak to allow the electrons to drift at the saturated drift velocity. The argon-carbon dioxide gas mixture used here does not allow the sense wire voltage to be increased much above 1.90 kV. This is not high enough to keep the region of low

152

field between the field wires small enough to be negligible.

5.4.2 How Well the Drift Relation Works Across the Cells

The figures in this section show how a polynomial drift relation up to the power 7 in drift time and after 10 iterations, fits the data across the small cells. The conditions describing the data are :

    a)   argon-carbon dioxide 90%-10%
    b)   sense wire voltage plateaued at 1.90 kV
    c)   dual threshold discriminators, applied threshold 1 Volt
    d)   magnetic field at 1 Tesla
    e)   track angle ϕ at ~ 0°

For this run, the best mean linear drift velocity is 43.8 μm/ns. The efficiency of keeping a track after fitting, which started with sufficient hits, is 83.75 %. The mean number of hits per track is 4.258 and the noise level is 2.89 %. The mean of the residuals in the left hand half of the cells is 2.06 μm, and in the right hand half it is 2.11 μm. The RMS of the residuals in the left hand half of the cells is 99.9 μm, and in the right hand half it is 98.2 μm. The total number of hits in the following figures is 25291 for the left hand side and 24689 for the right hand side of the cells.

Figures 3.71 and 3.72 show the mean of the residuals as a function of drift distance, for the left and right hand sides of the cells respectively.
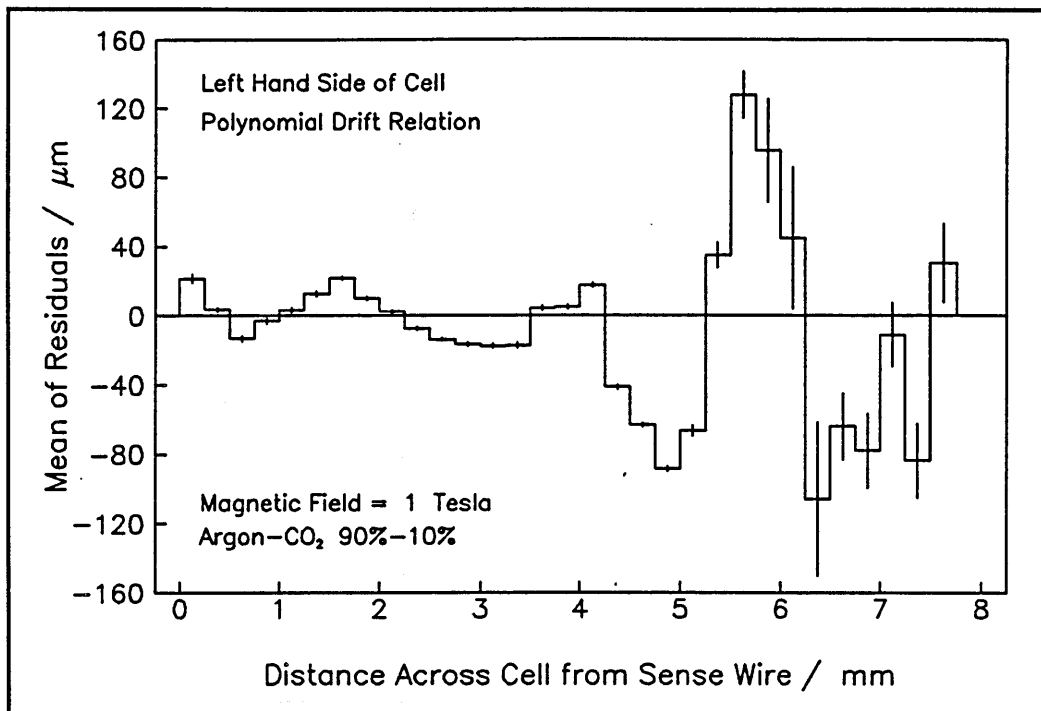
Fig 3.71 Mean of Residuals across Left of Cell
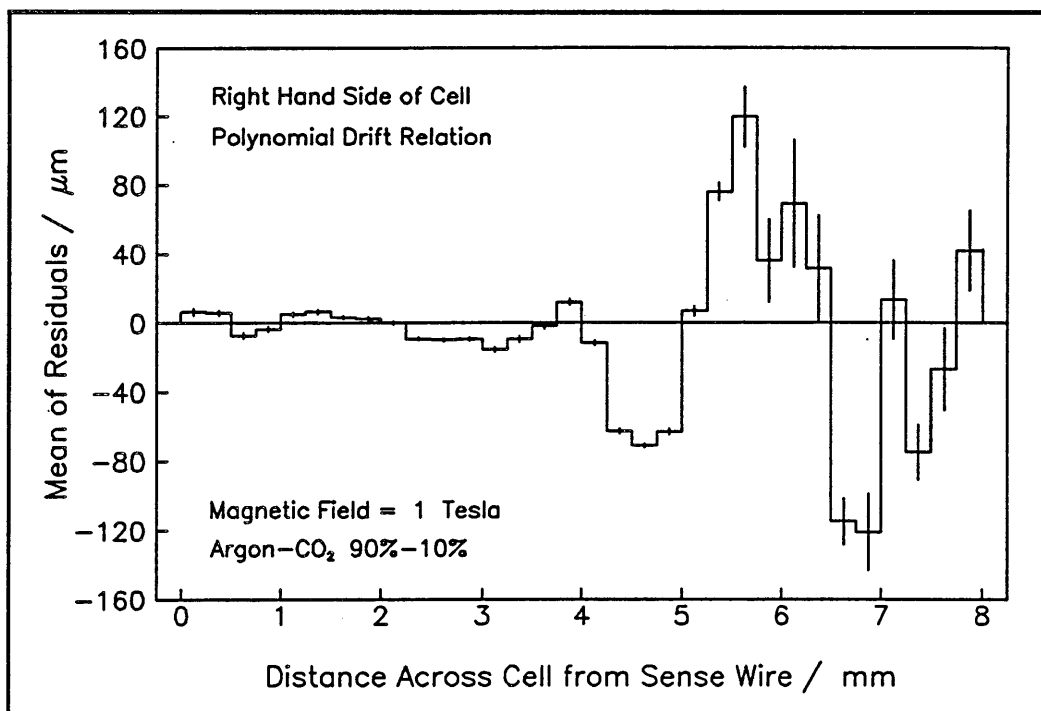
Fig 3.72 Mean of Residuals across Right of Cell

Figures 3.73 and 3.74 show the RMS of the residuals as a function of the drift distance for the left and right hand sides of the cells.

154
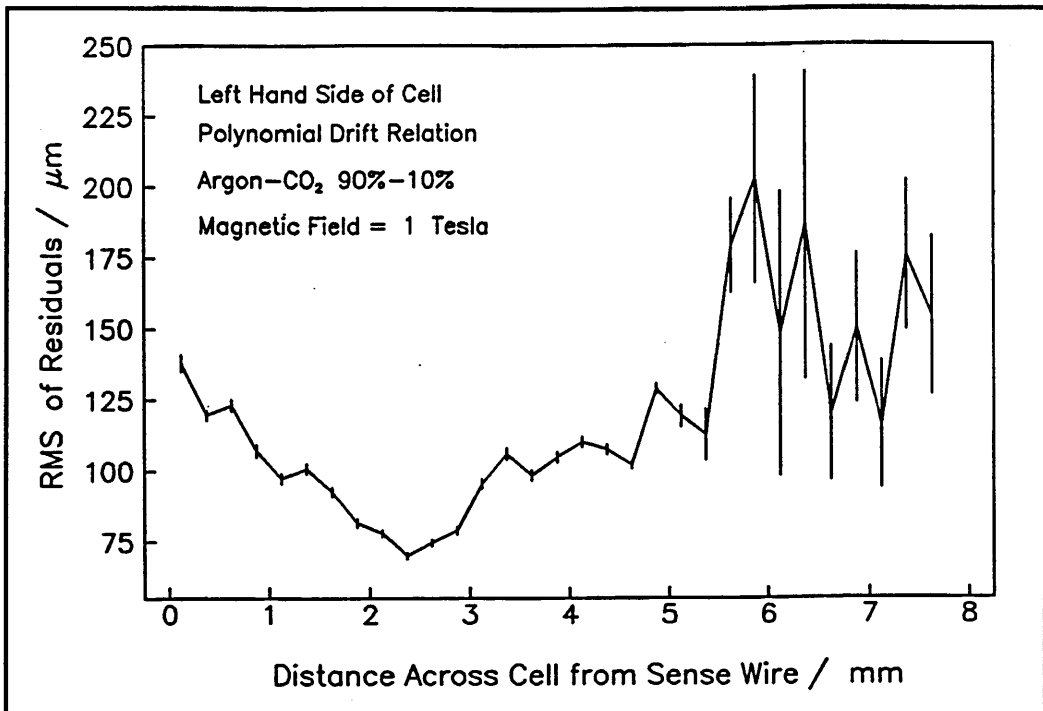
Fig 3.73   RMS of Residuals across Left of Cell
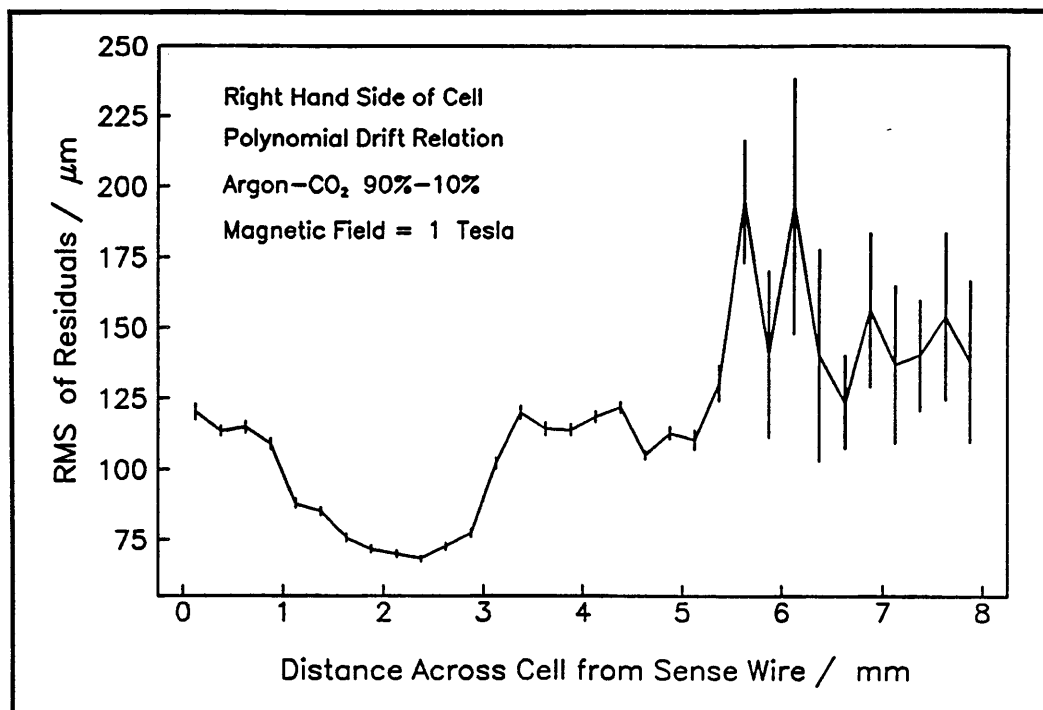
Fig 3.74   RMS of Residuals across Right of Cell

These results may be compared with those obtained from similar running conditions with argon-ethane gas, in Section 5.3.1. Over the first 5 mm of the cell, both drift relations behave in a similar manner for the means and RMSs of the residuals. The distance where the fit is best is

~ 2.5 mm, the same as that found for the argon-ethane data. Close to the sense wire and field wires, the fit is worse than across the centre of the cell. With the argon-ethane gas mixture, the fit is about twice as good as that for argon-carbon dioxide. Beyond about 5 mm drift distance, the data with argon-carbon dioxide is very poor, and cannot be well fitted by the polynomial. Large intrinsic errors from the region of low electric field mean that these apparently long drift distances are fitted worse than when using a simple linear drift relation with the argon-ethane data.

Figure 3.75 shows the hit distribution across the cell for the previous four plots. This may be compared with the TDC time distribution for argon-carbon dioxide shown in figure 3.70. Almost none of the hits with very long drift times have been kept and used in the fitting. The large peak of very short drift times seen in the hits kept was present in the raw data drift times too.

Fig 3.75   Hit Distribution across the Cell after
Track Fitting and Cuts
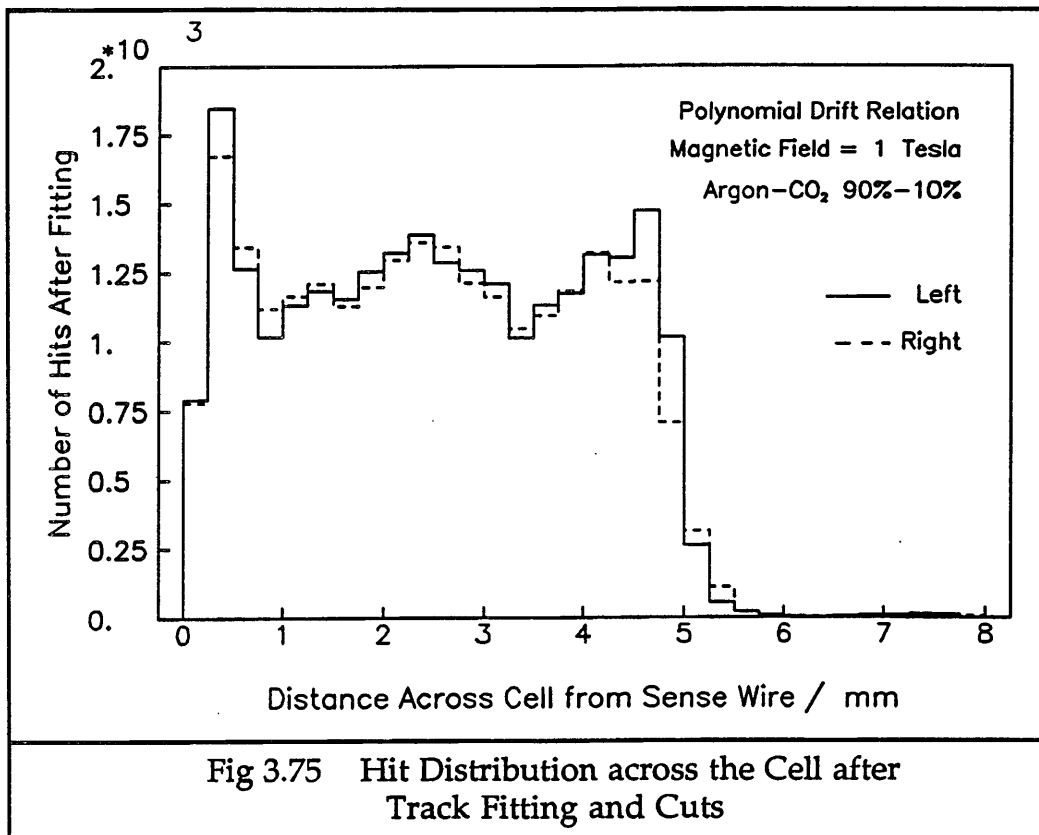
5.4.3   Changes with the Sense Wire Voltage

All the results in this section are based on runs taken with argon-carbon dioxide 80%-20% gas, magnetic field at 1 Tesla and track angle $\phi \approx 23.5°$. Figure 3.76 shows two TDC time distributions for this gas, with sense wire voltage at 1.85 kV and 2.10 kV.

Fig 3.76 TDC Time Distributions with Different Sense Wire Voltages
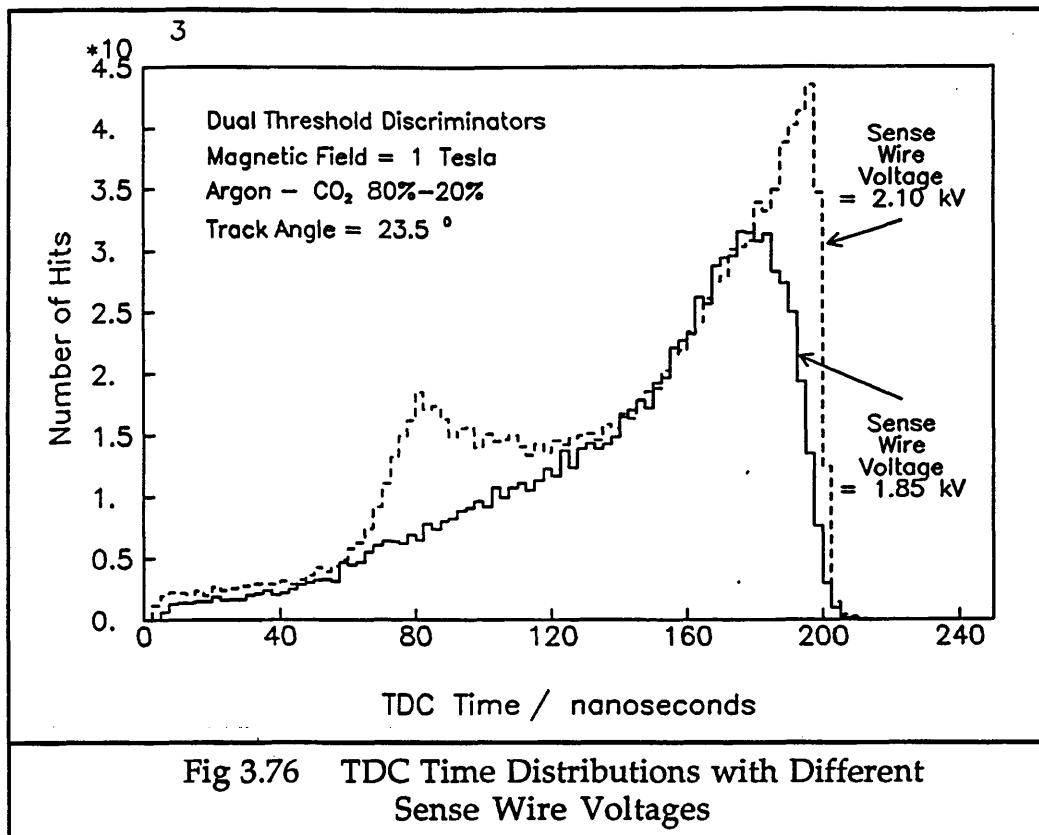
The smaller voltage is too low for the chamber to operate efficiently. The higher voltage has a much larger spike of hits from tracks near the sense wire, and a steeply rising leading edge. It also has a hump of TDC times from tracks near the field wires.

The TDC time distributions for the runs with $V = 2.00$ kV and $V = 2.10$ kV are almost identical.

The TDC time distribution with 2.10 kV may be compared to that obtained with argon-carbon dioxide 90%-10%, in figure 3.82, for instance. (Both these runs have the same track angle.) With the larger proportion of CO_2, and higher sense wire voltage, the chamber is still less efficient across the body of the cell than when less CO_2 is present.

As the sense wire voltage is raised, the best mean linear drift velocity increases, until the voltage goes past the efficiency plateau, when it decreases slightly. This can be seen in figure 3.77.
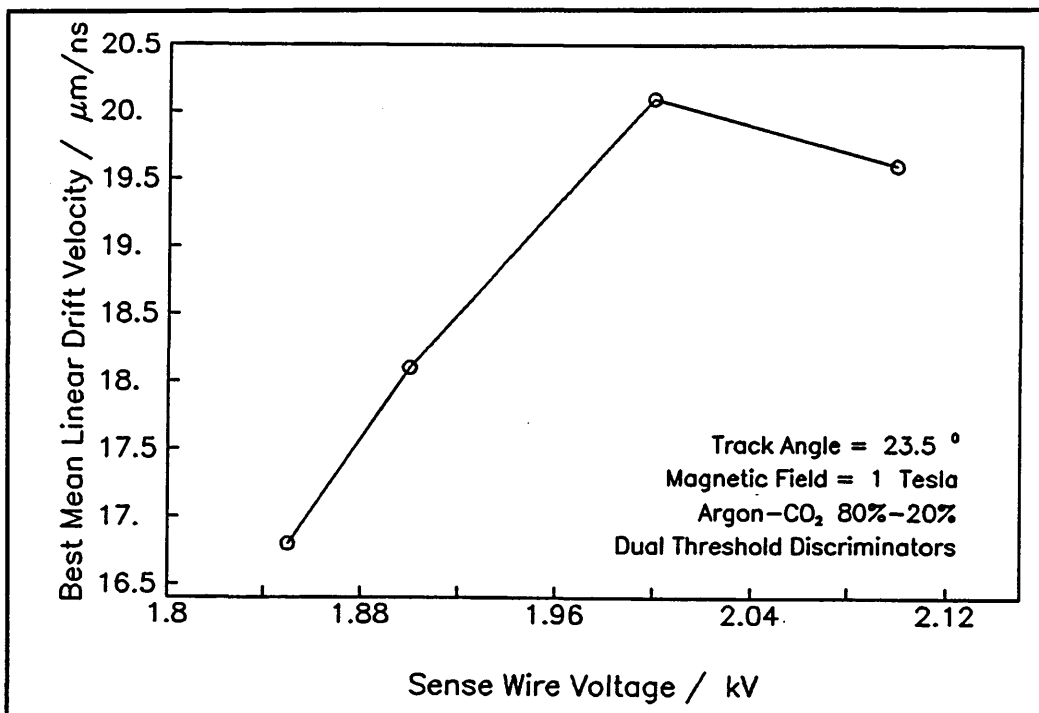
Fig 3.77   Mean Linear Drift Velocity versus Sense Wire Voltage

Figure 3.78 shows the electron drift relations for these four runs.
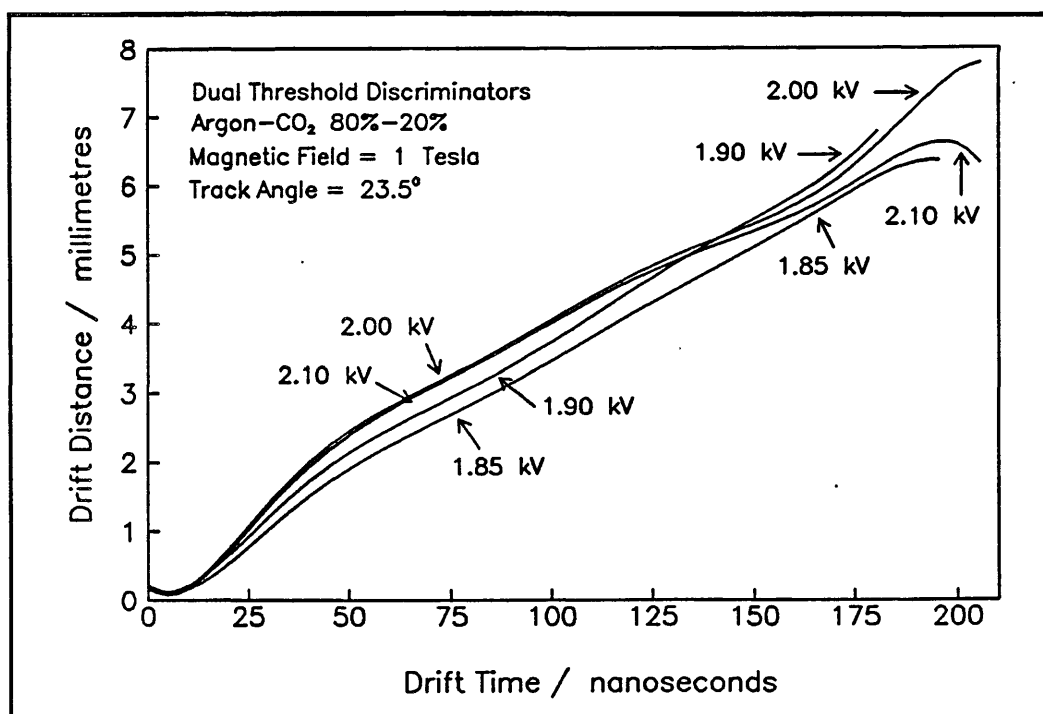
Fig 3.78   Electron Drift Relations with Different
Sense Wire Voltages

The fact that the drift relation changes so much, as the sense wire voltage is changed, would be very inconvenient when running the ITC,

since the drift relation would have to be re-evaluated if the voltage was changed, or if a block of wires was run at a different voltage to other blocks in its layer. With argon-ethane, there is almost no change in the drift relation across most of the cell when the sense wire voltage was changed (see figures 3.52 and 3.53).

The efficiency of the track fitting program in keeping a track which started off with sufficient hits increases as the sense wire voltage increases. This is shown in figure 3.79.

Fig 3.79   Track Keeping Efficiency versus Sense Wire Voltage
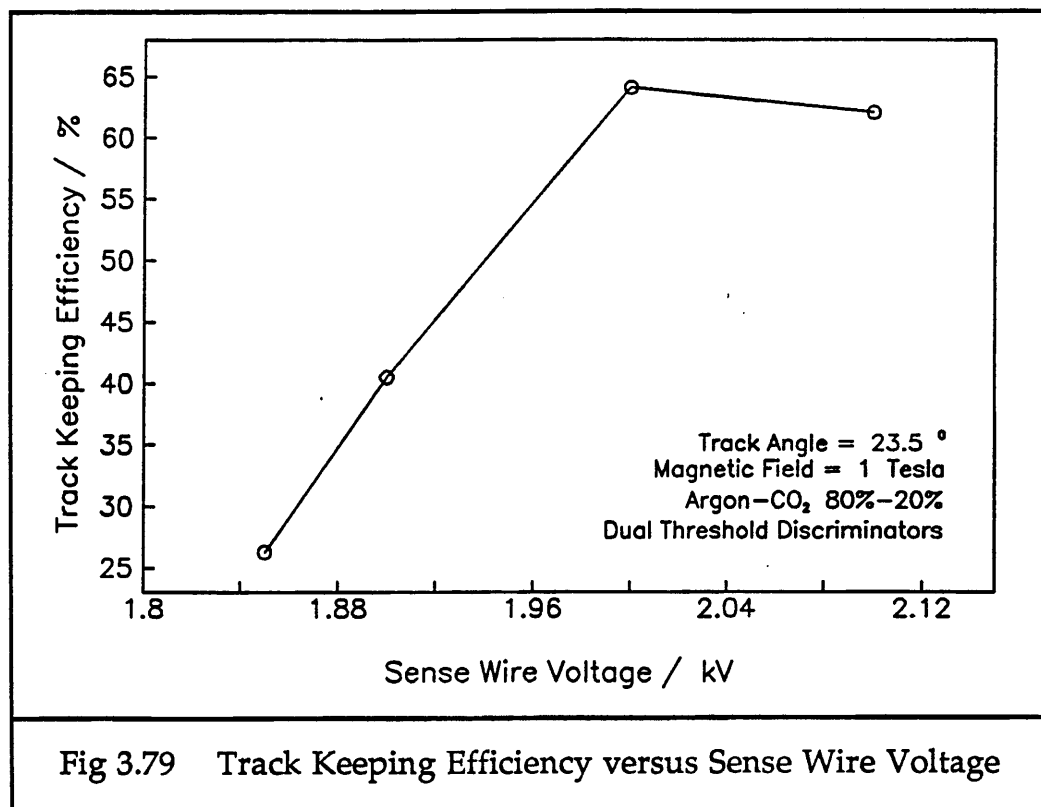
Figure 3.80 shows the mean number of hits per track, which also increases as the sense wire voltage is increased and the chamber becomes more efficient.

Fig 3.80   Mean Number of Hits per Track versus Sense Wire Voltage
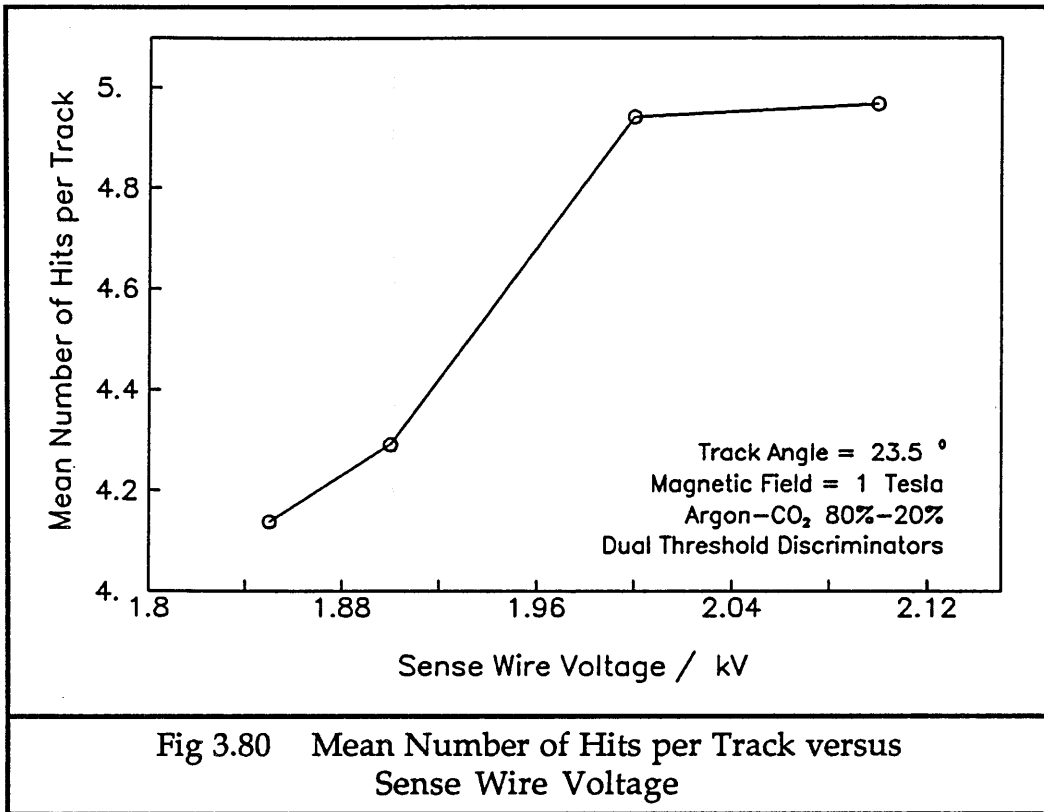
As the sense wire voltage is increased, the signals gain a sharper rise time, and the resolution obtainable with the dual threshold discriminators improves. This is seen in figure 3.81, which shows the RMS of the residuals versus sense wire voltage.

Fig 3.81   RMS of the Residuals versus Sense Wire Voltage
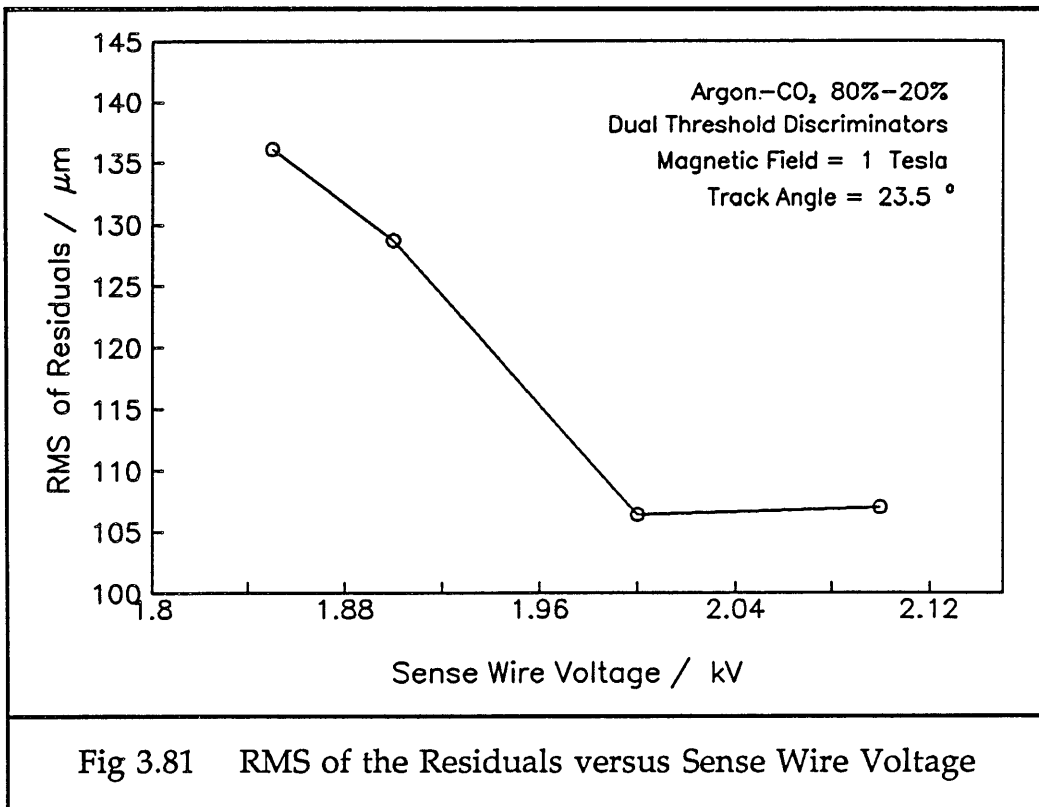
For these four runs, the noise level is between 2.07 % at 1.85 kV and 3.35 % at 2.00 kV.

5.4.4 Changes with the Magnetic Field

The results in this section are based on data taken with argon-carbon dioxide 90%-10% and track angle $\phi \approx 23.5°$.

Figure 3.82 shows the TDC time distributions for when the applied magnetic field is 0 and 1 Tesla. When the magnetic field is at 1 Tesla, there is an increase in long drift times and also a loss of efficiency across the cell. These effects here are much larger than those seen with argon-ethane gas, in figure 3.56.
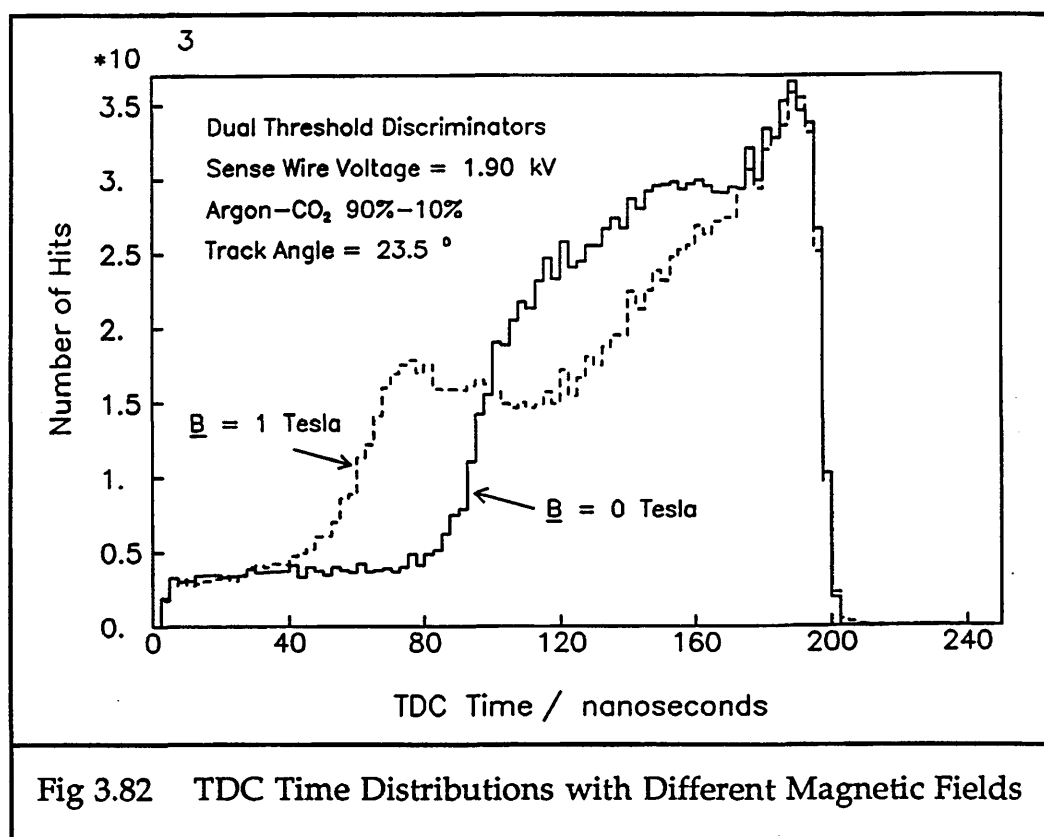
Fig 3.82   TDC Time Distributions with Different Magnetic Fields

The electron drift relation changes between $\underline{B}$ = 0 and 1 Tesla far more than with argon-ethane gas. The best mean linear velocity is shown as a function of the magnetic field in figure 3.83.

Fig 3.83   Mean Linear Drift Velocity versus Magnetic Field
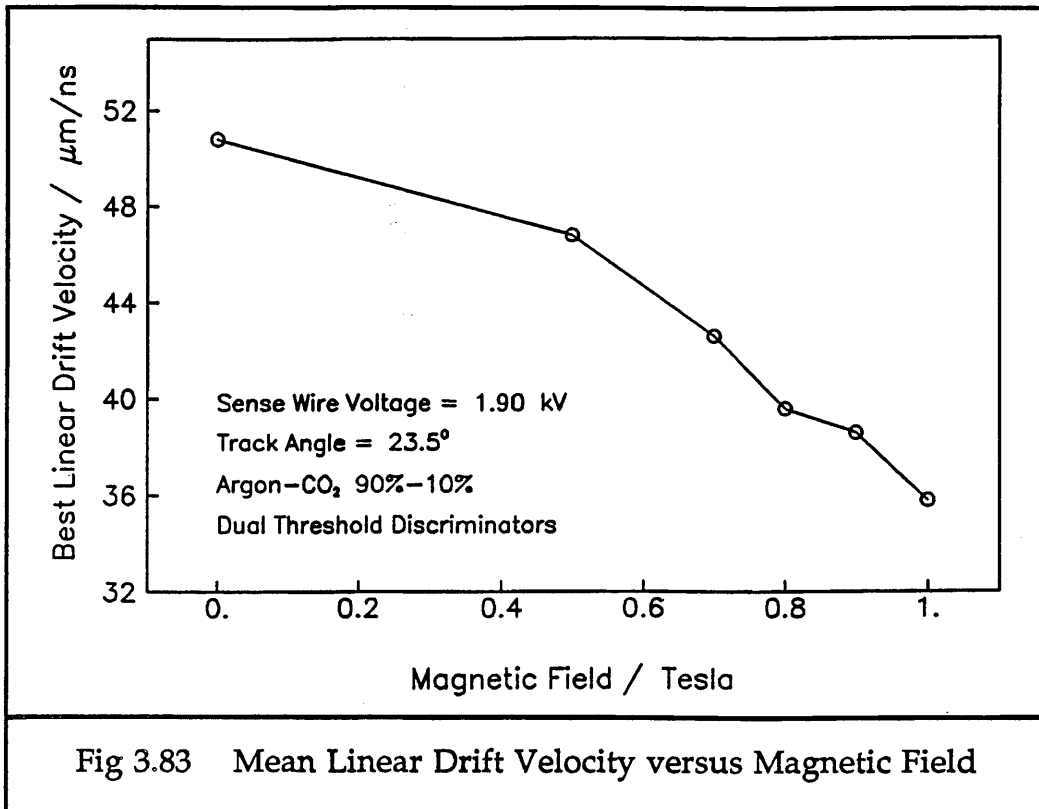
Comparing the drift velocities in figure 3.83 to those velocities found for argon-ethane (shown in figure 3.57), it can be seen that with no magnetic field, a faster linear drift velocity (50.8 μm/ns) is needed with argon-carbon dioxide than with argon-ethane (46.0 – 47.2 μm/ns). When the magnetic field is increased to 1 tesla, the best mean linear drift velocity for argon-carbon dioxide (35.8 μm/ns) is much slower than that needed for argon-ethane (41.6 – 44.2 μm/ns). It is not clear which of the many factors, such as gas type, sense wire voltage or track angle, is responsible for these observed differences.

Figure 3.84 shows the best drift relations for two runs at 0 and 1 Tesla. The running conditions are those shown in figure 3.83.

There is a much larger difference between the drift relations for these two runs than between those for argon-ethane (figure 3.58). Hits are also included in the argon-carbon dioxide data for much longer drift times, for an extra ~ 25 ns, both with and without the magnetic field. These are from the large region of low electric field between the field wires, and because the track angle is steeper. With the magnetic field at 1 Tesla, the electron drift relation is much less linear than that found using argon-ethane. This will be further commented on in Section 5.4.6.

162

Fig 3.84   Electron Drift Relations at Different Magnetic Fields
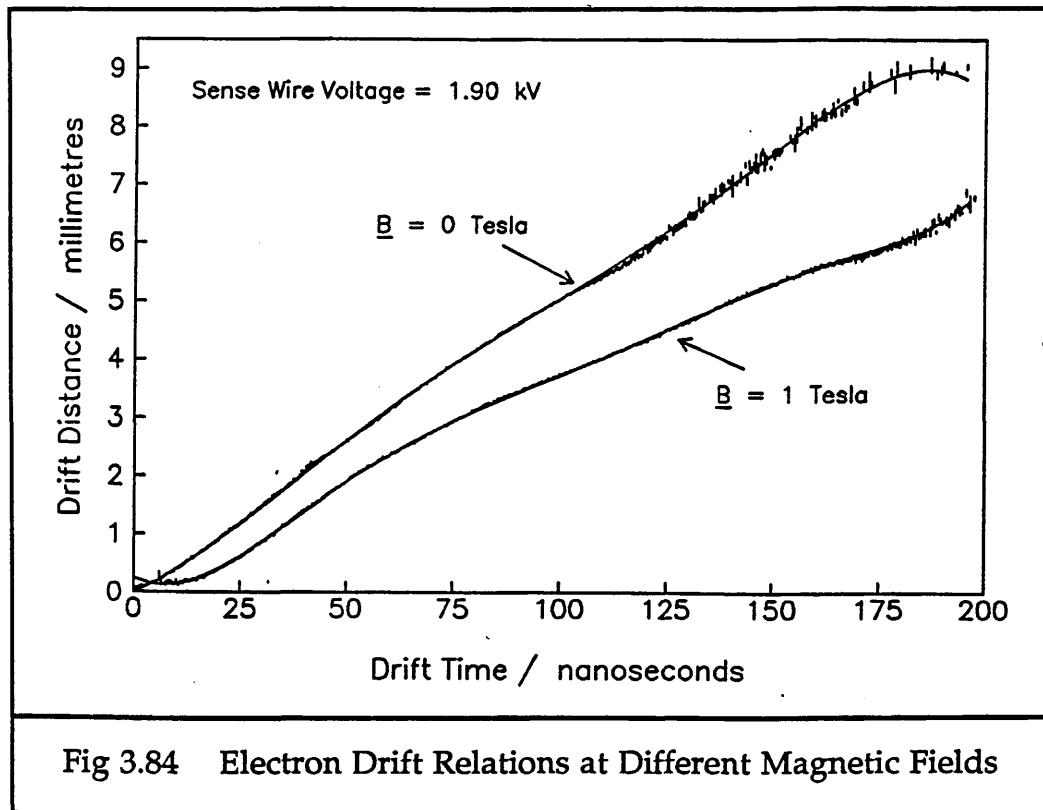
Figure 3.85 shows the amount of noise present in the chamber on the small cells with argon-carbon dioxide gas.

Fig 3.85   Percentage Noise Hits versus Magnetic Field
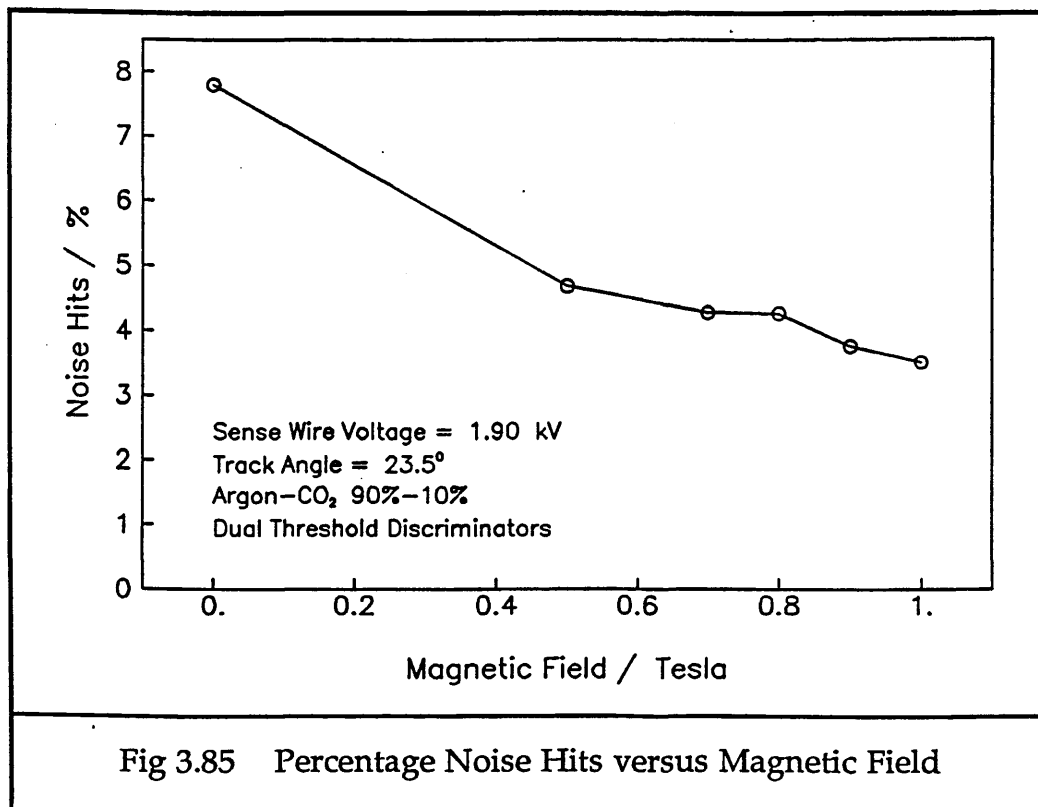
The reduction in the percentage of noise hits as the magnetic field increases is of the same magnitude as that found with argon-ethane gas (see figure 3.60). However, the overall level of noise is ~ 4.5 times that found with argon-ethane gas and sense wire voltage at 2.07 kV, and ~ 1.5 times that with argon-ethane gas and sense wire voltage of 2.40 kV. The track angle for the argon-carbon dioxide data here is $\approx$ 23.5°. For tracks with $\emptyset \sim 0°$, but all the other run conditions the same as here, the noise is slightly lower, at 2.89 %, but still higher than that found with any of the running conditions and argon-ethane gas.

Changing the magnetic field does not have much effect on the other parameters. The RMS of the residuals increases by ~ 4 µm from $\underline{B}$ = 0 to 1 Tesla. The mean of the residuals increases from 2.5 µm to 4.2 µm. The mean number of hits per track also increases from 4.98 to 5.11. Figure 3.86 shows the RMS of the residuals obtained for various values of the magnetic field, with argon-carbon dioxide 90%-10% gas. The RMSs of the residuals with argon-ethane for the two sets of data measured with dual threshold discriminators are also shown for comparison.
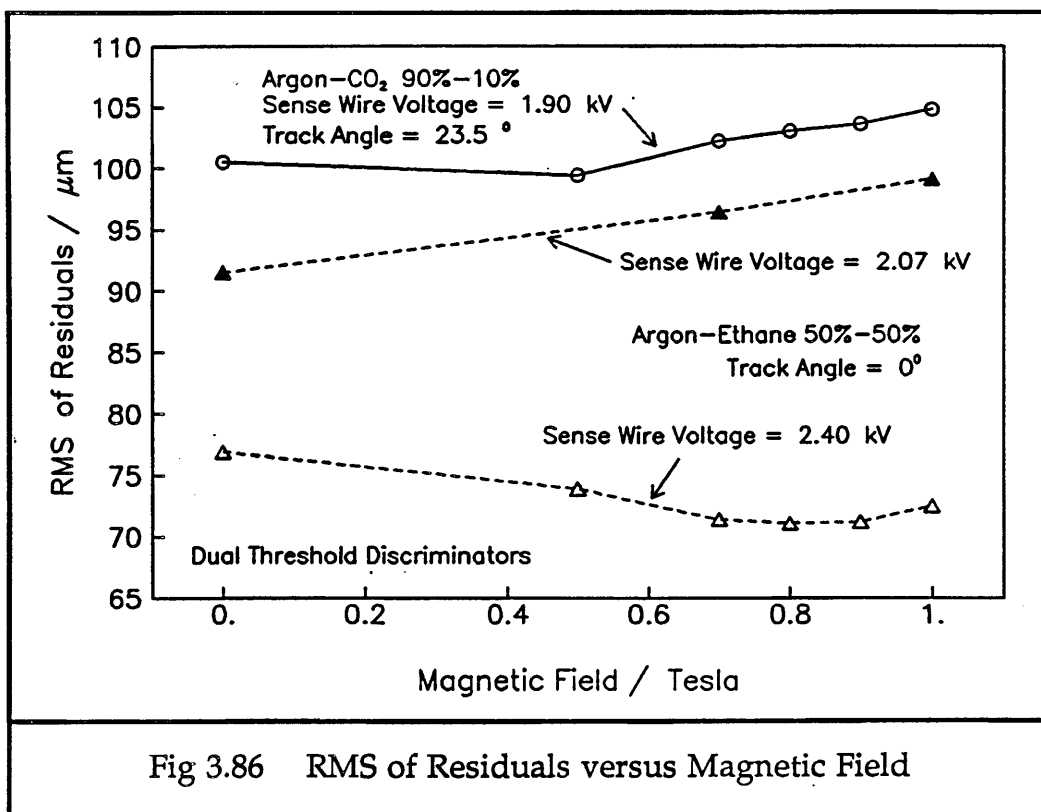
Fig 3.86   RMS of Residuals versus Magnetic Field

As can be seen from figure 3.86, results from argon-ethane gas consistently outperform those from argon-carbon dioxide gas, even when the sense wire voltage is rather low.

5.4.5 Changes with Track Angle ø

Figure 3.87 shows the TDC distributions for three runs with different track angle ø. There are much larger differences between these three distributions than there were between those taken with argon-ethane gas (see figure 3.65).
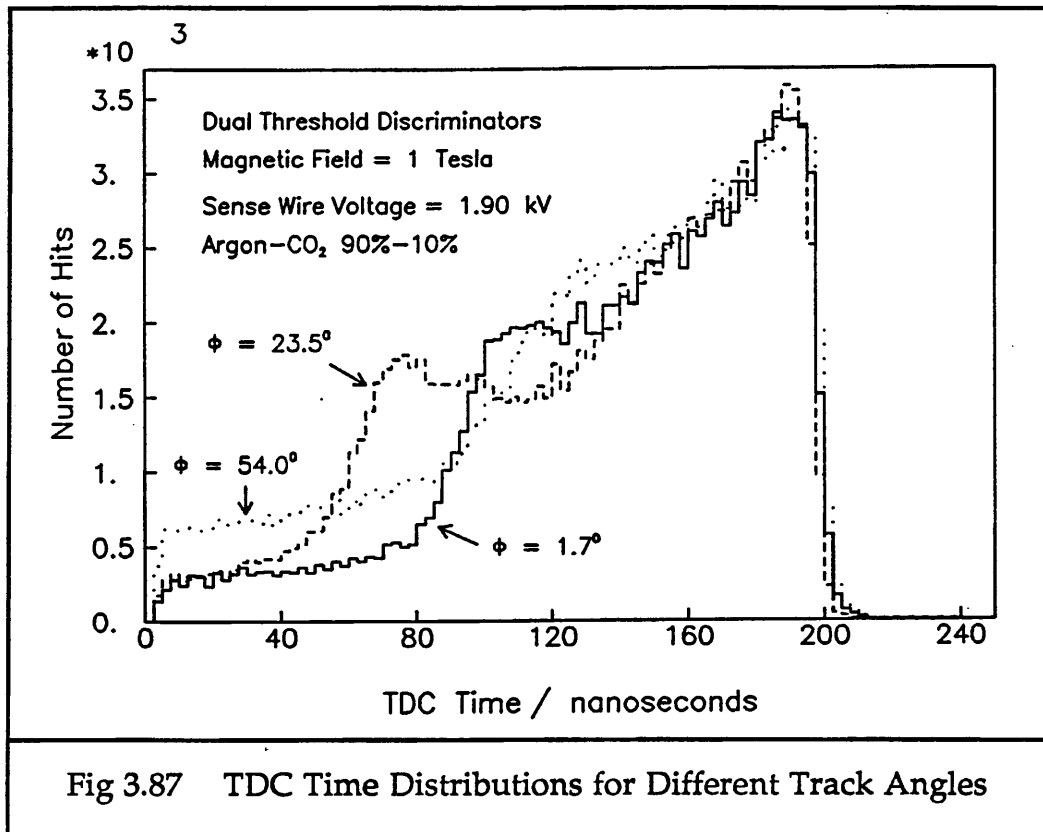
Fig 3.87   TDC Time Distributions for Different Track Angles

The increase in long drift times (and therefore short TDC times) is not simply proportional to the track angle ø. As ø increases from 1.7° to 23.5°, there are more long drift times, and the cells become less efficient for these long drift distances. However, increasing the track angle ø to 54.0° does not continue this pattern. The hump at the edge of the cell appears to occur for shorter drift times than for either of the other two runs. This behaviour is followed by the best mean linear drift velocities for these runs, which are 43.8 μm/ns for ø = 1.7°, 35.8 μm/ns for ø = 23.5°, and 46.2 μm/ns for ø = 54.0°.

Increasing the track angle increases the mean number of hits per track. This is shown in figure 3.88. The mean number of hits per track changes in a very similar way to that found with argon-ethane gas (shown in figure 3.68).

Fig 3.88   Mean Number of Hits per Track versus Track Angle
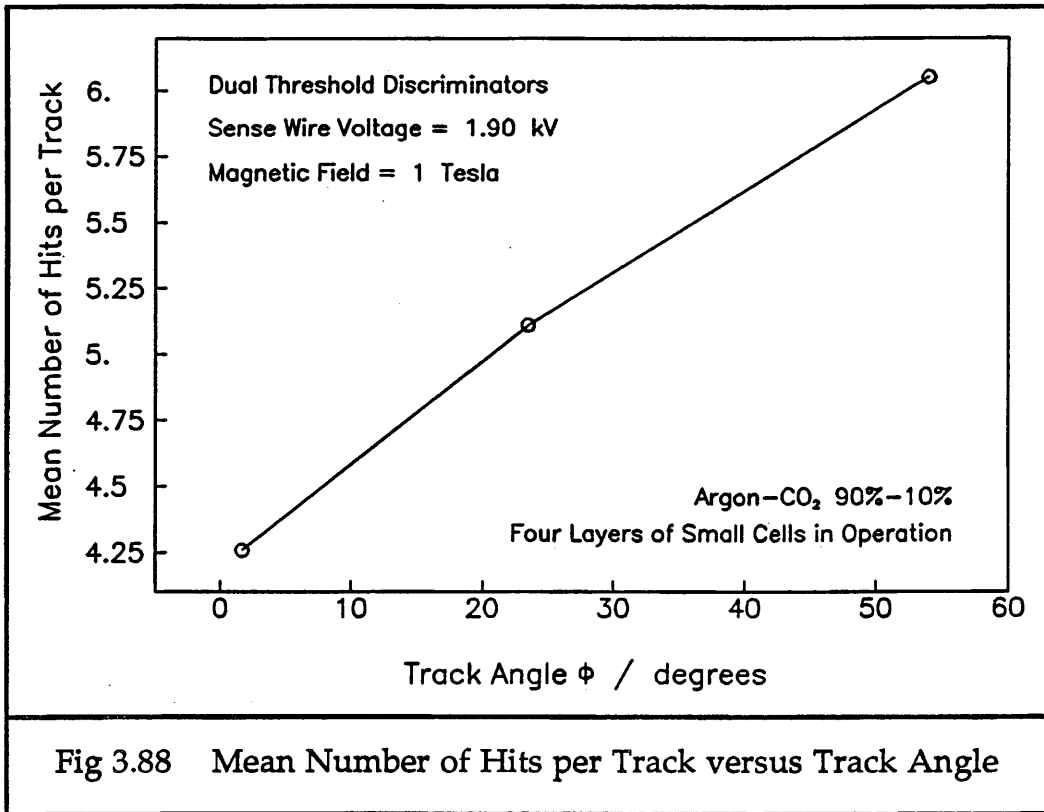
Other effects of increasing the track angle are small. The RMS of the residuals increases by a few microns. The percentage noise hits also increases slightly as $\varnothing$ increases.

5.4.6   The Electron Drift Relation

When a polynomial was used as a drift relation for runs with argon-ethane gas, there was very little improvement in the resolution of the chamber compared to when the best linear drift velocity was used. The electron drift behaviour across most of the cell was very linear and well modelled by using a drift relation with only one coefficient. However, this is not found to be so when argon-carbon dioxide gas is used. For tracks with $\varnothing \approx 0°$, $\underline{B} = 0$ T or very low sense wire voltage, the improvement in the RMS of the residuals is only a few microns. For runs with high sense wire voltage in the 80%-20% gas mixture, the improvement is ~ 32 μm. For runs at 1 T with track angle $\approx 23.5°$, the improvement is ~ 15 μm. For steeper angled tracks, such as $\varnothing \approx 54.0°$, the improvement is ~ 17 μm. All these values are obtained after 10 iterations to find the best drift relation coefficients.

Consequently, it is much more important when using argon-carbon dioxide gas to use a higher order drift relation to model the behaviour of the electrons in the gas, since this is much less linear than that found with argon-ethane.

166

6 Conclusions from the Analysis of the Test Data

The main conclusion to be made from the tests is that the behaviour of the chamber over the few hours of a run is fairly uniform and steady. The analysis has concentrated on the data taken with argon-ethane 50%-50% gas, since it is hoped that this will be used. Promising resolutions for the small cells under a variety of operating conditions have been obtained, which indicate that track fitting in the ITC using 8 layers of cells with a 1.5 Tesla magnetic field could be achieved with an overall resolution of $\sim 100\,\mu m$. Values better than $75\,\mu m$ for the RMS of the residuals have been obtained under optimal conditions with a 1 Tesla magnetic field.

Track fitting algorithms have been tested, and the method of weights has been shown to be fairly effective at choosing the correct ambiguities for the hits in each cell. Ways of parameterising the electron drift relation have been investigated, although once the best mean linear drift velocity has been found for runs with argon-ethane gas, higher order drift relations produce only negligible improvements. Using the best mean linear drift velocity instead of a nominal $52\,\mu m/ns$ improves the RMS of the residuals by $\sim 27\,\mu m$. The RMS is also improved by $\sim 16\,\mu m$ by introducing an individual zero time for each track to compensate for the jitter of the STOP signal to the TDCs.

For tracks which pass through the chamber at a steep $\varnothing$ angle, the number of hits per track rises, and the extra hits can be used in the track fitting. The RMS of the residuals gets worse as the track angle increases.

The investigation into which type of discriminator produces the best results shows that the constant fraction discriminator produces better resolutions than the dual threshold discriminator with the magnetic field at 1 Tesla. However, the resolution with the dual threshold discriminator can be improved by lowering the threshold applied, although if this is set too low, it will probably increase the amount of noise recorded. Raising the sense wire voltage improves the performance of the chamber with both types of discriminator.

Comparing the results found using argon-carbon dioxide with those obtained from argon-ethane, there are several effects worth noting. Argon-carbon dioxide has a very short plateau for the sense wire voltage, and this is at a much lower level than that for argon-ethane. Consequently, with the sense wire voltage low, the region of low electric field around the field wires is much larger than when the chamber can be operated with a higher sense wire voltage. This leads to longer drift times being measured with argon-carbon dioxide. Argon-carbon dioxide gas mixtures are much

less efficient across the body of the cell than the argon-ethane mixture, as shown by the TDC time distributions. Under all operating conditions tried, the RMS of the residuals for argon-carbon dioxide is larger than that for argon-ethane and so is the percentage of noise hits in the chamber.

The two reasons for using argon-carbon dioxide are to avoid an organic gas which might lead to carbon whisker growth if the electric field on the field wires were too high, and to avoid having an explosive gas in the chamber for reasons of safety.

To conclude overall, the construction and testing of the small test chamber have proved extremely useful for both the wiring of the ITC and in understanding how it will behave when in use in ALEPH.

SIGNAL PRODUCTION IN A DRIFT CHAMBER

This section contains a brief summary of the processes involved in the production of signals on the sense wires in a drift chamber. It is derived from the text by Fabio Sauli, in reference [2.12]. The generation of a signal may be divided into four stages.

1   Ionisation

When a charged particle travels through a gas, it ionises some of the nearby gas molecules. This happens because it interacts with the outer electrons and they gain enough of its energy to become unbound from their molecules. These primary ionisations produce secondary ionisation, since the primary electrons can have enough energy to ionise a second generation of electrons. The total number of ionisations from one charged particle travelling through a gas mixture of argon-ethane 50%-50% is :

$$n_T = \frac{\Delta E}{W_i} = \left(\frac{\Delta E}{W_i}\right)_{Argon} \times 50\,\% + \left(\frac{\Delta E}{W_i}\right)_{Ethane} \times 50\,\%$$

$$= \frac{2440}{26} \times 0.5 + \frac{1480}{28} \times 0.5 = 73 \text{ ion pairs/cm}$$

n_T = total number of ion pairs
ΔE = total energy loss in the gas volume considered
W_i = effective average energy to produce one pair

The average length travelled in a cell in the ITC for a particle with $\theta = 90°$ and $\varnothing = 0°$ is ~ 7.2 mm. Therefore, for these straight tracks, there is a total of ~ 53 electrons ionised on average per cell.

2 Drift and Diffusion

The liberated electrons drift towards the nearest positively charged sense wire, under the Lorentz force from the electric field and the magnetic field. Interactions with the gas molecules oppose these forces, and consequently the electrons drift at constant average velocity. They interact with nearby electrons in the gas molecules, but do not liberate the electrons, as they do not have enough energy. If the chamber is being operated on the voltage plateau, then the average drift velocity in argon-ethane 50%-50% is $\approx 52\ \mu m/ns$, with $\underline{B} = 1$ Tesla.

The electrons also diffuse through the gas, following a roughly Gaussian distribution, with the coefficient of diffusion being dependent on the electric field strength and gas type, both transverse to and longitudinal to the field direction. For gases close to the thermal limit, where the electrons do not gain energy from the electric field, the standard deviation of space diffusion σ_x for 1 cm of drift is $\approx 200\ \mu m$. In the ITC, all drift distances are < 1 cm.

3 Avalanche Region

Once the drifting electrons get within ~ 100 μm of the sense wire, the electric field becomes large enough that the electrons enter an avalanche region. They are accelerated by the electric field and start ionisations of their own once their energy is above the ionisation potential of the gas. The number of electrons in the avalanche approximately doubles at each ionisation.

4 Generation of the Signal on the Sense Wire

The large numbers of positive ions (~ 10^6) left in the vicinity of the positive sense wire are accelerated away from it down the potential gradient towards the field wires. Because the ions are much heavier than the electrons, this movement of large numbers of ionised molecules releases large amounts of potential energy into the electric field. This generates an electromagnetic shock wave on the sense wire, which is transmitted along the wire in both directions, away from the initial ionisations.

ELECTRON DRIFT PATHS IN THE ITC HEXAGONAL CELLS

1 Introduction

An investigation has been made into the electric fields in the ITC hexagonal cells, and into the electron drift paths with and without an applied magnetic field. Two computer simulation programs have been used to do this. The first one takes a grid of wires of given radii and voltage, and calculates the charge per unit length on the wires [3.B.1]. The second program uses these charge distributions to calculate the electric field and potential across a cell, and the electron drift paths in the cell under various conditions [3.B.2].

2 Calculation of the Charge Distributions

The charge per unit length on each wire in a given grid, is calculated by inverting the linear relation which gives the voltage on a wire in terms of the charges on this and all other wires. For two long parallel conducting wires, the charge induced on one wire by the voltage on the other is :

$$Q = \frac{V \pi \, \varepsilon_0}{\log_e (R/r)}$$

Q = charge induced per unit length of a long conductor A
V = potential of a nearby parallel long conductor B
R = distance between the two conductors
r = radius of conductor A

It is assumed that $r \ll R$, so that the charge distribution on the wires can be considered uniform. This relation is used to calculate the charge on a

wire from the potentials of all the wires in the grid, not just the nearest neighbour, by summing all the separate contributions. There is a boundary condition used in the calculation, that the total charge in the system is zero. This is necessary to prevent infinitely long wires from being at an infinite potential with respect to infinity. This boundary condition means that there has to be an arbitrary overall offset in the voltages.

3   Calculation of the Electric Field

Having calculated the charge distribution on the grid of wires, it is straightforward to calculate the electric field across a cell, and also the potential across the cell. The electric field around a long cylindrical conductor is given by :

$$\underline{E} = \frac{Q\,\hat{\underline{r}}}{4\,\pi\,\varepsilon_0\,r^2}$$

$$V = Q \log_e r$$

r = distance from wire
$\hat{\underline{r}}$ = unit vector perpendicular to wire surface
$\underline{E}$ = electric field at distance r from wire
V = potential at distance r from wire
Q = charge per unit length on wire surface

These relations are used by summing the contribution from every wire in the grid to the total electric field and potential at the point under consideration.

The electric field $\underline{E}$ and potential V have been calculated for the two cell sizes used in the small test chamber, which have the shortest and longest maximum drift distances of the eight cell sizes used in the ITC. Figure 3.B.1 shows the electric field in a large cell, and figure 3.B.2 shows the corresponding electric potential. The sense wire has 2.5 kV on it, in the centre of the cell. The electric field on the surface of the sense wire is -258.7 kV/cm. On the top and bottom field wires, the electric field is 14.7 kV/cm, and on the two pairs of side field wires, the electric field is 11.4 kV/cm. Across most of the body of the cell, the electric field is over

1 kV/cm, which ensures that the electron drift velocity in the gas is saturated. Between the side pairs of field wires however, the electric field drops very nearly to zero. In the surrounding region, up to a couple of millimetres away, the electric field is less than 0.5 kV/cm, and up to about 2 mm from the sense wire in this direction, the field is less than the drift velocity saturation level with the magnetic field at 1.5 T, of ~ 1.3 kV/cm. Therefore, tracks at the outer edges of the large cells will have very slow drifting electrons to start with, and will produce longer drift times than would be supposed from the electron drift path distances.

Figure 3.B.3 shows the electric field in a small cell, and figure 3.B.4 shows the potential across the cell. The sense wire is at 2.5 kV in these figures. The electric field on the surface of the sense wire is -256.1 kV/cm. On the top and bottom field wires, it is 12.0 kV/cm, and on the field wires at either side of the cell, it is 14.0 kV/cm.

Fig 3.B.1   Electric Field Across a Large Cell in the ITC

Fig 3.B.2   Potential Across a Large Cell in the ITC
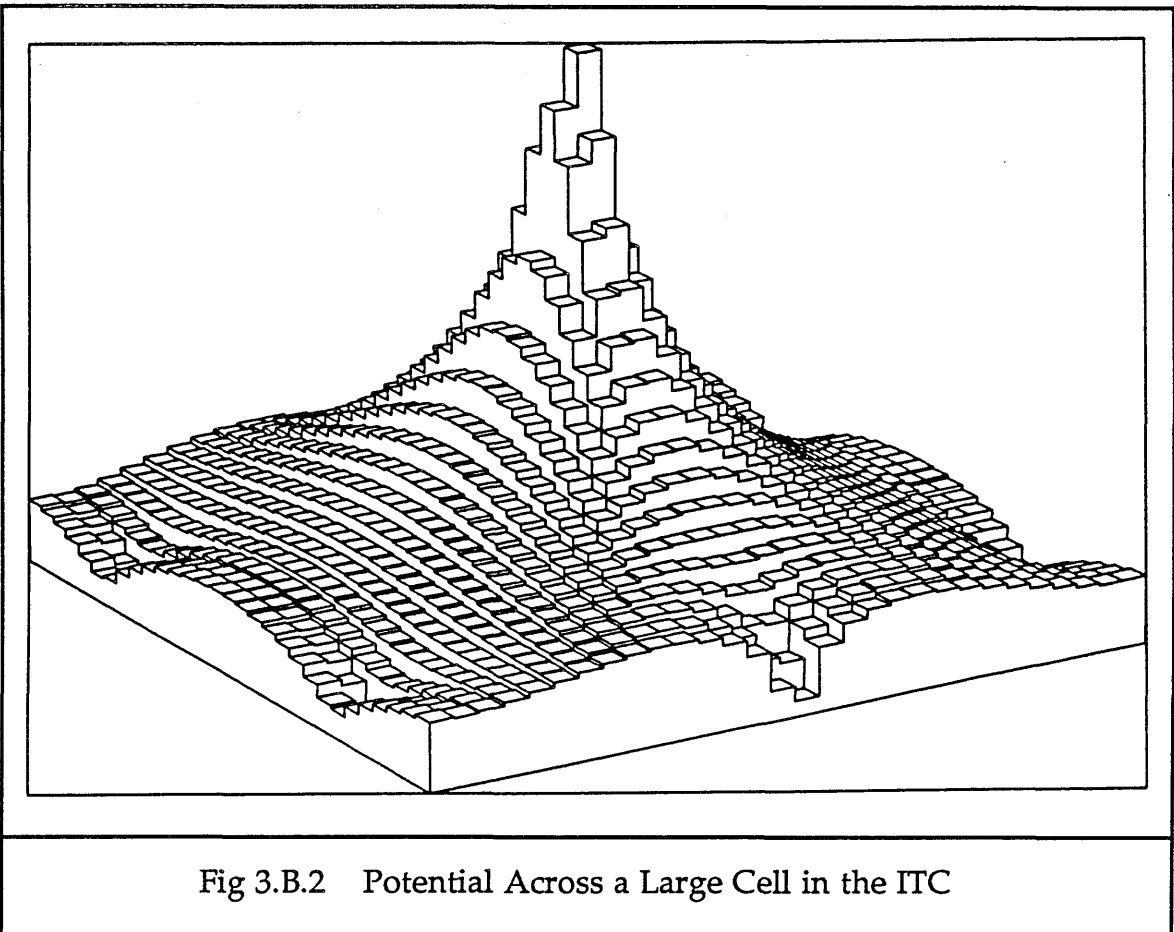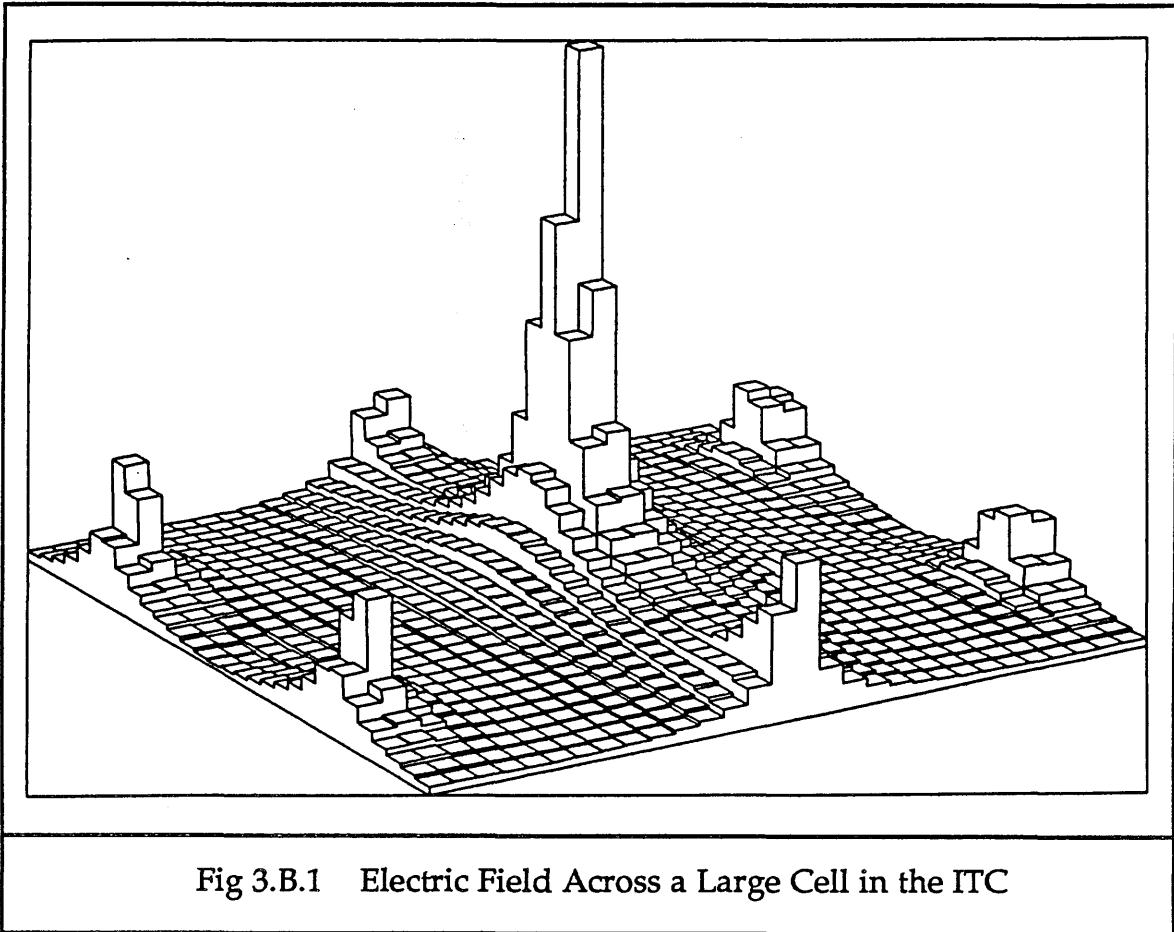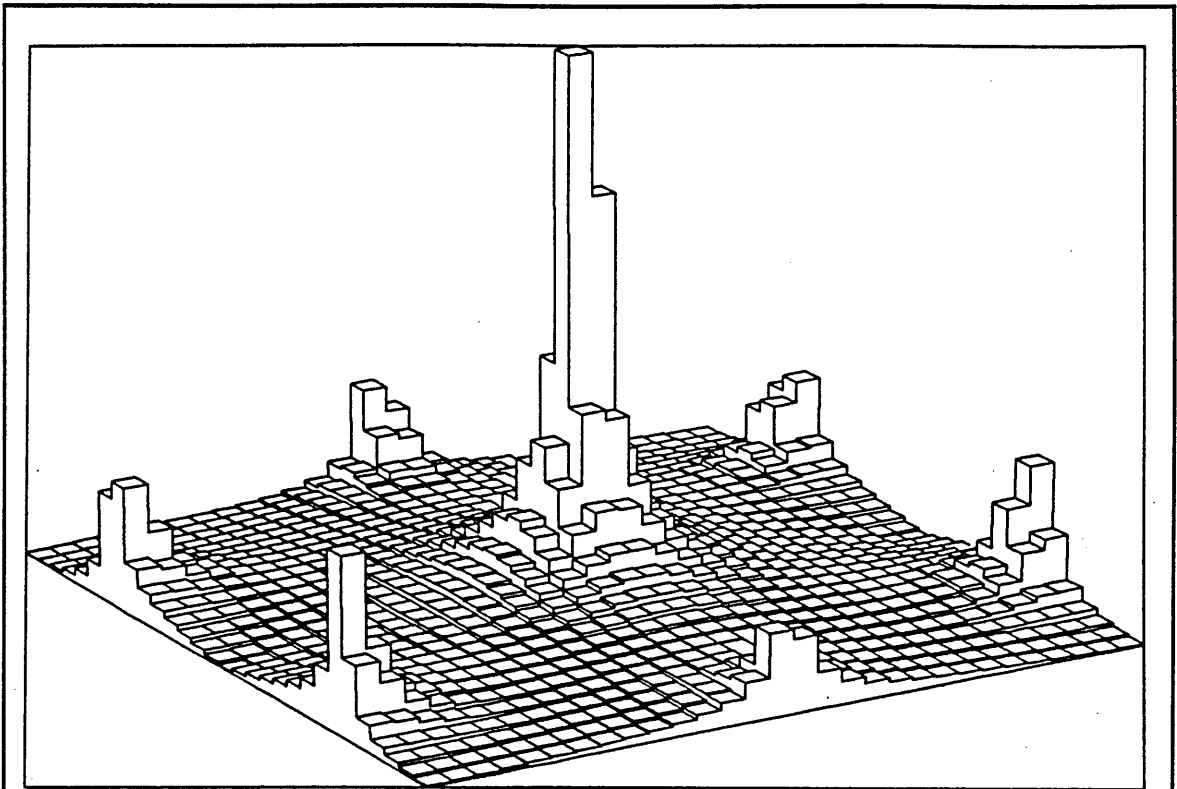
Fig 3.B.3   Electric Field Across a Small Cell in the ITC
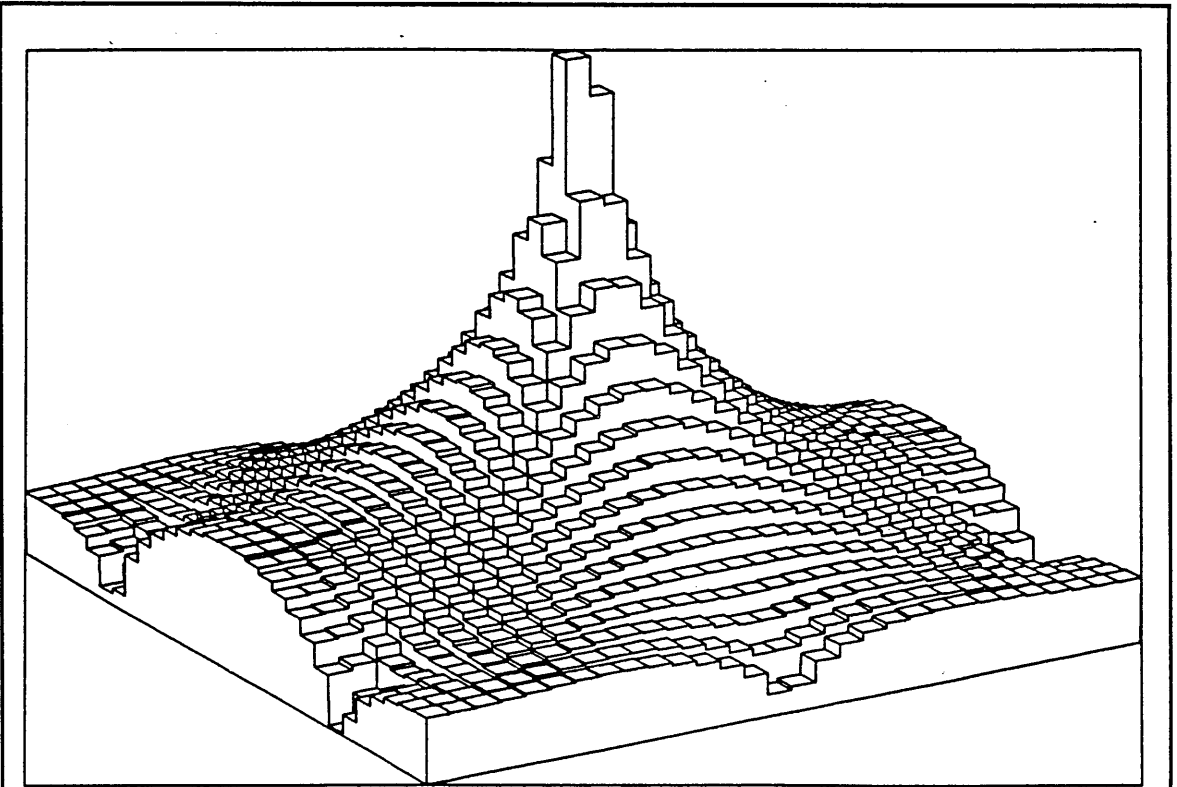
Fig 3.B.4   Potential Across a Small Cell in the ITC

4   Calculation of the Electron Drift Paths

Once the electric field has been calculated across a cell, the electron drift paths may also be calculated, when there is no magnetic field. The electron drift velocity in argon-ethane 50%-50% is parameterised using 8 straight line sections to represent the curve for $\underline{B} = 0$ T, as shown in figure 2.9 of Chapter 2. The electron paths follow the electric field lines. These can be seen in figure 3.B.5 for three large cells, and in figure 3.B.6 for three small cells, with 2.5 kV on the sense wires. For the large cells, there is no electron leakage between the two sublayers of the bilayer, but with the small cells, there is a small amount of leakage. The electric field between these sublayers is very low however, so the electron drift velocity is very much slower than the saturated value of ~ 53 µm/ns with $\underline{B} = 0$ T.

When the magnetic field is applied, then the electron paths no longer follow the electric field lines, but become curved because of the Lorentz force acting on them. The total force acting on the drifting electrons from the applied electric and magnetic fields is :

$$\underline{F} = Q\left(\underline{E} + \underline{v} \quad \times \underline{B}\right) \qquad\qquad \tan\theta_{Lorentz} = \frac{|\underline{v}_{B=0} \times \underline{B}|}{E}$$

Applying a magnetic field changes the average direction of the drifting electrons and modifies the energy distribution, and therefore the drift properties of the electrons. The change in energy distribution affects the drift velocity and the diffusion.

The mean angle of deflection of a drifting electron is the angle between its direction of travel and the electric field. It is found experimentally to be larger than the Lorentz angle. Figure 3.B.7 shows the mean deflection angle with various electric and magnetic fields, for argon-ethane 50%-50%.
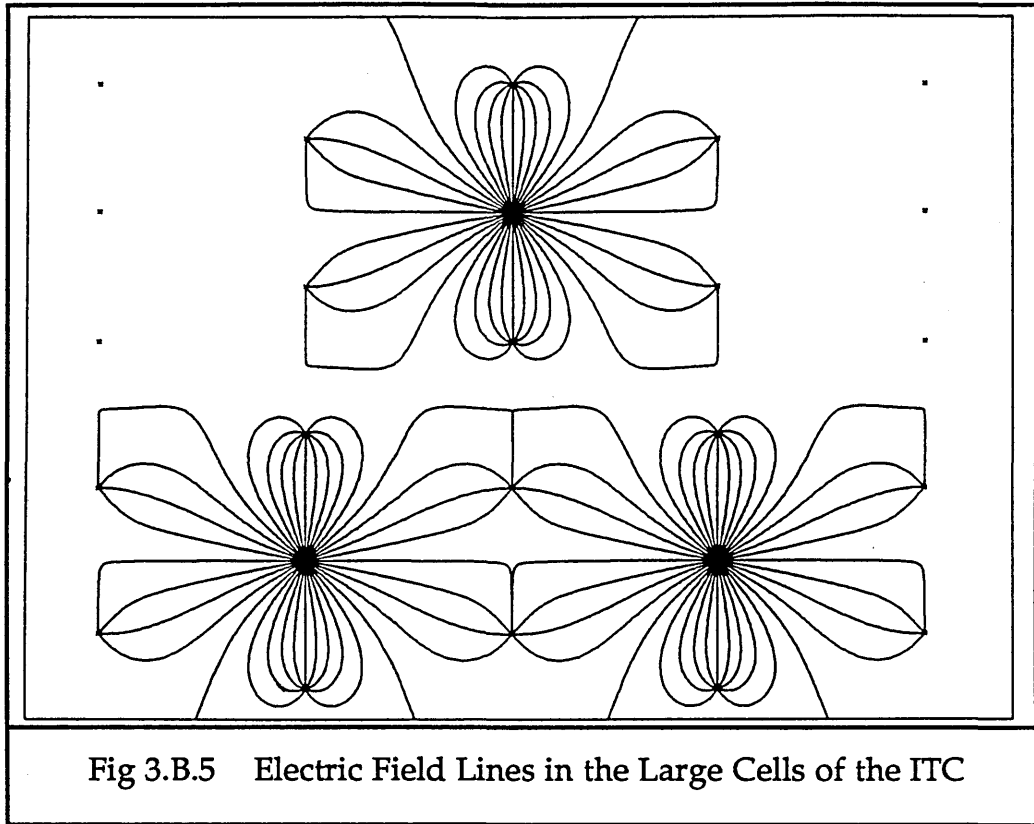
Fig 3.B.5   Electric Field Lines in the Large Cells of the ITC
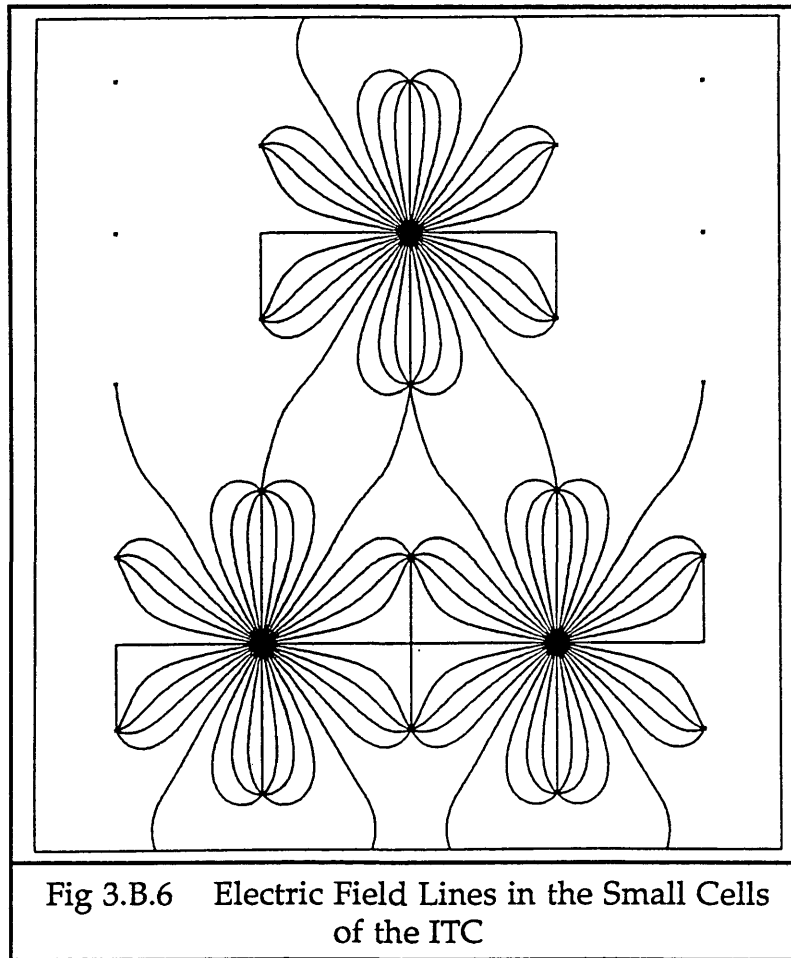
Fig 3.B.6   Electric Field Lines in the Small Cells
of the ITC

177
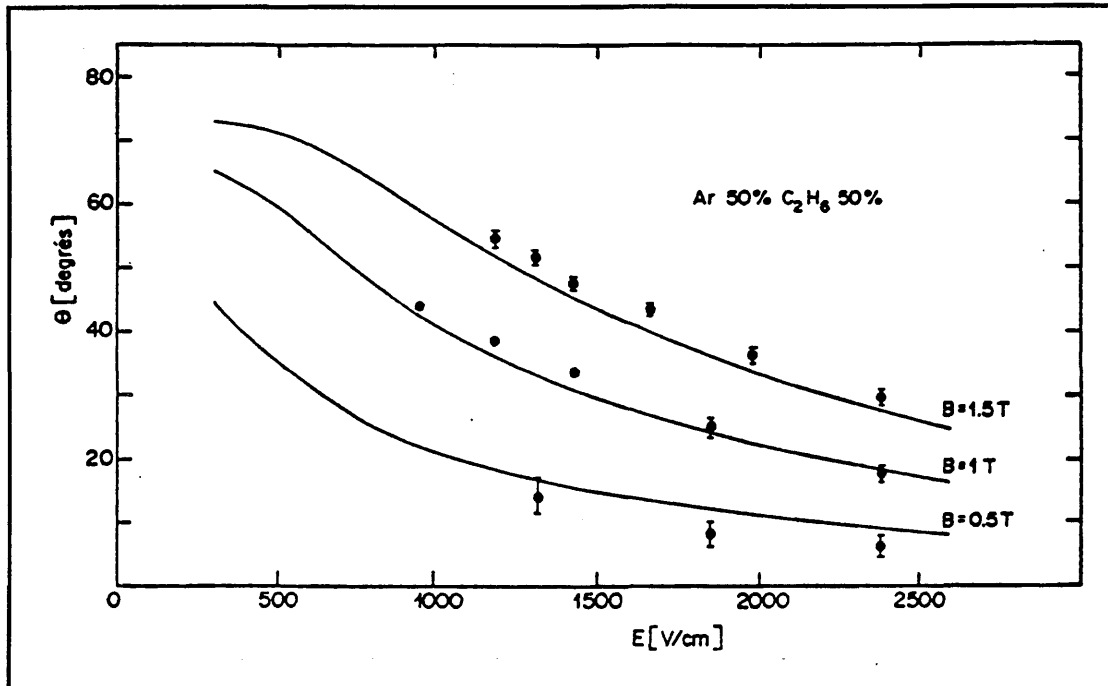
Fig 3.B.7   Deflection Angle with Electric and Magnetic Fields
in Argon-Ethane 50%-50%

The curves shown in figure 3.B.7 can be reproduced for the simulation program by the introduction of a constant k, as shown in figure 3.B.8.

$$\tan \theta_{Total} = \frac{k \left| \underline{v}_{\underline{B}=0} \times \underline{B} \right|}{E}$$
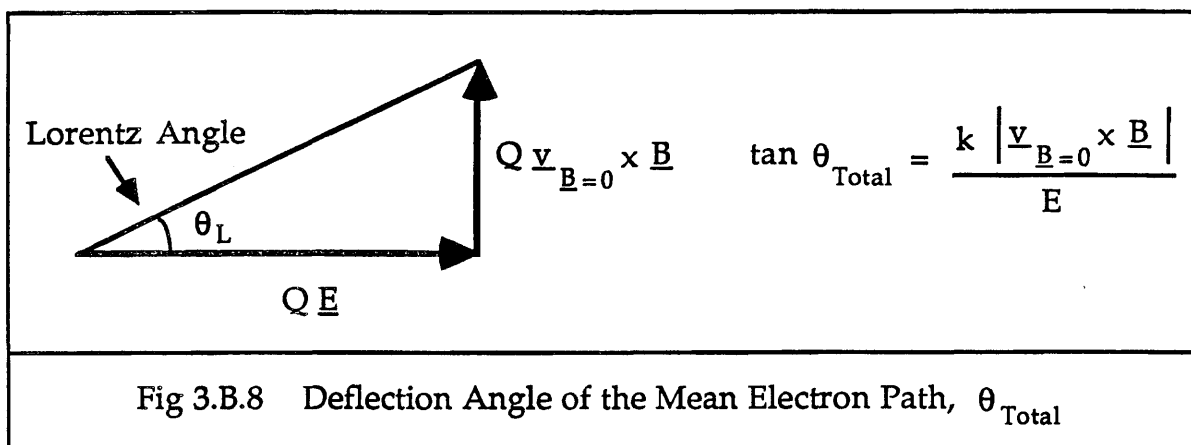
Fig 3.B.8   Deflection Angle of the Mean Electron Path, θ_{Total}

Using the drift velocity found when $\underline{B} = 0$ T, the value of k is found to be 2, in order to reproduce the deflection angle curve with $\underline{B} = 1.5$ T within 1 or 2 degrees. The other curves for smaller magnetic fields are also then reproduced fairly well.

Figure 3.B.9 shows the electron drift paths in a bilayer of large cells, with $\underline{B} = 1.5$ T and 2.5 kV on the sense wires. The drift velocity parameterisation used represents that found for $\underline{B} = 1.5$ T, shown in figure 2.9 of Chapter 2. Electron leakage from cell to cell within a sublayer can be seen, as well as across the region of low electric field from sublayer to

178

sublayer within the bilayer. Figure 3.B.10 shows the electron drift paths for the same conditions in the small cells.

Fig 3.B.9   Electron Drift Paths in Large Cells with $\underline{B}$ = 1.5 Tesla

Fig 3.B.10   Electron Drift Paths in Small Cells
with $\underline{B}$ = 1.5 Tesla
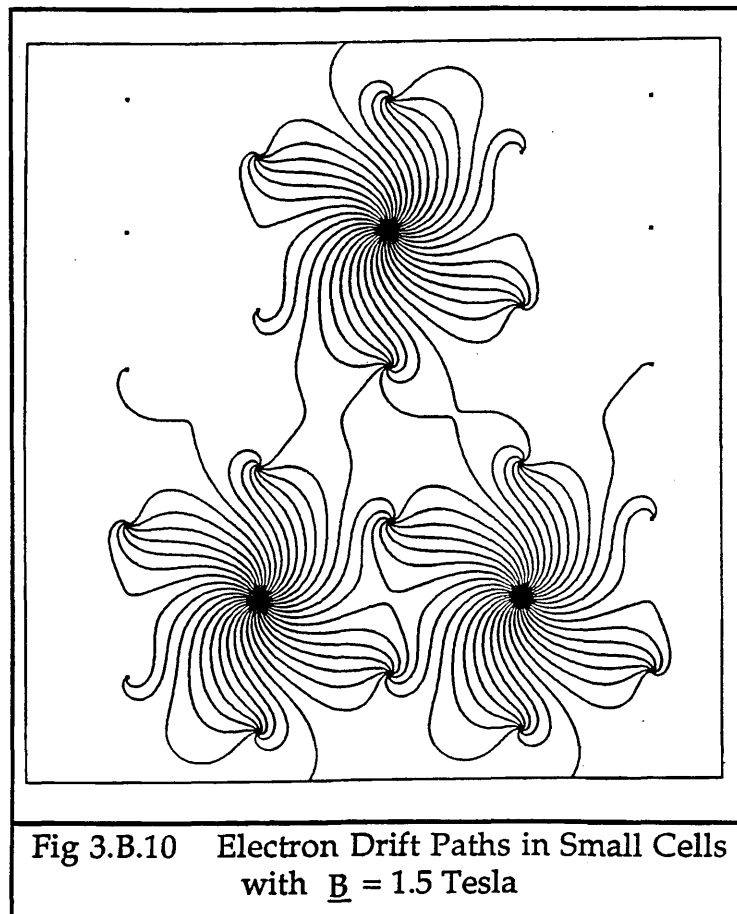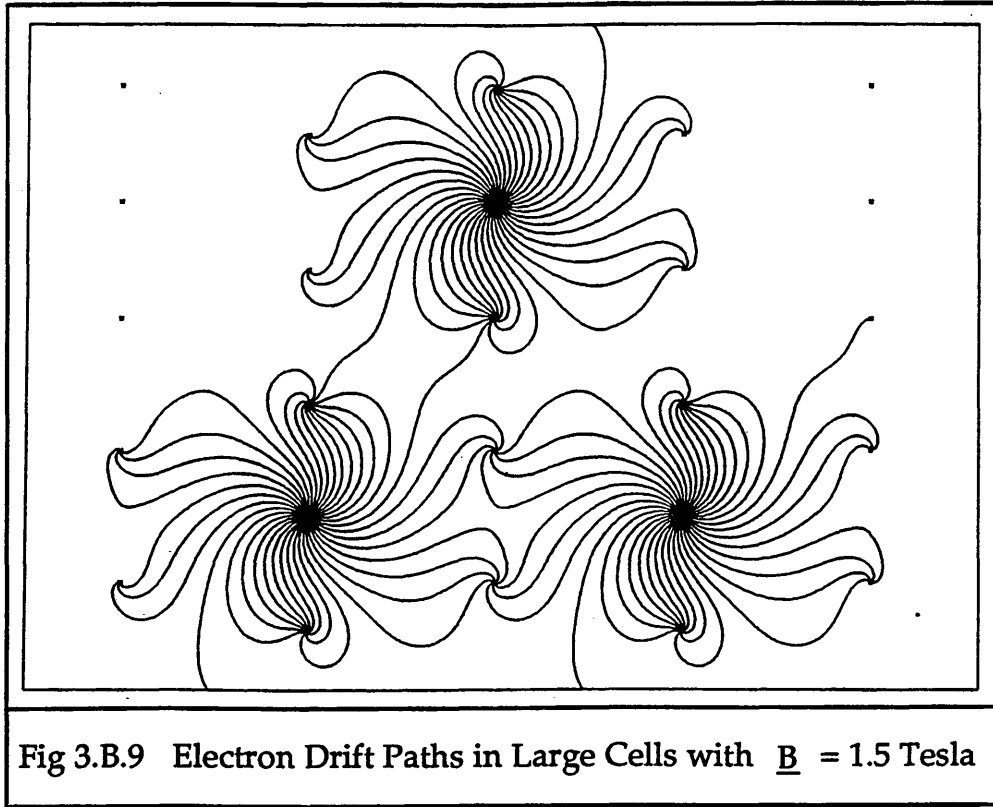
5 Investigation into the Effects of Dead Cells on the Electron Drift Paths

By setting the potential on some of the sense wires to 0 V in the simulation, it is possible to investigate the effect that dead cells have on the electron drift paths. There were many dead cells in the small chamber, and these affected the timing in neighbouring cells.

Figure 3.B.11 shows the electron drift paths in large cells when there are three dead cells.

Fig 3.B.11   Electron Drift Paths in Large Cells with Three Dead Cells
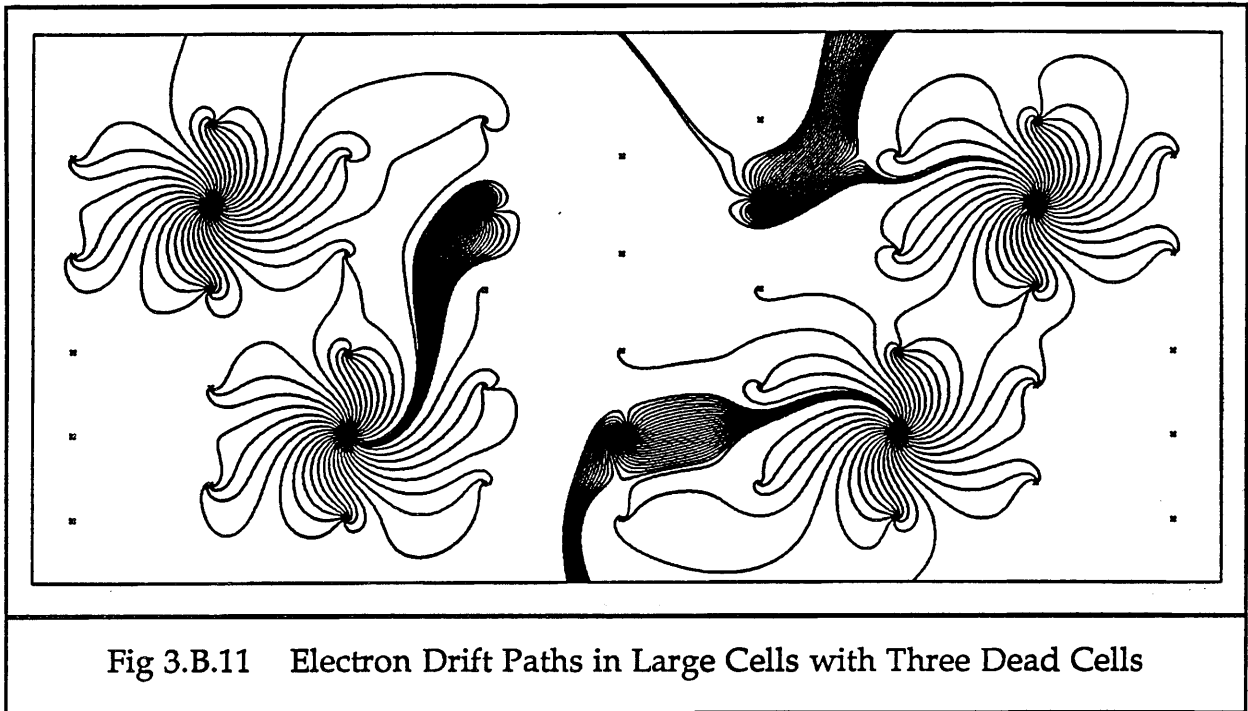
In figure 3.B.11, the earthed sense wires are now behaving like extra field wires. The electron drift paths in the normal cells do not appear to be greatly affected by the dead cells. There is a high level of asymmetry of the electron paths in the dead cells. Electrons liberated in the left hand dead cell of the upper sublayer, which has a live cell just below it, drift from one sublayer to the other. Electrons from the right hand dead cell in the upper sublayer mainly leave the bilayer altogether, although a few drift into the next cell along. In the lower sublayer, with just one dead cell, a signal will be detected in the next cell along for tracks in the right hand side, but tracks in the left hand side will probably not produce a signal, since the electrons all tend to drift out of the bilayer.

Figure 3.B.12 shows the same setup for a bilayer of small cells, with three dead cells.

Fig 3.B.12   Electron Drift Paths in Small Cells with
Three Dead Cells
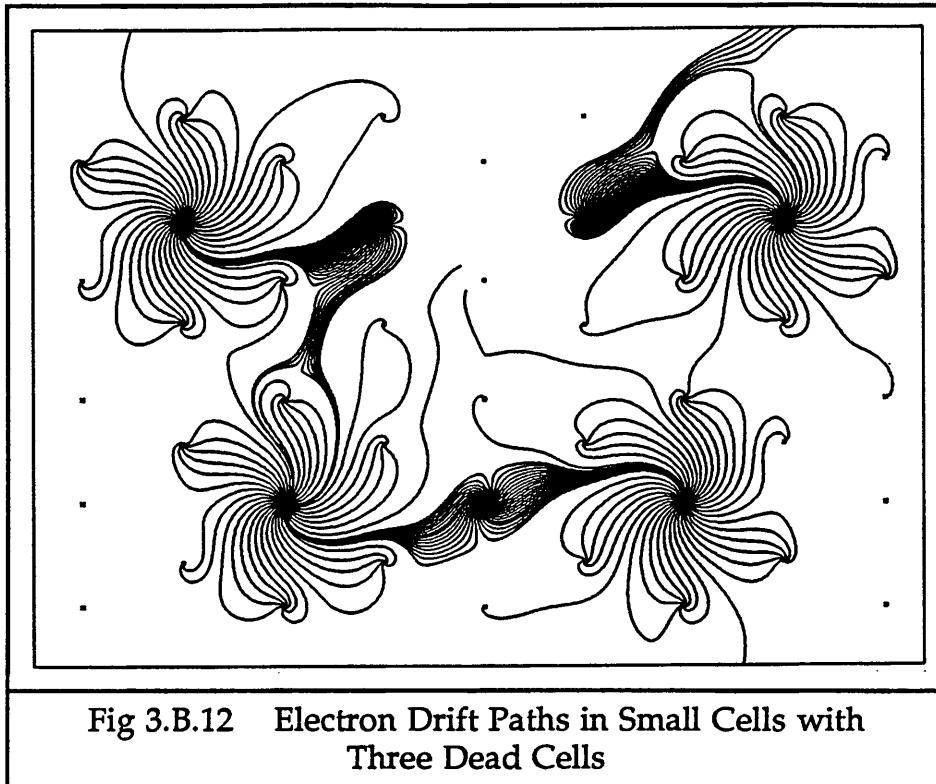
The effects with dead small cells are different to those in the large cells, because the sense wires are closer together. When a dead cell has only one live neighbouring cell within the sublayer, then electrons liberated in that dead cell will tend to drift to that live neighbour, or across to the other sublayer. With an isolated dead cell, drifting electrons are contained within the sublayer, and drift to the sense wires on either side.

6   Conclusions

The electric fields and electron drift paths in the ITC hexagonal cells are fairly complicated and non-uniform. There is a region of low electric field within the drift cells, between the pairs of side field wires, which means that tracks produced in this region at maximum drift distance from the sense wire, will have longer drift times than would be expected just from the electron drift paths, due to the low drift velocity. This is most noticeable with the large drift cells from layer 4 of the ITC. There is some leakage of electrons from one cell to another, which will produce pairs of hits in some layers associated with just one track. However, the design does not have very significant left-right asymmetry within the cells, and it also keeps the electric field below the critical value of ~ 20 kV/cm for carbon fibre whisker growth, on all the field wires.

Chapter 4

z POSITION MEASUREMENT

1 Introduction

In the ITC, the z position of hits along the sense wires is measured in order to provide a three dimensional trigger in ALEPH. The r-ø drift positions are measured to ~ 100 µm for good tracking resolution, but the r-ø hit coordinates alone do not provide a very sensitive trigger, since tracks in the ITC which do not originate from the interaction point cannot be distinguished from those that do. Therefore, if the third coordinate is available, then three dimensional tracks can be reconstructed, and those which do not come from the interaction point can be rejected.

Since the z coordinate is principally used in the trigger, the z resolution need only be better than ~ 5 cm for distinguishing tracks from near the origin. The interaction between the beams will take place with a spread of ~ 1.5 cm about the origin in the z direction. The main constraint on the z measurement system is the need to produce the trigger signal within ~ 3 µs of a beam crossing, in order to allow the Time Projection Chamber to set its gates. The necessity for this very high speed means that most standard z position measurement techniques are unsuitable for use in the ITC. Methods such as charge division or stereo wires require complex online or offline reconstruction, which make them too slow to be used in a fast trigger.

The method to be used in the ITC to produce fast online z position information for use in the r-ø-z trigger is that of time differences [4.1]. This method is also to be used by Zeus, in the Inner Detector [4.2], and by Opal, in the z Chambers [4.3].

2 z Position Measurement using the Method of Time Differences

2.1 How the Timing Method Works

When a charged particle travels through the ITC, it produces a signal on every sense wire it passes. Each signal travels along its sense wire and the time of arrival is measured at both ends of the wire. The signal arrival time from one end of the sense wire is used to reconstruct the drift distance in the r-ø plane. To calculate the z position, the difference in arrival times is found, using the following relation :

$$\Delta z = \frac{c}{2}\left(t_2 - t_1\right)$$

The arrival times t_1 and t_2 are shown in figure 4.1.

Fig 4.1   Calculation of Time Difference
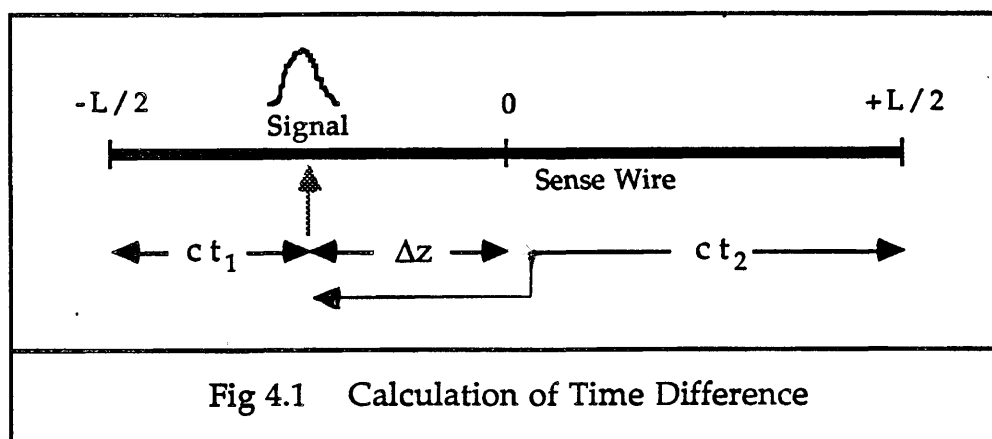
The signals travel at a speed of $c = 3 \times 10^8$ m/s along the wire, so it takes ~ 6.7 ns for a signal to travel the entire length of the wire. The signal rise time is a few nanoseconds, and to measure the z position to within a few centimetres, the timing must be done to within ~ 50 ps. In comparison, to obtain an r-ø resolution of ~ 100 μm, the signals need only be timed to within 500 ps.

The method of timing relies on the signals at each end of the wire being the same as each other, in order for the difference in arrival time to relate to the z position and not be dominated by any change in the shape of the leading edge of the signal. The timing method also needs very good calibration, since the cable lengths at each end of the chamber cannot be cut accurately enough not to add any offset to the z = 0 cm position in the centre of the chamber. Since the timing has to be done with such a high

degree of accuracy on the leading edge of the signal, the timing method is very vulnerable to interference from external high frequency noise, which if present, completely loses the timing signals.

2.2 How the Calibration Works

The calibration system is used to remove any effects in the z position measurement from the different cable lengths and readout channels. There is one calibration wire in each cell, as shown in figure 4.2. These wires are insulated from the end plates, and are connected together in blocks outside the end plates.
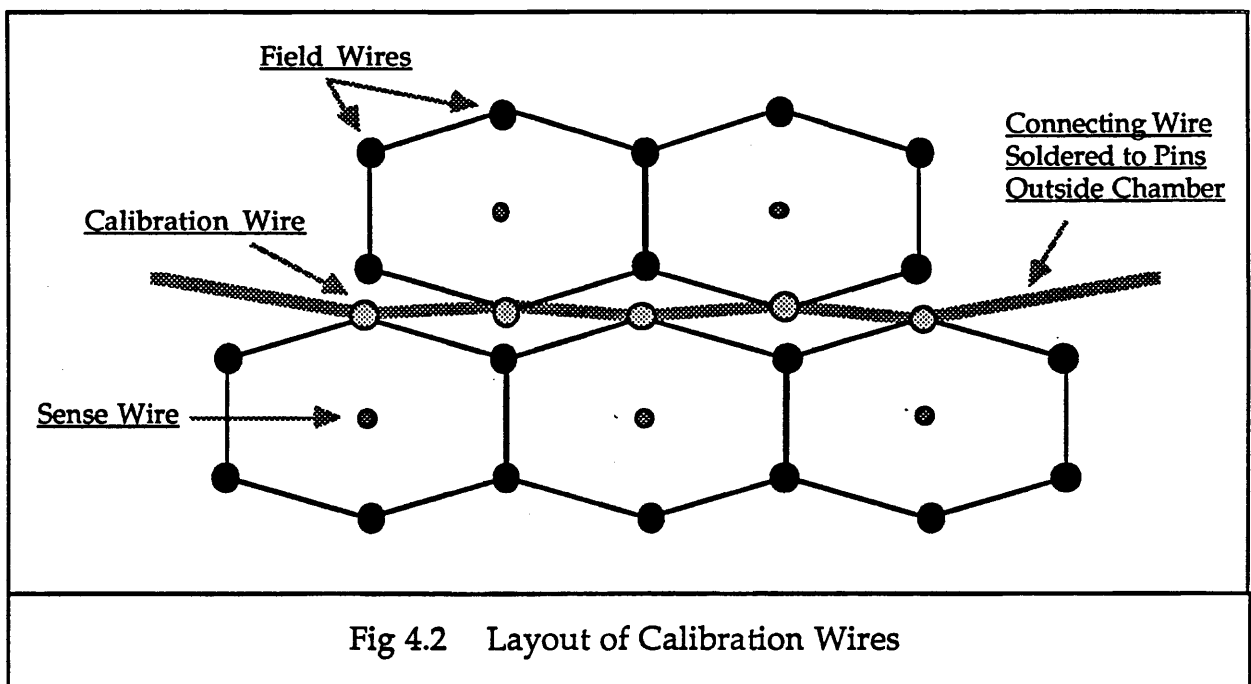
Fig 4.2 Layout of Calibration Wires

A calibration pulse is sent to each end of the chamber, so that all the calibration wires in a block are pulsed at both ends simultaneously. The calibration pulses induce signals onto the sense wires, which are then amplified and read out in the same way that chamber signals are. Since the calibration signals at each end of a wire are simultaneous, the signals seen on the sense wire should produce a zero time difference as if from a signal generated at the centre of the chamber. The calibration readout is used to trim the voltage levels on the Az time expansion boards, so that any irregularities between channels are removed before the z signals are used in the trigger. The calibration finds the centres of the wires to within ~ 1 cm.

2.3 Nonlinearity in the z Position using Time Differences

When the method of time differences was first tested for use in the ITC, a very significant nonlinearity was found from the expected $c/2$ gradient of z position with time difference. This nonlinearity is seen in figure 4.3, which shows data from the CERN beam tests of 1984, taken with a long test chamber. From its curved shape, the nonlinearity became known as the "S-bend".

Fig 4.3   CERN Test Beam Data Showing
S-Bend Nonlinearity from c/2
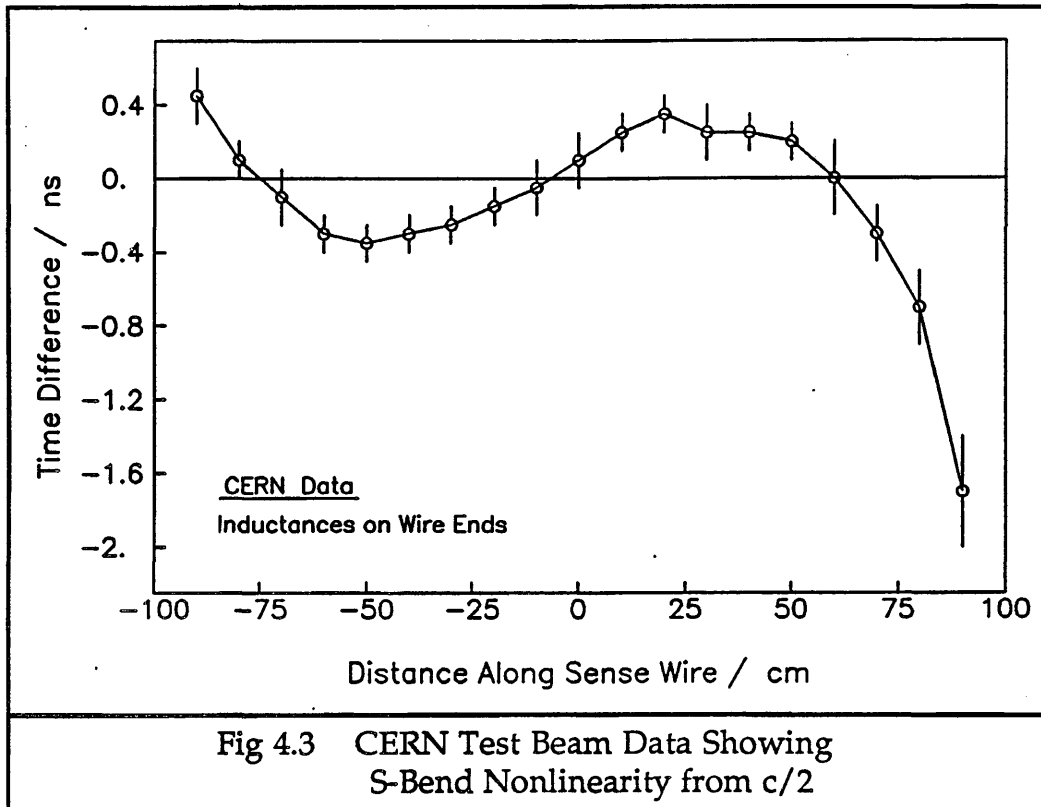
The vertical scale in figure 4.3 shows a time difference which is actually a combination of three time differences :

$$\Delta t = \Delta t_{ideal} - \left(\Delta t_{meas} - \Delta t_{calib} \right)$$

where Δt is the time difference plotted on the vertical scale,

$\Delta t_{ideal} = z \times 2/c$

Δt_{meas} is the measured time difference,

and Δt_{calib} is the calibration time difference.

These CERN data were taken with inductances on the ends of the sense wires, which reduce the magnitude of the nonlinearity. This effect is

examined in more detail in Section 5.5.1. The data in figure 4.3 are the only data presented where these inductances are present.

Initial investigations showed that the S-bend has more than one contributory cause. Signals on the sense wires in the chamber are reflected at the ends of the wires, and these reflections change the shape of the leading edges of the signals. These reflections cause the signals at each end of a sense wire to be different from one another and this affects the timing. A second contribution to the S-bend comes from the discriminators used to find the time of arrival of the signals. The shape of the S-bend is very much influenced by how the discriminator works and how high up the signal leading edge the timing is taken.

In order to investigate the nonlinearity, and also to test the stability of this z measurement system and the calibration method, a long test rig was constructed. This was used to make detailed measurements of the S-bend, and test the calibration system, using two different types of discriminator to see which type was most accurate and steady. The results from this test rig were then used to help construct a computer simulation of the z measurement system, and this model allowed the nonlinearity of the measurement system to be explained.

3   Experimental Tests

3.1   Objectives of the Tests

A series of tests of the method of time differences for z position measurement was undertaken using a 2 m long test rig at Imperial College, in order to establish how stable the system can be, and how often the calibration will be necessary. Tests were also made using different discriminators, in order to decide which type and setup will produce the best z position measurement.

3.2   Experimental Setup

The test rig used had 11 cells of wires strung between two aluminium end plates which were held 2 m apart with four metal rods. The cell pattern used represents a small section of a bilayer of ITC cells, with the dimensions of cells from layer 1 of the ITC. Three of these cells could be calibrated and

read out at each end. This cell layout is shown in figure 4.4.
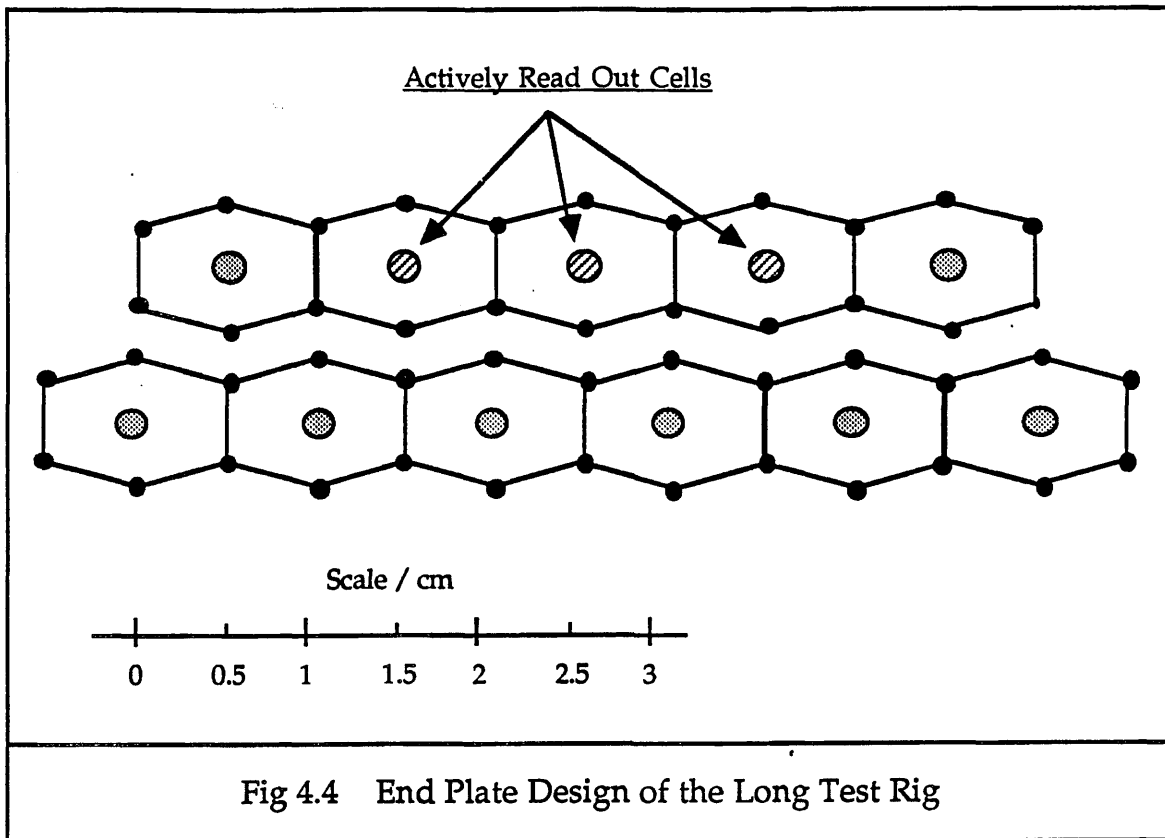
Fig 4.4   End Plate Design of the Long Test Rig

Most of the wires used in this rig were the same as in the ITC. That is, the sense wires were 30 μm diameter gold plated tungsten, and most of the field wires were 147 μm gold plated aluminium. Some of the field wires were 100 μm copper/beryllium. This difference had no effect on the results.

Signals were injected onto the sense wires using small wire hooks which just touched the wires, and which could be slid along the detector to produce signals anywhere along the wire from $z = 0$ cm at the centre of the test rig to $z = 90$ cm near one end. These hooks can be seen in figure 4.5. They are mounted in a perspex block.

Signals were produced on the sense wires from a pulse generator, via an attenuator, and a Lemo cable, which was coupled to the hooks via two resistors which also attenuated the signals.

Although the hooks enabled a wide variety of signal sizes to be injected onto the sense wires at any point along the wires, they caused additional signal reflections on the wires, which were not negligible, and which changed the shape of the S-bend from that seen in the ITC where there are no hooks. These additional reflections had to be included in the simulation program in order to reproduce the data successfully.
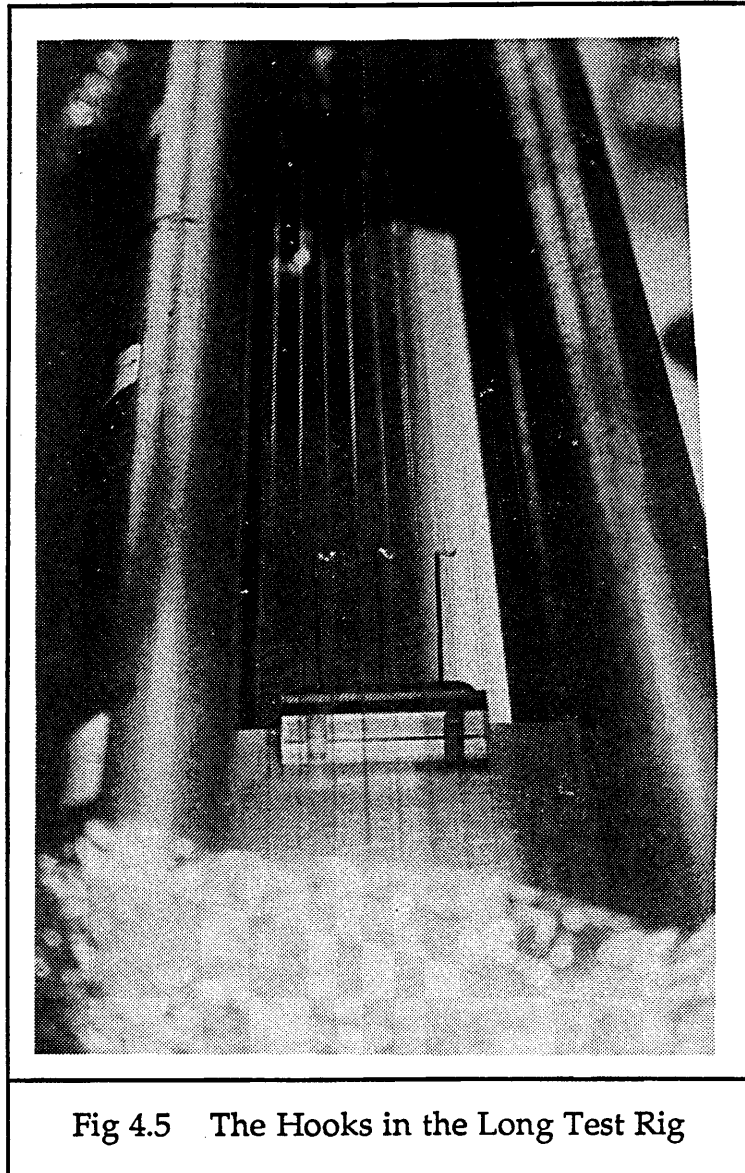
Fig 4.5   The Hooks in the Long Test Rig

The readout of the signals was achieved in a similar manner to that in the ITC, except that there was no time expansion, and so the timing had to be done using a much faster TDC. The time expansion process is explained in Chapter 5, since it is not used in this chapter. After time expansion, a TDC with 5 ns bin size is all that will be necessary to achieve the desired z position resolution, but in this series of tests, where no time expansion was carried out, a TDC with 50 ps bin size was necessary to obtain the same resolution.

The readout system used for these tests is shown in figure 4.6. An LSI-11 computer controlled the pulse generation, calibration, signal readout and data processing and recording.
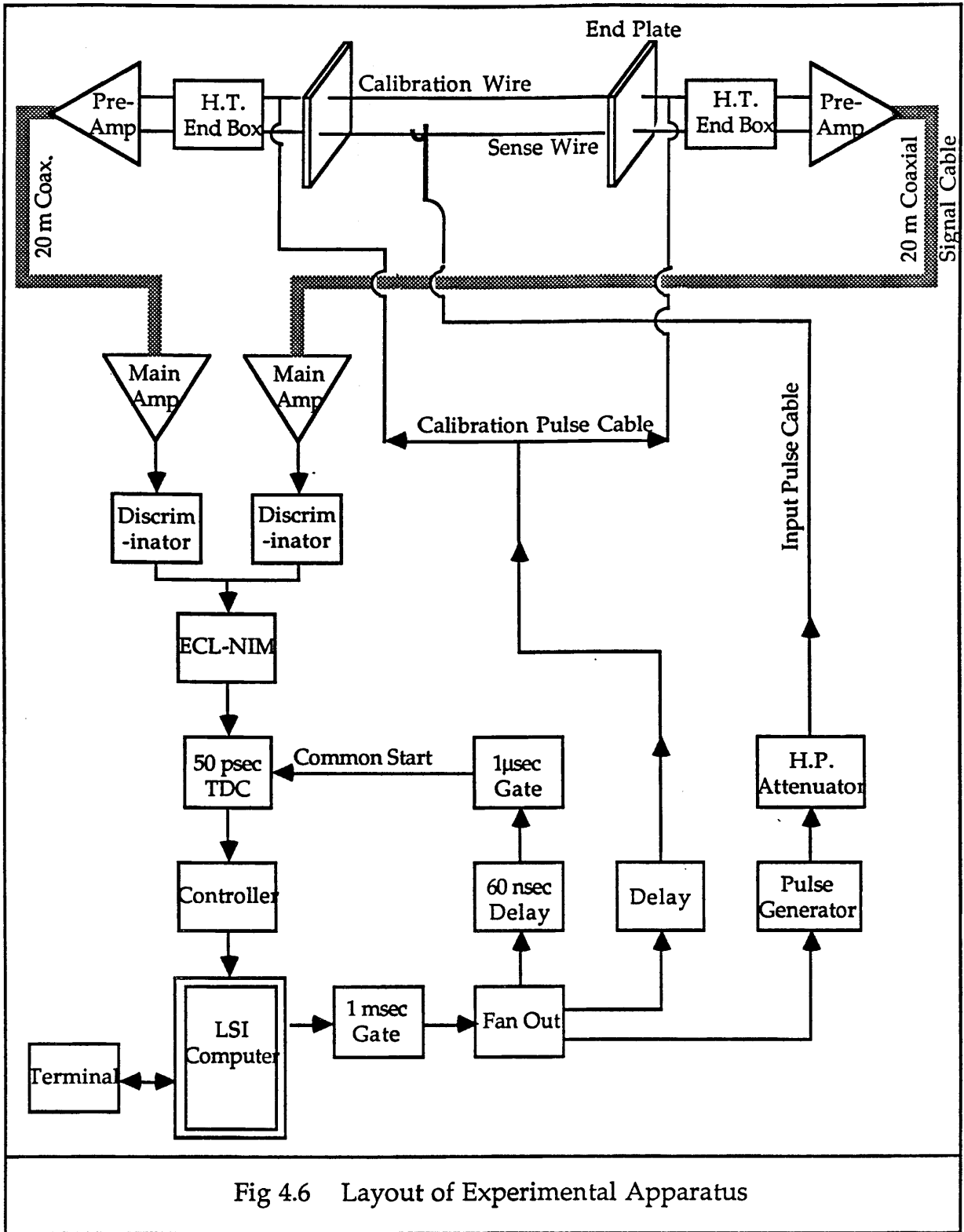
Fig 4.6   Layout of Experimental Apparatus

3.3   Experimental Details

3.3.1   Electrical Screening

In order to be able to read out any signals at all, the whole of the long test rig, including HT end boxes and preamplifiers, had to be electrically screened from high frequency interference by being wrapped in several

layers of aluminium foil. This foil covering was crucial to the z measurement system. If the foil screening was not tight along the whole length of the chamber, then the spread of time differences measured doubled or trebled. If there was a hole in the screening, then the timing was lost completely. Even with the screening, when the Iraqi embassy about 100 m away was broadcasting on its radio transmitter at ~ 20 MHz, or if the equally close Bulgarian embassy was transmitting at high frequency, then all measurements were lost during those periods.

3.3.2 Multiple Measurements

For the investigation of long term stability of the measurement system and measurements of the nonlinearity from c/2 of the z position from the time difference, signals were injected onto the sense wires at 10 cm intervals. At each point on the wires, a wide range of pulse sizes was used, and 1000 signals of each size were injected, in order to measure both the mean time difference and the spread of time differences at that position and pulse size. The spread is calculated as the root mean square of the time differences measured.

Before each set of tests was run, the test rig was calibrated. The hooks were placed in the centre of the test rig at z = 0 cm, so that reflections from them did not affect the calibration, and 5000 calibration signals were sent to the calibration wires and read out from the sense wires. The mean time difference measured from these was recorded as the calibration time, for later use.

3.4   Results on Stability

Two tests were done on the stability of the measurement system, by calibrating the system every half hour over several hours. Figure 4.7 shows the calibration time difference for the three sense wires taken during an 8 hour period, overnight. The absolute values for the time difference are not significant. Within this period, there is a slight drift of the time difference, but it is less than one TDC bin in magnitude.

Figure 4.8 shows another test, over 50 hours, on just one wire. There is no slow drift as in figure 4.7, but there is a shift of ~ 1 TDC bin after 20 hours. The 5 periods when the signal is lost correspond to broadcasts from the Iraqi or Bulgarian embassies between 8 and 9 am each morning, 1 and 2 pm each afternoon, and from 4 to 5 pm on the second afternoon.
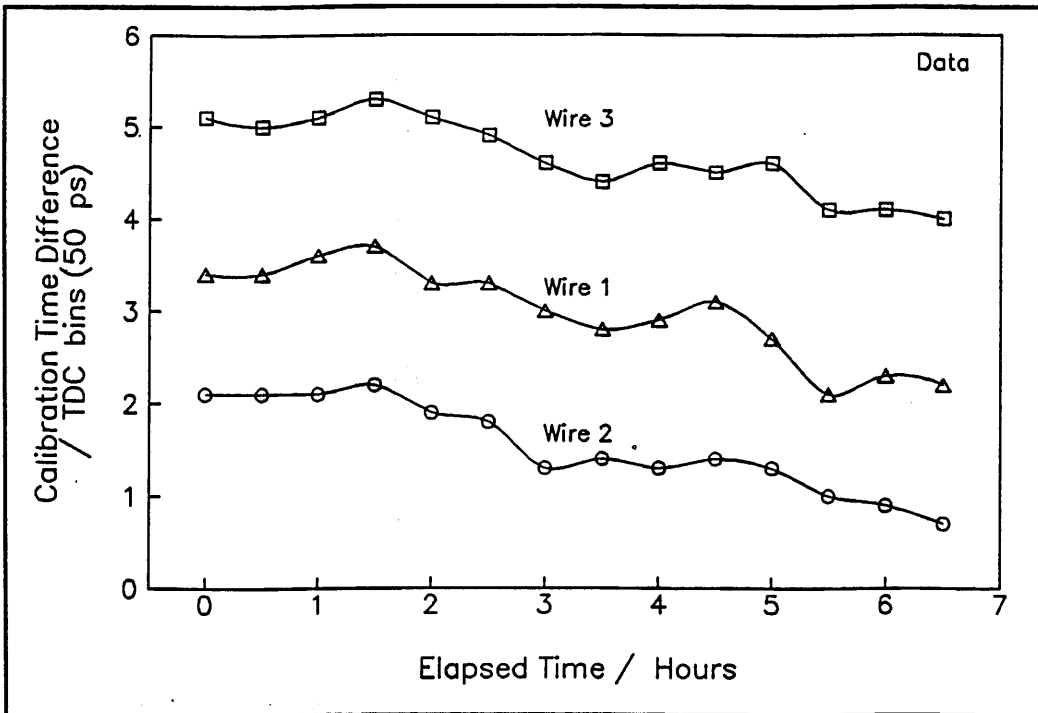
Fig 4.7   Long Term Stability of Calibration, Test 1
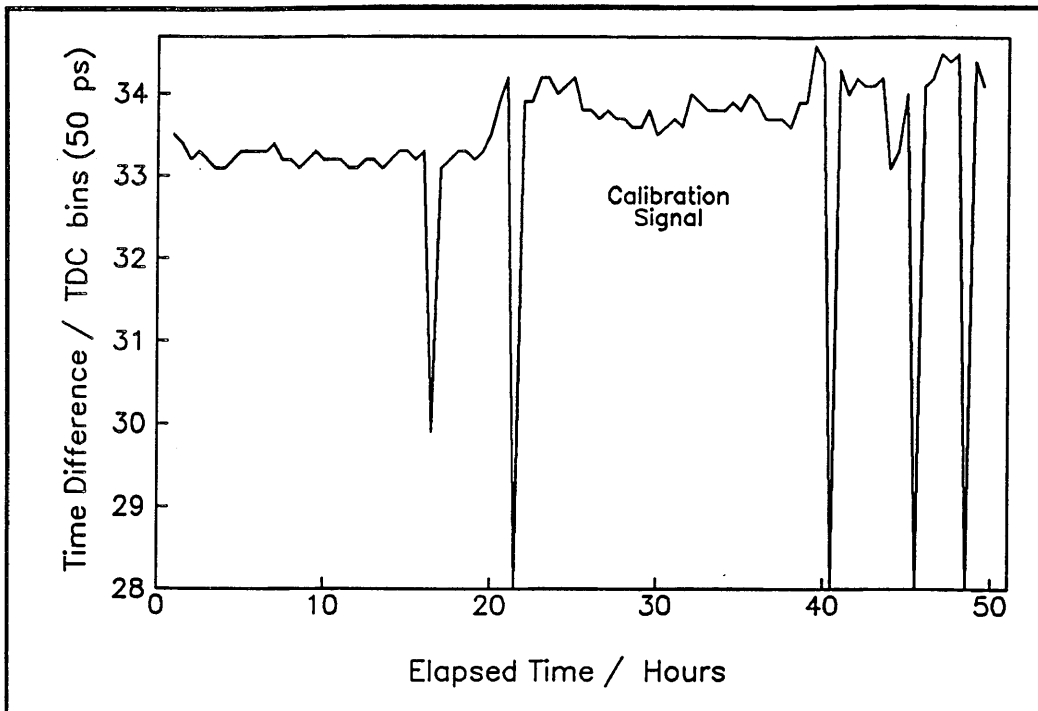
Fig 4.8   Long Term Stability of Calibration, Test 2

One conclusion from these tests is that the system can be made to operate steadily for many hours, provided that the chamber is completely screened from external high frequency signals. The calibration should only be necessary once every few hours to cope with the level of drift of the time

192

difference found. It should be sufficient to calibrate the system at the start of each data taking run in LEP, although it may be felt necessary to be able to do a calibration more often if needed, in case the running conditions inside ALEPH are not so good as for the long test rig.

4 Theory and Results from the Simulation

. This section gives details of how the z measurement system works and what is going on to produce the nonlinearity from c/2 in z position from the time difference. It will present results from the simulation based on calculations from the ITC and the long test rig, and will show signal profiles calculated at all stages through the readout system before discrimination.

The simulation program is written using double precision variables in order to retain the level of accuracy required throughout the calculation.

4.1 Transmission Lines

4.1.1 Brief Summary of Transmission Line Theory

The sense wire surrounded by field wires acts like a transmission line, because they are all long parallel conductors. These transmission lines in the ITC are lossy, which means that the signals travelling on them are both attenuated and distorted. At high frequencies, the equation governing the transmission of signals along a lossy transmission line approximates to :

$$V \approx V_0 \exp(i\omega t) \; \exp\left(\frac{-Rz}{2Z_0}\right)$$

V = Voltage amplitude after travelling distance z along line [V]

V_0 = Initial voltage amplitude [V]

ω = Angular frequency of signal [Hz]

t = Time of travel of signal [s]

z = Distance travelled along line [m]

R = Series resistance per unit length of the line (at frequency ω) [Ω/m]

Z_0 = Characteristic impedance of the line [Ω]

This is a damped wave equation.

The equation for the characteristic impedance at high frequencies approximates to the same relation as for ideal transmission lines :

$$Z_0 \approx \sqrt{\frac{L}{C}}$$

L = Series inductance per unit length [H/m]

C = Shunt capacitance per unit length [F/m]

These relations are derived in Appendix C at the end of this chapter.

4.1.2 Calculation of the Parameters for the ITC

In order to calculate the values of the transmission line parameters in the ITC, it is necessary to make the approximation that a sense wire surrounded by a hexagon of parallel field wires behaves rather like a coaxial cable with a gas dielectric. The cell can be seen in figure 4.9.

Field Wire

radius of sense wire

a = 15 μm

mean radius of cell

b = 5.167 mm

Sense Wire

Fig 4.9   Hexagonal Cell as a Coaxial Transmission Line
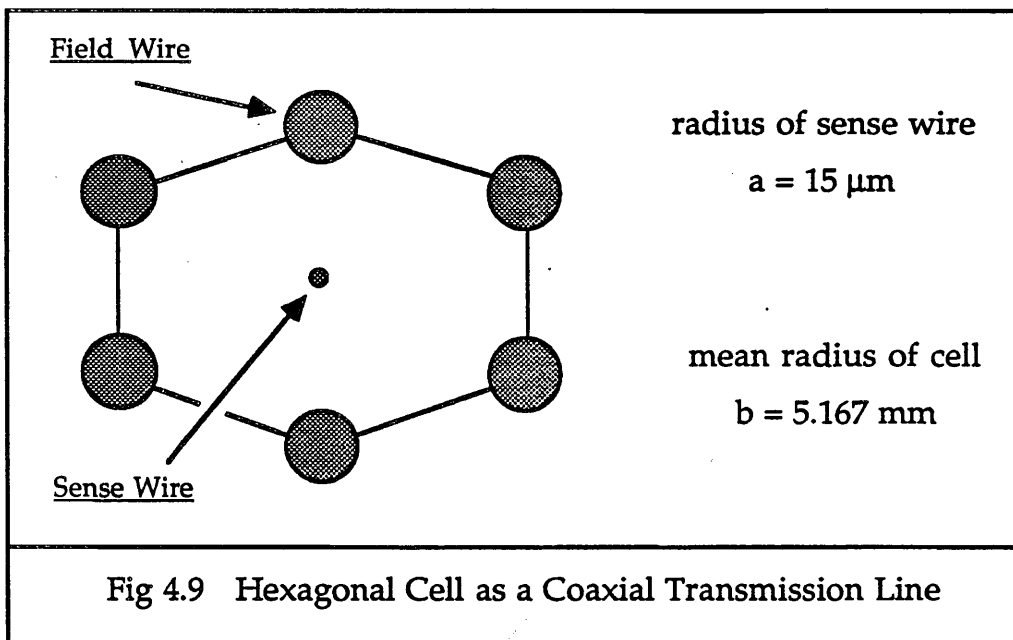
a) Series Resistance, R

This is measured to be 88 Ω/m in the ITC with zero frequency current. However, R is a frequency dependent quantity, and the very high frequency components of the signals are used for the timing. In Appendix D, there is a calculation of the "skin effect" which shows that for the upper frequencies in the signals on the sense wire in the ITC ~ 500 MHz, (corresponding to a signal rise time of ~ 1 ns), the series resistance R ~ 139 Ω/m. The series resistance is used as a variable in the simulation program because the

frequencies in the signals are not well known, and also because it is used to compensate for the distortion of the signals, since this effect is not included in the simulation model.

b) Series Inductance, L

For a coaxial cable, as shown in figure 4.10, current I is flowing in the inner conductor, and − I has been induced to flow in the outer conductor.

Fig 4.10   Series Inductance of a Coaxial Cable
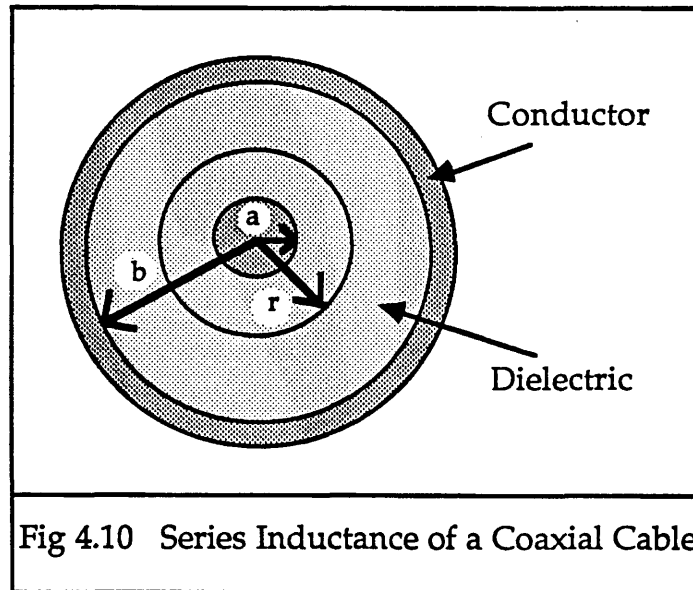
Apply Ampère's Circuital Law to find the magnetic field B due to these currents.

$$\int \underline{B} \cdot \underline{dl} = \mu\, \mu_0\, I = 2\,\pi\, r\, B$$

$$B = \frac{\mu\, \mu_0\, I}{2\,\pi\, r}$$

Join the conductors together at both ends of a section, length l, to get the total magnetic flux per unit length, and hence the self inductance per unit length :

$$\varnothing = l \int_a^b \frac{\mu\, \mu_0\, I\, dr}{2\,\pi\, r} = \frac{\mu\, \mu_0\, I\, l}{2\,\pi} \log_e (b/a)$$

$$L = \frac{\varnothing}{11} \quad \Rightarrow \quad L = \frac{\mu \mu_0 \log_e (b/a)}{2\pi}$$

Therefore, for the ITC, where the relative permeability $\mu = 1$, the self inductance per unit length is $L = 1.17$ $\mu H/m$.

c) Shunt Conductance, G

The shunt conductance is proportional to any leakage currents from the high voltage sense wire to earth and is measured in units of Ω^{-1}/m. When the small test chamber (see Chapter 3) was running properly, there was a total leakage current on the sense wires of much less than 0.1 μA. This was divided between 64 wires, giving a current per wire that is at most ≈ 1 nA, say, (with sense wire voltage at 2 kV). This gives a value of the shunt conductance per wire in the ITC at a maximum of $G = I / V$ $\sim 5.10^{-13}$ Ω^{-1}/m. This is so small as to be negligible, so take $G = 0$ Ω^{-1}/m.

d) Shunt Capacitance, C

This can be calculated as follows. Using the variable names as in figure 4.10, suppose there is a surface charge density σ on the inner conductor. This gives a charge per unit length of :

$$Q = 2\pi a \sigma$$

The electric displacement $\underline{D}$ is cylindrically symmetrical, and its magnitude is only dependent on the distance from the axis.

$$\int_S \underline{D} \cdot \underline{dS} = 2\pi r D(r) = 2\pi a \sigma$$

$$D(r) = \frac{a\sigma}{r}$$

Therefore

$$E(r) = \frac{a\sigma}{\varepsilon \varepsilon_0 r}$$

196

The potential between the inner and outer conductor is :

$$V = - \int_b^a \underline{E} \cdot \underline{dl} = - \int_b^a \frac{a\,\sigma}{\varepsilon\,\varepsilon_0 r}\, dr = \frac{a\,\sigma}{\varepsilon\,\varepsilon_0} \log_e (b/a)$$

The capacitance per unit length of the wires is C.

$$C = \frac{Q}{V} \quad \Rightarrow \quad C = \frac{2\,\pi\,\varepsilon\,\varepsilon_0}{\log_e (b/a)}$$

For the ITC, where the relative permitivity $\varepsilon = 1$, this gives $C = 9.52\,pF/m$.

e) Characteristic Impedance, Z_0

For high frequencies, in the cell size of the long test rig, $Z_0 = 350\,\Omega$. In the ITC, the mean cell radius varies from 5.167 mm to 5.915 mm, giving a range of characteristic impedances from 350 Ω to 358 Ω.

4.2   The Hook

A small metal hook was used to enable signals to be injected onto each sense wire. It was coupled from the signal attenuator cable to the sense wire with a pair of resistors. These attenuated the signals before they arrived on the wire, and also removed some of the high frequency components from the signals, giving them a slower rise time than when they were generated. This setup can be seen in figure 4.11.
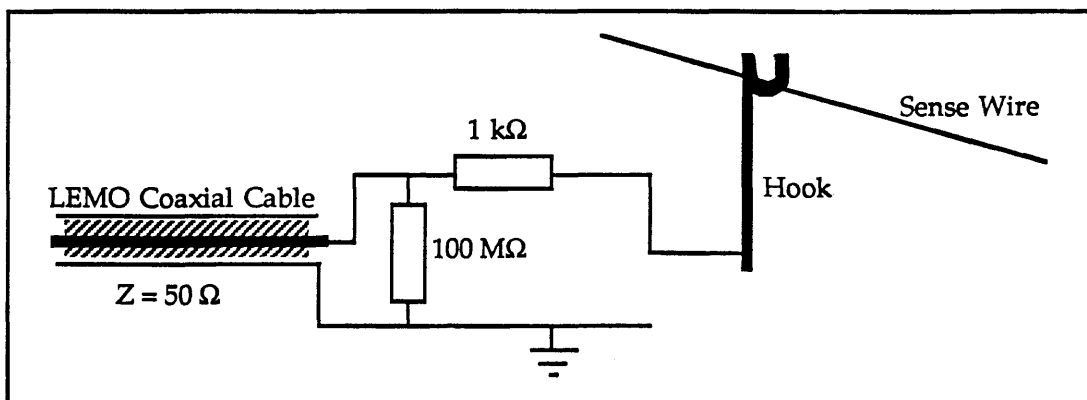
Fig 4.11   Coupling of Signal onto Sense Wire via Hook

Figure 4.12 shows the impedances involved at this junction with the hook. The sense and field wires form a transmission line of characteristic impedance 350 Ω, and from the hook, the input signal can travel in either direction down the sense wire, so the wires are shown as a pair of parallel impedances of 350 Ω.
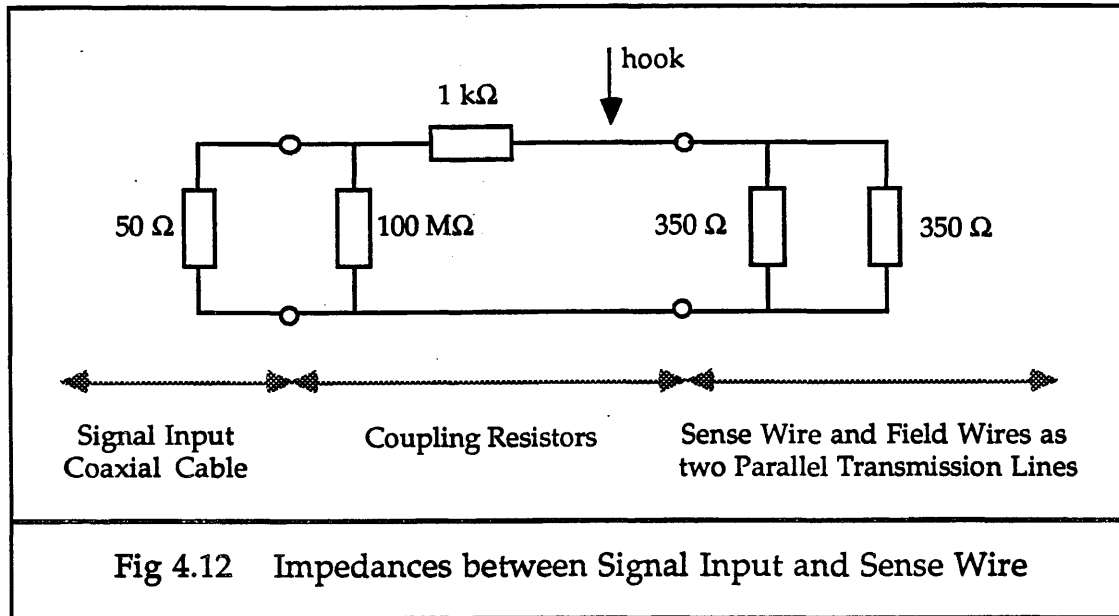
Fig 4.12   Impedances between Signal Input and Sense Wire

At high signal frequencies, the two coupling resistors each have a capacitance of about 0.5 pF associated with them. The 0.5 pF from the 100 MΩ resistor is in parallel with the capacitance of the LEMO cable, which is approximately 100 pF/m. Therefore, this extra capacitance can be neglected. The effect of the 0.5 pF from the 1 kΩ resistor is to act as a low pass filter with the resistors, and cut out some of the high frequency components of the signal. This gives the signal a slower rise time once it is on the sense wire.

The following calculations show the attenuation effect of the hook and resistors on signals being injected onto the sense wire, and for signals travelling along the sense wire, they show the extra reflections generated and the signal attenuation.

4.2.1   Transmission Coefficient for Injecting a Signal onto the Sense Wire via the Hook

Figure 4.13 shows the impedances seen by the signal as it approaches the sense wire from the signal generator.

Fig 4.13   Transmission of Signal onto Sense Wire
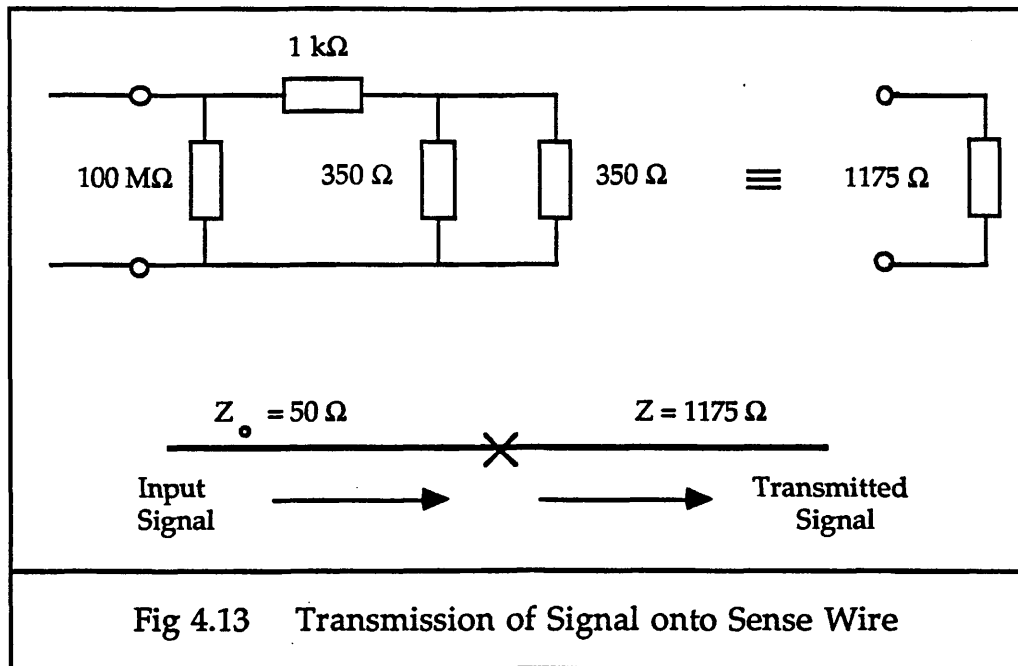
The signal approaches the hook on a LEMO cable of characteristic impedance 50 Ω. It sees a step in this impedance up to 1175 Ω, as shown in figure 4.13. Therefore, the total transmission coefficient is : ·

$$T_{total} = \left(\frac{2 Z}{Z + Z_0} \right) = 1.92$$

This is divided across the 1 kΩ resistor and the two parallel 350 Ω impedances, giving a transmission coefficient for the pulse onto the sense wire of :

$$T_{Hook} = \frac{175}{(1000 + 175)} \times 1.92 = 0.29$$

The signal charge then divides equally between the two directions of the sense wire, and two signal wave fronts are formed which travel away from each other to the ends of the sense wire.

There is also a positive reflection from this junction back down the coaxial cable, of amplitude 0.92 V per input Volt.

4.2.2   Coefficients for a Signal on the Sense Wire

The impedance shown to the signals travelling along the sense wire by the hook as a branch from the sense wire transmission line is calculated to be 1050 Ω, as shown in figure 4.14.
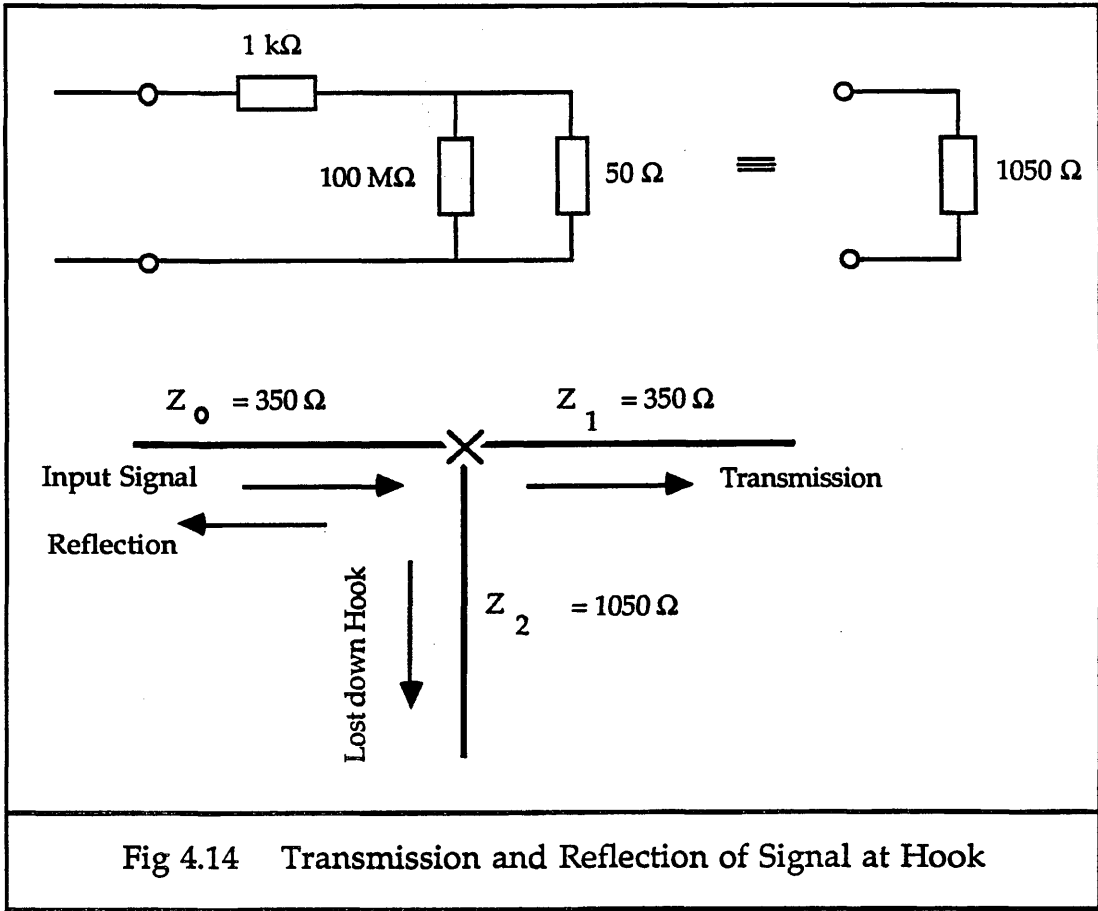
Fig 4.14   Transmission and Reflection of Signal at Hook

An experimental measurement of this value was made in order to check the validity of the approximations made. This was done by sending a square wave, which has many high frequency components, down a cable into an oscilloscope to measure its amplitude. The hooks were then attached to the cable as a branch, with the short LEMO cables at the base of the hooks, after the coupling resistors, correctly terminated with 50 Ω terminators to simulate the long cables used in the tests. The signal seen on the oscilloscope was attenuated because of this branch. From the amount of attenuation, the impedance of the hooks as a branch from the transmission line was then calculated to be 1000 ± 100 Ω. This agrees with the calculation, and so shows that the approximations used are valid.

The transmission coefficient for signals travelling along the sense wire will now be calculated. A signal on the sense wire approaching the hook sees a total impedance of :

$$Z = \frac{1}{(1/1050 + 1/350)} = 262.5 \ \Omega$$

Therefore, the voltage reflection coefficient at the hook is :

$$\rho = \left(\frac{Z - Z_0}{Z + Z_0} \right) = -0.14$$

The voltage transmission coefficient past the hook is :

$$T = \left(\frac{2Z}{Z + Z_0} \right) = 0.86$$

The current divides between the hook and the sense wire in the ratio of $350 : 1050 = 1 : 3$. Therefore, three quarters of the transmitted charge travels on down the sense wire at a potential of 86 % of the initial voltage, and one quarter of the transmitted charge at the same potential is lost down the hook. The transmitted and reflected parts of the signal, and those lost from the sense wire transmission line down the hook can be seen in figure 4.15.

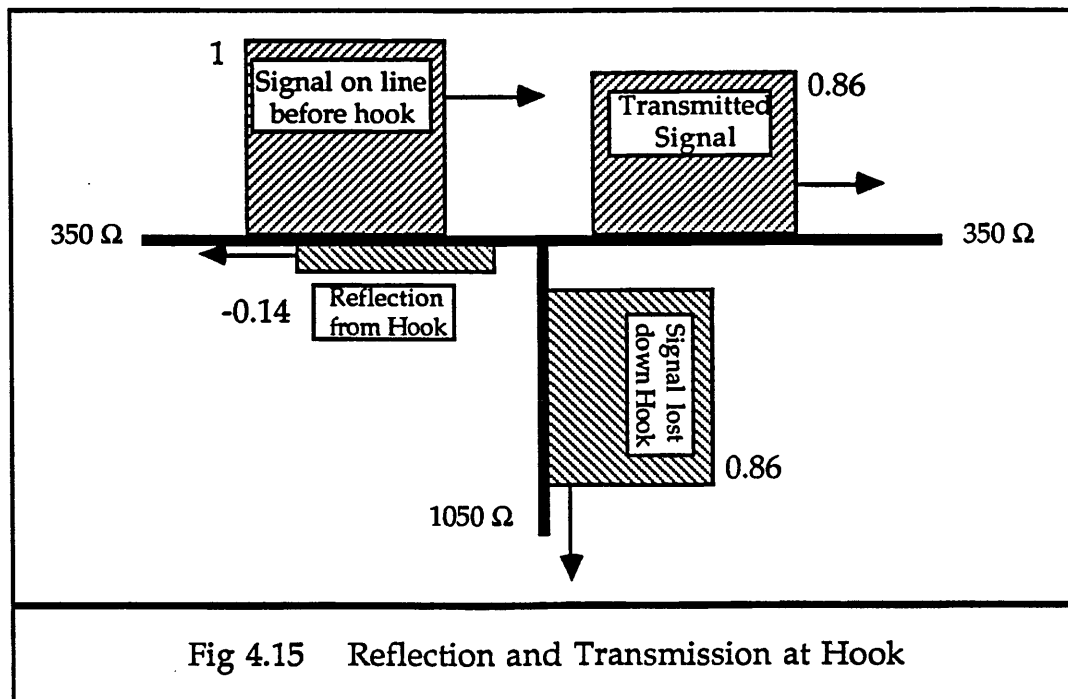Fig 4.15   Reflection and Transmission at Hook

4.3   Generation of the Signal

4.3.1   Drift Chamber Pulse Properties

The two main properties of drift chamber pulses are very fast rise times, of the order of 1 ns, and very long tails. The steep rise time is due to the acceleration away from the sense wire of the last generation of ions to be created in the avalanche, which is about half of the total number produced. The long tail is produced by the ions travelling from the sense wire to the field wire. These two properties are the same as those which distinguish surges of current on telegraph cables induced by nearby lightning. Drift chamber pulses may be considered to be like very small lightning surges on the sense wires.

4.3.2   Pulses Used in the Simulation

This type of pulse shape was produced in the long test rig from the attenuated square wave pulse with its upper frequencies removed by the hook and resistors. The test pulse had a rise time of a few nanoseconds once it was on the sense wire, and a very long, flat tail. Since the timing is always taken from the leading edge of the pulse, only a short section of the tail need be created for the simulation.

The pulse used in the simulation program was generated using the following relations :

$$\text{pulse height} \quad = 0.7439 \times t^3 \times \exp(-t) \qquad 0 \leq t \leq 3 \text{ units}$$
$$= -0.013889 \times t + 1.041667 \qquad t > 3 \text{ units}$$

It can be seen in figure 4.16.

This signal was then scaled by a given factor vertically, to give a range of pulse heights in milliVolts, and by another factor horizontally for $0 \leq t \leq 3$, to give a rise time in nanoseconds. These values correspond to the height and rise time of the pulse once it is on the sense wire.

In the simulation program, the signal is split into small step functions within this envelope, as shown in figure 4.17.
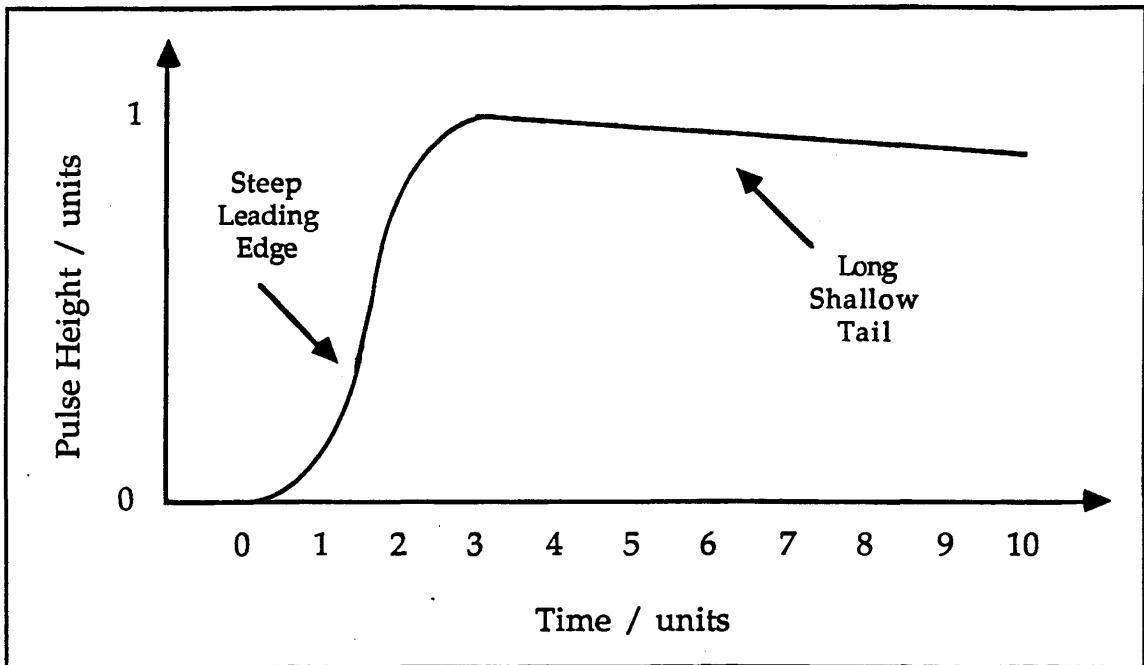
Fig 4.16   Pulse Generated for the Simulation Program, before Scaling
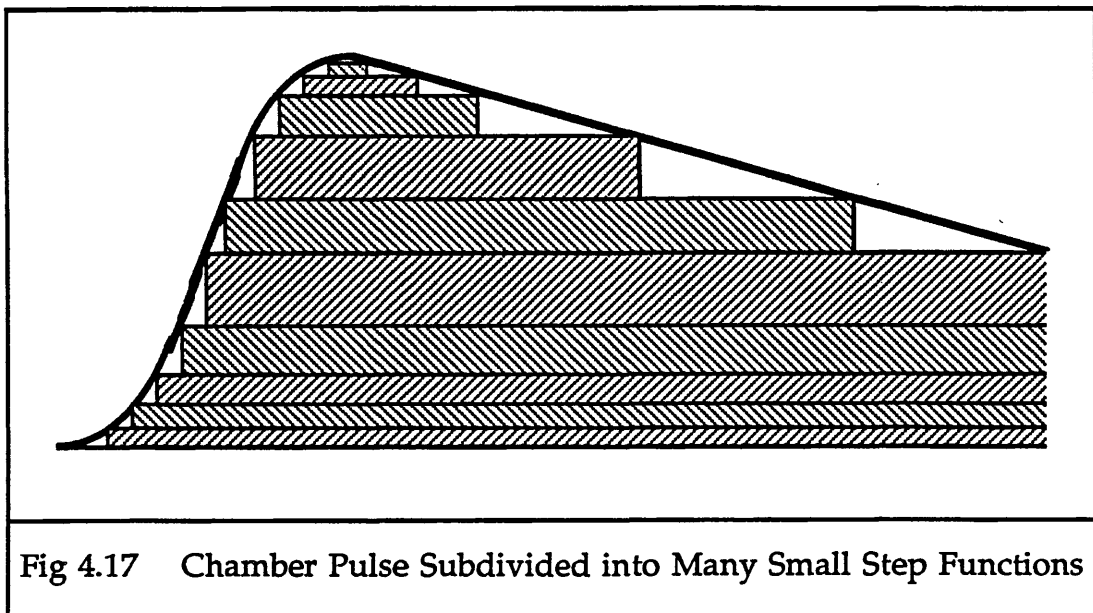
Fig 4.17   Chamber Pulse Subdivided into Many Small Step Functions

The reason for using these step functions is that it is very difficult to calculate the reflection and transmission of a complicated wave form, such as that shown in figure 4.16, but these calculations can be done for step functions. Since the transmission line system is linear, it is possible to calculate what happens to each of the step functions individually, and then to sum them up afterwards. In the simulation program, it was found that 60 steps from base to peak of the signal was sufficient to produce results where the granularity of the subdivision was not significant.

4.3.3 Frequencies Found in the Pulse

Without doing a Fourier transform of the pulse to find the different contributions from different frequencies, it is still possible to make an estimate of the maximum frequencies likely to be found in the pulse. These are the most interesting components, since the signals are capacitively coupled to the preamplifiers, and the timing measurement is made on the leading edge of the pulse. Even though the amplifiers have a 3 dB roll-off level of 120 MHz, frequencies above this level are still interesting, since they will be attenuated on the sense wire more than lower frequencies, and are also very important in the reflections. These effects lead to an increase in the signal rise time before it reaches the amplifiers.

—For a very fast typical chamber pulse, rise time ~ 1 ns.

—This can be considered as half the period of the highest frequency component of the signal, giving T ~ 2 ns.

—This gives maximum frequencies $\approx 1/T$ ~ 500 MHz.

4.3.4 Range of Pulse Heights

The signals used in the runs with the long test rig were generated from a pulse generator, which produced square pulses of amplitude 1.5 V. These signals were passed through a Hewlett Packard attenuator, which added no time delay to the signal when it attenuated it. The attenuator was used from 0 dB to 45 dB, where deciBels are defined as :

$$dB = -20 \log_{10} \left(\frac{V_{out}}{V_{in}} \right).$$

These signals were then attenuated by the hook and resistors by a factor of 0.29, (shown in Section 4.2.1), to produce a range of pulse heights on the sense wire of 435 mV – 2.4 mV. This spread of pulse heights covers a range of 178. Signals smaller than 2.4 mV did not pass an inbuilt threshold on the discriminators, and signals larger than 61 mV on the sense wire (17 dB on the attenuator) were just small enough not to saturate the amplifiers. Between this pulse size and the smallest ones used, there is a factor of 25 across the range.

This range of pulse heights can be compared with the range expected in the ITC. As calculated in Section 3.2.3 of Chapter 3, the range of pulse heights expected is ~ 100. This means that the range of pulse heights used in the tests covers this expected range more than adequately. It also means that some chamber signals will be large enough to saturate the amplifiers, so any effects from this must be investigated.

4.4 Reflection and Transmission

When a signal travelling along a transmission line arrives at a section with different characteristic impedance to that of its current section, there must be no discontinuity of current or voltage across the boundary. Consequently, a reflection is produced to balance the transmitted part of the signal. This section presents the reflection coefficients at a mismatched termination, as found at the end of the ITC sense wires. It then considers the effects that various combinations of termination resistance and capacitance have on a square pulse, and examines the multiple reflections found in the ITC and the long test rig. Finally, it shows what the signals look like in the long test rig and in the ITC after attenuation and reflection.

4.4.1 Reflection and Transmission Coefficients

The calculation of the reflection and transmission coefficients for a mismatched transmission line is shown in Appendix E. The resulting relations are :

$$T = \frac{2\,R}{R + Z_0}\left(1 - \exp\left(\frac{-\left(1 + R/Z_0\right)t}{R\,C}\right)\right)$$

$$\rho = \frac{R - Z_0}{R + Z_0} - \frac{2\,R}{R + Z_0}\exp\left(\frac{-\left(1 + R/Z_0\right)t}{R\,C}\right)$$

T = transmission coefficient

ρ = reflection coefficient

Z_0 = characteristic impedance of transmission line [Ω]

R = resistive component of termination [Ω]

C = capacitive component of termination [F]

t = time [s]

4.4.2 The Effects of Various Terminations on a Square Pulse

Figures 4.19 and 4.20 show what happens to a square pulse which travels along a transmission line of characteristic impedance Z_0, and then meets a termination of impedance Z, which is both resistive and reactive. The square input signal is shown in figure 4.18. The frequency used is ω.

Fig 4.18   Square Pulse used in
           Figures 4.19 and 4.20
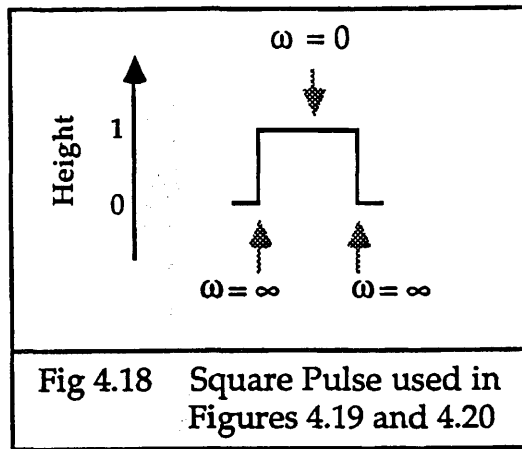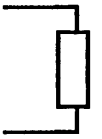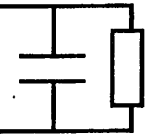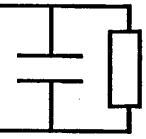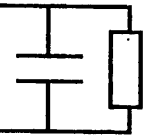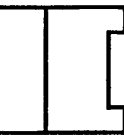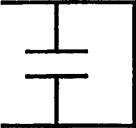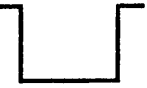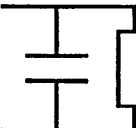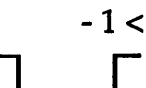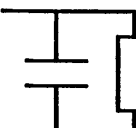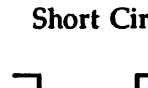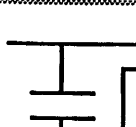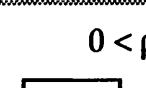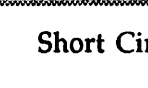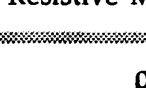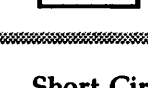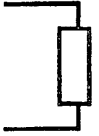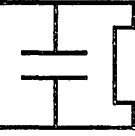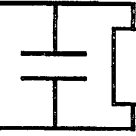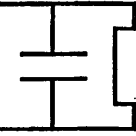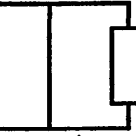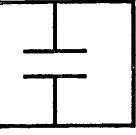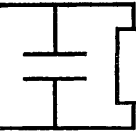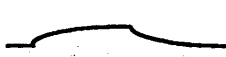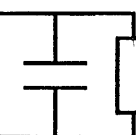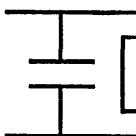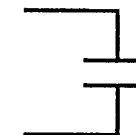
Figure 4.19 on page 207 shows the reflections from the square pulse for various terminations. The reflection coefficient is ρ.

Figure 4.20 on page 208 shows the transmitted pulses from the square pulse for various terminations. The transmission coefficient is T.

Capacitance at End / End Resistance	C = 0	C small	C medium	C large	C → ∞
R = 0	$\rho = -1$ Short Circuit	$\rho = -1$ Short Circuit	$\rho = -1$ Short Circuit	$\rho = -1$ Short Circuit	$\rho = -1$ Short Circuit
$0 < R < Z_0$	$-1 < \rho < 0$ Resistive Mismatch				Short Circuit $\rho = -1$
$R = Z_0$	$\rho = 0$ Matched				Short Circuit $\rho = -1$
$Z_0 < R < \infty$	$0 < \rho < +1$ Resistive Mismatch				Short Circuit $\rho = -1$
$R \rightarrow \infty$	$\rho = +1$ Open Circuit	Reactive Mismatch	Reactive Mismatch	Reactive Mismatch	Short Circuit $\rho = -1$

Capacitance at End / End Resistance	C = 0	C small	C medium	C large	C → ∞
R = 0	T = 0 — Short Circuit	T = 0 — Short Circuit	T = 0 — Short Circuit	T = 0 — Short Circuit	T = 0 — Short Circuit
$0 < R < Z_0$	0<T<1 — Resistive Mismatch				T = 0 — Short Circuit
$R = Z_0$	T = 1 — Matched				T = 0 — Short Circuit
$Z_0 < R < \infty$	1<T<2 — Resistive Mismatch				T = 0 — Short Circuit
R → ∞	T = 2 — Open Circuit	Reactive Mismatch	Reactive Mismatch	Reactive Mismatch	T = 0 — Short Circuit

4.4.3 Reflection and Transmission Coefficients in the ITC

By using the simulation program and tuning the variables to reproduce the data from the long test rig experiments, the values of the end resistance and capacitance are found to be :

$$R_{end} = 380 \,\Omega \qquad C = 15 \, pF$$

These will be compared with the calculated values in Section 4.5.1.4 of this chapter. They can be used to calculate the reflection and transmission coefficients found in the ITC, to give :

$$\rho = 0.04 - 1.04 \exp(-0.37\, t)$$

$$T = 1.04\,(1 - \exp(-0.37\, t))$$

where t is time, measured in nanoseconds.

These values of R_{end} and C give a time constant of 5.7 ns.

The reflection and transmission of a square pulse in the ITC are shown in figure 4.21.

Fig 4.21   Reflected and Transmitted Signals from a Square Pulse in the ITC
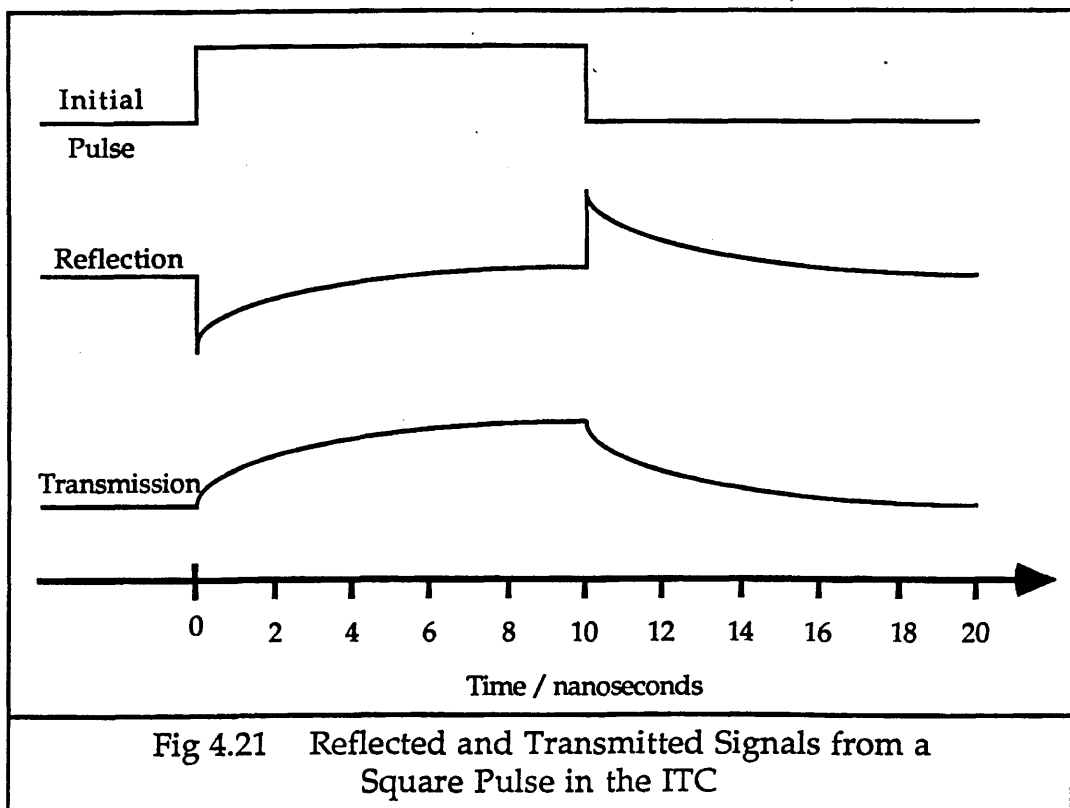
4.4.4   Multiple Reflections

a)   In the ITC

In the ITC, there is only one reflection which arrives in time to affect the leading edge of the signal whose time of arrival is to be measured. All higher order reflections arrive too late, and are too small to have any significant effect on the signal to be read out. The "direct signal" travels from where it was generated directly to the end at which the timing is being considered, the "timing end". The "primary reflection" travels in the opposite direction, reaches the end of the transmission line, the "far end", is reflected back and travels to the timing end where it combines with the direct signal to give the total signal to be transmitted for readout. This is shown in figure 4.22.

Fig 4.22   Direct Signal and Primary Reflection in the ITC
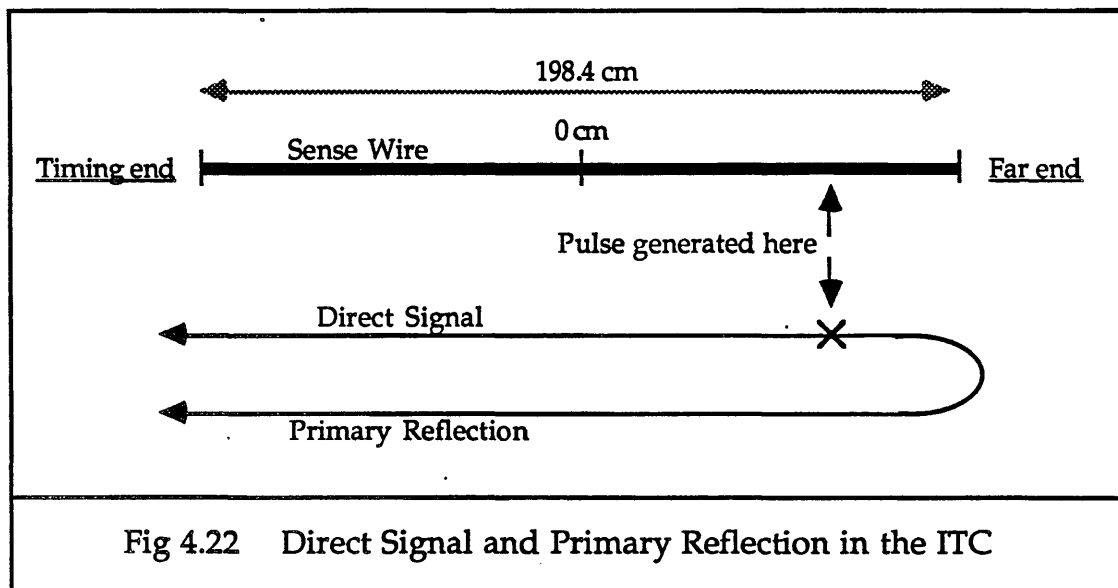
The timing is done at both ends of the chamber and the system is symmetrical. Therefore, when the far end is considered as the timing end, then the signal roles are reversed, with the primary reflection coming from what was formerly the direct signal. From now on, in this section, the timing at only one end will be considered, for simplicity.

For the ITC, the reflection coefficient at the end of the sense wire for the maximum signal amplitude is $\rho \sim -0.41$. The case when the reflection has the worst effect on the timing is when it is largest and there is minimum delay between the arrival times of the direct signal and the reflection. This is when the signal is generated at the far end of the chamber, and there is no delay between the direct signal and the primary reflection. The direct signal is attenuated by a factor of ~ 0.677 when it travels along the whole length of the wire, (using the relation derived in

Appendix C for voltage attenuation, and the series resistance of 139 Ω/m calculated in Appendix D). The reflection is also attenuated by this value. The resultant signals arriving at the timing end are shown in figure 4.23.

Fig 4.23   Worst Case Reflection in the ITC
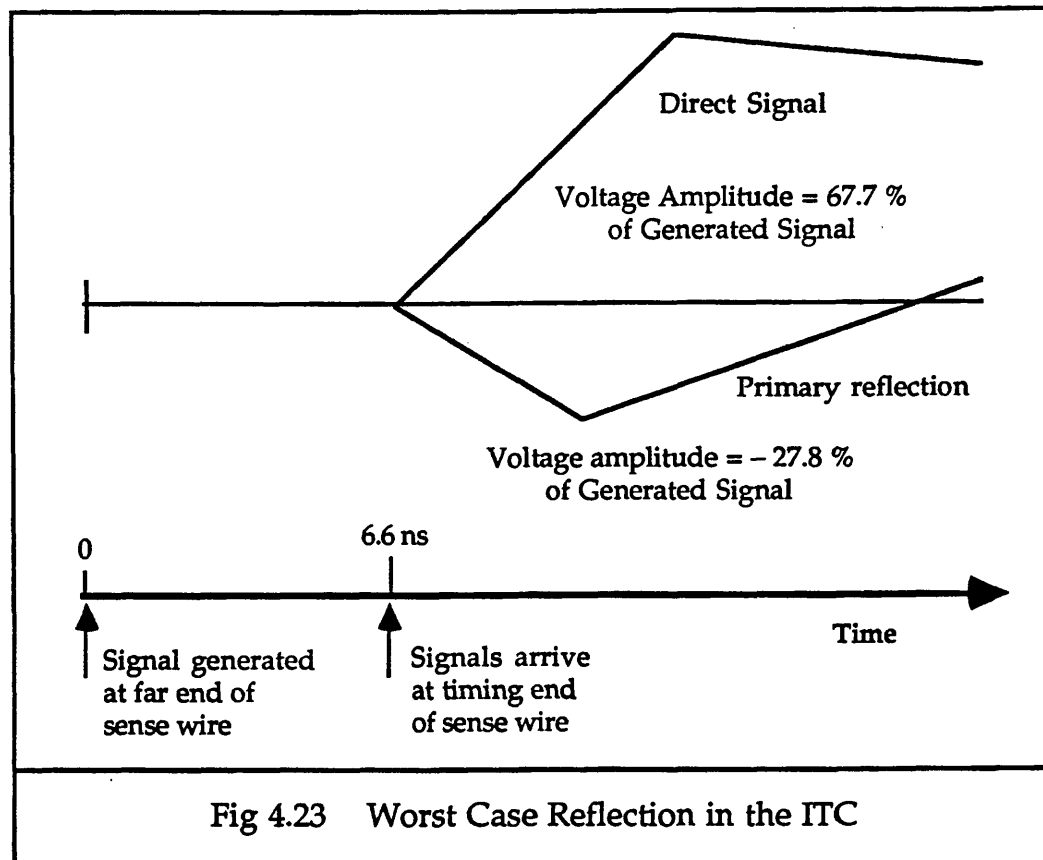
b) In the Long Test Rig

Multiple reflections in the long test rig are much more complicated than those in the ITC, due to the presence of the hook. This generates reflections which arrive early enough at the timing end to affect the signal being transmitted. The reflections which arrive soon enough to affect the leading edge of the direct signal are shown in figure 4.24. All other reflections not shown arrive too late to have any effect on the timing.

In the simulation program, these multiple reflections are included up to third order. Beyond this level, although the signals arrive in time to affect the direct signal leading edge, they have been attenuated so much that they are insignificantly small.

The primary reflection is not quite the same as the primary reflection in the ITC, since it has to travel past the hook, and is attenuated there.

Fig 4.24   Reflections Which Arrive in Time to Affect the
            Leading Edge of the Direct Signal in the Long Test Rig
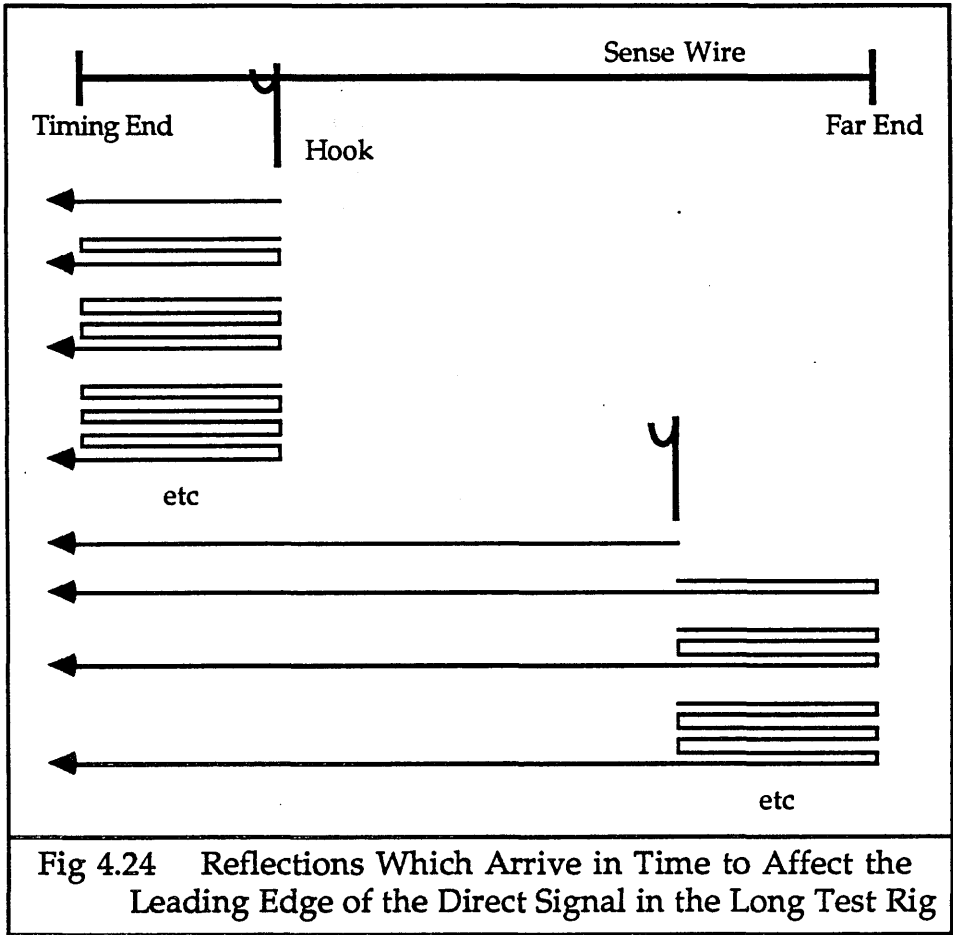
When the signal is generated at the far end of the test rig line, with the hook at $z = 90$ cm, then the primary and tertiary reflections have the worst effect. The reflection coefficient from the end of the chamber is ~ -0.41. The reflection coefficient at the hook is -0.14 and the transmission coefficient at the hook is 0.86. All these signals at the timing end in this case can be seen in figure 4.25.

Fig 4.25   Most Significant Primary and Tertiary Reflections
            in the Long Test Rig
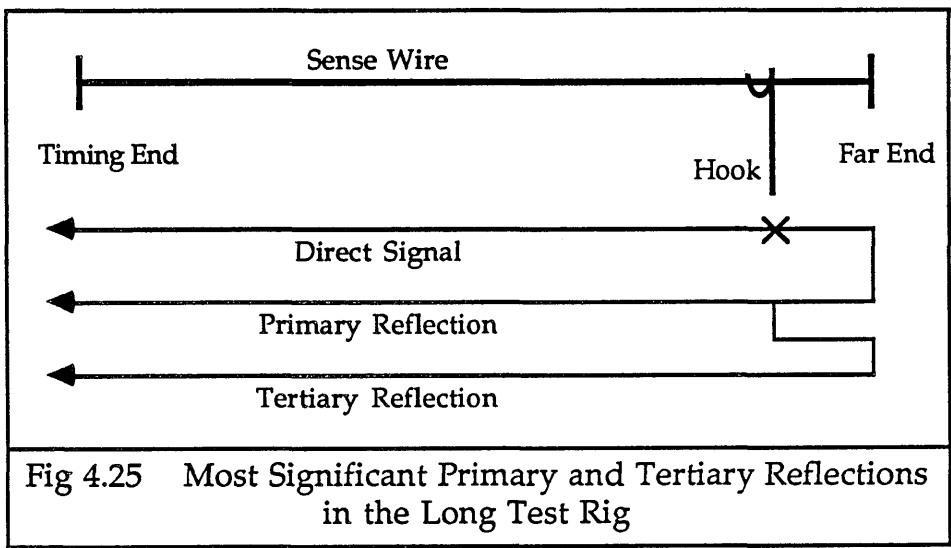
In the case shown in figure 4.25, for the worst primary and tertiary reflections, the direct signal is 68.9 % of the height of the initially generated signal. The primary reflection is − 23.6 % of the initial signal, and is delayed by 0.5 ns with respect to the arrival time of the direct signal. The tertiary reflection is + 1.3 % of the initial signal, and is delayed by 1 ns.

When the signal is generated at the timing end, with z = − 90 cm, then the only significant reflection is the secondary one. This can be seen with the direct signal in figure 4.26.

Fig 4.26   Most Significant Secondary Reflection
in the Long Test Rig
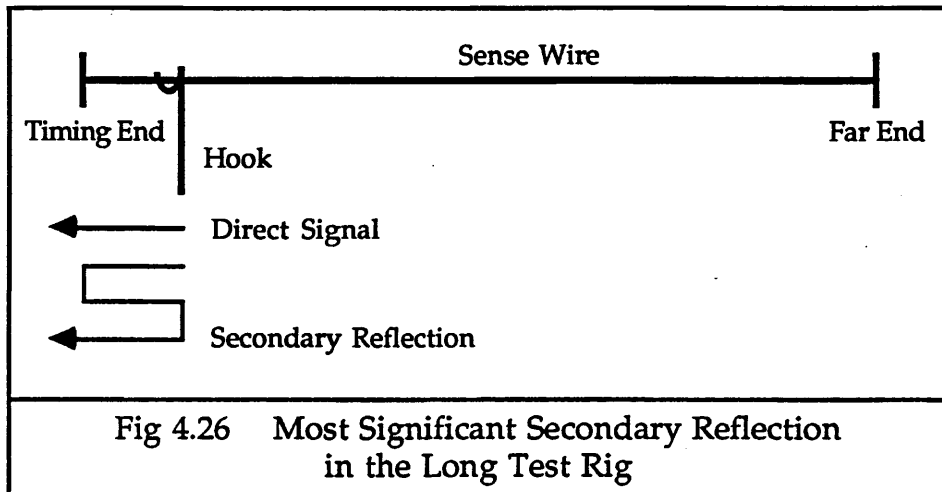
For the worst case secondary reflection in the long test rig shown in figure 4.26, the direct signal is 98.5 % of the height of the initially generated signal. The secondary reflection is − 5.5 % of the initial signal size, and is delayed by 0.5 ns with respect to the arrival time of the direct signal.

The stages of the calculation used to arrive at these signals are shown in figure 4.27.

213
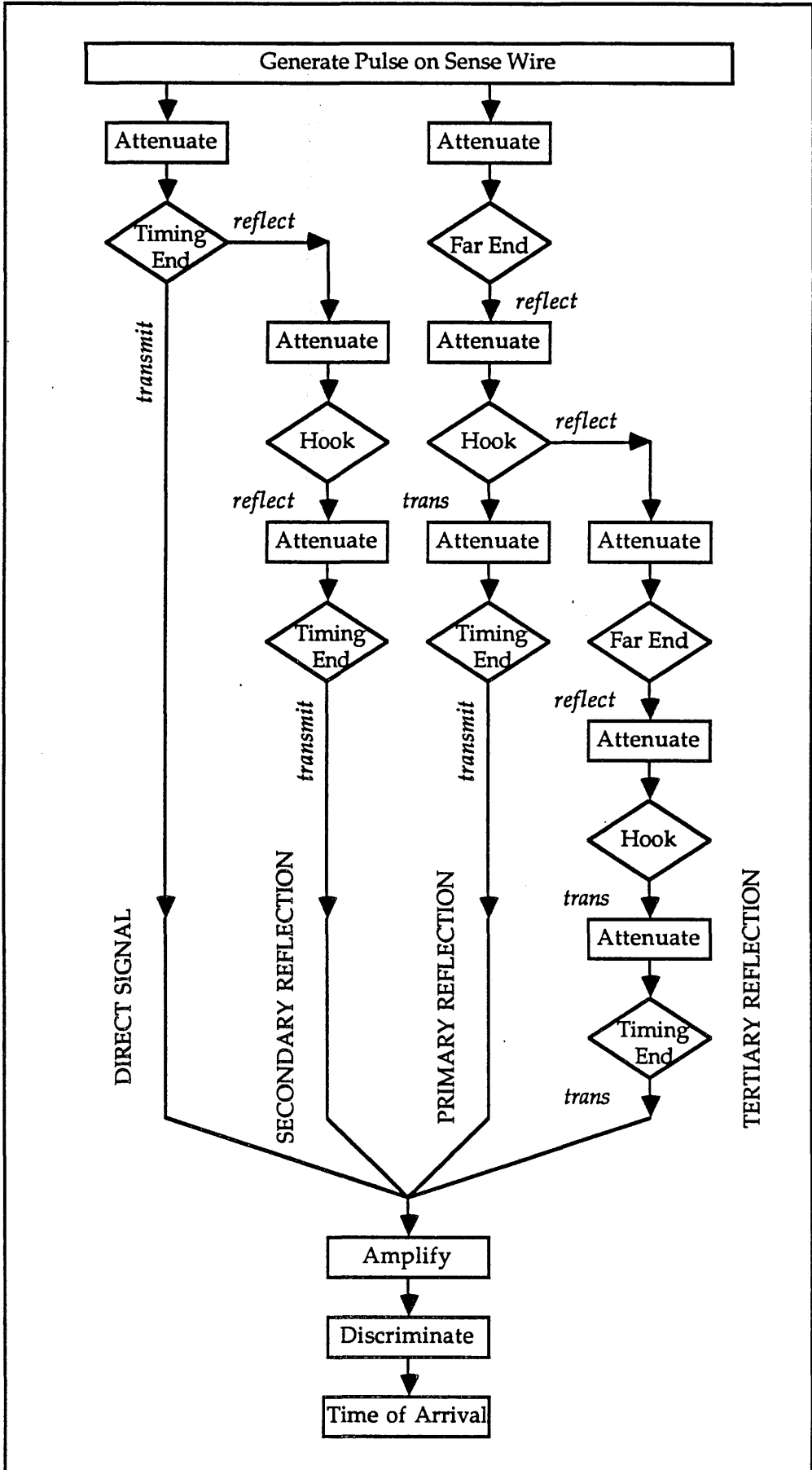
Fig 4.27 Production of Direct Signal, Primary, Secondary and Tertiary Reflections in the Long Test Rig

4.4.5 Reflected Signals in the ITC and the Long Test Rig

The simulation program can be used to calculate the signals in the ITC and in the long test rig. These are shown in the following seven figures. Figure 4.28 shows what the direct signals look like after travelling various distances down the sense wire. That is, the 11 signals shown were generated equally spaced along the sense wire, and all travelled to the timing end of the sense wire. The largest signal was generated at the timing end and has travelled no distance at all on the transmission line. The smallest signal was generated at the far end and has travelled the entire length of the sense wire. The initial signal amplitude on the sense wire was 56 mV.
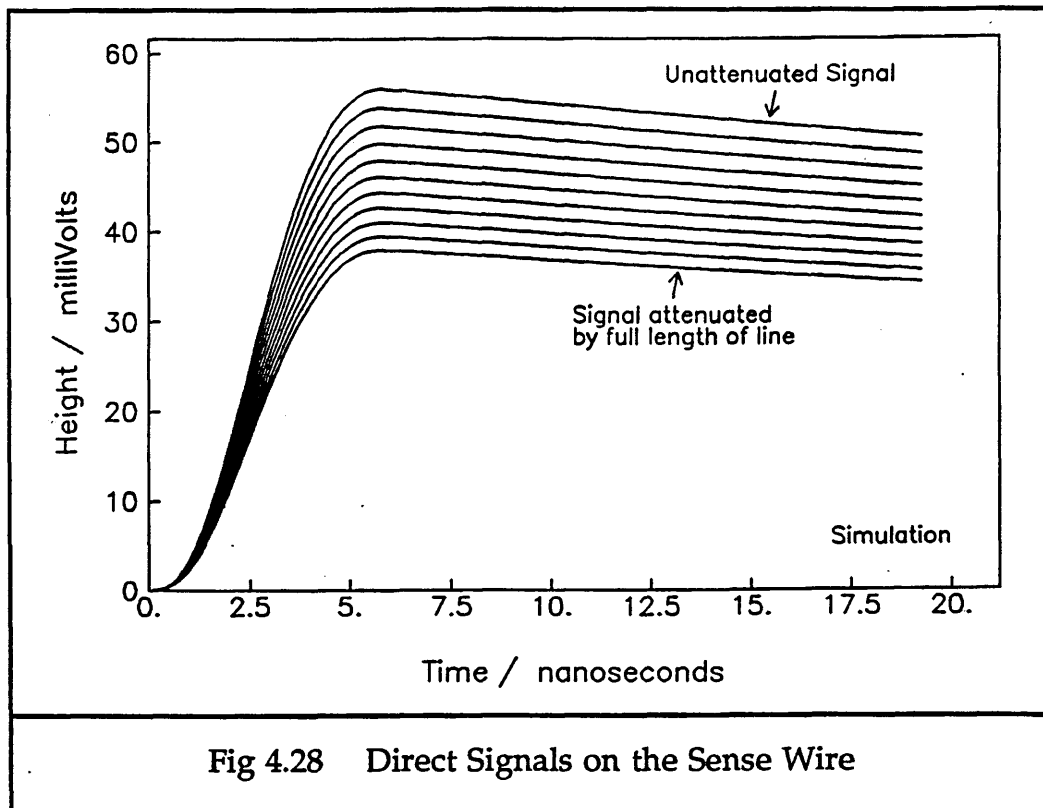
Fig 4.28   Direct Signals on the Sense Wire

The active length of the sense wire transmission line is not 2 m, the distance apart of the end plates, but is slightly less, because the signal reflection comes from the tip of the feedthrough inside the chamber. This will be shown in Section 4.5.4 of this chapter.

Figure 4.29 shows the primary reflections in the ITC. These have been inverted at the far end of the chamber. The largest negative signal was generated at the far end of the sense wire, and the smallest primary reflection was generated at the timing end, and has travelled twice the length of the transmission line. The initial signal size was 56 mV.

215
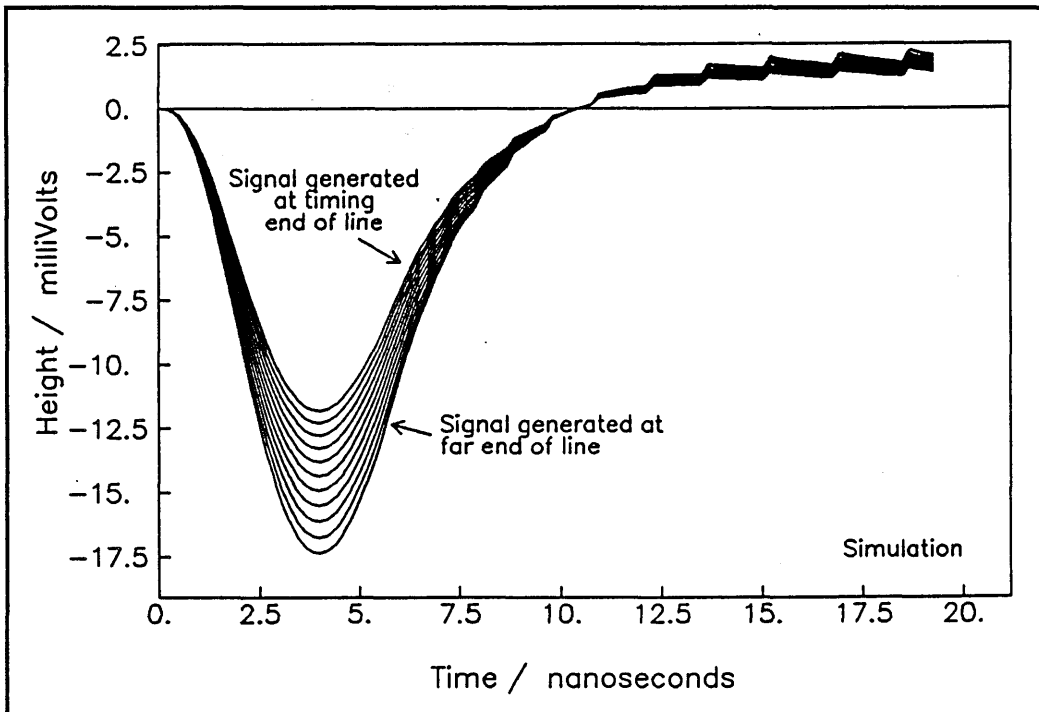
Fig 4.29   Primary Reflections in the ITC

The primary reflections in the ITC can be compared with the primary reflections in the long test rig, which are shown in figure 4.30. These are smaller than in the ITC, because of the extra attenuation across the hook.
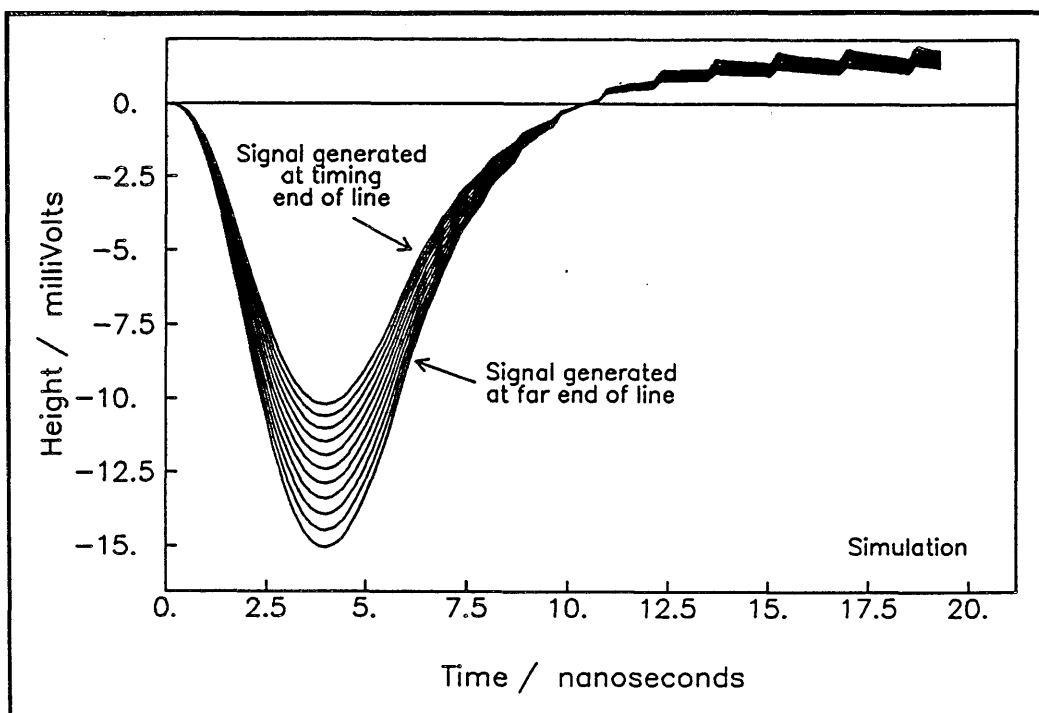
Fig 4.30   Primary Reflections in the Long Test Rig

The secondary and higher order reflections in the ITC arrive too late to be significant in the timing, so are not shown. However, those from the hook in the long test rig are significant, and are shown in figures 4.31 and 4.32. Figure 4.31 shows the secondary reflections in the long test rig. There have been two reflections, so the first part of the signal is no longer inverted. The largest secondary signal was generated from a signal which started at the timing end of the long test rig. The smallest comes from a signal generated at the far end. The initial signal size was 56 mV.

Fig 4.31   Secondary Reflections in the Long Test Rig
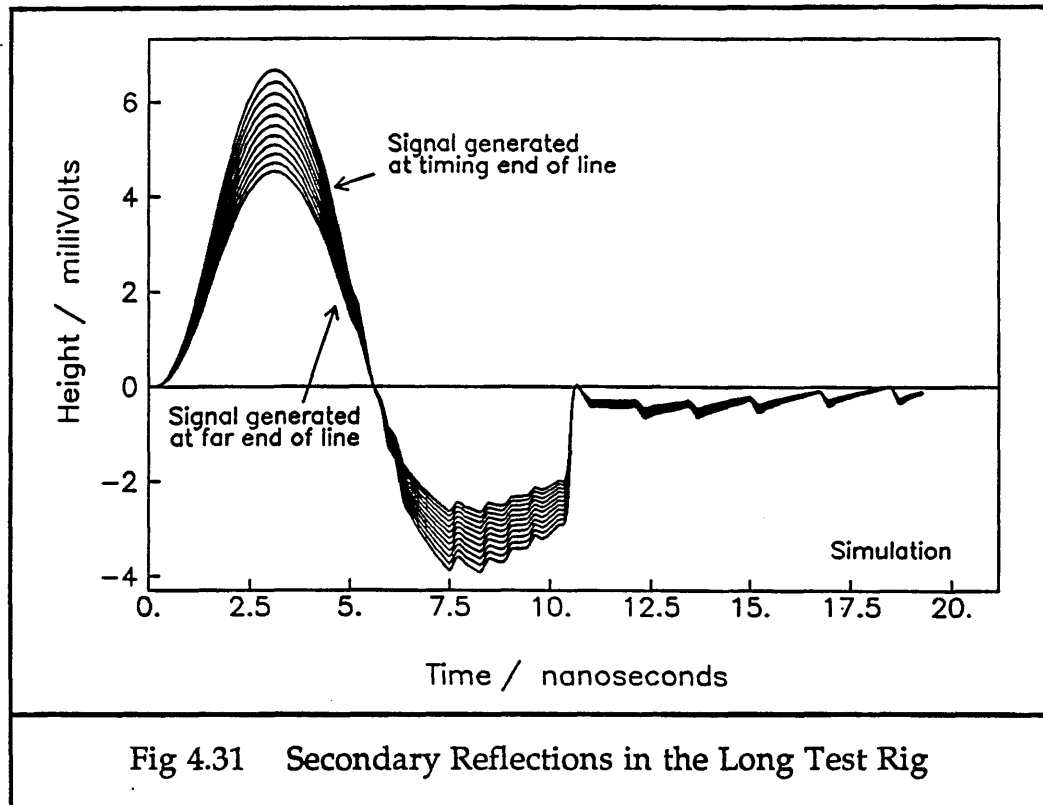
Figure 4.32 shows the tertiary reflections in the long test rig. These are inverted after three reflections, two from the end of the transmission line and one from the hook. The largest signal started at the far end of the rig, and the smallest started at the timing end. The granularity seen in the tails of these signals, and in the other reflections, is caused by the division of the initial signal into small step functions. These spikes are a product of the step functions, and do not represent the real signals in the test rig. The initial signal size was 56 mV.
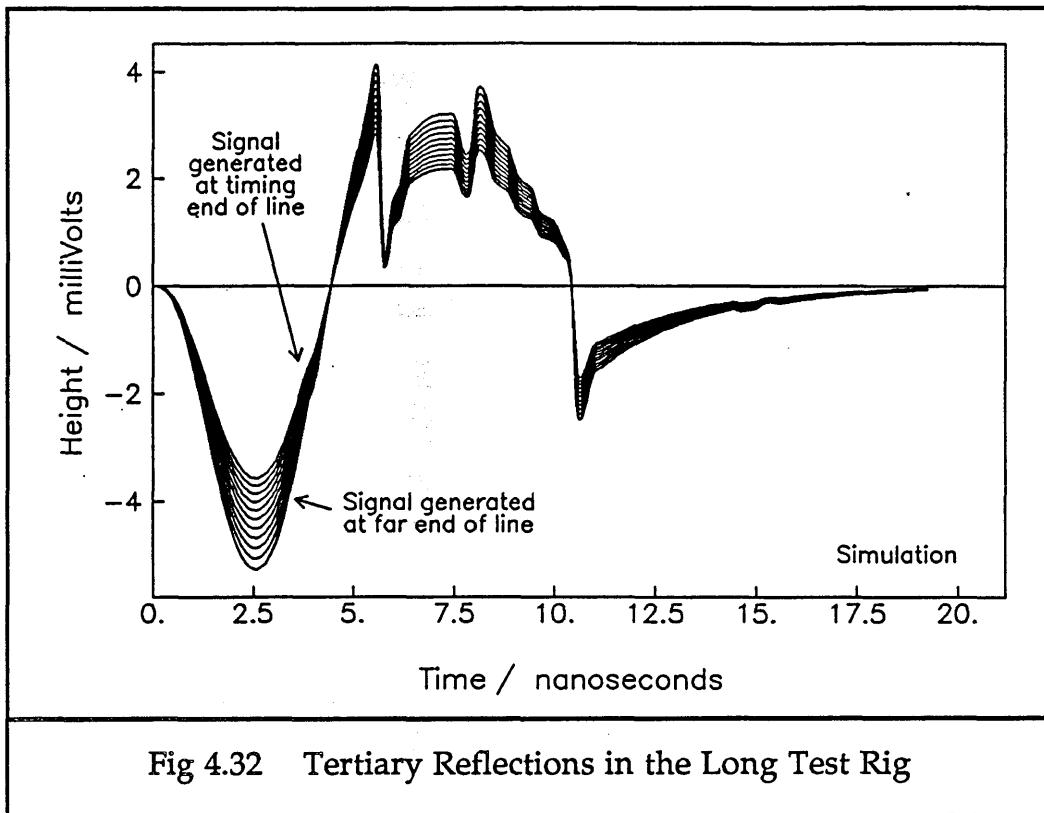
Fig 4.32   Tertiary Reflections in the Long Test Rig

Figure 4.33 shows what the sums of the direct signals and primary reflections look like in the ITC, just before they are transmitted through the end termination. The largest signal has travelled no distance along the sense wire, and has the smallest, latest reflection added to it. The smallest signal has travelled the whole length of the chamber, and has the largest reflection added to it, with no delay between their arrival times at the timing end.
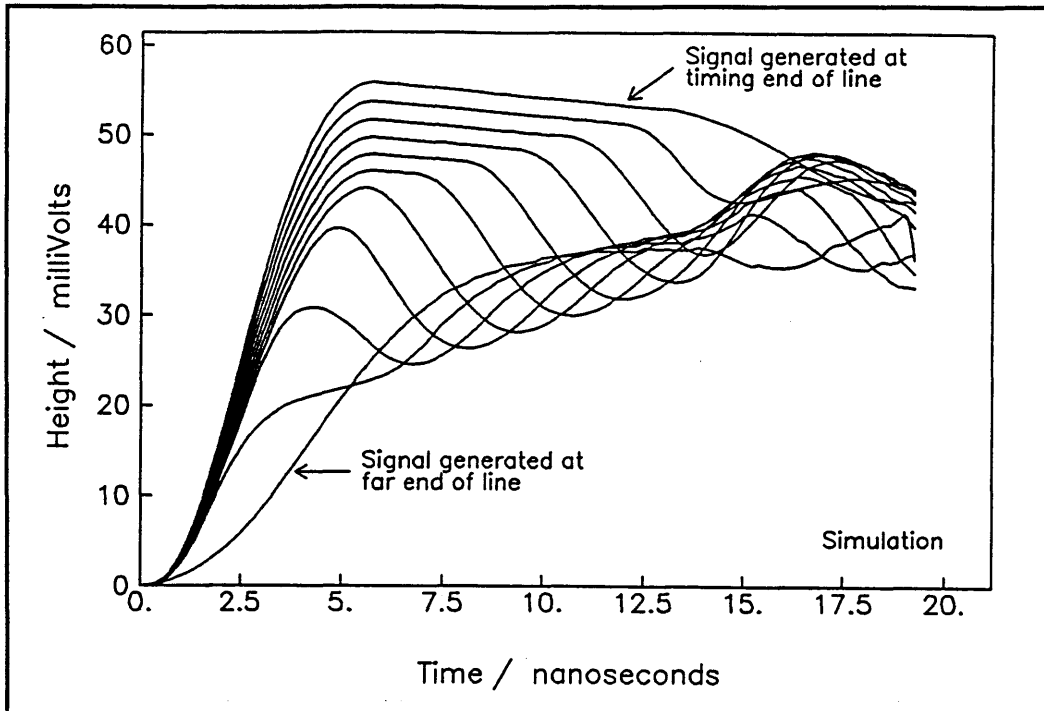
Fig 4.33   Signals Before Transmission in the ITC

Figure 4.34 shows the sum of the direct signals with the primary, secondary and tertiary reflections in the long test rig, just before transmission through the end termination.
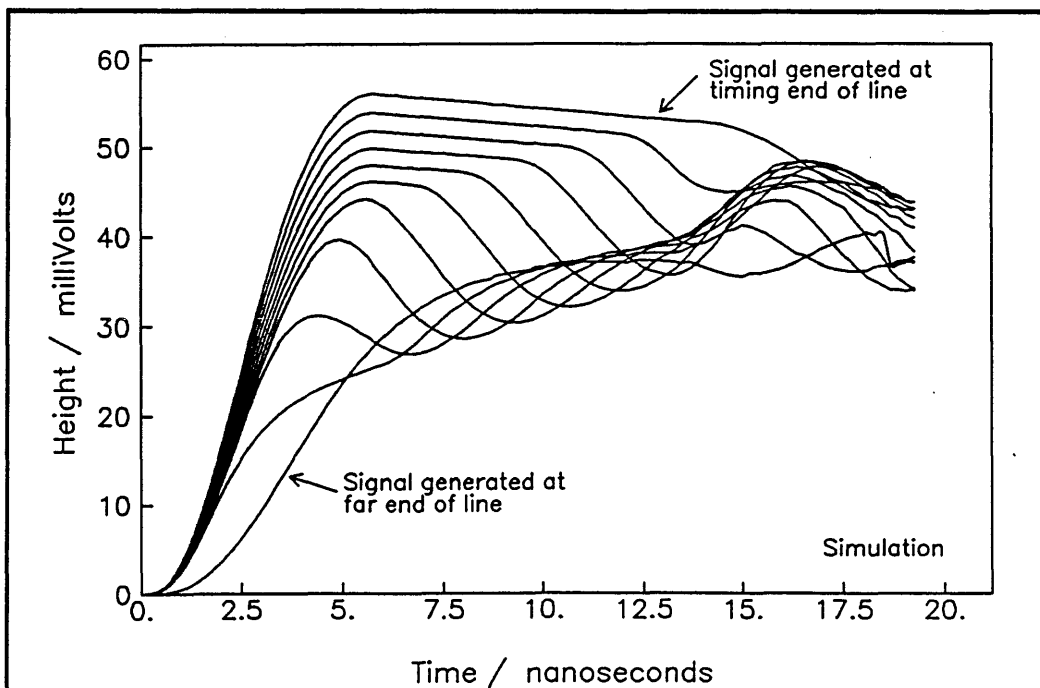
Fig 4.34   Signals Before Transmission in the Long Test Rig

4.5   Termination at the End of the Chamber

This section presents a calculation of the end impedance of the ITC for comparison with the values found with the simulation program. It shows how the termination was simulated, and also where the reflections occur in the chamber. The effect of power losses in the end plate is explained, and the amount of loss is predicted with the simulation program. The transmitted signals are then shown with all these effects included.

4.5.1   Calculation of the End Impedance of the ITC

The termination of the sense wire transmission line in the ITC is very complicated. Not only does it not match the characteristic impedance of the transmission line, but also the signal path through the end electronics ceases to behave as a transmission line and reverts to behaving as discrete electronic components. This is shown in Appendix D with the transmission line calculations. There are many separate contributions to the end impedance of the ITC and consequently it is not trivial to calculate it. This calculation will be done in several stages. It is important to know the end impedance, since the value and form of this governs the reflections produced in the chamber, and the reflections produce the nonlinearity in time difference which strongly affects the z position measurement.

4.5.1.1   Feedthrough and Pin in the End Plate

The stray capacitance and inductance are calculated here for the feedthrough and pin in the end plate, plus the wires on the end box connected to the pins with square tube connectors. The calculations have been made by using the approximation that the components, arranged in hexagons, behave like coaxial cables. One sample calculation is shown here, and then the capacitance and inductance at each part of the termination are shown in figure 4.36. Figure 4.35 shows a cross section through the pins and square tube connectors outside the chamber end plate.

This section of the termination is considered to be a short section of a transmission line.

Inner conductor radius	= a	= 1.270 mm
Radius to outer conductors	= b	= 3.897 mm
Length of transmission line	= l	= 14.5 mm
Mean relative dielectric constant	= ε	= 1.69
Capacitance per unit length	= C	

Fig 4.35   Pins and Square Connectors
Outside the End Plate
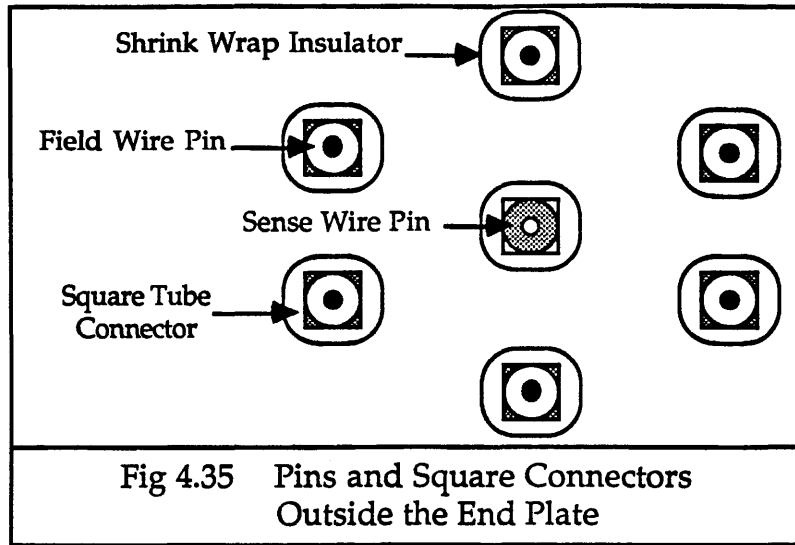
$$C = \frac{2 \pi \varepsilon \varepsilon_0}{\log_e(b/a)} = 84.00 \, \text{pF/m}$$

Total capacitance $= C1 = 1.22 \, \text{pF}$
Inductance per unit length $= L$

$$L = \frac{\mu \mu_0 \log_e(b/a)}{2 \pi} = 0.22 \, \mu\text{H/m}$$

Total inductance $= L1 = 3.19 \, \text{nH}$

The characteristic impedance is therefore :

$$Z \approx \sqrt{\frac{L}{C}} = 51 \, \Omega$$

For some of the calculations, there is not only air as the dielectric, but also glue, or plastic as in this example. The relative dielectric constant has been calculated as a weighted average of the dielectric constants of these materials, depending on their thicknesses.

Figure 4.36 shows the results of similar calculations to this for all the components on the end of the sense wire up to the end box in the ITC.

Total Capacitance	Capacitance / Unit Length	Length of Section	Dielectric	Mean Radius to Outer Conductor	Outer Conductors	Radius of Conductor	Inner Conductor	
18.89 pF	9.52 pF/m	1984 mm	Gas	5.167 mm	Field Wires	15 μm	Sense Wire	
0.14 pF	17.08 pF/m	8 mm	Glue, Gas and Feedthrough	5.167 mm	Field Wires	15 μm	Sense Wire	
0.59 pF	28.33 pF/m	20.8 mm	Gas and Feedthrough	1.588 mm	End Plate	15 μm	Sense Wire	
1.23 pF	293.61 pF/m	4.2 mm	Feedthrough	1.588 mm	End Plate	788 μm	Sense Wire Pin	
0.14 + 0.06 pF	175 + 75 pF/m	0.8 mm	Feedthrough and Gas	3.897 mm	Field Wire Pin	788 μm	Sense Wire Pin	
0.38 pF	90.35 pF/m	4.2 mm	Feedthrough and Gas	3.897 mm	Field Wire Square Tube	1.27 mm	Pin or Square Tube	
1.22 pF	84.00 pF/m	14.5 mm	Shrinkwrap and Gas	3.897 mm	Field Wire Square Tube	1.27 mm	Square Tube	
0.66 pF	21.90 pF/m	30 mm	Wire Insulation and Gas	10.0 mm	Earth Wires to End Box	0.2 mm	Wire to End Box	

Fig 4.36   Capacitance, Inductance and Characteristic Impedance at the Termination of the Sense Wire in the ITC

Inductance / Unit Length	Total Inductance	Characteristic Impedance	≈ Transmission Line Behaviour ?
1.17 μH/m	2.32 μH	350 Ω	yes
1.17 μH/m	9.36 nH	262 Ω	yes
0.93 μH/m	19.34 nH	182 Ω	no
0.14 μH/m	0.59 nH	22 Ω	no
0.32 μH/m	0.26 nH	36 Ω	yes
0.22 μH/m	0.92 nH	49 Ω	yes
0.22 μH/m	3.19 nH	51 Ω	yes
0.78 μH/m	23.47 nH	189 Ω	yes

Fig 4.36 (cont'd)

Figure 4.37 shows the characteristic impedance as a function of distance from the inside of the end plate for the ITC. It can be seen that as signals pass through the end plate, the characteristic impedance drops almost to nothing, before going up again in the HT end box to a level which more nearly matches the sense wire transmission line impedance.

Figure 4.38 shows the end impedance for the long test rig, for comparison with that in the ITC in figure 4.37. Two designs of end box leads are calculated for, because on the long test rig, the two end boxes were of different design at each end of the chamber. The old design end box had 2.5 cm leads bound together in signal-earth pairs. The later design end box had 5 cm leads which tapered in from the pins to the end box. These two designs had different capacitance and inductance in the leads. The final design of end box leads used in the ITC has 3 cm separated leads.
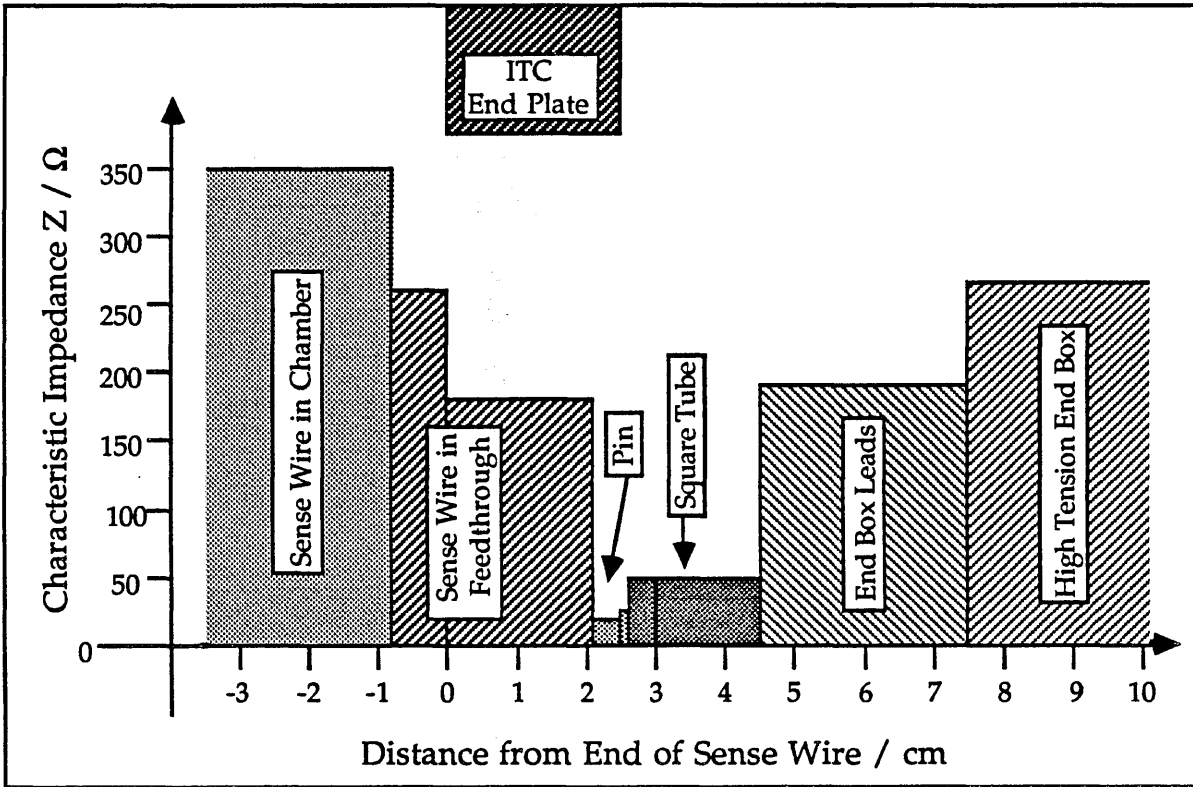
Fig 4.37   Impedance at the End of the Sense Wire
at High Frequencies in the ITC
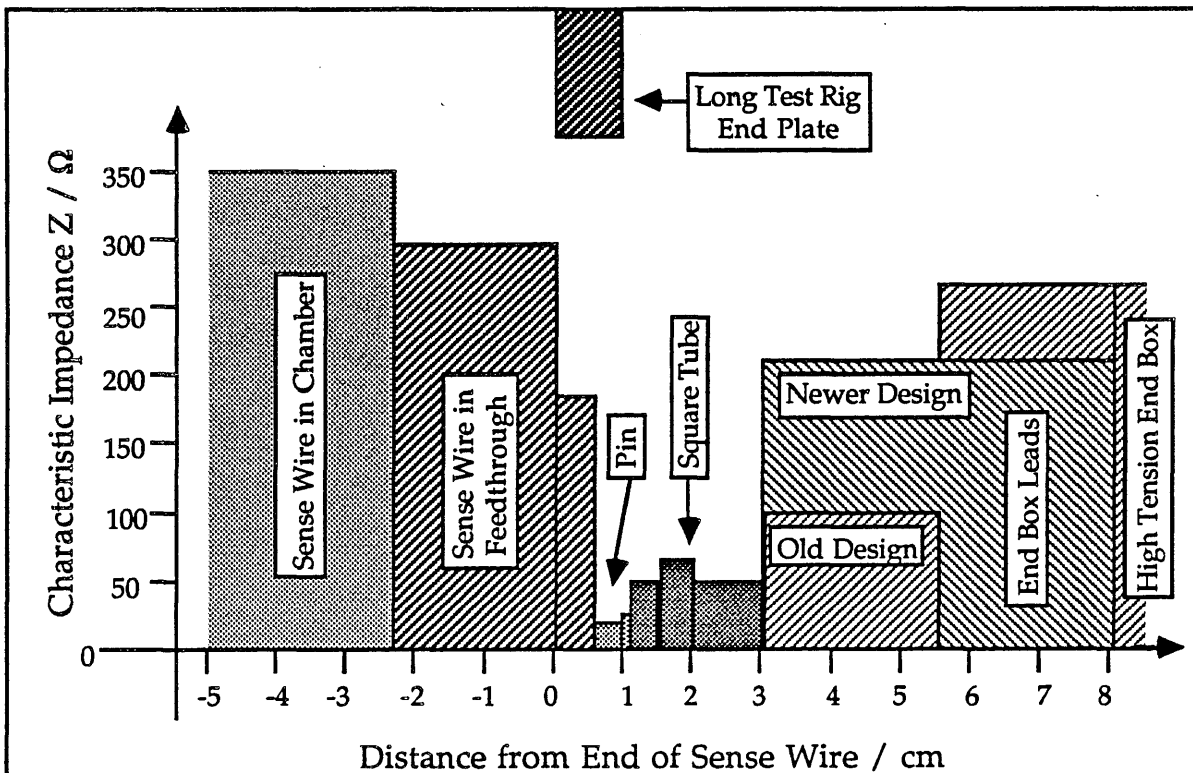
Fig 4.38   Impedance at the End of the Sense Wire at High Frequencies
in the Long Test Rig

224

The stray capacitance from this part of the termination in the ITC is:

$$C_{pin\ etc} = 0.14 + 0.59 + 1.23 + 0.14 + 0.06 + 0.38 + 1.22 + 0.33$$
$$= 4.1\ pF$$

In the long test rig, the stray capacitance from this part of the termination is $C = 4.2\ pF$.

There are probably about another couple of picoFarads stray capacitance in the long test rig not already included in the calculation, from the square tube and the pin to the outside of the end plate, and from the sense wire in the chamber to the inner face of the end plate. Therefore, the total stray capacitance from this section in the long test rig may be estimated at:

$$C_{total} \approx 6.2 \pm 1\ pF$$

4.5.1.2   The High Tension End Box

Each HT end box distributes the high voltage, about 2 - 2.5 kV, to a block of 16 sense wires, and earths some of the surrounding field wires. It capacitively couples the sense wire to the preamplifier so that only the interesting higher frequencies are let through.

This passive electronic component is made of a 50 μm thick Kapton sheet, coated on both sides with a 25 μm thick layer of adhesive and a 35 μm thick layer of copper. Areas of copper are etched away to leave copper strips on both sides of the sheet. The whole sheet is coated with a thin conformal layer of polyurethane. The sheet is then bent into a rectangular box shape. On the inside (the HT side), 3 mm wide copper strips, separated by 5 mm wide gaps, are all connected to a single HT lead via 10 MΩ resistors. The strips are 9.7 cm long, and are individually connected to sense wire pins via 5.5 cm long wire leads. On the outside of the Kapton sheet, 3 mm wide copper strips alternate with 1 mm wide strips, separated by 2 mm wide gaps. The 3 mm wide strips capacitively couple to the strips on the HT side and connect to the preamplifier signal pins. The capacitance due to the Kapton sheet is approximately 100 pF. The 1 mm strips are connected to field wire pins and to the preamplifier grounds. They shield the signals from one another and make the box look like a transmission line. A 100 kΩ resistor between each signal strip and the corresponding ground makes the impedance of this transmission line similar to that of the sense wires. The circuit diagram for one channel of the end box is shown in figure 4.39.
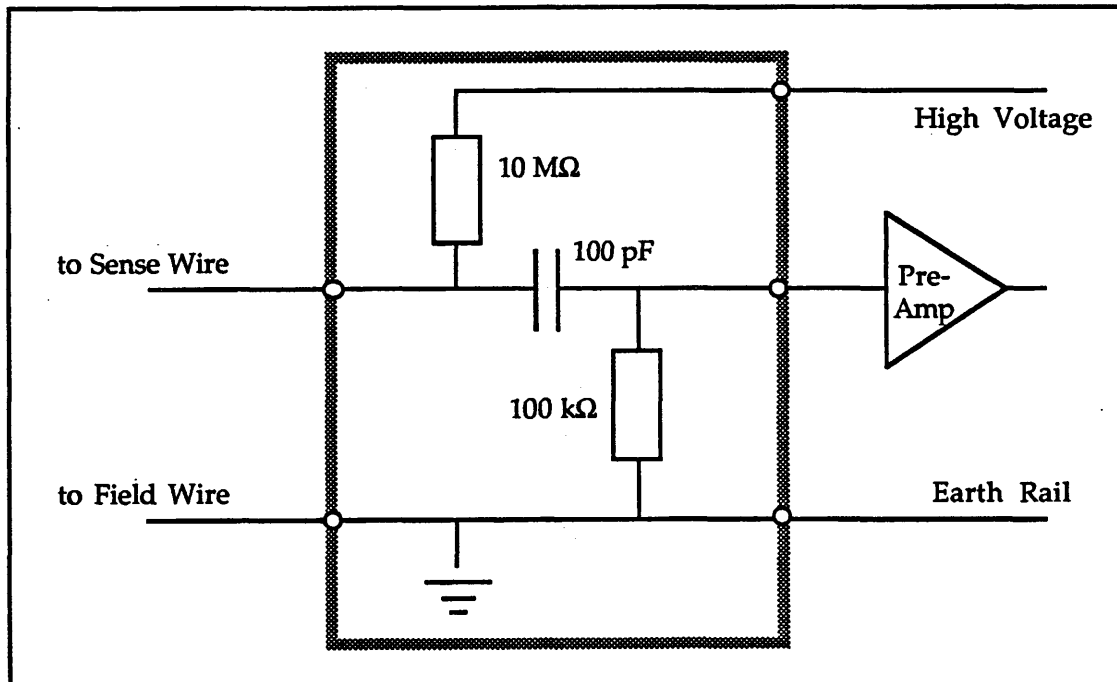
Fig 4.39   Circuit Diagram of a Channel of the High Tension End Box

Each resistor in the end box has a capacitance of ~ 0.5 pF associated with it at high frequencies, which is not shown in the circuit diagram. The 100 pF series capacitance is between the parallel copper strips on either side of the Kapton. These strips have associated with them a shunt capacitance and series inductance, between each signal copper strip and the two neighbouring earth copper strips on the same side of the Kapton. The series inductance is 1.64 μH/m and the shunt capacitance is 30.9 pF/m, over a length of 9.7 cm. Therefore, the end box acts as a transmission line with characteristic impedance of $\approx$ 263 Ω.

4.5.1.3   The Preamplifier

Each preamplifier is built on a double-sided printed circuit board, with surface mounted components. The preamplifier has 8 channels on each side, for reading out 16 sense wires. It also has the facility to enable a test pulse to be injected into all the channels.

A preamplifier is needed close to the chamber principally to drive the chamber signals down 23.5 m of 50 Ω coaxial cable. The signal on the sense wire is only a few milliVolts in amplitude and consists of only a very small amount of charge. The amplifier boosts the current, and hence the power, so that the signal is not attenuated across the boundary at the impedance drop. The circuit diagram for one channel of the preamplifier is shown in figure 4.40.

4.6 Volts

47R

10μF

1k2

BFT25

BFR 92

BFT 25

2k2

39R

INPUT 100R 22R 0.1μF

470pF

OUTPUT

2k2

10k 10nF 0.1μF 0.1μF

GROUND

BAV99

4k7

1k

Auto-
Calibration

51R

Next
Channel

Next
Channel
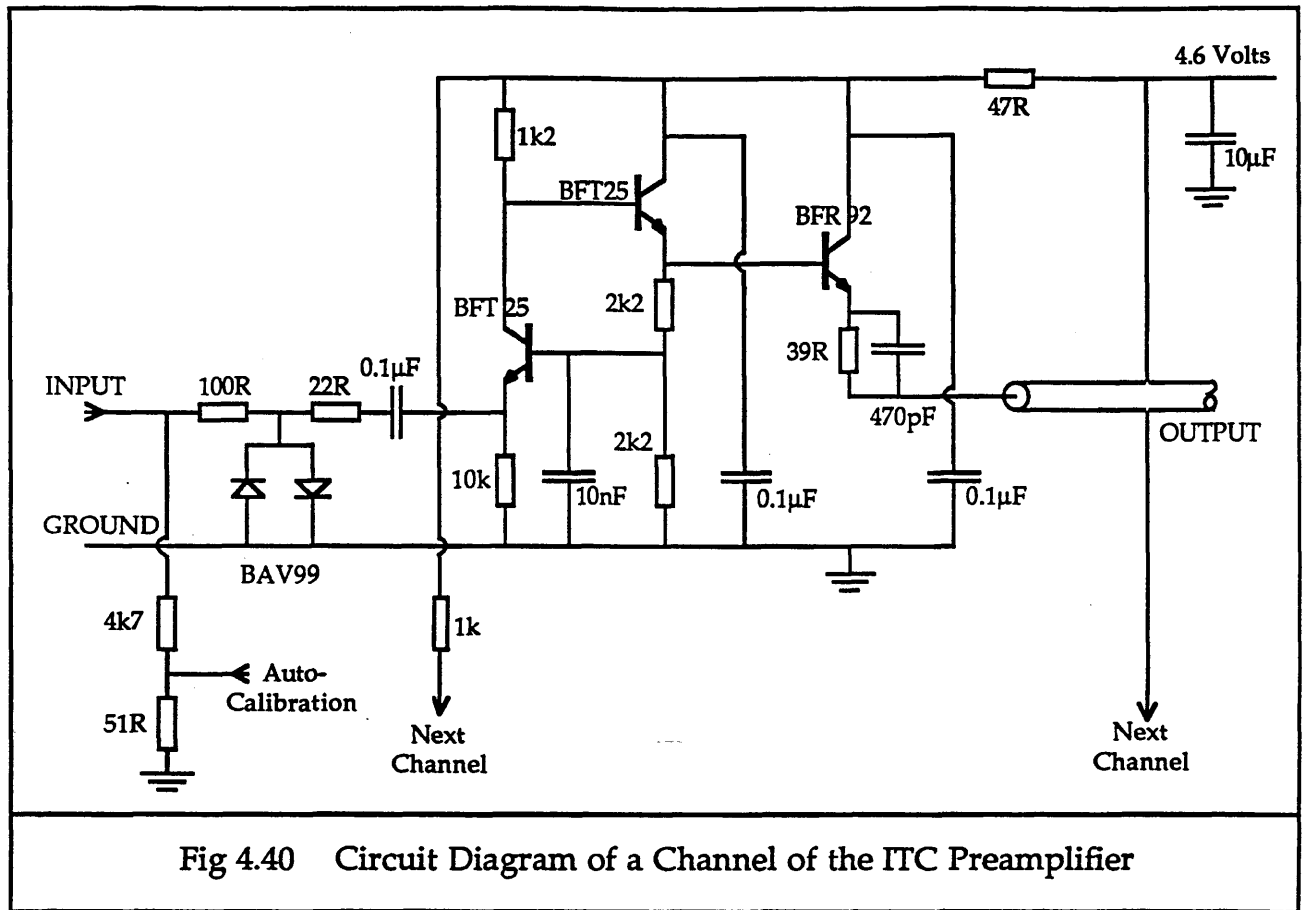
Fig 4.40 Circuit Diagram of a Channel of the ITC Preamplifier

The preamplifier is a charge sensitive device, which works in two stages. At the input stage of the preamplifier, there is a pair of diodes, which acts as a voltage limiter. It limits the voltage going past to ~ 0.6 - 0.7 Volts, in order to protect the subsequent transistors. The first stage transistor is a common base amplifier. This is a voltage amplifier with a gain ~ 2 at high frequencies. It has a high input impedance, of the order of a few hundred Ohms, which is needed to match the characteristic impedance of the sense wire transmission line. Its output impedance is a few MegaOhms.

The second stage of the preamplifier consists of two transistors used as emitter followers. The first of these feeds back into the first stage to keep it biased correctly. Their main purpose, though, is to amplify the power, by amplifying the current, in order to drive the 23.5 m cable. They have a very high input impedance and a very low output impedance, and so the signal does not lose any voltage amplitude as it is transmitted down onto the 50 Ω cable. If the preamplifier were not there, and the end box, with characteristic impedance 263 Ω were connected directly onto the 50 Ω cable, then the voltage transmission coefficient for the signal would be only 32 %. The published saturated gain of these two transistors is ~ 20 - 50 each. However, their actual gains are much smaller. This is because current saturation only occurs in the second BFT25 transistor (shown in figure 4.40) with a current

of 1 mA, and the BFR92 transistor (also in figure 4.40) needs 14 mA. The currents in the preamplifier are ~ 0.1 mA to start with, and less than 1 mA after the amplification. These low operating currents reduce the total current gain from ~ 1000 to ~ 100.

The amplification has been kept low in order to minimise the heat produced inside the gas volume of the ITC by the dissipated power. Each preamplifier channel dissipates about 10 mW, and there are 60 preamplifier cards at each end of the ITC, with 16 channels each, giving ~ 9.6 W released as heat at either end of the chamber. The temperature will be kept steady at ~ 20°± 2°C with cooling water in pipes running around this region.

Input Impedance of the Preamplifier

Figure 4.41 shows the components of the preamplifier which affect the input impedance. The extra capacitances shown are not real components, but arise from the resistors, diodes and connectors in the circuit when operated with high frequency signals.
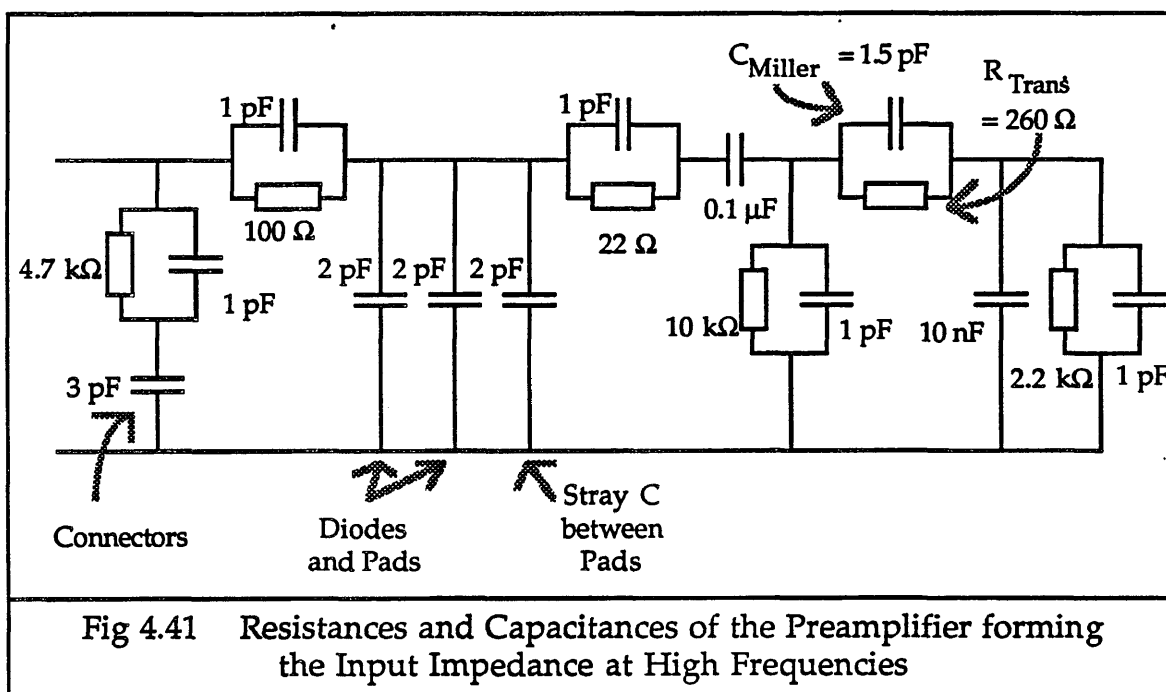
Fig 4.41   Resistances and Capacitances of the Preamplifier forming the Input Impedance at High Frequencies

The input impedance of the preamplifier is highly dependent on the input impedance of the first transistor BFT25. This has been used in the common base configuration so that the impedance is a few hundred Ohms instead of only a few Ohms obtained from the more usual common emitter configuration. The high impedance is needed so as to match the characteristic impedance of the sense wire transmission line at 350 Ω.

The input impedance of this transistor is considered to be almost totally resistive. There is a very small inductive part which is ignored.

$$Z_{transistor} = r_e + \frac{r_b}{\beta}$$

β = current gain between base and collector $\approx$ 30 at saturation currents of I_e = 1mA. The emitter current is actually only $\approx$ 0.1 mA, however, giving $\beta \sim 10$.

r_e = emitter resistance

$$r_e = \frac{k_B T_{abs}}{q_e I_e} = \frac{26}{I_e \text{ (mA)}} \quad \text{at room temperature.}$$

r_b = base resistance, which is the internal resistance of the silicon and is $\sim 5\ \Omega$ if there is very low noise.

Therefore :

$$Z_{transistor} = 260\ {}^{+15}_{-12}\ \Omega$$

The errors are calculated by allowing for an error on the emitter current of $\pm$ 0.005 mA, from the various resistor tolerances, and also allowing the base resistance to increase by $\sim 2\ \Omega$, to allow for any noise in the silicon. A rise in the temperature of the transistor, such as may happen inside the ITC, where the preamplifier boards are closely packed, will increase the input impedance of the transistor by $\approx 1\ \Omega$ for a 5 K increase in T_{abs}.

The next calculation is of the input capacitance of the preamplifier. The components used are all microcomponents, attached to the board with pads. Each pad has $\approx$ 0.5 pF associated with it at high frequencies. There is one pad for each diode and there are two for each resistor. There are also ~ 2 pF per channel for all the connections between the pads, because everything is very close together on the circuit board. The Miller effect across the first transistor must also be included. This is where the capacitance of the circuit beyond the transistor feeds back across the voltage gain part of the circuit.

$C_{Miller} = C_{ce} (1 + A) \approx 1.5$ pF
A = voltage gain ≈ 2
C_{ce} = collector emitter capacitance $\approx$ 0.5 pF

The 4.7 kΩ resistor, which couples together neighbouring signal lines, connects to earth through the stray capacitance of the preamplifier connector and the connector in the electrical end plate. Finally, each diode has ≈ 1 pF associated with it at high frequencies. The surface mounted resistors have a tolerance of 5 %.

The network shown in figure 4.41 reduces to a total resistance of :

$$R = 260 + 100 + 22 = 382 \pm 20 \ \Omega$$

and a total capacitance at high frequencies of :

$$C = 1.7 \pm 0.3 \ pF.$$

The errors here include those on the input impedance of the transistor, and the tolerances of the resistors. For the capacitance, the approximations for the connectors have been taken into account.

4.5.1.4   Total End Impedance

The behaviour of the various elements of the impedance at the end of the sense wire has been investigated in order to know what the change in impedance will be for a signal travelling along the line. This will determine the size and form of the reflection. The values given are approximate. Figure 4.42 shows the total impedance at the end of the sense wire in the ITC.
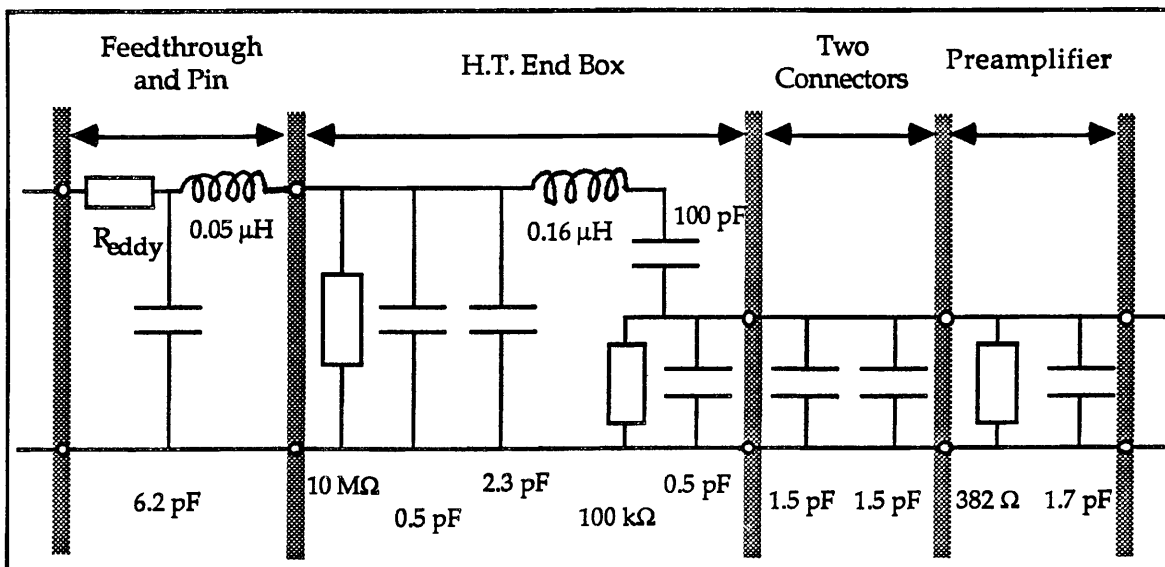
Fig 4.42   Total Impedance at the End of the Sense Wire

Every component resistor has a capacitance of $\approx 0.5\,pF$ associated with it at high frequencies. These capacitances have been drawn in on figure 4.42 as if they were real circuit elements. The series inductances of the end components and the end box have also been shown as discrete elements.

The high voltage rail of the end box and the earth are connected with a very large capacitance, so at very high frequencies the two rails can be considered to be the same, and have been drawn this way in figure 4.42. The series resistance R_{eddy} is due to eddy currents in the end plate, which will be shown to exist and calculated in the next section.

The resistive part of the termination is dominated by the resistive part of the input impedance of the preamplifier, and is therefore approximately $380 \pm 20\,\Omega$.

The total capacitance on the end at high frequencies reduces to a parallel capacitor with value approximately $13.9 \pm 1.3\,pF$.

These calculated values for R_{end} and C correspond within errors to the values found with the simulation.

Figure 4.43 shows the effective termination of the sense wire transmission line in the ITC for high frequency signals.

$Z_0 = 350\,\Omega$ $R = 380\,\Omega$ $C = 13.9\,pF$

Fig 4.43   Termination of Sense Wire as Calculated
for High Frequencies
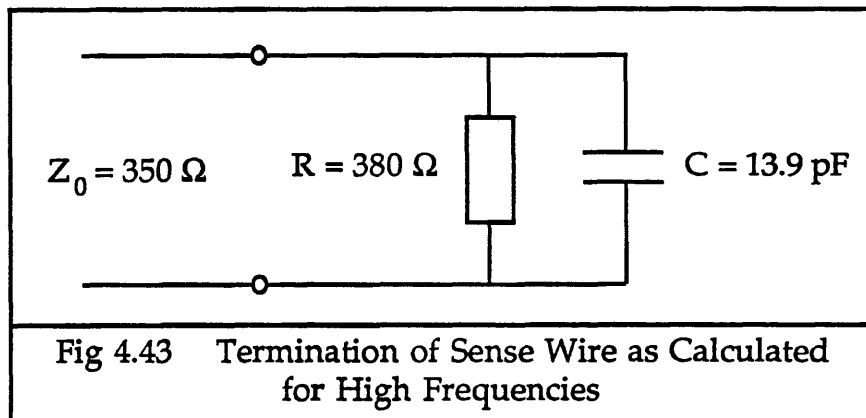
4.5.2 Power Losses in the End Plate

When the high frequency signals on the sense wires are transmitted through the end plate, this thick sheet of conducting material acts like the turn of a transformer and electromotive forces are induced in it. These cause eddy currents to flow in the end plate. The end plate is not laminated, and the resistivity of aluminium, at $4\,\mu\Omega/cm$, is lower than that for iron, at $9\,\mu\Omega/cm$, which is traditionally used in a transformer core. Therefore, the eddy currents here will be worse.

The eddy currents cause power to be dissipated as heat energy, with :

$$P = I^2 R$$

For a fixed flux amplitude,

$$\frac{\partial \varnothing}{\partial t} \propto \text{eddy current density} \propto \omega$$

$$\Rightarrow \quad \text{Power losses} \propto \text{frequency}^2$$

This power loss from the signal distorts it in a nonlinear way. The distortion is very difficult to simulate. It may be reproduced very approximately as simple attenuation, by inserting a large resistance in series with the transmission line. The feedthrough and pin in the end plate may thus be considered as a very short section of discrete components which highly distort and attenuate the signals, and which have a very low, complex characteristic impedance, produced by a large shunt capacitance, large series resistance, and low series inductance.

From the simulation program of the z measurement system in the ITC, a value of the series resistance R_{eddy} at the end plate at high frequencies has been found. The pulse size needed for saturation behaviour with the constant fraction discriminators was used to find R_{eddy}. This behaviour is presented in Section 5.4.3. The best fit value for the long test chamber is :

$$\text{Attenuation} = 0.7 \approx \exp\left(\frac{-Rz}{2Z_0}\right)$$

z = long test rig end plate thickness = 1 cm
Z_0 = mean characteristic impedance through end plate

$$Z_0 \approx \frac{5.8 \text{ mm} \times 182 \text{ } \Omega + 4.2 \text{ mm} \times 22 \text{ } \Omega}{10 \text{ mm}} \approx 115 \text{ } \Omega$$

(very approximately, assuming transmission line behaviour)

$$\Rightarrow \quad R \approx 8200 \text{ } \Omega/\text{m}$$
$$\Rightarrow \quad R_{eddy} \approx 82 \text{ } \Omega$$

In the ITC, the end plates are 2.5 cm thick, unlike the 1 cm thick end plates in the long test rig. Therefore, there is more power loss and greater attenuation in the ITC. This attenuation in the ITC can be calculated using

232

the same approximation to give:

$$Z_0 \approx \frac{20.8 \text{ mm} \times 182\ \Omega + 4.2 \text{ mm} \times 22\ \Omega}{25 \text{ mm}} \approx 155\ \Omega$$

$$\text{Attenuation} \approx \exp\left(\frac{-Rz}{2Z_0}\right) \approx 0.5$$

4.5.3 Termination Used in the Simulation

The termination used in the simulation program is shown in figure 4.44. The end resistance R_{end} and capacitance C are those used in the calculation of the reflected signals in the chamber, with values found from the simulation:

$$R_{end} = 380\ \Omega \qquad C = 15\,\text{pF}$$

Fig 4.44   Termination of Transmission Line
Used in Simulation Program
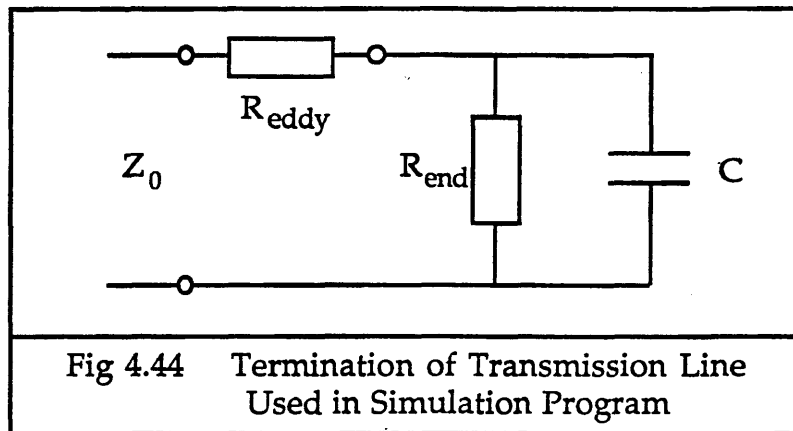
The total end impedance Z is calculated from R_{end} and C to be:

$$Z = \frac{1}{\left(1/R_{end} + i\omega C\right)} = \frac{R_{end}\left(1 - i\omega R_{end} C\right)}{\left(1 + \omega^2 R_{end}^2 C^2\right)}$$

The maximum of Im(Z) occurs at $\omega_0 = 1/R_{end}C$. This is also the 3 dB roll-off level of Re(Z). The end impedance can be seen in figure 4.45.

Fig 4.45   Characteristic Impedance from a Parallel
Resistance and Capacitance

The figure shows, with labels:

Characteristic Impedance Z

3 dB roll-off level of Re (Z)
at maximum of Im (Z)
at $\omega_0 = 1 / RC$

Re (Z)

R

$$Z = \frac{R(1 - i\omega RC)}{(1 + \omega^2 R^2 C^2)}$$

Im (Z)

ω_0

Angular Frequency ω
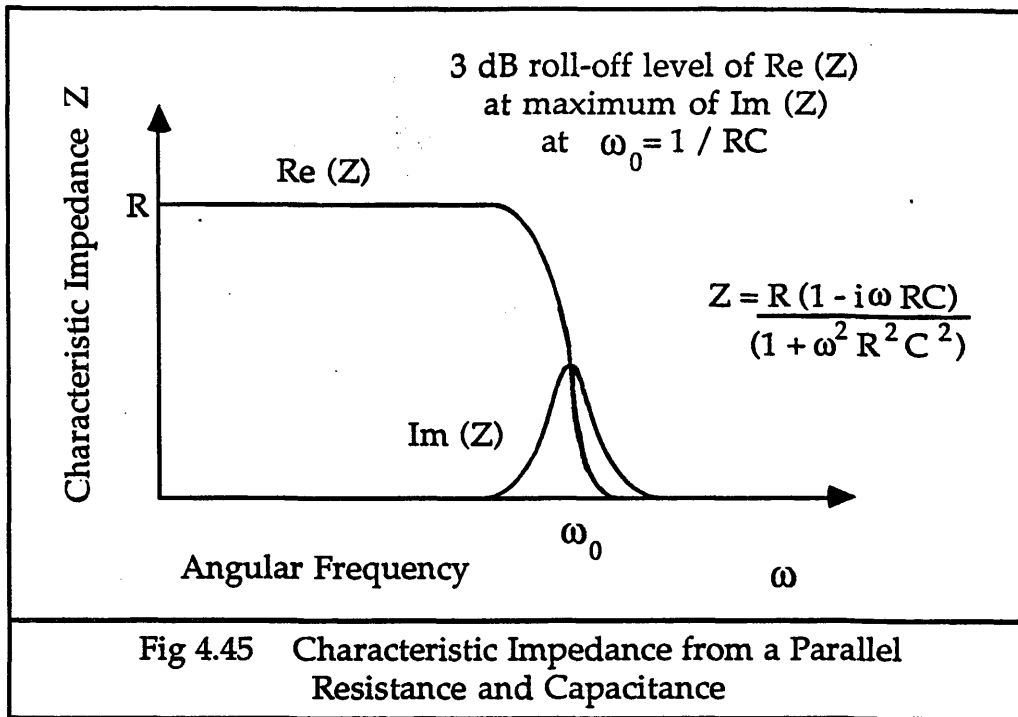
4.5.4 Where the Reflections Occur

Although the active length of the sense wires in the ITC along which signals can be generated is 2 m, the termination impedance is spread out from the tip of the feedthrough 23 mm (in the long test rig) or 8 mm (in the ITC) inside the end plate to the preamplifier 26 cm away from the end plate. Therefore, reflections do not necessarily come from exactly the ends of the sense wire. Using the simulation program, the only length of line which will reproduce the data from the long test rig is found to be :

$$l = 195.4 \text{ cm}$$

This was obtained by making the simulated "S-bend" for the dual threshold discriminator turn over at the correct position down the line, and also matching the simulated reflection effects for the constant fraction discriminator to the data.

The meaning of this shorter length is that the reflections in the long test rig appear to come from 23 mm in from the end of the wire, at the innermost tip of the feedthrough. Since the reflection is generated before the signal reaches the end plate, the reflection does not lose energy from eddy currents in the simulation program.

Since the reflection is generated at the tip of the feedthrough inside the chamber, then the effective length of the transmission line in the ITC is :

$$l = 198.4 \text{ cm}$$

234

4.5.5 Signals After Transmission

Figure 4.33 for the ITC, and figure 4.34 for the long test rig, show the signals on the sense wire after all the reflections have been added in, but before transmission through the end impedance to the preamplifier. Now that the attenuation through the end plate has been calculated, as well as the termination impedance, the effect of these on the signals can be shown. Figure 4.46 shows the signals in the ITC after transmission through the end plate and end box, just before amplification. The largest signal was generated on the sense wire at the timing end, and has travelled no distance on the wire. The smallest signal was generated at the far end of the wire, and has travelled the whole length of the wire. The signals are smaller than they were before transmission, despite being amplified by the step up in characteristic impedance, due to the power loss in the end plate via eddy currents.

Fig 4.46   Signals After Transmission in the ITC
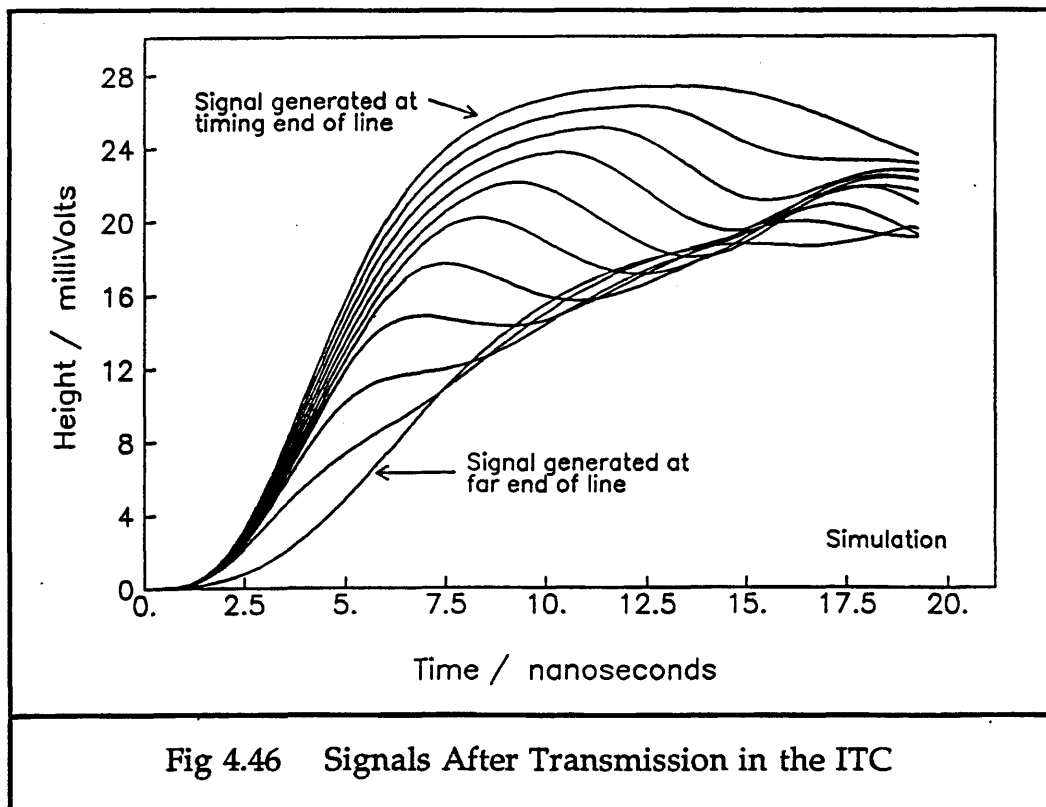
Figure 4.47 shows the signals in the long test rig after transmission through the end plate, but before amplification.
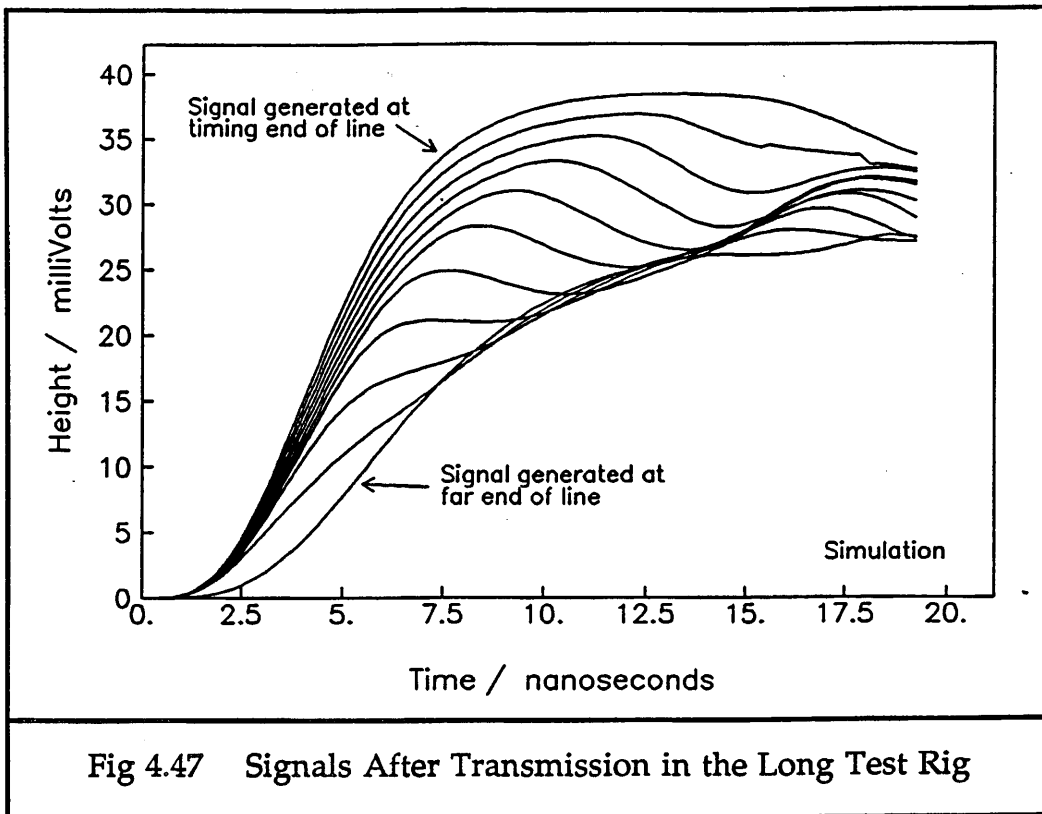
Fig 4.47   Signals After Transmission in the Long Test Rig

4.6   Amplification of the Signal

4.6.1   Increase in the Signal Amplitude

After the signals have been transmitted through the end plate, they travel through the preamplifier, 23.5 m of coaxial cable, and the main amplifier before reaching the discriminator. All of these stages have an effect on the signal amplitude. With the long test rig, in order to use the ITC preamplifier and cable length needed in ALEPH, and use the discriminators in the signal height range for which they were designed, it was necessary to have a terminator at the input of the main amplifier which reduced the signal voltage amplitude by half. The gains and attenuations of the various stages for the long test rig and ITC readouts for high frequency signals are shown in table 4.1. For these tests, the cable length used with the long test rig was 20 m, not 23.5 m as will be used with the ITC. With the ITC readout, a different main amplifier will be used to that used in the long test rig readout.

Table 4.1	Voltage Gain of Readout Systems	
Item	Gain of Long Test Rig	Gain of ITC
Preamplifier	2	2
Cable	0.6	0.705
Terminator	0.5	–
Main Amplifier	80	32
Total Net Gain	48	45

4.6.2 Increase in the Signal Rise Time

As the signals travel through the system, they lose some of their upper frequencies, from distortion on the sense wire and frequency cut-off in the amplifiers. This loss increases their rise time. In the ITC, signals will have very fast rise times, ~ 1 ns, when generated. After transmission through the end plate, this will have increased to several nanoseconds. The preamplifier and main amplifier both have 3 dB roll-off frequencies of 120 MHz. This significantly increases the signal rise time. In the long test rig, the signals started as square pulses, but after passing through the hook and coupling resistors, the signal rise time was ~ 3.5 ns. After transmission through the end plate, the rise time had increased to ~ 5 ns, and after the main amplifier, the rise time was measured to be ~ 12 ns at the 10%-90% level. From 0% to 100%, the rise time was ~ 20 ns. The increases in rise time from each stage of the readout process are added together in quadrature to produce the final value.

The effect of amplification on the signals after transmission is therefore not just to increase the voltage amplitude, but also to increase the signal rise time. The signal leading edge is slowed down so much that the dips and bumps of the reflections which were after the peak of the transmitted signal are now on the leading edge. Figure 4.48 shows the transmitted signals from figure 4.46 after amplification in the ITC readout. Figure 4.49 shows the transmitted signals from figure 4.47 after amplification in the long test rig readout. The initial amplitude of these signals on the sense wire was 56 mV.
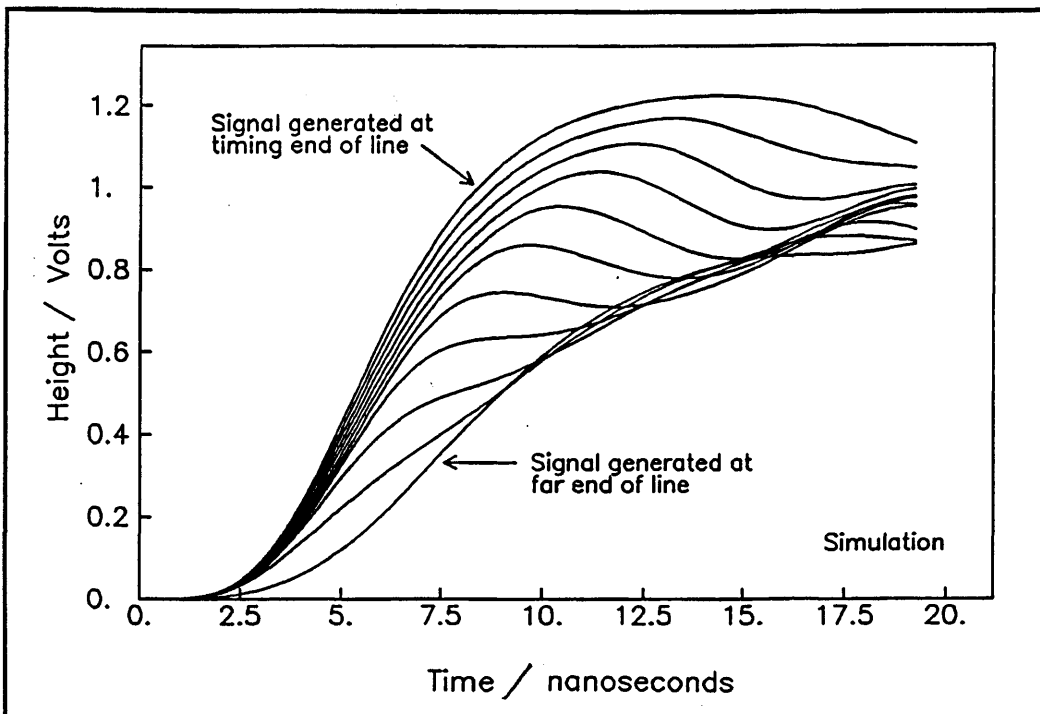
Fig 4.48   Signals After Amplification in the ITC
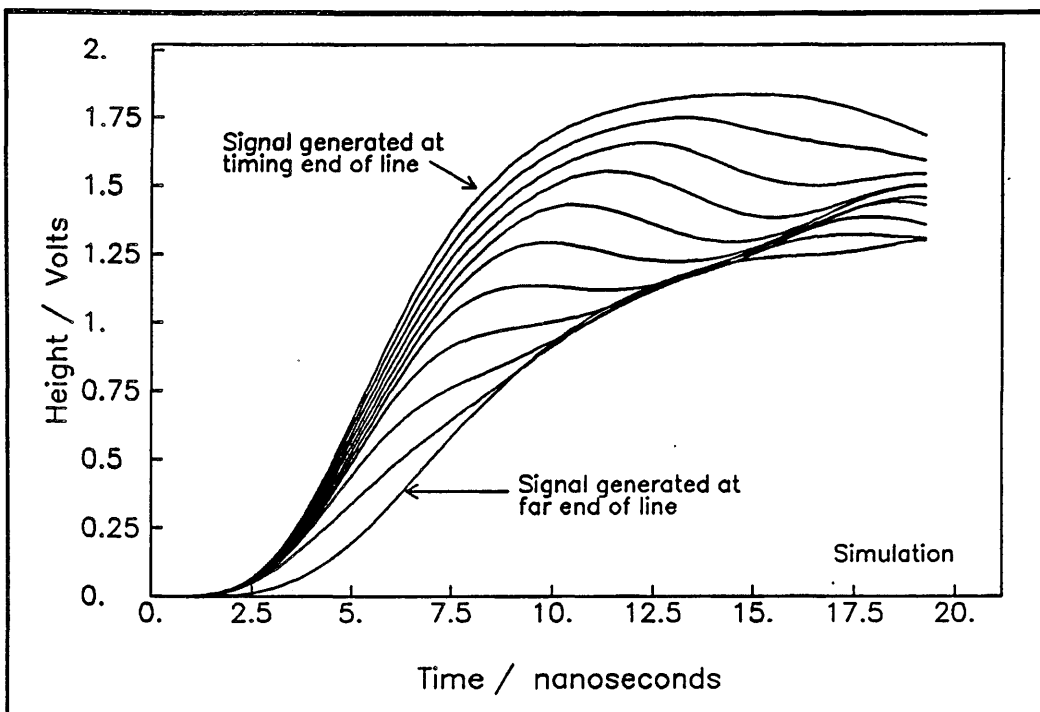
Fig 4.49   Signals After Amplification in the Long Test Rig

The 3 dB roll-off frequency is built into the simulation program by passing the signals through an RC low pass filter with time constant 1.3 ns, which gives the required roll-off frequency.

$$f_{max} = \frac{1}{2\pi RC} = 120 \text{ MHz}$$

In section 5.1 it will be shown that in order to compensate for the lack of distortion in the simulation program, and for a discriminator effect not possible to include accurately in the model, the series resistance of the sense wire has to have the value 400 Ω/m to reproduce the data. Figure 4.50 shows the effect this has on the long test rig signals as they arrive at the discriminator after amplification.

Fig 4.50   Signals After Amplification in the Long Test Rig with Series Resistance = 400 Ω/m
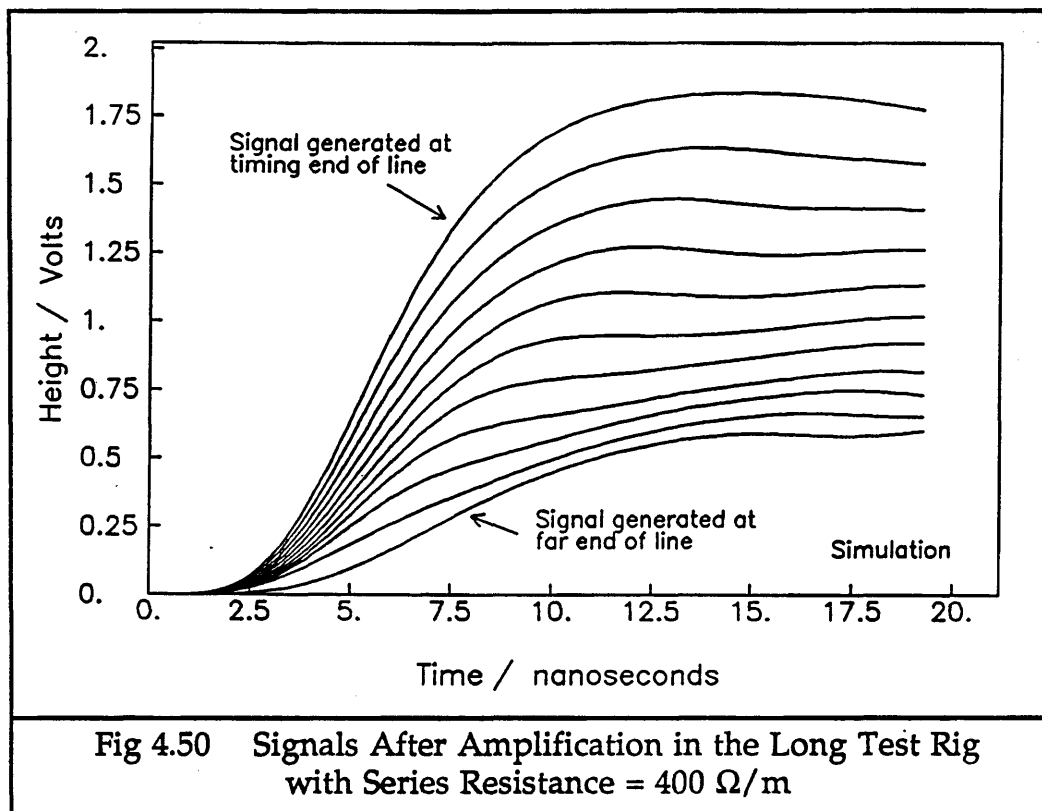
4.6.3 Saturation of the Amplifier

The main amplifier saturates on signals larger than 2 V in amplitude. The saturation has a marked effect on the nonlinearity from c/2 of the z position measured from time difference and has been included in the simulation program by not allowing signal amplitudes to increase above the 2 V level. The results of this can be seen in figure 4.51 for signals which started on the sense wire with an amplitude of 109 mV. Those signals which travel further than ~ 80 cm along the sense wire are attenuated sufficiently to avoid being affected by the saturation of the amplifier.

Figure 4.52 shows the amplified signals from the simulation program which started on the sense wire at 168 mV. Here, all the signals generated at any point on the sense wire are affected by the saturation of the amplifier.
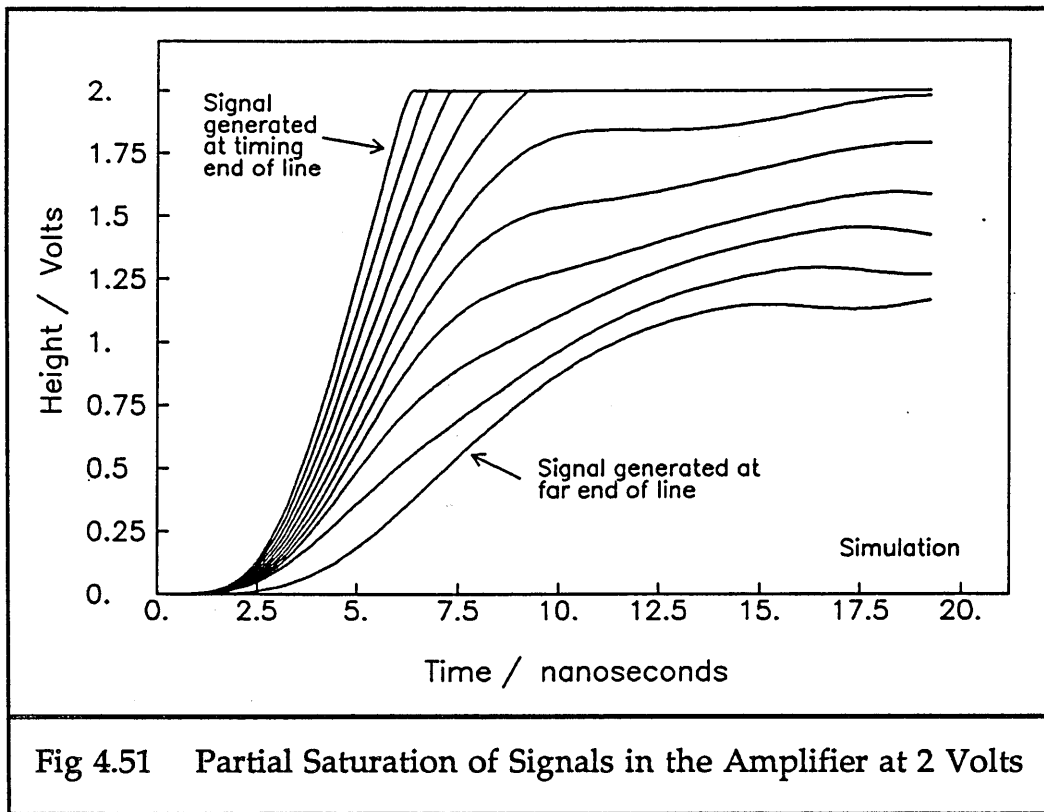
Fig 4.51   Partial Saturation of Signals in the Amplifier at 2 Volts

For both of these figures, the series resistance of the sense wire is 400 Ω/m, which will be explained in Section 5.1, to enable these signal sizes to saturate the amplifier and produce the modified discriminator S-bends at the levels found in the data, to be shown in Section 5.4.3.
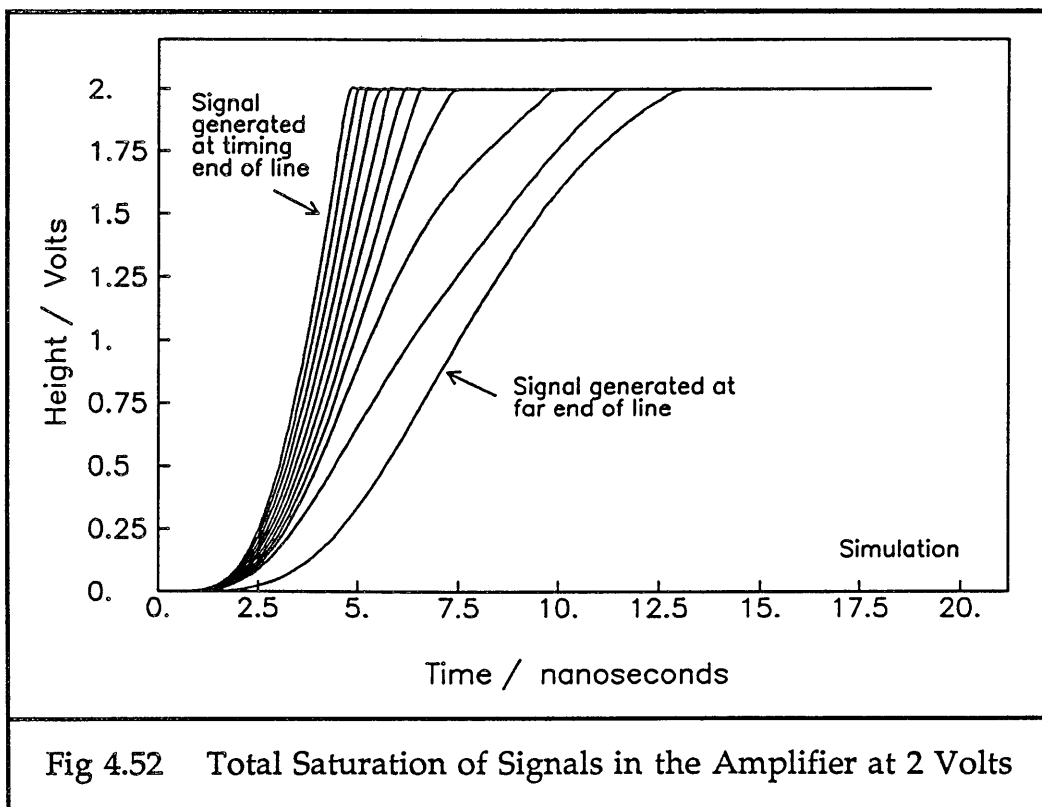
Fig 4.52   Total Saturation of Signals in the Amplifier at 2 Volts

This sudden cutoff at 2 V, used in the simulation program, is only an approximation to what happens in the real amplifiers, where the effect is smoother and not easy to reproduce. However, since the saturated S-bends can be reproduced from the simulation, the approximation is a valid one.

5 Discrimination

A discriminator is an electronic circuit which produces a signal after a threshold voltage level is reached by the input signal and sufficient charge has been accumulated. The signal produced by the discriminators to be used for the ITC is an ECL signal, which is a square wave pulse between - 0.75 V and - 1.5 V, of amplitude - 0.75 V. This signal is converted to a NIM pulse, which is defined as a 16 mA pulse. (When this is terminated through 50 Ω to ground, it gives a signal of - 0.8 V.) The NIM pulse is sent to the TDC to measure the time of arrival of the signal.

The next section discusses different designs of discriminator available, and their advantages and disadvantages. It then presents data results from testing two types of discriminator under consideration for use with the ITC readout system, together with the results from the simulation program about the behaviour of these discriminators. Finally, ways of compensating for the nonlinearity from c/2 are discussed. First however, a note must be made on the limitations of the simulation program.

5.1 Notes on the Simulation

The model used to simulate the behaviour of the z measurement system using the time difference method includes all the effects explained in the previous chapter, such as attenuation along the sense wire, multiple reflections, transmission through the end plates, complete with attenuation from power losses, and amplification, with high frequency loss, before discrimination. However, it has some limitations. There is no distortion of the signal on the sense wire from the change of series resistance with signal frequency included in the program. There is also a problem with the simulation of the discriminators. In the next section, it will be explained that the discriminators produce a slewed output signal, depending on the height of the input signal. The amount of slewing depends both on when the leading edge of the input signal passes a threshold level, and also on

how fast afterwards enough charge can accumulate to enable the output signal to be produced. These two effects cannot be separated when measuring the slewing of the discriminators, and so are only half included in the simulation, since how much charge is needed to produce an output signal is unknown. The result of these two deficiencies of the model is that another process in the production of the signal has to compensate for them. The effect of the distortion on the sense wire and the charge accumulation in the discriminators is to increase the difference in signal amplitude between the signals from each end of the sense wire. This signal height difference is reintroduced by the simulation program by artificially increasing the attenuation along the sense wire of the signals travelling on it. The predicted series resistance of the sense wire for the expected frequencies in the signal is ~ 139 Ω/m. However, for the simulation to reproduce the S-bends and other effects as found in the data, it is necessary for this value to be increased to 400 Ω/m.

All the signal profiles shown in the previous section, unless stated otherwise, have been calculated using the more realistic value of 139 Ω/m for the series resistance of the sense wire. However, all the S-bend lines shown in the next section have used 400 Ω/m in order to be able to reproduce the relations indicated by the data points. If signal distortion were to be in some way included in the model, then signal profiles shown in the previous section would be slightly different. Signals travelling along the sense wire would probably be smaller than shown, giving a greater difference between largest and smallest signals. The use of 400 Ω/m for the series resistance was the only way found to fit the data, and the values found for the other variables such as the length of the sense wire, the end capacitance, end resistance and attenuation in the end plate from eddy losses are also the only ones which enable the data to be fitted.

All these variables are highly correlated, and so it is not very meaningful to refer to errors on their values. A change in one variable beyond a certain small tolerance means that every other variable has to be changed to attempt to reproduce the features of the data. The effects in the data to which the simulation was fitted were the detailed shape of the S-bends for both the dual threshold and constant fraction discriminators, at various threshold levels, fractions and delays, the slewing of the S-bends with signal size and the effect on the S-bends of the saturation of the amplifiers.

The tolerances by which the variables can be altered individually without significantly degrading the overall fit of the simulated S-bends to the data points are as follows :

l   = transmission line length = 195.4 ± 0.1 cm

R_{end} = termination resistance   = $380 \pm 5 \, \Omega$

C   = termination capacitance = 15.00 ± 0.05 pF

R   = series resistance at high frequency = $400 \pm 5 \, \Omega/\text{m}$

Attenuation from eddy current power losses = 0.70 ± 0.01

This set of values is the only way found to successfully model the data. The values of R_{end} and C correspond within errors to those found from calculating the end impedance of the sense wire transmission line. The length of the transmission line corresponds to the length of the sense wire between the tips of the feedthroughs protruding inside the end plates of the long test rig. The attenuation in the end plate is not an unreasonable value, although it is very difficult to actually calculate what it should be. The anomalous series resistance at high frequency has been accounted for by the missing effects of signal distortion and discriminator charge accumulation in the simulation program.

5.2   Types of Discriminator

a) Single Threshold Discriminator

The single threshold discriminator is the simplest of discriminator designs. It works by producing a signal after a threshold level has been passed by the input signal, and after sufficient charge has been accumulated to enable the output signal to be produced. This is shown in figure 4.53.

There are two problems experienced when using this type of discriminator. The time of arrival of the signal is ideally the time of arrival of the first electron to arrive at the sense wire, since the route of this through the drift cell has had the least deviations from diffusion. Therefore, the discriminator threshold is set as low as possible. This also avoids some of the effects of the reflections on the leading edge of the signal, since these will be mostly above a low threshold. However, if there is any noise on the signal, from external high frequency interference, then there will be a jitter on the time of arrival measured. This type of discriminator is very susceptible to interference from noise.

Fig 4.53   Time of Arrival from a Single Threshold Discriminator
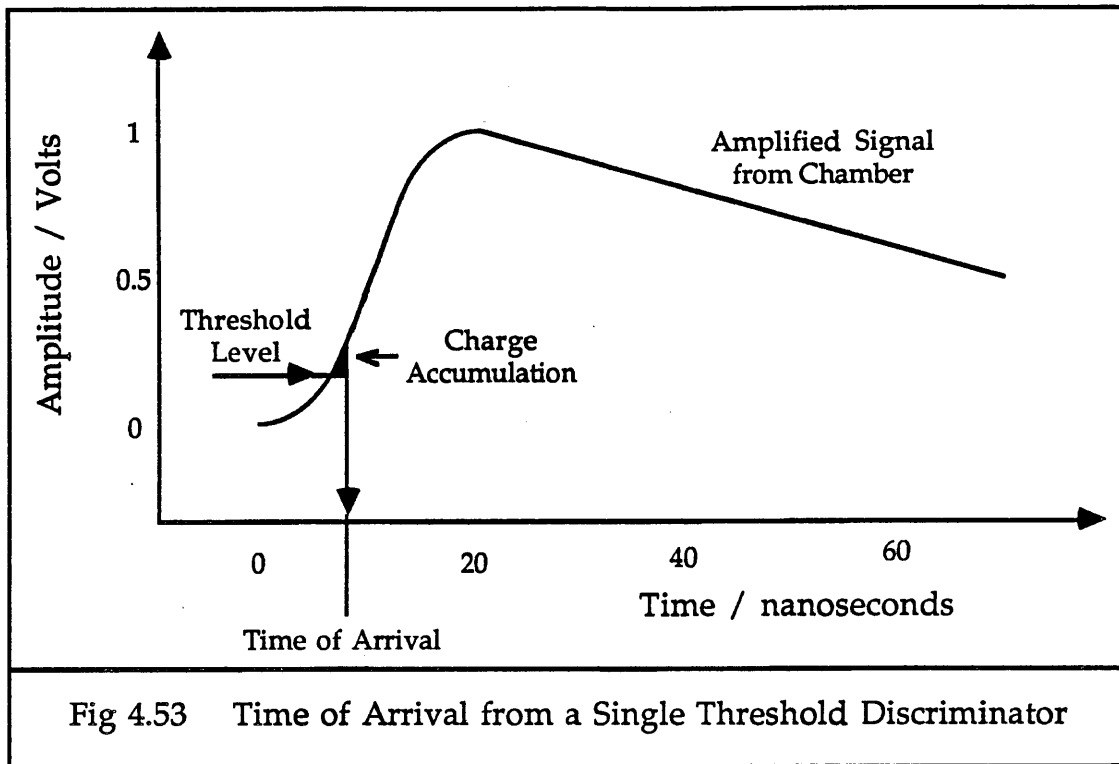
The second problem experienced is known as slewing. Signals from a drift chamber have a range of signal rise times, and the range of pulse heights will be ~ 100. These two parameters affect the speed of arrival of charge, and so lead to different times of arrival being measured from signals which were actually generated at the same time on sense wires in the chamber. This effect can be seen in figure 4.54, where the smaller pulse produces a discriminator signal after that from the larger pulse.

Fig 4.54   Slewing with Pulse Height in a
Threshold Discriminator
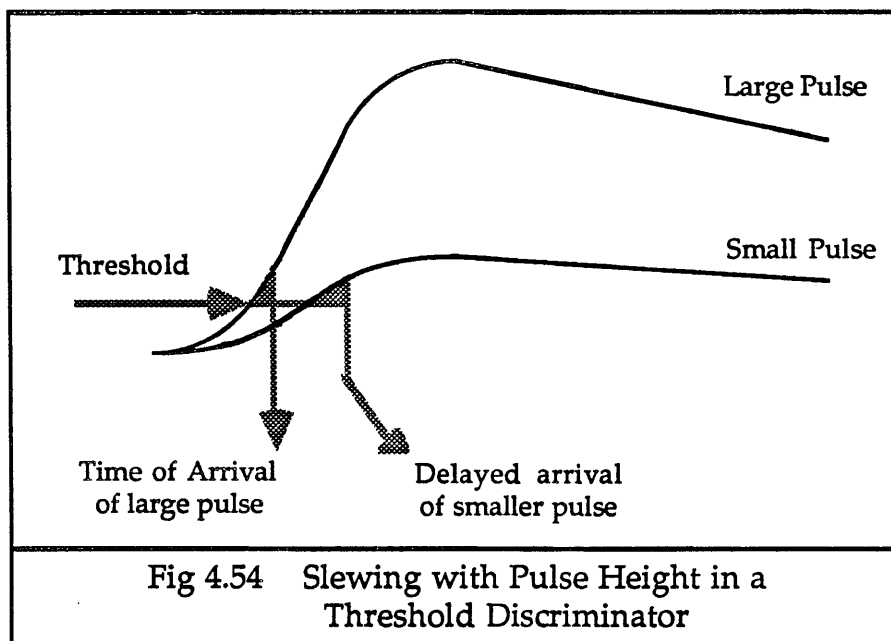
b) Dual Threshold Discriminator

One improvement that can be made to this discriminator design is to add a second threshold level. This can be seen in figure 4.55. The dual threshold discriminator is also known as the hi-lo discriminator.
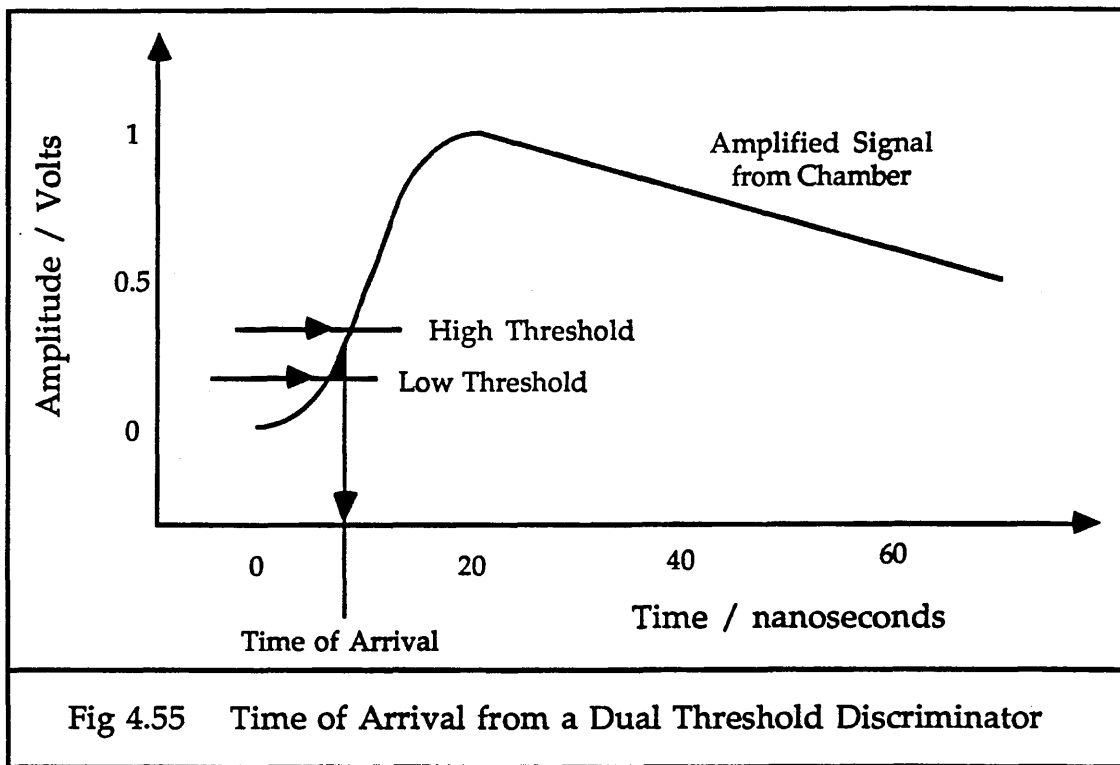
Fig 4.55   Time of Arrival from a Dual Threshold Discriminator

With this type of discriminator, a signal is only produced when a high threshold level is passed, but the timing signal is produced from when the lower threshold is reached. The low threshold can now be set lower than with the single threshold discriminator without producing a signal more often on the noise, and lowering the threshold helps to reduce the amount of slewing from the range of signal rise times and heights. However, the timing is still slewed and it still jitters from the noise on the signal.

c) Constant Fraction Discriminator

Another type of discriminator commonly used is known as the constant fraction discriminator. This gets away from setting a fixed level threshold by producing its output signal when a fixed fraction of the signal height has been reached. This is achieved by splitting the input pulse into two parts. One is delayed by a set time, and the other is attenuated to a set fraction of its original amplitude, and sometimes inverted. If the second signal is inverted, then the two signals are added back together again, and the discriminator output signal produced when the resultant signal changes sign from negative to positive. Otherwise, the two signals are

compared, and when they are equal in amplitude, then the discriminator signal is produced. The operation of the constant fraction discriminator can be seen in figure 4.56, with a fraction of 1/2.
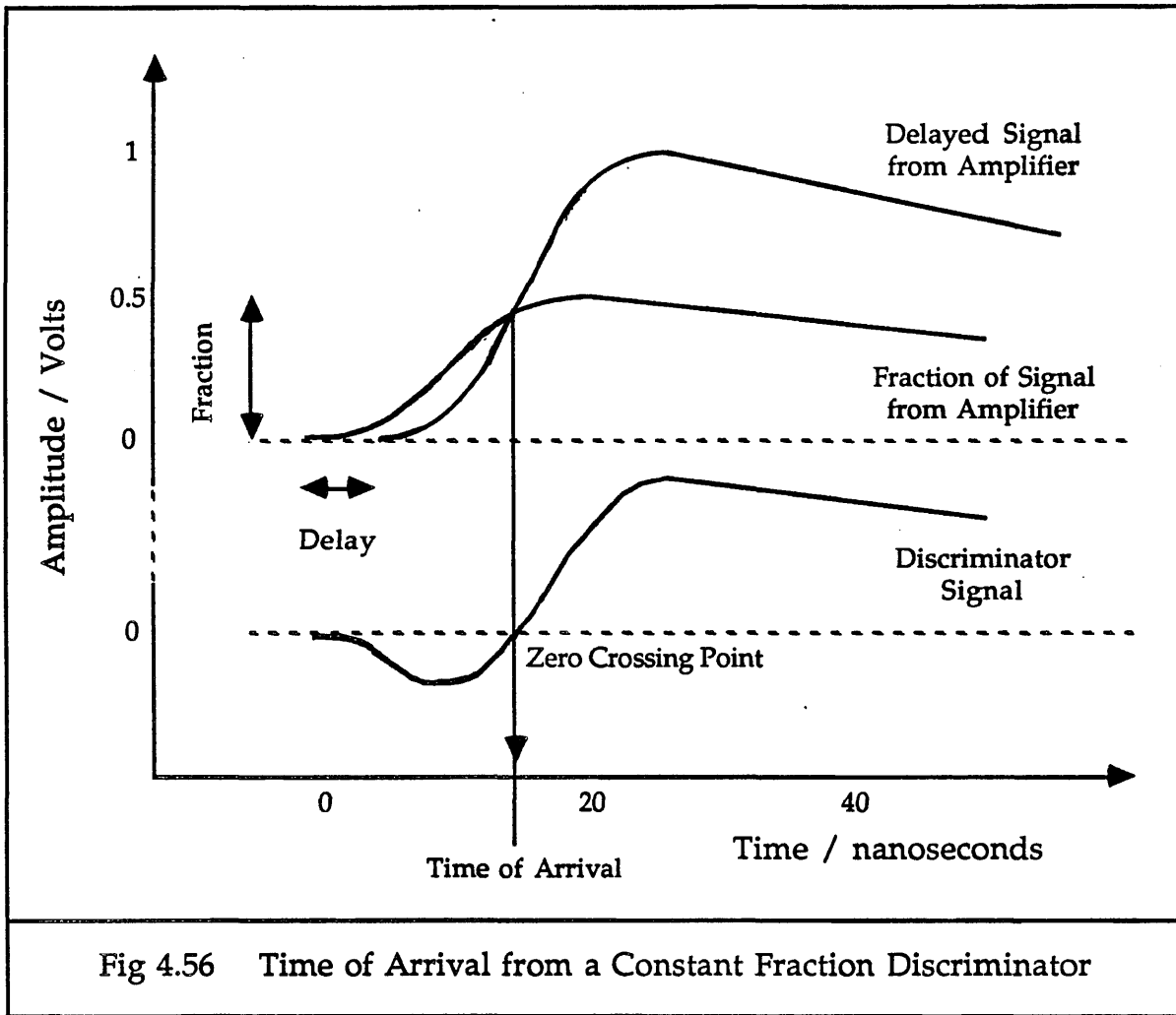
Fig 4.56   Time of Arrival from a Constant Fraction Discriminator

There are two advantages to this design of discriminator. Firstly, since the discriminator output signal is produced from high up the signal leading edge, the timing is hardly affected by noise on the signal. Secondly, since the timing is always taken at a fixed fraction of the leading edge of the signal, the timing of the discriminator signal becomes ideally independent of the signal amplitude. This is a very useful attribute when trying to time the arrival of drift chamber signals which have a very wide range of signal amplitudes. One disadvantage of this type of discriminator over the simpler threshold ones is that taking the timing from high up the signal leading edge makes it very susceptible to reflection effects. Another disadvantage is that the constant fraction discriminator needs more components to be built, and therefore costs more to produce.

5.3   Dual Threshold Discriminator

5.3.1   Details of How it Works

Figure 4.57 shows the logic diagram of a dual threshold discriminator [4.5].

Fig 4.57   Block Diagram of a Dual Threshold Discriminator
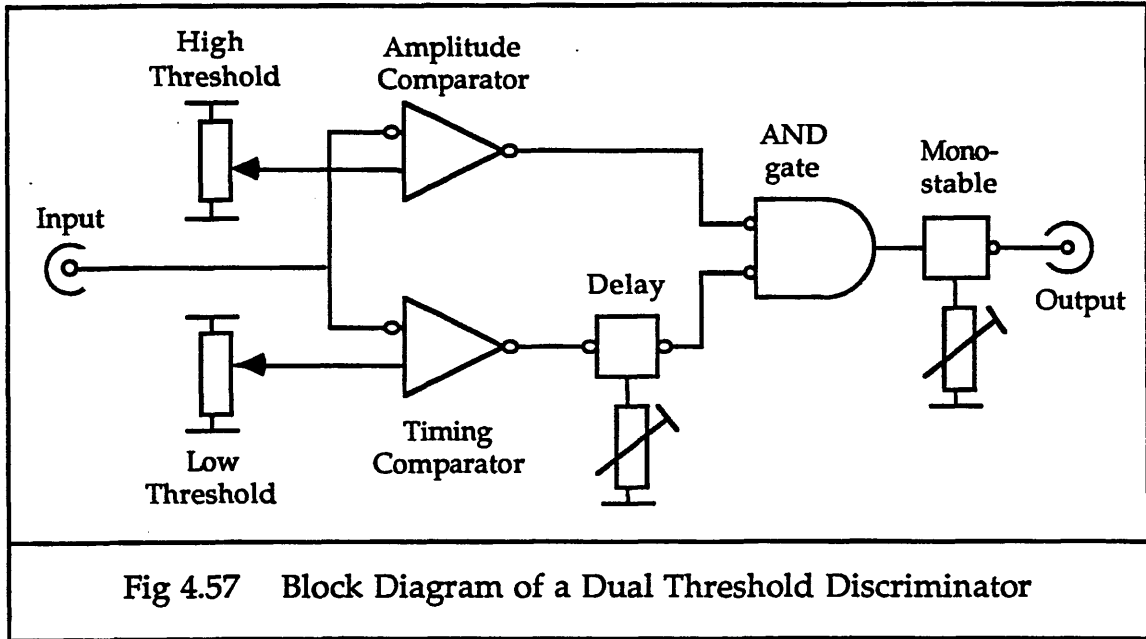
The threshold levels on the discriminators used with the long test rig were adjustable together, not individually. They are shown in figure 4.58.

Fig 4.58   Threshold Levels on the Dual Threshold Discriminator
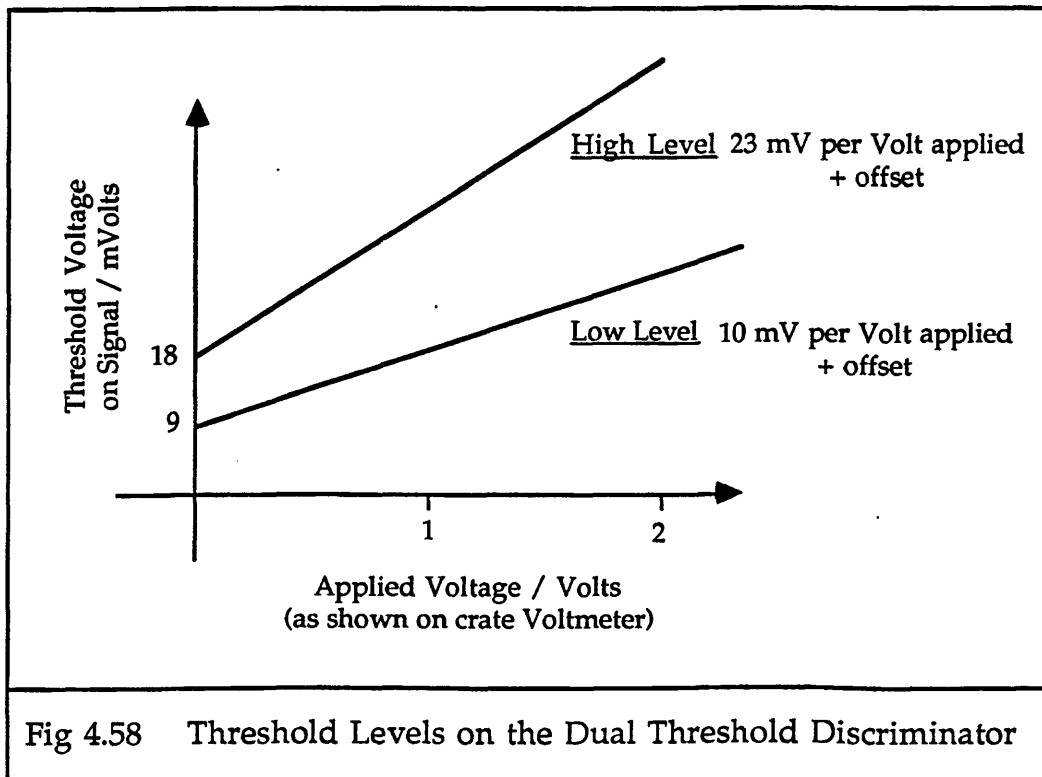
The "applied threshold voltage" is a term used in subsequent parts of this chapter and in other chapters, and the graph in figure 4.58 shows how it relates to the actual threshold levels on the input signal. For instance, most of the data taken with the dual threshold discriminators, both with the long test rig, and also with the small test chamber, had an applied threshold of 1 V. This means that for a pulse to produce a discriminator output signal, it had to have an amplitude greater than 41 mV after amplification, and the timing was taken from when the signal reached 19 mV, plus a small delay while the charge accumulated. The applied threshold could be varied from 0 V, giving high and low thresholds of 18 mV and 9 mV respectively, up to 10 V, giving 248 mV and 109 mV as high and low threshold levels.

5.3.2 "S-Bend" Results and Simulation

The nonlinearity from c/2 in the time difference does not form an "S" shape with dual threshold discriminators, but is still known as the S-bend, for compatibility with the constant fraction terminology. The dual threshold S-bend is shown in figure 4.59. The points are data from the runs with the long test rig. The line is from the simulation program. The data points are for signals which were 56 mV amplitude when they started on the sense wire. These are fairly large signals, but they are small enough not to saturate the amplifiers.

Fig 4.59   Standard Dual Threshold Discriminator "S-Bend"
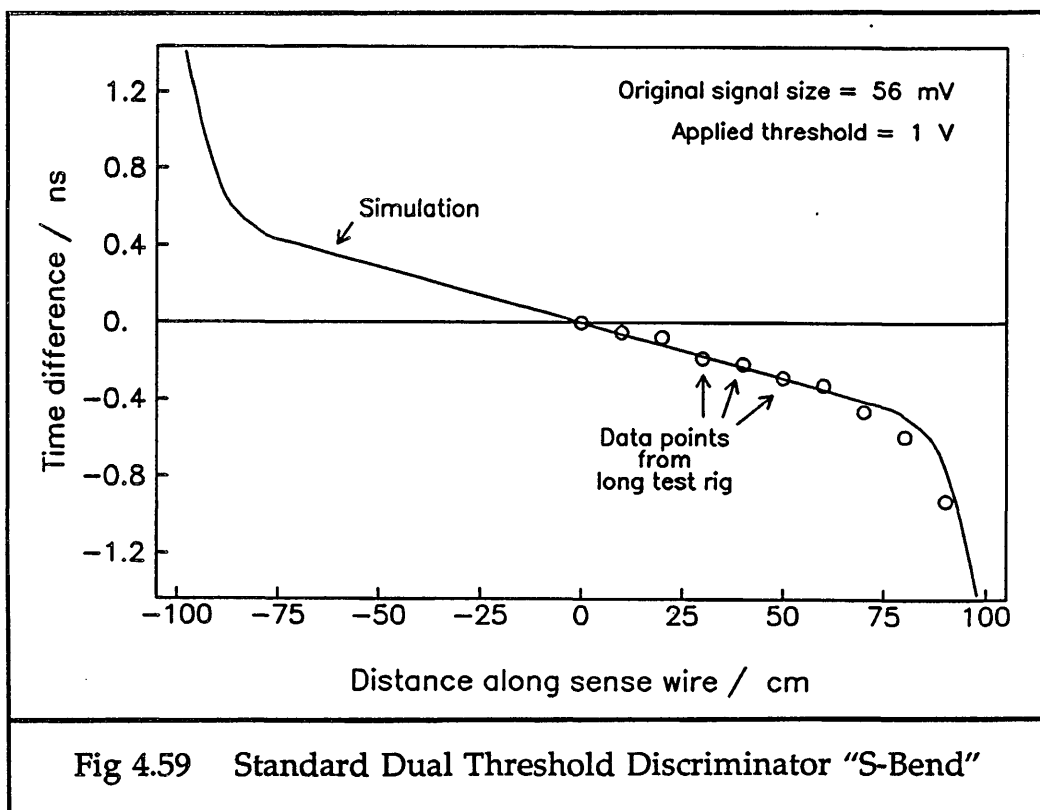
There are several points of interest here.

a) Zero Crossing of the Data

The data points lie on a line which crosses the origin in figure 4.59. Two corrections have been made to the time differences in order to achieve this. The first is the one made every time, using the calibration time difference to correct the time differences. This should make the line through the data points pass through the centre of the chamber. However, it does not, and all the points after subtraction of the calibration time difference are ~ 0.2 ns below where they would be if the line through them passed through the origin. A second correction is necessary, and this comes from the fact that the calibration pulses used in the tests no longer have the same amplitude as each other by the time they reach the discriminators. There is a variation in the gain between the preamplifier channels of ~ 10 %, causing another delay between the timing at one end of the chamber and the other, from the slewing caused by this difference in pulse size. Therefore, after amplification, the calibration signals may produce a time difference which no longer relates to the centre of the chamber. The time offset found on this particular wire corresponds to an offset in the calibrated chamber centre of 3 cm. One of the other wires tested had an offset of only 0.04 ns ($\equiv$ 0.6 cm), and the third wire tested had an offset of 0.48 ns ($\equiv$ 7.2 cm). If dual threshold discriminators are used with the ITC, then this effect in the calibration must also be calibrated and corrected from channel to channel. The finally corrected data points, as shown in figure 4.59, were used when finding the values of the variables in the simulation program by fitting the S-bend nonlinearity to the data.

b) Deviation from c/2

Along the central ~ 140 cm of the sense wire, the "velocity" of the change in z position is approximately 0.9 c/2. This apparent slowing down of the signal is caused by the attenuation of the signal as it travels along the sense wire. This leads to the signals at each end of the chamber having different amplitudes, so the time difference measured is larger than it should be ideally, because of the slewing of the discriminators, and the apparent velocity slows down to compensate.

This effect can be seen more clearly by looking at the signal profiles as they reach the discriminator. In figure 4.60, a 56 mV signal was generated at various points along the sense wire and has been attenuated, transmitted and amplified before reaching the discrimination stage. The largest signal shown in figure 4.60 travelled no distance on the sense wire, and the

smallest signal travelled the full length of the sense wire. The threshold level is shown at an "applied" level of 1 V, which corresponds to a low threshold level of 19 mV. This is very low down on the signal leading edge, so has been enlarged to be more easily seen.

Fig 4.60   Dual Threshold Discriminator Signals from the Long Test Rig
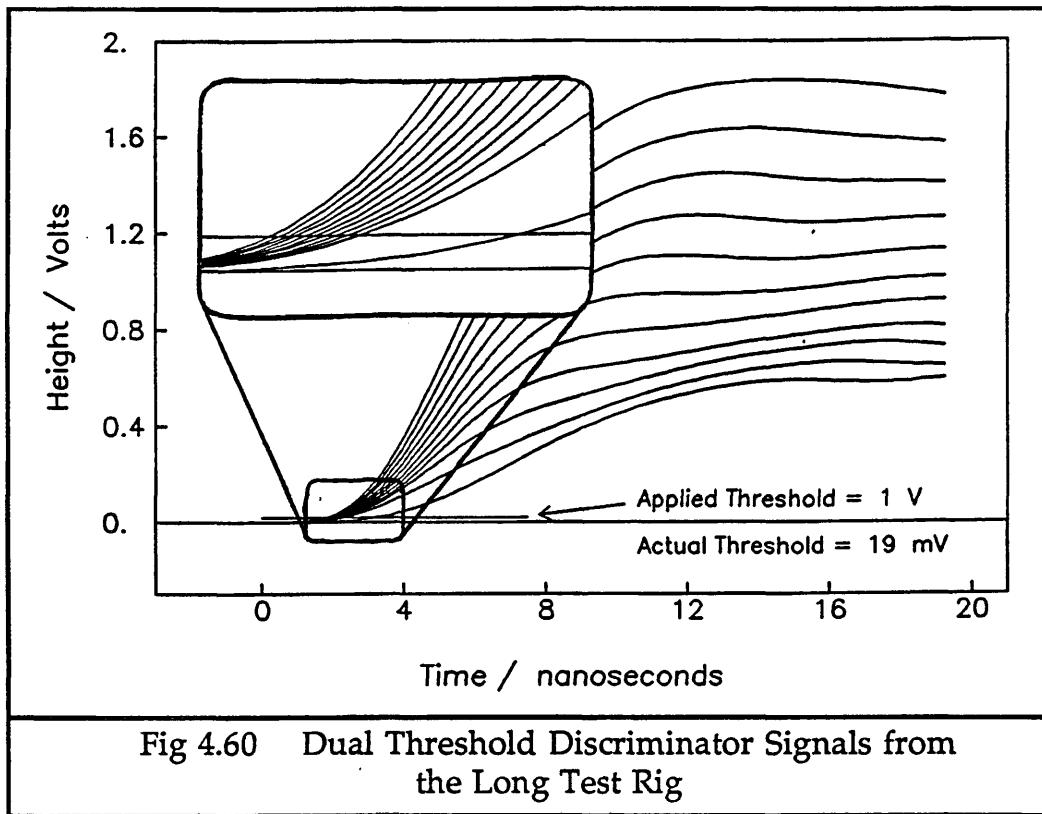
From figure 4.60, it can be seen that the time interval between each signal crossing the threshold level is fairly uniform for nearly all the signals, giving the linear slewing seen along the central 140 cm of the sense wire.

c) The "Tail" of the Nonlinearity

For signals which are generated near the ends of the sense wire, in the last ~ 20 cm of the chamber, the time difference measured is very much larger than can be accounted for simply by considering the attenuation of the signals on the sense wire. This can be explained by inspecting the smallest signal in figure 4.60, where it can be seen that this signal which has travelled the full length of the sense wire has its leading edge affected by the reflection at the low threshold level shown. This greatly increases the time difference measured for signals which start near the end of the sense wire, and produces the "tail" in the nonlinearity from $c/2$ in the z position from time difference at the ends of the chamber. For a signal of 56 mV generated on the sense wire at z = 90 cm, the z position measured will be 84.4 cm.

5.3.3   Variation of the S-Bend with Pulse Size

As the height of the signal on the sense wire varies, the dual threshold discriminator measures different times of arrival. This slewing of the output signal affects the form of the S-bends produced. Figure 4.61 shows the data points measured with the long test rig, with an applied threshold of 1 V, and a range of pulse sizes on the sense wire. As the pulse size gets smaller, a marked decrease in apparent velocity on the line can be seen. The only calibration done to the data is to subtract the calibration time difference.

Fig 4.61   Experimental Measurements of the Change in Dual Threshold "S-Bend" with Signal Height
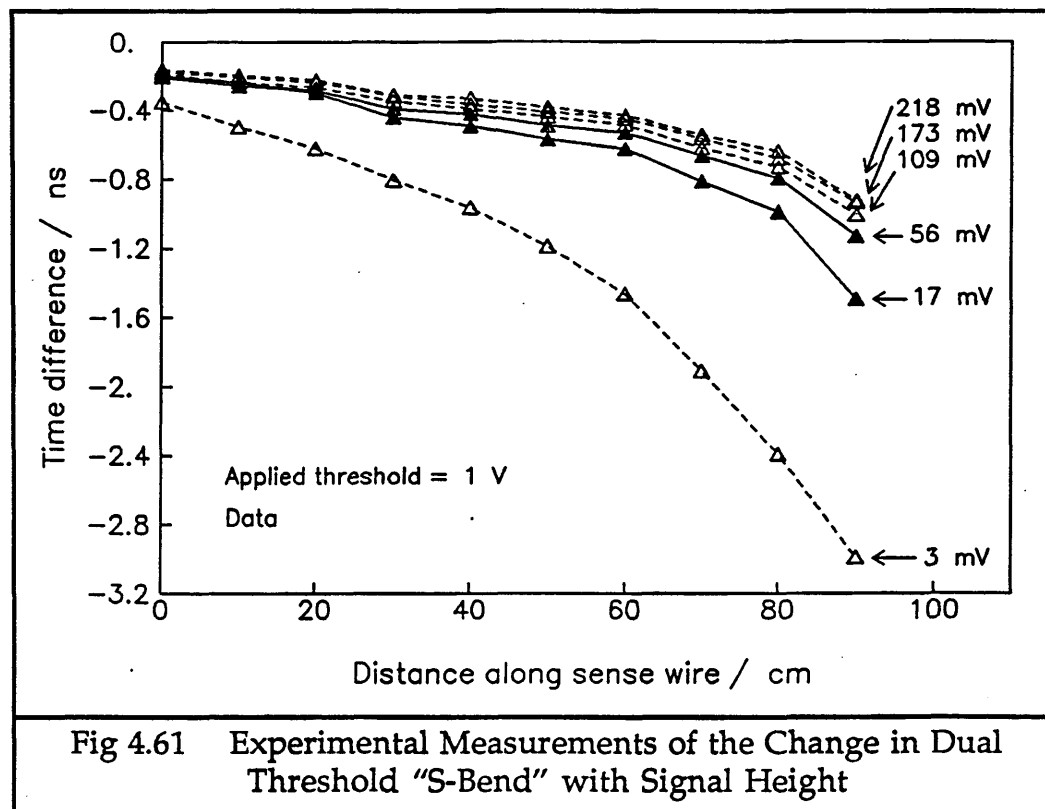
Figure 4.62 shows the results of the simulation of these S-bends with different pulse height. The trend of decrease in apparent velocity is well modelled, although the actual lines predicted for each pulse size do not exactly match those found in the data.
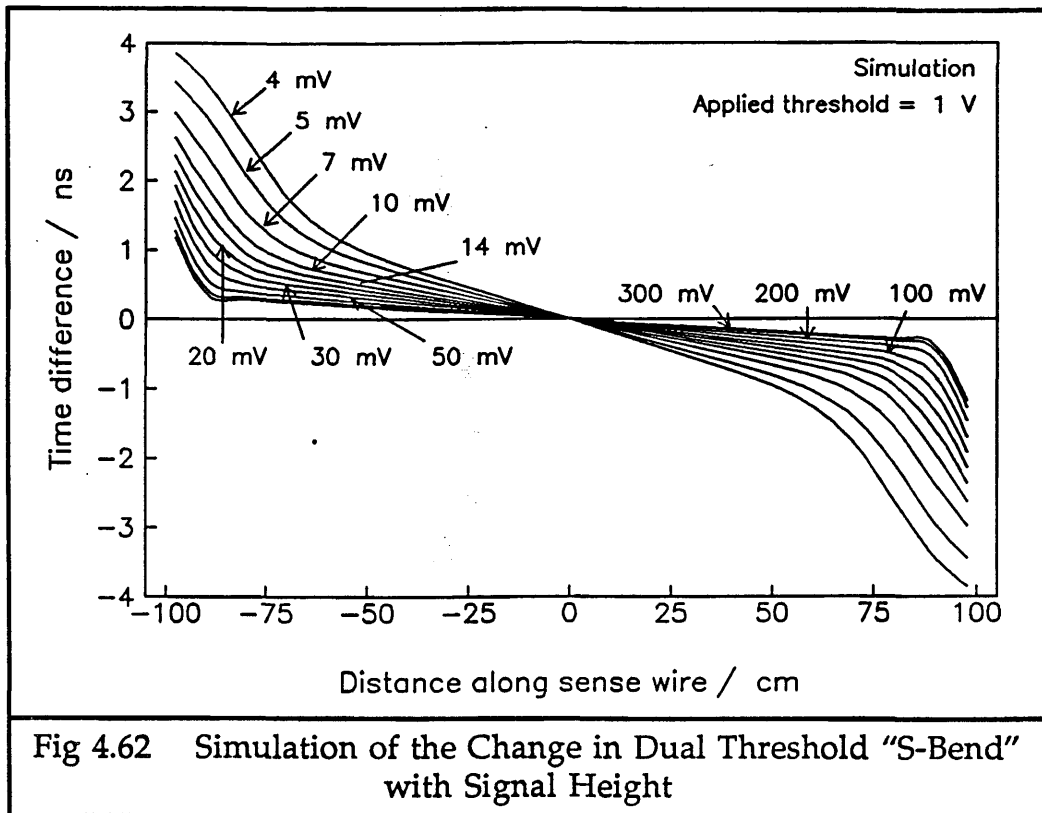
Fig 4.62   Simulation of the Change in Dual Threshold "S-Bend"
with Signal Height

In figure 4.63, the change in S-bend gradient, the apparent velocity, can
be seen as a function of pulse amplitude on the sense wire. The points on
the figure are data from the long test rig, and the line is from the
simulation.
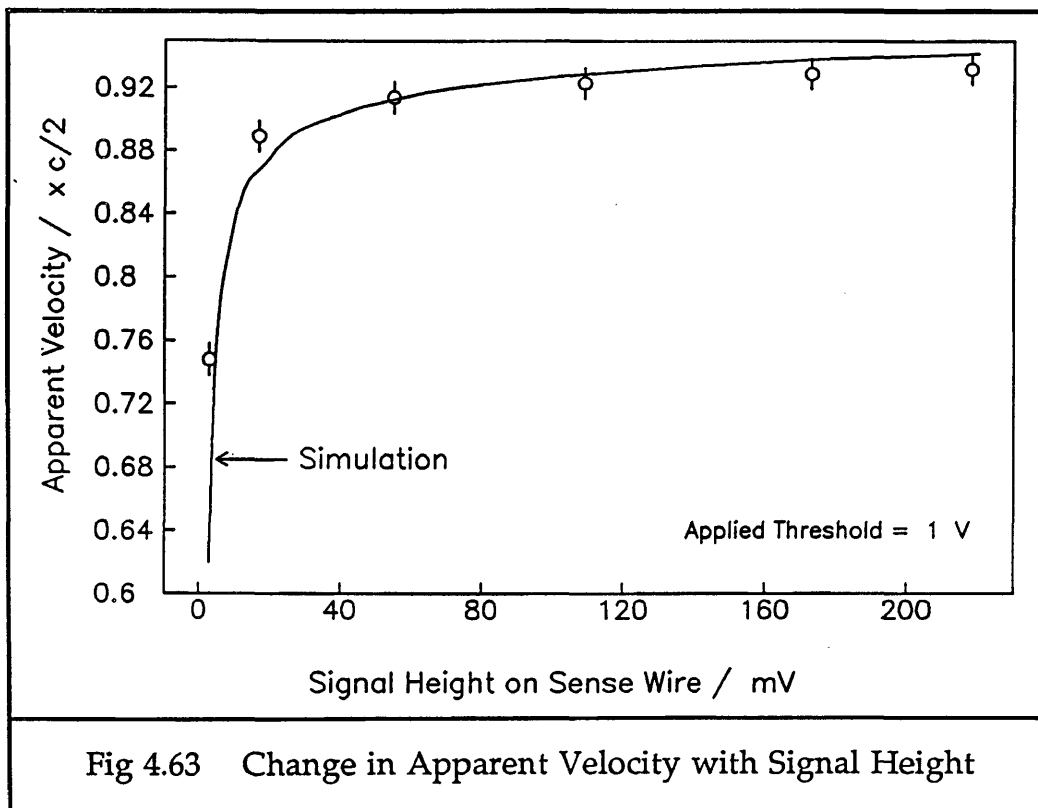
Fig 4.63   Change in Apparent Velocity with Signal Height

The worst effects of this change in S-bend are seen for small pulses near the ends of the sense wire. However, in the ITC, charged particles which produce signals near the end of the sense wires will be most likely to be travelling at small θ angles to the z direction from the interaction point. Therefore, they will traverse a long section of the cell, and this will lead to a large pulse being produced on the wire. This means that the very worst effects of the slewing of time difference with pulse size will be mainly avoided.

5.3.4 Spread of Values Measured

The root mean square of time differences, σ_t, taken at any point on the wire for any pulse height gives a measure of how reliable the result is under those conditions. It was calculated from 1000 readings in each position with each pulse height. Figure 4.64 shows the change of σ_t along the sense wire, for different pulse heights, for the dual threshold discriminator.

Fig 4.64   Variation of the Spread of Time Differences along the
Sense Wire with the Dual Threshold Discriminator
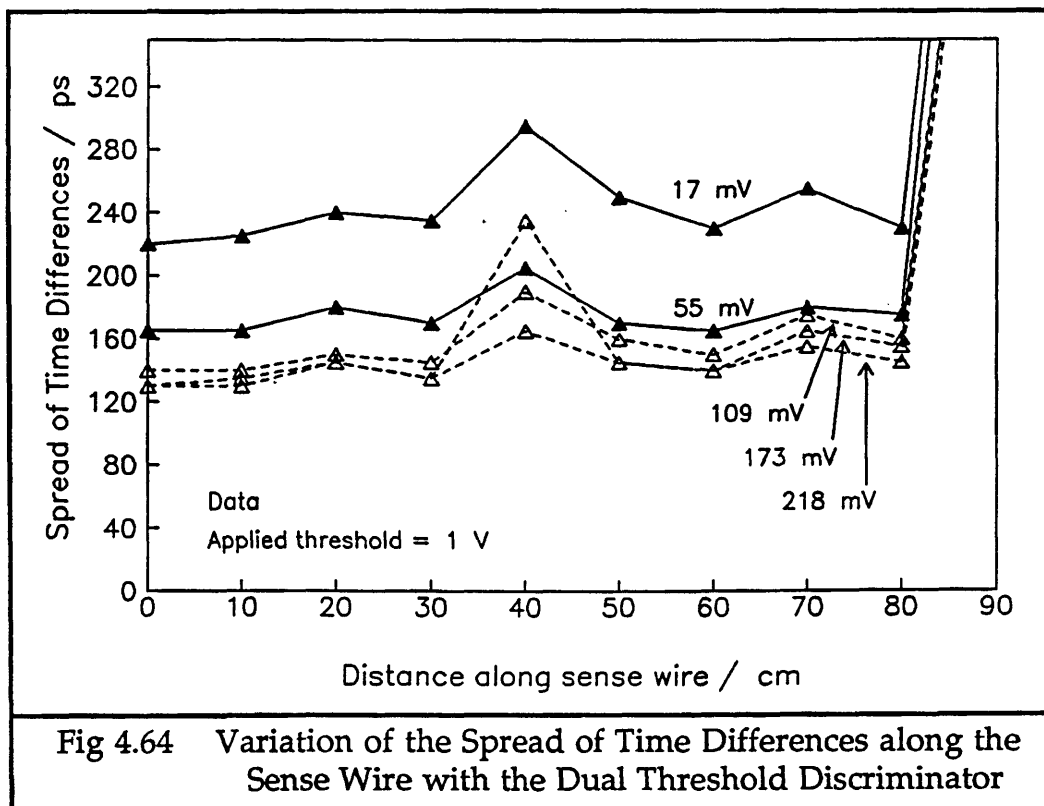
The apparent jump in values of σ_t at $z = 40$ cm for all the pulse heights is due to the fact that all the values for different pulse heights in one z position were measured together at the same time. The screening aluminium foil was then unwrapped to shift the hooks along the wires, and rewrapped. This meant that in each z position the screening against

253

external high frequency pickup was slightly different. Therefore, the irregularity in the value of σ_t, especially at z = 40 cm, is not a significant feature of the operation of the discriminators.

The very large increase in spread of time differences measured at z = 90 cm was not caused by loose wrapping of the aluminium foil, but is a real effect of the system.

The spread measured is approximately constant at any one z position for large pulses, but as they get smaller, the distribution widens, meaning that the position error in the chamber gets worse. This can be seen in figure 4.65, where the mean spread of time differences over the length of the chamber up to and including 80 cm, is shown against pulse size on the sense wire.

Fig 4.65   Variation of the Mean Spread of Time Differences with Signal Height and the Dual Threshold Discriminator
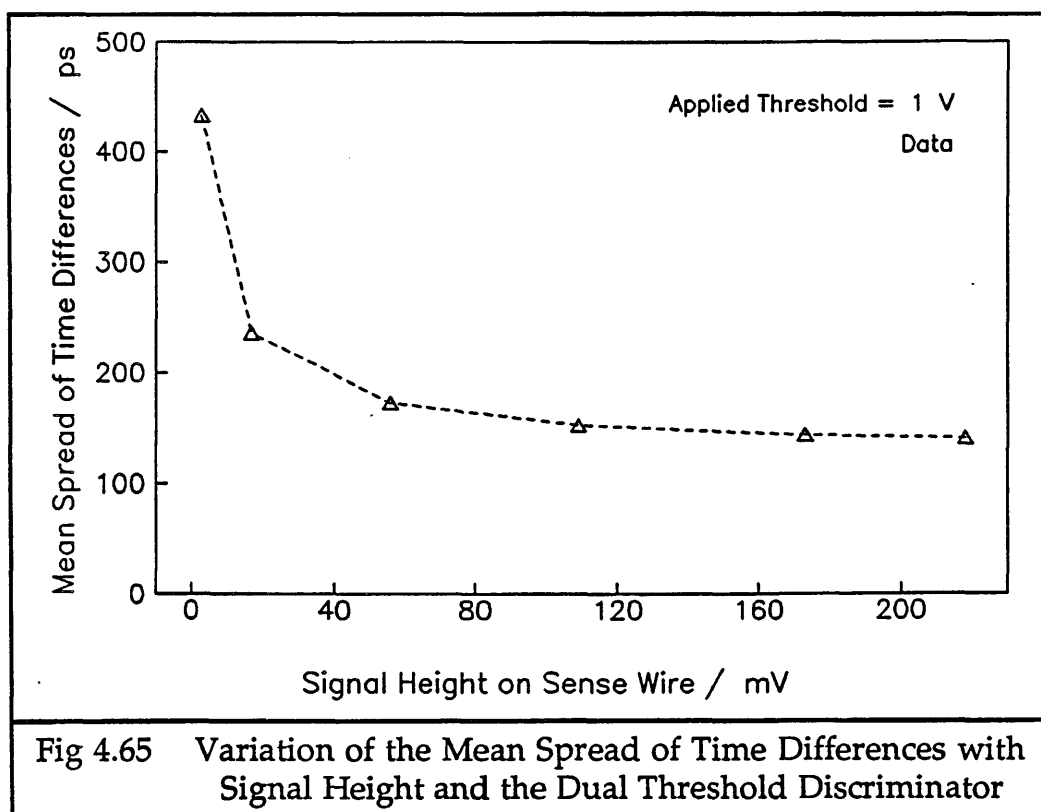
A mean value for σ_t can be calculated for the dual threshold discriminators, for later comparison with that from the constant fraction ones. Using the values for the signal sizes near the ends of the range of pulse sizes which do not saturate the amplifier, (ie. 17 mV and 56 mV), and from the next pulse size up (109 mV), which saturates the amplifiers if it travels less than ~ 1 m on the sense wire, and averaging along the whole length of the chamber, a value of σ_t = 495 ps is obtained. These signal sizes cover the range of sizes expected in the ITC.

5.3.5 The Effects of Changing the Threshold

a) Changes in the Spread of Values Measured

In order to reduce the spread of time differences measured, the threshold level can be raised to bring it above the noise on the signal. The effect of this from the test rig data, can be seen in figure 4.66. The mean spread of time differences over all signal sizes and averaged over the length of the chamber reduces to ~ 50 ps, the width of one TDC bin.

Fig 4.66   Variation of the Mean Spread of Time Differences
with Discriminator Threshold Level
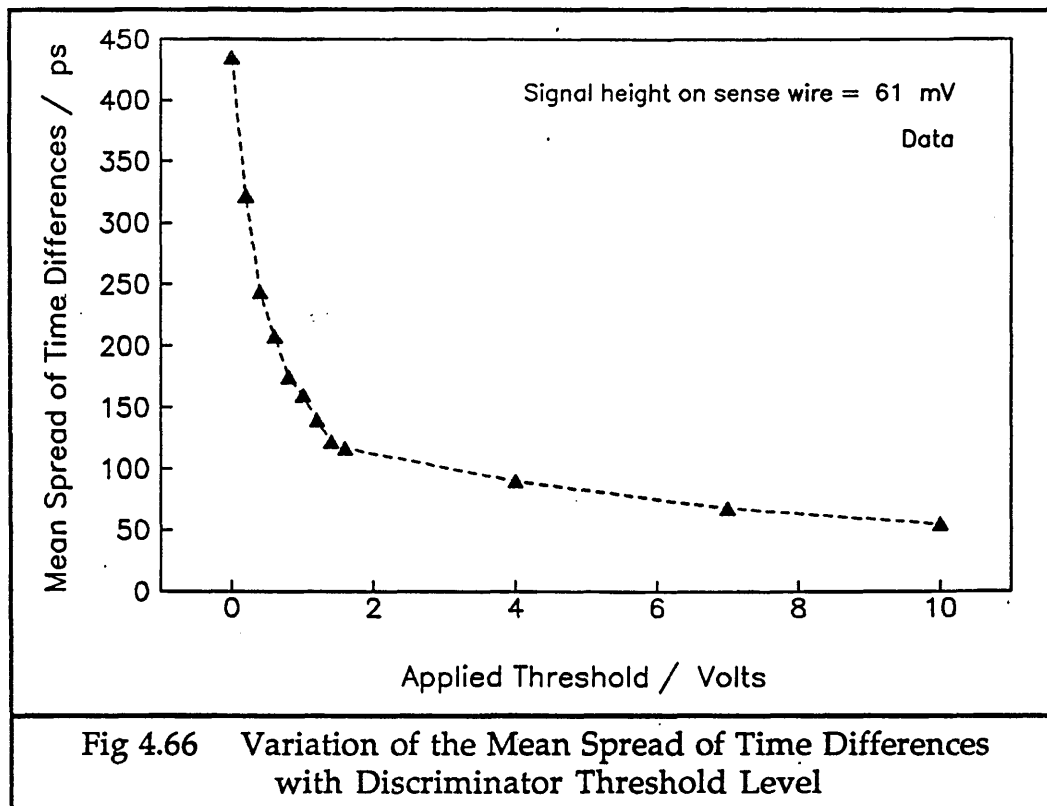
b) Changes in the S-Bend

If the threshold level on the dual threshold discriminator is raised, in order to reduce the spread of values measured, then the S-bend shape changes, because the higher threshold level sees more of the reflection on the leading edge of the signal. Figure 4.67 shows the results from the long test rig of increasing the threshold and the effect on the S-bend. An increase in the deflection of the tail of the curve is seen. These data points have only been calibrated with the calibration time difference.
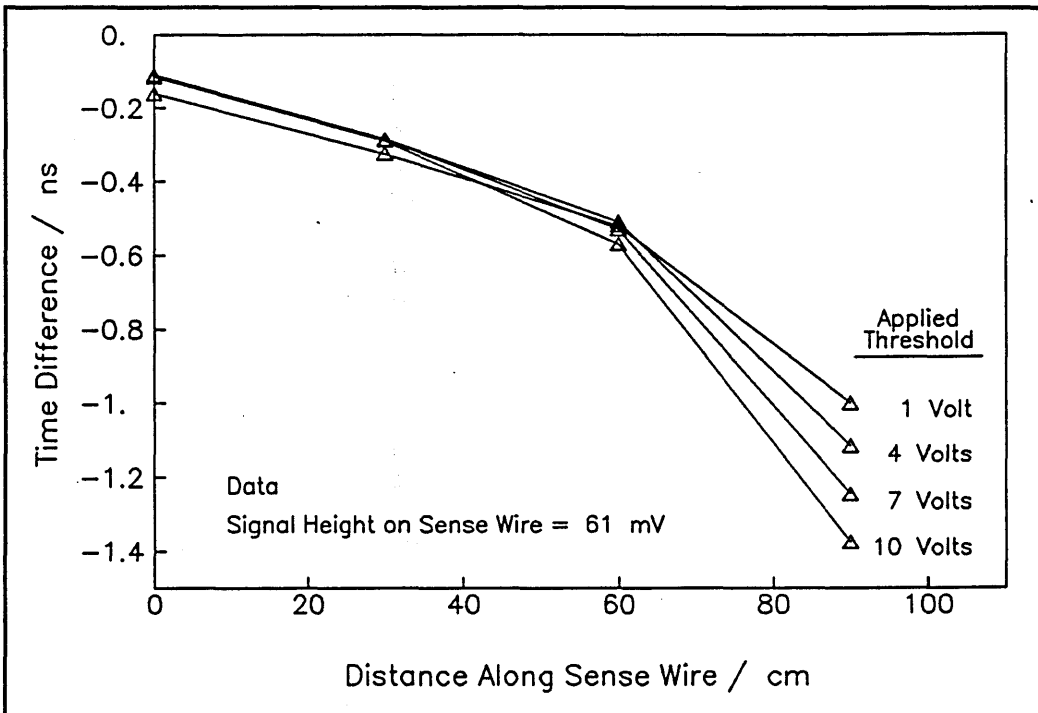
Fig 4.67   Experimental Measurements of the Change in the
"S-Bend" with Discriminator Threshold Level

Figure 4.68 shows the simulation results for these S-bends with
different threshold levels. The simulation results in figure 4.68
qualitatively reproduce the data in figure 4.67.
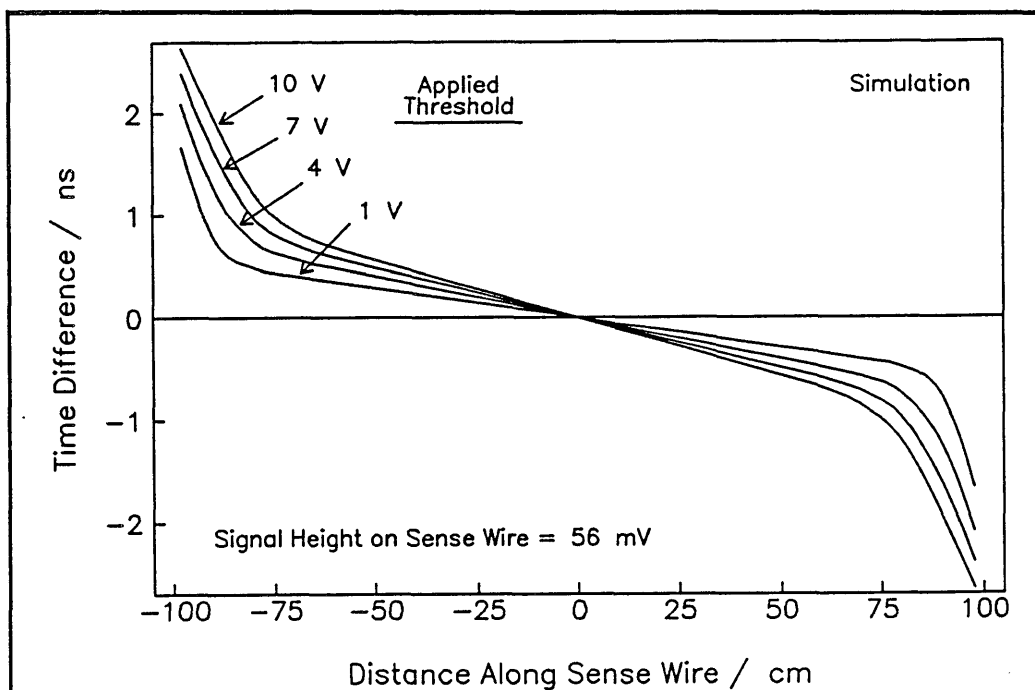
Fig 4.68   Simulation of the Change in "S-Bend" with
Discriminator Threshold Level

c) Changes in the Time Difference

The change in the S-bends can be further shown by looking at the difference in times measured at each end of the sense wire. Figure 4.69 shows the time difference measured, from the simulation, with different pulse heights at z = 42 cm on the sense wire. This position has been chosen in order for these results to be comparable with those for the constant fraction discriminator in Section 5.4.8. These time differences have not been subtracted from the ideal time difference and have no need of calibration.

| Fig 4.69 | Simulation of the Change in Measured Time Difference with Signal Height and Discriminator Threshold Level |
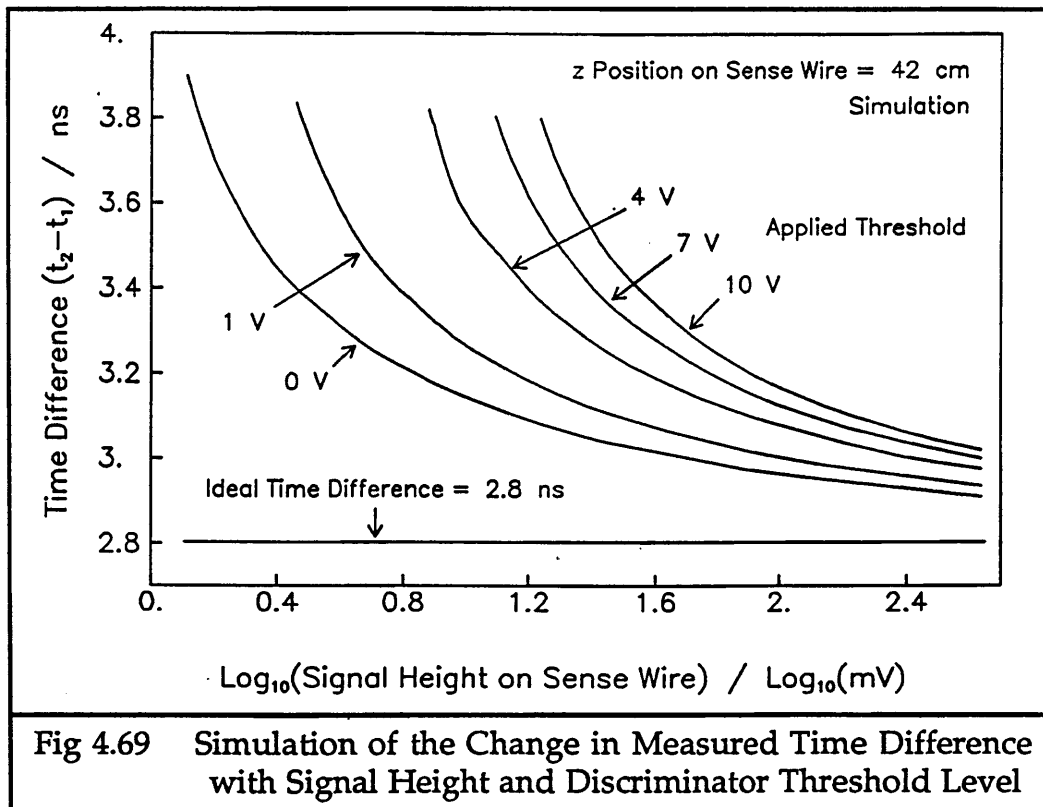
In figure 4.69, the range of pulse heights on the sense wire which do not saturate the discriminator goes up to 61 mV, $(\log_{10}(61\mathrm{mV}) = 1.79)$. Signal sizes in the ITC will be mainly in the region where there is the most rapid change in the time difference measured.

The difference in arrival times was measured with the long test rig for the calibration pulses, as a function of threshold. These results are shown in figure 4.70.

Fig 4.70   Change in Calibration Time Difference with
Discriminator Threshold Level
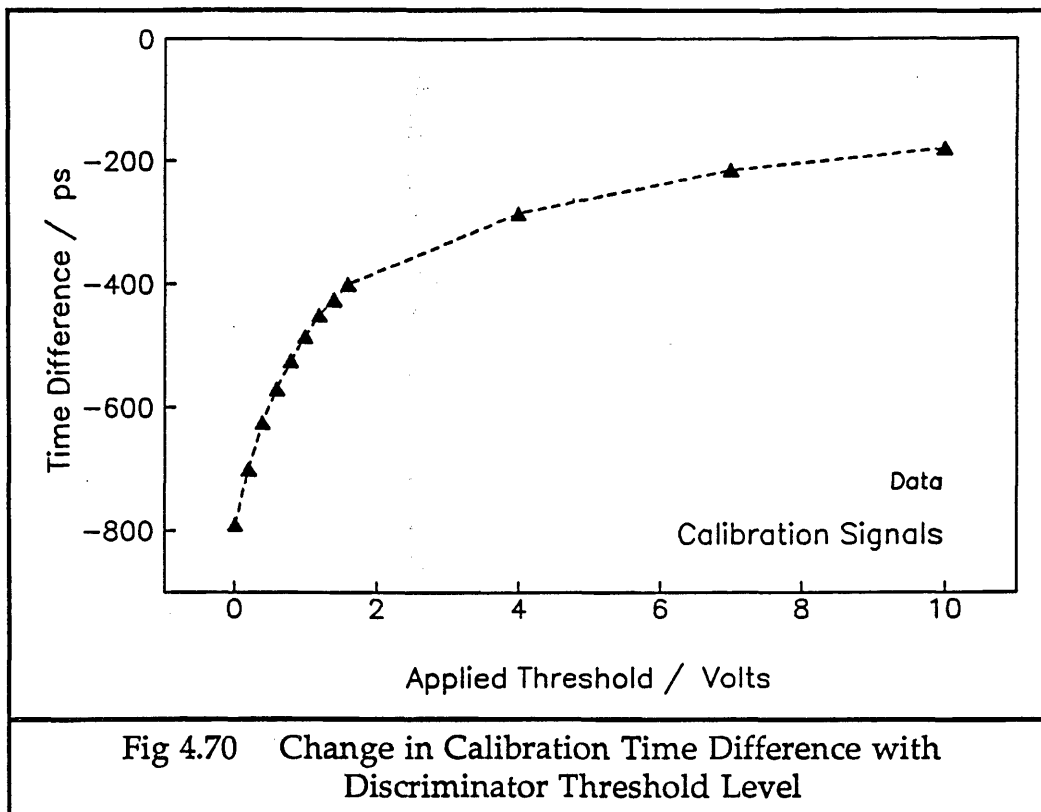
The shift in time difference with the calibration signals shows that the signals are not the same size when they arrive at the discriminators. This confirms the reason put forward for the non-zero crossing point of the dual threshold data for the S-bend, in Section 5.3.2 a).

d) Loss of Small Signals

As the threshold is raised, and the spread of time differences decreases, there is also an effect which is detrimental to the timing measurements. Small signals on the sense wires no longer reach the high threshold level and their times are lost from the readout. Figure 4.71 shows the signal heights in the ITC at which timing from small signals is lost as the discriminator threshold is raised, from the simulation.
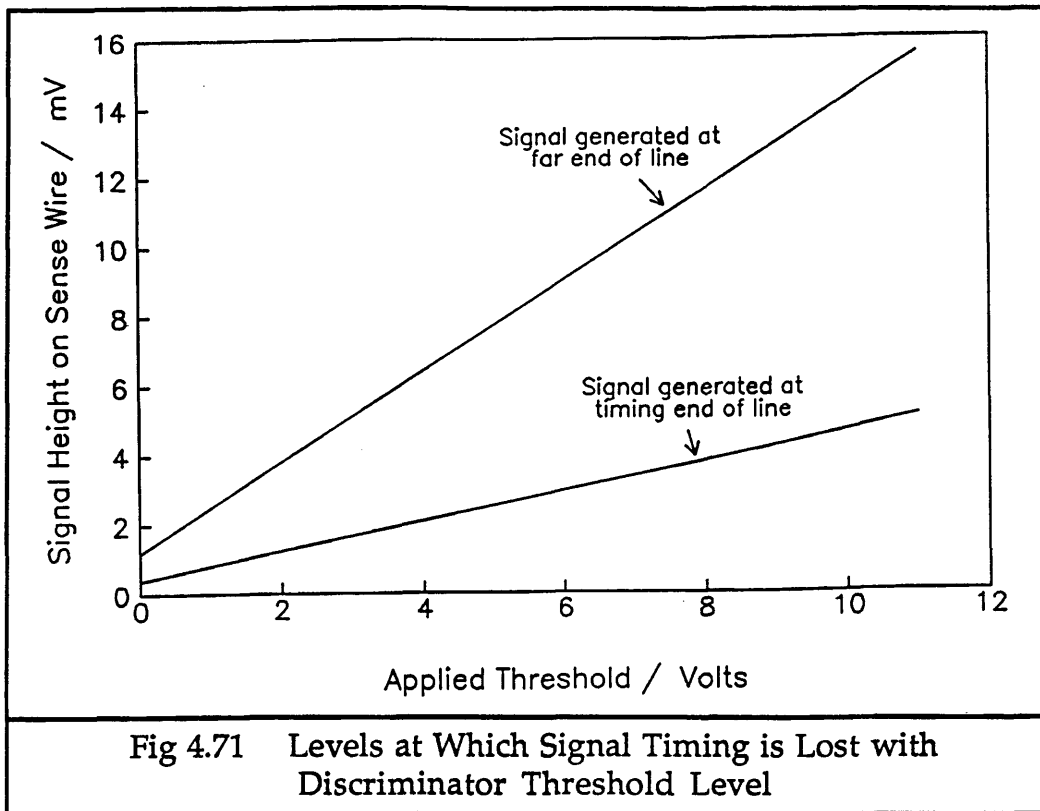
Fig 4.71   Levels at Which Signal Timing is Lost with
Discriminator Threshold Level

The lower line shows the minimum size a signal must have when it is at the timing end, and so is not attenuated by the sense wire before readout, for it to pass the discriminator high threshold and be read out. The upper line shows the minimum size a signal must have when it starts at the far end of the sense wire, and is attenuated by nearly 2 m of transmission line before it is read out, if it is to pass the high threshold. The series resistance used for this plot is 139 Ω/m. Therefore, for signals to be read out at both ends of the wire, no matter where along the sense wire they are generated, the height must be greater than the upper line in figure 4.71, at the appropriate threshold.

The implications of this are that if a threshold of 10 V, say, were to be chosen, in order to operate with a minimal spread of time differences, then no sense wire signals smaller than ~ 7 mV would be read out at all, and many of the signals between 7 mV and 10.4 mV would only be read out at one end of the chamber, sometimes producing a drift time for the r-ø readout, but not producing a time difference for the z position and the space point trigger. This would lose a large number of genuine hits from the trigger.

When distortion of the signal on the sense wire is taken into account, then the upper line on figure 4.71 will be higher than it is shown.

5.3.6 Miscellaneous Results from the Simulation Program
for the Dual Threshold Discriminator

The simulation program can be used to show the contribution to the S-bend nonlinearity from the end reflections and the attenuation along the wire, by removing these effects from the model, and comparing the S-bends produced.

Figure 4.72 shows the effect of having various series resistances on the shape of the S-bend, for a starting signal of 56 mV and an applied threshold of 1 V. The line for $R = 0 \, \Omega/m$ shows that the deviation from $c/2$ along most of the length of the sense wire is caused by the series resistance of the wire, since when it is removed, there is no deviation from $c/2$. $R = 88 \, \Omega/m$ is the value of the series resistance measured with direct current. $R = 139 \, \Omega/m$ is the estimated series resistance for the sense wire signals, and $R = 400 \, \Omega/m$ is the figure needed to compensate for the lack of distortion and for the lack of discriminator slewing in the simulation. This value of R reproduces the S-bend seen in the data.

Fig 4.72   Simulation of the Change in Dual Threshold "S-Bend" with Series Resistance of Sense Wire
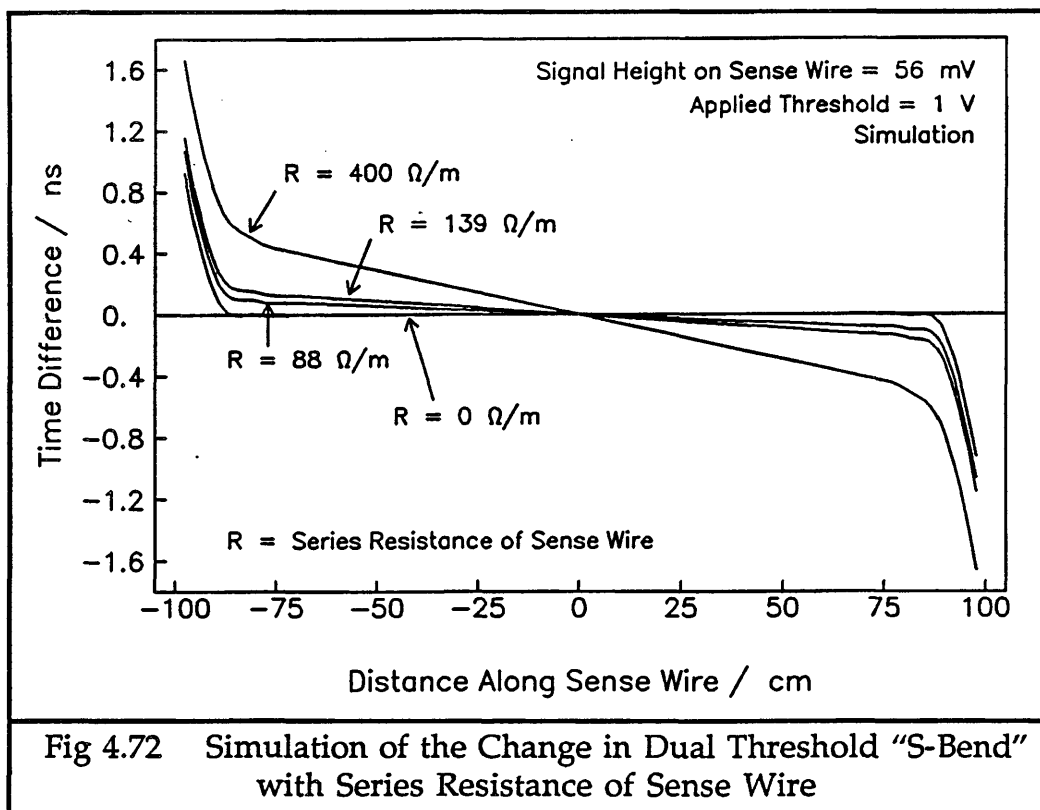
Figure 4.73 shows the dual threshold discriminator S-bend when the reflection is removed from the simulation model by setting $C = 0 \, pF$ and $R_{end} = 350 \, \Omega = Z_0$. This is compared with a standard S-bend, and it can be seen that there is a small contribution to the central linear section from the reflection, but most of the effect of the reflection is at the ends of the

chamber, where the tail of the distribution is produced.

Fig 4.73   Simulation of the Change in Dual Threshold "S-Bend"
with Sense Wire Termination
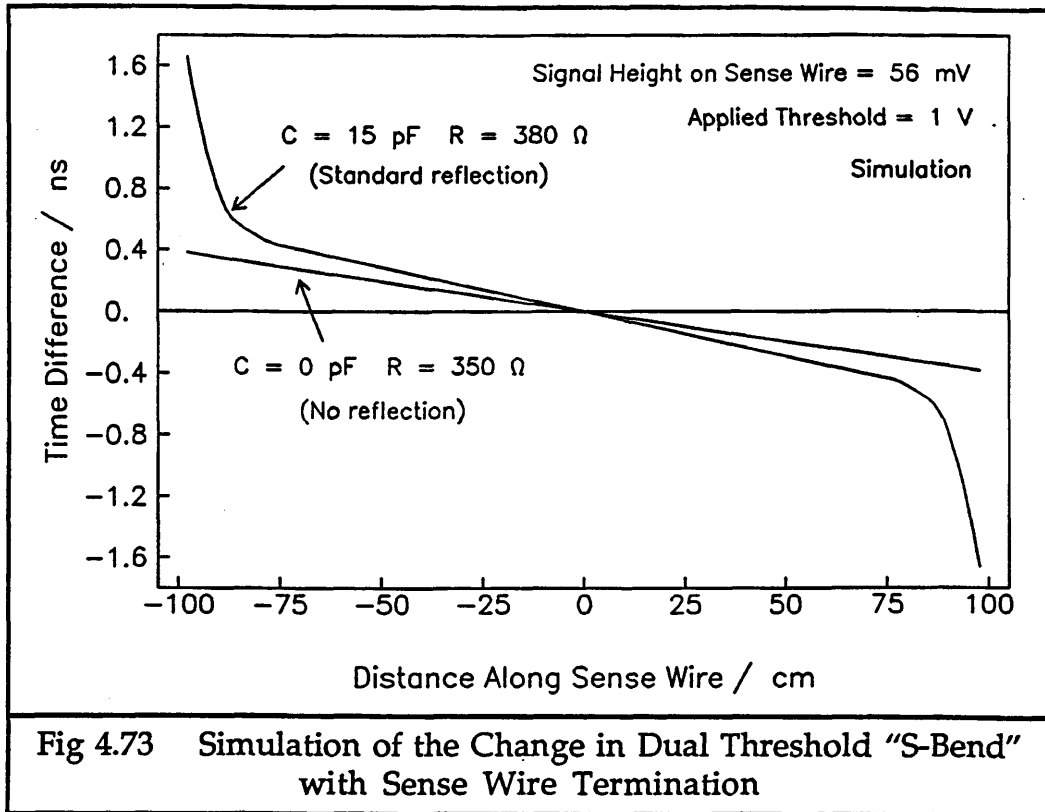
5.4   Constant Fraction Discriminator

5.4.1   Details of How it Works

The logic diagram for a constant fraction discriminator is shown in
figure 4.74.

Fig 4.74   Block Diagram of a Constant Fraction Discriminator
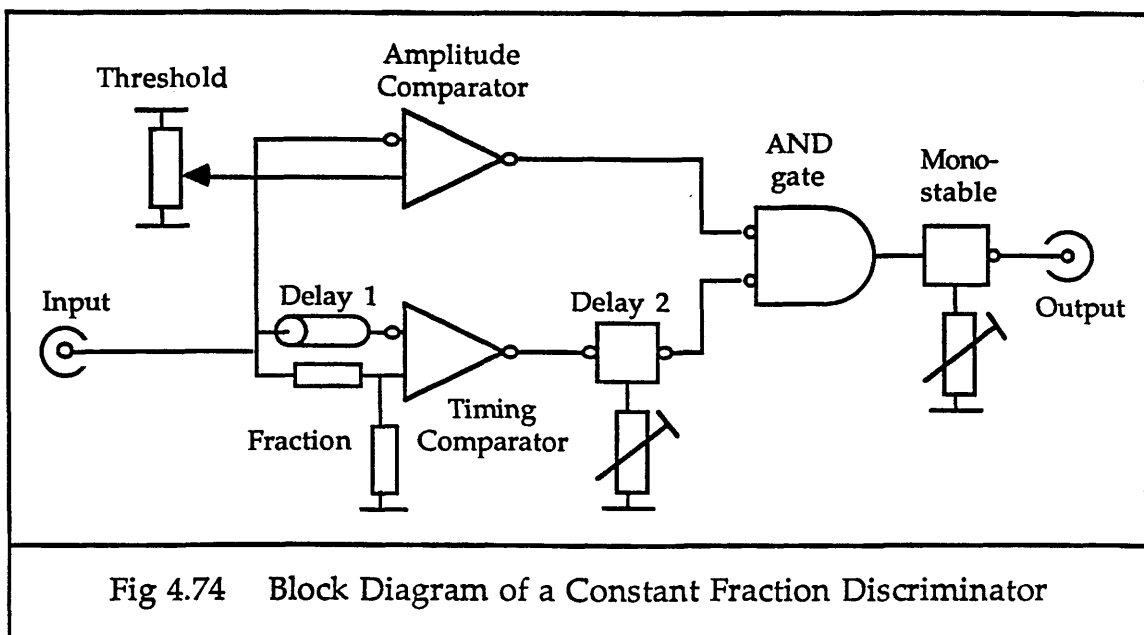
The standard values for fraction and delay are a fraction of 1/2 and a delay of 5 ns. These values are chosen with regard to the rise time of the signals to be discriminated. Other values were also used with the long test rig, in order to test the effects of changing the fraction and delay on the S-bend and spread of time differences measured. These were delays of 2.5 ns and 7.5 ns, and a fraction of ~ 0.36.

5.4.2 S-Bend Results and Simulation

The standard S-bend, produced with constant fraction discriminators having fraction 1/2 and delay 5 ns, and signals 56 mV in amplitude on the sense wire is shown in figure 4.75. The data points are from the long test rig, and the line is from the simulation.
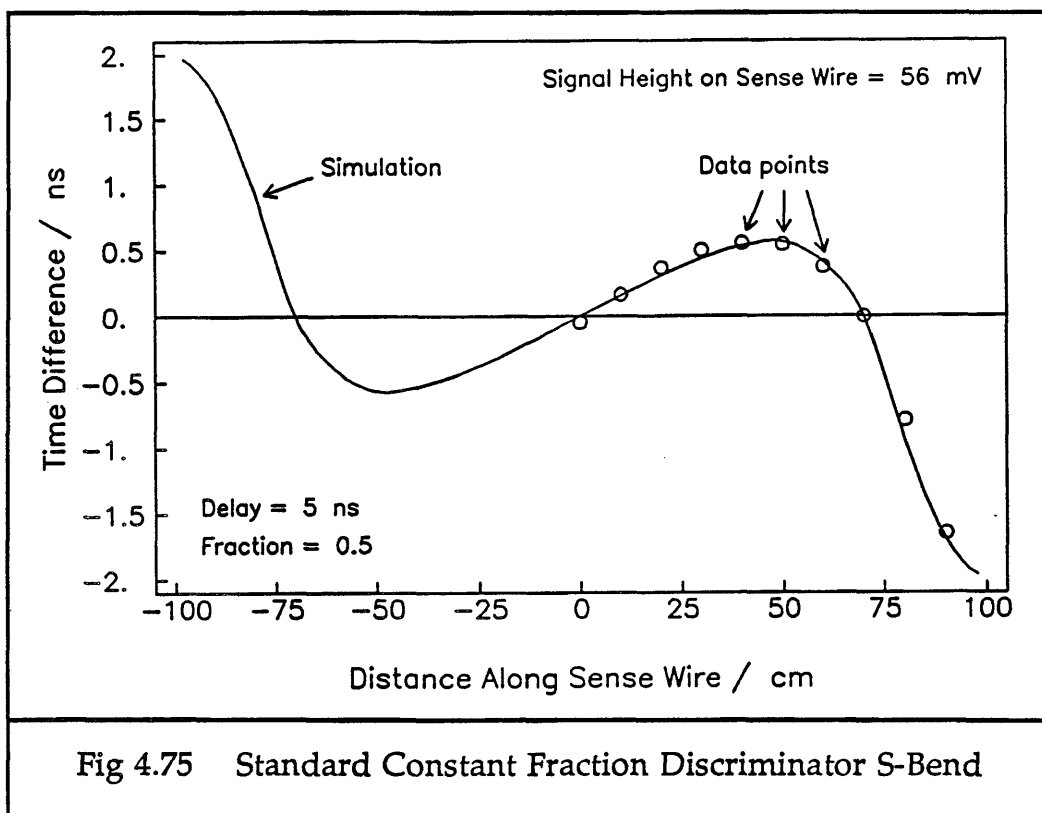
Fig 4.75   Standard Constant Fraction Discriminator S-Bend

There are several things worth noting about this nonlinearity from c/2 in the z position with time difference.

a) Zero Crossing

With the constant fraction discriminators, which are scarcely affected by variations in signal height in the range of the calibration pulse sizes, the calibration works successfully on the data, so that a line through the data points after calibration passes through the origin, within the tolerance of 1 cm.

b) Deviation from c/2

The output signal from the constant fraction discriminators is produced from half way up the signal leading edge (if the fraction used is a half). This is in a region where the leading edge of the signal is affected by the reflections in the chamber, wherever in the chamber the signal started. Therefore, the shape of the S-bend is dominated by the effects of the reflections, when using the constant fraction discriminator. This leads to an increase in the apparent velocity above c/2 in the central ~ 80 cm of the sense wire. This then slows down, and the apparent velocity decreases from here to the ends of the sense wire.

The cause of these effects can be seen in figure 4.76, which shows the summed discriminator signal after delaying half the signal by 5 ns, and inverting the other half and reducing it in height by a half, and then recombining them. The discriminator output signal is produced when this signal crosses the horizontal axis and changes sign.

Fig 4.76   Constant Fraction Discriminator Signals from the Long Test Rig
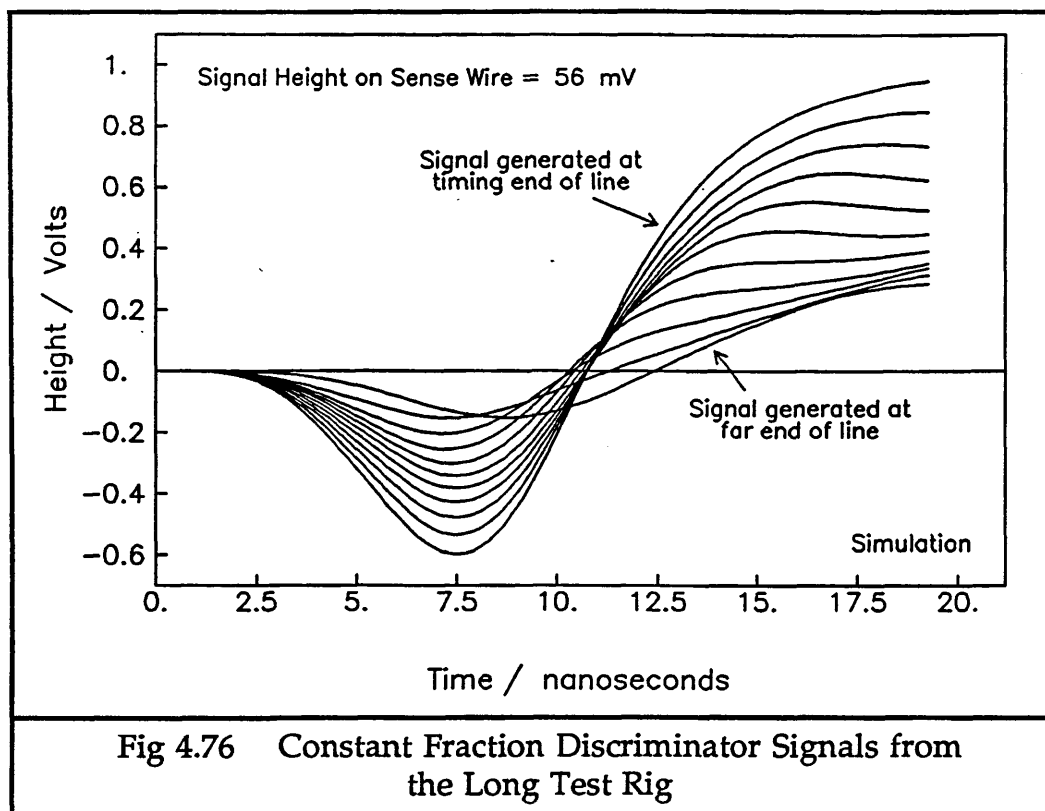
The signals in figure 4.76 started at 56 mV on the sense wire, with the largest signal starting at the timing end of the sense wire, and the smallest starting at the far end of the sense wire. The other signals in between started at equidistant intervals along the wire. For the signals which travel nearly the length of the sense wire, the large delaying effect of the reflection can be seen on the crossing time. Also, the change of direction of the effect can be

seen for the three signals which travel the furthest, leading to the tail in the S-bend which is similar to that seen with the dual threshold discriminator.

c) Variation of the S-Bend with Signal Size

For signals on the sense wire less than ~ 61 mV in amplitude, there is ideally no dependence of the S-bend shape or size on signal height. There is actually a very small effect from the intrinsic slewing of the constant fraction discriminator, which will be explained in Section 5.4.7, but this is not of any great significance provided that the discriminator circuits are set up carefully to minimise the effect. Figure 4.77 shows that the discriminator output signal is independent of the amplitude of the input signal.

Fig 4.77   The Effect of Pulse Size on Timing with the
Constant Fraction Discriminator
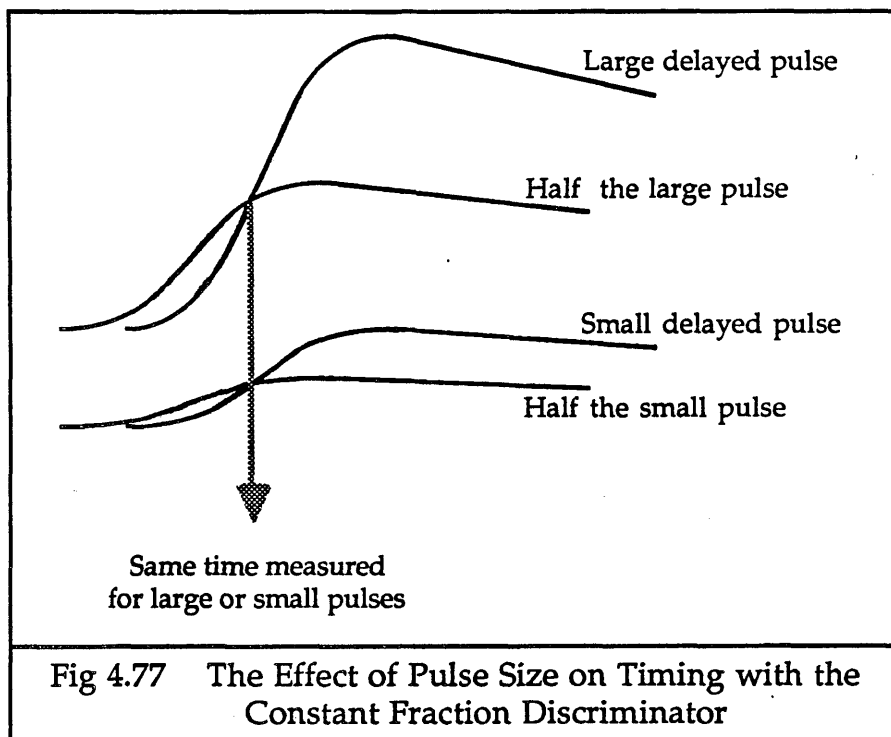
5.4.3   The Effect of Amplifier Saturation on the S-Bend

When the signals from the sense wire saturate the amplifiers, then the constant fraction discriminator no longer produces its signal at a fixed fraction of the leading edge of the signal, but behaves like a fixed threshold discriminator. This can be seen in figure 4.78.

As the amplifiers saturate first at one end of the sense wire and then at both ends, the S-bends produced from larger and larger pulses gradually change from having the shape in figure 4.75, until the nonlinearity resembles that found with the dual threshold discriminator. This can be seen in figure 4.79 for the data from the long test rig, with a discriminator of fraction 1/2 and delay 5 ns. The S-bend from the 3 mV signal is shifted

because of the inbuilt slewing of the discriminator, which is explained in Section 5.4.7.
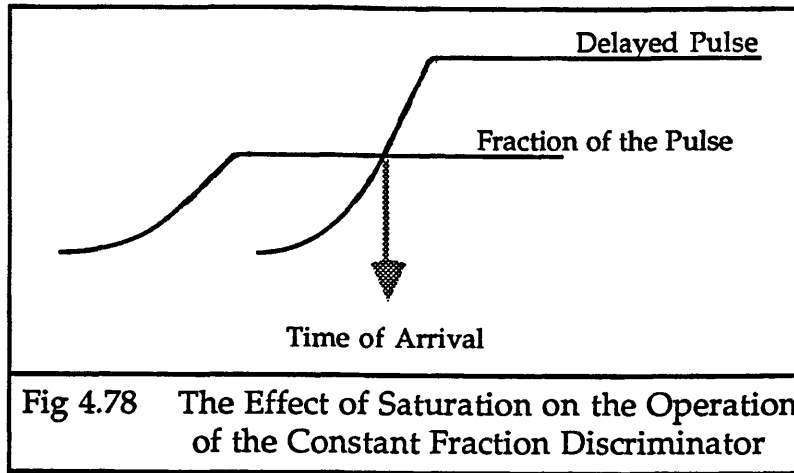
Fig 4.78   The Effect of Saturation on the Operation of the Constant Fraction Discriminator
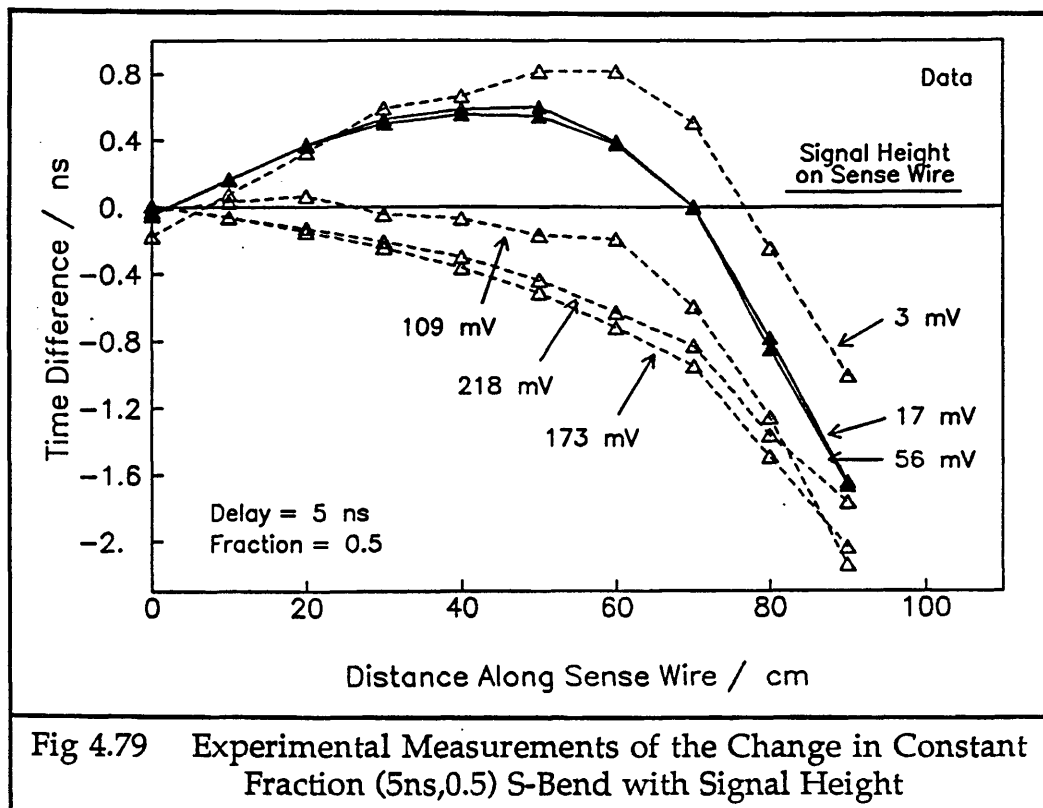
Fig 4.79   Experimental Measurements of the Change in Constant Fraction (5ns,0.5) S-Bend with Signal Height

Figure 4.80 shows the S-bends from the simulation program, for the same discriminator fraction and delay, for signals from when there is no saturation, to when the amplifiers are just saturated at both ends of the chamber, with a chamber pulse height of 170 mV. This qualitatively reproduces the data, although it does not saturate at exactly the same signal level.
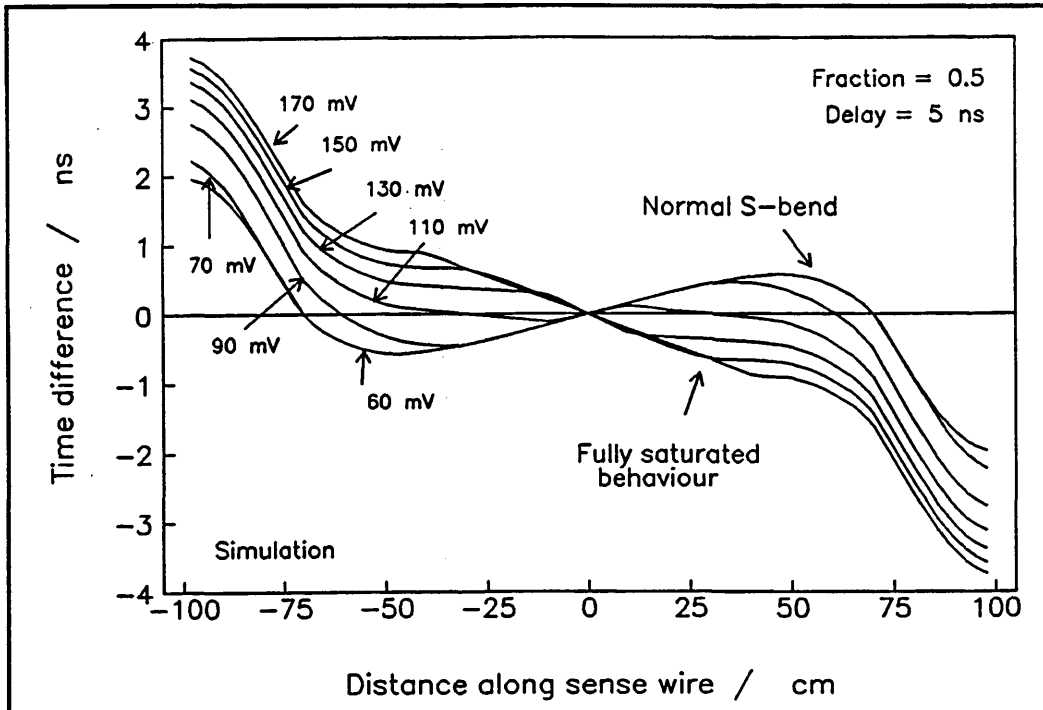
Fig 4.80   Simulation of the Change in Constant Fraction
(5ns,0.5) S-Bend with Signal Height

If the signal heights are allowed to continue to increase, then the apparent velocity in the S-bend increases slightly, in a similar effect to that seen with the dual threshold discriminator in figure 4.62 with large signals. This can be seen in figure 4.81. This effect is seen in the data in figure 4.79 with the pulse heights at 173 mV and 218 mV.
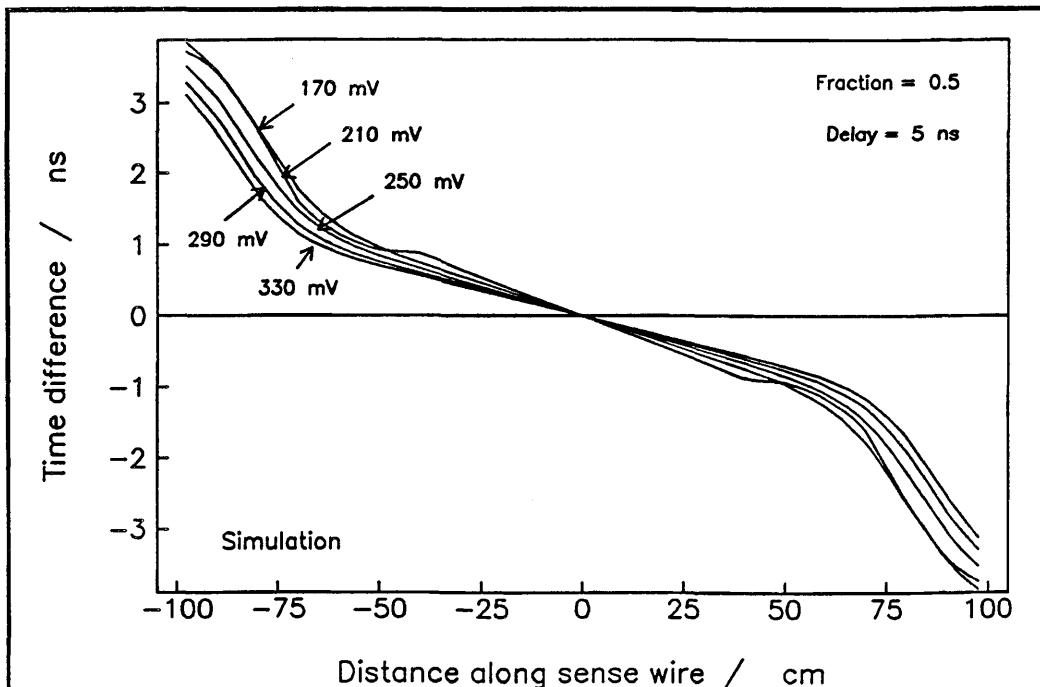
Fig 4.81   Simulation of the Change in Constant Fraction S-Bend
with Very Large Signals

5.4.4 The Effects of Discriminator Delay on the S-Bend

Figure 4.82 shows the data taken with a constant fraction discriminator of fraction 1/2 and delay 2.5 ns, for the same set of signal heights as in figure 4.78 for the discriminator with fraction of 1/2 and delay of 5 ns. Figure 4.83 shows the data taken with discriminators of fraction 1/2 and delay 7.5 ns.

As the delay between the split signals on the discriminator boards is increased, from 2.5 ns to 7.5 ns, the shape of the S-bend changes. The crossing points of the S-bend with the axis move in towards the centre of the sense wire. This is because when the delay is longer, the timing is taken from higher up the signal leading edge, so there is more interference from the reflections. The reflections are significant over most of the chamber.

Conversely, if the delay is decreased, then the crossing points of the S-bend move out towards the ends of the chamber. The timing is taken from lower down the pulse leading edge, so the effects of the reflection are observed only towards the ends of the sense wire. This relation between the length of the chamber over which the reflection affects the timing, and the delay used in the constant fraction discriminator can be seen in figure 4.84.

Fig 4.82   Experimental Measurements of the Change in Constant Fraction (2.5ns,0.5) S-Bend with Signal Height
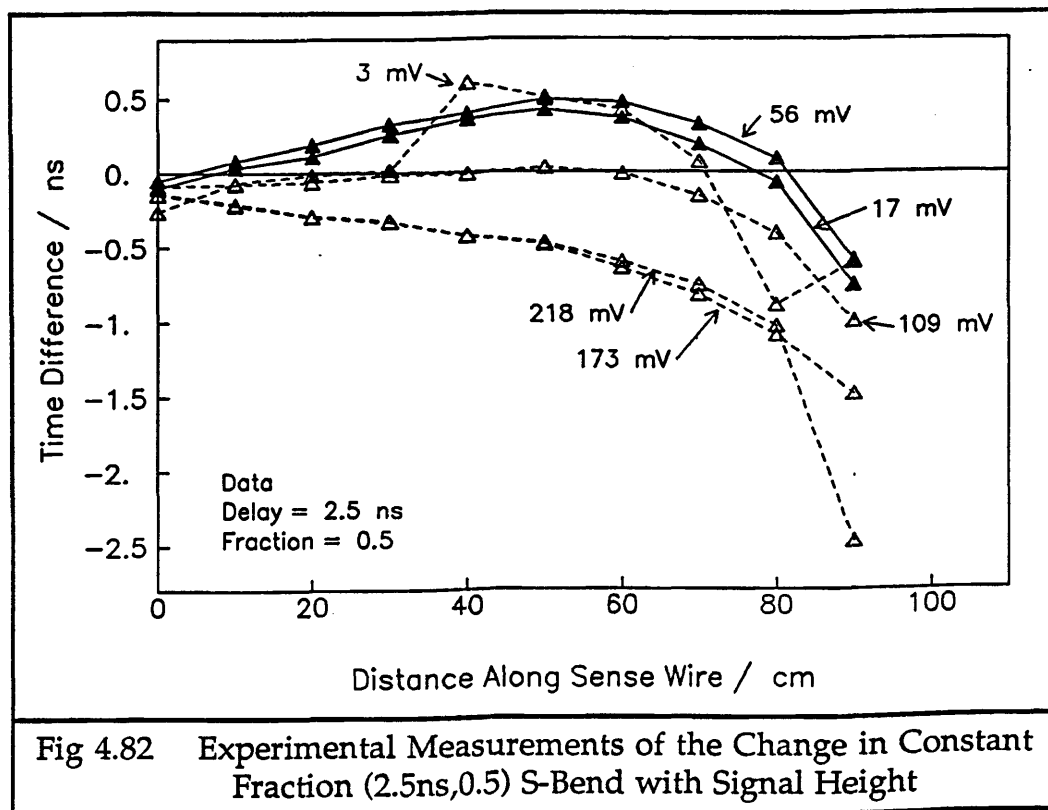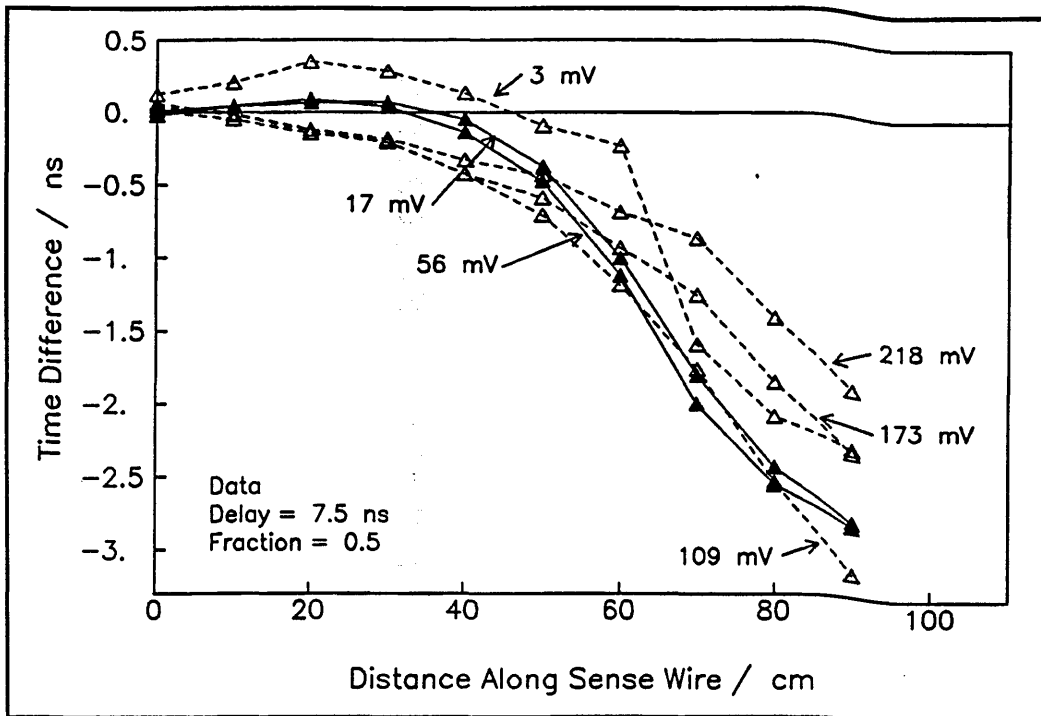
Fig 4.83   Experimental Measurements of the Change in Constant
            Fraction (7.5ns,0.5) S-Bend with Signal Height
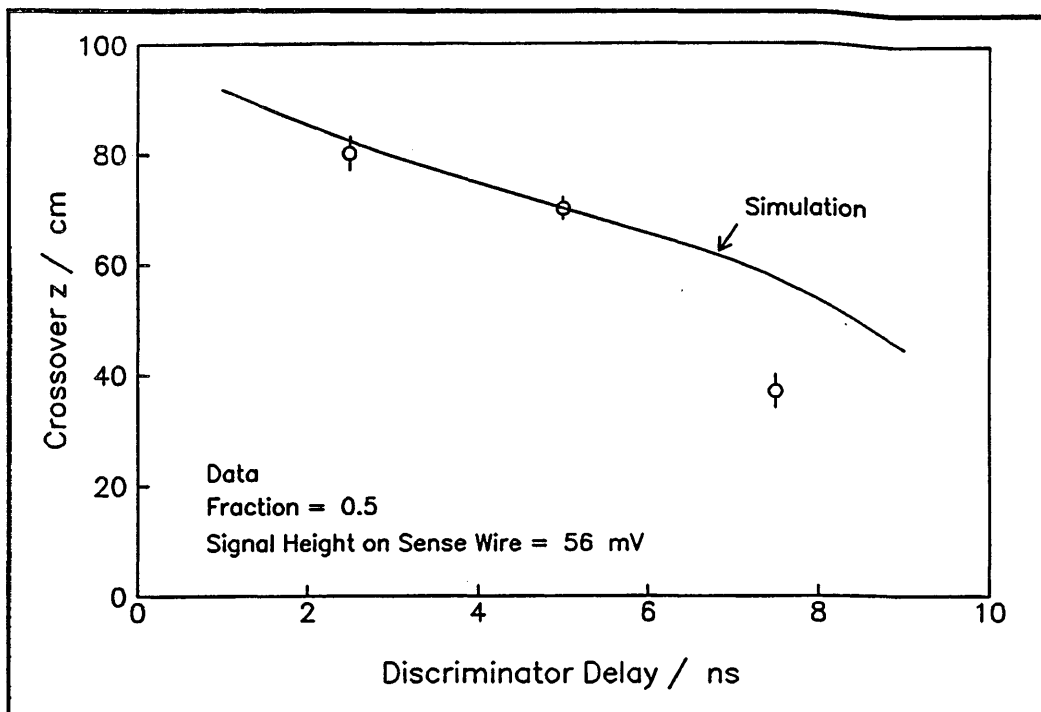
Fig 4.84   Change in S-Bend Crossover with Discriminator Delay

Figure 4.85 presents the results from the simulation, showing how
these three S-bends, from discriminators with different delays, vary with
respect to each other. The signal height on the sense wires was 56 mV.

Fig 4.85 Simulation of Change in S-Bend with Discriminator Delay
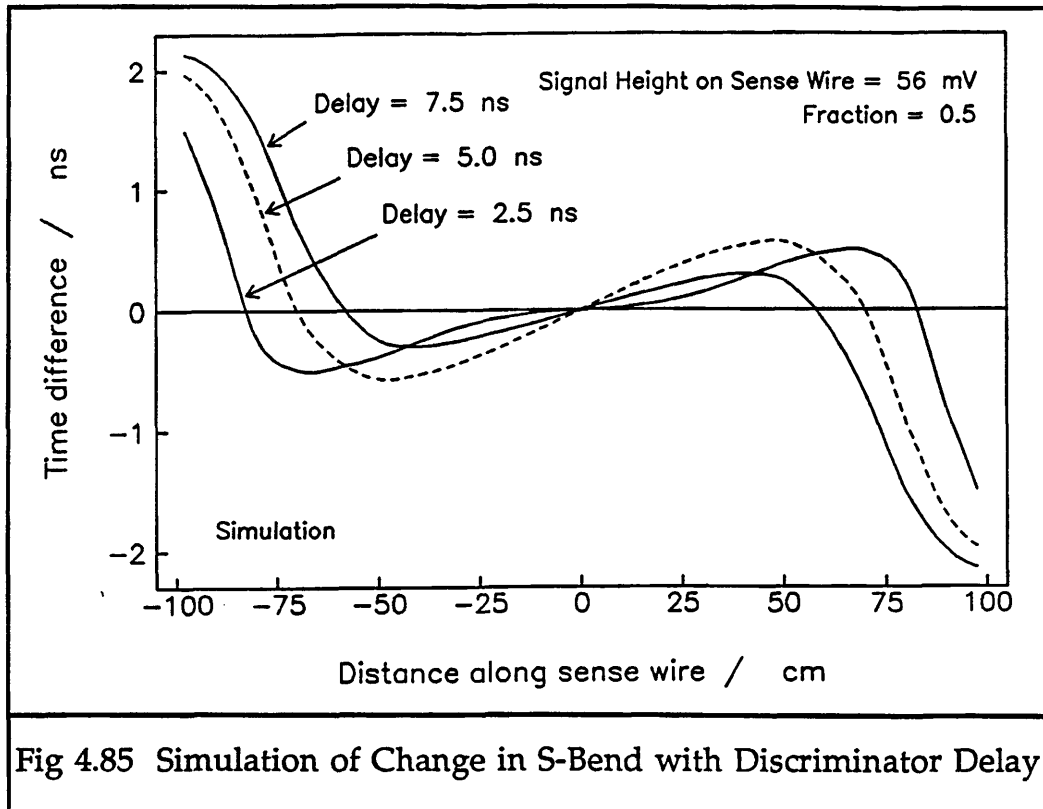
Figures 4.86 and 4.87 show the predicted behaviour of the S-bends when the signals saturate the amplifiers, for the discriminators of delay 2.5 ns and 7.5 ns.

Fig 4.86 Simulation of the Change in Constant Fraction (2.5ns,0.5) S-Bend with Signal Height
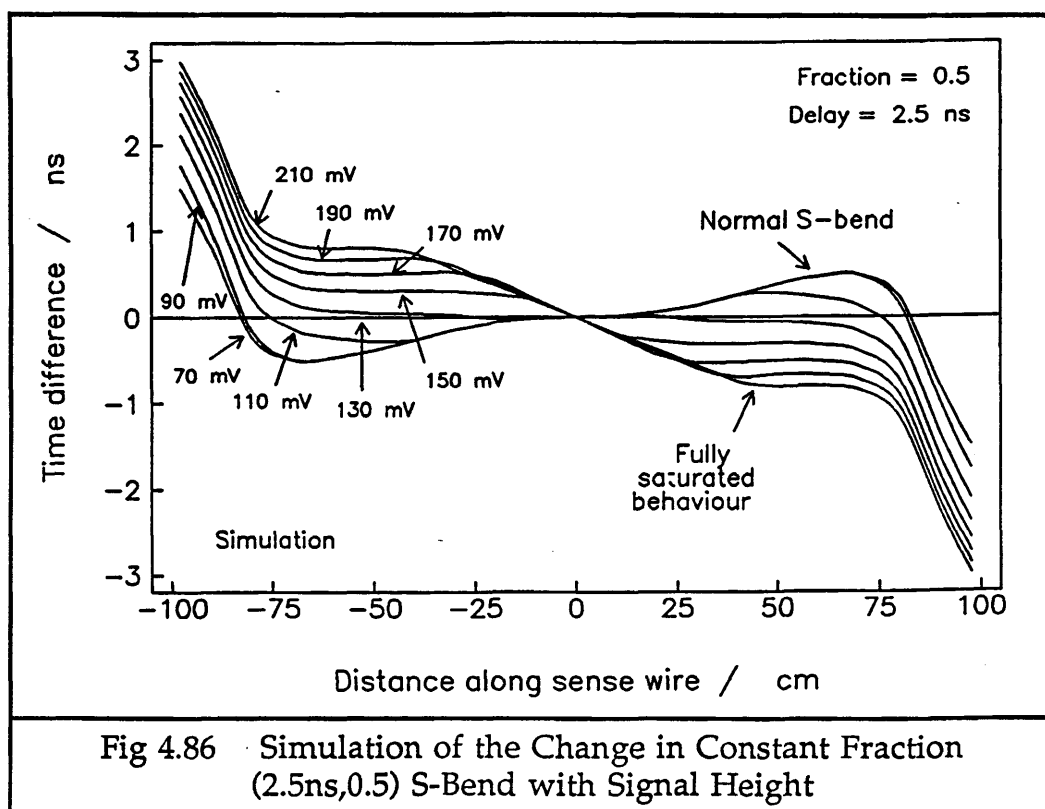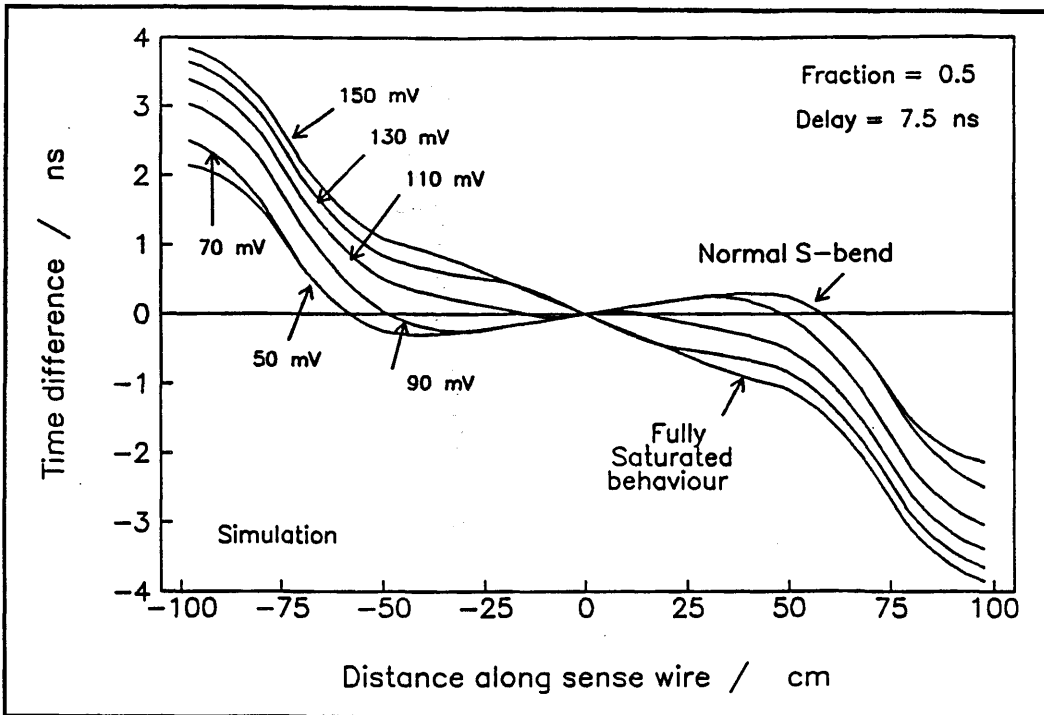
Fig 4.87   Simulation of the Change in Constant Fraction
            (7.5ns,0.5) S-Bend with Signal Height

5.4.5   The Effects of Discriminator Fraction on the S-Bend

Figure 4.88 shows the S-bends measured for a range of pulse heights in the long test rig using constant fraction discriminators with a delay of 5 ns and fraction of 0.36.
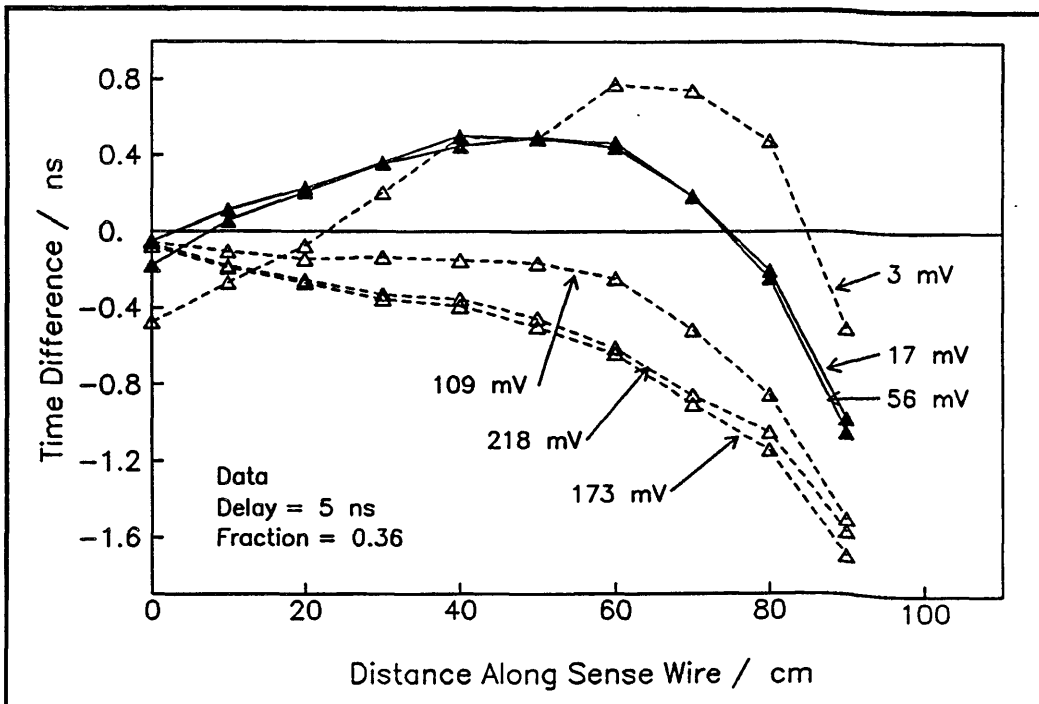
Fig 4.88   Experimental Measurements of the Change in Constant
            Fraction (5ns,0.36) S-Bend with Signal Height

The difference between this S-bend with mid-range pulse heights and that from the discriminator with 5 ns delay and fraction 1/2 is that there is less deviation from c/2 near the ends of the sense wire with the smaller fraction discriminator. This is because the timing is taken from lower down on the leading edge of the signals, so the effects of the reflection are less significant. This can be seen in figure 4.89.

Fig 4.89   The Effect on the Timing of Changing
the Fraction of the Pulse Used
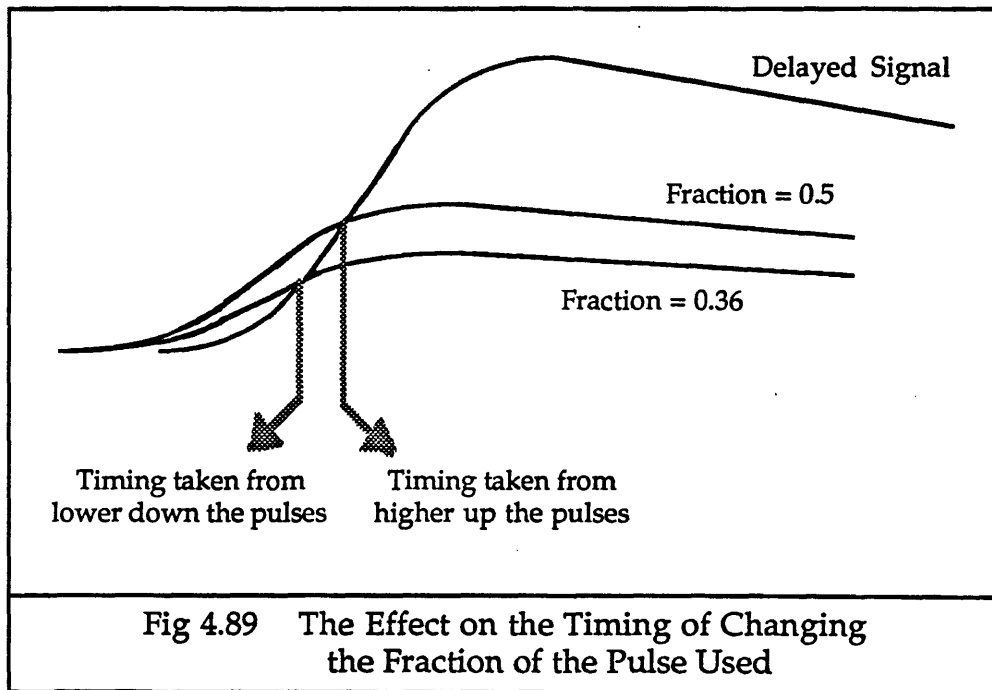
The shift in the crossover position on the axis of the S-bend with change of discriminator fraction can be seen in figure 4.90.
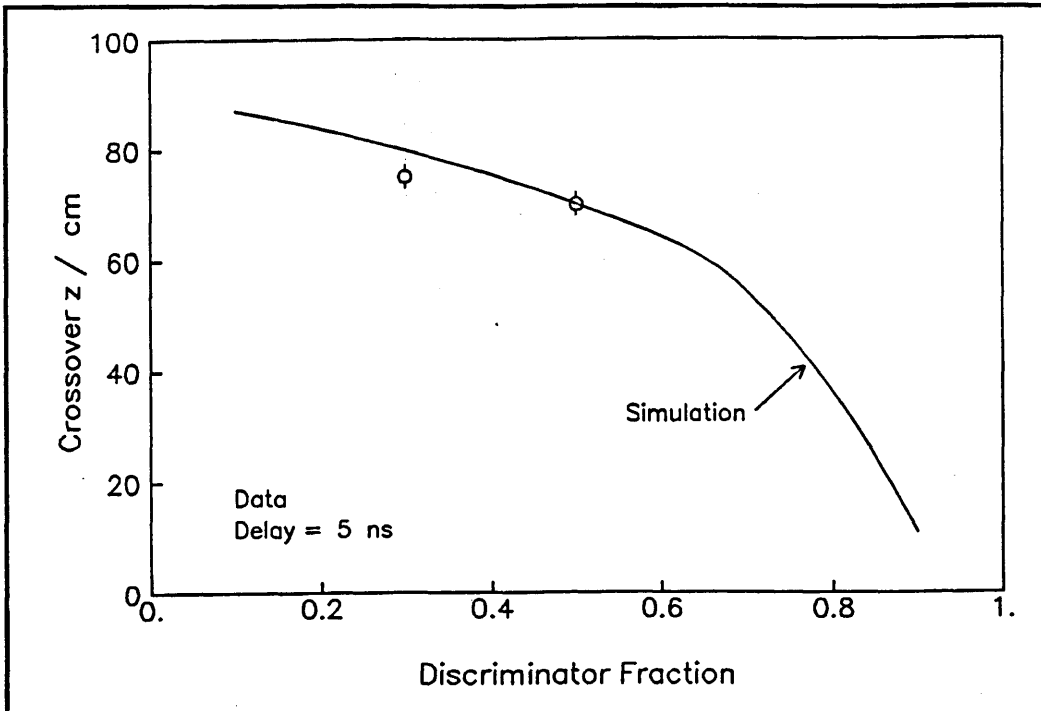
Fig 4.90   Change in S-Bend Crossover with Discriminator Fraction

Figure 4.91 shows the two S-bends at these fractions, 0.5 and 0.36, from the simulation program. The initial pulse height on the sense wire was 56 mV.
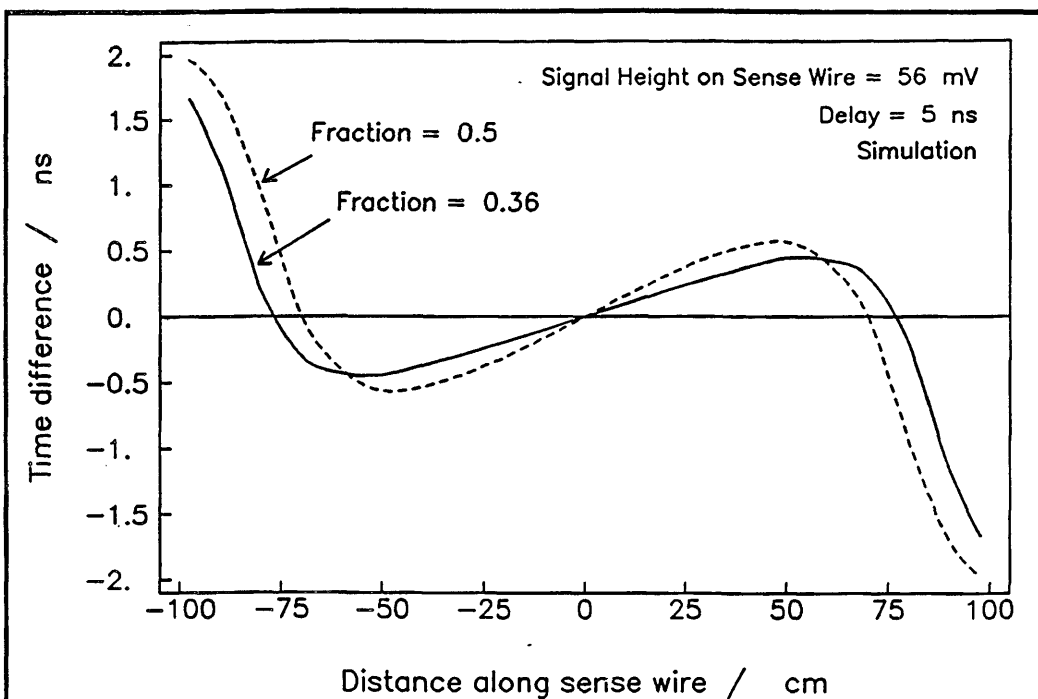
Fig 4.91   Simulation of the Change in S-Bend with
Discriminator Fraction

Figure 4.92 shows the change in the S-bends from the simulation for the discriminator with fraction 0.36, as the signal height increases and the amplifiers saturate.
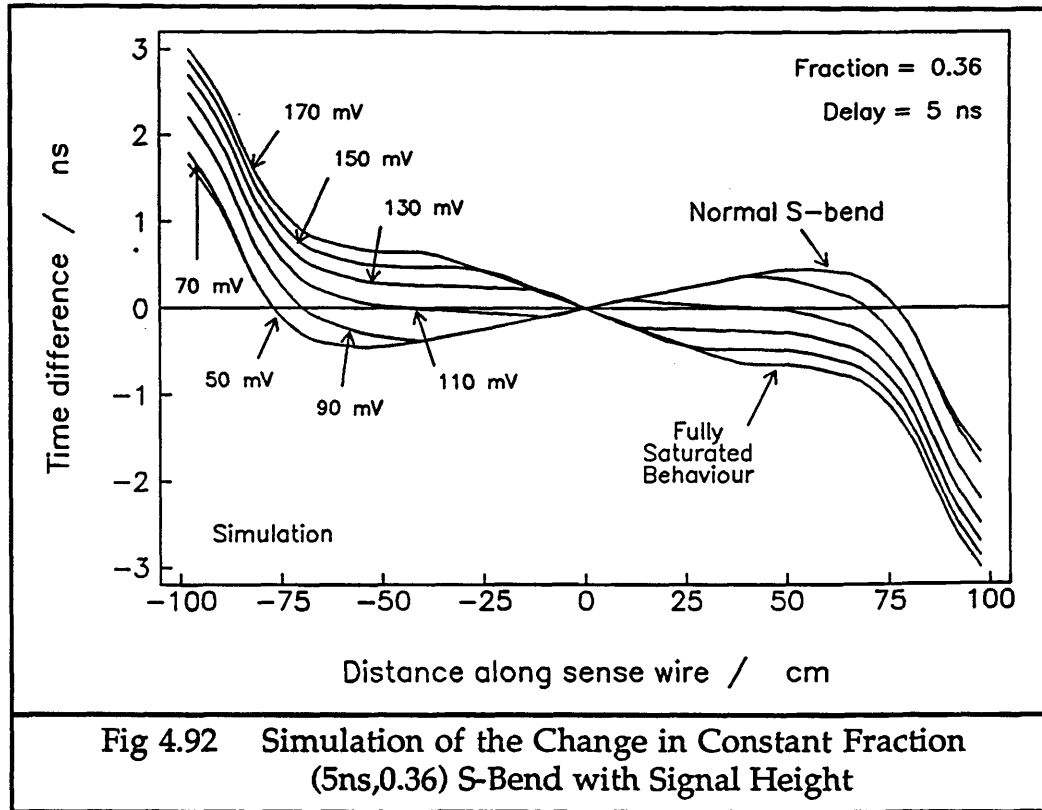
Fig 4.92   Simulation of the Change in Constant Fraction
(5ns,0.36) S-Bend with Signal Height

5.4.6   Spread of Values Measured

The spread of time differences, σ_t, measured in the long test rig with different signal sizes and at different z positions along the wire with constant fraction discriminators can be seen in figures 4.93, 4.94, 4.95 and 4.96.
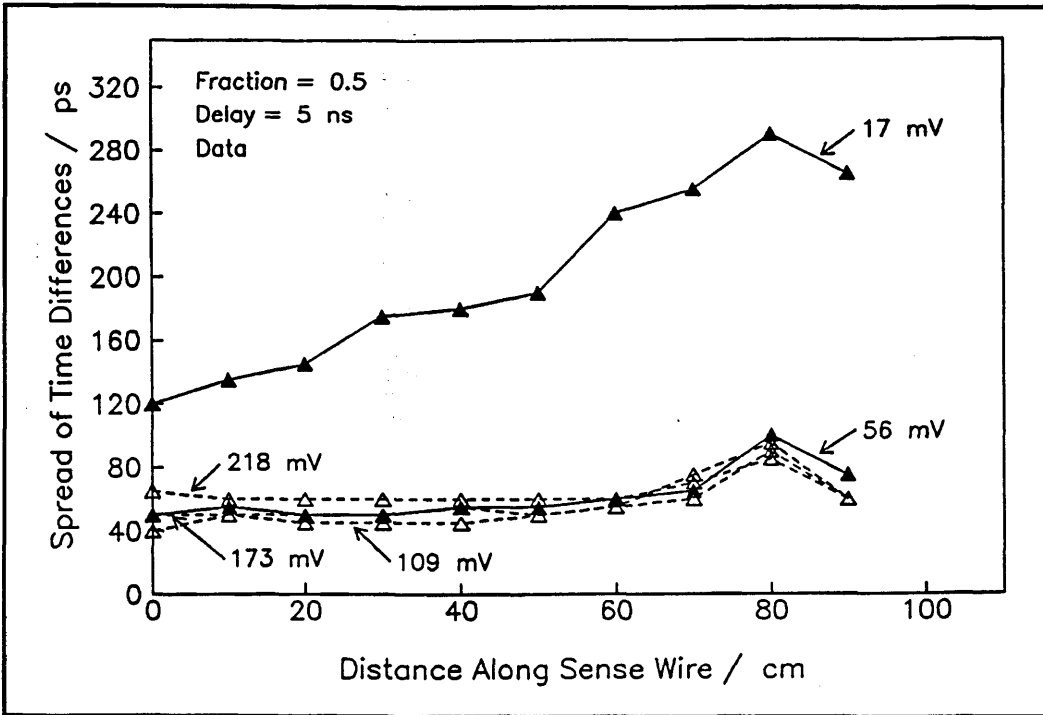
Fig 4.93   Variation of the Spread of Time Differences along the
Sense Wire with the Constant Fraction (5ns,0.5) Discriminator
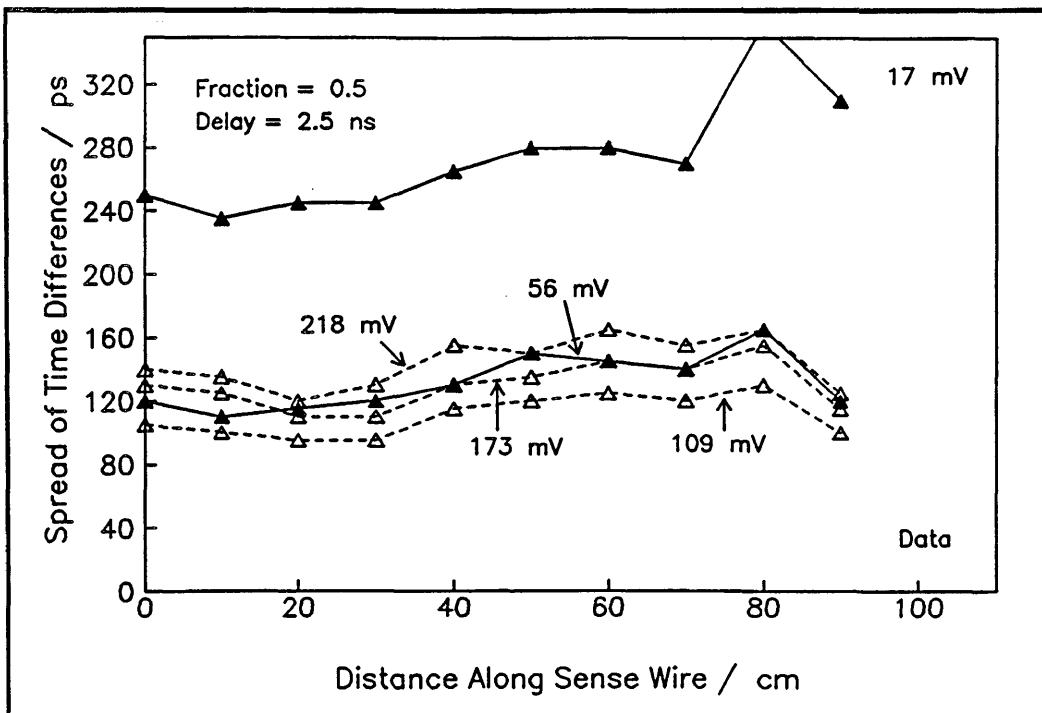
Fig 4.94   Variation of the Spread of Time Differences along the
Sense Wire with the Constant Fraction (2.5ns,0.5) Discriminator
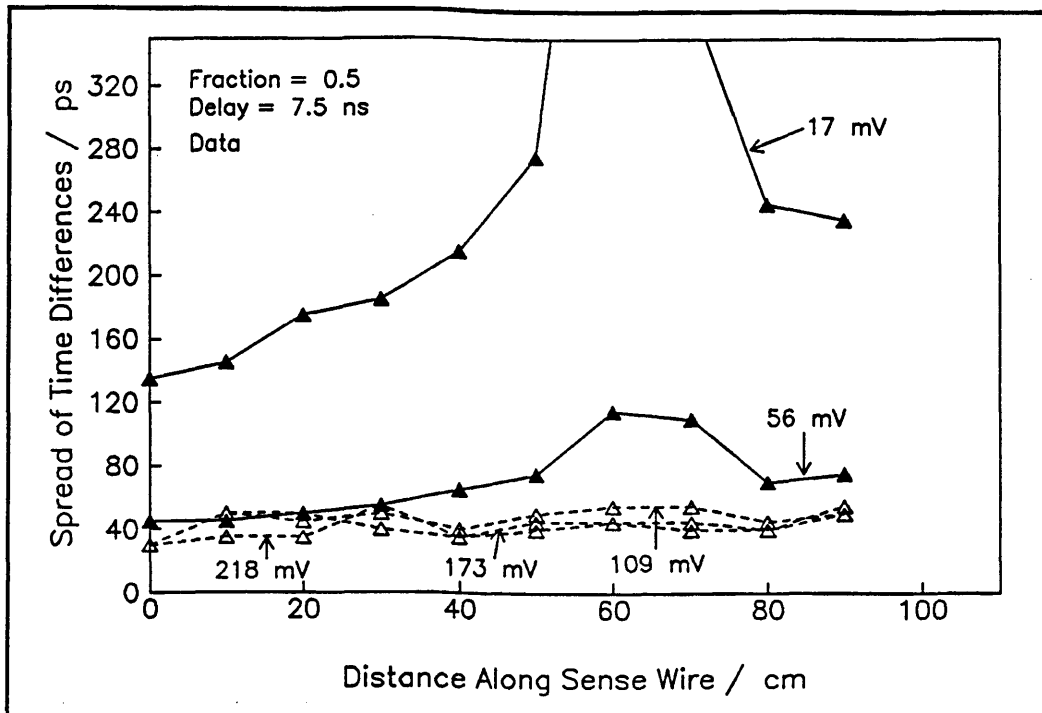
Fig 4.95   Variation of the Spread of Time Differences along the Sense Wire with the Constant Fraction (7.5ns,0.5) Discriminator
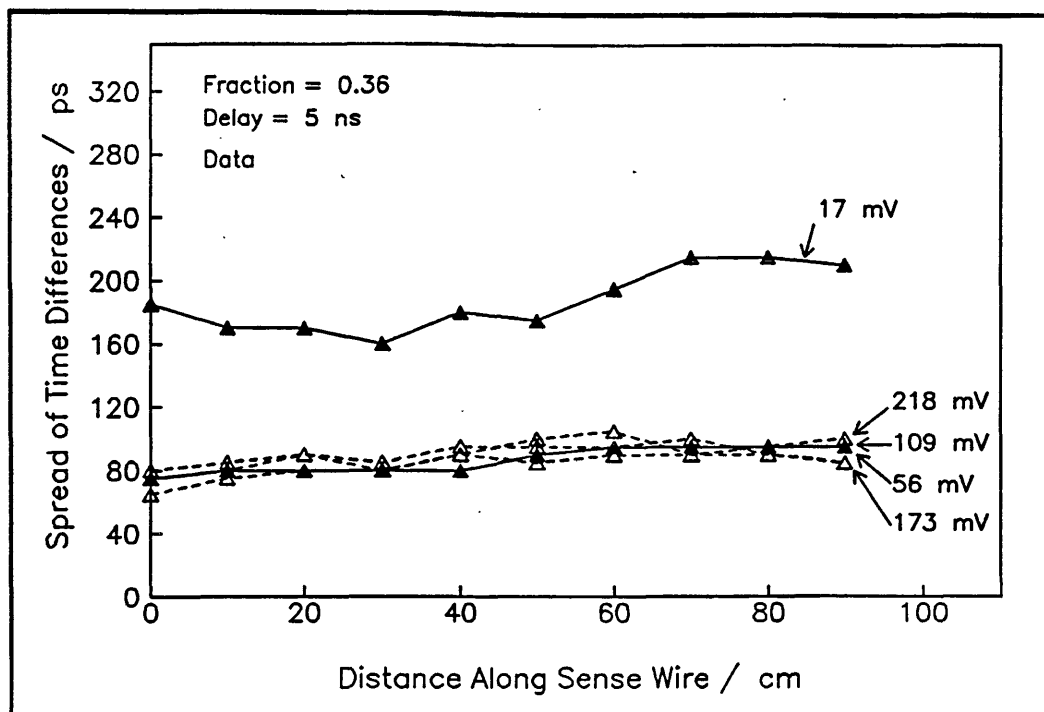
Fig 4.96   Variation of the Spread of Time Differences along the Sense Wire with the Constant Fraction (5ns,0.36) Discriminator

On the whole, the spreads of time differences are fairly steady for each discriminator type when the signals are fairly large, but small signals give a wider distribution. This can be seen in figure 4.97 for the four different setups of constant fraction discriminator tested. The mean spreads have

been calculated along the length of the sense wire.
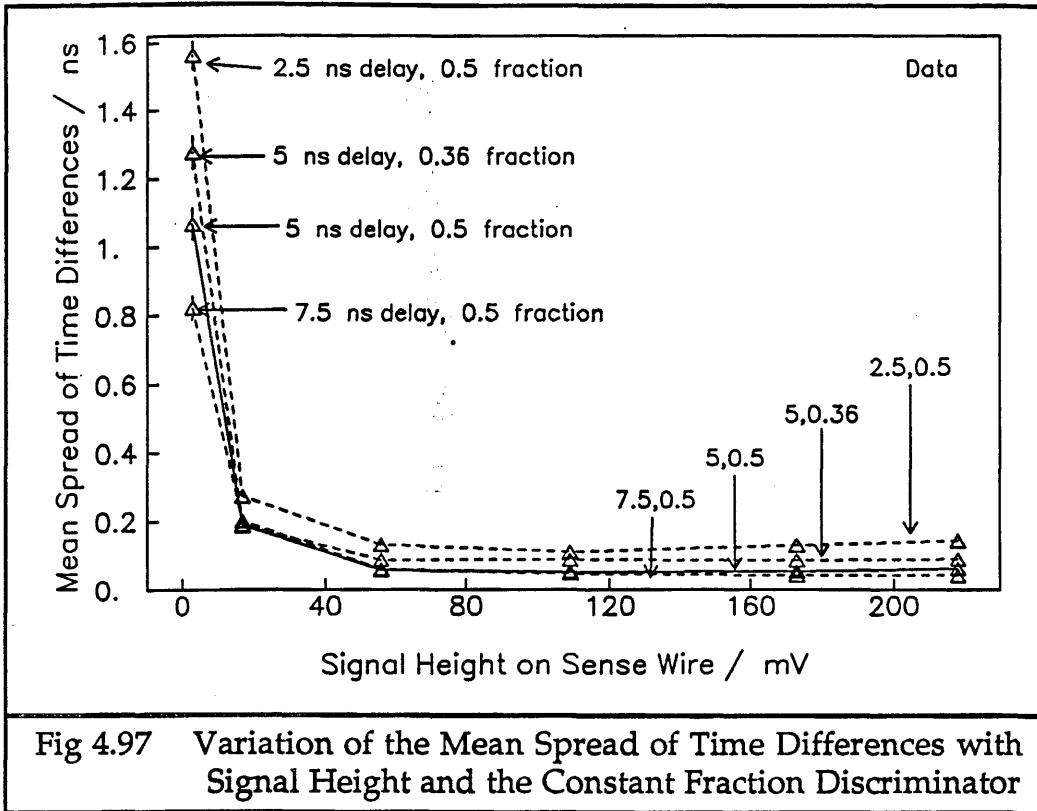
Fig 4.97   Variation of the Mean Spread of Time Differences with
Signal Height and the Constant Fraction Discriminator

Figure 4.98 shows the mean spreads of time differences taken over signal heights as well as z position, as a function of discriminator delay, with the results from the fraction 0.36 discriminator and for the dual threshold discriminator with an applied threshold of 1 V superimposed for comparison.

The mean spreads of time differences from all the various setups of the constant fraction discriminators tested are better than those from the dual threshold discriminator.

Calculation of an average spread of time differences for each discriminator setup, using signals at 17 mV, 56 mV and 109 mV, and averaging across the whole length of the sense wire produces values as shown in table 4.2, with the result from the dual threshold discriminator also shown for comparison. These signal sizes almost cover the range of signal heights expected in the ITC.

276
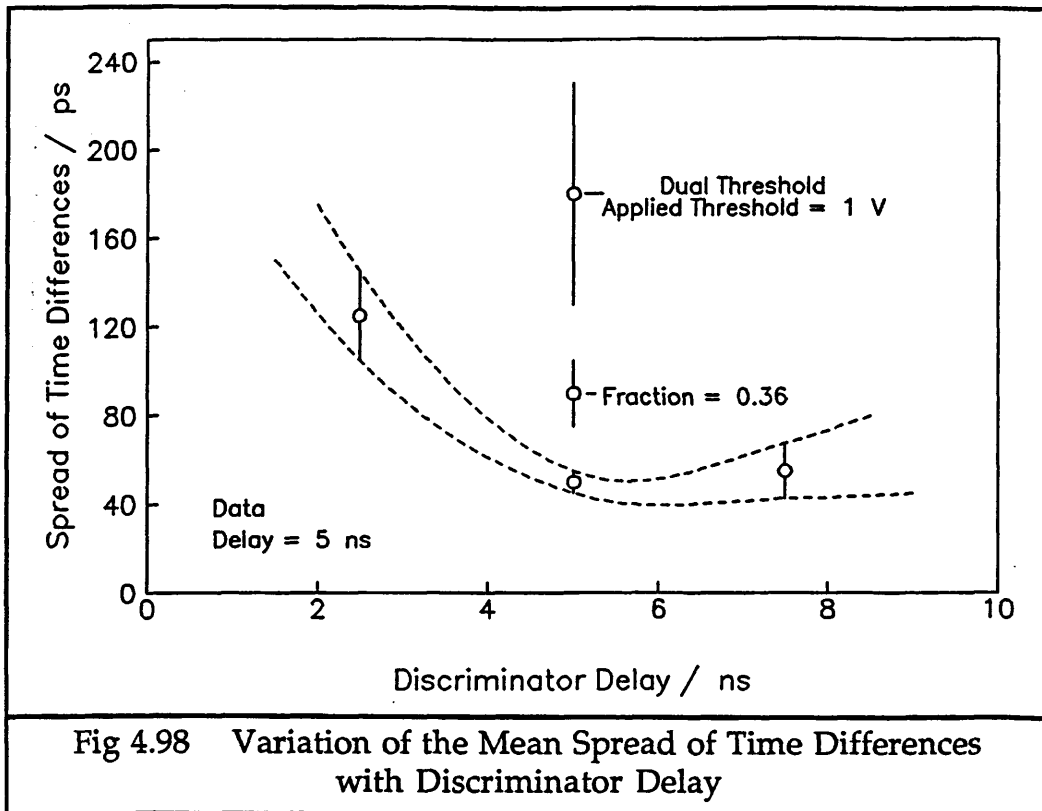
Fig 4.98   Variation of the Mean Spread of Time Differences
with Discriminator Delay

Table 4.2   Mean Spread of Time Differences
for Each Discriminator Setup

Constant Fraction Discriminator		$< \sigma_t >$
Delay / ns	Fraction	/ ps
5	0.5	106
2.5	0.5	172
7.5	0.5	109
5	0.36	121
Dual Threshold Discriminator		
1 V Applied Threshold		495

It is possible to gain an insight into why having a short delay time
should increase the jitter on the readout time by considering what is
happening to the signals in the discriminators. Figure 4.99 shows where the
timing is taken from with a long discriminator delay and with a short one.

277

i) Long Delay, Relative to Rise Time	ii) Short Delay, Relative to Rise Time
Timing taken from one leading edge and the other tail	Timing taken from both leading edges
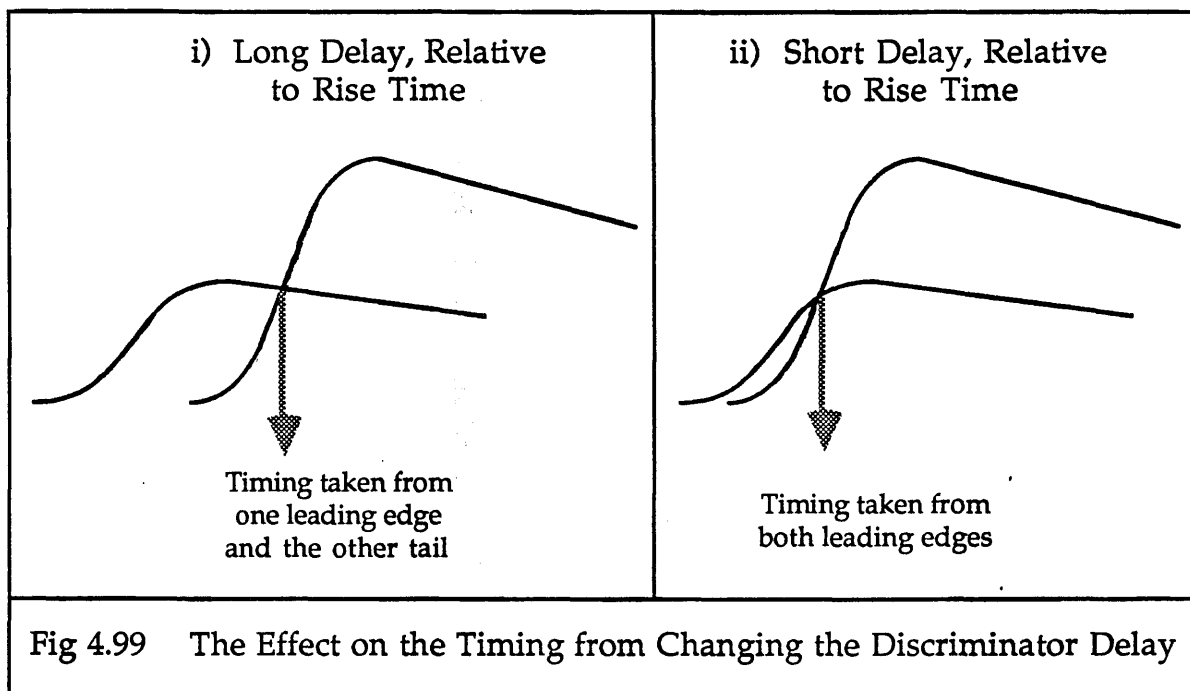
Fig 4.99   The Effect on the Timing from Changing the Discriminator Delay

If the delay is greater than half the signal rise time, then the timing is taken from the leading edge of one part of the split signal, and the trailing edge of the other part of the signal. This makes the timing less sensitive to interference from noise. If the delay is shorter than half the signal rise time, then the timing is taken from the crossing point of both leading edges. In this case there is much greater sensitivity to shifts in the leading edge from high frequency noise. The shorter the discriminator delay, the lower down the signals the timing is taken, and the worse this jitter will get. The discriminator design which will probably be used with the ITC, where delay = 5 ns (and fraction = 1/2) has a delay much less than half the signal rise time, which will probably be 12 - 15 ns at the 10% - 90% level. Therefore, this setup of discriminator will be operating in the mode which is more sensitive to interference from noise.

5.4.7   Inbuilt Slewing of the Constant Fraction Discriminator

Ideally, there is no slewing of the output signal from the constant fraction discriminators from input signals which are small enough not to saturate the amplifiers. However, in practice, there is a small amount of slewing which is unavoidable. This can be minimised before the discriminators are used by careful adjustment of two potentiometers on the circuit board, while observing the timing edge of the discriminator output signal on an oscilloscope, using a very wide range of input signal amplitudes. The optimum setting, causing the least slewing overall, is shown as the data points in figure 4.100.

Fig 4.100   Inbuilt Timing Slew on the Constant
Fraction Discriminator
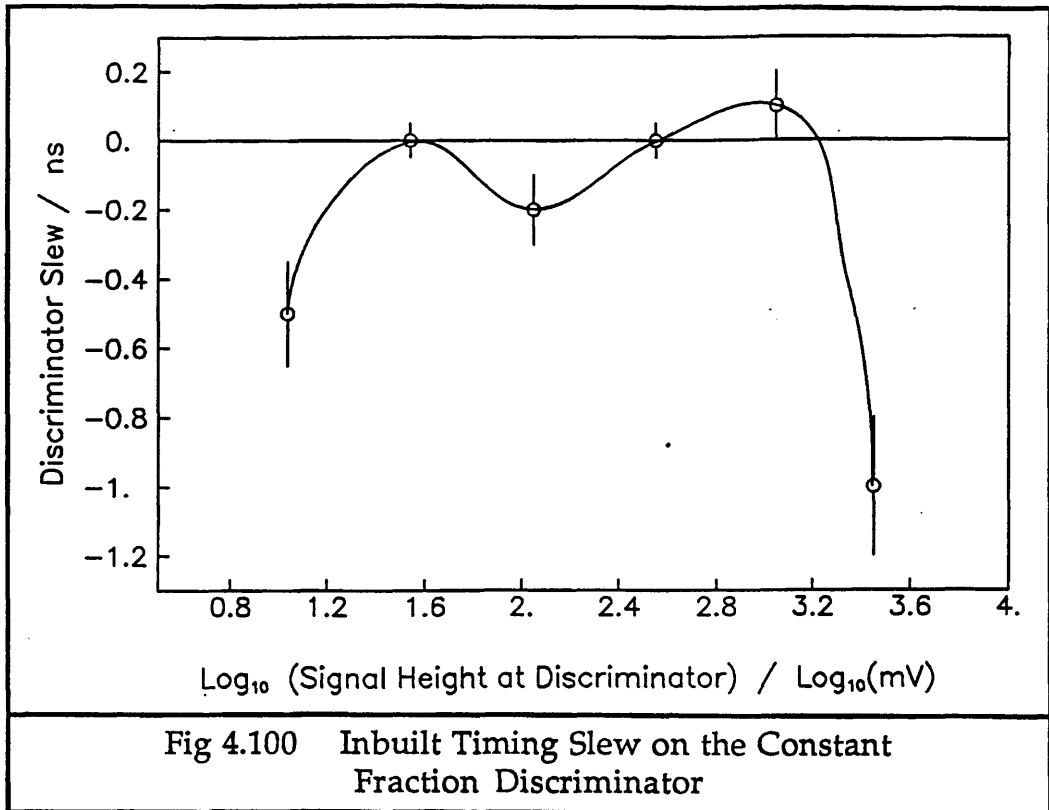
A simple five part fit to these points has been included as an option in the simulation program. Figure 4.101 shows the worst effects of this inbuilt slewing for a very small signal and for a fairly large, nonsaturating one.

Fig 4.101   The Effect of the Inbuilt Slewing on the Constant
Fraction Discriminator S-bends
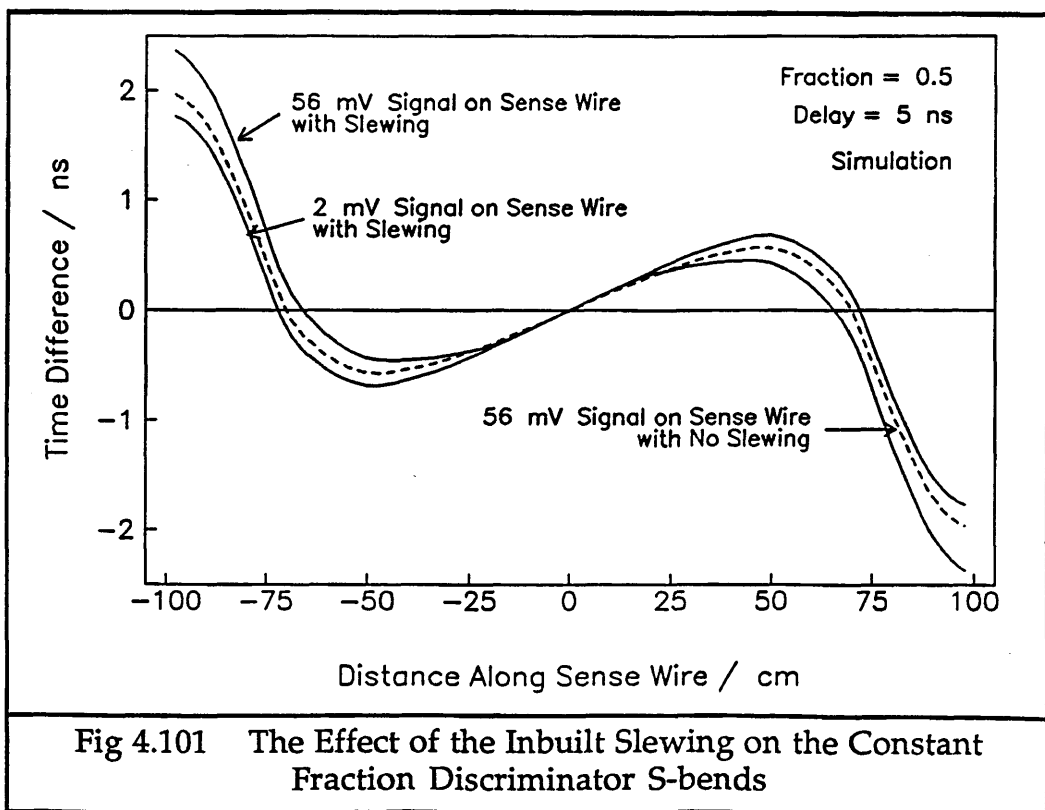
5.4.8 Time Differences Measured and Predicted

Figure 4.102 shows results from the data for the time differences measured on all three wires, before calibration and subtraction from the ideal time difference, with the constant fraction discriminators which have fraction = 1/2 and delay = 5 ns. Superimposed is the result from the simulation for this time difference. The three sets of data points and the simulation have been shifted on the time difference axis so that their "plateaux" coincide. The plateau is the region where the signal heights are large enough to pass the internal threshold of the discriminator, without being much affected by noise, and small enough not to cause the amplifiers at either end to saturate. It is reasonable to make this shift, since none of the data points have had the difference in cable lengths calibrated out from them, and so the actual time differences measured are not significant. The data and the simulation are produced with signals starting at z = 42 cm.
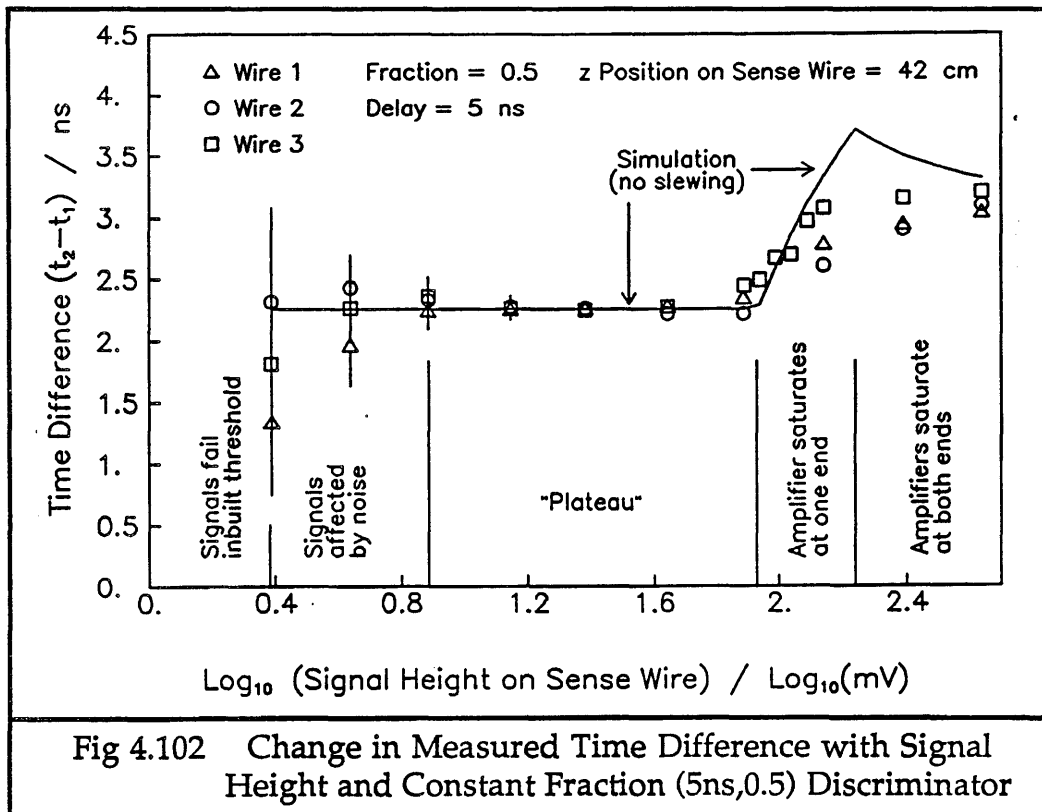
Fig 4.102   Change in Measured Time Difference with Signal
Height and Constant Fraction (5ns,0.5) Discriminator

The difference between the data and the simulation for large signals can be attributed to the inbuilt slewing of the constant fraction discriminators, which was not included in the simulation here.

Figure 4.103 shows the time differences measured from the simulation, with signals generated at z = 42 cm, for discriminators with fraction of 1/2 and delays of 2.5, 5, 7.5 and 10 ns. The long flat region is the plateau, where the signal sizes do not saturate the amplifiers, and there is ideally no

slewing of the signal in the discriminators. As this time difference increases with increasing signal size, the amplifier at one end of the chamber gradually starts to saturate. Once the peak in the time difference is reached, the amplifier at the other end of the chamber starts to saturate. As the signal size increases still further, both amplifiers continue to saturate, and the time difference measured decreases. This corresponds to the decreasing of the S-bend nonlinearity from the maximum deviation, with very large pulses, as shown in figure 4.81.
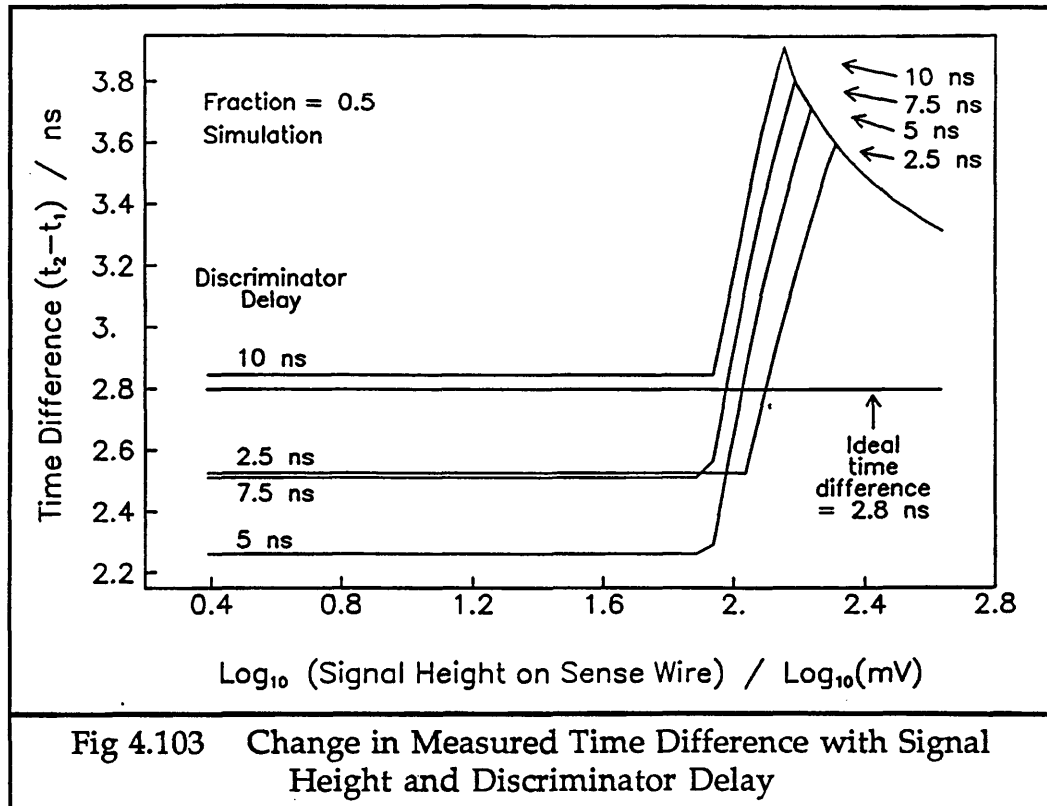
Fig 4.103   Change in Measured Time Difference with Signal
Height and Discriminator Delay

Figure 4.104 shows the time difference predicted from the simulation for discriminators with a delay of 5 ns and fractions of 0.3, 0.5 and 0.7.

The change in time difference when the amplifiers saturate is less extreme for smaller fractions.

Fig 4.104   Change in Measured Time Difference with Signal
Height and Discriminator Fraction
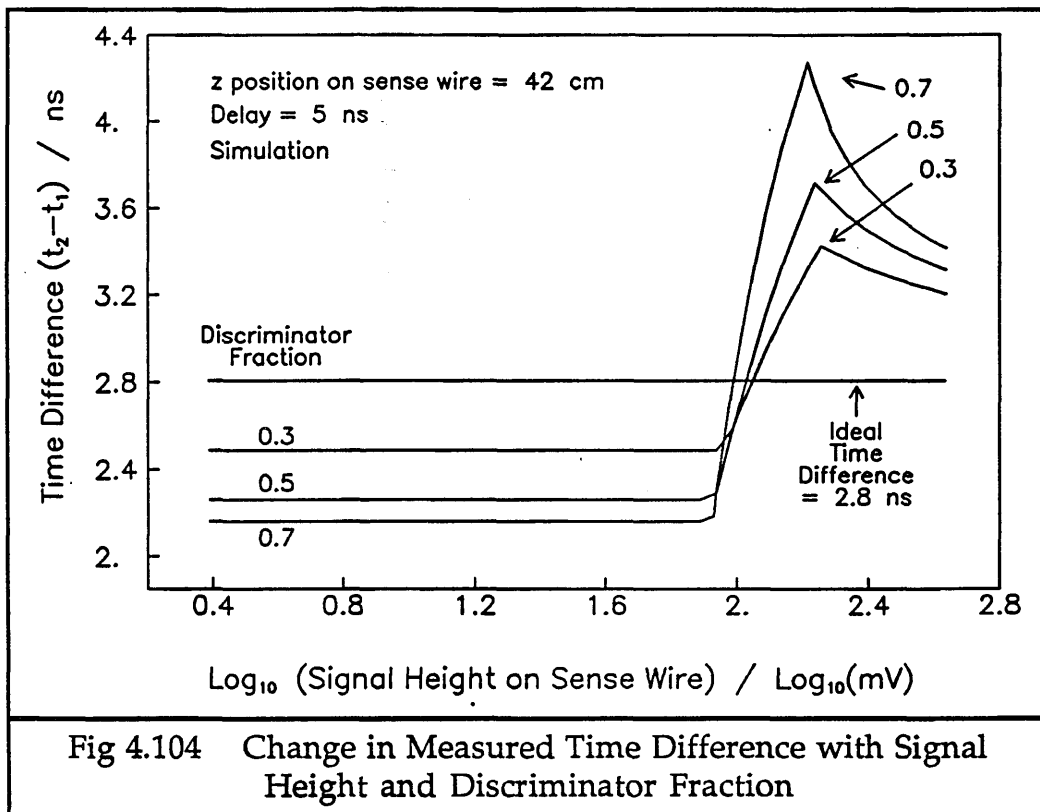
5.4.9   Comparison of the Different Setups of the Constant Fraction Discriminator

There are three main criteria which can be used to decide which fraction and delay for the constant fraction discriminator perform best for the conditions present in the ITC. These will be described here, and then a summary made of the different properties found.

a) Interference from Noise

The first criterion by which to judge the quality of discriminator behaviour is its susceptibility to interference from noise. This is not included in the simulation program. The mean spreads of time differences for each discriminator setup are shown in table 4.2, Section 5.4.6.

Decreasing either the delay or the fraction has an adverse effect on the susceptibility to interference from noise.

b) Plateau Behaviour

Another criterion for judging the performance of the discriminators is the length of the plateau. That is, how large can the pulses be before saturation behaviour occurs and the S-bend changes. The pulse sizes needed to trigger the change in S-bend behaviour for several setups of discriminator are shown in figures 4.105 and 4.106. These values are for z = 42 cm in the long test chamber, and are produced from the simulation.

282

Fig 4.105   Change in Plateau Length with Discriminator Delay

Fig 4.106   Change in Plateau Length with Discriminator Fraction
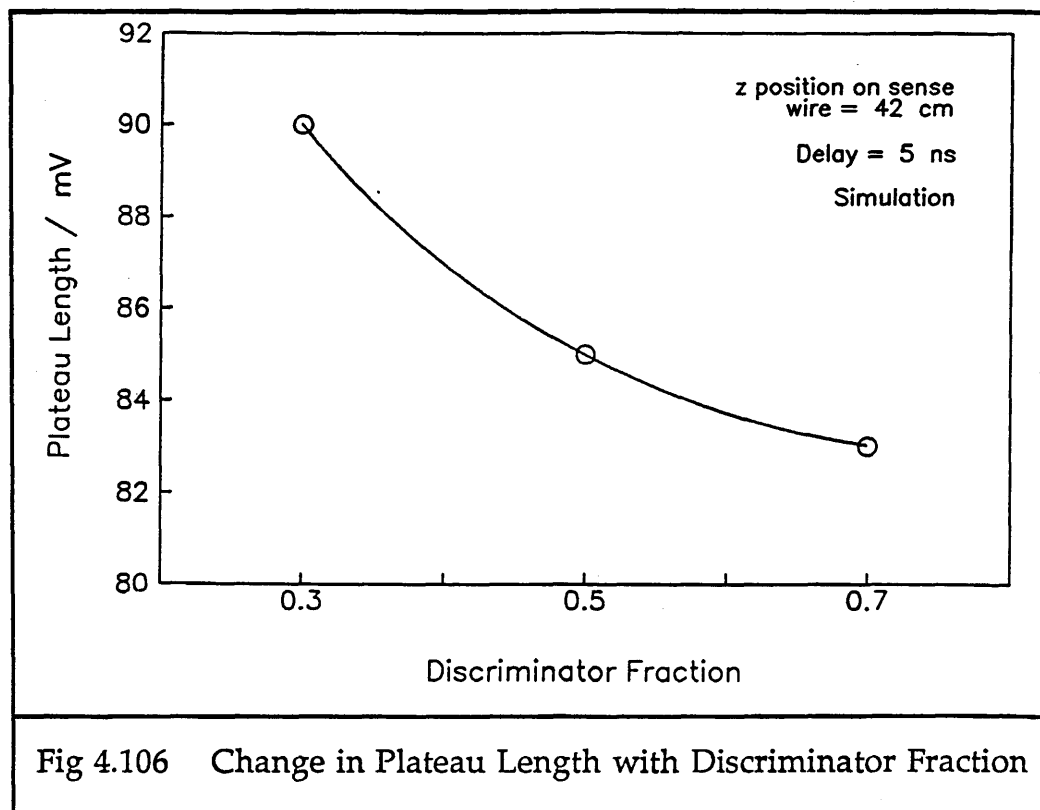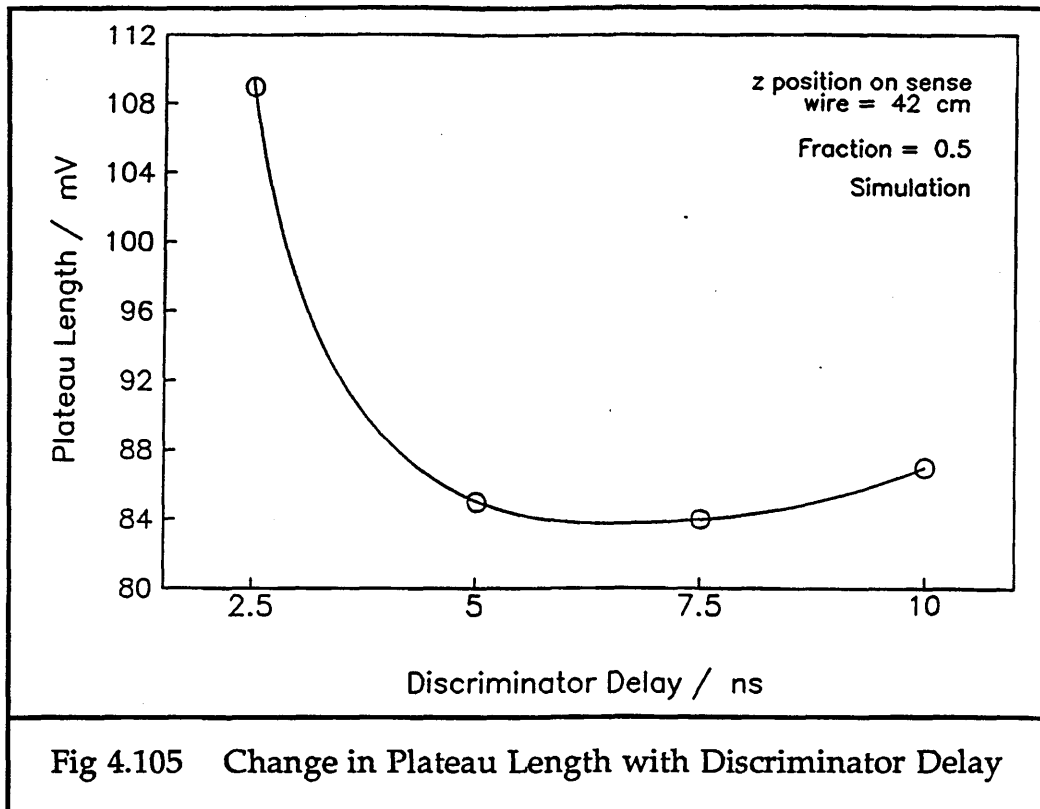
The plateau can be lengthened either by decreasing the delay, or decreasing the fraction. Also, once the delay is increased to about 10 ns, the plateau starts to get longer again.

c) The Difference Between Plateau and Saturated Behaviour

The worst aspect of the constant fraction discriminators is the radical changing of the S-bend for very large pulses. This will introduce the largest position errors. Therefore, it is very important to try to minimise the difference between the two modes of operation. Table 4.3 shows at which pulse sizes the maximum saturation behaviour occurs, from the simulation.

Table 4.3 Plateau and Maximum Time Differences for each Discriminator Setup with Signals at z = 42 cm				
Delay / ns	Fraction	Pulse Size for max. Δt / mV	Maximum Δt / ns	Plateau Height / ns
2.5	0.5	206	3.60	2.53
5	0.5	174	3.72	2.26
7.5	0.5	154	3.81	2.51
10	0.5	143	3.92	2.85
5	0.3	180	3.43	2.49
5	0.7	164	4.28	2.16

This gives the difference between the time difference at the peak to the time difference on the plateau as shown in figures 4.107 and 4.108, which is best if it is small.
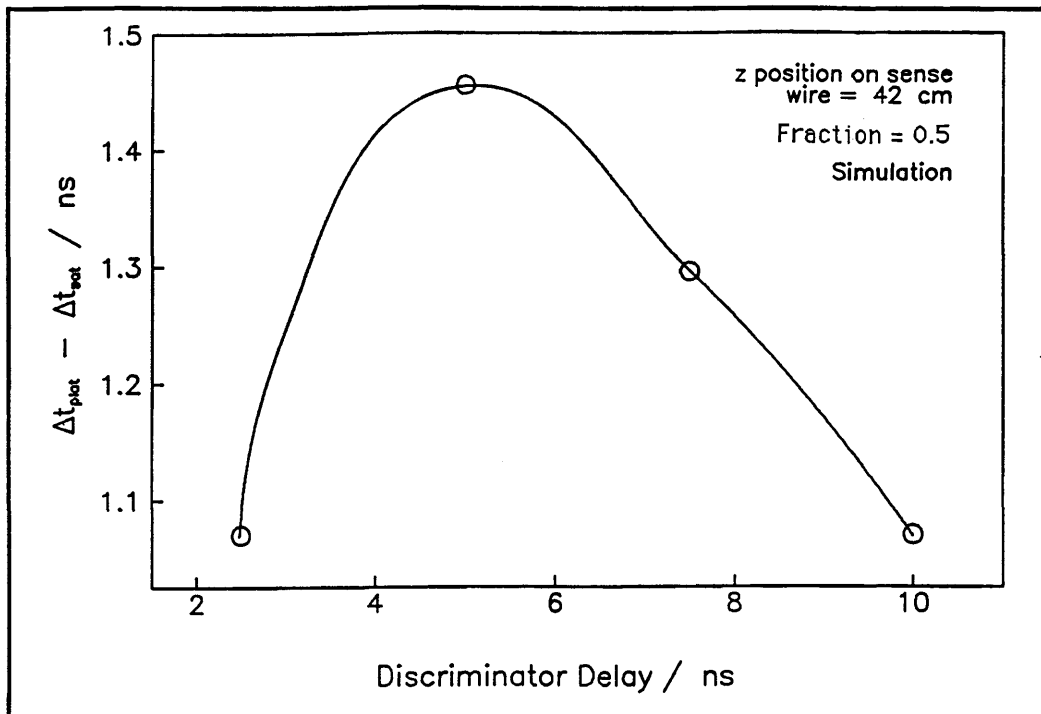
Fig 4.107   Difference Between Saturated and Plateau Time Differences with Discriminator Delay
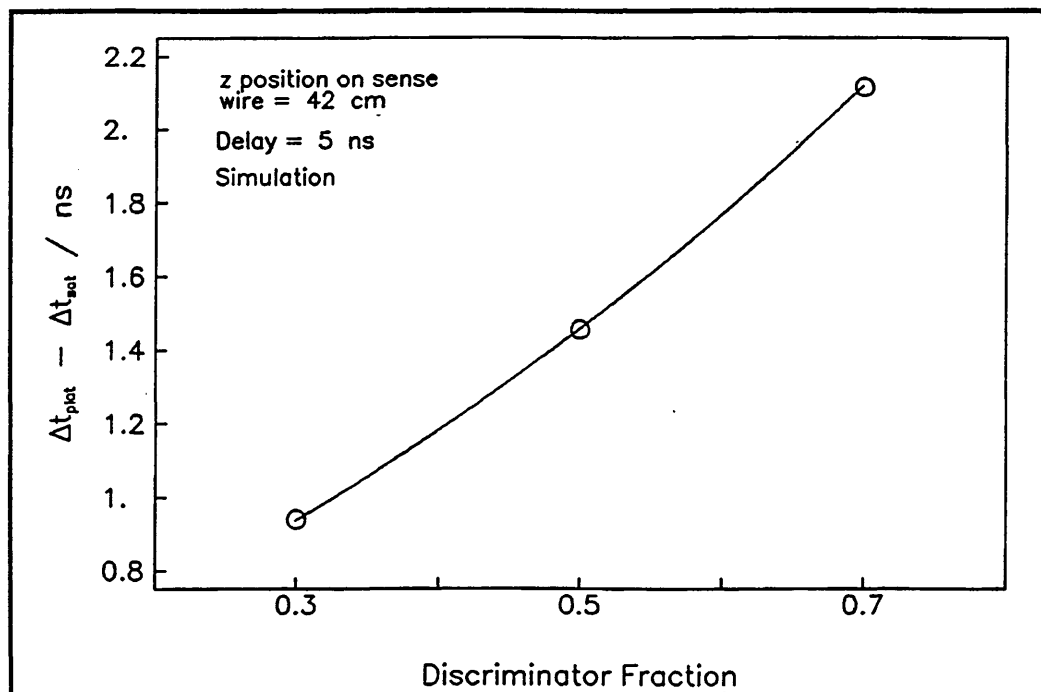
Fig 4.108   Difference Between Saturated and Plateau Time Differences with Discriminator Fraction

This difference can also be looked at with respect to the position on the sense wire, z, for the S-bends. In the following two figures, the simulation program has been used to generate two S-bends for each type of discriminator. The first was for a plateau sized pulse, and the second for the

pulse size which produced the maximum time difference, as shown in figures 4.103 and 4.104. The difference was then found between the two S-bends, and figures 4.109 and 4.110 show this difference as a function of z. This is the difference which should be as small as possible.
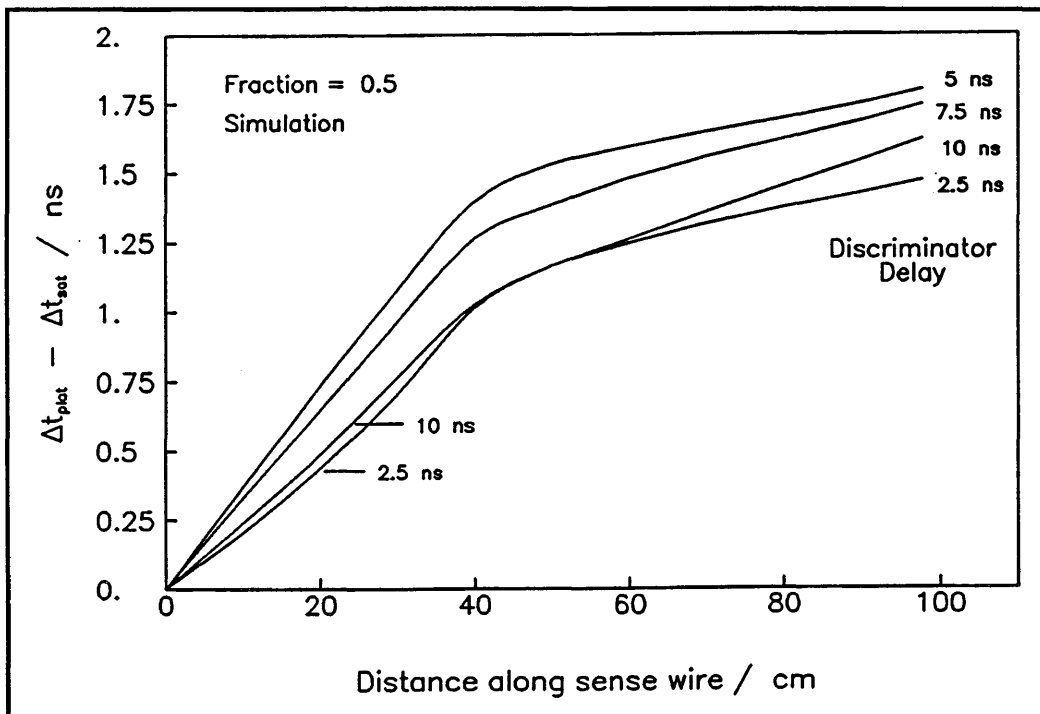
Fig 4.109   Difference Between Saturated and Plateau Time Differences with Position on Sense Wire and Discriminator Delay
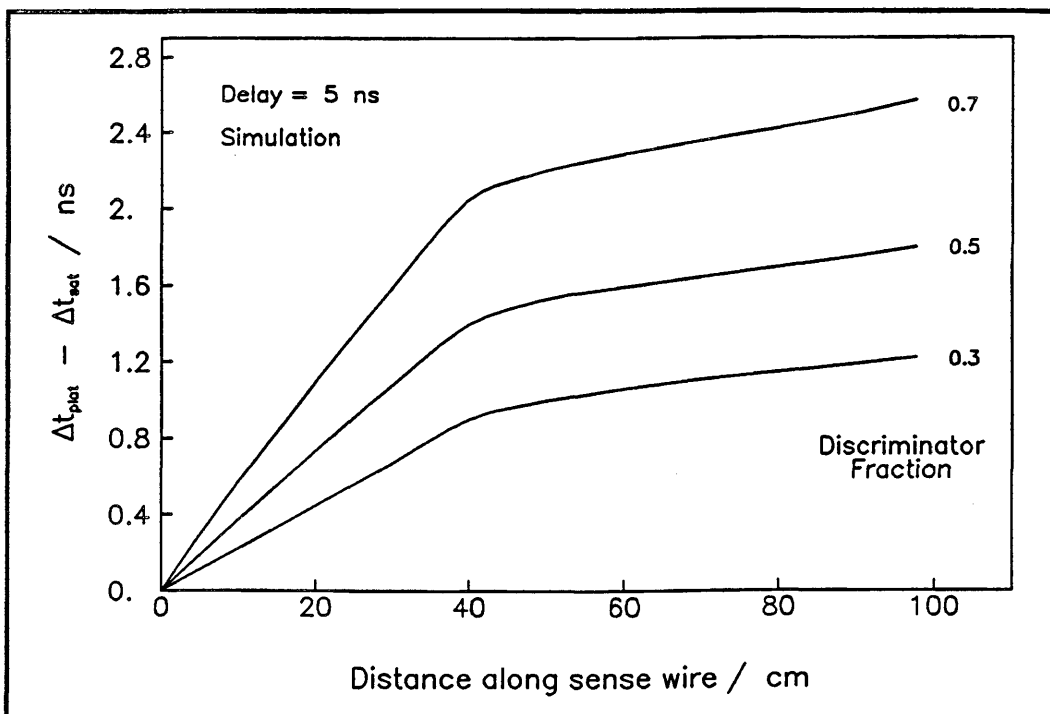
Fig 4.110   Difference Between Saturated and Plateau Time Differences with Position on Sense Wire and Discriminator Fraction

The mean values of this difference, averaged across the length of the sense wire, can be seen in figures 4.111 and 4.112.

Fig 4.111   Mean Difference Between Saturated and Plateau Time Differences with Discriminator Delay

Fig 4.112   Mean Difference Between Saturated and Plateau Time Differences with Discriminator Fraction
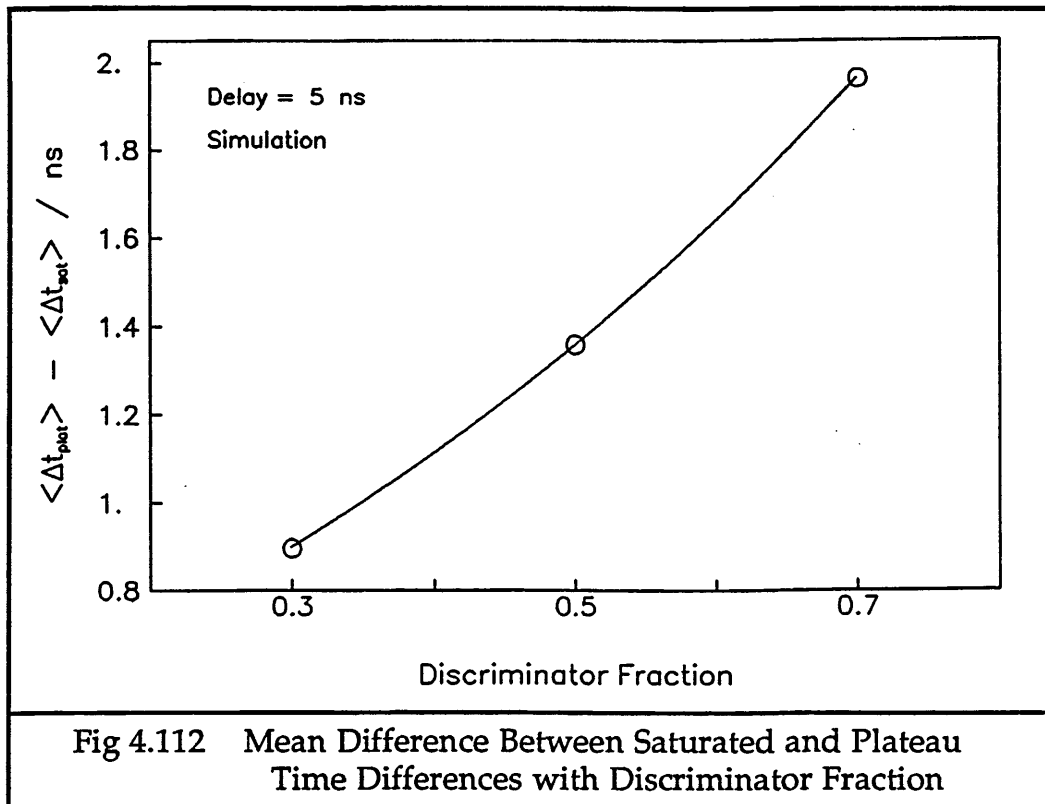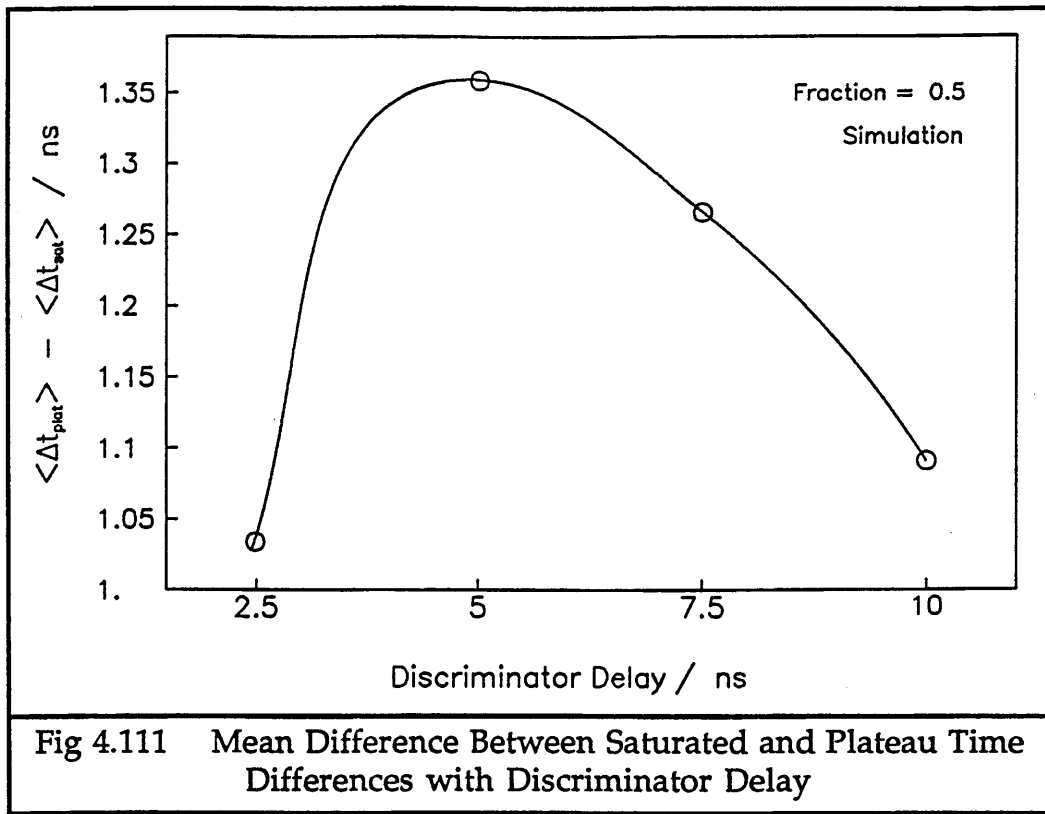
It can be seen that decreasing the delay from the standard 5 ns to only 2.5 ns improves the discriminator performance by 24 % using this criterion, and increasing it to 10 ns improves the performance by 20 %. Decreasing the fraction from the standard value of 0.5 to 0.3 improves the performance by 34 %.

A change in the time difference of 1.359 ns, which is the average value for the standard delay = 5 ns, fraction = 1/2 constant fraction discriminator, is equivalent to a shift in z position, using c/2 as the velocity, of 20.4 cm.

d) Summary

If noise were not important, then it can be seen that the best delay to use would be a shorter one than the standard 5 ns, such as 2.5 ns. This gives a 28 % increase in plateau length, and a decrease of 24 % in the difference between the two S-bends, from first saturation to the plateau. However, the 2.5 ns delay boards used in the experimental tests have an increase of 62 % in the mean spread of time differences over that from the standard 5 ns ones. (This still compares very favourably with the dual threshold boards, which have an increase of 367 % in the mean spread of time differences over that from the standard constant fraction model.) Alternatively, raising the delay to 10 ns will probably not increase the noise by much at all, and may even reduce it slightly (as shown in Section 5.4.6), and will improve the difference between the two extremes of S-bend by 20 %. The plateau length will also increase by 2 %, which although small, is better than a decrease in length.

When considering the discriminator fraction, decreasing this to 0.3 will increase the plateau length by 6 %, and decrease the difference in S-bends by 24 %. However, the mean spread of time differences from the tests, for a fraction of 0.36 was 14 % worse then the standard discriminator value, and would be ~ 20 % worse for a fraction of 0.3.

Therefore, if it were desired that a constant fraction discriminator should be used, because of the low spread of time differences from noise relative to that from the dual threshold discriminator, and also because of the long plateau with no slewing from pulse size, then a decision would have to be taken as to which was least desirable : an increase in σ_t or a larger difference between the plateau S-bend and the saturated S-bend.

5.4.10 Miscellaneous Results from the Simulation Program
for the Constant Fraction Discriminator

The simulation program can be used to show the contribution to the S-bend nonlinearity from the end reflections and the attenuation along the wire. The S-bends in the following two figures are produced.

Fig 4.113   Simulation of the Change in Constant Fraction S-Bend with Series Resistance of the Sense Wire
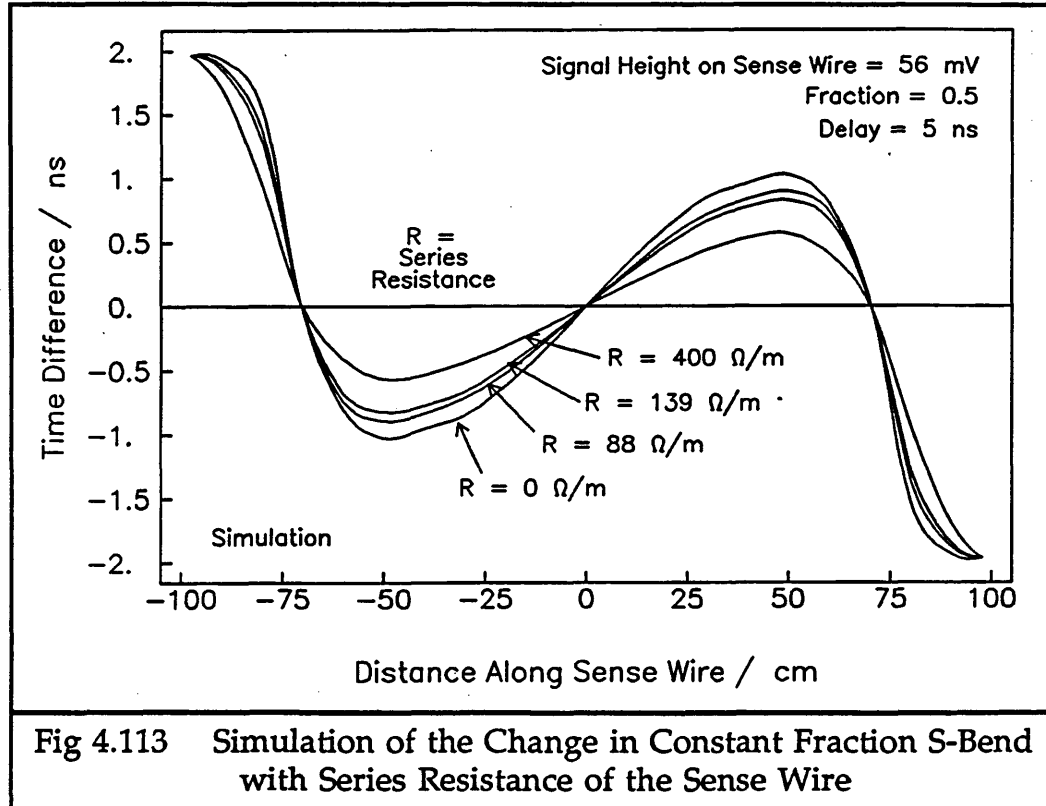
Figure 4.113 shows the effect of having various series resistances on the shape of the S-bend, for a starting signal of 56 mV and standard values for fraction of 1/2 and delay of 5 ns in the discriminator. As the series resistance increases, the effect on the S-bend is to decrease the deviation from c/2 all along the sense wire, except at the very ends, where the value of the time difference is dependent on the reflection and not the attenuation of the signals. The crossing point of the S-bends is also unchanged.

Figure 4.114 shows the effect of having an end capacitance of zero on the S-bends.
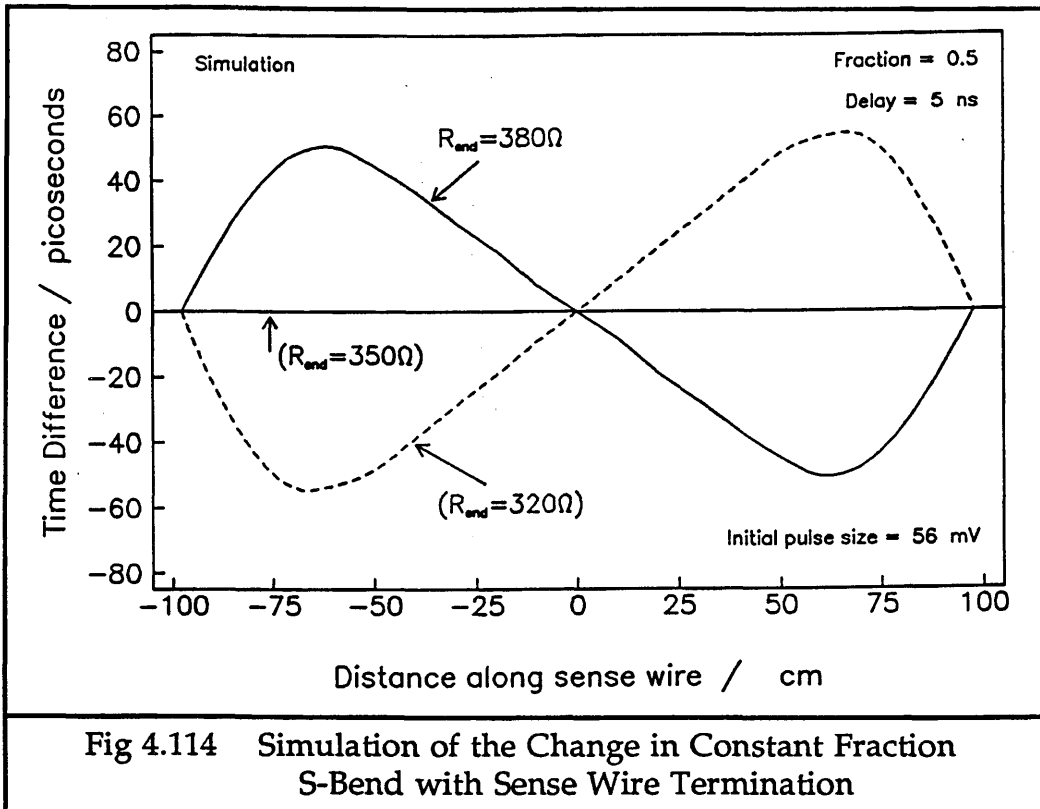
Fig 4.114   Simulation of the Change in Constant Fraction
S-Bend with Sense Wire Termination

If the end resistance exactly matches the characteristic impedance Z_0, of the transmission line, then there are no reflections, and there is no nonlinearity from $c/2$. If the end resistance is larger than Z_0, as in the ITC, then the S-bend actually bends in the opposite direction to that seen when $C > 0$ pF. When the end resistance is less than Z_0, then the S-bend is a mirror image of that for the larger end resistance. When $C = 0$ pF, then there is no deviation from $c/2$ at the ends of the transmission line. In figure 4.114, it should be noted that the vertical scale covers a much smaller range of time differences than that in figure 4.113.

5.5   Compensating for the S-Bends

There are two methods which have been considered to compensate for the S-bend non-linearities, in order to know the z position along the wire accurately. Both are effected with hardware, so that the corrected z value may be used for the trigger during a beam crossing in LEP.

5.5.1   Inductances

This method involves changing the properties of the termination of the transmission line in order to reduce the reflections. The reflections may be reduced by "loading" the line, which means adding a series inductance L,

as shown in figure 4.115.

Fig 4.115   Loading the Line with a Lumped Coil
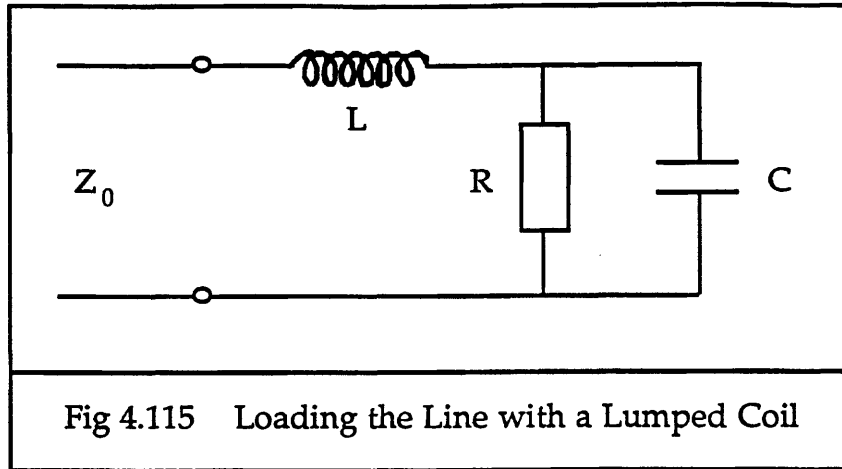
Loading decreases the attenuation and distortion, by increasing the characteristic impedance of the line, and improving the validity of the distortionless transmission line relationship. Increasing L also decreases the velocity of propagation, but this is not a problem, since the travelling time of the signal on the wire is negligible compared to the electron drift times in the cell. L can be increased by adding a coil at each end of the sense wire. This is called "lumped" or "coil" loading, and the effect is to increase the average inductance per unit length of the line. If an inductor is added to the end of the line, it acts with the stray end capacitance as a low pass filter. That is, high frequencies are filtered out. The reflections are composed principally of these high frequencies, and so increasing L decreases the amount of reflection which can be produced and transmitted and so decreases its effect.

Figure 4.116 shows a symmetrical Π section low pass filter, consisting of the end capacitance and inductance, plus the end resistance as termination.

Fig 4.116   Symmetrical Π Section Low Pass Filter
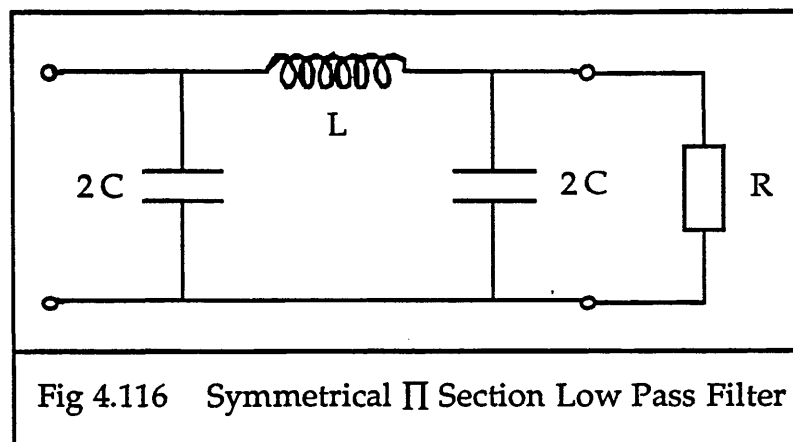
The inductive and capacitive reactances are :

$$\chi_L = \omega L \qquad\qquad \chi_C = -1 / \omega C$$

Cut-off frequency occurs at :

$$\chi_C + \frac{\chi_L}{4} = 0$$

$$\Rightarrow \quad f_{cut\text{-}off} = \frac{1}{\pi \sqrt{L C}}$$

For the ITC, $C \approx 15$ pF , and $L \approx 1$ μH has been tried, which gives :

$$f_{cut\text{-}off} \approx 82 \text{ MHz}$$

One disadvantage of adding inductors is that a row of closely packed inductance coils on the preamplifier board acts like a series of linked transformer coils, which leads to signals on one channel being induced into the others, which gives very bad crosstalk. This is very difficult to eliminate. Another problem is that inductances with a value of ~ 1 μH are rather large, having air cores. There is very little space on the closely packed preamplifiers at the ends of the ITC for large numbers of bulky inductors. Consequently, it has been decided not to use loading inductances.

5.5.2 Varying the Time Expansion Discharge Currents

Once the timing measurement has been made, then the S-bend non-linearities are intrinsically included. They can be removed before the time difference is used for the trigger, when the time expansion process occurs. The time expansion process is explained in Section 6.1 of Chapter 5. Ideally, if there were no S-bend nonlinearity, then the time expansion would be achieved by discharging capacitors with different voltage levels on them for the different layer radii. If the capacitors can be made to produce a nonlinear discharge, then the standard S-bend nonlinearity may be removed from the time difference. The saturated nonlinearities will of course not be corrected by these inbuilt variable voltage levels. This method will almost certainly be used with the ITC if constant fraction discriminators are chosen, and possibly also even if dual threshold ones are used.

6 Predictions for the ITC

6.1 Differences Between the Long Test Rig and the ITC

There are several physical differences between the ITC and the long test chamber. These all affect the shape of the S-bends slightly.

a) Thickness of the End Plate

The ITC end plates are 2.5 cm thick, whereas the long test rig end plates are only 1 cm thick. This affects the attenuation and distortion of the signal caused by the eddy currents induced in the end plate. Using the attenuation approximation, the attenuation changes from ~ 0.7 to ~ 0.5. This extra attenuation means that signals may be larger in the ITC than in the long test rig, before they saturate the amplifiers and change the S-bends.

b) Active Length of the Sense Wire

The distance between the end plates in the ITC is 2 m, the same as in the long test rig, but because the end plates are two and a half times as thick in the ITC as in the long test rig, the feedthroughs protrude into the chamber by only 0.8 cm instead of 2.3 cm. This makes the active length of the sense wires in the ITC 198.4 cm, while it was only 195.4 cm in the long test rig. This means that there is a slightly greater delay between the arrival at the timing end of a sense wire of a signal generated on it, and the arrival of the reflection from the far end. This will change the shape of the S-bend.

c) Capacitance at the End of the Sense Wire

The capacitance at the end of the sense wire changes slightly between the ITC and the long test chamber. Some contributions to the total capacitance are larger in the ITC, such as through the feedthrough, and some are smaller, such as in the end box leads. Consequently, in the simulation using the ITC conditions, the end capacitance has been left at 15 pF, since all the expected changes are very small.

d) Characteristic Impedance of the Sense Wire Transmission Line

The cells in the ITC are of different size in each layer. This means that each layer of cells has a different mean characteristic impedance Z_0. These values for Z_0 can be seen in table 4.4 for each of the 8 cell layers.

293

Layer in ITC	shortest distance / mm	longest distance / mm	mean radius / mm	Z_0 / Ω
1	4	5.752	5.168	350.3
2	4	6.081	5.387	352.8
3	4	6.538	5.692	356.1
4	4	6.872	5.915	358.4
5	4.9	5.497	5.298	351.8
6	4.9	5.748	5.465	353.6
7	4.9	6.071	5.681	356.0
8	4.9	6.330	5.853	357.8
Long Test Rig	4	5.752	5.168	350.3

Table 4.4   Characteristic Impedances of Each Cell Size in the ITC

The maximum effect this has on the S-bends for the constant fraction discriminator can be seen in figure 4.117. The effect this has on the dual threshold discriminator S-bend nonlinearity is negligible.

Fig 4.117   Change in the ITC Constant Fraction S-Bend with Cell Size
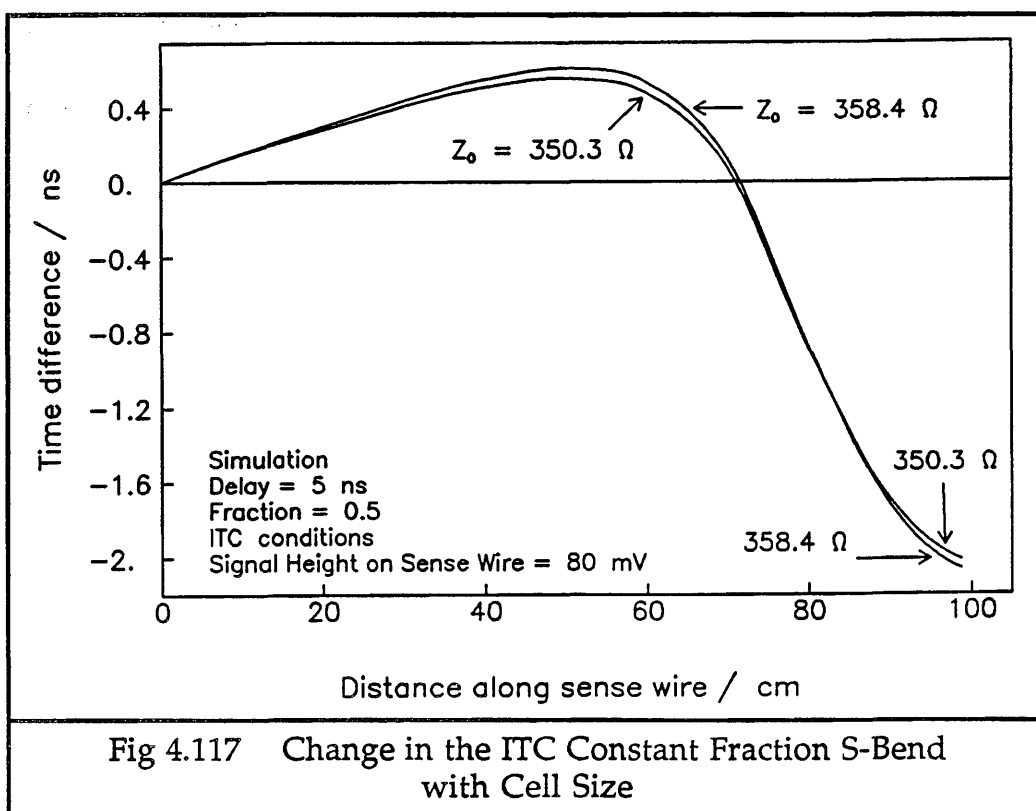
The S-bends will have to be compensated for layer by layer in the ITC readout, because of the different time expansion of each layer. Therefore,

the small effect from different characteristic impedances will not be very significant, and will be removed along with the S-bend.

e) The Hook

The main difference between the long test chamber and the ITC is the presence of the hook on the sense wire during the tests. When the hook is not there, the reflections are not attenuated across it, and so they have more effect on the timing. However, when there is no hook on the sense wires, then there are no significant multiple reflections, only the primary reflection. The effects of the hook can be removed from the simulation by setting R_{Hook} very large.

Figure 4.118 shows the S-bends produced with the standard constant fraction discriminator from the simulation program, for both the long test rig, with its multiple reflections and attenuation in the end plate of 0.7, and for the ITC, with no hook, and attenuation through the end plate of 0.5.

| Fig 4.118 | Comparison of ITC and Long Test Rig S-Bends with the Standard Constant Fraction Discriminator |
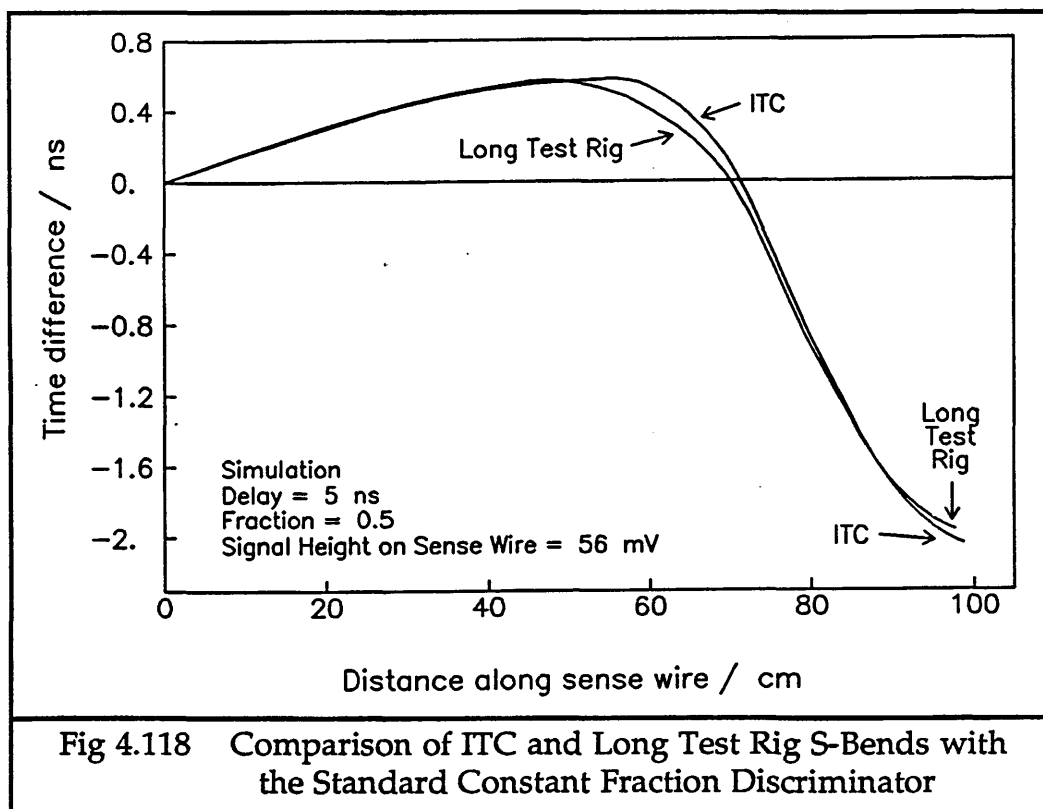
Figure 4.119 shows the S-bend nonlinearities from c/2 for the dual threshold discriminator with an applied threshold of 1 V, for the long test rig and for the ITC.

Fig 4.119   Comparison of ITC and Long Test Rig S-Bends with
the Dual Threshold Discriminator
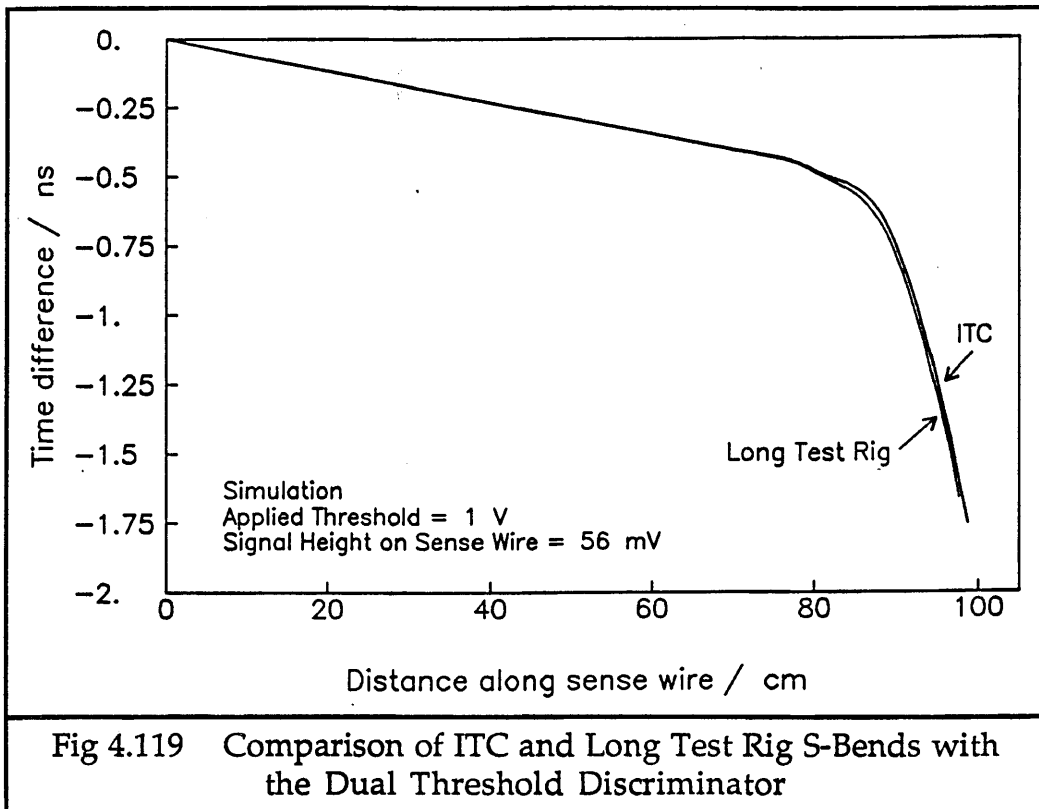
6.2   Changing the End Impedance

If the 23.5 m long 50 Ω cables, which take the chamber signals from the preamplifiers on the ends of the ITC to the main amplifiers in the electronics barracks, were attached directly onto the ends of the chamber, with no preamplifiers to drive the signal down the line, or if the preamplifier were to be designed with a low input impedance, by using the more usual common emitter mode instead of the common base mode, then the S-bends are changed quite dramatically. This effect has been investigated in case it is of interest in future detector readout systems. The different S-bends can be seen in figures 4.120 for the constant fraction discriminator and in 4.121 for the dual threshold discriminator.
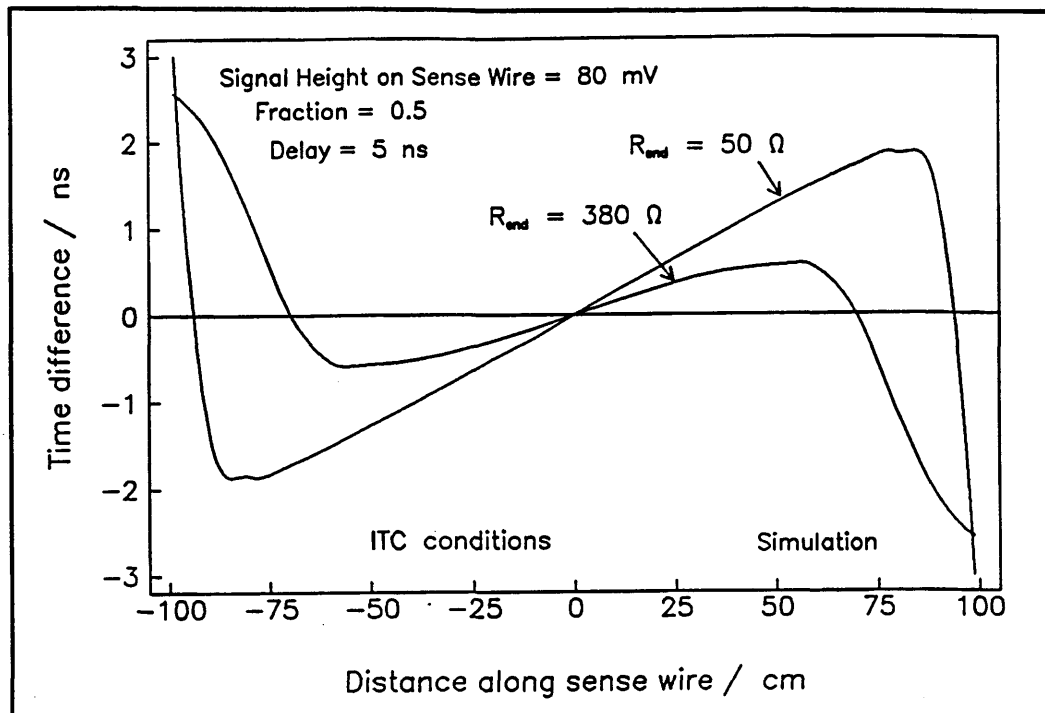
Fig 4.120   Comparison of Constant Fraction S-Bends with
             Large and Small Termination Impedances
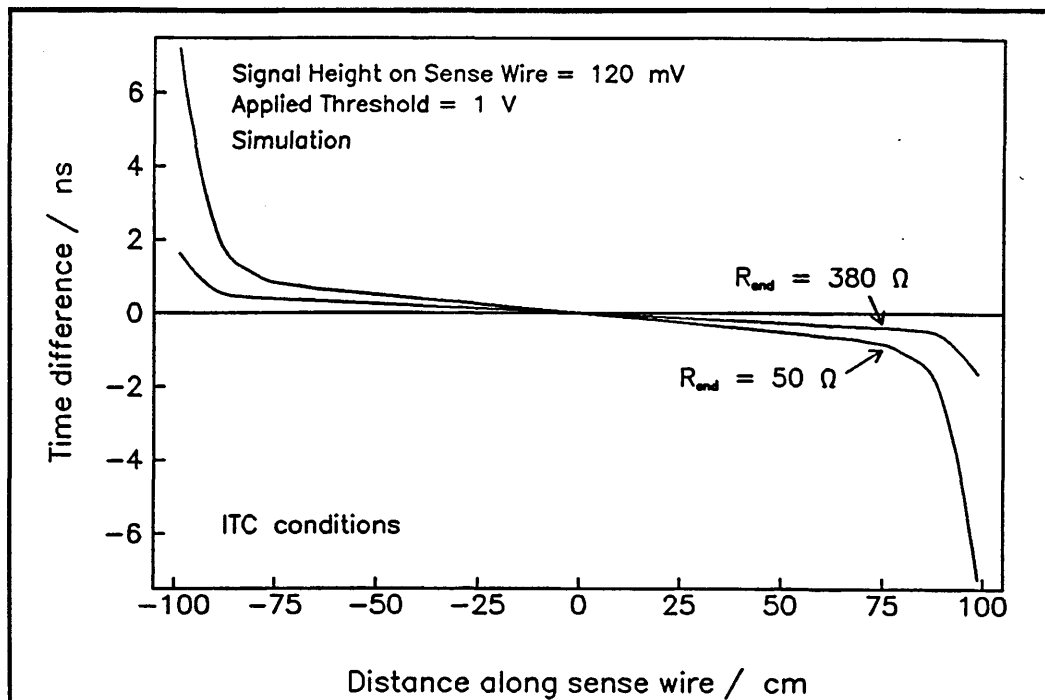
Fig 4.121   Comparison of Dual Threshold S-Bends with Large
             and Small Termination Impedances

As can be seen, for the dual threshold discriminator, the basic S-bend is very similar in shape for the two end impedances but with R_{end} = 50 Ω, the deviation from c/2 is very much magnified. There is no benefit from this behaviour. However, with the constant fraction discriminator, it can be

297

seen that for the central ~ 170 cm of the chamber, the deviation from c/2 becomes almost linear. For the outer 15 cm at each end, the deviation is also linear, but very much slower than c/2. This linear behaviour has some of the more easily correctable features of the normal dual threshold discriminator S-bends with R_{end} = 380 Ω, but still retains the feature of no slewing with pulse size which makes the constant fraction design such a good type of discriminator.

When the end impedance is mismatched with that of the line, with a step down such as 380 Ω to 50 Ω, then the transmission coefficient across this boundary is only 0.23. Therefore, more amplification would be needed to drive the signal to the discriminator and avoid the loss of timing from smaller signals.

6.3   Leakage Currents

The simulation program has been used to investigate the changes to the S-bends if there were a small leakage current from the sense wire (at ~ 2 - 2.5 kV) to ground. This could be due to cracks in the feedthroughs, as experienced with the small test chamber, growths of carbon fibre whiskers, or through the gas as the chamber ages.

The dual threshold discriminator S-bend shows very little change between I = 0 μA (G = 0 Ω^{-1}/cm) up until I ~ 1 mA (G $\approx$ 25 x 10^{-10} Ω^{-1}/cm), which is an enormous current per wire. The chamber would probably be set to trip and turn itself off if there were a current of a few microAmps. At this high value of I, the RMS difference in the z position measurement along the length of the chamber is ~ 0.5 mm.

The constant fraction discriminator z position measurement alters noticeably at a much lower current. A current of I = 1 μA, which gives G ~ 25 x 10^{-12} Ω^{-1}/cm, produces an RMS change in z position along the length of the chamber of 3.3 mm.

7   Conclusions

The method of z position measurement by timing can be made to work accurately and consistently. The system can be frequently calibrated online using pulses injected at both ends of one field wire per cell. This method works well and is both simple to build and to operate.

Two types of discriminator have been successfully tested. Constant fraction discriminators are reliable and give nearly no timing slew over a wide range of pulse sizes, as expected from a real chamber. If the pulses are too large for the amplifier, then saturation occurs and there is a radical change in mode of operation to that of a fixed threshold discriminator. This should be minimised by careful choice of the gas gain in the chamber, and the gain of the preamplifiers and main amplifiers. The spread of time differences of < 50 ps for a wide range of pulse heights, measured in any one place on the wire, corresponds to ~ 2 mm position error, and does not vary by much along the sense wire. The difference in timing between standard operation and saturated operation can be reduced by using a constant fraction discriminator with a longer delay than is at the present standard. A delay of 7.5 ns, or even 10 ns will reduce the difference between the timing of small and large pulses, without increasing the spread of time differences measured.

Dual threshold discriminators have several problems. The nonlinearity from c/2 is strongly affected by changes in pulse height. Changes in pulse height from 55 mV to 17 mV correspond to shifts in z position from 0 cm in the middle of the wire to about 9 cm at the end of the wire, and a 3.5 mV pulse gives a shift of 37 cm at the end of the wire. (These distances were calculated using the nominal speed of c/2.) It must be born in mind, however, that at the ends of the sense wire, mainly larger pulses are all that are expected. The spread of time differences measured with the dual threshold discriminators is ~ 4.5 x that for constant fraction boards, giving a further error in z position of ~ 9 mm. This can be reduced to ~ 3 mm by increasing the threshold fourfold. If the threshold is raised too high, however, then small signals from tracks close to the sense wires will be lost and reflection effects become more significant. The other problem found with the dual threshold discriminators is that it is not so easy to calibrate the centre of the sense wires with them, because of the slewing with signal rise time. Because of the variations from channel to channel of the gain of the preamplifiers, by the time the calibration pulses reach the discriminators from each end of a sense wire, they are no longer equal in amplitude. Therefore, the calibration time difference does not correspond very well to the centre of the sense wire.

TRANSMISSION LINE THEORY

1 Parameters of a Transmission Line

The properties of a transmission line can be described by four parameters :

R = series resistance per unit length [Ω/m]

L = series inductance per unit length [H/m]

G = shunt conductance per unit length [Ω^{-1}/m]

C = shunt capacitance per unit length [F/m]

The values of these parameters are frequency dependent.

They can be combined to give the characteristic impedance of the line :

$$Z_0 = \sqrt{\frac{(R + i\omega L)}{(G + i\omega C)}} \qquad [\Omega]$$

The parameters can be thought of as lumped elements in a circuit as shown in figure 4.C.1.
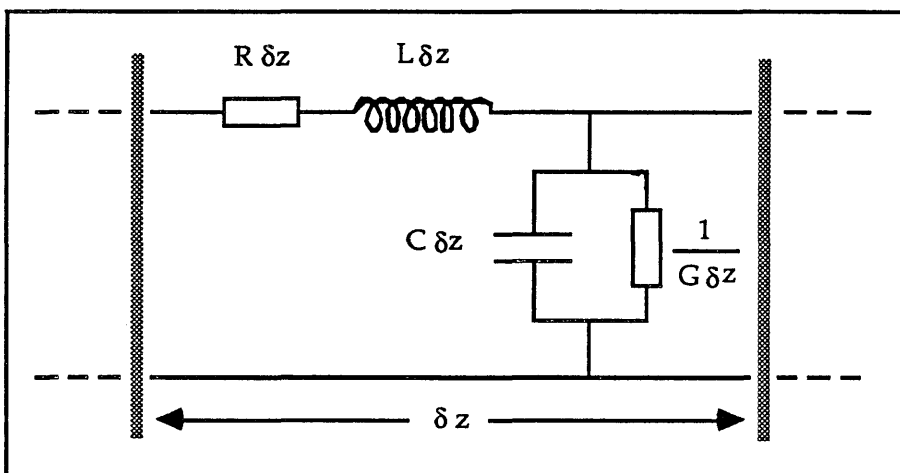
Fig 4.C.1   Elemental Section of a Lossy Transmission Line

2 Ideal Transmission Line

An ideal transmission line is lossless. A lossless line has :

$$R = G = 0$$

This gives :

$$Z_0 = \sqrt{\frac{L}{C}}$$

For a lossless line, the wave equation for the voltage will now be derived. Figure 4.C.2 shows a short section of lossless transmission line. Figure 4.C.3 shows the voltage and current on a short section of the line.

Fig 4.C.2 Elemental Section of a Lossless Transmission Line
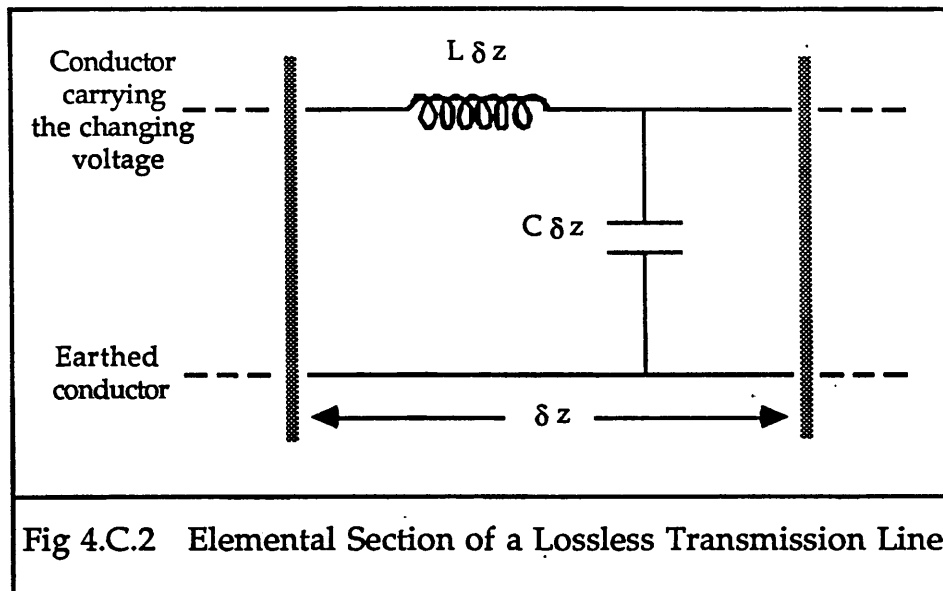
At a time t, the voltage and current at position z, as shown in figure 4.C.3, are $V(z,t)$ and $I(z,t)$. At position $(z+\delta z)$, the voltage changes to $V(z+\delta z,t)$ because there is a back electromotive force from the self inductance $L\delta z$.

The voltage change along the transmission line from z to $(z+\delta z)$ is calculated to be :

$$V(z+\delta z,t) - V(z,t) = \frac{\partial V}{\partial z} \delta z = -L \delta z \frac{\partial I}{\partial t}$$

$$\frac{\partial V}{\partial z} = -L \frac{\partial I}{\partial t} \qquad \text{------ 1}$$

Fig 4.C.3   Voltage and Current on a Transmission Line
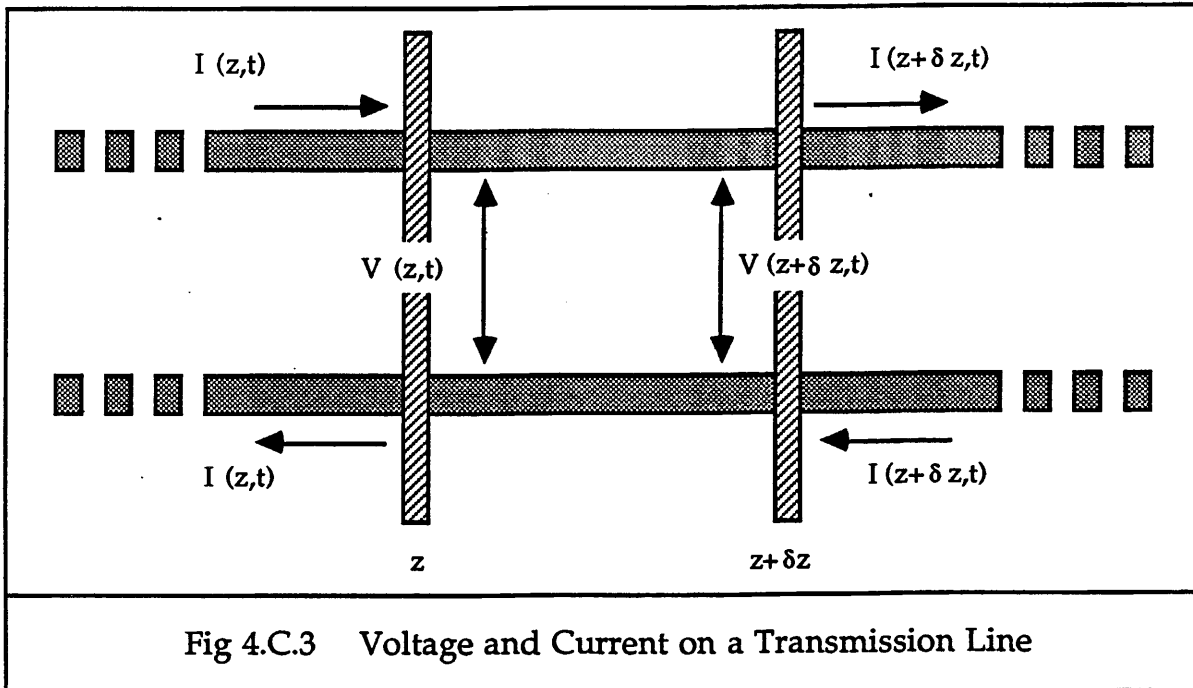
The current flowing in the two conductors also varies with z, because of the capacitance between them.

$$I(z+\delta z,t) - I(z,t) = \frac{\partial I}{\partial z}\,\delta z = -C\,\delta z\,\frac{\partial V}{\partial t}$$

$$\frac{\partial I}{\partial z} = -C\,\frac{\partial V}{\partial t} \qquad \text{---- } 2$$

Differentiating equations 1 and 2 gives :

$$\frac{\partial^2 V}{\partial z^2} = -L\,\frac{\partial^2 I}{\partial z\,\partial t}$$

$$\frac{\partial^2 I}{\partial t\,\partial z} = -C\,\frac{\partial^2 V}{\partial t^2}$$

Since z and t are independent variables, these two relations combine to give a wave equation :

$$\frac{1}{LC}\,\frac{\partial^2 V}{\partial z^2} = \frac{\partial^2 V}{\partial t^2}$$

302

Therefore, when a changing voltage is applied to a transmission line, voltage waves travel along it, at a velocity :

$$v = \frac{1}{\sqrt{LC}}$$

If the dielectric between the conductors has a relative permittivity of 1, such as for gases, then the velocity of the signal along the line = c, the velocity of light.

The solution to the wave equation for the lossless transmission line is of the form :

$$V(z,t) = V_0 \exp\left(i(\omega t - \kappa z)\right)$$

$$\kappa = \text{wave number} = \frac{\omega}{c} = \omega\sqrt{LC}$$

which is an unattenuated, undistorted wave.

3 Lossy Transmission Line

In real transmission lines, there are three sources of loss of signal from the line :

a) Copper Loss   Resistance of the sense wire leads to attenuation. This is important even at low voltages.

b) Dielectric Loss   Small conduction currents through the dielectric attenuate the signal. This is negligible with a gaseous dielectric, even for high frequencies.

c) Corona Loss   Occurs when the electric field at a point on the small radius sense wire is so high as to ionise the gas around that point. This only dominates at very high voltages and frequencies, and will not be a problem in the ITC.

All three losses increase with frequency.
Therefore, in the ITC, the only significant source of attenuation of the

signal is from the series resistance of the sense wires at high frequency.

For a lossy line, the two transmission line equations are :

$$-\frac{\partial V}{\partial z} = RI + L\frac{\partial I}{\partial t}$$

$$-\frac{\partial I}{\partial z} = GV + C\frac{\partial V}{\partial t}$$

which give the wave equation :

$$\frac{\partial^2 V}{\partial z^2} = RG\,V + (RC + GL)\frac{\partial V}{\partial t} + LC\frac{\partial^2 V}{\partial t^2}$$

This can only be fully solved for a special type of lossy line called the distortionless line, which has the special property :

$$\frac{R}{L} = \frac{G}{C}$$

That is, a line is distortionless when the two time constants RC and LG are equal.

Therefore, for this special case, the wave equation becomes :

$$\frac{\partial^2 V}{\partial z^2} = \alpha^2\,V + \frac{2\alpha}{v}\frac{\partial V}{\partial t} + \frac{1}{v^2}\frac{\partial^2 V}{\partial t^2}$$

where $\quad v = \dfrac{1}{\sqrt{LC}} \qquad \alpha = \sqrt{RG}$

Let $\qquad V = U\exp(-\alpha vt) = U\exp(-Rt/L)$

This gives :

$$\frac{\partial^2 U}{\partial z^2} = \frac{1}{v^2}\frac{\partial^2 U}{\partial t^2}$$

which is another wave equation.

Therefore, in a distortionless line, each component of the signal travelling on it is attenuated by a constant factor.

In the ITC, however, the shunt conductance per unit length, $G \approx 0 \ \Omega^{-1}/m$. Therefore, the full lossy line case must be considered.

In a lossy line, the solution to the full transmission line equation becomes that of a damped wave :

$$V(z,t) = V_0 \exp\left(i(\omega t - \kappa z)\right) \exp\left(-\alpha z\right)$$

$$= V_0 \exp\left(i\omega t - \sqrt{(R + i\omega L)(G + i\omega C)}\ z\right)$$

where κ = wave number = ω/c

          α = attenuation constant

In the ITC, the readout of the signals is done using the high frequency components, so to first order approximation at high frequency, this solution reduces to :

$$V \approx V_0 \exp\left(i\omega t\right) \exp\left(\frac{-(R/Z_0 + GZ_0)\ z}{2}\right)$$

For the ITC transmission lines there are almost no leakage currents, so $G \approx 0 \ \Omega^{-1}/m$, making the damping factor for the high frequency signals on the sense wire approximately :

$$\exp\left(\frac{-R\,z}{2Z_0}\right)$$

On the sense wire transmission line at high frequencies, giving $R \ll i\omega L$, and with $G \approx 0 \ \Omega^{-1}/m$, the characteristic impedance approximates to :

$$Z_0 = \sqrt{\frac{R + i\omega L}{G + i\omega C}} \approx \sqrt{\frac{L}{C}}$$

4   Validity of the Approximations for the Termination

The termination of the sense wire transmission line ceases to behave as a transmission line where the signals pass through the end plate, because some of the approximations made for transmission line behaviour cease to be valid. For the end impedance at high frequencies to be approximately equal to that for the ideal transmission line, with $G \approx 0 \ \Omega^{-1}/m$, it is necessary that $R \ll i\omega L$. When the high frequency signals pass through the end plate, the value of L drops almost to zero, and the value of R increases enormously, due to the eddy current power losses. Therefore, this approximation is no longer valid, and the signal path through the end plate does not behave as a transmission line, but as discrete components.

Appendix D

THE SKIN EFFECT

In order to calculate the increase in series resistance of the sense wire with frequency, it is necessary to consider the current density in this conductor. The current density in the sense wire is uniform at low frequencies, because the wire has uniform resistivity through it, and because it is non-magnetic and its diameter is small. However, as the frequency rises, the current density becomes less uniform, both in magnitude and phase. In a round wire, the current density varies with distance from the axis of the wire, and is greatest at the surface. At very high frequencies, almost all the current is confined to a very thin layer next to the surface of the wire. The thickness of this layer is called the "skin depth", and the movement of current density into this layer is called the "skin effect".

The consequences of the skin effect are an increase in series resistance and a decrease in internal inductance. The internal inductance has been neglected in calculations so far, because of this effect at high frequencies.

$$\text{Skin Depth} = \delta = \frac{1}{\sqrt{\mu \mu_0 \pi \sigma f}} \qquad \sigma = \text{conductivity}$$

The sense wires are made of gold-plated tungsten, as shown in figure 4.D.1.

The conductivities for tungsten and gold are always given as percentages of a standard value, the conductivity of copper.

$$\sigma_W = 31\% \ \sigma_{Cu}$$
$$\sigma_{Au} = 80\% \ \sigma_{Cu}$$
$$\sigma_{Cu} = 5.8 \cdot 10^7 \ \Omega^{-1}/m$$

Therefore, 2 μm of gold behaves like ~ 3.21 μm of tungsten, for high frequencies.

Fig 4.D.1   Cross Section Through Sense Wire
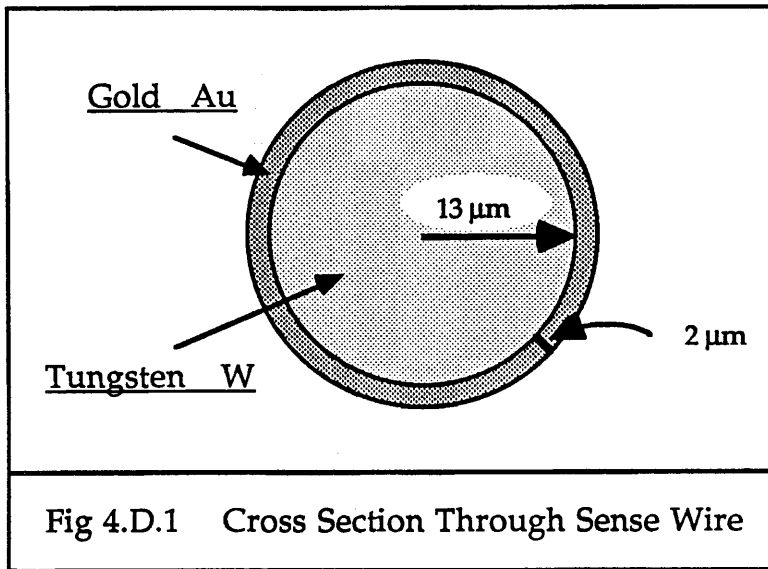
In the ITC, where $f_{max} \sim 500$ MHz,

$$\delta_W = 5 \ \mu m$$

and so over half of the high frequency components of the signal are contained in the gold plating.

If $\delta \ll$ radius of conductor = r, then :

$$R(f) = \frac{r \, R_{dc}}{2 \, \delta}$$

However, for the ITC sense wires, this condition on δ does not strictly hold. It is still possible to find out the resistance at high frequencies, though, by using a graph of results, such as that shown in figure 4.D.2 [4.4].

This gives for $f = 500$ MHz, a value of the series resistance of 139 Ω/m.
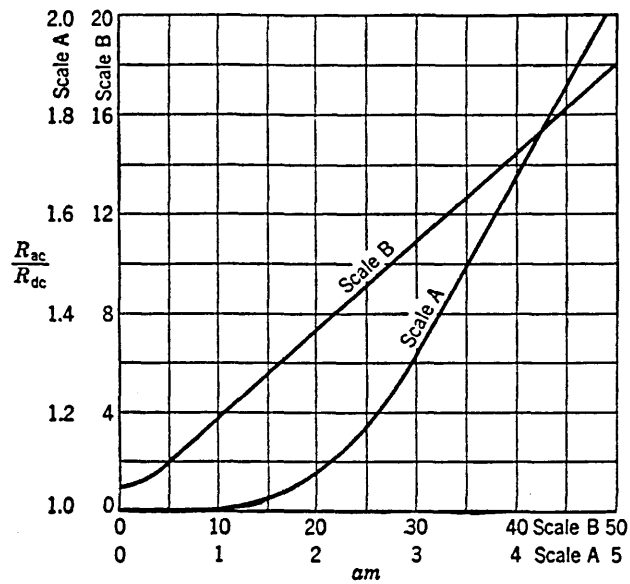
$$am = a \sqrt{\frac{\omega\mu}{\rho}} = 2.810 \times 10^{-3} a \sqrt{\frac{f\mu}{\rho\mu_0}}$$

$$= 1.585 \times 10^{-3} \sqrt{\frac{f\mu/\mu_0}{R_{dc}/l}}$$

where a is the radius of the wire (in meters).

μ is its absolute permeability (in henrys per meter).

μ/μ_0 is its relative permeability.

ρ is its resistivity (in meter-ohms).

R_{dc}/l is its d-c. resistance per unit length (in ohms per meter).

f is the frequency (in cycles per second).

$\omega = 2\pi f$.

Fig 4.D.2   Change in Series Resistance of a Conductor with Signal Frequency

THE REFLECTION AND TRANSMISSION COEFFICIENTS

Figure 4.E.1 shows a terminated transmission line, where the termination does not necessarily match the characteristic impedance of the line, and where it has both resistive and capacitive elements. This is the case for the sense wire termination in the ITC.

Fig 4.E.1   Mismatched Termination of a
Transmission Line
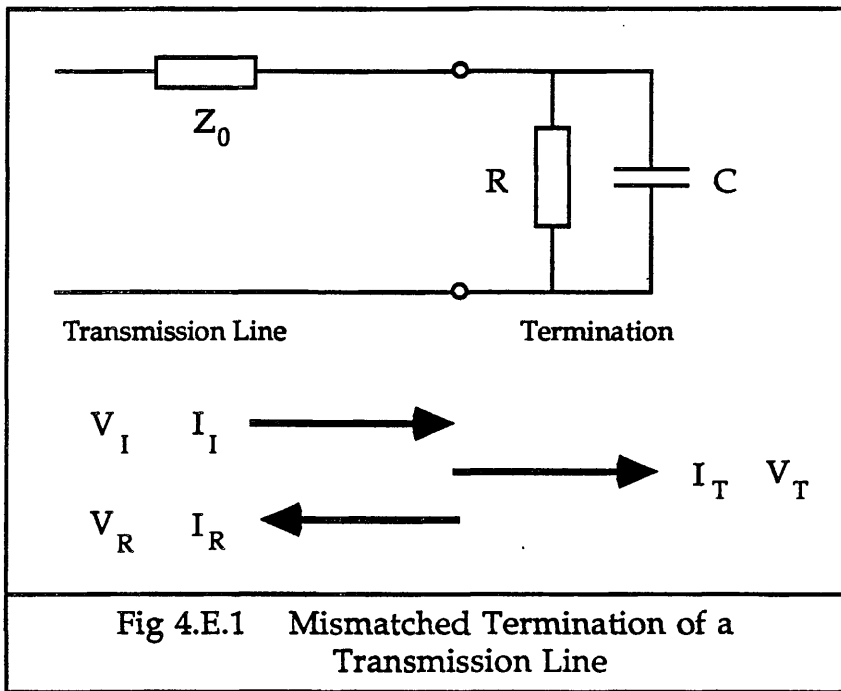
Across this junction, there must be continuity of both voltage and current, giving the following two relations :

$$I_I + I_R = I_T \qquad\text{------------ 1}$$
$$V_I + V_R = V_T \qquad\text{------------ 2}$$

I = input
R = reflection
T = transmission

The currents and voltages are related to each other as follows :

$$I_I = \frac{V_I}{Z_0} \qquad I_R = \frac{-V_R}{Z_0} \qquad I_T = C \frac{dV_T}{dt} + \frac{V_T}{R}$$

Substitution of these currents into equation 1 gives :

$$\frac{V_I}{Z_0} - \frac{V_R}{Z_0} = C \frac{dV_T}{dt} + \frac{V_T}{R}$$

Replacement of V_R using equation 2 gives :

$$2 V_I - V_T = Z_0 C \frac{dV_T}{dt} + \frac{Z_0}{R} V_T$$

Separation of variables and integration gives :

$$\int \frac{dt}{Z_0 C} = \int \frac{dV_T}{2 V_I - V_T (1 + Z_0/R)} + A$$

$$\frac{t}{Z_0 C} = \frac{\log_e \left(2 V_I - V_T (1 + Z_0/R) \right)}{-(1 + Z_0/R)} + A$$

Applying the boundary condition that $V_T = 0$ at $t = 0$, gives the value of the constant A :

$$0 = \frac{\log_e (2 V_I)}{-(1 + Z_0/R)} + A$$

Putting this back into the previous equation obtained after integration, and rearranging gives the transmitted voltage as :

$$V_T = V_I \left(\frac{2 R}{R + Z_0} \right) \left(1 - \exp \left(\frac{-(1 + R/Z_0) t}{RC} \right) \right)$$

311

Using equation 2, the equivalent relation for the reflected voltage is :

$$V_R = V_I \left(\frac{R - Z_0}{R + Z_0} - \frac{2R}{R + Z_0} \exp\left(\frac{-\left(1 + R/Z_0\right)t}{RC} \right) \right)$$

The transmission coefficient T, and the reflection coefficient ρ are defined as :

$$T = \frac{V_T}{V_I} \qquad \rho = \frac{V_R}{V_I}$$

At the boundary :

Direct Signal + Reflection = Transmitted Signal

If the signal is a step function of height 1, then :

$$1 + \rho = T$$

Therefore, the transmission coefficient is :

$$T = \left(\frac{2R}{R + Z_0} \right) \left(1 - \exp\left(\frac{-\left(1 + R/Z_0\right)t}{RC} \right) \right)$$

The reflection coefficient is :

$$\rho = \left(\frac{R - Z_0}{R + Z_0} - \frac{2R}{R + Z_0} \exp\left(\frac{-\left(1 + R/Z_0\right)t}{RC} \right) \right)$$

Chapter 5

SIMULATION OF THE ITC TRIGGER
– Using Data from the TASSO Vertex Detector

1   Introduction

The two triggers provided for ALEPH by the ITC form part of the level 1 trigger. They each provide a YES signal when conditions inside the ITC directly after a beam crossing indicate that there may have been an interaction between an electron and a positron from the beam bunches. The beam crossing rate in LEP will be ~ 44 kHz. It is aimed to reduce this to ~ 500 Hz by using the level 1 trigger. The ITC trigger does not have to achieve this level of rejection alone, but works with the e-γ calorimeter, the hadron calorimeter and the luminosity monitors to do it. The final trigger rate after the level 3 trigger, which is written onto tape, will be ~ 1 Hz. Therefore, 99.8 % of the level 1 triggers will be false. This chapter describes an investigation made into these false triggers, using the ITC r-ø trigger on two random trigger samples of data from the TASSO vertex detector [5.1]. This detector has sufficient similarity with the ITC to make this a valid investigation. In this chapter first of all, a comparison is made between these two detectors and the beam conditions. There then follows a description of the data samples used and the hit multiplicity distributions produced in the small vertex detector. The ITC r-ø trigger is explained, and then applied to the TASSO data. This gives the number of false triggers produced under these conditions. The question of whether the random trigger data produces hits which are correlated in some way, or truly random is next addressed, and some random events are generated which follow the hit multiplicity distributions of the real data for comparison. Finally, a third coordinate is added to the TASSO data to show the potential improvement of the ITC space point processor over the r-ø processor.
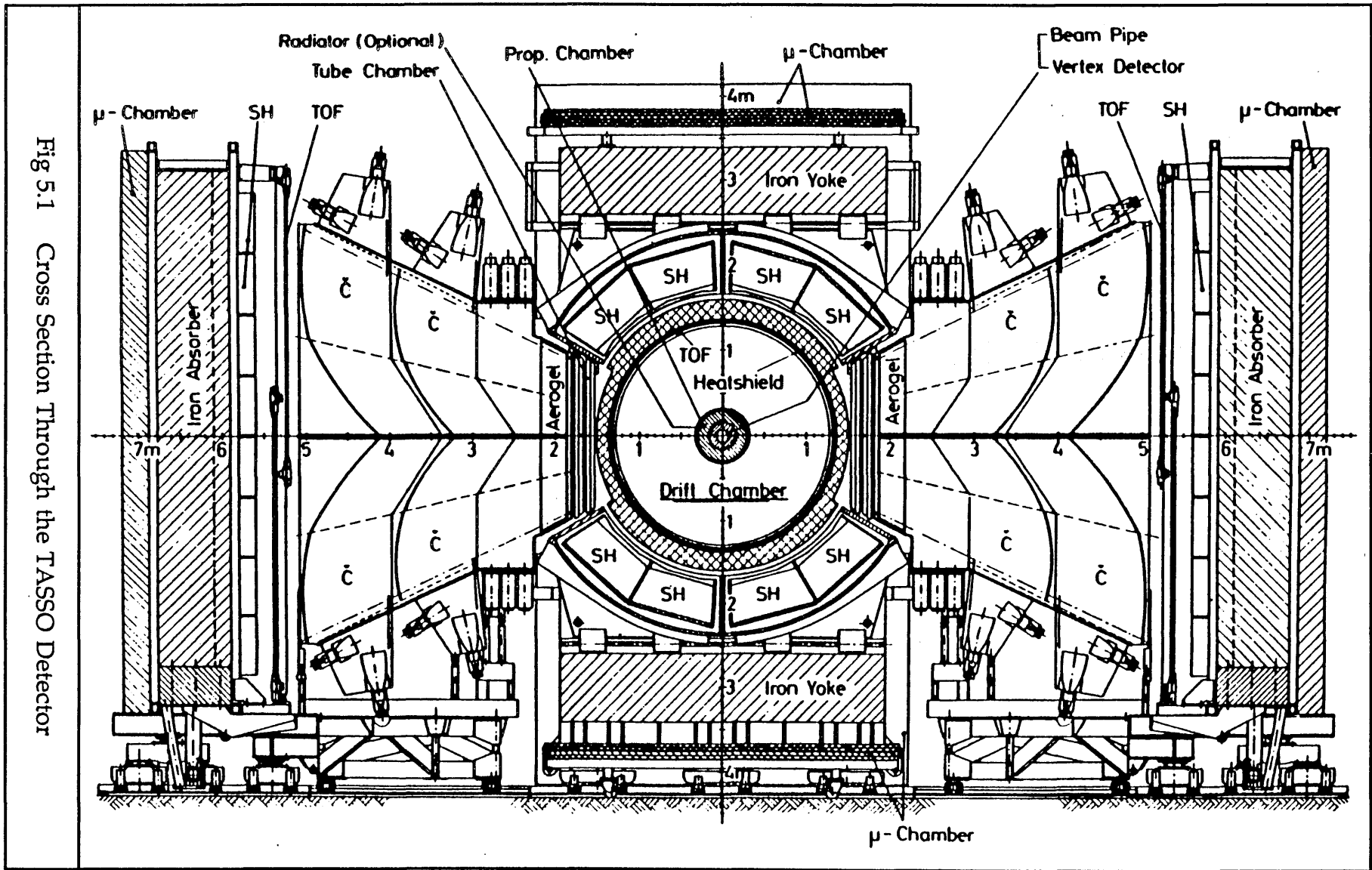
Fig 5.1 Cross Section Through the TASSO Detector

314

2   The TASSO Vertex Detector

The TASSO (Twin-Armed Spectrometer SOlenoid) detector was one of four large experiments on the PETRA (Positron Elektron Tandem Ring Anlage) e^+e^- storage ring at DESY (Deutsches Elektron Synchrotron) in Hamburg. TASSO ran from May 1979 to November 1986. After the summer of 1982, a small vertex detector was added, between the innermost detector and the beam. It is data from this detector which has been used to test the ITC trigger algorithms.

. .   A cross section through the TASSO detector can be seen in figure 5.1. This goes along the beam pipe and through the twin arms, after which the detector is named.

Figure 5.2 shows the vertex detector itself. It is a multiwire drift chamber, which works on the same principles as the ITC. A cross section through the vertex detector across part of one end plate can be seen in figure 5.3.

Fig 5.2   The TASSO Vertex Detector

Fig 5.3   The TASSO Vertex Detector Cell Layout
and Walls
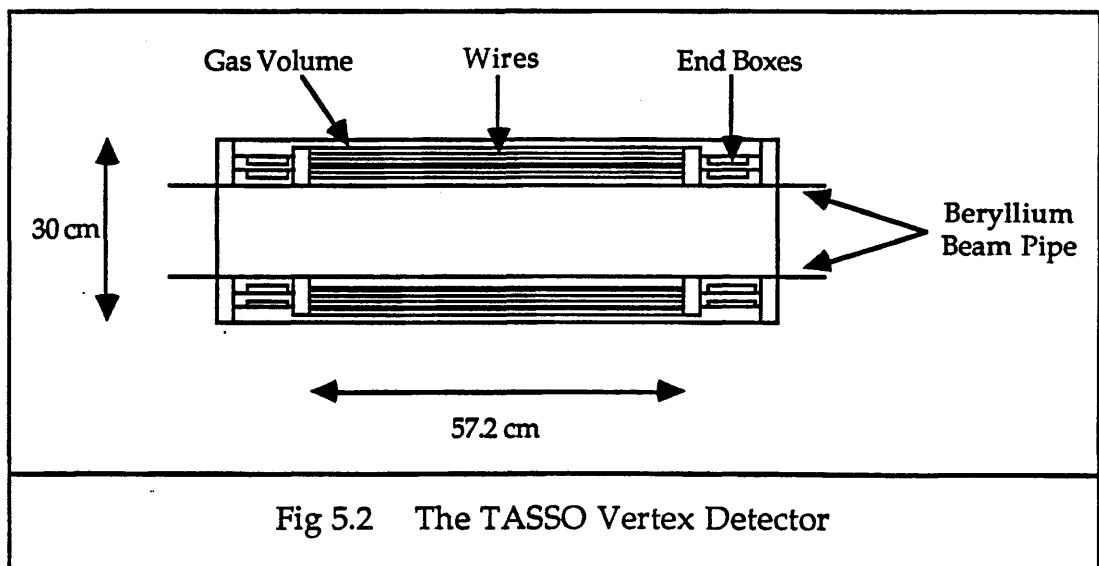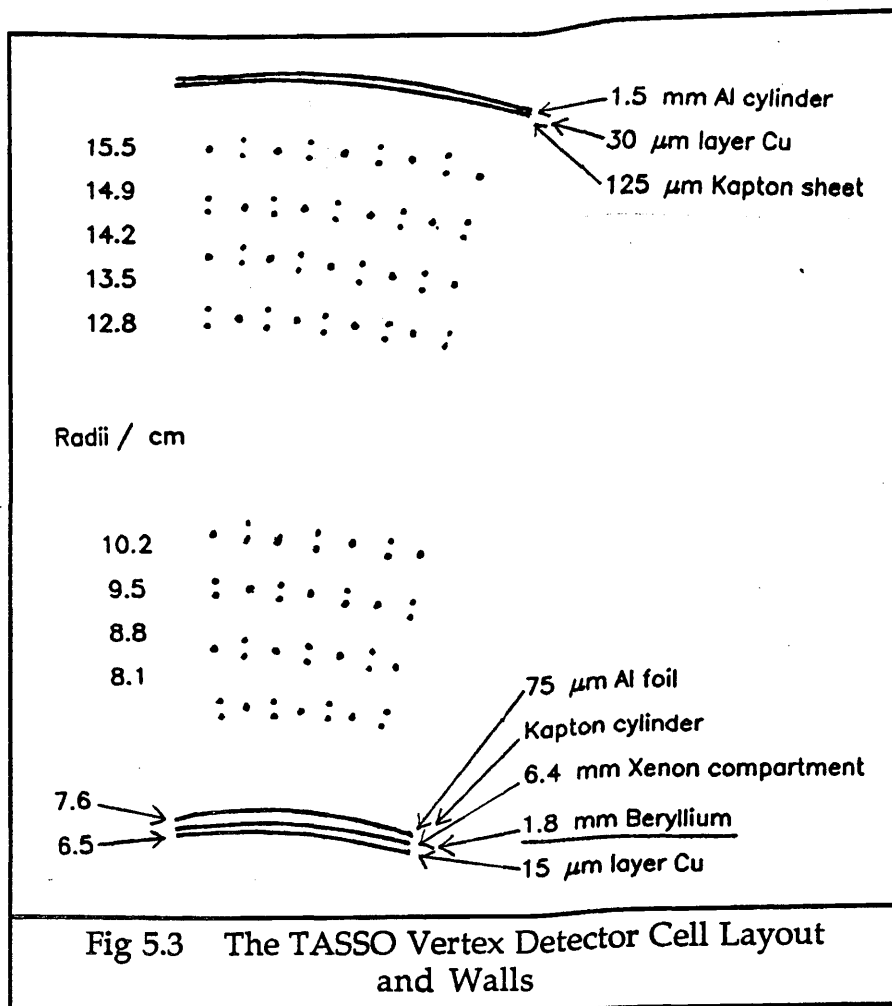
2.1   Material Between the Beam and the Detection Volume

The inner shell of the vertex detector forms a section of the beam pipe. Its inner radius is 6.5 cm and it is ~ 1.1 cm thick. It is principally composed of a 1.8 mm thick layer of beryllium, which was chosen for its low atomic number of Z = 4 and high modulus of elasticity. It had to be strong enough to maintain the vacuum inside the beam pipe, and allow a pressure of ≤ 4 bar inside the chamber. The inner wall of the vertex detector also had to have a minimal percentage radiation length, whilst being as opaque as possible to the flux of synchrotron radiation photons from the beam. However, beryllium is almost transparent to the low energy photons which are the predominant component of the reflected photon flux incident on the pipe. To counteract this, the inner surface of the beam pipe was coated with a 15 µm layer of copper, which has a very high absorption for photons of energy < 50 keV. Unfortunately on absorbing a photon, copper fluoresces at an energy of 8 keV. Most of these photons were then absorbed by a 75 µm layer of aluminium on the outside of the beam pipe. If this had not proved enough to stop these 8 keV photons from causing large currents in the

chamber, then xenon gas could have been introduced into a thin compartment within the beam pipe wall. Xenon has a very high attenuation coefficient at this energy level. However, in the runs used for the following analysis, the xenon cavity was not used.

2.2 Wires in the Chamber

The TASSO vertex detector had 8 layers of cells, divided into two groups of four, which were separated in order to give as long a lever arm as possible for vertex reconstruction. The radii of the sense wire layers can be seen in figure 5.3. The important innermost radius is 8.1 cm. There are 720 sense wires, made of 20 μm diameter tungsten-rhenium. These are arranged to give 72 cells per layer in the inner 4 layers, and 108 cells per layer in the outer 4 layers. Between each sense wire was a pair of field wires, giving a total of 1440 field wires. These were made from 100 μm diameter beryllium-copper. The active length of the chamber was 57.2 cm, which was chosen to match the acceptance of the outer tracking detectors. The average maximum drift distance of the rectangular cells in the vertex detector was 4 mm.

2.3 Gas Used in the Chamber

The gas type used in the chamber was argon-carbon dioxide 90%-10%. The argon was bubbled through water and the CO_2 was bubbled through ethanol. This gas mixture was used because tests with argon-ethane 50%-50% produced growths of carbon fibre whiskers from the field wires to the positive sense wires. The chamber was then being run with a gas pressure of 4 bar and the sense wire voltage was at 5 kV. Consequently, less extreme operating conditions were chosen, with pressure at 3 bar and sense wire voltage of 2.7 kV. These conditions in the argon-carbon dioxide gas mixture gave an average drift velocity of the electrons in the gas of 38 μm/ns.

The relevant properties of the TASSO Vertex Detector and the ITC are summarised in table 5.1.

317

SET UP	TASSO VERTEX DETECTOR	ALEPH ITC
Table 5.1 Comparison of the TASSO Vertex Detector and the ALEPH ITC		
Detector Type	Small Cell Multi-Wire Drift Chamber	Small Cell Multi-Wire Drift Chamber
No. of Layers of Wires	8	8
Sense Wires in Inner Layer	72	96
Sense Wires in Outer Layer	108	144
Radius of Inner Layer	8.1 cm	16.11 cm
Radius of Outer Layer	14.9 cm	26.02 cm
Average Max. Drift Distance	4 mm	5.6 mm
Interactive Length	57.2 cm	200 cm
Gas Pressure	3 bar	1 bar
Gas Mixture	argon 90 % CO_2 10 % ethanol, water	argon 50 % ethane 50 % ethanol

3 The Data Samples

Two data samples were used for the tests of the ITC trigger. These were triggered in TASSO and recorded after a fixed number of beam crossings, independently of any physics triggers. The beam conditions were reasonable when the data was taken. The two sets consist of :

15 135 events   at   38 GeV

15 347 events   at   44 GeV

The plots in figures 5.4 and 5.5 show the hit multiplicity distributions for each layer of the detector, of these two data sets at the different energies. It should be noted that even at the lower of the two energies the inner 4 layers almost always have at least one hit per layer each.
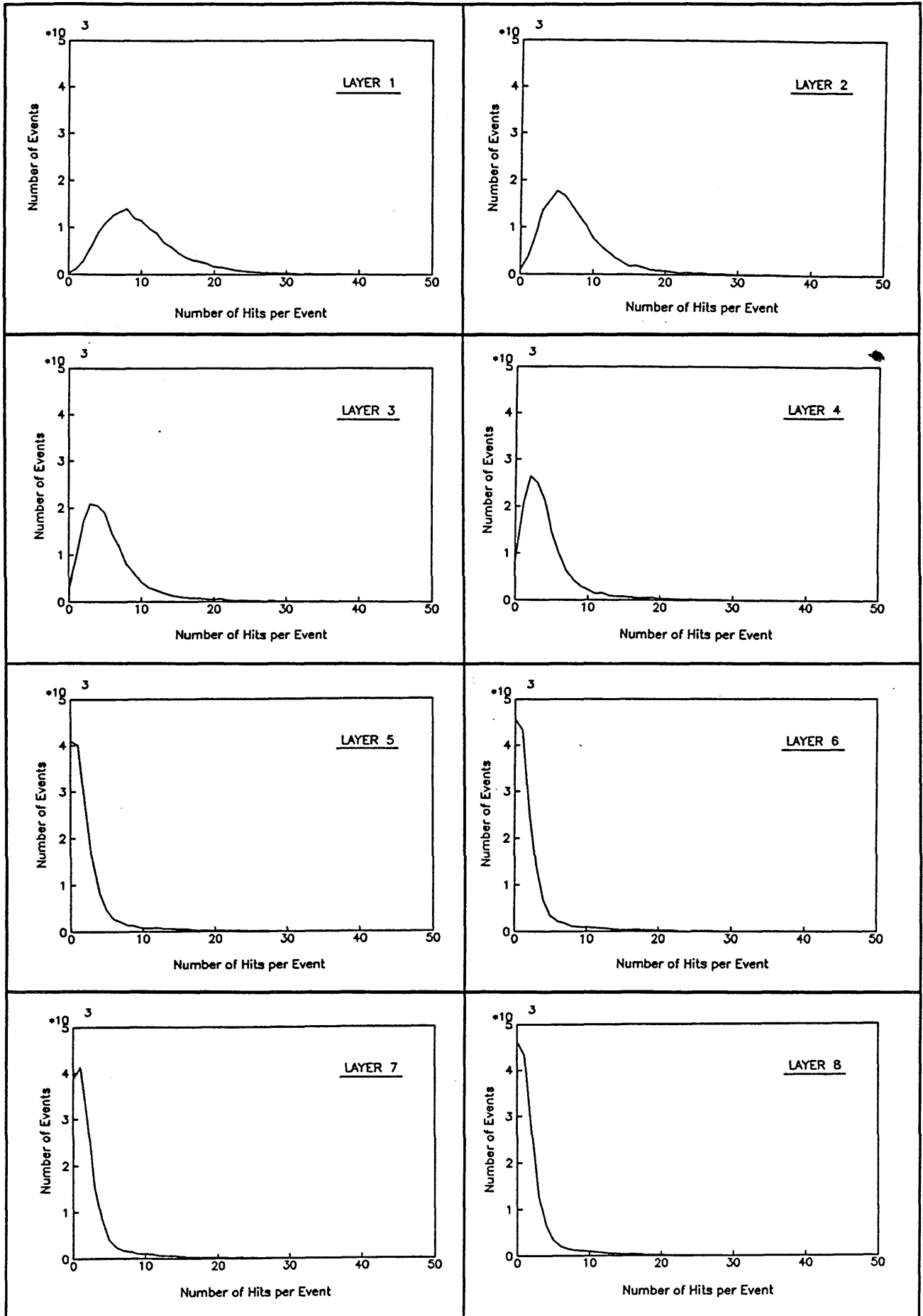
Fig 5.4   Hit Multiplicity Distributions for Each Layer at 38 GeV
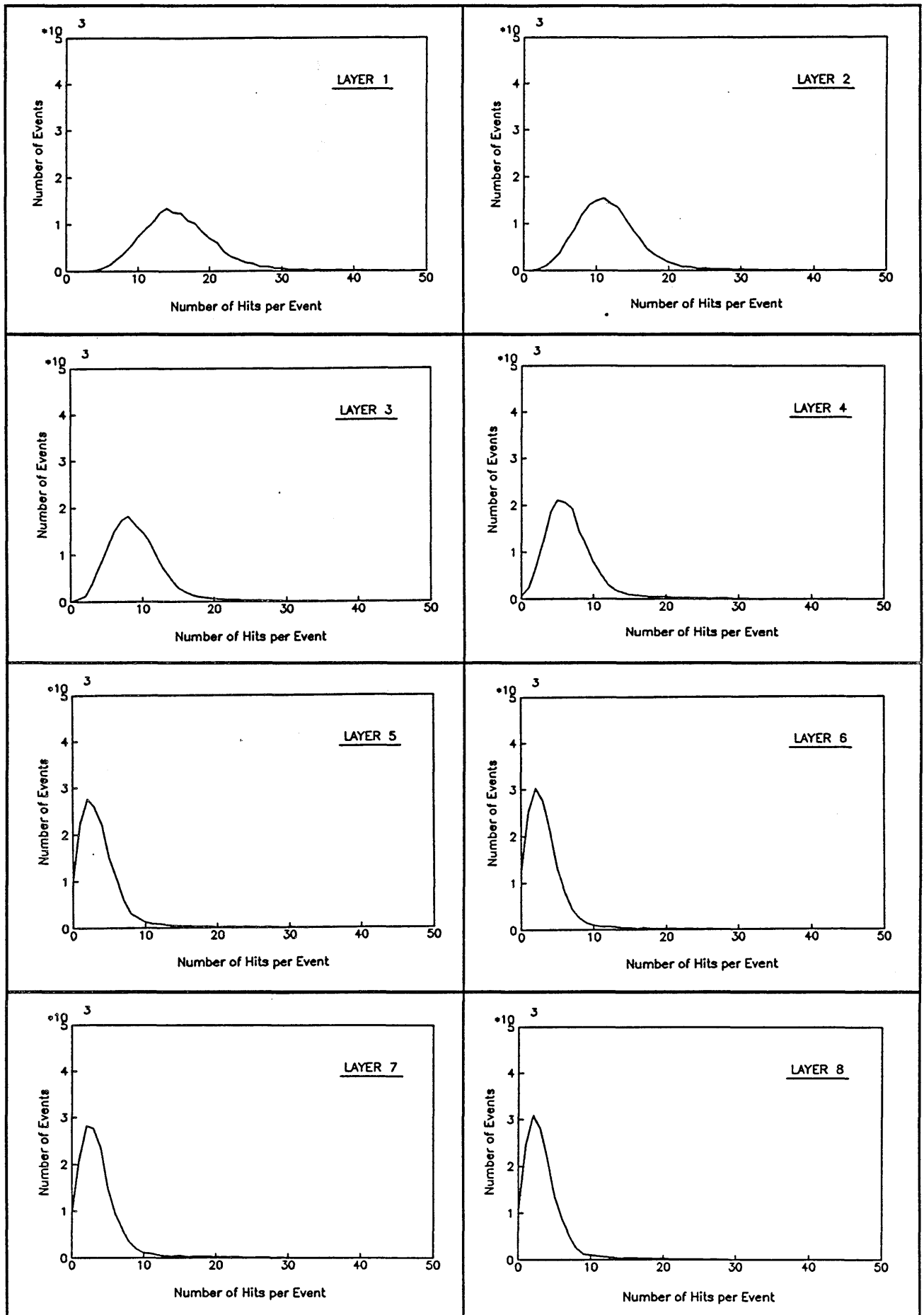
Fig 5.5   Hit Multiplicity Distributions for Each Layer at 44 GeV

320

The mean hit multiplicities can be shown as a function of the distance of the cell layer from the interaction point. This can been seen in figure 5.6 for both the data samples.
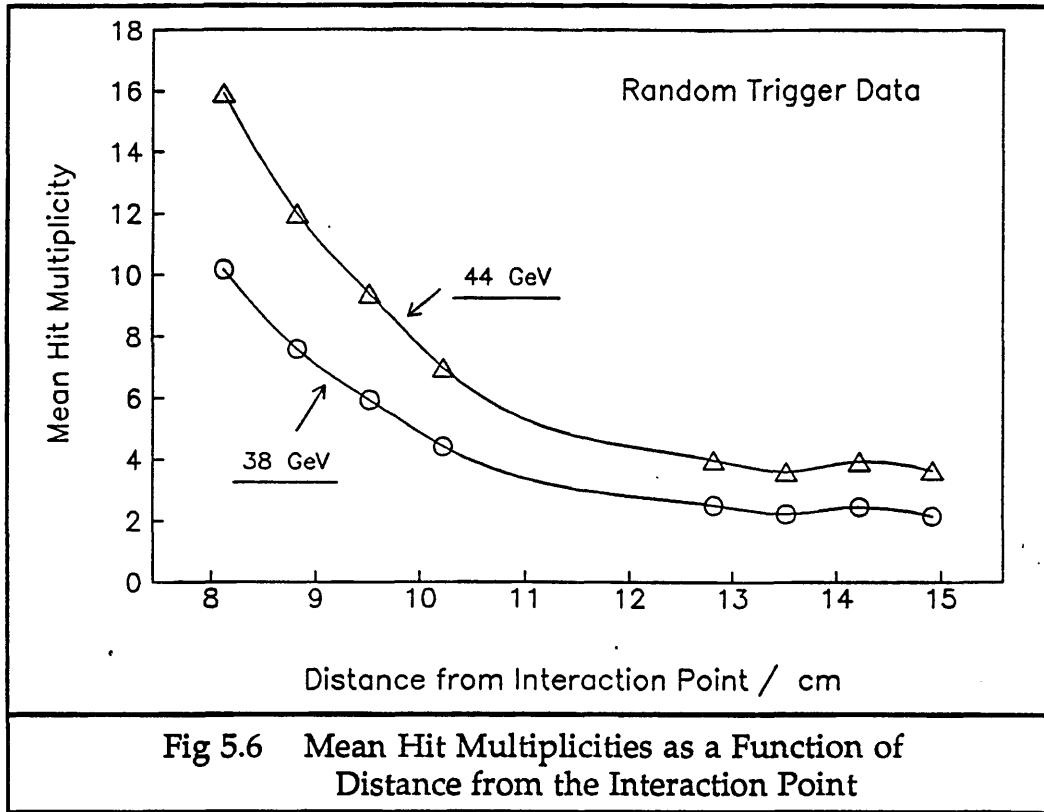
Fig 5.6   Mean Hit Multiplicities as a Function of
Distance from the Interaction Point

4   The ITC r-ø Trigger

The r-ø trigger is one of two trigger processors in the ITC. It works at the simplest level of hits on the wires, and does not use the drift times or any information about the z positions. It has to give a positive trigger with better than 99 % probability if a single track with transverse momentum p_t greater than some cut-off leaves the origin at the interaction point. The trigger should reject noise and tracks with low momentum or those with a large impact parameter with respect to the origin.

4.1   The Trigger Masks

The r-ø trigger operates by superimposing a pattern of masks onto the cell layout on the end plate [5.2]. There are 288 masks in the ITC r-ø trigger. These are based on the cells in the outer layers of the detector, where there are 144 cells per layer. The two types of mask can be seen in figure 5.7.
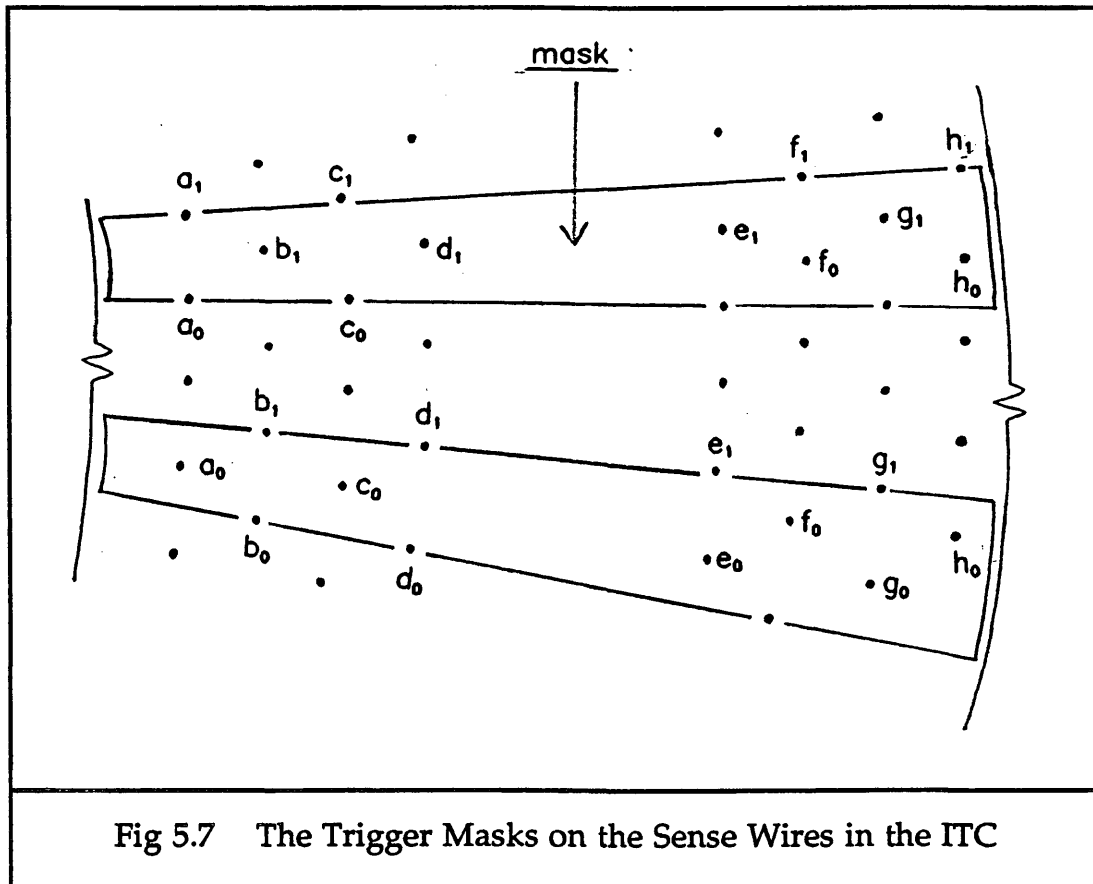
Fig 5.7   The Trigger Masks on the Sense Wires in the ITC

Sample algorithms for a mask with 8 hits in it are as follows :

1) a_0.AND.$(b_0$.OR.b_1).AND.c_0.AND.$(d_0$.OR.d_1).AND.
      $(e_0$.OR.e_1).AND.f_0.AND.$(g_0$.OR.g_1).AND.h_0

2) $(a_0$.OR.a_1).AND.b_1.AND.$(c_0$.OR.c_1).AND.d_1.AND.
      e_1.AND.$(f_0$.OR.f_1).AND.g_1.AND.$(h_0$.AND.h_1)

These masks are set up with a fixed number of hits required in them. In the following analysis, the number of hits needed in at least one mask for a trigger is varied from 4 to 8. The number of hits needed in the ITC can be individually set for each mask. This means that areas of the chamber which are turned off or are very noisy will not influence the overall number of triggers from the ITC. Also, in the ITC, the position of the hits within a mask can be specified. For instance, it could be required of a trigger that it has at least one hit in both an inner layer and an outer layer, to make sure that there is a sufficiently long lever arm for track fitting and predicting the distance of closest approach of the track from the origin. Alternatively, a hit in the innermost and outermost layers could be required. In the following tests, the effects of these special restrictions on the trigger efficiency are not investigated. A straight forward lower limit on the number of hits in any one mask is the trigger algorithm tested.

4.2 Applying the ITC r-ø Trigger to the TASSO Vertex Detector

The geometry of the TASSO vertex detector is similar enough to that of the ITC that the trigger masks described above can be applied to the cell pattern there. To fit the vertex detector cell pattern, 216 trigger masks are needed which map onto the outer layers of cells, where there are 108 cells per layer.

4.3 The ITC r-ø Trigger on the Two Data Samples

The percentage of events in each data sample which pass the trigger masks when the   number of hits required in at least one mask is varied from 4 to 8 is shown in figure 5.8.

Fig 5.8   Frequency of Random Trigger Events Passing the Trigger
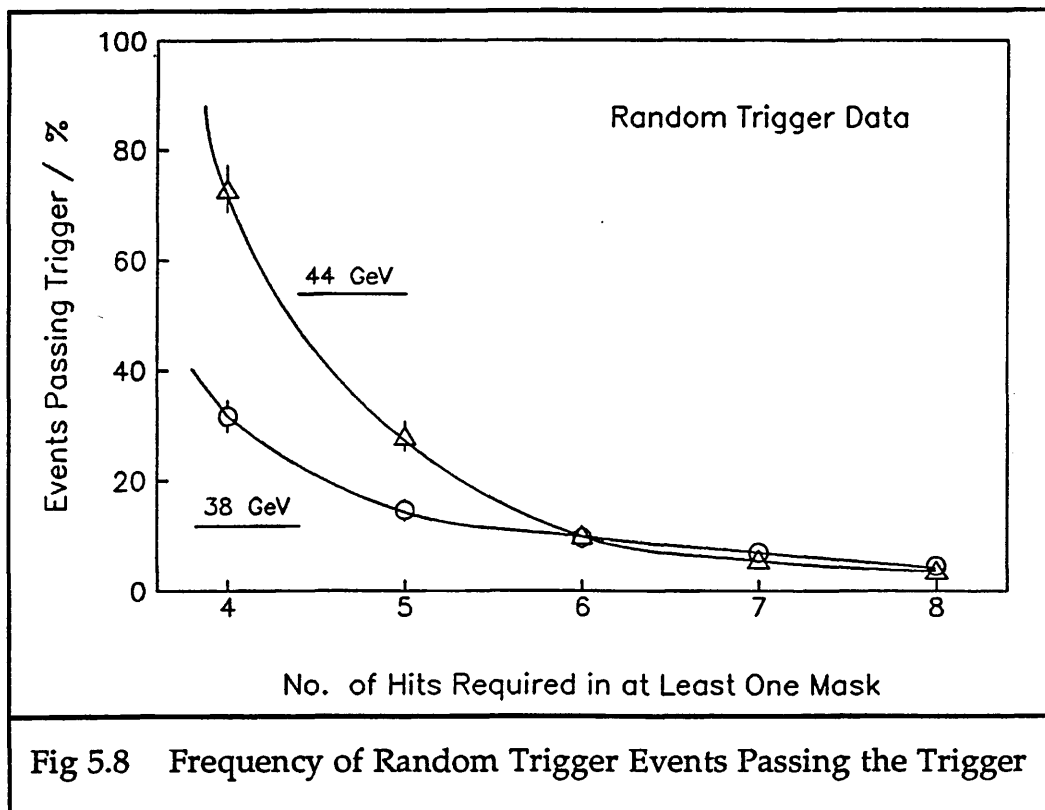
There are 8 cell layers in the TASSO vertex detector, so to require 8 hits in at least one mask is the maximum number possible in a mask as defined. As can be seen in the figure, the 44 GeV data produced a much higher trigger rate than the 38 GeV data, when only 4 or 5 hits were required in any one trigger mask. When all 8 wires in any one mask were required to be hit, then 4.6 % of the events from this random trigger data at 38 GeV passed the

trigger and 3.9 % of the events passed the trigger at 44 GeV beam energy.

For the ITC trigger, in conjunction with the other Level 1 trigger detectors, to reduce an interaction rate of 44 kHz down to 500 Hz, only about 1 % of beam crossings must pass the trigger.

Some sample events which pass the trigger can be seen in figures 5.9 - 5.14.

Figure 5.9 shows a typical random trigger in the TASSO vertex detector from the 44 GeV data which has no masks with 4 or more hits in them.

Figure 5.10 shows an event from the same data sample which passes the trigger with a requirement of at least one mask with 4 hits in it.

Figure 5.11 shows an event which passes a trigger cut of 7 hits in one or more mask. The fact that these filled masks are not produced by charged particles from the interaction point at the origin can be seen in figure 5.12, which shows a cross section through the whole tracking area of TASSO. The vertex detector is only small in the middle of this plot, surrounded by a thin detector called the CPC or Cylindrical Proportional Chamber, which has four active layers, and then the large Central Detector, in which no tracks at all can be seen.

Figure 5.13 shows a typical random trigger event in the vertex detector which passes the requirement of at least one mask having all 8 wires hit. As can be seen, far more than one mask has been completely filled up. This event has also not been caused by an annihilation of an electron and a positron at the interaction point, but is just beam noise. This can be seen in figure 5.14, where there are no obvious tracks in the central detector.
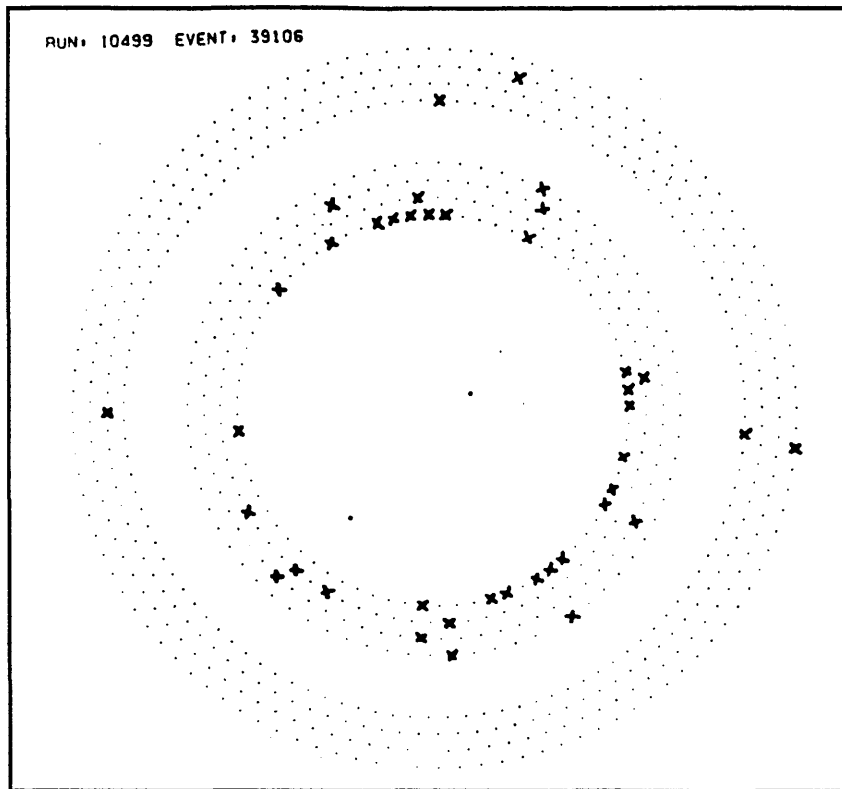
Fig 5.9   A Typical Event at 44 GeV Which Passes
No Trigger Masks

Fig 5.10   A Typical Event at 44 GeV Which Passes
the Trigger Requirement of
at Least One Mask With 4 Hits in It

RUN: 10499 EVENT: 35052

Fig 5.11   A Typical Event at 44 GeV Which Passes
the Trigger Requirement of
at Least One Mask With 7 Hits in It
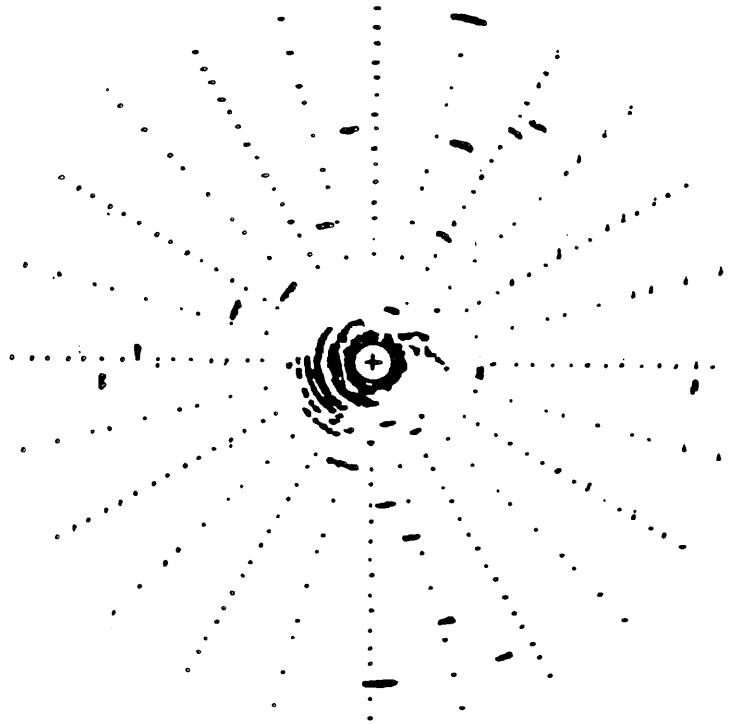
Fig 5.12   An Event With 7 Hits in at Least One
Trigger Mask, Shown Through All
the Tracking Detectors in TASSO

326

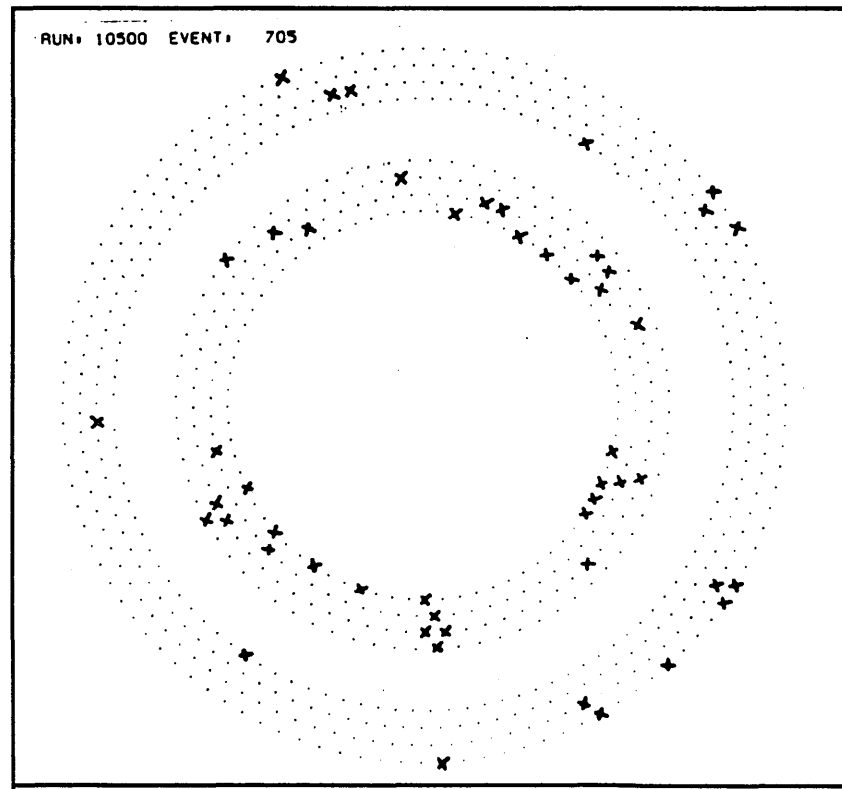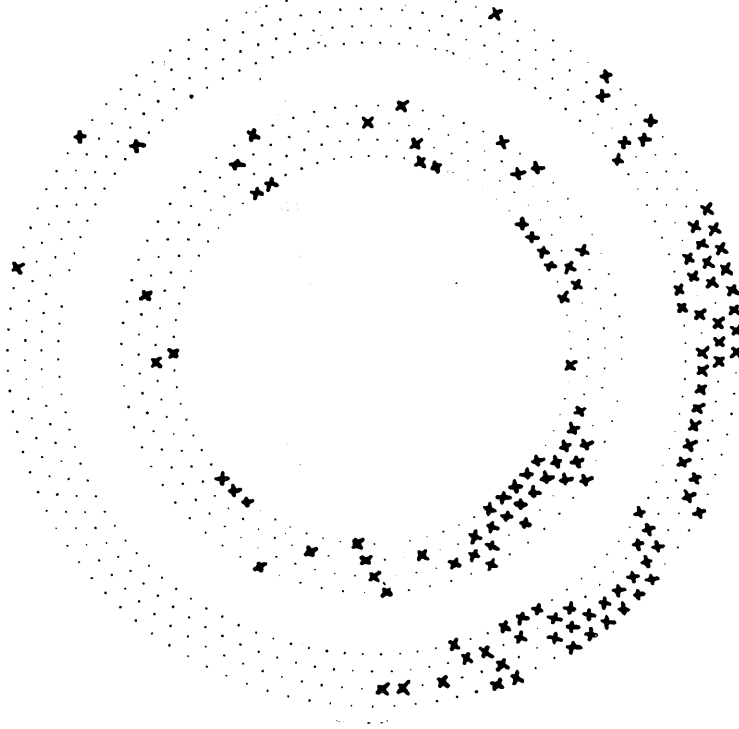RUN: 10499 EVENT: 37303
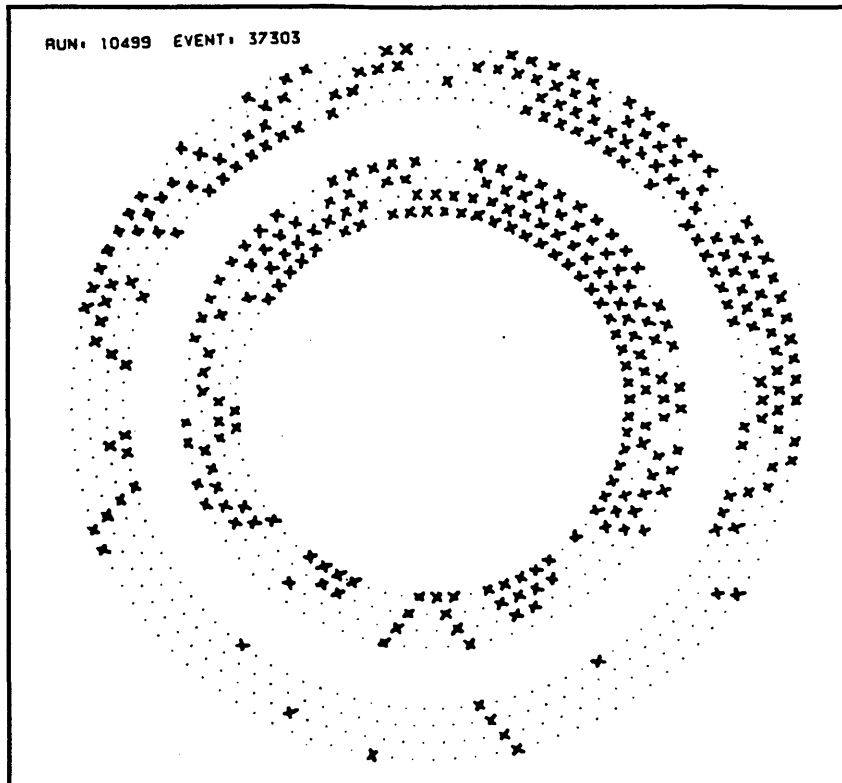
Fig 5.13   A Typical Event at 44 GeV Which Passes
the Trigger Requirement of at Least
One Mask With 8 Hits in It
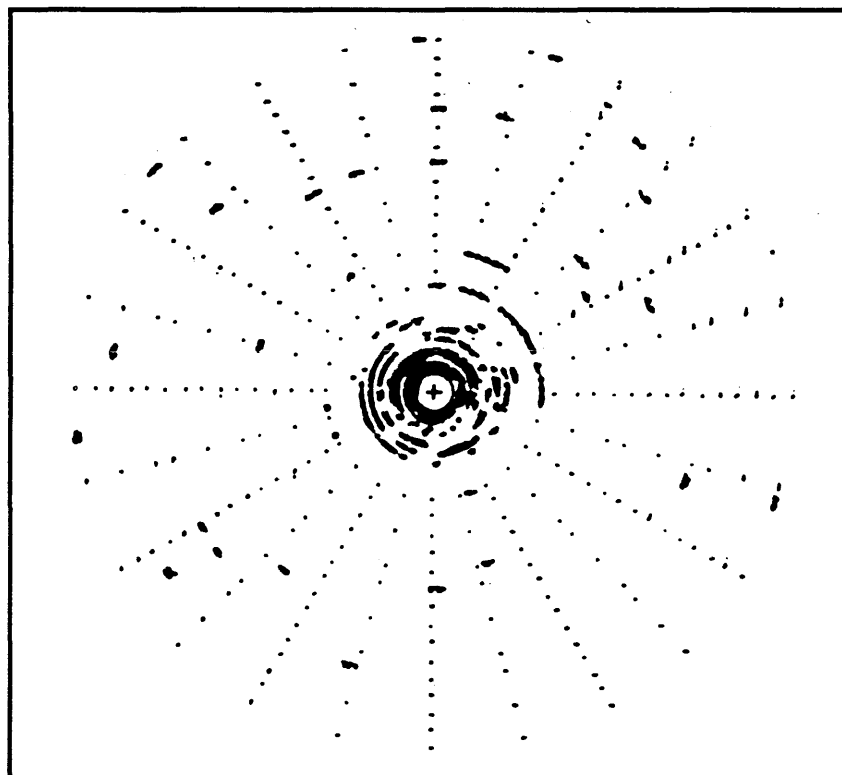
Fig 5.14   An Event With All 8 Hits in at Least
One Mask, Shown Through All
the Tracking Detectors in TASSO

4.4 Source of Noise in the Vertex Detector

Most of the hits in the vertex detector which were not associated with beam interaction products were concentrated in the plane of PETRA on the inside of the ring. This indicates that the source of these hits was not synchrotron radiation, which would be on the outside of the ring, and so must have been effectively absorbed by the copper coating on the beryllium of the beam pipe. The 8 keV fluorescence from the copper accounted for about 10 % of the current drawn by the chamber. The remaining current was caused by off-momentum particles, which showered in the beam pipe before they reached the detector [5.1]. This source of noise hits in the detector indicates that the randon trigger data hits are not truly random within the detector but are in some way correlated. This possible correlation will be investigated in the next section by generation of random events and comparison of the trigger pass rate with that of the real data.

5 Simulation of the Random Hits

In order to test the hypothesis that the random trigger data hits were correlated in some way within the TASSO vertex detector, a Monte Carlo generator was used to produce hits on the cell layers. These hits were made to reproduce the distributions of the number of hits per layer for each of the two beam energies, as shown in figures 5.4 and 5.5. The number of events generated were :

15 000 events	with	38 GeV hit distribution
15 000 events	with	44 GeV hit distribution

The percentage of events from these uncorrelated data sets which pass the ITC r-ø trigger at various hit levels per mask can be seen in figure 5.15. They are shown in relation to the random trigger data for comparison.

As can be seen in the figure, when a high number of hits in at least one mask is demanded, almost none of the Monte Carlo data events pass the r-ø trigger. When a demand is made of at least one mask having all 8 layers hit, then no Monte Carlo events at either energy level pass the ITC r-ø trigger.

Therefore, it can be seen that the hits seen in the TASSO vertex detector in the random trigger data events are correlated, and that this greatly increases the number of false positive triggers produced.

Fig 5.15 Random Trigger Data and Monte Carlo Data Trigger Efficiencies for Various Mask Hit Levels
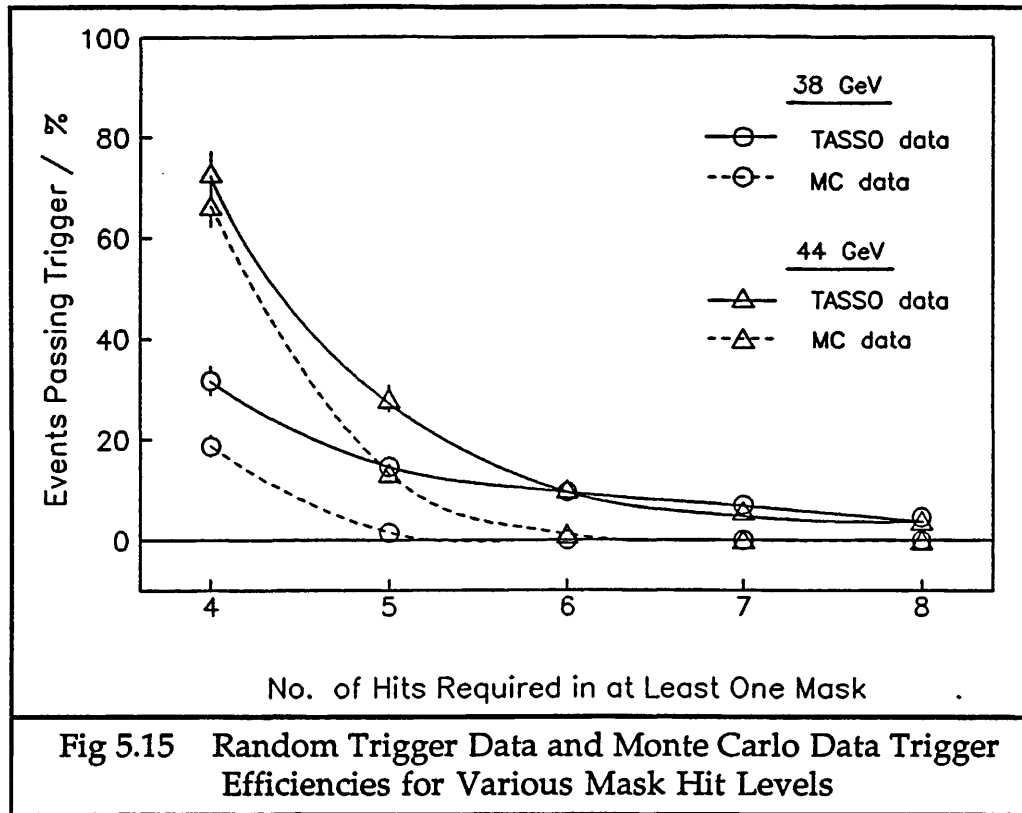
6 The ITC Space Point Processor

The next investigation is into the ITC space point processor to see if this can be used to overcome the hit correlation problems. In the ITC, unlike in the TASSO vertex detector, there is not only r-ø information about the tracks seen in the detector, but also there is a z coordinate associated with each r-ø coordinate. This means that every track can be reconstructed in three dimensions instead of just two, and this extra piece of information should reduce the false trigger rate. Therefore, the next investigation is to see by how much the trigger rate can be reduced by using the z coordinate in the ITC trigger.

The ITC space point processor does not use the drift times measured, just the hit wire information, coupled with the z position information after it has undergone a time expansion process.

6.1 The Time Expansion Process

The hits along the track of a particle which starts at or near the interaction point and travels out at any angle through the ITC are made to coincide in time at the space point processor by the use of a method known

as time expansion. The signals are read out from both ends of a hit wire, amplified and discriminated, and time difference between them is found for each hit wire. These time differences then undergo the time expansion process, where they are multiplied by factors which are inversely proportional to the radii of the sense wire layers. The net result of this is that signals from a track at any polar angle θ all arrive at the space point processor within a short time window. This effect is shown in figure 5.16 for three tracks in the ITC. One track has a large polar angle $\theta = 90°$, another has $\theta = 14.7°$, which is the lowest value angle for a track to still cross all 8 cell layers. The third track does not emanate from the interaction point, but from further along the beam pipe.

Fig 5.16   Time Expansion for the Space Point Trigger
Processor in the ITC
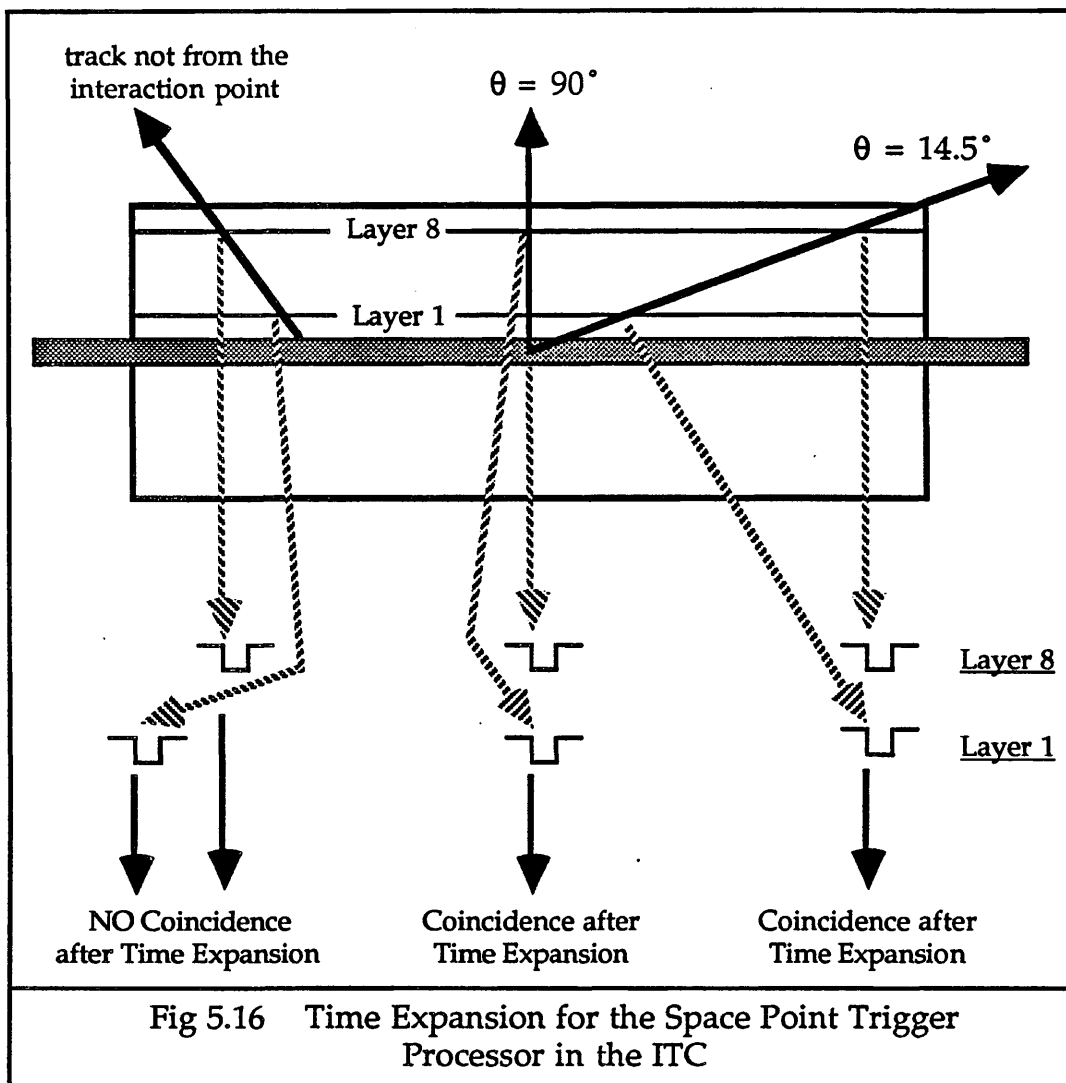
As can be seen in figure 5.16, the two tracks from the interaction point both produce coincident z signals after time expansion, despite their different polar angles. The track which does not come from the interaction point will not produce a space point trigger, because its expanded time differences do not coincide.

6.2 Adding a z Coordinate to the TASSO Vertex Detector Hits

There is no z information from the TASSO vertex detector. However, a random z coordinate can be assigned to each of the hits in the events from the TASSO random trigger data. This will enable a test to be made of the improvement that the space point processor gives on this data. Adding a random z coordinate to the TASSO random data is a rather artificial test, but does give some indication of the effectiveness of the r-ø-z trigger.

For the z coordinates, it is assumed that the spread of tracks in z is uniform throughout the chamber after time expansion. The time expansion factors used for the TASSO vertex detector are from 80 to 150, corresponding to the radii of the cell layers in that detector. The resolution used for z was 100 ns in expanded time, which corresponds to an error in z of $\sigma_z \sim 7$ cm, but this varies from layer to layer because of the different time expansion factors. The addition of a random z coordinate to each hit was only done with the 38 GeV data, since the results will probably be very similar for the 44 GeV data.

6.3 The Effectiveness of the Space Point Trigger

Figure 5.17 shows the percentage of events from the 38 GeV random trigger data which pass trigger requirements of various numbers of hits in at least one mask, both as the data came from TASSO and also with a random z coordinate associated with each hit.

It can be seen that when tracks are looked for using all three coordinates, then the false trigger rate is much lower than from the r-ø trigger alone.

Now consider the difference between trigger rates from the uncorrelated Monte Carlo data and the three coordinate data, where only the z coordinate is totally uncorrelated. This is shown for the 38 GeV data in figure 5.18.
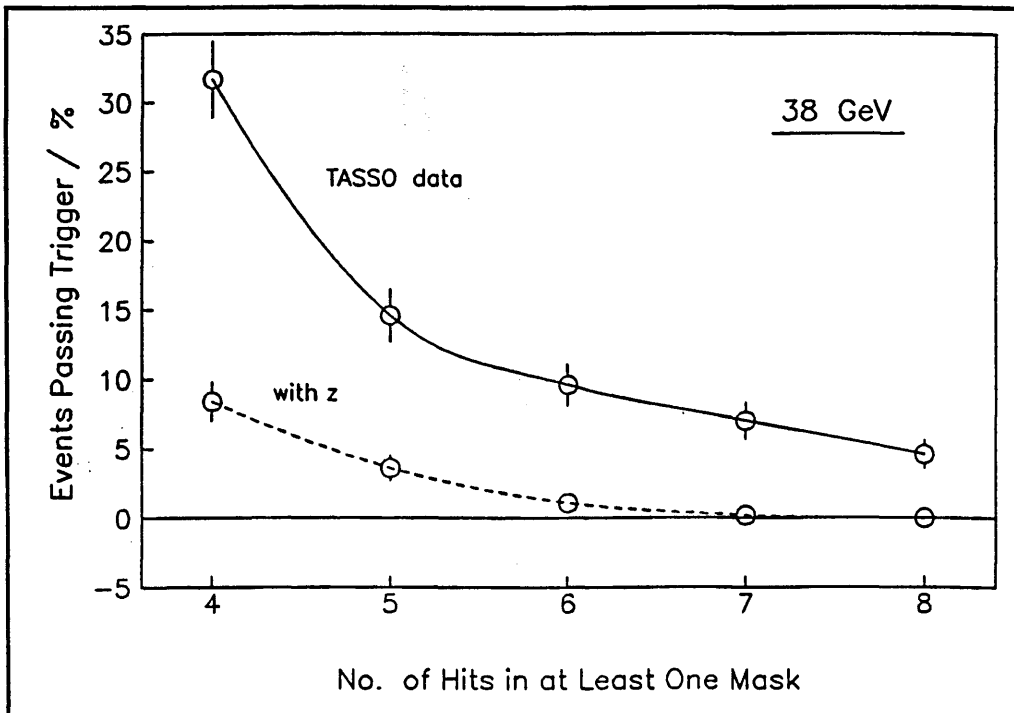
Fig 5.17   Frequency of r-ø-z Points Passing the Trigger at 38 GeV
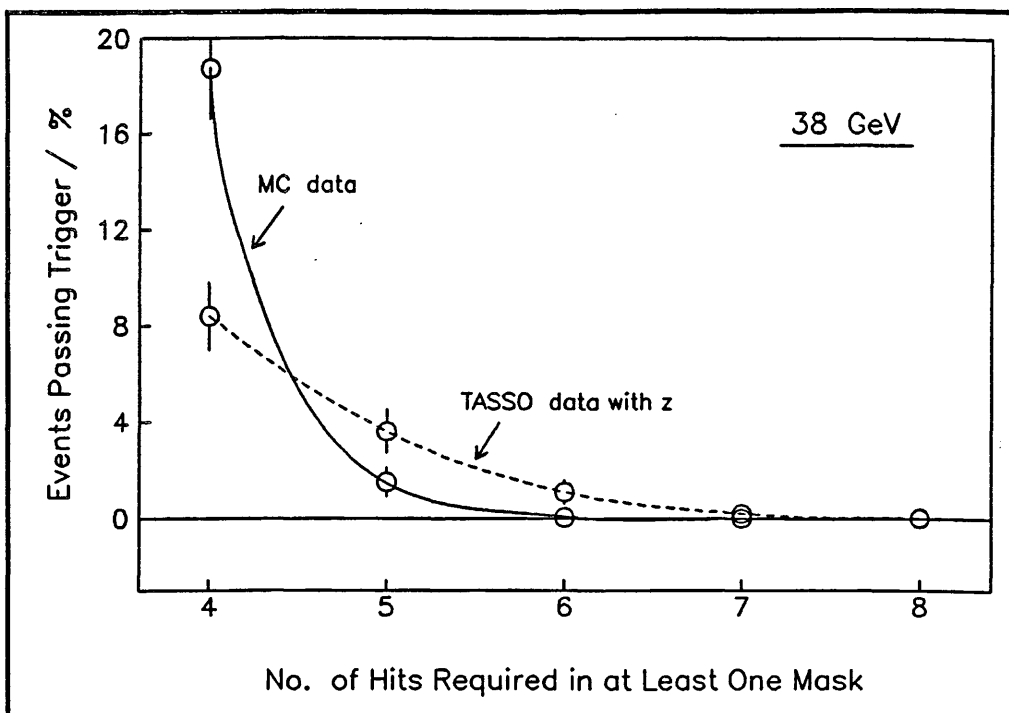
Fig 5.18   Comparison of Trigger Rates Between r-ø-z Points
and Uncorrelated Monte Carlo r-ø Points

When all three coordinates are used, but the r-ø points are correlated, then the trigger rate is less than half that obtained from the r-ø trigger using totally uncorrelated data, when only 4 hits are required in a mask. However, this improvement gained from using the z coordinate is not so

good for higher numbers of hits in a mask. Uncorrelated r–ø data produces no triggers when all 8 hits are required in a mask, and even when just 6 hits are required then only 0.05 % of the events pass the trigger. When three coordinates are used, but the r–ø coordinates are correlated, then 0.03 % of the events pass the trigger when all 8 layers are required to have been hit in at least one mask. If only 6 layers need have been hit in any one mask, then the space point trigger processor would pass 1.1 % of the events. This is at the level which the Level 1 trigger needs to be to reduce the beam crossing rate down to a manageable rate for the outer detectors to be operated.

7   Conclusions

There are several conclusions which can be drawn from this study. There are also several provisos which will be pointed out afterwards about how relevant the situation in the TASSO vertex detector was to the conditions which the ITC trigger processors will have to work with in ALEPH.

Firstly, the hits seen in the TASSO vertex chamber from random beam crossings are correlated. It is quite possible that any noise in the ITC in ALEPH will also be correlated in some way, depending upon the source of the noise.

Simulation of the ITC r–ø trigger using the random trigger data from TASSO suggest that in ~ 5 % of all crossings at least one mask will have ≥ 7 hits in it. Also, almost every beam crossing in both of the different energy runs investigated has at least one hit in all of the 4 inner cell layers, and quite often has hits in the outer layers too. Therefore, if this is the same for the ITC then the ITC r–ø trigger may be ineffective for the veto of a single photon trigger, such as is produced by :

$$e^+ e^- \rightarrow \nu \bar{\nu} \gamma$$

Now consider the not insignificant differences between the conditions in the two detectors.

a)   The TASSO vertex detector was much closer to the beam than the ITC will be in ALEPH. The radius of the inner layer of sense wires was 8.1 cm in the vertex detector, whereas it will be 16.11 cm in the ITC. This should reduce the amount of noise from off-momentum beam particles

and synchrotron radiation in the ITC from the level it would have been if its inner layer had been that much closer to the beam pipe.

b)   The beam pipe in TASSO was made of beryllium, which is much more transparent to soft photons than the aluminium one to be used in ALEPH. Therefore, the ITC should be better shielded from noise caused by pair production from these photons.

These two differences between the experiments should improve the conditions in the ITC relative to those in the TASSO vertex detector. However, the following differences will act against them and degrade the ITC conditions.

a)   The ITC is nearly four times as long as the TASSO vertex detector. It has an active length of 200 cm compared with the active length of the TASSO vertex detector of only 57.2 cm. This means that it has a much higher probability of having particles pass through it which have not originated from an interaction at the centre of the detector. This will increase the false trigger rate.

b)   The most important difference between the running conditions of the two detectors is that each was used or will be used with different accelerators. PETRA, with centre of mass energy $\sqrt{s}$ = 36 GeV or 44 GeV, was running at a much higher level than designed for. Therefore, the noise level was much higher than when running at the lower design energies. LEP will be operated, initially, at $\sqrt{s}$ = 96 GeV, which is only half its design energy. Therefore, it is hoped that there will not be lots of noise from LEP's beams.

Until LEP is running and the beam conditions are seen, it is not really possible to make an estimate of how these various factors will affect the amount of noise found in the ITC and how many false triggers will be seen. What can be concluded from this study however is that the space point processor for the ITC should give a very useful improvement in cutting down the rate of false triggers which would otherwise result if only the r-ø trigger were in operation.

REFERENCES

Chapter 1   Introduction

1.1   Design Study of a 22 to 130 GeV e^+e^- Colliding Beam Machine (LEP), CERN/ISR–LEP/79–33.

1.2   S.L. Glashow, Nucl. Phys. 22 (1961) 579;
A. Salam, J.C.Ward, Phys. Lett. 13 (1964) 168;
S. Weinberg, Phys. Rev. Lett. 19 (1967) 1264.

1.3   P.W.Higgs, Phys. Lett. 12 (1964) 132;
Phys. Rev. Lett. 13 (1964) 508;
Phys. Rev. 145 (1966) 1156;
F.Englert, R.Brout, Phys. Rev. Lett. 13 (1964) 321;
G.S. Guralnik, C.R. Hagen, T.W.B. Kibble, Phys. Rev. Lett. 155 (1967) 1554

1.4   ALEPH handbook (forthcoming, Sept 1988)

Chapter 2   The Inner Tracking / Trigger Chamber – Design and Construction

2.1   Proceedings of the Workshop on Radiation Damage to Wire Chambers, Jan 16-17, 1986, LBL-21170.

eg.   Analysis of TPC Inner Drift Chamber Wire Coatings, M.C. Williams;
Ageing Effects in Gaseous Detectors and the Search for Remedies, A. Dwurazny, Z. Hajduk and M. Turala;
Summary of Aging Studies in Wire Chambers by AFS, DELPHI, and EMC Groups, H.J. Hilke.

2.2   Calculation of end plate deflections by A.P.White and M.Cattaneo (IC).

2.3   Calculation of sense wire hole positions in the end plates by M. Cattaneo (IC).

2.4   Proceedings of the Workshop on Radiation Damage to Wire Chambers, Fourth Discussion Period, D.M. Binnie.

2.5   The crimp pins and feedthroughs are described in :
Design and Construction of the CLEO II Drift Chamber, D.G. Cassel et al., CLNS 86/717, Feb. 1986.

2.6 See the introduction to :
Drift and Diffusion of Electrons in Gases : a Compilation,
A. Peisert and F. Sauli, CERN 84-08.

2.7 P. Ramanantsizehena, Thesis, Université de Strasbourg,
CRN-HE 79-13 (1979).

2.8 C.M. Ma et al., MIT Technical Reports 129 and 130 (1982)

(The relevent parts of references 2.7 and 2.8 are both included in 2.6)

2.9 Proceedings of the Workshop on Radiation Damage to Wire
Chambers, LBL-21170;

eg. Plasma Chemistry in Wire Coating, D.W. Hess.

2.10 Alignment of the ITC, R. Forty, ALEPH - Note 87-015.

2.11 Radiation Length Presented to Tracks by the ITC and its Supports,
P.J. Dornan, ALEPH 86-63.

2.12 Principles of Operation of Multiwire Proportional and Drift
Chambers, F. Sauli, CERN 77-09.

Appendix B   Electron Drift Paths in the ITC Hexagonal Cells

3.B.1 This program is based on one by Va'Vre (SLAC), and modified by
G. Hall, A.P. White and W. Cameron (IC).

3.B.2 This program was written by W. Cameron (IC) and modified by
myself.

Chapter 4   z Position Measurement

4.1 The method of time differences was first presented in :
Second Coordinate Readout in Drift Chambers by Timing of the
Electromagnetic Wave Propagating Along the Anode Wire,
IEEE Trans. Nucl. Sci., Vol. NS-28, No.1, Feb. 1981,
R.A. Boie, V. Radeka, P. Rehak and D.M. Xi.

4.2 Details of the z measurement system used in the Zeus Central
Tracking Chamber may by found in :
The Zeus Detector Status Report 1987,
section 7.5.4, z Readout of the CTD, PRC 87–02.

4.3 OPAL Status Report (1984) CERN LEPC/84–17, LEPC/M–51.

4.4 Lightning induced signals on telegraph cables are described in :
Electrical Transmission of Power and Signals, (Wiley, 1949),
E.W. Kimbark.

4.5 Figure 4.57 for the dual threshold discriminator and figure 4.74
for the constant fraction discriminator are based on drawings by
D. White (RAL).

Chapter 5   Simulation of the ITC Trigger –
Using Data from the TASSO Vertex Detector

5.1   The TASSO Vertex Detector, D.M. Binnie et al.,
       NIM 228 (1985) 267-277.

5.2   The ITC r-ø Processor, J.K. Sedgbeer, ALEPH-Trigger 85-4.

ACKNOWLEDGEMENTS

There are many people I would like to thank for their contributions towards the work of this thesis. I have learnt a lot from them and enjoyed working with them.

For their work on the small test chamber, I would like to thank the following people : Ray Beuselinck, Chris Bishop, Bill Cameron, Ron Campbell, Dave Clark, Peter Dornan, Dave Garbutt, John Hassard, Mike MacDermott, Andy Rochester, S. Sriranganathan, Alan Watson and Andy White.

With the z measurement work, thanks are due to : Andy Belk, David Binnie, Chris Bishop, Bertrand Blau, Bill Cameron, Dave Garbutt, Dave Price and Les Toudup.

I would like to thank my supervisor Peter Dornan for his help with the work on the trigger, and for general advice throughout my studentship.

Financial support from the SERC for three years is acknowledged, and also three months funding from the High Energy Physics group under David Binnie. I have enjoyed my time in the group and am privileged to have been able to study here.

Most of all, I would like to thank my parents and John Ellison, for their love and support, without which none of this would have been possible.